MAGNETIC RESONANCE IMAGING IN FOOD SCIENCE

BRIAN HILLS
Institute of Food Research
Norwich Research Park
Colney, Norwich
United Kingdom

A Wiley-Interscience Publication
JOHN WILEY & SONS, INC.
New York · Chichester · Weinheim · Brisbane · Singapore · Toronto

This book is printed on acid-free paper. ♾

Published simultaneously in Canada.

Library of Congress Cataloging-in-Publication Data:
Hills, Brian, 1949–
Magnetic resonance imaging in food science / Brian Hills.
p. cm.
"A Wiley-Interscience publication."
Includes bibliographical references and index.
ISBN 0-471-17087-9 (cloth : alk. paper)
1. Food—Analysis. 2. Magnetic resonance imaging. I. Title.
TP372.5.H55 1998
664'.07—dc21 97-37413

Printed in the United States of America.

10 9 8 7 6 5 4 3 2 1

PREFACE

I have written this book in the belief that magnetic resonance imaging (MRI) has the potential of revolutionizing food manufacturing science. The word *potential* has to be emphasized, because most applications of MRI to foods at the time of writing are little more than feasibility exercises. This, to my mind, is not a disadvantage but rather an exciting opportunity for future research, so that throughout the book I have tried to direct the reader to these opportunities. Of course, the magnitude of the scientific and technical challenges to be overcome in fully realizing the potential of MRI in food science should not be underestimated. Food displays an enormous range of structural and compositional complexity. The spatial heterogeneity in many foods can extend over distance scales ranging from the molecular to the macroscopic and contains hints of fractal geometry, self-similarity, and spatial chaos. Moreover, there is an intimate relationship between this structural complexity and the dynamic changes associated with food processing and storage. From the perspective of an NMR spectroscopist, having at his or her disposal an almost endless variety of pulse sequences for measuring spin density, relaxation, diffusion, flow, and high-resolution solid or liquid spectra, this structural and dynamic complexity presents a lifetime of research possibilities. Fortunately, finding the motive to continue this research effort is not difficult. Besides the purely scientific motivation, there are many compelling pragmatic reasons for seeking to maximize the potential of MRI in food science. Providing safe and nutritious food for the ever-increasing human population is a daunting global challenge and one that has immediate importance to hungry sections of the world population. The technical challenges in achieving this objective remain considerable, and include the optimization of all stages of food production. This involves the procurement of the best crop strains by selection and genetic manipulation, optimization of the crop yield, and optimization of postharvest processing for improved food quality, safety,

and energy efficiency. It also entails the discovery of the best choice of storage and transportation conditions so as to be able to market safe, high-quality food as cheaply and efficiently as possible.

In writing this book I have had to speculate somewhat about future research possibilities and have not shied away from presenting topics that are still under development. This entails the risk that the shortsightedness of my speculations will be revealed by future developments. Nevertheless, if my speculations serve to inspire other research workers, this is a risk I gladly embrace. To keep the book reasonably concise, I have had to assume that the reader is familiar with the basic ideas of NMR and MRI and have simply summarized some of the major concepts in the introductory chapter. This, I trust, is not unreasonable since there are already many excellent textbooks on NMR and MRI, including the wonderful treatise entitled *The Principles of Nuclear Magnetism* by Abragam, who by delving into the depths of spin physics, appears to have encompassed most of the well-charted and it often seems, even uncharted oceans of NMR. The principles of MRI have been explained lucidly in an excellent book by Callaghan entitled, *The Principles of NMR Microscopy*, and during the preparation of this book, all eight volumes of the encyclopedia of NMR and MRI have appeared in print. I therefore refer the reader to these excellent works for details of pulse sequences and NMR concepts. However, the emphasis of these texts is on the principles of NMR and MRI rather than their application to food science, so I do not hesitate to offer this new book to the reader. Throughout I have attempted to incorporate more recent MRI developments, such as STRAFI, gradient-echo imaging, and functional imaging, and point out their relevance in food science. Key references to the original literature have been included, but these citations make no claim to completeness and I apologize beforehand to any researcher who feels aggrieved because his or her work is not mentioned. They need only send me a reprint, and if there is ever a future edition, I will endeavor to amend my oversight.

Because "food" is such a diverse and complex collection of biological materials, some rational organization of this book is essential if the reader (and author) are not to get hopelessly confused. The book is therefore divided into three parts according to the distance scale being probed by the MRI studies. Part One deals with the macroscopic distance scale, Part Two with the microscopic, and Part Three with the (macro-)molecular, although the boundaries between these scales is necessarily somewhat blurred. At each distance scale I have attempted to classify each MRI study according to the dynamic changes being investigated. This reflects my belief that using MRI simply to look at a static, unchanging food structure is to underuse the technology and risks competition with other techniques that can provide far better spatial resolution, such as optical and electron microscopy, or in the case of the macroscopic distance scale, with a knife and the human eye! Having organized the material by exploiting the space and time dimensions, I have, wherever appropriate, included mathematical models of the dynamic process being imaged, because, ultimately, most of the processes being imaged find their explanation in the (bio-)physics of heat, mass, and momentum transport.

This book should be of value to all food scientists and technologists who seek a better understanding of the present and future role of MRI in their discipline, and conversely, to NMR and MRI specialists who wish to explore the potential of this wonderful technique in the arena of foods. Chapters 7, Whole Plant Functional Imaging, and 9, Macroimaging and NMR Microscopy, will also be of interest to plant physiologists and Chapter 4, Flow Imaging and Food Rheology, to fluid hydrodynamicists.

BRIAN HILLS

Norwich, United Kingdom

Contents

PART ONE

MACROSCOPIC DISTANCE SCALE

1

RÉSUMÉ OF MRI METHODOLOGY

1.1 INTRODUCTION

It is common practice with books on nuclear magnetic resonance (NMR) to begin at the level of a nuclear spin and describe the quantum-mechanical origin of the signal and of nuclear spin interactions. This quantum-mechanical approach is mandatory if one is to understand high-resolution liquid- or solid-state NMR spectroscopy where the sample is spatially homogeneous and the main purpose is to elucidate details of molecular structure and dynamics. However, in imaging, it is the *spatial* distribution of the signal throughout the sample that is of principal concern, and this requires an understanding of phase coherence and Fourier relationships. Some familiarity with the quantum aspects of NMR will therefore be assumed and the scene will be set for subsequent chapters by beginning with a brief résumé of MRI from the perspective of phase coherence and Fourier conjugate relationships.

1.2 PHASE COHERENCE AND FOURIER CONJUGATE VARIABLES IN NMR

The power of NMR and MRI techniques arises, primarily, because they exploit phase coherence. Radio-frequency pulses and magnetic field gradients are used to phase encode the transverse spin magnetization so that it evolves coherently in space and time with a phase factor $\exp(i\phi)$, where ϕ is the spin phase. This is possible because the radio-frequency field is itself highly coherent (i.e., has a well-defined phase and frequency). The possibility of generating highly coherent radio-frequency radiation is determined by the Heisenberg uncertainty relationship relating the phase uncertainty $\Delta\phi$ and the uncertainty in the number of photons

per unit frequency per mode of oscillation, Δn, such that $\Delta\phi\ \Delta n \geq h/2\pi$ (19). Because of their very low frequency and therefore low energy, $h\omega/2\pi$, there are astronomically large numbers of photons even in a low-intensity radio-frequency wave, so Δn can be large in absolute magnitude, permitting $\Delta\phi$ to be extremely small. This high phase coherence together with the ease of electronically generating and controlling radio-frequency pulses sets NMR (and MRI) apart from all other forms of spectroscopy.

The nuclear spin phase ϕ is itself the dimensionless product of two conjugate Fourier variables, one of which is characteristic of the spin, such as its resonance frequency, while the other characterizes some external operation on the spin, such as the phase evolution time. For example, when the equilibrium proton magnetization in pure water is rotated from its initial alignment in a perfectly homogeneous external magnetic field B_0 through 90° by a spatially homogeneous radio-frequency pulse, the water proton spins precess coherently (i.e., in phase) throughout the sample with a phase factor $\exp(i\omega_0 t)$, where ω_0 is the spin resonance frequency γB_0 and γ is the proton gyromagnetic ratio. This situation does not last forever because molecular motions and spin interactions ensure that each spin experiences a fluctuating local magnetic field, and this gradually causes the spins to get out of phase with each other (i.e., to dephase) and the phase coherence decays exponentially in time as $\exp(-t/T_2)$, where T_2 is the characteristic dephasing time (the transverse relaxation time), which for pure water is about 2.5 s. If the applied magnetic field is not perfectly homogeneous, spins in different subregions of the sample (called *spin isochromats*) will precess with slightly different frequencies, resulting in a much faster dephasing, characterized by $\exp(-t/T_2^*)$, where T_2^* is a shorter effective dephasing time.

In this example the NMR signal observed, $S(t)$, called the *free induction decay* (FID), is $\exp(i\omega_0 - T_2^{*-1})t$. More formally, the signal is the ensemble average of the phase of the transverse magnetization arising from all the spins in the sample, which can be written

$$S(t) = \langle \exp(i\phi) \rangle = \int d\omega\, P(\omega) \exp(i\omega t) \tag{1.1}$$

Here $\langle \cdot \rangle$ denotes an ensemble phase average and $P(\omega)$ is their frequency probability distribution, in other words, the *spectrum*. The exponential phase factor in equation (1.1) makes the signal, or FID, $S(t)$, a complex function, and it is usual to observe both its real (in-phase) and imaginary (out-of-phase) components by quadrature detection. The phase factor in equation (1.1) also means that the time-domain signal $S(t)$ is a Fourier transform, so the complex spectrum can be obtained by Fourier inversion of the FID:

$$P(\omega) = \frac{1}{2\pi} \int dt\, S(t) \exp(-i\omega t) \tag{1.2}$$

If all the spins precess perfectly coherently at the resonance frequency, the signal $S(t)$ is $\exp(i\omega_0 t)$ and Re $P(\omega)$, usually called the spectrum, is simply a delta

function, $\delta(\omega - \omega_0)$. In practice, dephasing broadens this delta function into a Lorentzian probability distribution

$$\text{Re } P(\omega) = \frac{T_2^{*-1}}{(\omega - \omega_0)^2 + T_2^{*-2}} \tag{1.3}$$

corresponding to the FID, $\exp(i\omega_0 - T_2^{*-1})t$. The relationship between the time and frequency domains is illustrated in Figure 1.1. The effective transverse relaxation time T_2^* can be obtained either from the width at half-height of Re $P(\omega)$, which for the Lorentzian in equation (1.3) is πT_2^{-1}, or in the time domain, from the slope of *ln* $S(t)$ versus t, provided that the FID is acquired *on-resonance*, so that the oscillating component of $S(t)$ is removed and it becomes the simple exponential function $S(0) \exp(-t/T_2^{-1})$. It often happens in complex food systems that the on-resonance FID, $S(t)$, has more than one decaying component and can be represented as a multiple exponential. Figure 1.2 shows an example in which there are fast- and slow-decaying components in the on-resonance FID. As we shall see, there are various mathematical procedures for extracting the component exponentials from $S(t)$, including a procedure that yields a continuous distribution of relaxation times, and examples are presented in Part Two of the book. The molecular origins of the intrinsic transverse dephasing, characterized by T_2, is discussed more fully in Part Three.

Other types of NMR experiments arise because the phase, ϕ, can be made to depend on different pairs of Fourier conjugate variables by the introduction of various sequences of radio-frequency and magnetic field gradient pulses in *pulse sequences*. Consider, for example, the effect of introducing a time-dependent spatially linear magnetic field gradient $\mathbf{G}(t)$ across the water sample after a 90° excitation radio-frequency pulse. Now the spin resonance frequency varies across the sample as $\omega(\mathbf{r},t) = \omega_0 + \gamma\mathbf{G}(t) \cdot \mathbf{r}(t)$. The phase shift experienced by a spin as it moves in this field gradient is therefore

$$\phi(t) = \int_0^t dt' \gamma\mathbf{G}(t') \cdot \mathbf{r}(t') \tag{1.4}$$

Provided that the water is undergoing coherent translational motion (as apart from random diffusion, perfusion, or chaotic turbulent motion, for example), the position of the spin $\mathbf{r}(t)$ in equation (1.4) is simply

$$\mathbf{r}(t) = \mathbf{r}(0) + \mathbf{v}t + \frac{\mathbf{a}t^2}{2} \tag{1.5}$$

where $\mathbf{v}$ is the mean fluid velocity and $\mathbf{a}$ is its acceleration. Substitution of equation (1.5) into (1.4) identifies the Fourier conjugate pairs for spatial imaging, flow imaging, and acceleration (or jerk) imaging, respectively. Spatial imaging arises from the first term and is based on the conjugate Fourier variables $\mathbf{k}$ and $\mathbf{r}(0)$, where $\mathbf{k}$ is seen to be proportional to the zeroth moment of the gradient pulse

$$\mathbf{k} = \gamma \int_0^t dt' \mathbf{G}(t') \tag{1.6}$$

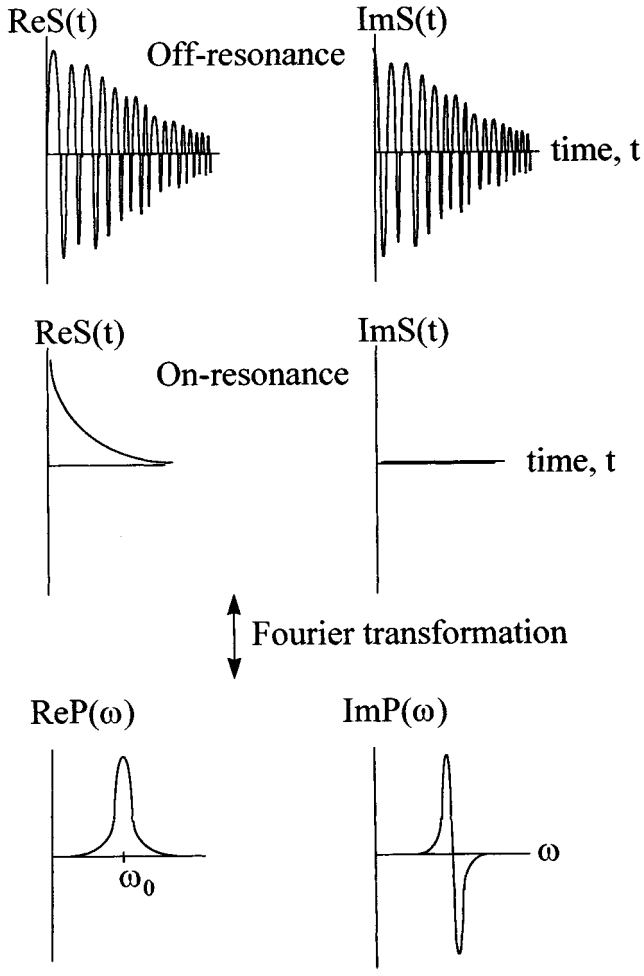

Figure 1.1. Schematic of the real and imaginary parts of an off-resonance FID (top); the same FID acquired on-resonance (middle); and the real and imaginary parts of the spectrum obtained by Fourier transforming either the on- or off-resonance FID (bottom).

For a rectangular gradient pulse of constant amplitude and direction applied for a duration t, the wavevector $\mathbf{k}$ is simply $\gamma \mathbf{G} t$. Flow imaging arises from the second term in equation (1.5) and is based on the conjugate pair $\mathbf{p}$ and $\mathbf{v}$, where $\mathbf{p}$ is the first moment of the gradient pulse, $\mathbf{G}$, such that

$$\mathbf{p} = \gamma \int_0^t dt'\, t' \mathbf{G}(t') \tag{1.7}$$

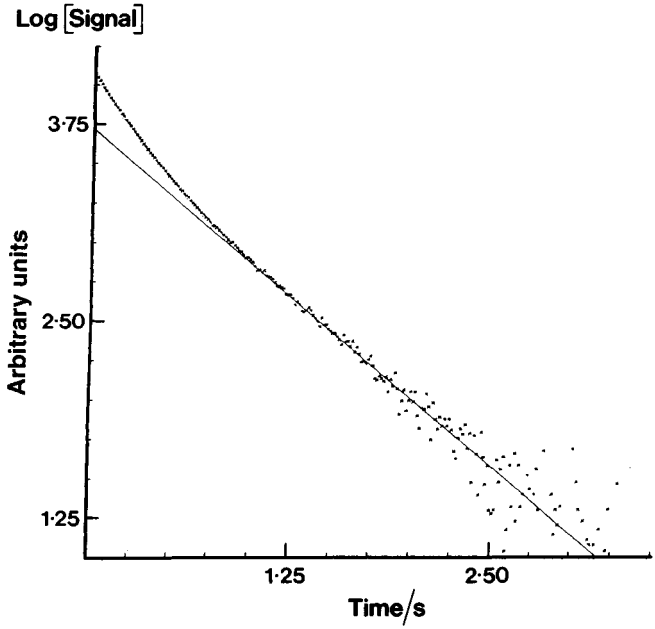

Figure 1.2. Typical plot of ln[Re $S(t)$] versus time for an on-resonance FID. The effective transverse relaxation time T_2^* is obtained from the straight-line slope. Note the presence of the faster-relaxing component at short times and the increased noise at long times.

To make the pulse sequence sensitive only to the flow velocity and not to the initial spatial distribution of the spins, the zeroth moment of the gradient [equation (1.6)] must be zero and the first moment [equation (1.7)] nonzero. This can be achieved by using, for example, a bipolar gradient pulse, as shown in Figure 1.2.

The third team gives rise to *acceleration,* or *jerk imaging,* which is seen to be based on the conjugate pair **a** and **b,** where **b** is the second moment of the applied gradient pulse, such that

$$b = \frac{\gamma}{2}\int_0^t dt'\, t'^2 \mathbf{G}(t') \tag{1.8}$$

For acceleration-sensitive imaging the gradient pulses must therefore have no zeroth or first moment and a nonzero second moment. A possible gradient waveform satisfying these conditions is illustrated in Figure 1.3. Analogously to equation (1.1), ensemble averaging gives Fourier relationships between these various

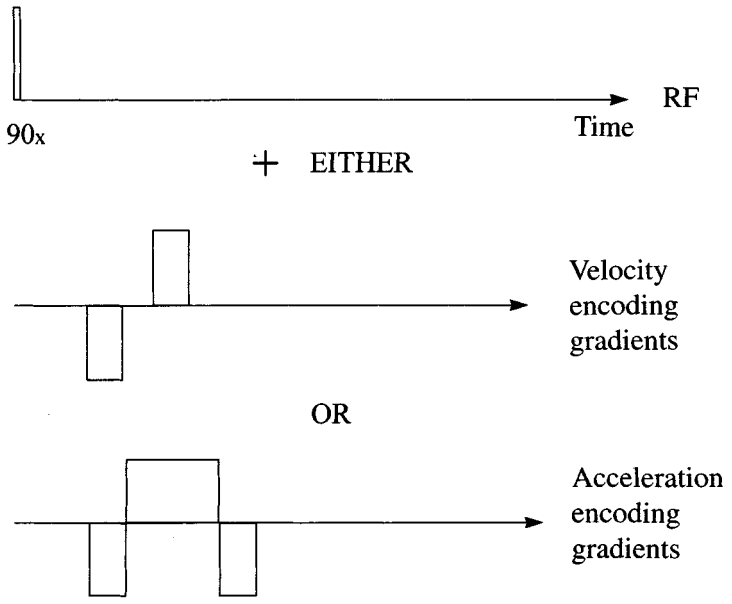

Figure 1.3. Simple gradient pulse sequences for velocity- and acceleration-sensitive phase encoding.

conjugate pairs, and these define the various types of imaging discussed in later sections. Simple *spatial imaging* is defined by the Fourier relationships

$$S(\mathbf{k}) = \int d\mathbf{r}\, P(\mathbf{r}) \exp(-i\mathbf{k} \cdot \mathbf{r}) \tag{1.9}$$

and

$$P(\mathbf{r}) = \frac{1}{2\pi} \int d\mathbf{k}\, S(\mathbf{k}) \exp(i\mathbf{k} \cdot \mathbf{r}) \tag{1.10}$$

In this case the probability distribution $P(\mathbf{r})$ is the spatial distribution of the transverse spin magnetization density, conventionally called the *image*. Because the Cartesian components of the wavevector $\mathbf{k}$ for rectangular gradient waveforms are the products $(\gamma G_x t_x, \gamma G_y t_y, \gamma G_z t_z)$, it can be varied in any direction, i ($=x$, y, or z) either by fixing the phase evolution time t_i and ramping through a raster of gradients (e.g., from $-G_i$ to $+G_i$), or alternatively, by fixing the gradient G_i and varying the phase evolution time t_i. Both possibilities have been used in Fourier imaging, but the former method based on a fixed evolution time has the advantage that image intensity attenuation by relaxation remains uniform over the imaging raster. The various types of k-space imaging based on these relationships are discussed in

greater detail later. Of course, it is not necessary to confine imaging sequences to rectangular gradient waveforms and we shall see in Section 5.5 that sinusoidally varying gradients have an important role to play in imaging solids.

Velocity phase-encoding imaging (or *flow imaging*) is seen, by the derivation in equations (1.4) to (1.5), to be defined by the Fourier relationship

$$S(\mathbf{p}) = \int d\mathbf{v}\, P(\mathbf{v}) \exp(-i\mathbf{p} \cdot \mathbf{v}) \tag{1.11}$$

so that Fourier inversion gives the velocity distribution function $P(\mathbf{v})$:

$$P(\mathbf{v}) = \int d\mathbf{p}\, S(\mathbf{p}) \exp(i\mathbf{p} \cdot \mathbf{v}) \tag{1.12}$$

Velocity imaging is discussed in greater detail in Chapter 4. In a similar way, acceleration imaging is characterized by the Fourier relationship

$$S(\mathbf{b}) = \int d\mathbf{a}\, P(\mathbf{a}) \exp(-i\mathbf{b} \cdot \mathbf{a}) \tag{1.13}$$

so that the acceleration image is

$$P(\mathbf{a}) = \int d\mathbf{b}\, S(\mathbf{b}) \exp(i\mathbf{b} \cdot \mathbf{a}) \tag{1.14}$$

There are many other ways of manipulating the phase evolution of spin magnetization and introducing Fourier conjugates. Displacement spectroscopy (also known as q-space microscopy) arises when the applied gradient $\mathbf{G}(t)$ consists of two short rectangular pulses of duration δ separated by a phase evolution time Δ, as illustrated in Figure 1.4. These gradient pulses are situated either side of a phase-reversing 180° pulse, so that if the spins do not move in the time Δ, their phase is completely refocused as an unattenuated echo (neglecting relaxation). If, however, they move through a displacement $\mathbf{R}$ in the time Δ, they suffer a phase change,

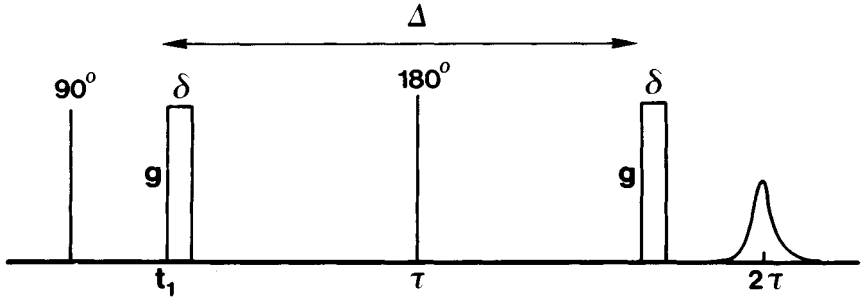

Figure 1.4. Basic Stejskal–Tanner pulsed gradient spin-echo (PGSE) pulse sequence used for displacement spectroscopy (or q-space microscopy). The echo time TE is 2τ and the displacement time is Δ.

$\mathbf{q} \cdot \mathbf{R}$, where the wavevector $\mathbf{q}$ is $(2\pi)^{-1}\gamma\mathbf{G}\delta$ and the echo intensity $S(\mathbf{q},\Delta)$ is attenuated. It can be shown (5) that $\mathbf{q}$ and $\mathbf{R}$ are Fourier conjugates such that

$$S(\mathbf{q},\Delta) = \int d\mathbf{R}\, P(\mathbf{R},\Delta) \exp(i\mathbf{q} \cdot \mathbf{R}) \tag{1.15}$$

so that the probability distribution for the displacement of spins through a distance $\mathbf{R}$ in time Δ is obtained by Fourier inversion,

$$P(\mathbf{R},\Delta) = \int d\mathbf{q}\, S(\mathbf{q},\Delta) \exp(-i\mathbf{q} \cdot \mathbf{R}) \tag{1.16}$$

Because the wavevector $\mathbf{q}$ is the product $(2\pi)^{-1}\gamma\mathbf{G}\delta$, it is possible to vary it by fixing $\mathbf{G}$ and varying δ, or by varying δ at fixed $\mathbf{G}$. As with spatial imaging, it is usually best to keep δ fixed (and as short as possible) to avoid variable and other artifacts. As we shall see, the displacement probability distribution can be used to probe flow and distribution in microheterogeneous systems.

1.3 HIGHER-ORDER COMBINATIONS OF FOURIER CONJUGATES

The Fourier relationships mentioned so far define some of the main types of NMR and MRI experiments. However, there are many other ways of manipulating the spin phase, and these give rise to a wide diversity of NMR and MRI protocols, limited only, it seems, by our ingenuity. It is this flexibility that is one of the main attractions of NMR. For example, the Fourier relationships above involve only single pairs of conjugate variables but there is no reason to be restricted to single pairs. Two-dimensional high-resolution NMR spectroscopy (2) uses a series of radio-frequency pulses to define two independent phase-encoding time delays t_1 and t_2 (with conjugates, ω_1 and ω_2) separated by a fixed mixing time t_m. Figure 1.5 shows a general schematic of the two-dimensional strategy, where the t_1 time domain is obtained by repeating the entire acquisition process for increasing values of t_1 and t_2 is the time during which the signal is acquired. A complex two-dimensional Fourier transform now relates the signal $S(t_1,t_2)$ to the two-dimensional spectrum $P(\omega_1,\omega_2)$ analogously to equation (1.1).

$$P(\omega_1,\omega_2) = \iint dt_1\, dt_2\, S(t_1,t_2) \exp(-i\omega_1 t_1 - i\omega_2 t_2) \tag{1.17}$$

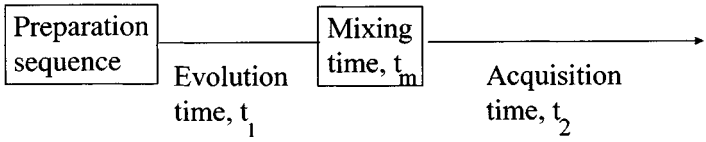

Figure 1.5. Protocol for two-dimensional spectroscopy, showing the preparation, evolution, mixing, and acquisition steps.

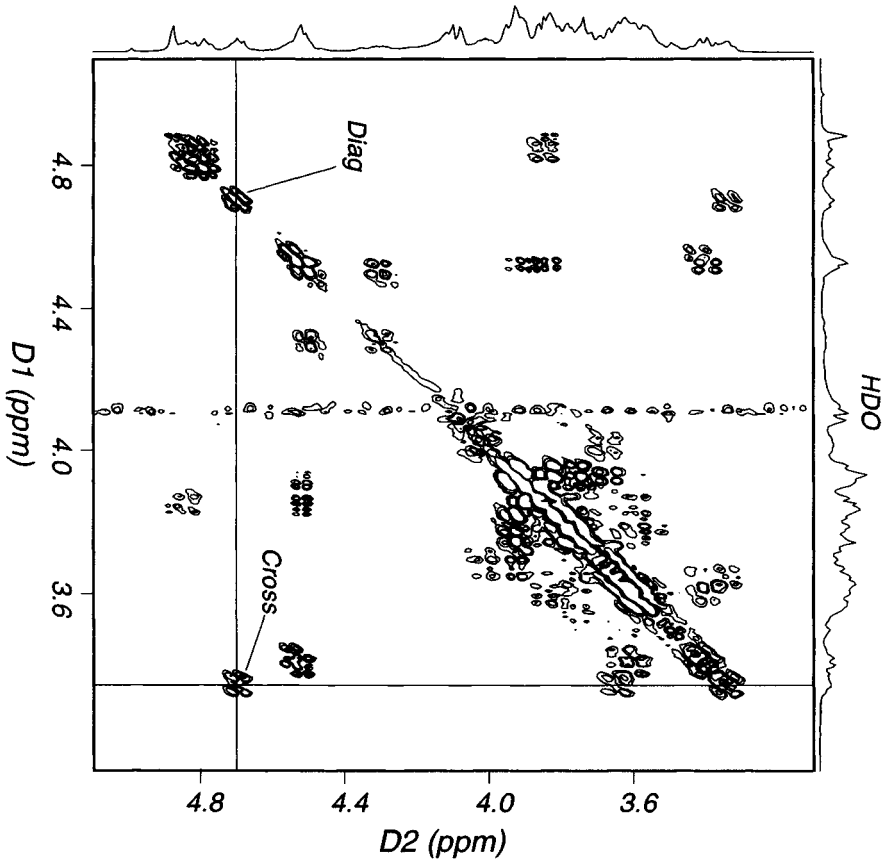

Figure 1.6. Example of a two-dimensional high-resolution spectrum. (Courtesy of Dr. I. J. Colquhuon.)

This entire class of spectroscopy can therefore be denoted $[(\omega_1,t_1);(\omega_2,t_2)]$-spectroscopy. An example of a two-dimensional spectrum is shown in Figure 1.6. New information arises in a two-dimensional spectrum whenever there is exchange or interaction of magnetization between different spins during the mixing time t_m, and the many different types of $[(\omega_1,t_1);(\omega_2,t_2)]$-pulse sequences are designed to produce different types of exchange interaction during the mixing period, which is especially useful in elucidating details of molecular structure and dynamics. For a detailed discussion of $[(\omega_1,t_1);(\omega_2,t_2)]$-spectroscopy, the reader is referred to the excellent book by Ernst et al. (2).

Diffusion-ordered spectroscopy (DOSY) is based on the combination $[(\mathbf{q},\mathbf{R}),(\omega,t)]$, which cross-correlates a high-resolution spectrum with simultaneous measurements of molecular diffusion. This combination is useful for analyzing complex mixtures in solution since it permits spectral peaks to be assigned to

particular molecular species. Other second-order combinations that play an important role in subsequent chapters include *chemical shift imaging,* which is based on the conjugate pairs [(**k**,**r**),(ω,*t*)] and is discussed in greater detail below, and the combination [(**q**,**R**);(**k**,**r**)], sometimes called *displacement imaging* or *dynamic NMR microscopy* (5). The latter is described by the two-dimensional Fourier relationship

$$S(\mathbf{k},\mathbf{q},\Delta) = \int d\mathbf{r} \int d\mathbf{R}\, P(\mathbf{r},\mathbf{R},\Delta) \exp\left(i\mathbf{q} \cdot \mathbf{R} + i\mathbf{k} \cdot \mathbf{r}\right) \tag{1.18}$$

where

$$P(\mathbf{r},\mathbf{R},\Delta) = \int d\mathbf{q}\, P(\mathbf{r},\mathbf{q},\Delta) \exp(-i\mathbf{q} \cdot \mathbf{R}) \tag{1.19}$$

Comparison with equation (1.16) shows that each voxel in the **r**-space image is now weighted by the displacement probability function $P(\mathbf{r},\mathbf{R},\Delta)$. In a fluid flowing with velocity $\mathbf{v}(\mathbf{r},t)$, the flow displacement will be $\mathbf{v}(\mathbf{r},t)\Delta$, and since there is always random displacement caused by diffusion, $P(\mathbf{r},\mathbf{R},\Delta)$ also has a spreading Gaussian component if there is unrestricted diffusion. For combined flow and unrestricted diffusion, the displacement probability function therefore has the Gaussian form

$$P(\mathbf{r},\mathbf{R},\Delta) = (4\pi D\Delta)^{-3/2} \exp\left\{\frac{-[\mathbf{R} - \mathbf{v}(\mathbf{r})\Delta]^2}{4D\Delta}\right\} \tag{1.20}$$

This shows that it is possible to extract both the velocity map and a diffusion map from a careful analysis of the dynamic displacement imaging experiment. Velocity imaging can therefore be performed using either bipolar phase-encoding gradients and the Fourier relationship in equation (1.12) or displacement imaging and the Fourier relationships in equations (1.17) to (1.20). The various advantages and disadvantages of these two approaches are discussed more fully in Chapter 4. When the velocity flow patterns in a fluid are especially complicated, there are advantages in abandoning velocity images in favor of direct two-dimensional plots of displacement probability functions in the displacement-position space [i.e., $P(\mathbf{r},\mathbf{R})$] as a function of increasing displacement time Δ plotted as a third dimension. The application of this to imaging Taylor flow vortices is discussed in Chapter 4.

Before leaving the combination [(**q**,**R**);(**k**,**r**)] it is worth pointing out that most moist solid foods are microscopically heterogeneous and contain water "compartmentalized" in pores and/or (sub-)cellular compartments. For these materials, water diffusion is restricted by pore walls and membrane barriers, and the simple Gaussian displacement probability distribution in equation (1.20) no longer applies. In such cases the (**q**,**R**) conjugate pair contains microstructural information, and the (**k**,**r**) pair, the macroscopic distance scale information (depending on the voxel dimensions). The microstructural aspects are considered in greater detail in Part Two of the book.

Velocity exchange spectroscopy (VEXSY) provides another way of using displacement probability functions to study complex flow patterns (1). VEXSY can be described symbolically as $[(q_1,\mathbf{R}_1),(q_2,\mathbf{R}_2)]$ and consists, in essence, of two sequential displacement pulse sequences separated by a mixing (or exchange) time t_m as shown in Figure 1.7. It is therefore analogous to two-dimensional high-resolution spectroscopic techniques, where the two-dimensional Fourier transforms describing VEXSY now assume the form

$$S(\mathbf{q}_1,\mathbf{q}_2,t_m) = \iint d\mathbf{R}_1\, d\mathbf{R}_2\, P(\mathbf{R}_1,\Delta)\, P(\mathbf{R},t_m \mid \mathbf{R}_2,\Delta) \exp(i\mathbf{q}\cdot\mathbf{R}_1 + \mathbf{q}_2\cdot\mathbf{R}_2) \qquad (1.21)$$

This expression involves the function $P(\mathbf{R},t_m \mid \mathbf{R}_2,\Delta)$, which is the conditional probability that a molecule that experienced a displacement $\mathbf{R}_1$ in the displacement time Δ will be displaced a distance $\mathbf{R}_2$ in the same displacement time Δ after the mixing or exchange time t_m. An inverse Fourier transformation with respect to $(\mathbf{q}_1,\mathbf{q}_2)$ therefore yields the two-dimensional displacement spectrum $P(\mathbf{R}_1,\Delta)P(\mathbf{R},t_m \mid \mathbf{R}_2,\Delta)$. Diagonal peaks in this $(\mathbf{R}_1,\mathbf{R}_2)$ space correspond to stationary flow where the spin experiences exactly the same displacement (in magnitude and direction) during the second displacement time Δ as during the first and therefore contains no really new information. However, off-diagonal peaks arise when this is not the case, and their intensity and distribution are sensitive probes of complex flow patterns, especially the transition from stationary flow to correlated randomized flow as the mixing time t_m is increased.

Third-order spectroscopic and imaging techniques involving combinations of three Fourier–conjugate pairs have also been developed. For example, the DOSY–TOCSY experiment combines diffusion measurements with two-dimensional spectral measurements and can therefore be denoted $[(\mathbf{q},\mathbf{R}),(\omega_1,t_1),(\omega_2,t_2)]$-spectroscopy. Cross-correlation imaging is based on the three Fourier pairs $[(\omega_1,t_1);(\omega_2,t_2);(\mathbf{k},\mathbf{r})]$ and is

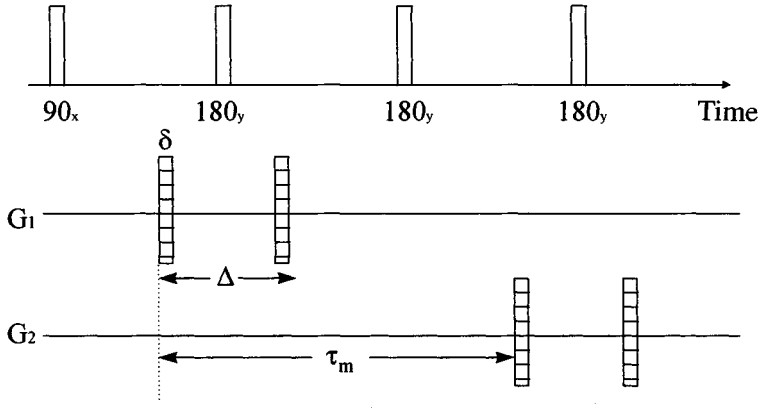

Figure 1.7. Basic VEXSY pulse sequence.

useful for imaging solute distributions. It is interesting to note that the VEXSY experiment involves acquiring an echo in the absence of external gradients. There is therefore the possibility of exploiting chemical shift information by Fourier transforming the echo in $[(q_1,\mathbf{R}_1),(q_2,\mathbf{R}_2),(\omega,t)]$-spectroscopy or for combining it with spatial imaging in the combination $[(q_1,\mathbf{R}_1),(q_2,\mathbf{R}_2),(\mathbf{k},\mathbf{r})]$. These last two possibilities have yet to be implemented and serve to illustrate the almost endless range of possibilities available in pulse sequence design.

Fourth- and higher-order combinations can be envisaged and it is an imaginative exercise to construct multidimensional matrices of Fourier conjugates $[(x_1,y_1),(x_2,y_2),(x_3,y_3), \ldots ,(x_n,y_n)]$ and speculate about hitherto unexplored types of NMR and MRI experiments. Indeed, it is difficult to keep abreast of the research literature dealing with the development of new pulse sequences and new types of NMR and MRI experiments. The interested reader will find details of the more popular pulse sequences and experimental protocols in standard textbooks dealing with the principles of NMR and MRI and listed in the references. Many other sequences can be found in the research literature published, for example, in the journals *Magnetic Resonance Imaging, Journal of Magnetic Resonance, Magnetic Resonance in Medicine, Annual Reports of NMR Spectroscopy, Journal of Magnetic Resonance Analysis,* and others.

1.4 MODULUS AND PHASE IMAGES

The Fourier conjugate relationships above involve complex variables. There are therefore real and imaginary parts in the image or spectrum $P(\epsilon)$, where ϵ denotes one of the Fourier variables, such as frequency (ω), position ($\mathbf{r}$), velocity ($\mathbf{v}$), acceleration ($\mathbf{a}$), or displacement ($\mathbf{R}$). In many applications only the real part or modulus image $|P(\epsilon)|$ is required, as, for example, when the proportionality between the transverse magnetization density and the proton spin density is used to produce images of moisture-content distribution (see Chapters 2 and 3). However, other applications, such as phase-encoding velocity imaging, make use of both the real and imaginary parts of the image. A common implementation of velocity imaging uses only a single velocity-encoding bipolar gradient corresponding to a single vector, $\mathbf{p}'$, so that the signal $S(\mathbf{p})$ in equation (1.12) is $\rho\delta(\mathbf{p} - \mathbf{p}')$ and the complex velocity image $P(\mathbf{v})$ is $\rho \exp(i\mathbf{p}' \cdot \mathbf{v})$, where ρ is the spin density. The complex image therefore has a real part $\rho \cos(\mathbf{p}' \cdot \mathbf{v})$ and an imaginary part $\rho \sin(\mathbf{p}' \cdot \mathbf{v})$, so the spin density ρ and phase image $\mathbf{p}' \cdot \mathbf{v}$ can be obtained by computing the image modulus and argument. Figures 1.8 and 1.9 show an example for Poiseuille flow in a cylindrical pipe.

In chemical shift temperature mapping, temperature changes induce a change in the water proton chemical shift, and this causes a phase shift in the echo observed using a gradient-echo imaging sequence. The temperature distribution can therefore be obtained from the phase image calculated as the argument of the image, $\text{Arg}(P(\epsilon))$. Temperature imaging is discussed in greater detail in Chapter 2.

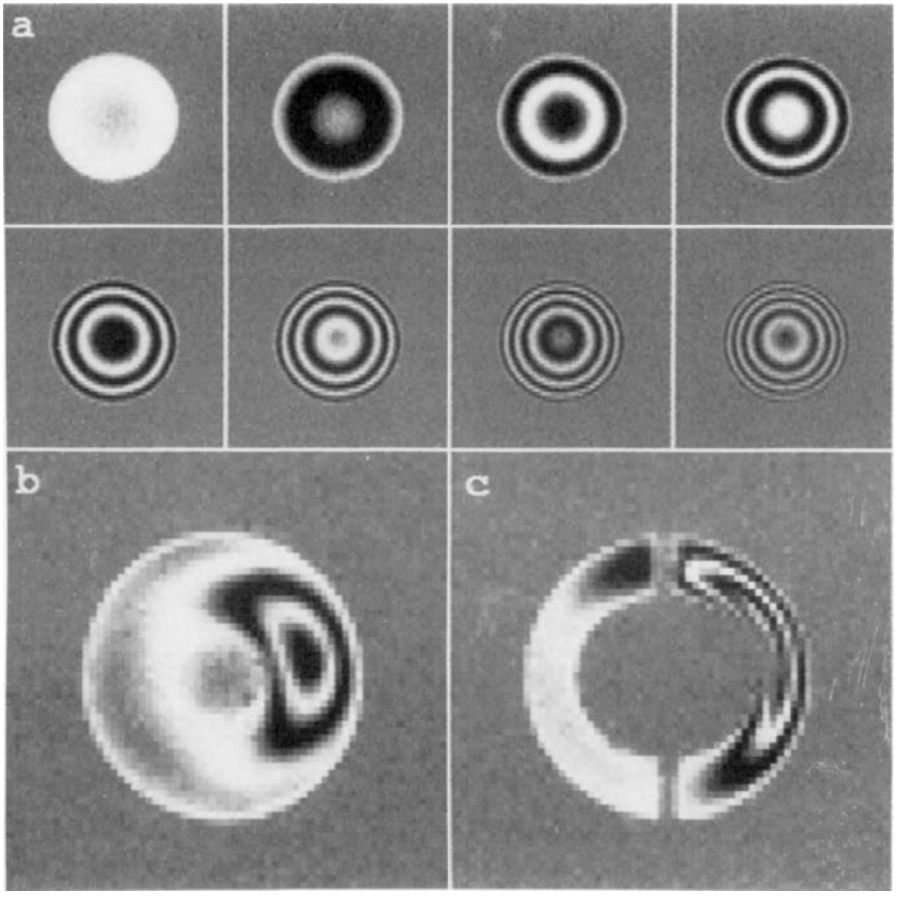

Figure 1.8. (*a*) Real and imaginary velocity-phase-sensitive images for Poiseuille flow of water in a cylindrical tube. (*b* and *c*) Flow around a sphere placed inside the cylindrical tube, acquired at two different planes across the tube. (Courtesy of the Herschel Smith Laboratory, Cambridge.)

1.5 STATISTICAL ASPECTS OF MRI

It is important to realize that the image $P(\epsilon)$ is actually a probability distribution. There is therefore always some degree of statistical noise in $P(\epsilon)$ and it is always possible to manipulate the image with a wide variety of statistical methods, such as MEM (maximum entropy methods), edge-sharpening algorithms, and chemometric techniques. These methods fall outside the scope of this book and have been treated, in detail, in a number of texts, including Ref. (6).

In many applications discussed in later chapters, such as imaging plant tissue, the statistical aspects of the Fourier relationship are of secondary consideration (provided

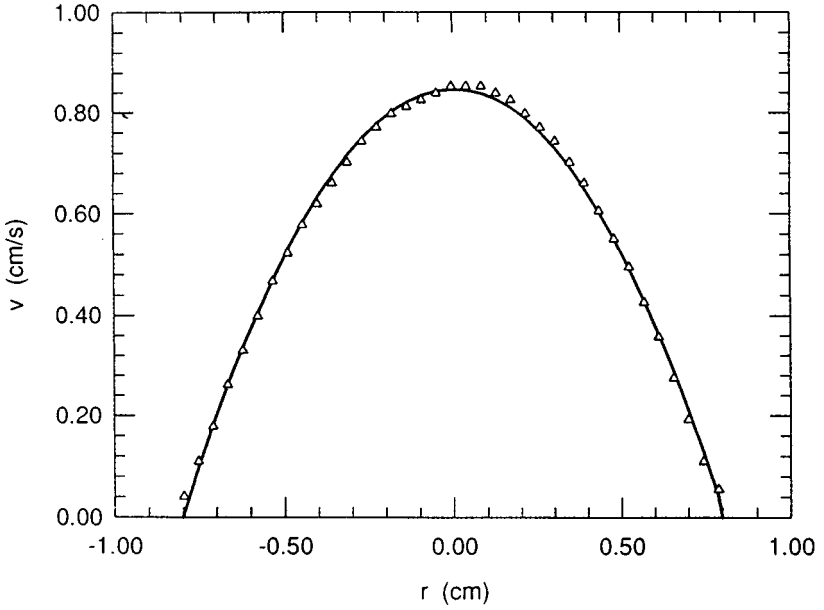

Figure 1.9. Radial velocity profile $v(r)$ extracted from the phase-sensitive images in Figure 1.8. (Courtesy of the Herschel Smith Laboratory, Cambridge.)

that the signal-to-noise ratio is sufficient) and the structural information is readily interpreted simply by looking at the image of the plant and, if necessary, comparing it with optical micrographs. However, this is not always the situation, and nature abounds with examples in which the inherent statistical aspect of a phenomenon is prevalent. For example, the eye is poor at extracting quantitative structural information such as pore size distributions and pore connectivities from structural images of porous media, so a statistical approach to imaging porous media is desirable. Extracting flow information from velocity-encoded images of a fluid undergoing spatially chaotic turbulent motion also requires statistical analysis.

When the inherent statistical aspects of a phenomenon are prevalent, the Wiener–Khintin theorem (4) for Fourier conjugates is a useful method for analyzing the raw NMR data. The Weiner–Khintin theorem relates autocorrelation functions in one Fourier domain to the square of their transform in the other. For the conjugates (**k**,**r**) in spatial imaging, this states that

$$<P(\mathbf{r})P(\mathbf{r}+\Delta\mathbf{r})> = \frac{1}{(2\pi)^3 V}\int d\mathbf{k}|S(\mathbf{k})|^2 \exp(i\mathbf{k}\cdot\Delta\mathbf{r}) \qquad (1.22)$$

In other words, all phase-encoding information is first removed from the signal $S(\mathbf{k})$ by squaring its modulus before it is Fourier transformed. The result is not an image

describing the actual location of spin density in space, but rather, an autocorrelation function revealing statistical correlations between different parts of the image, such as mean object sizes, excluded volumes, and nearest-neighbor distances. This approach is sometimes called *Patterson function analysis* because the autocorrelation function is analogous to the Patterson function of X-ray scattering theory.

The top part of Figure 1.10 shows a cross-sectional two-dimensional MRI image of a sample consisting of 0.11-mm nylon fibers packed lengthwise into a 6-mm cylinder. The autocorrelation function (or Patterson function) for the same data is shown in the bottom part of the figure. The width of the central peak indicates the mean fiber diameter, the low-intensity ring shows the excluded volume surrounding each fiber, and the rings clearly reveal the first and second nearest-neighbor distances. It can be seen that if this statistical information is the main quantity of interest and the sample is isotropic, it is not necessary to undertake lengthy two-dimensional imaging with slice selection. The same information can be obtained more simply from one-dimensional data using the autocorrelation function approach. The impressive information content in most spatially resolved images has made many investigators reluctant to throw away the phase-encoding information and use Patterson function analysis. Nevertheless, many real foods, such as freeze-dried materials, breads, and foams, have a porous structure that could be characterized more easily by this alternative approach.

1.6 FOURIER TRANSFORMATION OF THE RADIO-FREQUENCY WAVEFORM: SLICE SELECTION

It is, in principle, possible to perform all the NMR and MRI experiments mentioned above with only field gradients and *hard radio-frequency pulses* (i.e., coherent radio-frequency pulses of short duration T, high field amplitude B_1, and frequency ω_0). For example, a typical hard 90° pulse would have a short duration T of 2 μs, for example, and induce a rotation of the magnetization through an angle $\gamma B_1 T$ of 90°. The range of frequencies excited by this hard pulse (the excitation bandwidth) is of order $1/T$, which is about 0.5 MHz for a 2-μs pulse and centered on the radio-frequency ω_0, which is certainly sufficient to excite all the protons in a liquid or soft solid food sample. However, a new aspect of NMR and MRI is made available by using longer, lower-amplitude radio-frequency pulses (called *soft pulses*), whose amplitude, $B_1(t)$, is modulated in time. Here again a Fourier transform relates the time-domain waveform, $B_1(t)$, to the spectrum of frequencies contained in the radio-frequency pulse and hence the frequency response of the spin system. An infinite-duration, perfectly coherent radio-frequency wave, $\exp(i\omega_0 t)$, has a frequency spectrum, obtained by Fourier transformation, of $\delta(\omega - \omega_0)$. Any finite-duration pulse of waveform $B_1(t)$, even if generated at a single frequency ω_0, contains a frequency distribution $F(\omega)$ given by the Fourier transform

$$F(\omega) = \int_{-\infty}^{\infty} dt\, B_1(t) \exp(i\omega t) \tag{1.23}$$

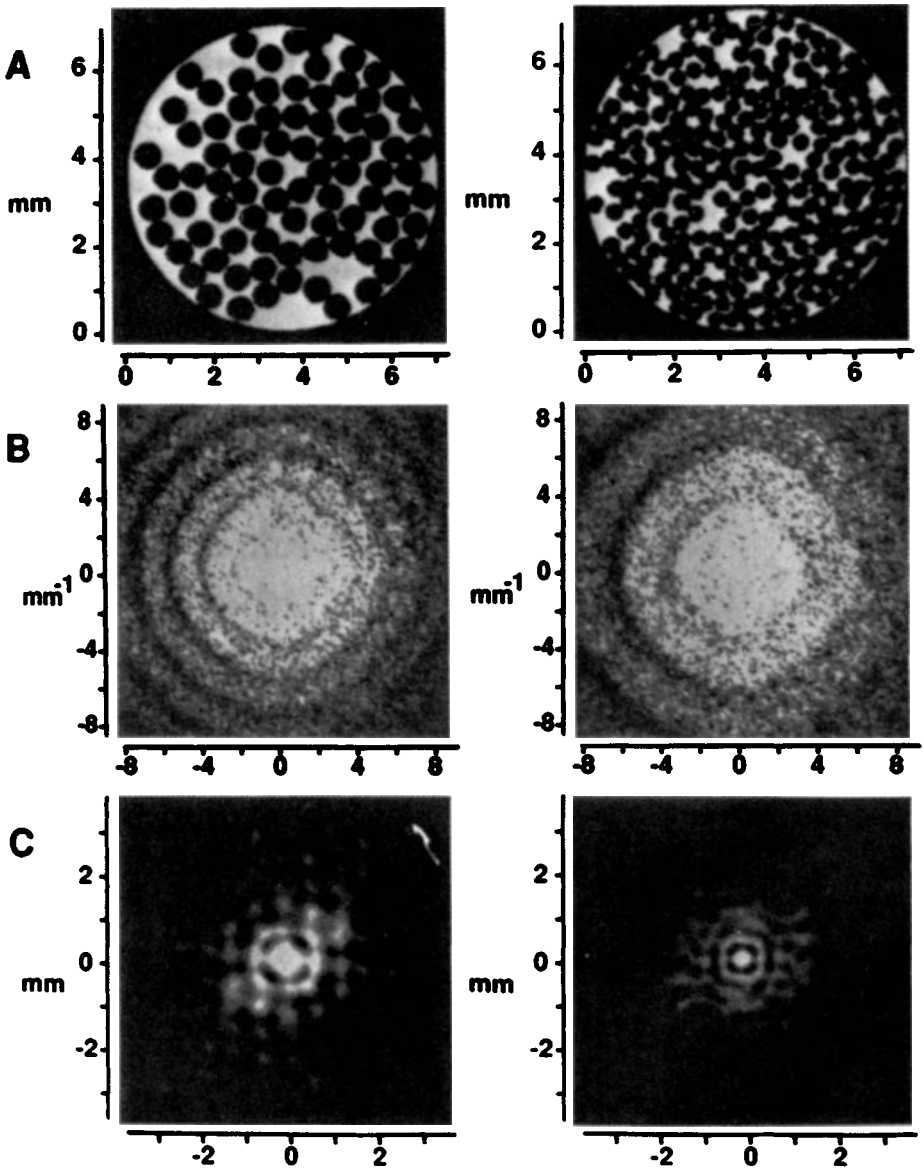

Figure 1.10. Slice images, NMR diffraction patterns, and Patterson functions for nylon fibers immersed in water-filled tubes. On the left are shown data for 0.56-mm fibers; on the right are shown data for 0.33-mm fibers. The diffraction pattern shown in (*B*) is the square of the data used to generate the images (*A*) by Fourier transformation. The transformation of the diffraction patterns yields the Patterson functions shown in (*C*), which show the fiber size and packing fraction. (From Ref. 57.)

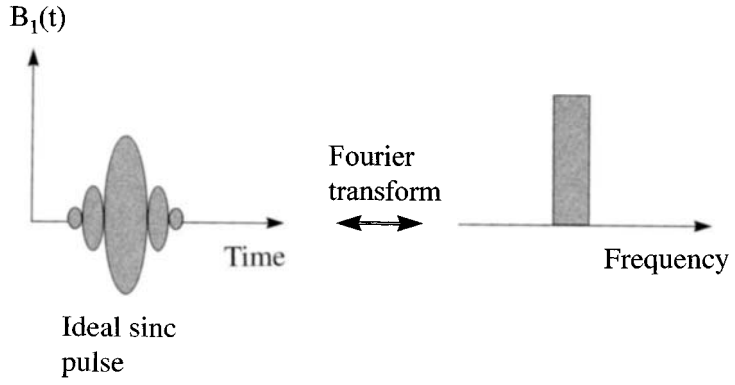

Figure 1.11. Ideal rectangular frequency distribution in a sinc-function radio-frequency pulse, $B_1(t)$.

Equation 1.23 shows that a narrow Gaussian-shaped pulse $B_1(t)$ will also excite a narrow Gaussian-shaped frequency band, because the Fourier transform of a Gaussian is itself a Gaussian. This is often used to excite only a single spectral line in chemical shift imaging (see below). Similarly, an ideal sinc-shaped pulse will give a rectangular frequency excitation (see Figure 1.11).

Another important application arises when a shaped pulse is applied at the same time as a linear field gradient. The gradient, let us say G_z, creates a linear distribution of resonance frequencies across the sample in the z-direction. The response of the spin system to the soft pulse in the presence of the gradient can be calculated using the Bloch equations (7), which show that the spatial distribution of the transverse magnetization, $M_+(z)$, $[=M_x(z) + iM_y(z)]$, is given as the modified Fourier transform

$$M_+(z) = -\gamma M(0) \exp(-i\gamma G_z z T). \int_{-T}^{+T} dt\, B_1(t) \exp(-i\gamma G_z z t) \qquad (1.24)$$

This shows that a rectangular slice of transverse magnetization can be excited in the x–y plane by applying a linear gradient in the z-direction (called the *slice-selection gradient*) using a sinc-function-shaped radio-frequency pulse to excite the magnetization (see Figure 1.12). The phase factor $\exp(-i\gamma G_z z T)$ in equation 1.24 is the phase shift across the excited slice and can be removed by applying an opposite sign z-gradient $(-G_z)$ for a time T, which refocuses the magnetization in the slice. Alternatively, the $B_1(t)$ waveform can be tailored to make the excitation pulse selective and self-refocusing (5).

By systematical change of the resonance frequency offset $\Delta\omega_0$ of the selective pulse it is possible to excite neighboring planes in a sample and undertake multislice three-dimensional imaging. By using selective pulses and gradients in orthogonal directions, either planes, lines, or small rectangular voxels can be excited in a sample. This gives rise to sequential plane, line, or point imaging in which a three-dimensional image is built up by sequentially exciting planes, lines, or voxels, respectively (2).

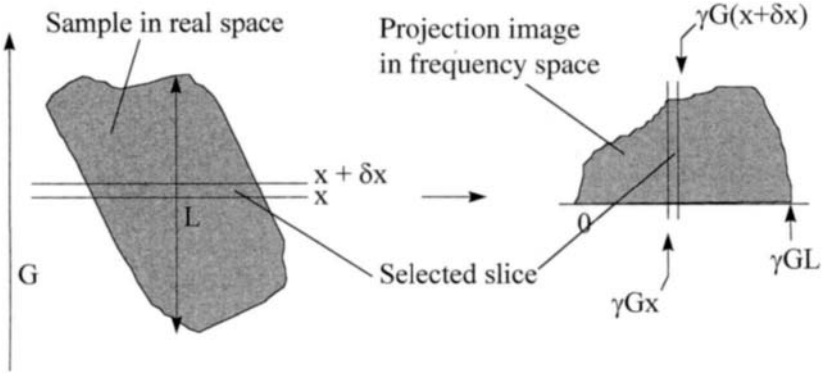

Figure 1.12. Schematic illustrating slice selection with a soft excitation pulse in a linear field gradient G. The linear gradient spreads the resonance frequencies into the one-dimensional spectrum shown on the right. A soft radio-frequency pulse excites a slice of frequency width $\gamma G\ \delta x$, corresponding to an excitation slice thickness δx.

1.7 FOURIER TRANSFORMATION OF THE GRADIENT MODULATION: MOTIONAL SPECTRA AND SPECTRA FD-MG-NMR

So far we have considered Fourier transforms of the signal, where they define various types of NMR experiments, and Fourier transforms of radio-frequency waveforms, where they define various types of slice and chemical shift selection. It is also possible to consider Fourier transforms of gradient waveforms [i.e., generalized time-modulated applied field gradients $G(t)$], and this gives rise to another type of NMR experiment, *frequency-domain modulated-gradient NMR* (FD-MG-NMR). This type of NMR is especially valuable for probing random velocity fluctuations in fluid systems on a frequency scale of 0.01 to 10 kHz. To see the relationship of this technique to the previous ones, we must return to the derivation of the Fourier transforms for velocity and acceleration imaging based on coherent motion in equation (1.5). This derivation assumed coherent fluid motion, so it neglected the attenuation of the signal due to random velocity fluctuations as they occur in Brownian motion, perfusion, and turbulence, for example. These velocity fluctuations can be characterized by the motional spectrum $D_{ij}(\omega)$, defined as the Fourier transform of the velocity autocorrelation function

$$D_{ij}(\omega) = \int_{-\infty}^{\infty} dt \, <v_i(0)v_j(t)> \exp(i\omega t) \tag{1.25}$$

A more rigorous analysis (5) of the effect of a modulated field gradient pulse $\mathbf{G}(t)$ shows that besides the complex phase factor $\exp[i\phi(t)]$, useful for studying coherent fluid motion, the signal is also attenuated by a real factor $\exp[-\alpha(t)]$, related to the velocity fluctuations, where

$$\alpha(t) = \gamma^2 \int_{-\infty}^{\infty} d\omega \, D_{ij}(\omega) \mid G(\omega,t) \mid {}^2\omega^{-2} \tag{1.26}$$

The key to this expression is $G(\omega,t)$, which is the Fourier transform of the gradient modulation function

$$G(\omega,t) = \int_0^t dt'\, G(t') \exp(-i\omega t') \tag{1.27}$$

By designing appropriate applied gradient waveforms $G(t)$, it is possible to probe the motional spectrum $D(\omega)$ over frequencies ranging from 0.01 to 10 kHz. Figure 1.13 shows an example of a gradient waveform $G(t)$, which on Fourier transformation gives a gradient spectrum that can be used to probe motions at frequencies of 0 and ω_m, where ω_m is π/t and t is the period. As indicated in Figure 1.13, because a hard 180° pulse reverses all spin phases, this gradient waveform is most conveniently generated with a CPMG pulse sequence in a constant applied gradient G. Alternatively, a sinusoidally varying applied gradient amplitude of frequency ω_m applied in the z-direction gives an echo attenuation factor of the form

$$\alpha(t) = \gamma^2 G^2 t \omega_m^{-2} [D_{zz}(0) + 0.5 D_{zz}(\omega_m)] \tag{1.28}$$

which also permits the motional spectrum $D(\omega)$ to be probed at a frequency ω_m. This approach has been used to study fluids flowing through packed particle beds where there are velocity contributions from local random velocity fluctuations, perfusive spreading motions induced by the microscopic tortuosity of the bed, and local coherent flow around the microscopic particles (3).

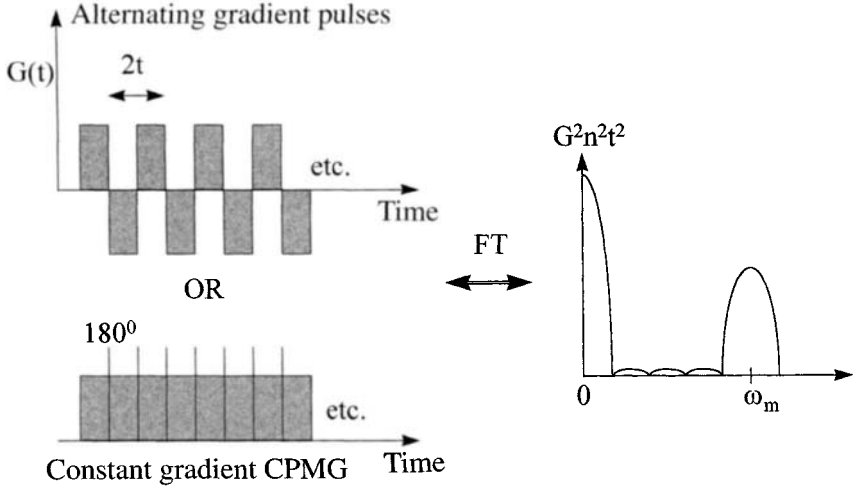

Figure 1.13. Fourier relationship between the time-domain gradient waveform $G(t)$ and the gradient spectrum. The alternating gradient waveform is equivalent to a constant gradient and a series of hard 180° radio-frequency pulses.

1.8 SPIN AND GRADIENT ECHOES: CONTRAST IN *k*-SPACE IMAGING

Most *k*-space imaging pulse sequences based on equations (1.9) and (1.10) use combinations of radio-frequency pulses or gradient reversal pulses to refocus the spin phases in an echo occurring at a time *TE* (called the *echo time*) after the initial spin excitation pulse. The signal is then acquired by recording the time dependence of the echo amplitude. An echo can be generated in various ways. *Spin echoes* are created by reversing the spin phase with radio-frequency pulses, and the most commonly used types involve the *Hahn echo,* created by reversing the phase with a 180° pulse, and the *stimulated echo,* resulting from the application of two 90° pulses separated by a short time delay. Of course, soft pulses can be used to create spin echoes in selected regions of the sample or for selecting resonance lines of particular chemical species. A *gradient echo* (sometimes called a *gradient-recalled echo*) involves reversing the phase built up by evolution in one applied gradient by reversing the sign (i.e., direction) of the gradient. Figure 1.14 shows a standard imaging sequence, called the *spin-warp sequence,* based on the Hahn echo. The soft pulse is used for slice selection in the *z*-direction, the phase encoding for spatial resolution in the *y*-direction, and the readout gradient for the *x*-direction.

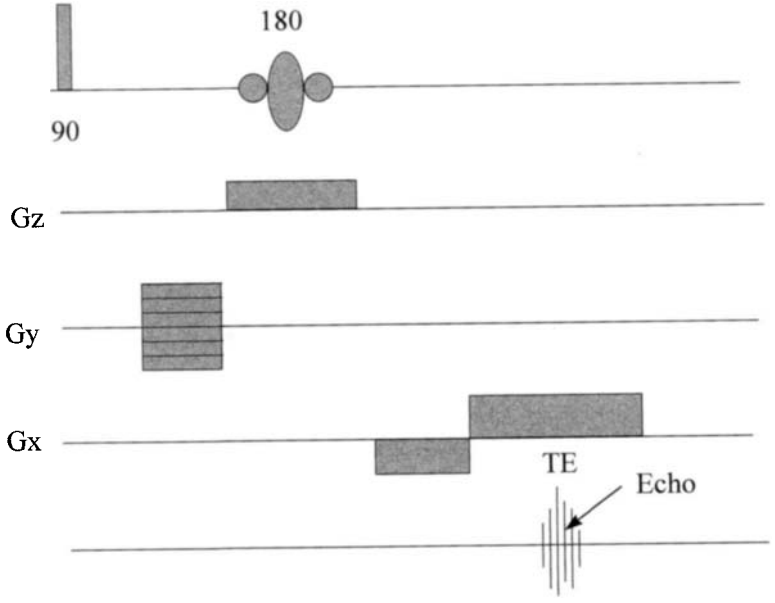

Figure 1.14. Basic spin-warp imaging sequence. Slice selection in the *z*-direction is achieved with a soft 180° radio-frequency pulse in a gradient G_z. Spatial resolution in the *y*-direction is achieved by phase encoding with a ramped gradient G_y. The readout gradient G_x gives spatial resolution in the *x*-direction. *TE* is the echo time.

Refocusing magnetization in spin or gradient echoes is an essential aspect of MRI because it affects the image contrast (i.e., the spatial distribution of image intensity). This is apparent if we recall that the modulus image $|P(\mathbf{r})|$ calculated from the Fourier transform of the echo signal $S(\mathbf{k})$ is the spatial distribution of the transverse magnetization density remaining in the sample at a time *TE* after excitation. Because of transverse relaxation, this is proportional to the initial magnetization density $M(\mathbf{r}, t = 0)$ (i.e., the equilibrium longitudinal magnetization per unit volume) attenuated by various amounts of transverse relaxation occurring during the time *TE*. As we have seen, most imaging sequences involve repeated excitation of the transverse magnetization with a 90° pulse where each repeated cycle has a different phase-encoding gradient. For maximum signal, the time between repeats (called the *recycle delay, TR*) must be long compared to the time it takes the longitudinal magnetization to recover to its initial equilibrium value $M(\mathbf{r}, t = 0)$, called the *longitudinal relaxation time* T_1. Otherwise, the signal will be attenuated because the longitudinal magnetization has failed to recover completely and the image intensity will be weighted by various amounts of longitudinal relaxation, with regions of short T_1 having the most signal.

The exact amount of transverse and longitudinal relaxation in each region of the sample will depend on the precise nature of the imaging pulse sequence and on the spatial distribution of transverse and longitudinal relaxation times, $T_2(r)$, and $T_1(r)$, respectively. For a simple gradient-echo pulse sequence, the image will be

$$|P(\mathbf{r})| = M(\mathbf{r}, t = 0) \exp\left[\frac{TE}{T_2^*(\mathbf{r})}\right] \left\{1 - \exp\left[\frac{-TR}{T_1(\mathbf{r})}\right]\right\} \tag{1.29}$$

Note that generating the echo by reversing the applied field gradient refocuses only dephasing caused by the applied gradient, not that caused by any other factor. Accordingly, the image contrast involves the effective relaxation time $T_2(\mathbf{r})^*$, which is measured in a free induction decay and not the true transverse relaxation time $T_2(\mathbf{r})$. The gradient-echo imaging sequence is therefore sensitive to intrinsic field inhomogeneities created by susceptibility discontinuities in the sample, for example.

On the other hand, a spin echo generated by a 180° radio-frequency pulse or a stimulated echo will refocus the dephasing arising from all field gradients experienced by the spins in the sample, including those from susceptibility distortions and field inhomogeneities. Accordingly, the image contrast will now depend on the intrinsic transverse relaxation time $T_2(\mathbf{r})$ and not $T_2(\mathbf{r})^*$. For a simple Hahn-echo imaging sequence there will also be an additional correction for the inversion of the residual longitudinal magnetization by the 180° pulse. The Hahn-echo image therefore has the more complicated form

$$|P(\mathbf{r})| = M(\mathbf{r}, t = 0) \exp\left[\frac{TE}{T_2(\mathbf{r})}\right] \left\{1 - 2\exp\left[\frac{TR - 0.5\,TE}{T_1(\mathbf{r})}\right] + \exp\left[\frac{-TR}{T_1(\mathbf{r})}\right]\right\} \tag{1.30}$$

Equations (1.29) and (1.30) show that the image can be T_2-*contrasted* by increasing TE and keeping TR greater than $5T_1$. Equations (1.29) and (1.30) can then be used to compute $T_2(\mathbf{r})$, in other words, to extract T_2 *images* (also known as T_2 *maps*). Conversely, the image can be T_1-*contrasted* by keeping TE as short as possible and decreasing TR so that $T_1(\mathbf{r})$ (i.e., T_1 *maps*) can be extracted. A spin density map $M(\mathbf{r}, t = 0)$ is obtained in the limits $TE \ll T_2(\mathbf{r})$ and $TR \gg T_1(\mathbf{r})$. Of course, different k-space imaging pulse sequences will be associated with relaxation contrast expressions differing in detail from equations (1.29) and (1.30), but the essential concept remains the same. Figure 1.15 shows $T_2(r)$, $T_1(r)$, and $M_0(r)$ maps for raw carrot, although quantitative gray scales have been left out for simplicity.

Applications of $M_0(\mathbf{r})$, $T_2(\mathbf{r})$, and $T_1(\mathbf{r})$ maps are discussed in subsequent chapters. However, it should be remembered when using these maps that the foregoing

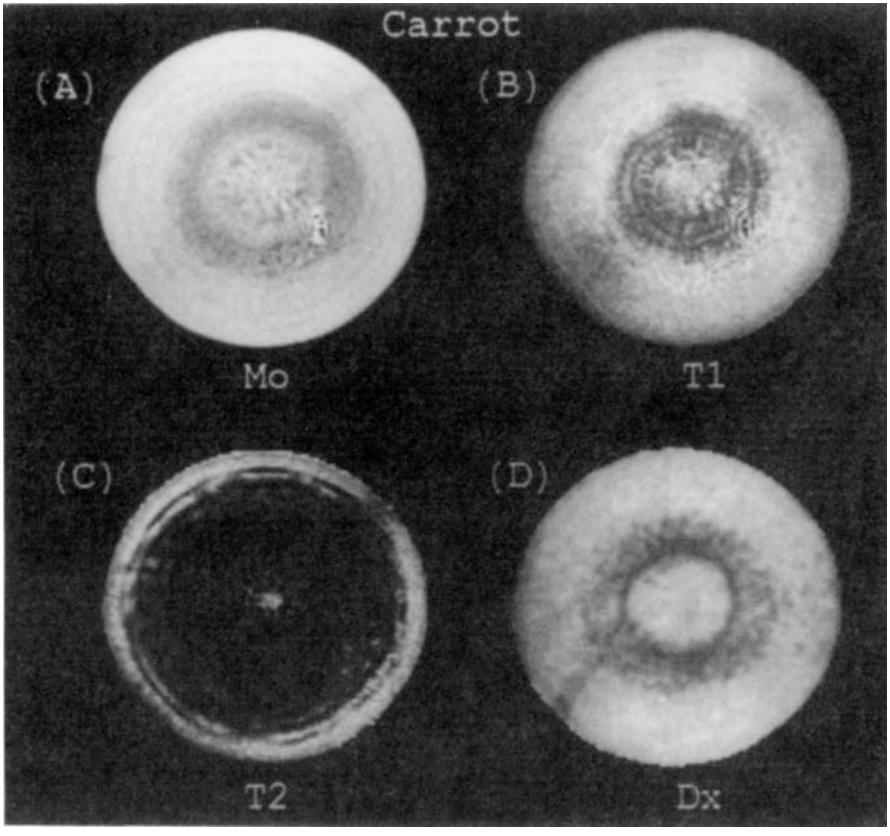

Figure 1.15. Maps of initial spin density (M_0), the longitudinal (T_1) and transverse (T_2) relaxation times, and the water self-diffusion coefficient in the transverse direction (D_x) for raw carrot. (Courtesy of the Herschel Smith Laboratory, Cambridge.)

analysis assumes single exponential relaxation, which, as we shall see in Part Two, is not always valid in microscopically compartmentalized samples or when the signal arises from various proton pools, such as lipids, biopolymers, and water. The relaxation-time maps are therefore best regarded as maps of "effective" relaxation times unless independent measurements confirm single exponential decay.

The procedure described above is satisfactory for generating simple relaxation and spin-density maps, but if maps of other NMR parameters are required, such as diffusion coefficients, magnetization transfer rates, or rotating-frame relaxation times ($T_{1\rho}$), a more systematic approach is to *precondition* the spin system immediately before the imaging sequence with a nonspatially resolving NMR pulse sequences designed to weight the magnetization with the NMR parameter chosen (Figure 1.16). For example, a spin-locking sequence applied immediately before a spatially resolving imaging sequence can be used to attenuate the magnetization by relaxation in the rotating frame before it enters the imaging sequence. Acquiring the image with varying spin-locking times can then be used to compute $T_{1\rho}(\mathbf{r})$ maps. A similar approach can be used to map many other NMR parameters. If the echo in the spatially resolving imaging sequence is acquired in the absence of an applied gradient, Fourier transformation will give a frequency spectrum containing chemical shift information (see Figure 1.10). This is a convenient strategy for volume-selective spectroscopy and at least in principle, permits each spectral peak arising from a subvolume of sample to be relaxation-time weighted with a preconditioning sequence. An alternative method for creating rotating-frame relaxation contrast using rotating-frame imaging is considered in Chapter 8. The microstructural and molecular origins of relaxation and diffusion contrast are considered in Parts Two and Three, respectively.

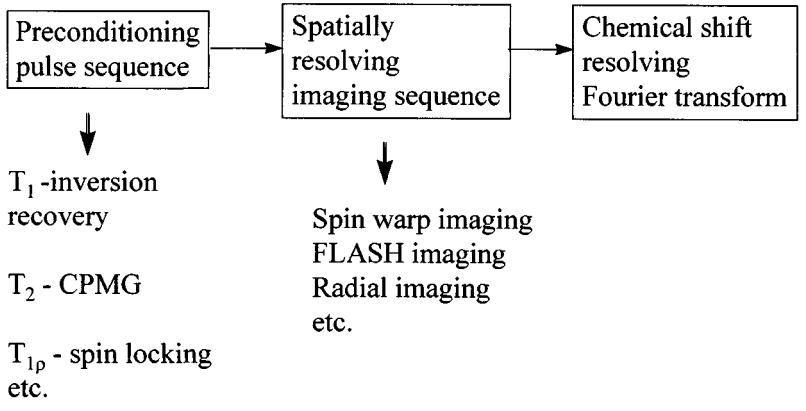

Figure 1.16. General scheme for generating NMR parameter maps. The preconditioning pulse sequence weights the image contrast with the chosen parameter. An imaging sequence creates spatial resolution, and if required, chemical shift resolution can be introduced by Fourier transforming the echo acquired in the absence of external gradients.

1.9 FAST IMAGING METHODS

Many of the processes discussed in later chapters, such as freezing, involve rapid changes in the sample composition and temperature and therefore of image intensity. To follow these changes in real time requires imaging techniques that are fast compared to the time scale of the sample changes. A number of such techniques have been developed and these can be classified into four main types: (1) FLASH imaging, (2) FAST imaging, (3) EPI methods, and (4) projection imaging.

1.9.1 FLASH Imaging

The first type, typified by the pulse sequence FLASH (an acronym for *fast low-angle shot*), uses smaller tip angles during the excitation step. Instead of a hard 90° radio-frequency pulse, a smaller tip angle, θ° (typically about 5°) is used, so that after one radio-frequency (RF) excitation or *shot,* the transverse magnetization is $M_0 \cos \theta$ and the residual longitudinal magnetization is $M_0 \sin \theta$. The existence of residual longitudinal magnetization permits repeated rapid sampling of the FID, such that after n shots the signal will be proportional to $M_0 \sin \theta \cos^n \theta$. This can be rapid because it is not necessary to wait for recovery of the longitudinal magnetization by relaxation, so the recycle delay TR can be much shorter than T_1. Each shot can be combined with gradient pulses and used to sample k-space. Two-dimensional imaging times as short as 100 ms can be achieved in this way. The price paid for this increased speed is a reduced signal-to-noise ratio (since $M_0 \sin \theta \cos^n \theta$ is less than M_0 and rapid digitation means wide bandwidths), resulting in poorer spatial resolution. Gradient-echo methods must be used with FLASH sequences because spin echoes would perturb the residual longitudinal magnetization between shots. As we have seen, a gradient-echo sequence weights the image by T_2^* relaxation, which is sensitive to susceptibility effects. If $T_2(\mathbf{r})$ maps are required, a Hahn-echo preparation sequence before the FLASH sequence can be used. Similarly, because there is little T_1 weighting in FLASH imaging, $T_1(\mathbf{r})$ maps are best acquired using an inversion recovery preparation sequence before the FLASH sequence. Pulse gradient incrementing during k-space sampling helps avoid the onset of steady-state effects (see Section 1.9.4), but it is usual to destroy the coherence of the transverse magnetization between cycles by the application of an additional short, pulsed field gradient (a spoiling pulse) immediately before the next low-angle excitation pulse.

1.9.2 FAST Imaging

A second approach to rapid image acquisition is to use steady-state free precession. Repeating RF excitation pulses on a time scale t_p shorter than $5T_1$ sets up a steady-state longitudinal magnetization which is less than the equilibrium value M_0. In like manner, if t_p is shorter than $5T_2$, there is residual coherent transverse magnetization from the preceding pulse and a steady-state situation is established such that the FID decays immediately after an excitation pulse and is refocused in a *time-*

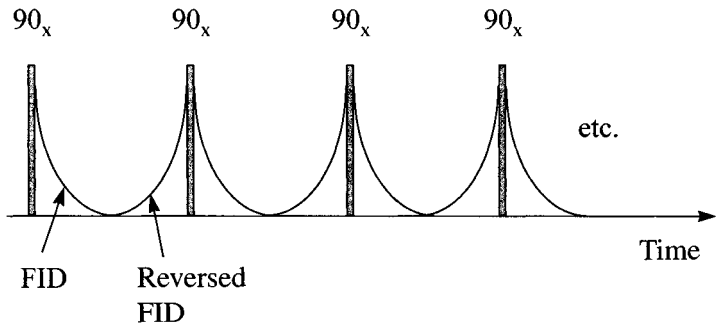

Figure 1.17. Idealized pulse sequence generating a steady state. A train of rapidly repeated 90° radio-frequency pulses creates an alternating sequence of FIDs and reversed FIDs.

reversed FID which builds up coherent transverse magnetization before the next excitation pulse (9) (see Figure 1.17). This steady-state situation is not removed even if T_2^* is much less than t_p, because each spin isochromat in the sample forms its own time-reversed FID, much like a Hahn echo.

The FAST imaging sequence uses the steady-state coherent transverse magnetization set up in a rapidly repeated imaging sequence to sample k-space. Rapidly repeating a standard gradient-echo or spin-echo imaging sequence will not establish a steady-state because the amplitude of the phase-encoding gradient pulse is ramped through a k-space raster in successive cycles. Coherence in the transverse magnetization is therefore lost between successive cycles. In the FAST imaging sequence, transverse coherence is maintained between cycles in a steady state by unwinding the phase built up in the phase-encoding pulse before the echo by application of an equal and opposite gradient pulse after the echo and before the next cycle of the sequence (see Figure 1.18). This steady-state strategy permits recycle times TR to be much less than T_1 or T_2^*. Like FLASH, a gradient-recalled echo is used and not a 180° spin echo, and a soft slice-selective excitation pulse with a tip angle of less than 90° can be used if necessary. Several variants of FAST have been proposed, including the CE-FAST and FADE imaging sequences. For details the reader is referred to Ref. (5).

1.9.3 EPI Methods

A third approach to rapid image acquisition is to use *echo planar imaging* (EPI). Coherence in the transverse magnetization is maintained in an FID for a time on the order of T_2^*. During this time a two-dimensional image can be obtained from a single FID by acquiring it in a weak readout gradient (let us say, G_x) and creating a series of echoes with a strong, rapidly switched G_y gradient as shown schematically in Figure 1.19. Each echo can be regarded as a separate experiment where the phase is encoded in the nth echo with the wavevectors $k_x = \gamma G_x n t_1$ and $k_y = \gamma G_y t_2$. A two-dimensional image is therefore obtained by Fourier transformation of the signal $S(k_x,k_y)$. Three-dimensional images are obtained using multislicing with a soft

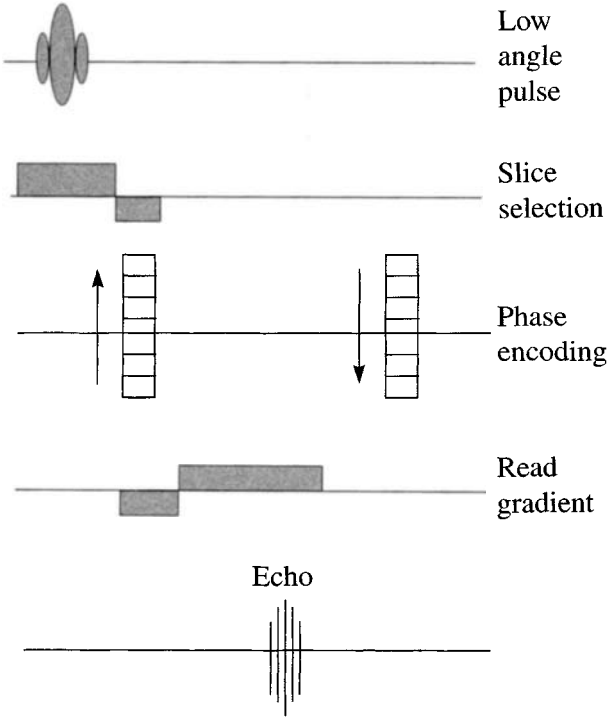

Figure 1.18. FAST imaging sequence, showing how transverse phase coherence is maintained by application of equal and opposite gradient pulses after the echo and before the next acquisition cycle.

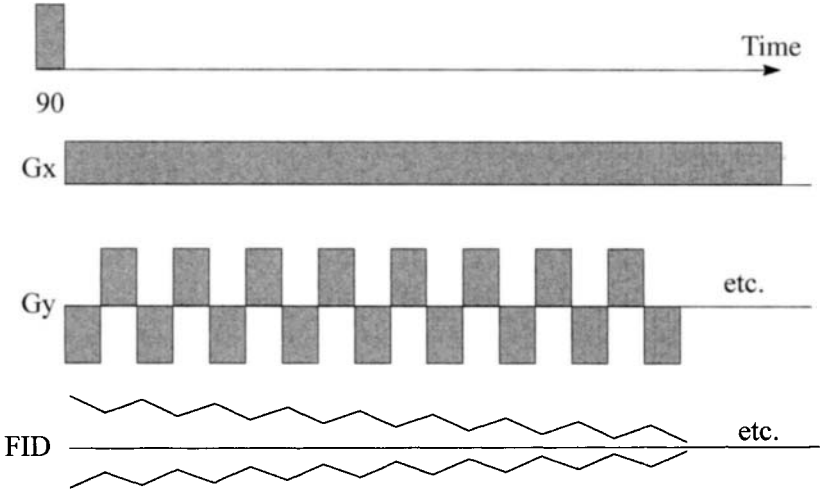

Figure 1.19. Basic echo-planar imaging sequence. Note the requirement for rapid gradient switching.

slice-selective excitation pulse. With EPI, complete images can be acquired in less than 100 ms; however, the price to be paid for this tremendous imaging speed is a low signal-to-noise ratio and the need to use rapid gradient switching, which requires specially screened gradient coils to avoid eddy currents being induced in the surrounding probe and magnet. Because it uses a single FID, EPI is also restricted to an imaging time of order T_2^*, so it is best used when there are very rapid changes, on a (sub-)second time scale. As with FLASH and FAST, there are several variants of the basic EPI method, such as FLEET, BEST, and MBEST, and details can be found in Callaghan's book (5).

1.9.4 Projection Imaging Methods

The last approach to fast imaging uses projection imaging, which exploits the sample geometry rather than special pulse sequences. In food processing it is usually the transport of mass, heat, and momentum that is of paramount importance, not three-dimensional structural imaging. In this situation there are many advantages to simple one-dimensional projection imaging, which assumes that the food can be cut or molded into cuboids or cylinders and then processed so that mass and heat transport occur only along one of the principal axes of the cuboid, or in the case of the cylinder, either along the axis or in a radial direction (i.e., across the cylinder). The one-dimensional image profile (or projection) is then obtained by imaging with a linear field gradient applied along one of these principal directions. The profile obtained by projecting across a cylinder is weighted by the curvature of the cylinder (e.g., the projection across a uniform cylinder is a semiellipsoid shape; see Figure 1.20). In this case the geometric distortion can be removed by calculating the inverse Abel transform of the projection, which generates the radial profile [i.e., the one-dimensional profile $P(r,t)$, where r is the radial distance from the cylinder

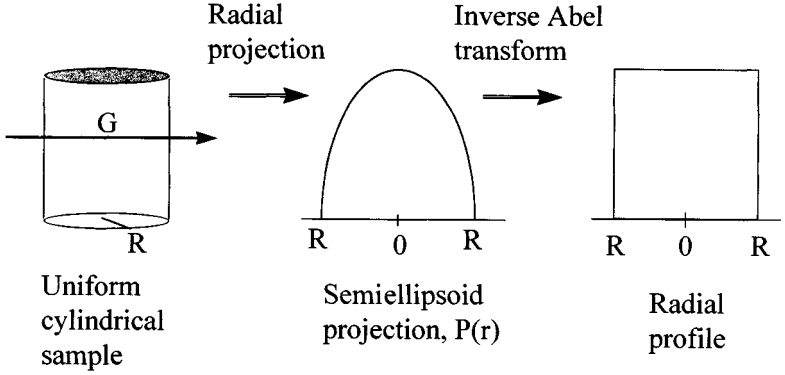

Figure 1.20. Radial projection imaging of a uniform cylinder. The true radial profile (a tophat function in this case) is obtained by inverse Abel transforming the radial projection Re $P(r)$, which is itself obtained by Fourier transforming the echo $S(t)$ obtained in the presence of a transverse external gradient G.

center]. For example, the semiellipsoid projection obtained from a uniform cylinder is converted into a tophat function by the inverse Abel transform (see Figure 1.20). Figure 1.21 shows the experimental radial profiles for two concentric NMR tubes, where the outer tube contains water and the inner tube is either empty or contains a Sephadex microsphere suspension. This figure shows that an inverse Abel transform

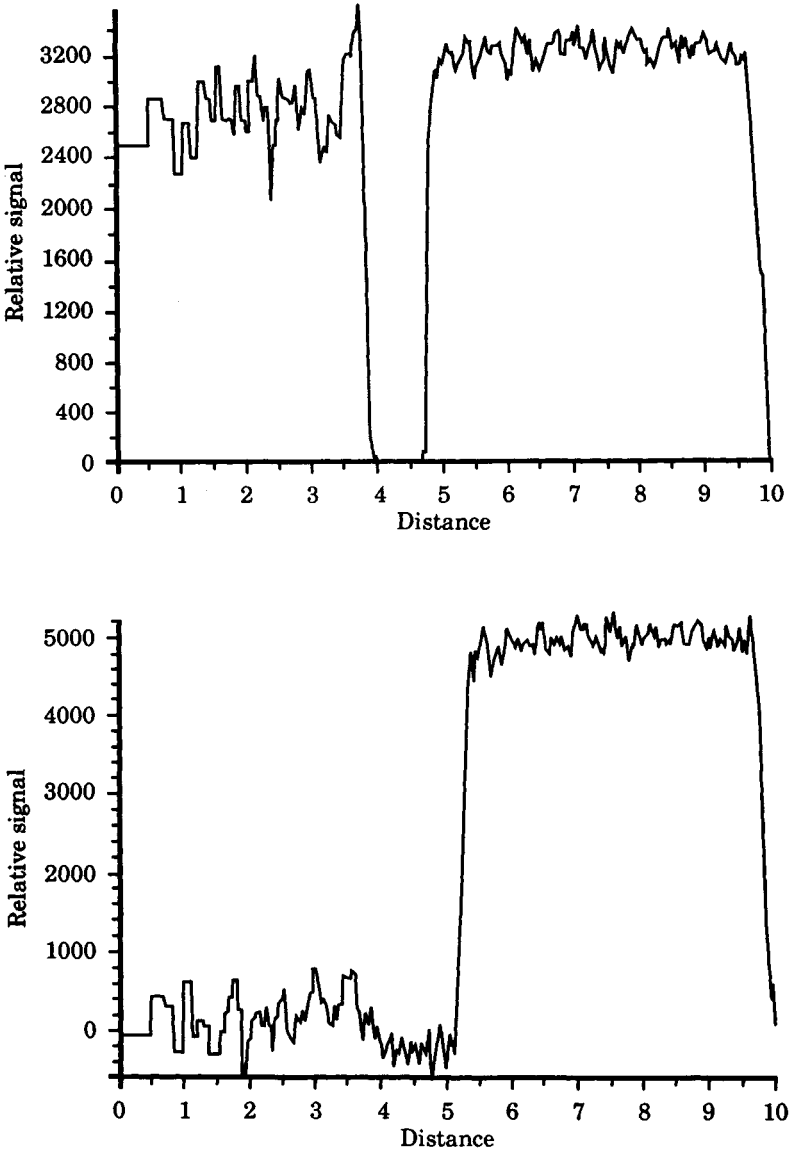

Figure 1.21. Experimental radial profiles for two concentric NMR tubes, the outer containing water and the inner either (*a*) containing a water-saturated uniform bed of Sephadex microspheres or (*b*) empty.

increases the noise near the axis of the cylinder (where the number of voxels is least). This shortcoming can, to some extent, be overcome by optimizing the inverse Abel transform with maximum entropy image enhancement.

Where its use is appropriate, one-dimensional projection imaging is necessarily faster than two- or three-dimensional imaging because the need for repetitive acquisition with ramped phase-encoding gradients is obviated. Moreover, the signal-to-noise ratio is better because each projection records signal from the entire sample. Unlike FLASH, FAST, or EPI fast imaging methods, one-dimensional projection imaging therefore permits a combination of high spatial resolution with high speed. The price to be paid is the assumption that geometric symmetry (e.g., cuboid or cylindrical symmetry) is maintained throughout the sample at all times. In many real samples this symmetry maintenance is only an approximation, so that spatial information is lost and one-dimensional imaging will give only average values. An advantage of projection imaging is that fitting the imaging data with a mathematical model is much easier in one spatial variable than it is in a general asymmetric three-dimensional morphology. Moreover, once the model has been developed in one dimension, it is a straightforward computational exercise to generalize it to more complex sample morphologies and processing conditions.

Of course, the various fast imaging protocols presented in this section are not all mutually exclusive. It is entirely feasible to combine one-dimensional projection imaging with low-tip-angle excitation or with the steady-state acquisition mode, for example, and this could be advantageous in a case such as when maps of several NMR parameters are required on as short a time scale as possible during a rapid food processing operation.

1.10 CHEMICAL SHIFT IMAGING

Up to now the discussion of imaging has neglected the fact that most biological systems, including foods, are complicated mixtures of many different chemical species. We are all aware that the chemical composition of a food is one essential factor determining its quality. In this section we review methods for spatially resolving chemical information: that is, *chemical shift imaging* (CSI), also called *NMR spectroscopic imaging*. There are three main approaches to CSI: CHESS (chemical-shift selective) techniques, four-dimensional Fourier imaging, and echo-time encoded spectroscopic imaging.

1.10.1 CHESS

In the CHESS technique, soft selective pulses (see above) applied in the absence of field gradients are used to excite transverse magnetization only in the spectral region of interest. Once excited, one of the **k**-space imaging methods are used to resolve its spatial distribution. If a Hahn-spin-echo imaging method is used, it is usual to make the 90° pulse chemical-shift selective. The stimulated-echo imaging

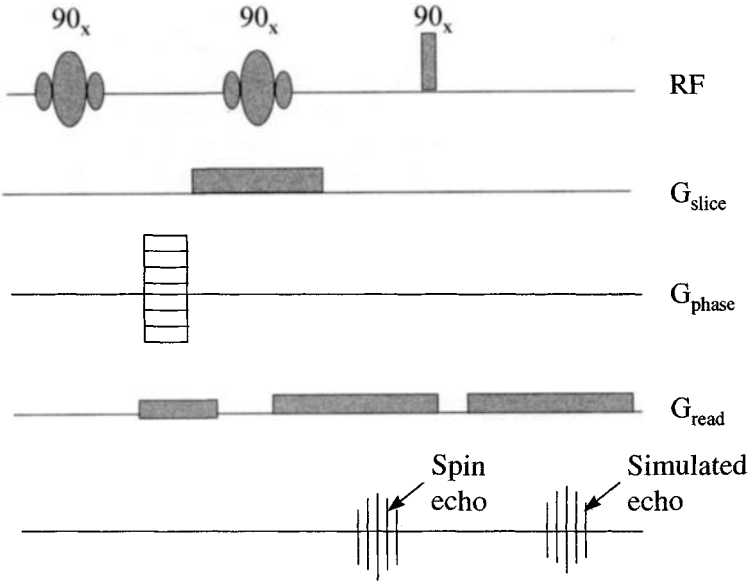

Figure 1.22. Basic three-dimensional CHESS pulse sequence. Chemical shift selection is accomplished by the first soft 90° pulse and three-dimensional imaging by the slice, phase-encoding, and readout gradient pulses.

sequence is especially useful with CHESS because it uses three 90° pulses, so that either the first or last pulse can be made chemical-shift selective and one of the others used for multislice selection. A typical CHESS pulse sequence is shown in Figure 1.22. Note that a spin echo occurs after the second 90° pulse and can also be used for imaging.

CHESS can also be used in a reversed sense for selective removal of particular chemical species from the image. For example, if there are only two frequency-resolved spectral peaks (such as water and lipid), a 180° pulse can be made chemical-shift selective by using a rectangular pulse so that the frequency response given by the Fourier transform in equation (1.23) is a sinc function. The 180° pulse duration is then adjusted so that the spectral peak of interest falls in the central lobe of the sinc function while the other peak falls on the zero node of the sinc function and is therefore suppressed. An alternative strategy in peak suppression, especially useful if the chemical species have very different longitudinal relaxation times, is to use the T_1-*null method* (see Figure 1.23). Here all the magnetization is initially inverted by a hard 180° pulse, after which it begins to recover as the function $[1 - 2\exp(-t/T_1)]$. This shows that the longitudinal magnetization will have recovered to zero after a time T_1 *ln* 2. If one chemical species, such as water, has a very different relaxation time, T_{1w}, then the others, introducing a delay T_{1w} *ln* 2 after the 180° pulse and before the imaging sequence will remove it from the image.

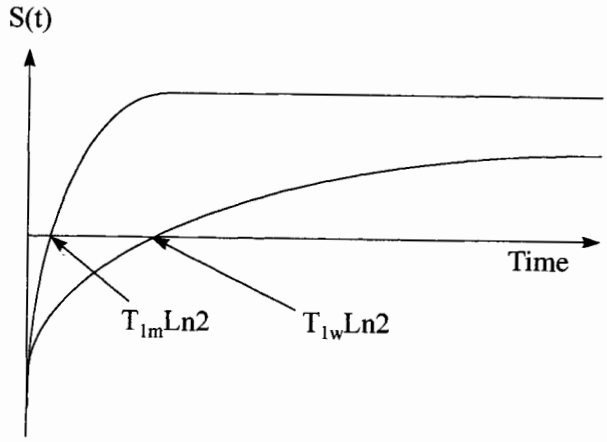

Figure 1.23. T_1-null method for selectively removing the signal from one proton pool.

1.10.2 Four-Dimensional Fourier Imaging

Four-dimensional Fourier imaging could be called [(**k**,**r**);(ω,*t*)]-spectroscopy because it simply uses slice selection and/or phase encoding to resolve the three spatial dimensions and the echo is acquired in the absence of an external (readout) gradient, so that it retains full chemical shift phase information in the time dimension. Fourier transformation of the echo in the wavevector and time domains then gives an image in which each voxel (or slice if only two-dimensional space encoding is used) contains a spectrum in the frequency dimension. Stated formally, the signal observed is

$$S(\mathbf{k},t) = \iint d\mathbf{r}\, d\omega\, P(\mathbf{r},t) \exp(-i\mathbf{k} \cdot \mathbf{r} - i\omega t) \tag{1.31}$$

so that the spectrum in each voxel or slice is obtained by Fourier inversion,

$$P(\mathbf{r},\omega) = \iint d\mathbf{k}\, dt\, S(\mathbf{k},t) \exp(+i\mathbf{k} \cdot \mathbf{r} + i\omega t) \tag{1.32}$$

For example, a spectrum from each voxel could be obtained by acquiring a Hahn echo with nonselective hard 90 and 180° pulses and phase encoding the three spatial directions with ramped gradients (G_x,G_y,G_z) applied between the 90 and 180° pulses. The major drawback with this approach is the long imaging time, which in this example would be $N_xN_yN_zTR$, where TR is the recycle delay and N_i is the number of pixels in the ith direction.

1.10.3 Echo-Time Encoded Spectroscopic Imaging

As its name implies, the basic idea behind this chemical shift imaging technique is the introduction of a new time variable, t', by progressively stepping out the echo time in an imaging sequence in N discrete steps. This shifts the echo position and

introduces a new phase factor, $\exp(-i\omega t')$, where ω contains the chemical shift spectral information. If the echo is acquired in a readout gradient (e.g., along the y-direction), there is also a phase factor from the chemical shift and the applied gradient, $\exp(-i\omega t_y - ik_y y)$, or equivalently, $\exp(-ik_y[y + \omega/\gamma G_y])$. If the x-direction is used for phase encoding and the z-direction for slice selection, the Fourier relationship within a z-slice is therefore

$$S(k_x,k_y,t') = \iiint dx\, dy\, d\omega\, P(x,y,\omega) \exp\left\{-i\left[k_x x + k_y\left(\frac{y+\omega}{\gamma G_y}\right) + \omega t'\right]\right\} \quad (1.33)$$

The required spatially resolved spectrum, $P(x,y,\omega)$, is obtained by inverse Fourier transformation,

$$P\left(x,\left(\frac{y-\omega}{\gamma G_y}\right),\omega\right) = \iiint dk_x\, dk_y\, dt'\, S(k_x,k_y,t') \exp[+i(k_x x + k_y y + \omega t')] \quad (1.34)$$

The image is shifted by $\omega/\gamma G_{y1}$ which is easy to correct by a simple frequency shift after the Fourier inversion. Either the Hahn-echo imaging sequence can be used with step increases in the 90 to 180° pulse spacing, or if a stimulated-echo imaging sequence is used, the separation between the first two 90° pulses can be varied.

The advantage of the echo-time encoding method over the four-dimensional Fourier imaging method is that the number of points in the spectral frequency domain (i.e., the spectral resolution) can be controlled by varying the number of echo-shift steps. If only two spectral peaks need resolving, only a few echo shifts are required and imaging times can be greatly reduced. Even more rapid techniques have been developed by combining chemical shift imaging with the rapid imaging methods mentioned before. Thus EPI–chemical shift methods exist, although the increased imaging speed results in low spatial resolution.

This brief résumé of MRI has probably been sufficient to permit the focus to shift away from the MRI techniques themselves and onto their applications, both realized and potential, in food science. They are the subject of the remaining chapters.

2

MRI AND FOOD PROCESSING: MAPPING MASS TRANSPORT AND PHASE BEHAVIOR

2.1 INTRODUCTION

The fact that water and lipid distributions can be imaged noninvasively accounts for the enormous impact that MRI has had in medical diagnosis, and the reader has no doubt seen examples of the beautifully detailed anatomical images generated in clinical imaging. Similar anatomical detail is important when monitoring the physiological changes in food-bearing plants as they ripen and are subjected to varying environmental conditions. These aspects are considered in Chapter 7. Once a food crop has been harvested, it usually undergoes some form of industrial processing, such as extrusion, cooking, or drying, and here again, the noninvasive attribute of MRI makes it an almost ideal tool for monitoring the processing operation. However, despite this potential, MRI has yet to have a significant impact in industrial food processing, and the reasons are not hard to discern.

To begin with, it is technically demanding to use MRI in a dynamic mode to follow changes in food materials in real time as they undergo processing operations. It is much easier to use MRI to observe *static* food structure in an analogous way to imaging human anatomy, and the early literature abounds in beautiful images of various types of food system, ranging from peach slices to oranges. However, a little reflection shows that there is little to be gained from such noninvasive structural imaging of foods because, unlike humans, they can be physically sectioned with impunity. Moreover, the very best resolutions attainable with MRI (currently, a few microns with specially designed NMR microscopes) cannot seriously compete with those routinely available with transmission electron microscopy (a few nanometers) or even light microscopy (1 to 2 μm). Even a sharp knife and a magnifying glass can give better resolutions than MRI on some large food samples for a fraction of the cost! Such considerations show that unlike clinical imaging, the true potential of

MRI lies not in *static* structure determination of food anatomy but in following, noninvasively, in real time, *dynamic* changes as the foods are processed and stored. Relevant processing operations in the food industry include drying, rehydration, heating, blanching, frying, microwaving, extrusion, curing, mixing, drainage, freezing, and freeze-drying, and even this long list is not exhaustive. Being noninvasive, MRI is well suited for real-time and on-line investigations of all of these processes.

Another reason for the relatively slow exploitation of MRI in food processing science is that providing meaningful information about any of these processes requires the *quantitative* aspect of MRI to be exploited fully. Qualitative observations of changes in image contrast, which are often all that are needed to make a diagnosis in clinical imaging, are usually insufficient in materials science, where the transport of mass, heat, and momentum, and their effect on material properties, is of chief concern. Quantitative MRI is very demanding, and developing appropriate mathematical models for quantitative data analysis also presents an outstanding challenge.

The high cost of imaging facilities is another hindrance to the exploitation of MRI in food science. Few research laboratories specializing in materials science can afford the luxury of a wide-bore superconducting imager and all the associated facilities justifiably needed in clinical imaging. Yet even this situation is changing as it is realized that unlike clinical imaging, it is not always necessary to use state-of-the-art wide-bore imagers to monitor food processing operations. Even one-dimensional profiling with an imager based around a low-cost permanent or resistive magnet can sometimes be all that is needed to follow a mass transport operation. A number of instrument manufacturers are therefore developing low-cost low-field imagers for materials science applications at a fraction of the cost of clinical imaging, and these are beginning to be marketed. There is also a lot of basic research that can be done with a low-cost imaging accessory added on to a conventional high-resolution or high-power NMR spectrometer, especially at microscopic resolutions. For this reason the last five years have seen an ever-accelerating pace of research activity into the development and exploitation of quantitative, dynamic MRI in food and materials science, and it is the author's belief that in future years MRI will have as great an impact in food science as it has had in clinical diagnosis.

2.2 MRI AND PROCESS OPTIMIZATION

The dynamic information emerging from MRI is contained in real-time changes in the NMR parameter maps (or images) referred to in Chapter 1. Depending on the imaging protocol, these include spatial maps of spin number density, relaxation times, magnetization transfer rates, or self-diffusion coefficients. (Velocity maps are considered in Chapter 4.) Figure 1.15 shows some MRI parameter maps for raw carrot and illustrates how each parameter has a characteristic spatial distribution in the tissue. With careful calibration, such NMR parameter maps can be converted into maps of quantities such as moisture content, temperature, and food quality needed for optimizing food processing conditions.

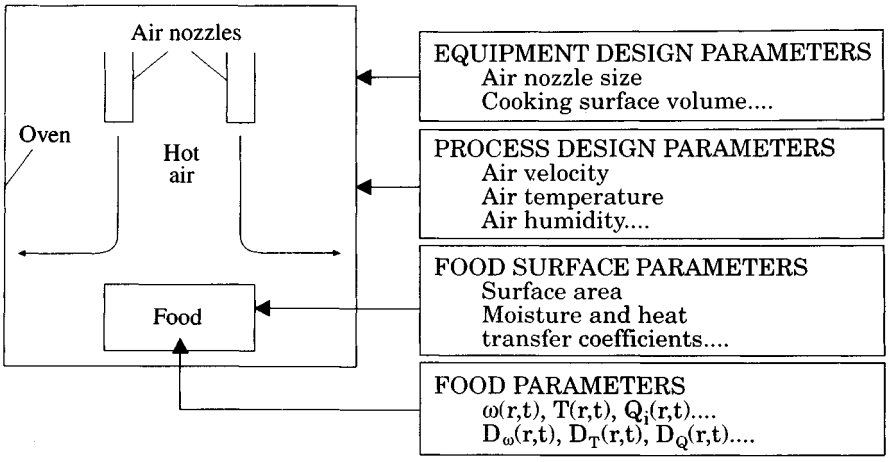

Figure 2.1. Schematic of a dry cooking process in an industrial oven. The various types of parameter needed to simulate the cooking process are listed.

To appreciate the potential impact of MRI in food processing, it is necessary first to review some of the basic ideas underlying process optimization in the food industry. Consider, for example, a dry cooking process as used for industrial roasting, baking, drying, or toasting. A schematic of a baking oven is shown in Figure 2.1. Hot air is blown over a food, such as dough, as it passes on a conveyor through an oven. In this and all other types of food processing the manufacturing operation has to be optimized to produce the desired food quality with minimum cost. Process design and analysis (162) attempts to do this by combining a theoretical simulation of the entire process with selective measurement of parameter values. Parameters in the simulation enter at various levels, which are indicated in Figure 2.1. There are those associated with the equipment design, such as the size of the air nozzles and the oven area-to-volume ratio. Others characterize the process design, such as air velocity, temperature, and relative humidity. Then there are parameters characterizing the food surface, such as the moisture and heat transfer coefficients. Finally, there are parameters characterizing the macroscopic state inside the food, including the time-dependent moisture content distribution $w(r,t)$, temperature distribution $T(r,t)$ food quality factors $Q_i(r,t)$, as well as their associated transport parameters, such as moisture diffusivity, thermal diffusivity, solute diffusivities, and chemical reaction rates. These parameters are functions of time t and of the position $\mathbf{r}$ (which denotes the coordinate x,y,z) within the food sample.

MRI can facilitate the optimization of the entire processing operation by providing real-time measurements of $w(r,t)$ and $T(r,t)$ and, in some cases, $Q_i(r,t)$, both in the bulk food and at the food surface, and each is considered in the following sections. As we shall see, MRI can produce images of $w(r,t)$, $T(r,t)$, and $Q_i(r,t)$ over spatial distances ranging from the microscopic to the macroscopic. In this part of

the book we focus on the macroscopic distance scale; changes on the microscopic scale are considered in Part Two, and the dependence of image contrast on (macro-) molecular characteristics is addressed in Part Three. One of the outstanding research challenges is to relate the MRI information obtained on the microscopic scale to the macroscopic observations, and this is a continuing theme throughout the book.

Ideally, MRI measurements should be made in real time under conditions identical to those used in the industrial processing operation. This is straightforward with processes such as freezing or surface air drying because most imaging probes can be thermostated between -100 and $+100$°C by passing air or nitrogen over the sample. But processes such as high-temperature dry cooking require the design of special heat-shielded cooking equipment that fits inside the bore of the imaging magnet. A less satisfactory but easier alternative is to abandon real-time imaging and remove food samples from various stages of the production line, halt the processing by, for example, freezing in liquid nitrogen, and then image the samples after rapid thawing in the probe.

2.3 DRYING

2.3.1 Drying and Process Optimization

The schematic in Figure 2.1 describes the basic idea behind optimizing food dehydration, but there are many different designs of industrial drying equipment, and this will be reflected in different equipment and processing design parameters in the theoretical models. The list of industrial drying equipment includes the following:

1. *Air dryers.* Hot low-humidity air is passed over the surface of the food in either batch or continuous mode. Batch dryers include simple kiln dryers, suitable for grains, fruits, and vegetables, where food is placed in a grill over a slotted floor and hot gas is blown through the bed from below. Tray dryers are similar except that the food is arranged in racks of trays. Rotary dryers involve agitation of the food in the drying gas and vary in design from simple shaking of the trays to actual rotation of large containers of granular food material in a hot gas stream. In continuous-mode dryers the food material is moved on a conveyor belt along a tunnel through which hot dry gas is passed.
2. *Vacuum dryers.* Used for heat-sensitive foods, especially in the form of slurries, granules, and sheets, the food is dried in a semivacuum. Heat transfer occurs by conduction and radiation (especially through the use of radiant heaters), so drying occurs at much lower temperatures than in air dryers where the hot air provides the major heat source.
3. *Drum dryers.* Suitable for drying liquids and slurries, the liquid flows as a thin film over the surface of an internally heated, rotating drum in a vacuum. The dry powder, or flakes, are then scraped off the drum surface. Milk and soup powders are commonly produced in this way.

4. *Fluidized-bed dryers.* Food particles, usually between 20 μm and 1 cm in size, are suspended in a dry airstream flowing upward through the bed of particles. The air-suspended particles behave, enmasse, like a fluid. Drying is usually fast and can be handled in either batch or continuous mode.

It is, in principle, possible to use MRI to investigate these drying processes directly by designing special small-scale nonmagnetic versions of these various industrial dryers suitable for use inside the core of a whole-body imager. However, this is not really a necessary or desirable thing to attempt because the relevant information needed for process optimization can be obtained more easily in less direct ways. For example, the equipment and process design parameters for each type of dryer can be measured directly in the industrially relevant context and incorporated into equations expressing overall conservation of heat and mass. The main role of MRI is then to obtain the food surface parameters and the internal food parameters needed for process optimization. Before discussing MRI drying studies it is necessary to understand the general features of food drying: in particular, the significance of the constant- and falling-drying-rate periods.

2.3.2 Constant-Drying-Rate Period

Initially, the food surface can be assumed to be water saturated. The rate-limiting step is then transport of moisture from the saturated surface across a thin film of surface air into the bulk of the flowing air. This moisture flux is driven by a gradient of chemical potential of moisture vapor. The initial flux of moisture F from the surface (i.e., the loss of mass per unit area of surface per unit time) can be written

$$F = k_m(W_s - W_b) \tag{2.1}$$

where k_m is the surface mass transfer coefficient, W_s the moisture content of the air at the surface of the solid (which can be assumed to be that of the water-saturated gas), and W_b the moisture content of the air in the bulk gas phase. Provided that the food surface remains wet enough to keep W_s constant, F will also remain constant during drying. This will be the case if the flux of water through the bulk food phase to the surface is fast compared to the flux lost from the surface. The time period over which F is constant is called the initial *constant-drying-rate period* and F is then independent of the mechanism of moisture transport within the food matrix itself. The constant-rate period is, of course, still associated with some decrease in water content at the food surface and with gradients of moisture within the bulk of the sample, which can be monitored with MRI. However, from the viewpoint of the drying kinetics, MRI can add very little new information during the constant-drying-rate period because F is easily measured by direct weighing of the moisture loss, while W_s and W_b can be measured for the gas phase, and the mass transfer coefficient k_m can be calculated from equation (2.1). For process optimization it is necessary to know how k_m depends on process variables such as gas velocity and temperature, but this can be more easily measured than predicted theoretically,

although expressions relating k_m to these variables have been derived (310). During the constant-rate period the surface temperature remains constant and equal to the wet bulb temperature of the air, so the flux of heat q to the surface is simply $F\lambda$, where λ is the molar latent heat of water at the wet bulb temperature.

2.3.3 Falling-Drying-Rate Period

As soon as internal moisture transport to the surface becomes rate limiting, the constant-drying-rate period ends and the drying rate begins to fall. Usually called the *falling-drying-rate period,* the drying rate now depends on the rate of transport of moisture through the food matrix, which is determined by the mechanism of internal moisture transport. Moisture and temperature gradients are set up within the bulk of the food and the loss of moisture causes various amounts of shrinkage, depending on the relative changes in porosity and volume. If the spatial distribution of the shrinkage is not uniform, stress fields will be set up within the food matrix, and if these exceed a critical value, stress cracking can result. The rate of drying can also affect how fast countergradients of dissolved solutes, such as salts and sugars, can be established. This, in turn, determines whether phase changes, such as sugar crystallization, occur at the surface and in the bulk. Rapid surface drying when there are significant concentrations of solutes such as sugars can cause the surface to harden (e.g., enter a glassy state) and act as a moisture permeability barrier, a phenomenon known as *case hardening.* Quantitative modeling of these various changes presents a considerable theoretical challenge, and real-time MRI measurements of moisture gradients $W(\mathbf{r},t)$, temperature gradients $T(\mathbf{r},t)$, diffusion maps $D(\mathbf{r},t)$, solute concentration gradients $Q_s(\mathbf{r},t)$, and changes in the food matrix itself provide a unique window on these complicated processes and can greatly assist in the construction of drying models needed for process optimization. The MRI drying investigations are discussed according to the principal moisture transport mechanism operating during the falling-drying-rate period.

2.3.4 MRI Studies of the Diffusive Drying Mechanism

In the diffusion model it is assumed that viscous forces and permeability barriers within the microstructure of the food prevent coherent velocity flow of water so that moisture movement occurs by random molecular diffusive motion. The only driving force for moisture movement in the diffusion model is therefore the gradient of water chemical potential set up between the drier surface and the rest of the material. Because viscous forces increase with decreasing particle size, materials usually characterized by a diffusive transport mechanism have heterogeneity on a submicron distance scale (e.g., $<10^{-2}$ μm) and include gels, doughs, pasta, and fine pastes. Cellular material such as fruit and vegetable tissue also approximate to the diffusive model because the cell membranes and cell walls act as permeability barriers, preventing coherent fluid flow.

In the diffusion model the moisture distribution $W(\mathbf{r},t)$ is calculated by solving the diffusion equation

$$\frac{\partial W(\mathbf{r},t)}{\partial t} = \nabla\cdot[D(\mathbf{r},t)\,\nabla W(\mathbf{r},t)] \tag{2.2}$$

with appropriate spatial boundary conditions. Very often, equation (2.2) is solved analytically by making simplifying assumptions. For example, by assuming that D is a constant, that the surface moisture content remains constant at w_s, and that there is no shrinkage or case hardening, the solution for a sphere of radius R is found to be

$$\frac{W(t) - w_s}{W(0) - w_s} = \frac{6}{\pi^2}\sum_{n=1}^{\infty}\frac{1}{n^2}\exp\left(\frac{-n^2Dt}{R^2}\right) \tag{2.3}$$

where $W(t)$ is the total integrated water content and $W(0)$ is the initial total moisture content, assumed to be uniform. This relationship shows that the diffusion coefficient can be estimated by fitting the experimental drying data plotted as $\ln[W(t) - w_s]/[W(0) - w_s]$ against t, where $W(t)$ is measured by periodically weighing the sample as it dries.

There are a number of difficulties with this somewhat naive approach. First, the water diffusivity D is not usually a constant but depends on the local moisture content and can become time dependent if there are changes in the food matrix that are slower than the moisture diffusion rate. Second, the surface moisture content usually decreases during drying and is therefore not constant. Instead, a flux boundary condition needs to be used, involving the interfacial mass transfer coefficient h, which will itself depend on process variables such as airspeed, humidity, and temperature as well as on the moisture content and temperature of the surface. Third, there is usually some degree of shrinkage during drying, and this, in general, will not be uniform throughout the sample but will itself depend on the spatial water content distribution. Fourth, the calculation above assumes isothermal drying conditions, which may not be valid if thermal transport is slow compared to the mass transport.

These more complicated phenomena can, in principle, be described using a more general diffusion model that couples the equations of heat and mass transport

$$\frac{\partial W(\mathbf{r},t)}{\partial t} = \nabla\cdot[D(\mathbf{r},t)\,\nabla W(\mathbf{r},t)] \tag{2.4}$$

$$\frac{\partial T(\mathbf{r},t)}{\partial t} = \nabla\cdot[K(\mathbf{r},t)\,\nabla T(\mathbf{r},t)] - C_p\frac{\partial W(\mathbf{r},t)}{\partial t} \tag{2.5}$$

Here C_p is the heat of vaporization and the last term in equation (2.5) is the heat required to evaporate the water, which couples the two equations. Of course, the diffusion coefficient $D(\mathbf{r},t)$ and thermal diffusion coefficient $K(\mathbf{r},t)$ also couple the equations because both are dependent on the local values of $W(\mathbf{r},t)$ and $T(\mathbf{r},t)$:

$$D(\mathbf{r},t) = F_1(W(\mathbf{r},t),T(\mathbf{r},t)) \tag{2.6}$$

$$K(\mathbf{r},t) = F_2(W(\mathbf{r},t),T(\mathbf{r},t)) \tag{2.7}$$

Unfortunately, the form of the functions $F_1(\cdot)$ and $F_2(\cdot)$ is not, in general, known and has to be determined either independently or by fitting the MRI data. Equations (2.4) to (2.7) need to be solved with appropriate surface boundary conditions involving changing surface moisture content and temperature. Nonuniform shrinkage also needs to be taken into account during numerical solution of the equations, which for simple geometries can be done with finite-element methods. If the moisture transport is associated with counter transport of solutes, a third coupled equation describing solute transport is needed.

Attempts have been made to solve such systems of equations numerically and compare the results with weight-loss data and measurements of temperature using thermocouples located at various points in the sample. However, measurements of overall weight loss or even of weight loss in finite-sized slices cut with a microtome are too crude to provide adequate tests of the model. It is in this context that the value of MRI becomes apparent. By providing real-time noninvasive maps of the moisture distribution $W(r,t)$, surface moisture content $W(\text{surface},t)$, shrinkage factors, temperature maps $T(r,t)$, and diffusion maps $D(r,t)$, MRI can greatly assist in testing and refining generalized diffusion models and in providing values for parameters such as the surface mass and heat transfer coefficients. In principle, once a satisfactory model with quantitative parameter values has been determined in this way, it can be incorporated, together with the equipment and processing variables, into the process optimization routines.

Despite the attractiveness of this scheme, progress in implementing it has been slow. There have been several examples where MRI has been used to provide moisture maps $w(r,t)$, but to date there are no examples of real-time combined MRI moisture, temperature, and diffusion mapping of a food drying process and this remains an outstanding future challenge. Moreover, the MRI data have so far served merely to highlight the inadequacies of the diffusion model, even in the general form expressed in equations (2.4) to (2.7).

One of the first examples of a quantitative MRI drying study, undertaken by Schrader and Litchfield (181), involved drying a cylinder of agar gel containing microcrystalline cellulose, which, although a model system, exhibits many of the characteristic features of food materials and is expected to conform to a diffusion-controlled drying mechanism. The gel was dried in a radially symmetric airstream of controlled humidity, velocity, and temperature inside the MRI probe. Two-dimensional spin-echo images were acquired with slice selection across the middle part of the cylinder with a short echo time (TE) and long repetition time (TR) to

minimize relaxation weighting. The two-dimensional images were converted into moisture content maps by calibrating signal intensity against moisture content (actually, solid content) using a series of homogeneous gel samples dried to known moisture contents and allowed to equilibrate for at least 24 h. Figure 2.2 shows some representative cross-sectional moisture contents determined in this way. The MRI results in Figure 2.1 reveal the true complexity of the drying process even for this model gel system. It is obvious that the simple diffusion model with a constant diffusion coefficient, equation (2.2), fails to provide a quantitative fit to the moisture profiles. In particular, the experimental profiles do not have the characteristic parabolic shape predicted by Fickian diffusion with a constant diffusion coefficient but are flatter in the middle and decrease more rapidly near the surface. Moreover, the surface moisture content is seen to decrease during drying and is accompanied by shrinkage. Attempts to model the experimental profiles in the isothermal limit with equations (2.4) to (2.7) with a diffusion coefficient that varied with local moisture content also failed to provide a quantitative fit to the profiles. A yet more sophisticated model incorporating nonuniform shrinkage and variable surface boundary conditions is undoubtedly needed but was not implemented in this exploratory MRI study.

The drying of extruded pasta has also been investigated with MRI by the author and colleagues. During the manufacture of pasta such as spaghetti, the extrusion step is followed by drying in a hot airstream so that the spaghetti can be packed and stored as the familiar bundles of straight, hard spaghetti cylinders. The drying step has to be optimized very carefully because drying at too fast a rate sets up severe moisture gradients in the pasta, which causes differential shrinkage, bending, and stress cracking. On the other hand, drying too slowly in a hot, humid atmosphere permits the growth of spoilage microorganisms. To optimize the drying conditions it is therefore necessary to understand the mechanism of pasta drying. For this purpose the drying kinetics have been investigated with fast radial microimaging (see Chapter 1). To permit unhindered shrinkage and a radially symmetric flow of dry air around the pasta, a specially designed holder is required. This is shown in Figure 2.3 for pasta freezing (see Section 2.5), but the same design applies to the drying experiment.

In this MRI study no attempt was made to simulate real industrial drying conditions in the probe. Rather, the purpose was to investigate the drying mechanism itself. Accordingly, the drying process was made essentially isothermal using an air temperature of 26°C, which is only slightly above room temperature. The small dimensions of spaghetti also meant that moisture gradients were established rapidly, so the imaging acquisition time was minimized by exploiting the cylindrical symmetry of the sample by taking only one-dimensional projections across the pasta cylinder (after slice selection) and using an inverse Abel transform to extract the radial signal profile $P(r,t)$ (see Chapter 1). A maximum entropy signal optimization algorithm was also used to smooth and enhance the radial profiles. In this way profiles could be acquired every few seconds with spatial resolutions of about 30 μm. A set of projections and their corresponding maximum entropy inverse Abel transforms are shown in Figures 2.4 and 2.5.

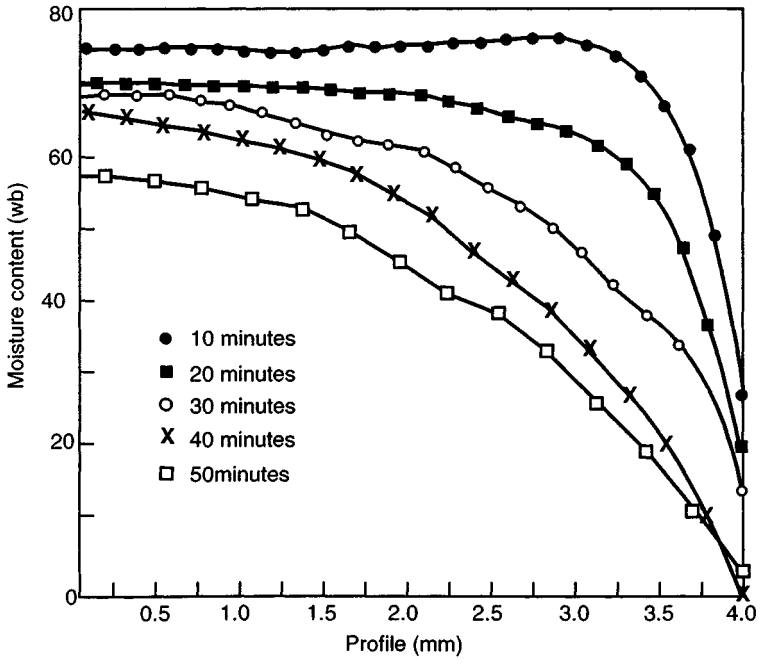

Figure 2.2. Moisture profiles of a model food gel during drying at 30°C scaled to adjust for shrinkage. The center of the cylinder is at 0.0. (From Ref. 181.)

Like the previous gel study, the MRI results reveal the real complexity of the pasta drying process. Shrinkage is observed both in the images and with a traveling optical microscope with samples dried under conditions similar to those used in the probe. Comparison of the MRI and optical radii suggests that a type of case hardening may be occurring in which the surface rapidly dries to form a drier shell around the wet inner core. The existence of this drier shell makes it difficult to determine the time dependence of the surface moisture content because this depends critically on the choice of the position of the outer edge of the pasta cylinder. Moreover, in this sample the initial moisture distribution is not uniform because the outside of the pasta is more hydrated than the inside. Not surprisingly, attempts to model these observations with equations (2.4) and (2.6) were only partly successful. The function F_1 was assumed to have an exponential form such that

$$D(r,t) = A \exp[BS(r,t)] \tag{2.8}$$

where $S(r,t)$ is the local degree of saturation defined as the ratio of the actual moisture content to that for the saturated sample. A crude attempt to model nonuniform shrinkage was made by reducing the number of cells in the numerical simulation

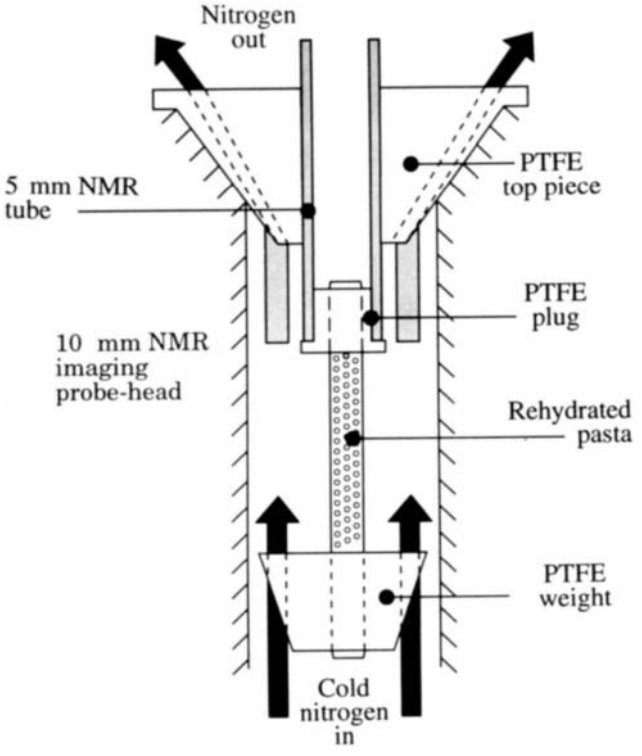

Cross section of
top piece and weight

Figure 2.3. Probe arrangement for the drying and freezing of cylinders of pasta and potato. For drying, the cold nitrogen gas used for freezing is heated and dried to the desired temperature and humidity.

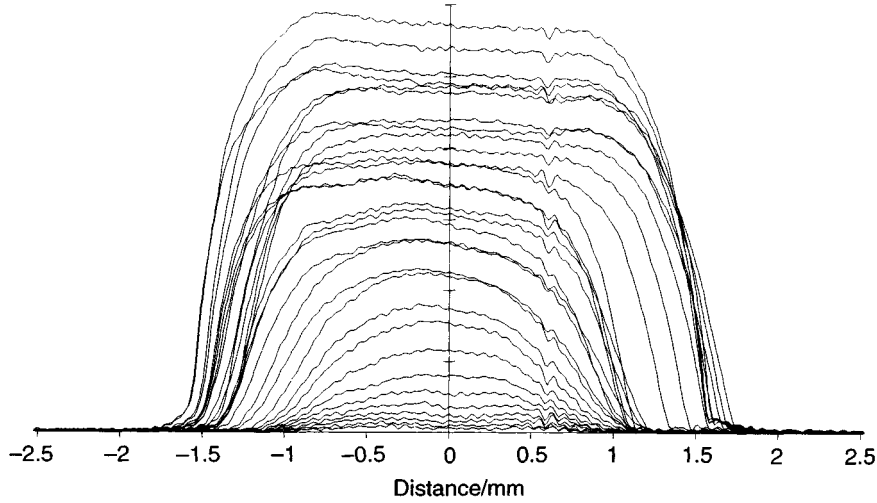

Figure 2.4. Transverse projections of rehydrated pasta during drying in the apparatus in Figure 2.3. Each profile was the result of a single acquisition with slice selection along the cylinder axis and a single gradient applied across the cylinder. The distortion near 0.5 mm is probably a small air bubble.

using the measured dependence of shrinkage on moisture content and the equation expressing local conservation of mass in a cylindrical geometry. To incorporate the rapid surface drying, the surface was assumed to dry essentially instantaneously, giving a boundary condition $W(R,t) = 0$, where R is the cylinder radius. The theoretical moisture profiles are reproduced in Figure 2.6 and succeed in reproducing the qualitative trends in the data, such as shrinkage and profile shape, but fail to provide a good quantitative fit to the data. Here again the MRI results highlight the need for more sophisticated drying models where case hardening is more explicitly treated, perhaps as a rubber–glass transition.

MRI has also been used to image moisture profiles in cellular tissue such as potato and apple during air drying. Potatoes are the leading vegetable crop in the world, with more than 340 million tons being produced annually at a value of nearly $30 billion. Understanding water transport in the raw tissue is important since it affects the quality and structural changes in potatoes during storage and handling and during processes such as freeze-drying, freezing-thawing, and cooking. Ruan et al. (180) used MRI to study moisture profiles during the air drying of raw potato cylinders (see Figure 2.7). The ends of 2-cm-diameter potato cylinders were coated with wax to prevent end drying and a two-dimensional spin-warp imaging sequence was used for a slice selected near the center of the 7-cm-long potato cylinder. Figure 2.6 shows typical moisture profiles during the potato drying, taken from Ruan et al. To minimize relaxation effects, TR was much longer than T_1 and TE was adjusted to equal the average T_2 for the mean moisture content at each drying time. In this way the factor $\exp(-TE/T_2)$ was kept essentially constant so that image intensities were proportional to moisture contents. The image intensi-

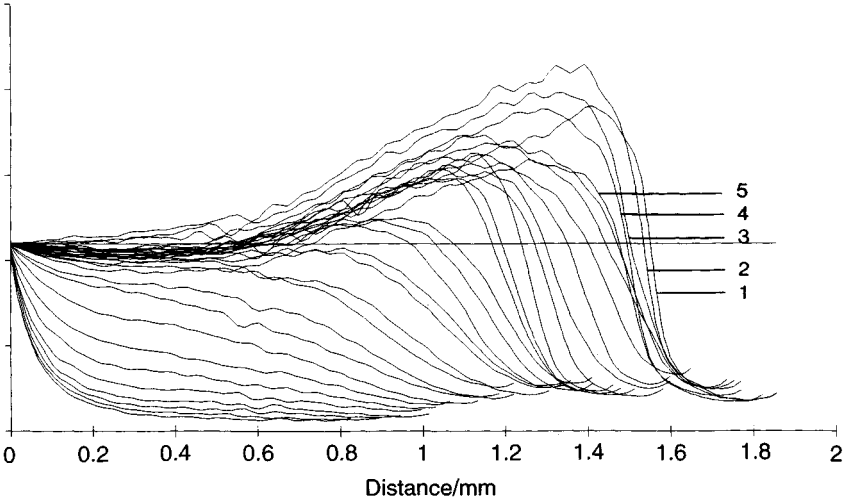

Figure 2.5. Radial profiles resulting from the inverse Abel transformation of the projections in Figure 2.4. The signal-to-noise ratio has been optimized by the maximum entropy method (MEM). The zero on the distance scale corresponds to the center of the cylinder.

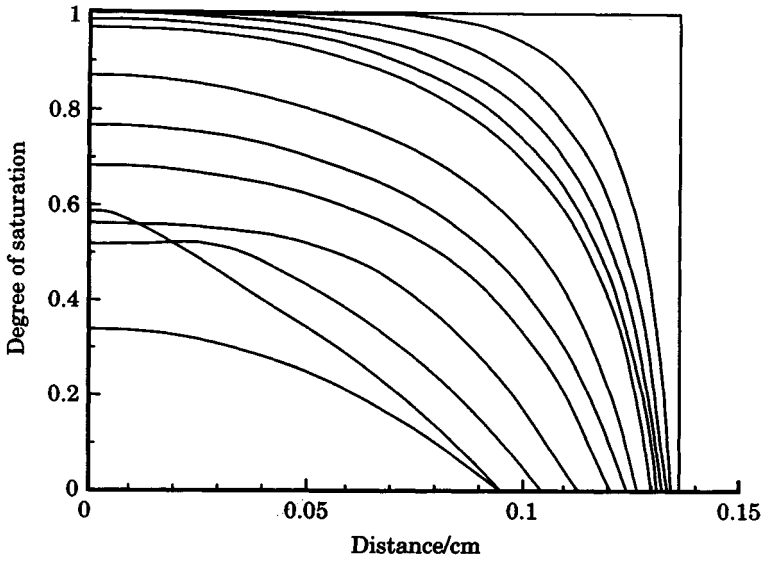

Figure 2.6. Theoretical profiles for moisture distribution during the drying of spaghetti. An attempt has been made to incorporate nonuniform shrinkage and moisture-dependent diffusivities into the model. Only semiquantitative agreement is found with the experimental profiles in Figure 2.5. The penultimate profile is a shrinkage artifact.

ties were calibrated against moisture content using equilibrated slices of various moisture contents which were determined by vacuum drying to constant weight. Air drying within the probe was achieved using low humidity air at 60°C, and the temperature gradients within the sample were measured every 30 min using positioned thermocouples.

The experimental moisture and temperature profiles were modeled by solving equations (2.4) and (2.5) with a variable moisture-dependent diffusion coefficient. This was done by first solving the moisture diffusion equation, then calculating the moisture loss from the sample and the resulting heat loss by evaporation. Finally, the thermal transport equation was solved using the calculated heat loss. The functional form F_1 in equation (2.6) was determined from the moisture profiles by least-squares fitting the MRI profiles with the simple Fick's law [equation (2.2)] so that an average diffusion coefficient was obtained as a function of average moisture content, which was obtained by integrating the moisture profile. This approximate procedure gave an exponential functional form similar to equation (2.8). Even when the coupled heat and mass transport were taken into account, the theoretical profiles still failed to provide a quantitative fit to the data. As with the gel and pasta samples, this could arise because of an inadequate treatment of shrinkage, since only an average shrinkage effect was incorporated at each step based on an independently measured shrinkage curve. The possible existence of surface case hardening may also need to be explicitly treated.

A spin-warp imaging sequence with $TR \gg T_1$ has been used to follow apple drying by McCarthy and Perez (179). Unlike the previous studies, a $5 \times 5 \times 2$ cm rectangular slab of apple was used so that a one-dimensional model could be used to fit the data. Fortunately, T_2 was independent of moisture content over the range of interest, so the measured image intensities were proportional to moisture content and could be scaled to the initial, gravimetrically determined moisture content (on a volume basis). The moisture profiles are shown in Figure 2.8 and again reveal the

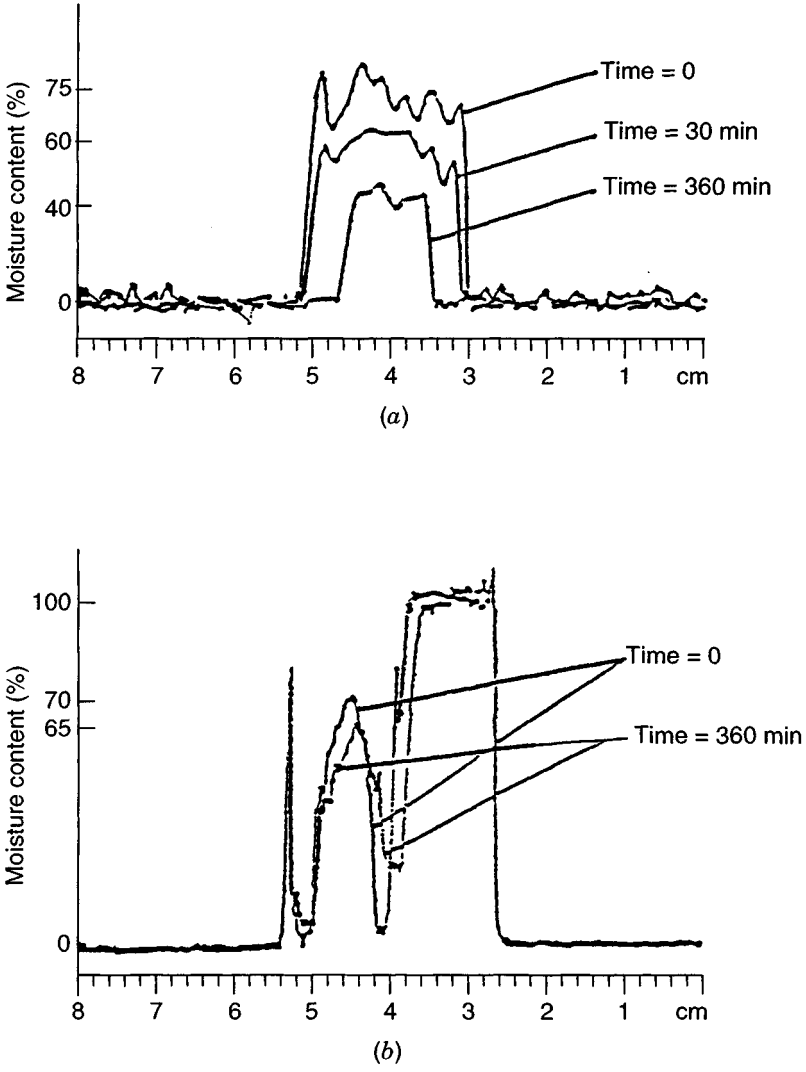

Figure 2.7. Moisture profiles for the drying and rehydration of potato cylinders. (From Ref. 180.)

non-Fickian nature of the drying process. The profiles also show that shrinkage can be neglected, so it is a pity that no attempt was made to model them. Instead, an effective moisture-dependent diffusivity was extracted using an integral form of the Fick's law relationship,

$$D(W^*) = -0.5\partial\left(\frac{x/t^{0.5}}{\partial W^*}\right)\int_0^{W^*} dW^* \frac{x}{t^{0.5}} \tag{2.9}$$

where W* is the dimensionless factor, $[W(0) - W(x)]/W(0)$, measured from the image profiles as a function of distance x (179). The possibility of modeling the drying of cellular tissue by explicitly treating its cellular microstructure is considered in Chapter 9.

MRI drying studies have also been performed on several intact fruits and vegetables, although because of the increased morphological complexity, no attempts were made to model the results with diffusion equations. Song and Litchfield have undertaken three-dimensional imaging of the drying in a corn kernel (182,185). This research also explored the origins of stress cracking in kernels and determined the effects on crack development of factors such as variety, drying temperature, and moisture content. The oil signal was eliminated by subtracting images from the initial image at successive time intervals. This permitted the areas of the corn kernel having the greatest changes in moisture content to be seen. A drying front was observed to move gradually from the kernel surface into the central area. In addition, a second moisture transfer route through the glandular layer of the scutellum was observed during drying. While considering the drying of plant tissue, it is worth mentioning that Pope et al. (72, 93) have imaged the distribution of water in sultana grapes before and after drying for 24 h at 40°C. However, a fuller discussion of the application of MRI to plants will be delayed until Chapter 7. Clearly, the MRI data so far presented highlight the true complexity of food drying, even in cases where the diffusion mechanism is believed to occur. An even greater degree of complexity is encountered when other transport mechanisms are considered, such as transport induced by capillary forces, to which we now turn.

2.3.5 MRI Studies of the Capillary Drying Mechanism

Many foods exhibit structural heterogeneity on a microscopic distance scale ranging from 0.1 to several hundreds of microns. In these course-grained materials, frictional forces are not necessarily capable of preventing localized percolative fluid flow within the porous matrix so that, besides the gradient of water chemical potential (μ), other forces, such as capillary forces and gravity, which drive coherent flow need to be included in the transport equation. On a macroscopic distance scale, the equation for the fluid velocity flow $\mathbf{v}(\mathbf{r},t)$ can be written (220):

$$\mathbf{v}(\mathbf{r},t) = \frac{-K_r K^0}{\eta}(\nabla p - \mathbf{g}\rho) - L\nabla\mu \tag{2.10}$$

Here K^0 is the Darcy permeability coefficient for the pure fluid, expressing the proportionality between the flow rate and the pressure gradient, which has contributions from capillary forces (the term ∇p) and from gravity (the term $\mathbf{g}\rho$). K_r ($0 \leq K_r \leq 1$) is the relative Darcy permeability for water and air, η the shear viscosity, ρ the fluid density, and L the Onsager coefficient for diffusion (306). Equation (2.10) can be combined with the equation expressing mass conservation,

$$\frac{\phi \partial(\rho S)}{\partial t} = -\nabla \cdot (\rho \mathbf{v}) \tag{2.11}$$

where ϕ is the porosity and $S(r,t)$ ($0 \leq S \leq 1$) is the degree of saturation, defined as the ratio of the volume of fluid per unit volume of sample located at r, divided by the same ratio in the saturated sample. Substituting equation (2.10) into (2.11) and assuming fluid incompressibility and the absence of external pressure gradients, we obtain a more general diffusion-type equation for isothermal drying:

$$\frac{\partial S}{\partial t} = \nabla \cdot [(D_\mu(S) + D_c(S)] \nabla S - \left(\frac{g\rho K^0}{\phi \eta}\right) \nabla K_r(S) \tag{2.12}$$

where

$$D_\mu(S) = L\phi^{-1}\left(\frac{\partial \mu}{\partial S}\right)_T \tag{2.13}$$

$$D_c(S) = K^0 K_r(S) \phi^{-1} \eta^{-1} \left(\frac{\partial P}{\partial S}\right)_T \tag{2.14}$$

$D_\mu(S)$ is the usual diffusion coefficient arising from the gradient of chemical potential, while the capillary force term has been written in the form of a diffusion equation with a diffusion coefficient, $D_c(S)$. The final term in equation (2.12) is the gravity effect.

Various limiting cases of equation (2.12) can be considered. If frictional forces are very strong, the Darcy coefficient K^0 will be negligible compared to the chemical potential gradient term and the equation reduces to the conventional Fickian diffusion equation (2.2). In the opposite limit, when frictional forces are negligible, as in coarser-grained wet granular foods having pores in excess of 100 μm, it can usually be assumed that a steady-state capillary profile exists resulting from a balance between capillary and gravitational forces. Setting D_μ and $\partial S/\partial t$ to zero, equation (2.12) then reduces to

$$D_c(S) \frac{\partial S}{\partial x} = \frac{g\rho K^0}{\phi \eta} K_r \tag{2.15}$$

Substituting $D_c(S)$ from equation (2.14), the water profile $S(x,t)$ in the direction of gravity is obtained by solution of the equation

$$\frac{\partial S}{\partial x} = g\rho \frac{\partial S}{\partial P_c} \tag{2.16}$$

This shows that the MRI measurement of the moisture profile $S(x,t)$ is, in this limit, also a measurement of $S(P_c)$ or conversely, of $P_c(S)$, the dependence of the capillary suction pressure on the degree of saturation. Equation (2.16) can be integrated by noting that $\partial S/P_c = (\partial S/\partial x)\ (\partial x/\partial P_c)$, which shows the linear dependence of the suction pressure on distance, $P_c(t) = g\rho x + P_s(t)$, where $P_s(t)$ is the surface suction pressure at time t. Equation (2.16) is therefore merely a change of variables from x to $P_c/g\rho$ and shows that the MRI profiles of $S(x)$ are sections through the $S(P_c)$ curve so that MRI profiles in capillary-porous materials can be used to determine $S(P_c)$. Figure 2.9 shows an example of this correspondence for an initially water-saturated randomly packed bed of 400-μm-diameter spherical glass microspheres after 800 min of surface air drying under controlled conditions. In this example the glass microsphere bed was set up in a 5-cm-diameter cylindrical vessel and had a depth of 6.5 cm. Spin-echo images were taken by slice selecting down the center of the cylinder and then projecting the slice across the cylinder. The left-hand side of the profile corresponds to the bottom of the bed and remains water saturated, whereas the surface degree of saturation is seen to have fallen to 0.2 after 800 min of drying.

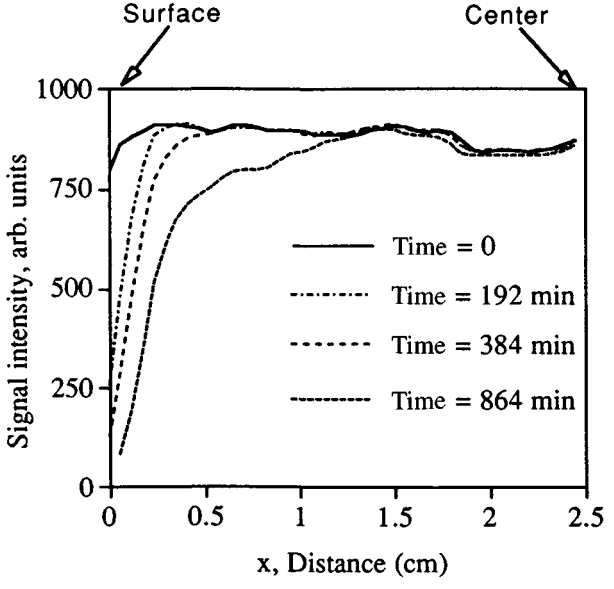

Figure 2.8. Moisture profiles as a function of time and position for the drying of an apple slab. The surface is at $x = 0$ at time zero. (From Ref. 179.)

The inset in Figure 2.9 shows the dependence of the degree of saturation S on capillary suction potential P_c, determined independently for a glass bead bed, and confirms that the MRI profile is indeed a section through the $S(P_c)$ curve.

As the pore size becomes smaller, $\partial S/\partial P_c$ decreases, so according to equation (2.16), the slope, $\partial S/\partial x$, also decreases and the MRI moisture profiles become flatter. In the limit of very small pores a completely flat moisture profile is predicted because capillary forces, which flatten the profile, far exceed the gravitational force, which causes a gradient in the direction of gravity. This prediction has been tested in the glass microsphere bed by varying the capillary force term, given approximately as γ/R, by changing the surface tension γ of the water by addition of a surfactant and using microspheres of varying radius R. A comparison of profiles A and B in Figure 2.10 confirms the tendency of the MRI profiles to flatten with increas-

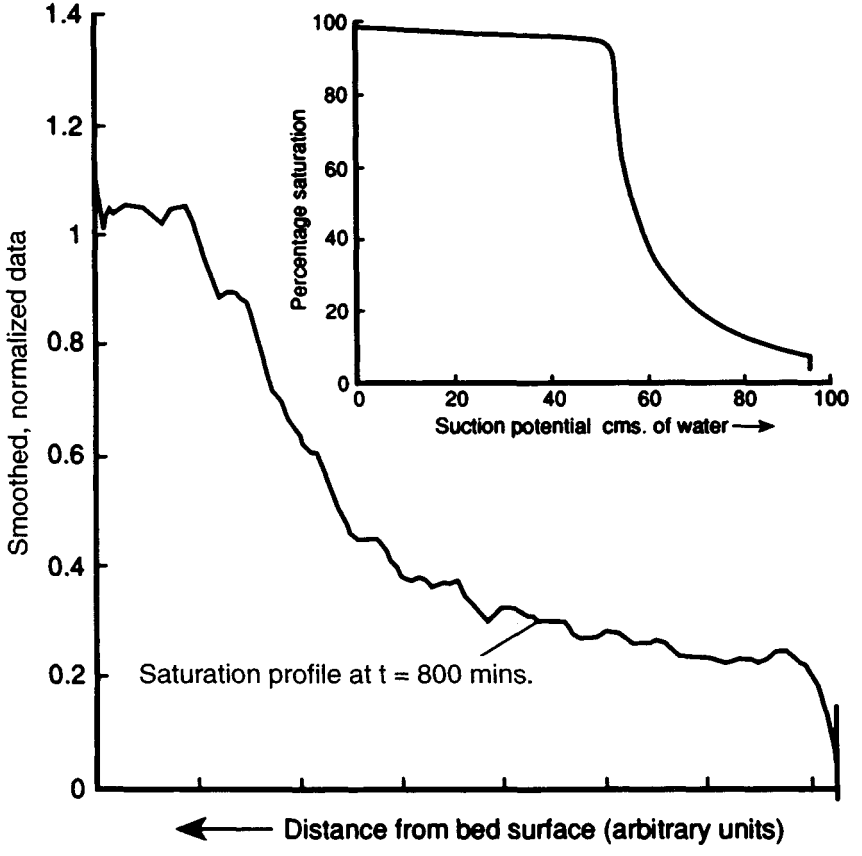

Figure 2.9. Moisture profile (degree of saturation) through a bed of glass microspheres after 800 min of drying. The bottom of the bed is at the left-hand edge and is still saturated. The surface has reached a degree of saturation of about 0.2. The profile has a shape similar to that of the suction potential, which is shown in the inset.

ing γ/R. However, it is also noticeable that at high capillary suction pressures, irregularities appear in the profiles (see, profiles *C* and *D* in Figure 2.10). These irregularities are a result of the inhomogeneous packing of microspheres in the bed and arise because capillary forces draw water preferentially out of large pores in regions of low packing density. Profile *D* is an extreme case of such irregularity in that this sample actually dries fastest at the closed lower end of the bed rather than at the exposed surface because the packing density is lowest at the bottom of the bed, where the existence of the glass wall hinders dense packing of the microspheres.

Another characteristic feature of capillary drying mechanisms is the existence of rapidly fluctuating transients in the moisture profiles. These are caused by the percolative counterflows of air and water through the material. This phenomenon has been imaged by Maneval et al. (307), who compared two-dimensional images taken at various positions across glass microsphere beds during surface air drying. This type of image should provide detailed tests of percolation theories of the transport, especially if a statistical analysis of correlation lengths is undertaken on various distance scales using, for example, Patterson function analysis (see Chapter 1). Such statistical information is difficult to obtain with conventional invasive techniques such as physical slicing and weighing.

Although we have considered the countertransport of water and air during the drying of capillary-porous materials, very similar considerations apply to multiphase transport of water and oil in these materials. These phases can be separated either by chemical shift imaging or by perdeuterating one of the phases (e.g., using D_2O instead of water) or by using fluorine imaging with a fluorinated oil phase.

The capillary-gravitational transport mechanism applies only to the fluid-phase transport and therefore ceases to function when the amount of fluid phase is too small to maintain connectivity throughout the bed. In the language of percolation theory, this critical fluid content is called the *percolation threshold,* and in soil science, the state of *zero fluid connectivity* or the *pendular state,* because the liquid water is believed to be located only at the point of contact between the particles comprising the insoluble solid phase. Below the percolation threshold, moisture transport proceeds by vapor-phase diffusion, to which we now turn.

2.3.6 Vapor-Phase Diffusive Transport Mechanisms

The basic ideas underpinning theories of vapor-phase transport have been presented in books by Crank (178) and Sahimi (187). It is appropriate to low-water-content porous media where there is local equilibrium between water in the vapor phase and water in a condensed phase, either within micropores in granules or perhaps as a surface layer of adsorbed water. Within each phase the transport is determined by simple Fickian diffusion such that

$$\frac{\partial W_v}{\partial t} = \frac{\partial}{\partial x} D_v \frac{\partial W_v}{\partial x} - \frac{\partial F}{\partial t} \tag{2.17}$$

$$\frac{\partial W_s}{\partial t} = \frac{\partial}{\partial x} D_s \frac{\partial W_s}{\partial x} + \frac{\partial F}{\partial t} \tag{2.18}$$

where W_v and W_s are the vapor- and condensed-phase water concentrations, respectively, and D_v and D_s are the corresponding diffusion coefficients. For simplicity it is assumed that the diffusion coefficients are constants, independent of moisture concentration, but this is not a necessary assumption. $\partial F/\partial t$ is the exchange rate between the two phases, which is unknown but can be eliminated by simple addition of the two equations, which gives

$$\partial \frac{(W_v + W_s)}{\partial t} = \frac{\partial}{\partial x}\left(D_v \frac{\partial W_v}{\partial x} + D_s \frac{\partial W_s}{\partial x}\right) \tag{2.19}$$

Because it is assumed that there is rapid exchange of water molecules between the two microphases, local equilibrium exists, so the concentrations are related by the equilibrium sorption isotherm. For mathematical simplicity an exponential form of isotherm can be assumed, but a similar analysis can be performed with other, more general forms of isotherm. An exponential isotherm can be written:

$$W_v = W_v^0 \exp\left(\frac{W_s}{W_s^0}\right) \tag{2.20}$$

Noting that

$$\frac{\partial W_v}{\partial x} = \frac{dW_v}{dW_s}\frac{\partial W_s}{\partial x} = \frac{W_v^0}{W_s^0}\exp\left(\frac{W_s}{W_s^0}\right)\frac{\partial W_s}{\partial x} \tag{2.21}$$

and that $W_p \gg W_v$, it follows that

$$\frac{\partial W_s}{\partial x} = \frac{\partial}{\partial x} D_{\text{eff}} \frac{\partial W_s}{\partial x} \tag{2.22}$$

This is in the form of a diffusion equation with an effective concentration-dependent diffusion coefficient given as

$$D_{\text{eff}} = D_s + \frac{D_v W_v^0}{W_s^0}\exp\left(\frac{W_s}{W_s^0}\right) \tag{2.23}$$

Equations (2.22) and (2.23) have been used by Hughes, McDonald, and co-workers (16,17) to fit the MRI profiles observed during the drying of zeolites and porous rocks. The profiles were measured with the gradient-echo solid-state imaging method because of the low water contents and short transverse relaxation times. Solid imaging techniques are only now beginning to be used to study water transport during the drying of low-water microporous food materials. The potential for this type of study is discussed more fully in Chapter 5.

2.4 REHYDRATION

2.4.1 Rehydrating Pasta

Most dried foods are rehydrated by the consumer before eating, so it is important to ensure that the rehydrated product has a satisfactory quality. A detailed MRI study of rehydration of spaghetti has been reported. With spaghetti, the stickiness and cohesion after rehydration are important quality factors and the rehydration rate should obviously not be too slow. These quality considerations affect both the choice of wheat used to make the spaghetti and the extrusion temperature. Hard durum wheat, soft wheats, and mixtures of the two types can be used in the extrusion process, and the choice profoundly alters the rehydration kinetics. MRI can assist in optimizing the choice of raw material by providing detailed information about the moisture profiles within individual spaghetti strands during rehydration (228). To do this, dry spaghetti, extruded from various types of wheat, was immersed in water at 80°C and samples removed every few minutes for radial imaging with a spin-echo sequence. Because the water content of dry pasta is very low and remains low during the early stages of rehydration, the radial images have to be compensated for signal loss due to fast relaxation. This problem was circumvented by directly imaging radial maps of the effective water proton transverse relaxation time measured by increasing the number of echoes in a CPMG preparation sequence introduced before the radial imaging pulses sequence. The T_2 maps were then converted to water-content maps using a calibration curve obtained for small, uniformly rehydrated pasta samples of varying gravimetrically determined water content. Figure 2.11 shows the radial moisture profile obtained 2 and 7 min after immersion of the spaghetti in water at 80°C.

The rehydration results were modeled in an analogous way to drying by numerically solving the diffusion equation, taking account of sample expansion during rehydration as well as the dependence on local water content of the water self-diffusion coefficient. The dashed lines in Figure 2.11 show the theoretical fit to the data. Although the theory provided only a semiquantitative explanation of the imaging data, it clearly establishes that increasing the proportion of soft wheat in the extrusion mix shifts the diffusion kinetics away from case II Fickian diffusion kinetics, observed with hard wheat pasta, toward the profiles expected for classical Fickian diffusion (178, 228).

The fact that rehydration starts with a dry food suggests the use of solid-imaging techniques. This has not yet been attempted with pasta, although a STRAFI solid-imaging study (see Chapter 5) on the rehydration of a related model system (a starch glass) by liquid water and by water vapor has been reported by I. Hopkinson and R. A. L. Jones, of the Cavendish Laboratory, Cambridge (abstract at the British Radiofrequency Spectroscopy Group meeting at Surrey, April 1997). The MRI profiles showed that rehydration by water vapor followed Fickian diffusion kinetics. In contrast, rehydration with liquid water followed case II diffusion kinetics, at least semiquantitatively.

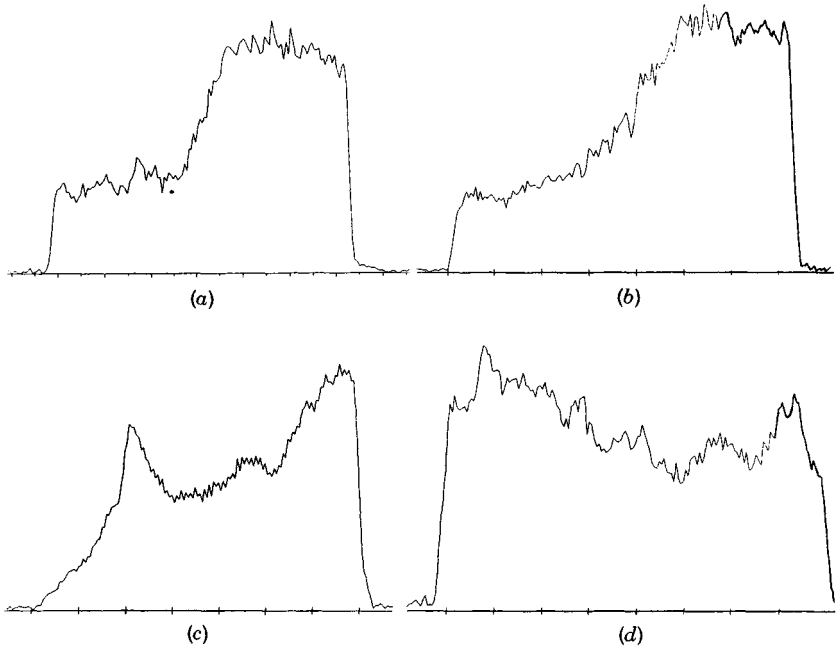

Figure 2.10. Effect of varying bead radius and surface tension on the drying profile at 500 min for randomly packed glass bead beds. The change from a sharp capillary profile in (*a*) to flat, but irregular, profile in (*d*) is apparent. The distance scale is arbitrary: (*a*) 400 μm, 1 m*M* SDS surfactant; (*b*) 400 μm, pure water; (*c*) 150 μm, 1 m*M* SDS surfactant; (*d*) 150 μm, pure water. (From Ref. 220.)

2.4.2 Glassy-State Rehydration Kinetics

The previous examples of the rehydration of spaghetti and starch are representative of the more general problem of the rehydration of glassy materials by a liquid solvent. Most research on this problem has focused on the ingress of organic solvents into plastics, and the results have been interpreted with non-Fickian diffusion models such as that of Thomas and Windle (315). In this model the rehydration process is considered to be the diffusion of water (or, more generally, penetrant) down an activity gradient into the glass coupled with time-dependent mechanical deformation of the polymer glass in response to the swelling stress. Besides a concentration-dependent penetrant diffusion coefficient, D, the Thomas–Windle model takes explicit account of the kinetics of the glassy polymer disentanglement and expansion, by incorporating the viscous flow rate, $1/\eta_0$. Swelling of the glassy polymer is modeled by assuming that a volume element within the glass experiences a swelling pressure, P, given by the osmotic expression

$$P = \frac{RT}{V_1 N} \ln \frac{a}{s} \tag{2.24}$$

where s is the ratio of the volume fraction of penetrant divided by the equilibrium volume fraction under conditions of zero extra swelling pressure and unit activity, V_1 the molar volume of penetrant, and N is Avogadro's number. The response of the volume element to the swelling pressure is assumed to be given by the viscosity relationship

$$\frac{ds}{dt} = \frac{P}{\eta k} \tag{2.25}$$

where k is a constant and the viscosity η decreases with increasing penetrant concentration according to the relationship

$$\eta = \eta_0 \exp(-Ms) \tag{2.26}$$

where η_0 is the viscosity of the unswollen glass and M is a constant. Substitution of equations (2.25) and (2.26) into (2.24) gives the swelling equation for a volume element i

$$\left(\frac{ds}{dt}\right)_i = \frac{-RT}{V_1 N k \eta_0} \ln\left(\frac{s}{a}\right)_i \exp(-Ms) \tag{2.27}$$

The swelling kinetics of a thin surface layer can be obtained by integrating equation (2.27) with $a = 1$, which assumes that the surface layer is instantly penetrated by solvent which reaches unit activity. More generally, equation (2.27) must be solved for each volume element in the sample, and this requires independent knowledge of the spatial dependence of the activity a. In the Thomas–Windle model this is given by Fick's first diffusion law, stated in the form

$$J = -D\left(\frac{s}{a}\right)\frac{da}{dx} \tag{2.28}$$

Equations (2.27) and (2.28) are then solved numerically with finite element methods by first determining the change in activity profile in a small time interval for a fixed concentration profile, and then, using the modified activity profile, determining the change in the concentration profile. The new concentration profile is then used to calculate a new activity profile and the process is iterated to convergence. It is further assumed that the diffusion coefficient D increases exponentially with penetrant concentration.

The Thomas–Windle model predicts a wide range of observed transport phenomena from Fickian diffusion kinetics when the glass relaxation kinetics is fast compared to diffusion; to case II kinetics when it is not. The case II situation is shown to be associated with a sharp solvent front ingressing into the glassy matrix with constant velocity, and in the Thomas–Windle model this arises because the region immediately ahead of the solvent front is preceded by a low concentration of solvent experiencing an extremely high swelling pressure and therefore an activity

that is much higher than the concentration (see Figure 2.12). The values of the pressure are those that are being resisted by the polymer network and which relax as the polymer glass deforms. At the solvent front itself, rapid transport down the steep concentration gradient is opposed by an equally steep pressure gradient in the opposite direction. Most interestingly, the model also shows that a diffusion coefficient

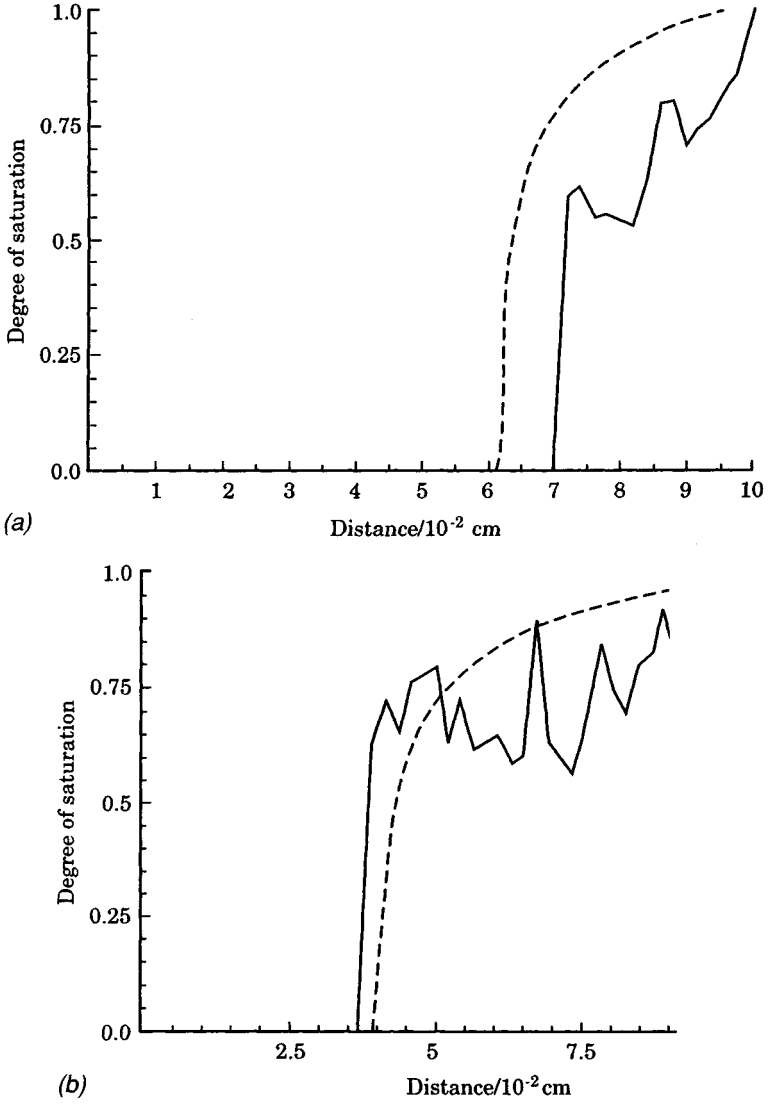

Figure 2.11. Radial moisture profile (solid line) inside a single strand of spaghetti made from hard wheat after 2 min (*a*) and 7 min (*b*) rehydration in water at 80°C. The origin corresponds to the center of the strand. The dashed line is the fit of a non-Fickian diffusion model to the data. (From Ref. 228.)

D, which increases markedly with concentration, is also an additional requirement for linear sorption kinetics (i.e., a linear dependence of total solvent adsorption versus time). To date, the Thomas–Windle model has been mostly applied to plastic–solvent systems, but it can obviously be used to model the rehydration of glassy foods.

2.4.3 Rehydrating Cereal Grains

The rehydration of cereal grains is an essential step in the manufacture of many types of extruded cereal products, from shredded wheat to rice crispies. Shapley and co-workers (199) have used MRI to compare the rehydration of wheat grains by boiling and steaming. The moisture images were obtained by compensating the spin-echo signal for transverse relaxation and by calibration of the spin density map with gravimetric measurements of water content. It was found that during boiling, water penetrates evenly into the wheat grain from all points on the boundary, including the inside of the crease. The moisture profiles show a clearly defined water front ingressing into the center of the grain. A perfectly sharp water boundary would suggest case II Fickian diffusion (178), which arises when the rate-limiting step is relaxation of the biopolymer (mainly starch) matrix rather than water diffusion. In contrast, steaming gives slower rehydration and a gradually increasing, spatially uniform water content throughout the grain. This suggests that with steam, the transport through the grain surface is the rate-limiting step, not the diffusion of water within the bulk of the grain. Why this should be so remains unclear.

Heil et al. (186) have imaged the uptake of water into dry beans. Here the major processing requirement is to optimize the water uptake rate and water holding capacity while decreasing splitting of the beans. If the beans split, the seed coats often separate and expose the cotyledons. The processing equipment usually discards these beans, causing reduced yields. If exposed cotyledons escape detection and end up in the finished canned product, they cause *starching*, whereby the starch in the cotyledon dissolves in the aqueous liquor. This changes heat transfer coefficients, increasing thermal processing requirements. Moreover, the product may no longer comply with quality standards specifying the number of separated seed coats, or damaged or hard beans. The MRI study was therefore undertaken to gain insight into the rehydration kinetics. The results showed that water uptake by undamaged dry beans occurs in two phases. The first appears to be controlled by natural barriers, such as the seed coat, and the rehydration dissolves the middle lamella (i.e., the region binding the seed coat to the cotyledon). The released seed coats are water permeable and become taut as the cotyledon expands during rehydration. Nevertheless, the beans remain intact. During this first phase the rate of rehydration is constant and the overall gravimetric uptake could be modeled using the simple equation $dW/dt = K_1$, where W is the total water content and K_1 is a constant. During the second phase the rehydration rate decreases as the total water content approaches equilibrium, and this phase could be modeled as $dW/dt = K_2(W^* - W)$, where W^* is the equilibrium water content of the rehydrated bean. Not surprisingly, the rate of rehydration of beans with damaged seed coats is substantially higher

than the intact bean and the seed coat often separates from the cotyledon. Although detailed image profiles of signal intensity were obtained during rehydration, no attempt was made in this exploratory study to convert them to quantitative moisture content maps.

2.4.4 Rehydration of Potato

Ruan et al. have imaged the rehydration of an air-dried raw potato cylinder immersed in water (180) and representative profiles through the center of the cylinder are reproduced in Figure 2.7. As with the potato drying experiment, the recycle time, TR, was chosen to be $\gg T_1$, and TE was made equal to the average T_2. In this way image intensities were proportional to the moisture content. The high-intensity regions in the outer regions of the profiles correspond to bulk water outside the potato cylinder. It was found that the hard layer produced on the outside of the potato during drying (i.e., through case hardening) acted as a permeability barrier to rehydration, which was therefore much slower than the initial stages of drying. The structural changes induced in the surface layers by case hardening also resulted in a much slower and smaller volume expansion during rehydration than the volume shrinkage observed during drying. This and the previous examples emphasize the importance of incorporating case hardening into theoretical models of tissue drying and rehydration.

2.5 FREEZING AND FREEZE-THAWING

Since its commercialization by Birdseye in the United States in 1923, the frozen food sector has grown into a worldwide industry producing 25 million tons of frozen food per annum. Despite its commercial importance, the underlying mechanisms of food freezing are still poorly understood. The difficulty arises because, in general, foods freeze over a range of temperatures, and each subzero temperature is characterized by a particular ratio of unfrozen water and ice. At the molecular level this arises because a biopolymer surface alters the structural and dynamic state of the water molecules adjacent to it and prevents them forming a regular ice lattice. Accordingly, a fraction of water within a biopolymer solution remains unfrozen even at temperatures as low as -15°C. Because different subcellular organelles in cellular fruit and vegetable tissue have different biopolymer and solute contents, they also exhibit different freezing behavior. For example, the starch granules and cell wall compartments in potato retain unfrozen water even at -25°C. This makes the a priori prediction of the amount of unfrozen water and ice at any subzero temperature extremely difficult and creates uncertainty in the amount of latent heat liberated at each point within a food as it is progressively frozen. MRI can help resolve this complex freezing problem by imaging the spatial distribution of ice and unfrozen water in the sample in real time during freezing. This is possible because ice has such a short transverse relaxation time that it contributes no signal in MRI,

so only the unfrozen water contributes image intensity. The MRI data can then be used to test and refine theoretical models of food freezing, which, in turn, facilitates optimization of the industrial freezing process.

Figure 2.3 shows the probe arrangement for radial imaging the freezing process, Figure 2.13 shows the radial projections of unfrozen water in rehydrated spaghetti as it is frozen by passage of cold nitrogen gas inside the imaging probe, and Figure 2.14 shows the radial profiles obtained after inverse Abel transformation. The radial imaging protocol (see Chapter 1) was used to acquire these profiles since this exploits the cylindrical sample symmetry and permits relatively fast imaging with good spatial resolution. The increase in noise toward the center of the cylinder is very noticeable in the profiles in Figure 2.14, and this is characteristic of the radial imaging protocol. To some extent this noise problem can be alleviated by performing the inverse Abel transform with a maximum entropy signal optimization routine. The results (see Figure 2.15) are smoother and suffer less from the nonuniform noise problem. The profiles in Figure 2.15 show that in the case of rehydrated pasta, there is a sharp ice front moving into the sample. However, this is not always the case, especially where there are subcellular compartments with different freezing characteristics. The corresponding radial profiles of unfrozen water in a cylinder of raw potato (Figure 2.16) show that there is gradation of ice and unfrozen water extending right through the sample. The detail provided by the imaging experiments provides a challenging test of current freezing models. Two such models are worthy of special mention since they are commonly used to model the freezing process.

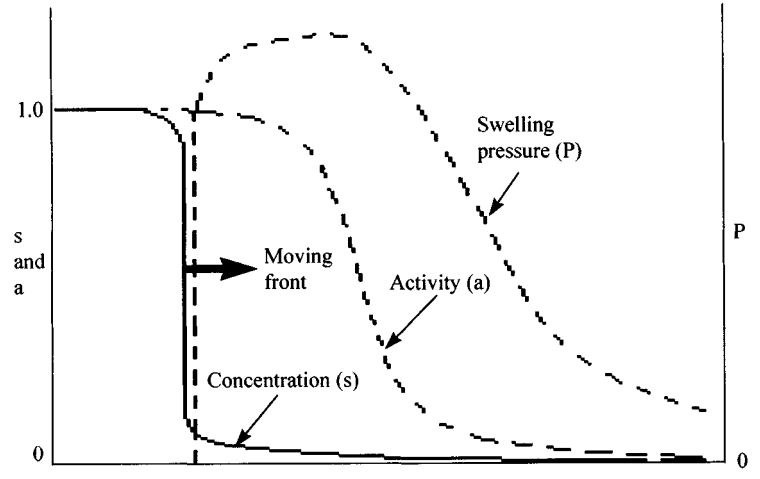

Figure 2.12. Spatial dependence of moisture concentration s, water activity a, and swelling pressure P, corresponding to the rehydration of a glassy polymer in case II diffusion according to the Thomas–Windle model. Curves are purely illustrative but are based on those calculated for the ingress of methanol into PMMA by Thomas and Windle. (From Ref. 315.)

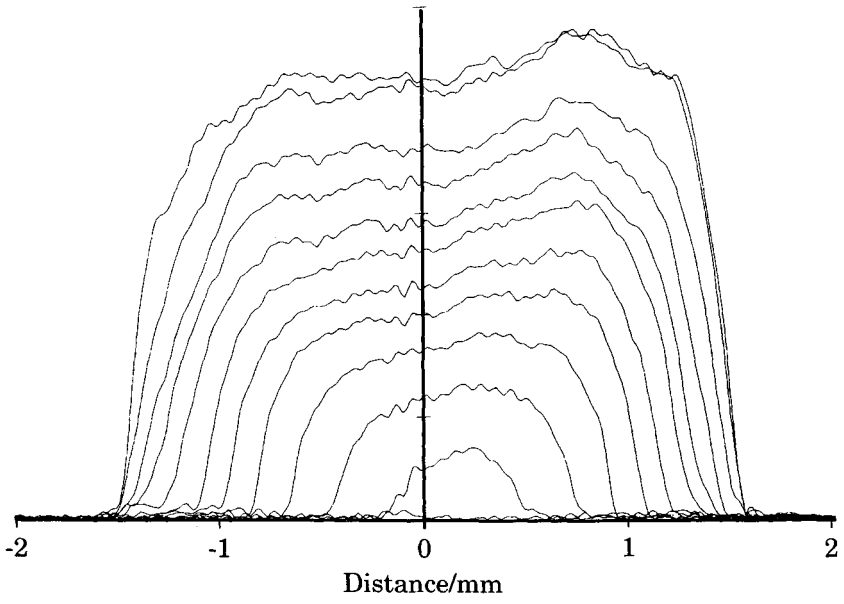

Figure 2.13. Image projections across a single cylinder of rehydrated pasta (spaghetti) during freezing taken every 10 s using the sample arrangement shown in Figure 2.3.

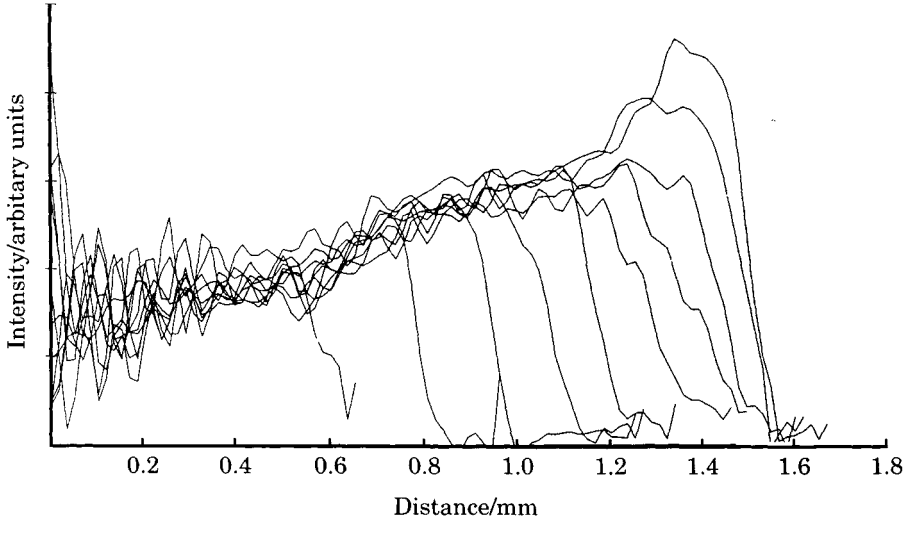

Figure 2.14. Radial profiles of unfrozen water in spaghetti during freezing obtained from Figure 2.13 by inverse Abel transformation. Note the increase in noise toward the center of the spaghetti cylinder.

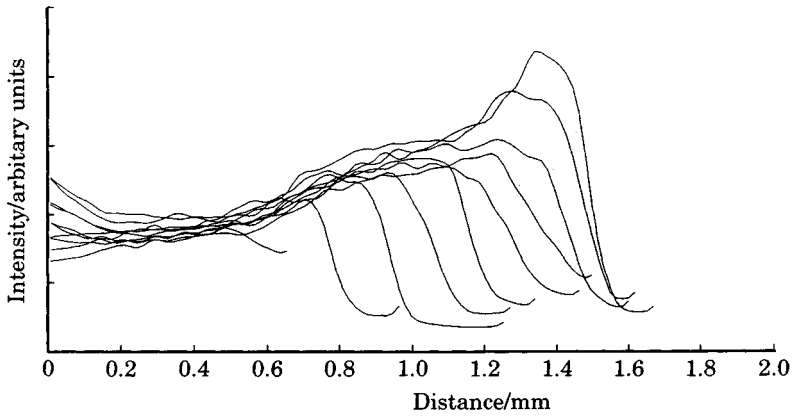

Figure 2.15. Radial profiles of unfrozen water in spaghetti during freezing obtained from Figure 2.13 by inverse Abel transformation with maximum entropy optimization of the signal-to-noise ratio. Note how the profiles are smoother than those in Figure 2.14.

2.5.1 Plank Freezing Model

The Plank model relies on three major assumptions: (1) there is a sharp ice front that ingresses into the sample during freezing, (2) physical parameters such as the thermal conductivity are constant, and (3) there is a constant outside temperature. The first condition is not always correct, especially if there are several water compartments characterized by different freezing behavior. The second condition is also questionable if the amount of unfrozen water in the sample varies with temperature. Despite these shortcomings the Plank model is sufficiently simple to permit analytic solutions for the freezing time and for the time dependence of the ice front position. As an example of the Plank model the equations will be presented for the freezing of a cylinder, assuming steady-state thermal transport. The predictions can then be compared with the MRI freezing profiles.

The amount of heat liberated at the ice front, Q_{lat}, is simply $-\lambda \cdot 2\pi\rho r l(dr/dt)$, where λ is the latent heat, ρ the density, l the cylinder length, and r the radial position of the ice front. This can be equated with the heat lost from the cylinder surface, Q_{surf}, which is $h \cdot 2\pi R l(T_{surf} - T_{out})$, where R is the outside radius, giving the equation for the velocity of the ice front

$$\frac{dr}{dt} = \frac{hR}{\lambda r}[T_{surf}(t) - T_{out}] \tag{2.29}$$

T_{surf} can be eliminated by equating the heat liberated from the surface, Q_{surf}, to that conducted through the ice phase, Q_{ice}, which has the form

$$Q_{ice} = \frac{k \cdot 2\pi l\,(T_{surf} - T_{ice})}{\ln(r/R)} \tag{2.30}$$

where k_{ice} is the thermal conductivity of ice, assumed constant, and T_{ice} is the freezing temperature. This gives the condition

$$T_{surf} = \frac{hRT_{out}\,\ln(r/R) - k_{ice}T_{ice}}{hr\,\ln(r/R) - k_{ice}} \tag{2.31}$$

By substituting this expression for T_{surf} into equation (2.29), and knowing T_{out}, an equation for the time dependence of the position of the ice front, $r(t)$, can be obtained by integration. This can be fitted to $r(t)$ obtained from the experimental imaging data and used to obtain the surface heat transfer coefficient h, which is the major unknown parameter.

When applying the Plank approach it is important to note that it assumes that an ice front always exists in the sample, so it takes no account of the time required to cool the surface to its freezing point. This can be partly corrected by shifting the time origin to the beginning of freezing.

2.5.2 Thermal Diffusion Freezing Model

In many foods, such as the raw potato profiles in Figure 2.16, MRI reveals that there is not a simple, sharp ice front ingressing into the sample during freezing as assumed in the Plank model, but rather, time-dependent profiles of the amount of ice and unfrozen water varying throughout the sample. To calculate these profiles a more sophisticated approach is required, based on numerical solutions to the thermal diffusion equation. In cylindrical coordinates the thermal diffusion equation assumes the form

$$C(w)\rho(w)\frac{dT}{dt} = \frac{d}{dr}k(w)\frac{dT}{dr} + \frac{k(w)}{r}\frac{dT}{dr} \tag{2.32}$$

Here $C(w)$, $\rho(w)$, and $k(w)$ are the apparent specific heat, the density, and the thermal conductivity, respectively. These three quantities themselves depend on the ice fraction $w(r,t)$ at each temperature and radial position in the sample. For the apparent specific heat, this functional dependence has the form

$$C(w) = C(0) - wY\,\Delta C_P - Y[\lambda + \Delta C_P\,(T - T_0)]\frac{dw}{dT} \tag{2.33}$$

where w is the ice fraction at temperature T, $C(0)$ the specific heat of the unfrozen sample, Y the water content of the unfrozen sample, ΔC_P the difference in the spe-

cific heats of ice and water, assumed constant and λ the latent heat of crystallization of water at T_0. The first two terms give the change in the specific heat of the sample when the water is converted to ice; the last two terms give the latent heat liberated during freezing. The initial value of the unfrozen sample $C(0)$ can be assumed to be constant and determined by the composition of the food. If the amount of protein, carbohydrate, fat, and so on, is known, an estimate can be made by assuming a linear dependence on the weight fractions:

$$C(0) = 1.424X_C + 1.549X_P + 1.675X_F + 0.837X_M + 4.18X_W \qquad (2.34)$$

where X_C is the weight fraction of the carbohydrate component, X_P is the weight fraction of the protein component, X_F is the weight fraction of the fat component, X_M is the weight fraction of the mineral components, and X_W is the weight fraction of water.

The thermal conductivity can also be assumed to depend linearly on the ice fraction,

$$k(w) = k_{\text{sample}} + Yw(k_{\text{ice}} - k_{\text{sample}}) \qquad (2.35)$$

where k_{sample} is the thermal conductivity of unfrozen food sample and k_{ice} that of ice, assumed to be temperature independent over the range of interest. The amount of ice, $w(T)$, and unfrozen water, $1 - w(T)$, at each temperature in the sample can be determined independently by measuring the loss of signal in the FID for samples held at uniform temperatures because only the unfrozen water contributes to the signal.

Having defined the various parameters in the model, the time dependence of the temperature and ice-fraction radial profiles can be calculated by numerically solving equation (2.32) with the following conditions:

$$\begin{aligned}
&t = 0: && T = 273\ \text{K} && 0 \leqslant r \leqslant R \\
&t > 0: && \frac{dT}{dr} = 0 && r = 0 \qquad (2.36) \\
&t > 0: && \frac{dT}{dx} = \frac{h}{k_{\text{gas}}}[T_{\text{surf}}(t) - T_{\text{out}}(t)] && r = R
\end{aligned}$$

Here h is the surface heat transfer coefficient and k_{gas} is the thermal conductivity of the cooling gas in the stagnant gas layer at the sample surface. T_{out} is the temperature of the cooling gas, and the time dependence of the surface temperature, $T_{\text{surf}}(t)$, is used to modify the boundary condition at each iteration of the calculation. Solution of the coupled equations gives the temperature profiles, $T(r,t)$, the corresponding ice-fraction profiles, $w(r,t)$, and unfrozen water profiles, $1 - w(r,t)$. By fitting the experimental MRI unfrozen water profiles it is therefore, in principle, possible to determine the surface heat transfer coefficient h.

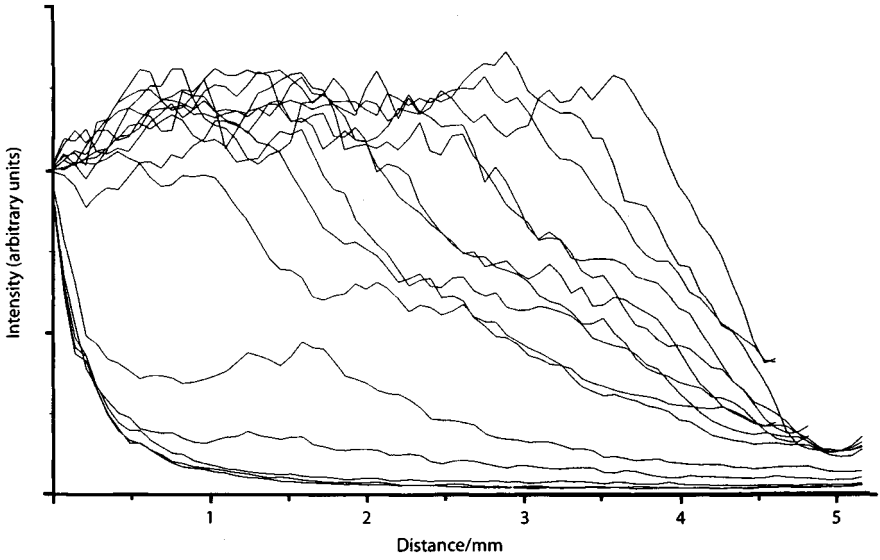

Figure 2.16. Radial profiles of unfrozen water in potato during freezing obtained by inverse Abel transformation with maximum entropy optimization of the signal-to-noise ratio. The origin is the center of the potato cylinder.

Figures 2.17 and 2.18 show the results of fitting the integrated signal intensity and the position of the ice front for the cases of pasta and potato by both the Plank and thermal diffusion approaches. It would appear that the Plank model provides a better fit to the data than does the more complex numerical model. This apparent agreement is, however, deceptive, at least in the case of potato, because the MRI profiles in Figure 2.16 show that there is no sharp ice front in the potato sample as assumed by the Plank model. In fact, neither the Plank nor the thermal diffusion model provide a quantitative fit to the data, and this highlights how the MRI profile data are beginning to challenge conventional theories of food processing.

In the industrial freezing situation, such as a spiral belt freezer, there is the possibility that on-line MRI could be used to determine freezing times (i.e., the time required for complete freezing of a product) and to ensure product quality. This will prevent unnecessary energy expenditure in overfreezing and prevent underfreezing of products, especially in their central regions. The potential of low-cost on-line MRI methods is discussed more fully in Chapter 6. Of course, most foods are thawed and cooked before consumption and the thawing process can also be followed by MRI. An important aspect of freeze-thawing is the sale of frozen-thawed meat as "fresh" meat at a higher price. MRI has a useful role to play in detecting this illegal activity, as it has been found (308) that the freeze-thawing process causes denaturation of the myofibrillar proteins in the muscle and a decrease in pH, resulting in a more rigid protein matrix and an enhanced rate of magnetization transfer between water and protein protons (see Chapter 12). Although the magnetization transfer rates can be measured on a sample-by-sample basis, a faster

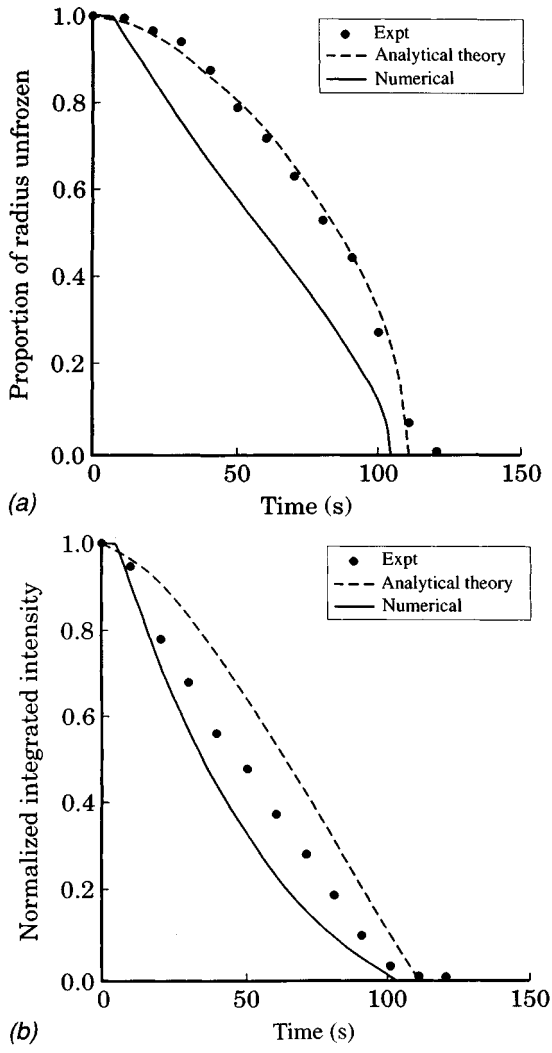

Figure 2.17. Comparison of the experimental position of (*a*) the ice front and (*b*) the integrated image intensity during the freezing of rehydrated spaghetti determined by radial imaging. The dashed lines show the fit with the analytic Plank model, and the full line shows the fit with numerical solutions based on the thermal diffusion equation.

throughput was achieved using MRI to measure transfer rates simultaneously for hundreds of meat samples (taken as cylindrical meat plugs drilled from the meat) placed in trays inside the imager (308).

MRI can, perhaps, be used to test whether foods have been refrozen after freezing and thawing, but this remains to be investigated. Different freezing rates in the two freezing steps would be expected to create regions of differing ice crystal size

and presumably of differing distributions of unfrozen water, which might be reflected in the image contrast. So far, only the ice–water phase transition has been discussed. However, similar concepts apply to lipid crystallization in materials such as oil-in-water emulsions and chocolates. These phase transitions will be discussed in Chapter 3 since they are largely responsible for changes in quality factors during storage rather than in the primary processing stage.

2.6 FREEZE-DRYING

Freeze-drying involves removal of water by the sublimation of ice into vapor under vacuum (110,111) and requires several stages. First, a large food sample is usually sliced, diced, or minced so as to maximize surface area and reduce the freeze-drying time. The sliced food is then frozen and the ice removed by sublimation under vacuum in what is conventionally called the *primary drying stage*. This is followed by the *secondary drying stage*, where residual unfrozen (adsorbed) water is removed by heating the product under vacuum. This leaves a very porous product with typically less than 2% moisture by weight. Finally, the dry product is conditioned to equilibrate residual moisture gradients and the vacuum removed.

In many ways the freezing stage is the most important in freeze-drying because the rate of freezing must be controlled for each product so as to optimize the size, orientation, and connectivity of ice crystals. This is important because each ice crystal becomes an air-filled pore during the primary drying phase, and the pore size distribution and pore connectivity determine the rate of heat transport and the rate of vapor-phase transport through the dried layer of food during the subsequent ice sublimation stage. In industrial freeze-driers the product is usually frozen by contact with cooled metal plates, but some foods are fast-frozen by spraying with liquid nitrogen. Because only the ice is sublimed in the primary drying phase and not residual unfrozen water, it is important to minimize the amount of unfrozen water by using temperatures well below $-20°C$.

During the primary drying phase the ice crystals are sublimed out of the frozen food by keeping the temperature below $-20°C$ and the pressure below about 1.33 mbar. Heat must be supplied continuously to the subliming ice front to supply the latent heat of sublimation. Industrial freeze-driers place the product in trays between heated metal plates, so heat transport proceeds by radiation to the product surface and by conduction through the outer, dried-out layers to the subliming ice front. In this arrangement heat conduction through the dried layers is rate limiting and can be increased only by raising the temperature of the surface, subject to the restraint that the outer layers do not experience heat damage. Of course, it is also vital that the surface of the frozen ice core does not melt. The thermal conductivity of the dried layer will be determined, in part, by the size and connectivity of the pores left by the sublimed ice crystals, which is why the rate of freezing is so important. The water vapor liberated from the food during the primary drying stage is usually removed by condensation in a separate refrigerated unit under the vacuum. A schematic of a freeze-drier is shown in Figure 2.19.

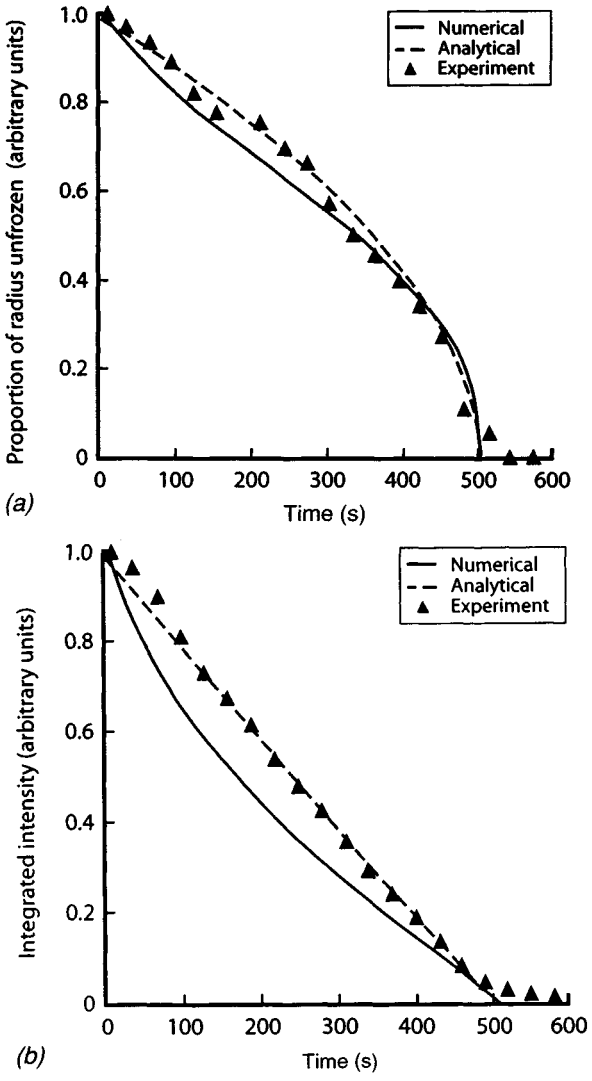

Figure 2.18. Comparison of the experimental position of (*a*) the ice front and (*b*) the integrated image intensity during the freezing of a cylinder of raw potato determined by radial imaging. The dashed lines show the fit with the analytic Plank model, and the full lines show the fit with numerical solutions based on the thermal diffusion equation.

The secondary drying stage begins, ideally, after all the ice has been removed by sublimation, leaving only residual unfrozen water, usually associated as an adsorbed layer around macromolecules. This residual water is removed by heating the food under vacuum to between 10 and 50°C, although some processes use desiccants such as silica gel and keep subzero temperatures. Residual water should not usually exceed 2% if the product is to be stored for long periods.

The dried product is then conditioned, which, in industry, involves storage of product dried from different parts of the drier in sealed containers for at least a day to achieve uniform moisture distribution. Finally, the vacuum is broken, usually with dry nitrogen gas, and the product sealed in airtight packaging. This is essential for preventing not just moisture adsorption but also the infusion of oxygen, which spoils the product via lipid oxidation. Lipid oxidation can be very rapid in freeze-dried foods because of their high porosity and large surface area.

In view of the earlier statement that ice gives no signal in MRI, it is perhaps surprising that MRI has been used to follow the kinetics of the primary stage of the freeze-drying of potatoes (109). This is possible because there is usually sufficient unfrozen water distributed among microscopic compartments in the frozen core of the food matrix to provide a signal under high receiver gains. Figure 2.20 shows a series of images of the frozen central part of a cylinder of potato undergoing freeze drying. The signal-to-noise ratio is not particularly good because of the small amount of unfrozen water, but it is sufficient to follow the ice core shrinkage noninvasively and provide a test of the theoretical models of the primary freeze-drying stage. With solid imaging techniques (see Chapter 5) it might be possible to image the secondary drying stage, but the author is unaware of any attempt to do this.

A complete theoretical description of the primary drying stage is very complicated because it involves the coupled equations of heat and mass transport, including transfer between the solid and gaseous phases. Details (but not solutions) can be found in a review by Athanasios and Bruttini (110). A simplified theoretical model of the primary freeze-drying stage that gives a reasonable fit to the MRI potato data in Figure 2.20 is based on the assumption that the sublimation process proceeds by a series of pseudosteady states where all the heat supplied to the ice front is used for sublimation (109). This means that

$$h(T_{gas} - T_{ice}) = L_s\beta(P_{ice} - P_{cond}) \tag{2.37}$$

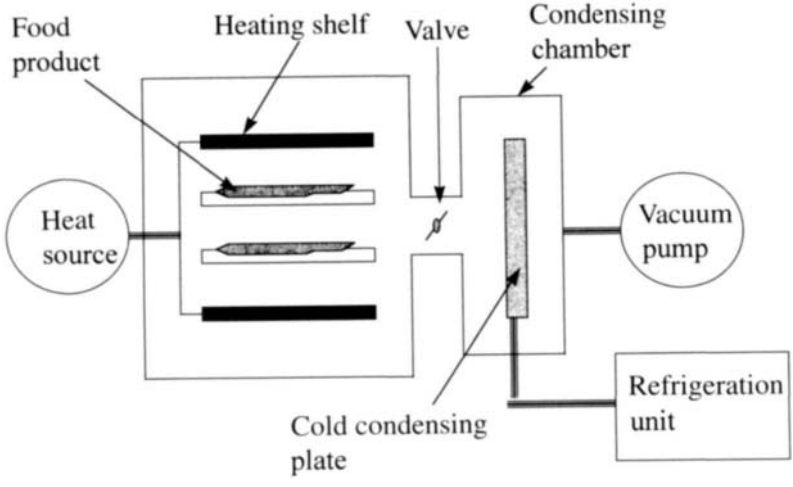

Figure 2.19. Schematic of a freeze-drier.

where T_{gas} is the temperature of the gas phase outside the sample, T_{ice} the temperature of the ice front, h the effective heat transfer coefficient between the gas and ice phases, L_s the latent heat of ice sublimation, β the effective mass transfer coefficient between the ice and gas phases, P_{ice} the partial pressure of water at the frozen core surface, and P_{cond} the partial pressure of water vapor of ice at the condenser unit. If it is assumed that the ice front is at equilibrium with vapor at the sublimation front, its temperature and equilibrium vapor pressure are related through an equation such as that of Clausius and Clapeyron (309)

$$P_{ice} = \exp\left(\frac{a}{T_{ice}} + b\right) \tag{2.38}$$

where a and b are known constants. A similar relation holds for P_{cond}. Equations (2.37) and (2.38) can be solved for the temperature and vapor pressure of the ice front, T_{ice} and P_{ice}. The result can be substituted into the mass transfer equation governing the rate of loss of mass from the ice front, dm/dt

$$\frac{dm}{dt} = A(t)\beta(P_{ice} - P_{cond}) \tag{2.39}$$

Here $A(t)$ is the surface area of the ice front. Knowing dm/dt from equation (2.39), it is possible to calculate the time evolution of the radius of the ice front, dR/dt, because

$$\frac{dm}{dt} = A(t)\rho\phi\frac{dR}{dt} \tag{2.40}$$

where ρ is the density of ice and ϕ is the porosity of the product. The solution is best performed numerically by iterating each step beginning with appropriate initial conditions. The resulting values of $R(t)$ can be compared directly with the values measured from the MRI images as well as those observed visibly after destructive dissection of the sample. The results for the MRI study on freeze-drying potatoes are shown in Figure 2.21.

The equations above involve effective transfer coefficients β and h between the gas phase outside the sample and the ice front inside the sample. In reality these are composite coefficients because the actual transfer involves two steps: external transfer between the outside gas and the food surface, and internal transfer between the food surface and the subliming ice front. Expressions for the effective transfer coefficients β and h in terms of more fundamental single-phase quantities, such as the external heat and mass transfer coefficients, and the internal thermal and mass diffusivities of the dried layer, can be obtained by solving the coupled Fourier flux equations governing the external and internal transfers. The equations are too lengthy to reproduce here, but the interested reader will find details in the paper by Rutledge et al. (109).

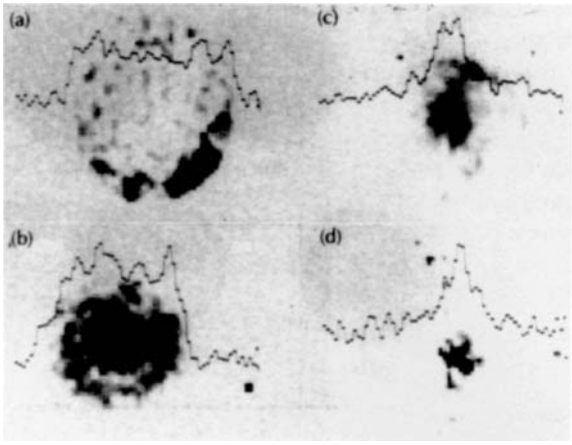

Figure 2.20. Imaging the time course of the freeze drying of potato cylinders. The black areas correspond to the frozen core of the potato cylinder after the freeze-drying times indicated: (*a*) 0 min; (*b*) 105 min; (*c*) 165 min; (*d*) 185 min. The dry material outside the core gives negligible MRI signal. The dark patch in (*a*) arises from sample nonuniformity, made visible by the use of a lower-contrast setting for this image only. Images were acquired at the INRA, Station de Recherche sur la Viande, Theix, France. (From Ref. 109.)

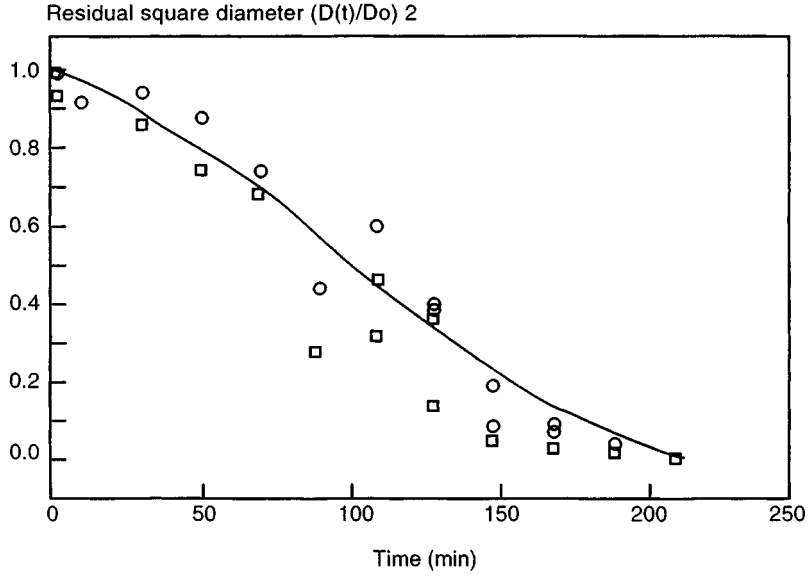

Figure 2.21. Time dependence of the square of the theoretical and observed residual diameters, $[D(t)/D(0)]^2$, of the ice core in raw potato during freeze drying. Squares, visual measurements; circles, MRI measurements. The line is the fit of the theoretical model. (From Ref. 109.)

The internal mass and heat transfer coefficients depend sensitively on the microscopic pore size distribution and pore connectivity in the dried outer layers. A variety of NMR relaxation and diffusion techniques have been developed to measure pore size distributions and connectivities in porous rocks and sandstones (motivated by the need to maximize oil extraction from porous rocks in the oil industry). These techniques involve saturating the porous matrix with water or brine solution and rely on the dependence of the relaxation time on pore size and the principles of q-space microscopy, both of which are discussed more fully in Part Two. Provided that the water is replaced by an inert nonaqueous solvent, similar techniques could, in principle, be used to study the pore structure in freeze-dried foods. A number of research groups are investigating this possibility, but results, although promising, are only preliminary.

Current models of freeze-drying assume a homogeneous dried outer layer characterized by spatially independent mass and heat diffusivities. In reality, the different rates of freezing in different parts of the sample may mean that there is a spatially dependent pore size distribution and hence a spatially inhomogeneous dried outer layer. In principle, relaxation-time-weighted imaging could cast light on this complication by probing the spatial distribution of pore sizes in the dried outer layer.

2.7 MRI AND MISCELLANEOUS PROCESSING OPERATIONS

Heating ovens during the baking of cookies and bread is expensive, so maximizing the throughput while maintaining quality is an industrial priority. In cookie manufacture, too rapid baking results in steep moisture gradients with the cooked dough, which results in stress cracking during cooling and storage. Modeling the baking process is difficult because it involves simultaneous heat transport, moisture migration, and all the chemical reactions associated with baking. For cookies this includes color formation, sugar caramelization, and starch gelatinization. Imaging the baking process is also difficult because fat contents are usually high (especially in cookie doughs), and water contents become very low and transverse relaxation times short, especially toward the end of the baking process. In addition, the crumbly, porous morphology creates susceptibility-induced local field gradients that broaden the spectral lines and usually prevent chemical shift separation of the water and oil images. As we shall see in Chapter 5, many of these problems can, in principle, be overcome with solid imaging techniques. To date, however, liquidlike spin-echo imaging has been used to follow qualitative changes during baking. Heil and co-workers (294) have used localized spectroscopy and MRI to study void formation, lipid migration, and moisture loss during cookie baking in the United States. The results show an increase in moisture content in the center of the cookie but little lipid migration. Hall (295) has quantified the moisture migration by calibrating image intensity against gravimetric water loss. Their lower limit on detectable water content is about 15%, which can be compared to a typical moisture content of 3 to 4% in a baked (English variety) cookie. Clearly, there is a long way

to go before MRI can be used routinely to monitor baking processes. Imaging studies of the staling changes in baked products during their subsequent longer-term storage will be discussed in Chapter 3.

Frying involves simultaneous heat transport, pressure-driven flow of water vapor to the surface, and ingress of oil into food. In French fries this results in the formation of a porous crust a few millimeters thick which is oil-rich and in which the chemical reactions responsible for browning and flavor formation are prevalent. Inside the crust is the water-rich region where starch gelatinization progresses as heat penetrates through the crust. This is usually associated with nonuniform shrinkage. Optimizing the temperature and blend of frying oils is especially important to minimizing oil loss, maximizing quality, and in responding to the changing consumer fat consumption patterns and the trend to less saturated oils (297). Not surprisingly, MRI studies of this complicated process are still at an early stage. Farkas et al. (296) have imaged oil–water interfaces in 2-cm-diameter potato cylinders after frying 6 min at 190°C and compared the results with SEM. The two-dimensional images were not corrected for relaxation losses so could not be quantified for oil and water content, but they confirmed the formation of an oil-rich crust with a fairly sharp oil–water interface. Clearly, the potential not only for monitoring the oil–water interface but also for imaging the degree of starch gelatinization in the core, and even for temperature mapping during frying, is considerable and as yet unexplored.

2.8 MRI AND NEW PROCESSING TECHNOLOGIES

A number of new processing technologies are being developed for commercial exploitation. These are primarily intended to extend food shelf life by destroying spoilage microorganisms and pathogenic bacteria while retaining high food quality, defined, for example, as high nutritional status and retained texture, color, and taste. The list of emerging techniques is quite extensive and includes ultrasonic and high-pressure treatments, the use of high electric field pulses (aptly called HELP technology), high magnetic field pulses, sous-vide (vacuum) cooking, microwave and radio-frequency heating, and many others. Much basic research is still needed if these new technologies are to be used widely over the next decade. Most probably, these novel sterilization and pasteurization processes will need to be used in combination with traditional processing operations such as drying and freezing.

As an example, the HELP technique could be used before convective drying, but these two processes are not necessarily independent. The high electric fields used in HELP are thought to induce transmembrane potentials, resulting in thinning and permeabilizing of cell membranes. This not only kills or injures unwanted microorganisms but also breaks down the cell permeability barriers to transport in cellular tissue, such as fruits and vegetables, and therefore changes the subsequent drying and rehydration kinetics. Here again, MRI is uniquely suited for investigating these changes both at a microscopic distance scale (see Part Two) and as we have seen, at the macroscopic scale.

Other techniques also present new processing possibilities. Under high pressure, foods can be cooled to low temperatures (e.g., −20°C) without ice crystal formation. Sudden removal of the pressure causes extremely rapid ice crystallization, resulting in very small ice crystals and minimal damage to the food matrix. Ultrasound treatment has also been found to reduce the size of ice crystals by increasing the rate of ice crystal nucleation. MRI can potentially help investigate the effectiveness of these novel techniques by imaging the ice crystal formation and the subsequent thawing kinetics, as well as moisture and heat transport in the frozen-thawed product.

3

MRI AND FOOD PROCESSING: MAPPING TEMPERATURE AND QUALITY

3.1 MRI AND TEMPERATURE MAPPING

In this chapter we continue the theme of process optimization begun in Chapter 2 by exploring how MRI can be used in temperature mapping and in the measurement of food quality factors. Heat transfer during food processing is, of course, every bit as important as mass transfer, and in most processes, such as drying and baking, they occur simultaneously, together with changes in quality factors. In MRI, heat transfer is followed indirectly from measurements of time-dependent temperature maps $T(r,t)$, which are obtained from maps of temperature-sensitive NMR parameters, or more usually, from maps of signal intensity acquired using pulse sequences weighted by temperature-sensitive NMR parameters. In principle, any NMR parameter that shows significant dependence on temperature over the range of interest can be used to map temperature changes in foods. All that is required is a calibration curve between the NMR parameter and temperature (at constant composition), and this can be determined in nonspatially resolved NMR experiments. NMR parameters that have been used for temperature mapping include the water proton relaxation times, especially the longitudinal relaxation time T_1, the water self-diffusion coefficient, and the water proton chemical shift.

Temperature maps are important in their own right, for identifying hot or cold spots in processing operations such as pasteurization and sterilization, but they are especially valuable for testing and refining theoretical models of heat transfer and for determining unknown thermal quantities such as surface heat transfer coefficients and thermal conductivities. These parameters can be determined by invasive methods using thermocouples, thermistors, and fiber optic sensors, but these measure temperatures only at a single point and can perturb the heat flow. Moreover, there are many dynamic processes where it is difficult to use probe sensors. One

example that has received intense interest by the food industry is aseptic heat processing of multiphase, solid-in-liquid foods. To ensure sterilization and complete cooking, it is essential that the temperature inside the solid particles reaches appropriate values during heating of the suspension. Failure to ensure this has led to legal restrictions on the production and sale of certain food particle suspensions until they are proved to be safe and reliable. Attempts to model asceptic heat processing mathematically are hindered by our lack of knowledge of the fluid-to-particle convective heat transfer coefficient k_{fs}, which is difficult to measure for the systems of interest under realistic flow conditions. As we shall see, MRI temperature mapping not only provides the temperatures inside the suspended particles, but enables k_{fs} to be extracted.

By mapping more than one NMR parameter, such as D, T_2, T_1, and spin density, with multislice multiecho pulse sequences, it should be possible, at least in principle, to image simultaneously temperature and other variables, such as moisture content, and quality factors, such as local microstructure or solute concentration, during nonisothermal processes such as drying, rehydration, and cooking which involve concurrent mass and heat transport and microstructural changes. To achieve this it will be necessary to find NMR parameters that show significantly different dependencies on temperature and moisture content and also to develop imaging protocols sufficiently fast to permit multiparameter determination in a time short compared to the rate of temperature change. This should be possible with fast imaging techniques, such as snapshot FLASH and echo planar imaging (EPI), discussed in Chapter 1, but to date, the author is unaware of any attempts to develop this multiparameter approach. Nevertheless, fast temperature mapping techniques are being developed. Figure 3.1 shows the temperature profile acquired in only 2 s with a precision of about 1°C determined using an inversion-recovery snapshot-FLASH MRI technique (167). The sample in this case was only a cylindrical agar gel phantom having a steady radial temperature gradient (see Figure 3.1), but the success of this rapid temperature mapping technique bodes well for future applications to real-time food processing.

3.1.1 Diffusion Mapping of Temperature

The effective water self-diffusion coefficient increases with increasing temperature and has been used to produce two-dimensional temperature maps in a model food gel during heating and cooling (21). The gel consisted of a cylinder of agar, microcrystalline cellulose, and water (1.95:6.55:200) and was heated, or cooled, by circulation of hot or cold water around the cylinder (see Figure 3.2). The effective water diffusion coefficient was measured by insertion of the usual pair of gradient pulses on either side of the 180° pulse in the standard spin-warp imaging sequence (see Figure 3.3). The signal intensity $S(r,t)$ is then proportional to $\exp(A)\exp(-bD)$, where A includes all factors, such as spin density and relaxation contrast, and b is the constant factor $\gamma^2G^2\delta^2(\Delta - \delta/3)$. The diffusion map can therefore be calculated as the ratio $b^{-1}\ln(S_1/S_2)$, where S_1 and S_2 are the images acquired with and without the diffusion gradients, respectively. The effective diffusion coefficient increases exponentially with

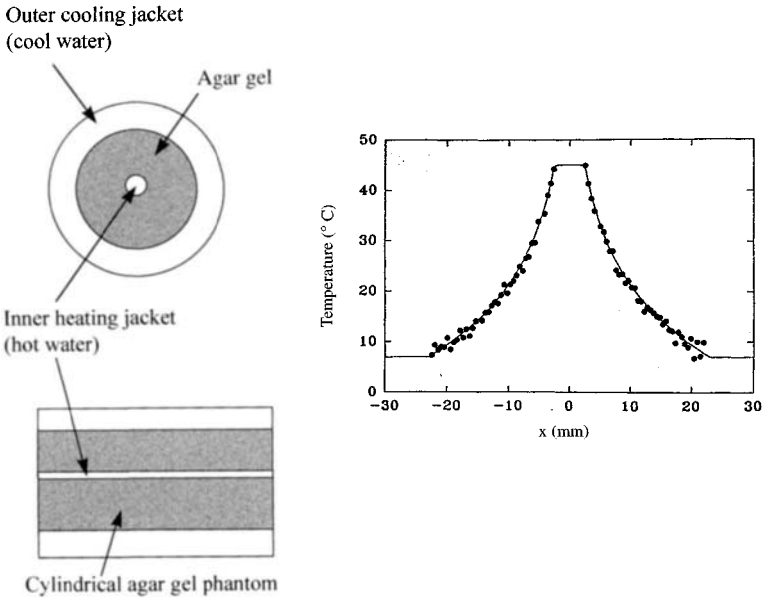

Figure 3.1. (*Left*) Geometry of the agar gel phantom used to test the rapid inversion-recovery snapshot-FLASH MRI temperature mapping technique. The cylindrical cooling jacket and axially centered glass capillary are maintained at constant temperature by circulating water. (*Right*) Radial temperature profile determined in 2 s with a precision of 1°C. The line shows the theoretical temperature distribution. (From Ref. 167.)

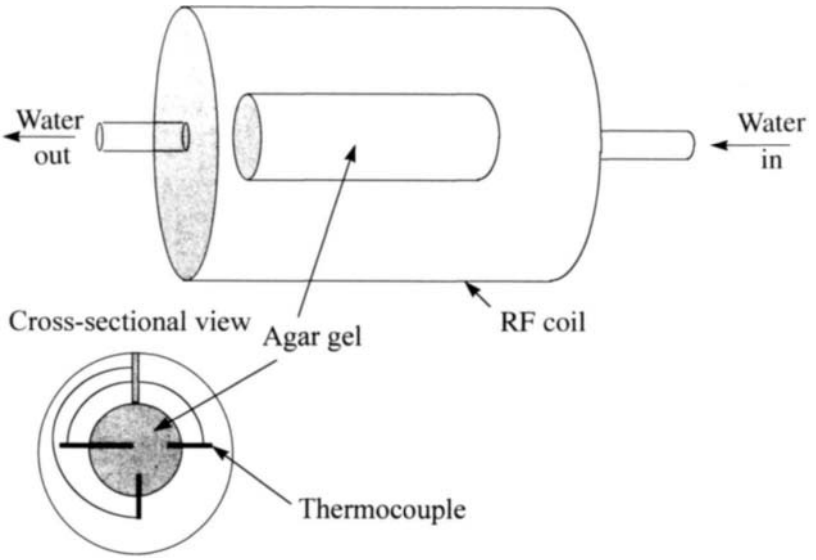

Figure 3.2. Temperature mapping an agar gel cylinder. Heating or cooling water is flowed around an agar gel cylinder at sufficient velocity to remove its signal. The cross section shows the arrangement of thermocouples within the gel. (From Ref. 166.)

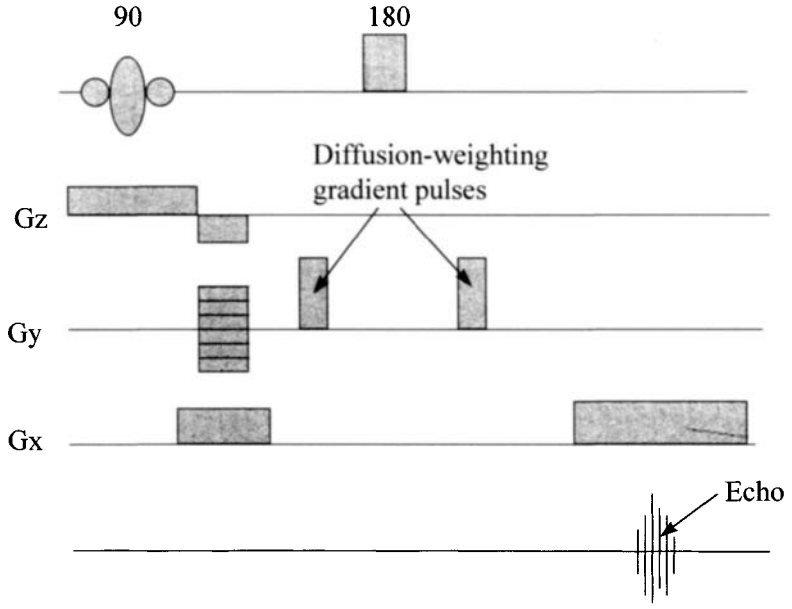

Figure 3.3. Diffusion-weighted imaging sequence used in temperature mapping the agar gel in Figure 3.2. (From Ref. 166.)

temperature as $D \propto \exp(-E/kT)$, where the dependence of the activation energy E on temperature can be neglected over a sufficiently narrow temperature range. It follows that $dD/dT = (E/kT^2)D$, so that for a finite temperature interval from a reference temperature T_r,

$$T = T_r + \frac{kT_r^2}{E}\frac{D - D_r}{D_r} \tag{3.1}$$

showing that there is a linear relationship between the relative increase in the diffusion coefficient and the temperature provided that the activation energy is constant. This linear relationship is shown for raw potato in Figure 3.4. The problem with this protocol is that it requires at least two acquisitions at each temperature, one with the diffusion gradient G and one without. This slows the measurement process and introduces errors due to temperature changes during measurement. An alternative protocol is therefore to measure the image in the absence of a diffusion gradient at the reference temperature and then use only one acquisition in the diffusion gradient G at all other temperatures. In this case the measurements will not be those of the actual self-diffusion coefficient but of a pseudodiffusion coefficient, which differs from it by the factor $(A_1 - A_2)/b$. Another way of reducing the acquisition time is to acquire only half k-space in the phase-encoding direction (which is the slowest direction because it requires repetition of the sequence with each phase-encoding gradient increment). Quantitative high-speed mapping of the diffusion

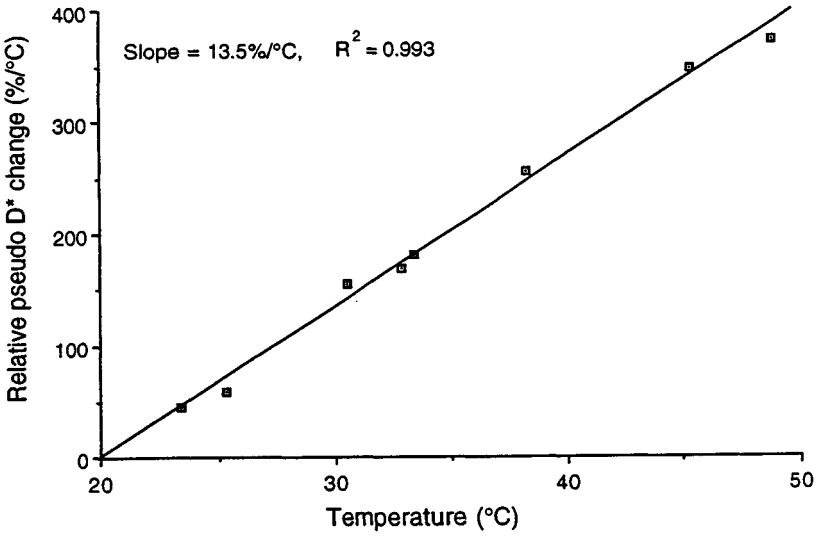

Figure 3.4. Linear relationship between the relative apparent water self-diffusion coefficient and temperature for potato. (From Ref. 165.)

coefficient is possible using fast gradient-echo imaging or echo-planar imaging. However, the price paid for increased speed in these sequences is decreased signal-to-noise ratio and decreased spatial resolution, but if the application does not require high spatially resolved temperature maps, these would be the sequences of choice.

The experiments reported by Sun and co-workers (166) simply involved heating a cylinder of the model gel in a plastic container, initially at 18°C, by flowing water at 35°C around it. The water flow was sufficiently fast that no signal was obtained from it. The MRI temperature maps were then compared with thermocouple measurements, which verified the maps to within a degree. As such, this was merely a feasibility study. Subsequently, the method was used to investigate the heating of a cylindrical plug of potato tissue (165) in direct contact with the circulating water, and the sample was heated from 20 to 50°C (see Figure 3.5). However, no attempt has yet been made to model the temperature maps with thermal transport equations and extract thermal parameters, such as the particle-fluid heat transfer coefficient, which would be the parameter of interest in asceptic processing.

3.1.2 T_1 Mapping of Temperature

T_1 mapping of temperature has a number of advantages compared to diffusion temperature mapping. There is a higher signal-to-noise ratio because short echo times can be used in T_1 imaging to avoid attenuation by transverse relaxation. Diffusion measurements are also more sensitive to gradient pulse imbalances, eddy currents,

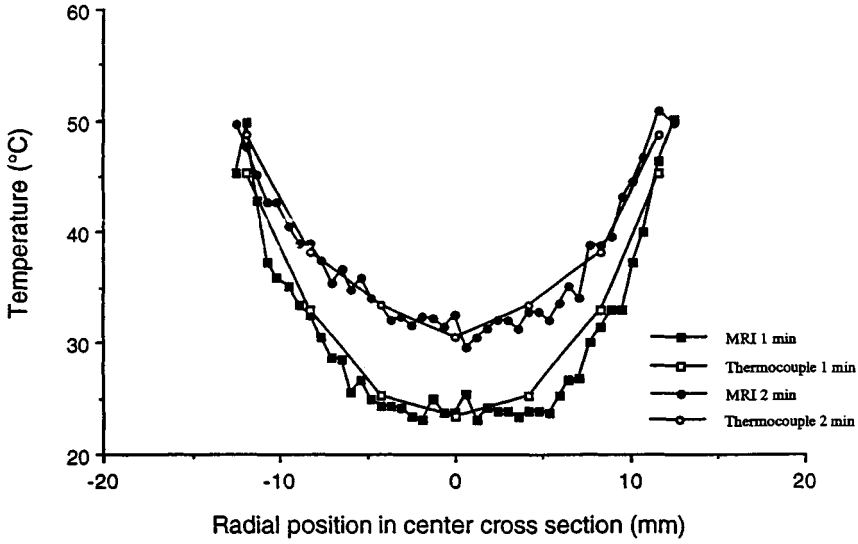

Figure 3.5. Comparison of the MRI and thermocouple radial temperature profiles for a cylindrical plug of potato using the arrangement in Figure 3.2. The initial temperature was 18°C and it was heated by water at 50°C. Measurements were taken after 1 and 2 min, as indicated. (From Ref. 165.)

and motional artifacts such as convection and perfusion. As discussed in Chapter 1, if a standard gradient-echo imaging sequence is used to measure T_1, and the echo time TE is made much shorter than T_2, the signal intensity is simply $S(r,t) = M(0)[1 - \exp(-TR/T_1)]$, where attenuation due to diffusion in the phase-encoding gradients and readout gradients has been neglected. Both $M(0)$ and T_1 are temperature dependent. The temperature dependence of $M(0)$ can be deduced from the Boltzmann factor of equilibrium statistical mechanics. For spin-$\frac{1}{2}$ nuclei, $M(0)$ is proportional to the difference in the spin-state populations ($N_{up} - N_{down}$), and according to the Boltzmann factor, N_{up}/N_{down} is proportional to $\exp(\Delta E/k_B T)$, where ΔE is the energy difference between the spin states and k_B is the Boltzmann constant. It follows that

$$M(0) \propto N_{down}\left[\exp\left(\frac{\Delta E}{k_B T}\right) - 1\right] \tag{3.2}$$

or, since $(\Delta E/k_B T \ll 1$, that $M(0) \propto \Delta E/k_B T$. In other words, $M(0)$ is inversely proportional to the temperature. Accordingly, we can write

$$\frac{S(T)}{S(T_{ref})} = \frac{(273 + T_{ref})\,[1 - \exp(-TR/T_1)]}{(273 + T)\,[1 - \exp(-TR/T_{1ref})]} \tag{3.3}$$

where T_1 is the relaxation time at temperature T and T_{1ref} is the relaxation time at the reference temperature in degrees Celsius. If the relationship between T_1 and temperature is known independently from nonspatially resolved calibration experiments, equation (3.3) can be solved iteratively to produce a temperature map from $S(t)$. In this way, only a single measurement of $S(T)$ is required rather than repeated measurements of a T_1 map using, for example, standard inversion-recovery weighted measurements, which would be too slow.

The protocol discussed above was tested by heating a precooked carrot in a rapidly flowing stream of water (164). Figure 3.6 shows the linear dependence of T_1 on temperature for raw carrot, and Figure 3.7 shows the dependence of $S(T)/S(T_{ref})$ on temperature from equation (3.3). Figure 3.8 shows the resulting temperature maps for heating cooked carrot (164). The initial water temperature was 20°C, and at time zero this was replaced by water at 83°C. Image acquisition times were about 24 s using a short repetition time of 0.74 s. A precooked carrot was used to help smooth out spatial heterogeneity arising from vascular bundles and growth rings. In this way the feasibility of the method was established, but no attempt was made to model the heat transfer process.

An alternative solution to the problem of long T_1 measurement times is the use of fast imaging methods such as inversion-recovery snapshot-FLASH imaging (167), discussed in Chapter 1. This approach has been tested on a phantom consisting of a cylinder of a $CuSO_4$-doped gel formed between a central glass tube containing cooling water at 7°C and an outer glass jacket containing water at 45°C. The measured radial temperature profile in this steady-state experiment agreed with the calculated radial

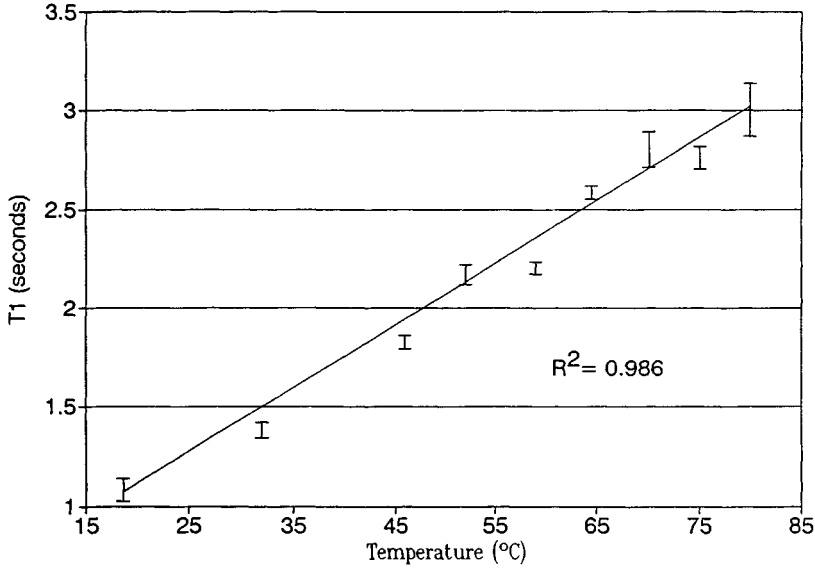

Figure 3.6. Linear relationship between the longitudinal relaxation time and temperature for cooked carrot. (Courtesy of Hulbert et al., Ref. 164.)

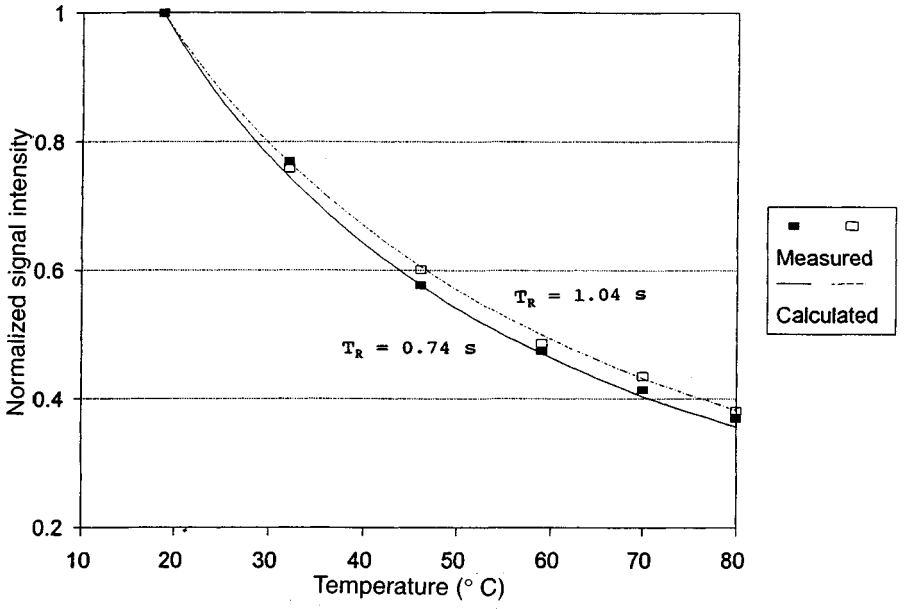

Figure 3.7. Temperature dependence of the normalized signal intensity $S(T)/S(T_{ref})$ for cooked carrot. (Courtesy of Hulbert et al., Ref. 164.)

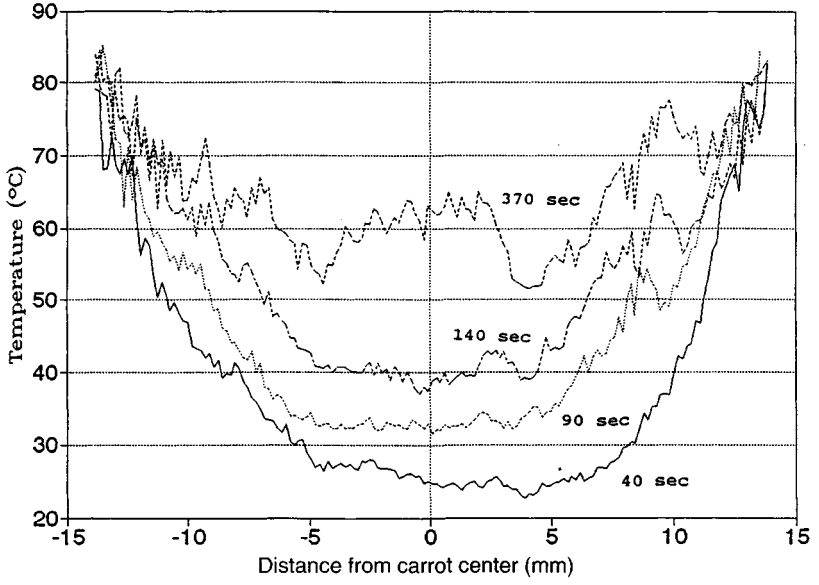

Figure 3.8. Experimental MRI temperature profiles for cooked carrot heated with 83°C water from an initial temperature of 20°C. The first profile was acquired before heating, and subsequent images were acquired after heating for the specified time. (Courtesy of Hulbert et al., Ref. 164.)

dependence to within 0.72°C with a relatively low spatial resolution of 0.4 × 0.8 mm. This establishes the feasibility of the fast temperature mapping method, but dynamic time-dependent temperature mapping was not attempted, and a less artificial apparatus would be needed for meaningful measurements of thermal properties because, in many samples, the glass or plastic walls of a container will be the rate-limiting thermal barrier to heat transfer to and from the sample.

3.1.3 Chemical Shift Mapping of Temperature

The water proton chemical shift σ increases linearly with temperature by about 0.01 ppm/degree over a wide temperature range, and this can be used to map temperature. The temperature dependence arises because the proton in water is screened from the applied magnetic field B_0 by the electronic charge density in the water molecule, and the charge density is perturbed by interactions with neighboring water molecules, primarily through hydrogen bonding. The amount of perturbation depends on the average number and strength of the hydrogen bonds, and this changes with temperature. It is not, of course, the chemical shift itself that is imaged but rather, the small change in phase, $\Delta\phi(\mathbf{r})$, induced by a temperature change, $\Delta T(\mathbf{r})$. For a gradient-echo sequence the phase shift $\Delta\phi(\mathbf{r})$ is equal to the frequency shift $\Delta\omega(\mathbf{r})$ times the echo time TE. Because $\Delta\omega(r)$ is related to the change in chemical shift, $\Delta\sigma(r)$, we can write

$$\Delta\phi(\mathbf{r}) = \gamma B_0 TE \frac{d\sigma}{dT} \Delta T(\mathbf{r}) \tag{3.4}$$

where $\Delta T(\mathbf{r})$ is the desired temperature change. There are two subtleties in this simple relationship and both relate to the magnitude of the applied field B_0. The first concerns the assumption implied in equation (3.4) that the amplitude of the external field B_0 does not vary in space or time during the course of the experiment. Any drift in the average value of B_0 from the magnet and probe will induce a zero-order phase shift that is material and temperature insensitive and can be taken into account with a reference phantom that remains at constant temperature. In many cases, however, the field drift is not uniform over the entire sample, and it is then necessary to use several reference samples located at different positions in the field. A first-order space-dependent phase drift arising from changing $B_0(\mathbf{r})$ can then be reconstructed.

The second subtlety concerns the effect of temperature-dependent susceptibility effects. The chemical shift σ in equation (3.4) is the proportionality constant between the local magnetic field felt by a water proton located at $\mathbf{r}$, $B_{loc}(\mathbf{r})$, and the external applied field, $B_0(\mathbf{r})$. However, there is also an effect from the bulk volume susceptibility of the material being examined. As a good approximation, this bulk susceptibility effect can be written

$$B_{loc}(\mathbf{r}) = \left[\frac{1 - 2\chi(\mathbf{r})}{3 - \sigma(\mathbf{r})}\right] B_0 \tag{3.5}$$

This shows that temperature changes can induce phase changes not just via the chemical shift, $\sigma(\mathbf{r})$, but also through changes in the local volume susceptibility of the material, $\chi(\mathbf{r})$. The extent to which the observed phase changes depend on the chemical shift or the susceptibility depends on the nature of the material. For many materials the susceptibility effect can be ignored. However, in fat tissue susceptibility changes are comparable to those of the chemical shift, and this makes temperature calibration of the phase shift very difficult in certain foods (168).

The temperature mapping protocol is illustrated in Figure 3.9. The four small circles are cylindrical phantoms kept at constant temperature throughout the experiment.

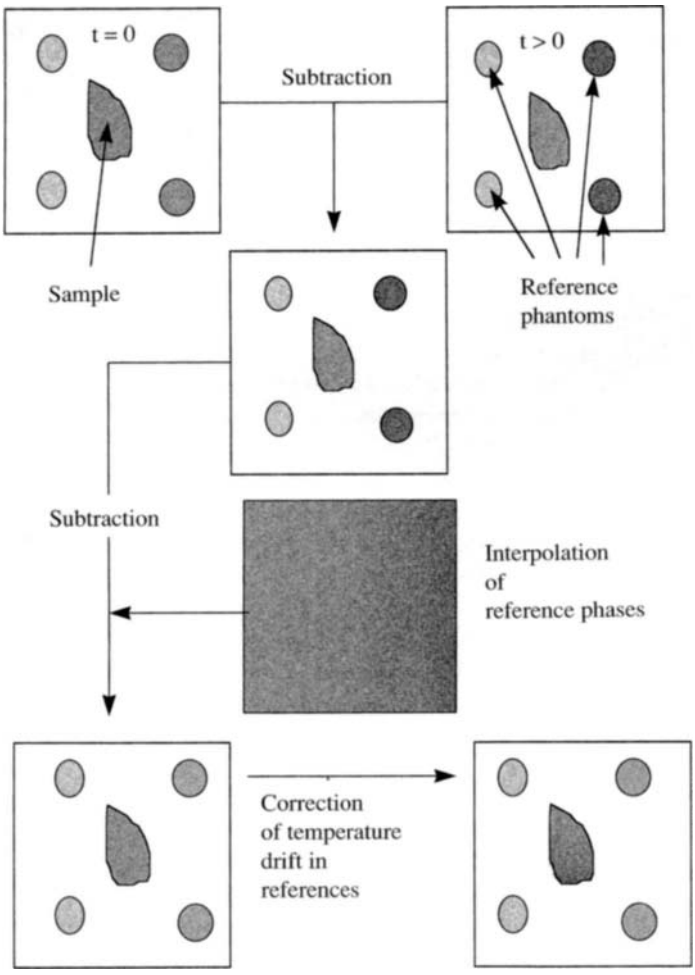

Figure 3.9. Chemical shift temperature mapping protocol. The four smaller circles represent phantoms for compensating phase shifts. (From Ref. 169.)

The changes in their phase is used to provide a zero- and first-order phase correction due to the drift in the applied field during the course of the experiment. This is done by spatial interpolation of the phase changes observed in the three constant-temperature phantoms, followed by subtraction of the resulting smoothed phase-drift map. Only phase differences are needed, so the first step involves subtraction of the initial map for the thermally equilibrated sample. This protocol has been tested on an agar gel and then used to map temperature in human leg muscles in vivo (169). Most recently, a similar protocol has been used by Litchfield and co-workers to study aseptic food processing (see below).

3.1.4 Surface Heat and Mass Transfer Coefficients

The efficiency of a processing operation such as drying or baking depends on the magnitude of the heat and moisture transfer rates at the food surface. However, the temperature, chemical state, and moisture content of a food surface change during processing, and this causes the magnitude of the surface heat and moisture transfer coefficients to vary. It is therefore essential to monitor the changing conditions of the food surface during processing and storage. Surface temperatures can sometimes be determined by painting with liquid-crystal temperature indicators whose color depends on temperature, but these materials may themselves perturb the moisture distribution and transport. Insertion of thermocouples only measures temperature at a point, and the presence of the thermocouple can perturb the heat flow. Here again, MRI can assist by providing real-time values of surface and interior temperature $T(r,t)$. The heat transfer coefficient can then be obtained, as a function of surface temperature and moisture content, by modeling $T(r,t)$. This approach, together with simultaneous MRI observations of the time-dependent surface moisture content, should permit a thorough scrutiny of the actual heat and mass transfer boundary condition during processes such as drying and cooking.

MRI is also being used to measure fluid-to-particle convective heat transfer coefficients (h_{fp}) which are needed to model aseptic food processing. Such measurements are not merely of academic interest, because the U.S. Food and Drug Administration has authorized the use of mathematical models to predict sterilization values (334). However, experimental values of h_{fp} are needed to validate the models, and MRI temperature mapping is the technique of choice. At the time of going to press, Kantt, Litchfield, and co-workers at the University of Illinois have reported MRI measurements of h_{fp} for lumps of raw, white potato suspended in a carrier fluid consisting of 6% gelatinized starch (private communication of work submitted to *J. Food Science*). A 20% w/w potato in carrier dispersion was used with varying potato sizes and flow rates, the smallest potato size category being $9.5 \times 9.5 \times 12.7$ mm at a flow rate of 21.2 L/min. The carrier was first made by adding starch to water and gelatinizing the dispersion by heating in a blend tank to temperatures between 70–80°C, with stirring. The potato pieces were then added, mixed, and held for 20 minutes at 80°C to obtain a uniform temperature. The mixture was then pumped through heat exchangers where the temperature of the carrier fluid was raised by up to 45°C to aseptic temperatures. The suspension exiting the heat ex-

changer was passed through the imaging magnet where the temperature distribution in the potato pieces was measured using the chemical shift mapping method (section 3.1.3). Even 45 seconds after exiting the heat exchanger the larger potato pieces still showed temperature differences ($T_{surface} - T_{center}$) of up to 22°C. A finite element method was used to fit the temperature maps within the potato pieces and extract a value of h_{fp}. In this calculation an average residence time was calculated from the average flow rate since the actual residence time of the particles being imaged was unknown.

3.2 MRI AND FOOD QUALITY FACTORS

Temperature changes are important in optimizing thermal transport and energy efficiency, but a processing or storage operation is designed to optimize food quality as well as energy efficiency. There are many factors that determine the quality of a food. A partial list would include color, taste, aroma, texture, and chemical composition, including the concentration of factors such as vitamins, sugars, and lipids; the extent of denaturation and gelatinization of biopolymers and the changing phase structure of the food caused, for example, by polymorphic transitions in lipids and fats, crystallization of sugars, and retrogradation processes associated with biopolymers. In addition, there can be slow enzymic and nonenzymic chemical spoilage reactions whose rates depend on local water content and temperature. For notational convenience these various quality factors will be labeled $Q_i(r,t)$, where the subscript i refers to the quality factor of interest. Of course, not all quality factors are amenable to MRI analysis, color being an obvious example, but in principle, any factor causing a change in the chemical composition or the dynamic state of molecules in the food should affect such NMR properties as relaxation times, diffusion rates, signal intensities, and/or chemical shifts and result in changes in image contrast. Examples of MRI being used to monitor changes in food quality can be found in most classes of food, including confectionery, fruits and vegetables, fish and meat, and cereal and dairy products. The range of possible applications is extensive and growing rapidly. Rather than attempting a comprehensive survey, the principles will be illustrated with a few representative examples, beginning with chocolate confectionery.

3.2.1 Quality Factors Associated with Solid–Liquid Ratios and Polymorphic Transitions in Fats

The long-term storage stability of fat-containing foods can be affected by fat crystal growth and polymorphic transitions in the solid fat phase. Other quality factors associated with rheology (such as hardness and mouth-feel) and flavor perception also depend critically on solid–liquid fat ratios. Bench-top low-resolution NMR measurements of the transverse relaxation times based on an FID or CPMG sequence are now used routinely for the determination of solid–liquid fat ratios (121), and transverse relaxation-time-weighted MRI can obviously add spatial discrimination

to these measurements. Adding spatial dimensions is not a trivial extension because the crystallization kinetics can depend critically on the shape and size of the food material and complicate the industrial scale-up of laboratory processes. Moreover, in solid lipid-based foods it is not only the solid–liquid phase transition that can be imaged but also the spatial distribution of different polymorphic crystalline or amorphous lipid phases in the apparently "solid" product because these are also associated with different proton relaxation times (118).

Chocolate is one particular high-fat product of obvious commercial importance that has been studied by NMR and MRI. The MRI signal from chocolate originates from the protons in cocoa butter and milk fat. Cocoa butter is primarily a mixture of triglycerides of palmitic (P), oleic (O), and stearic (S) fatty acids, with major contributions from the combinations POS, POP, and SOS; milk fat consists of large numbers of different triglycerides. The amount of solid and liquid fat in the chocolate will obviously vary with temperature, most chocolate being in the liquid state at 60°C and "solid" at room temperature. The other solidlike ingredients in solid chocolate, such as finely ground cocoa mass, sugar particles, and dried whole milk, do not contribute to the MRI signal because of their short transverse relaxation times. The triglycerides in cocoa butter exhibit polymorphism in their crystalline states. Six polymorphs have been identified (125), and which polymorph is present depends on the thermal history of the chocolate. For example, slowly cooling cocoa butter produces the more stable number 5 (or β) polymorph, whereas more rapid cooling gives the less stable number 3 or 4 (or β') polymorphs and larger amounts of a solid amorphous phase exhibiting greater chain mobility and a longer transverse relaxation time (120).

The MRI signal from cocoa butter arises from regions of high chain mobility and so depends both on the solid-liquid ratio and because each polymorph is associated with different chain mobility, on the polymorphic state of the solid components. For this reason, transverse relaxation-time-weighted MRI has been used to distinguish regions of chocolate that have melted and resolidified from those that have remained solid throughout (118). *Blooming* is an important quality factor in solid chocolate. Blooming is caused by polymorphic transitions in the cocoa butter and tends to occur during long-term storage of the chocolate and is accelerated by temperature cycling in high-humidity environments. It results in a loss of surface gloss, a whitish appearance, and is associated with changes in flavor and hardness. Because different polymorphic states have different proton transverse relaxation times, it should be possible to use MRI noninvasively as an early detector of chocolate blooming, although this possibility has yet to be investigated systematically.

The migration of liquid lipid components between two phases in multilayer confectionery products greatly affects the long-term quality of the product. For example, the transport of liquid triglycerides from a praline or hazelnut filling into a surrounding solid chocolate layer in a filled chocolate sweet can alter thermal stability and accelerate blooming on the chocolate surface. MRI lends itself naturally to this type of problem and has been used to image the transport of liquid lipids into chocolate in a model lamellar two-layer chocolate product consisting of a layer of

hazelnut oil and sugar layered over with dark chocolate. The lamellar structure permitted a 100-μm spatial resolution to be achieved, and the time course of the lipid migration was followed over an 84-day period for two samples stored at 19 and 28°C (305). Intensity changes in the profiles were converted to liquid lipid concentrations by calibrating with homogeneous samples of known liquid fat content (which was determined independently by the nonspatially resolved high-power NMR method). Figure 3.10 shows the time course of the liquid lipid profiles and reveals nondiffusive profiles and very different behavior at the two temperatures. At 19°C the liquid lipids tend to accumulate at the interface between the hazelnut oil and chocolate layers. In contrast, at 28°C the lipid accumulates at the chocolate surface. The reasons for these differing transport patterns has yet to be clarified and represents a challenging and important theoretical problem. Other examples of MRI use to image lipid transport and its effect on quality include the migration of fat into bread from peanut butter (171) and the separation of cream from milk over a 9-h period (172).

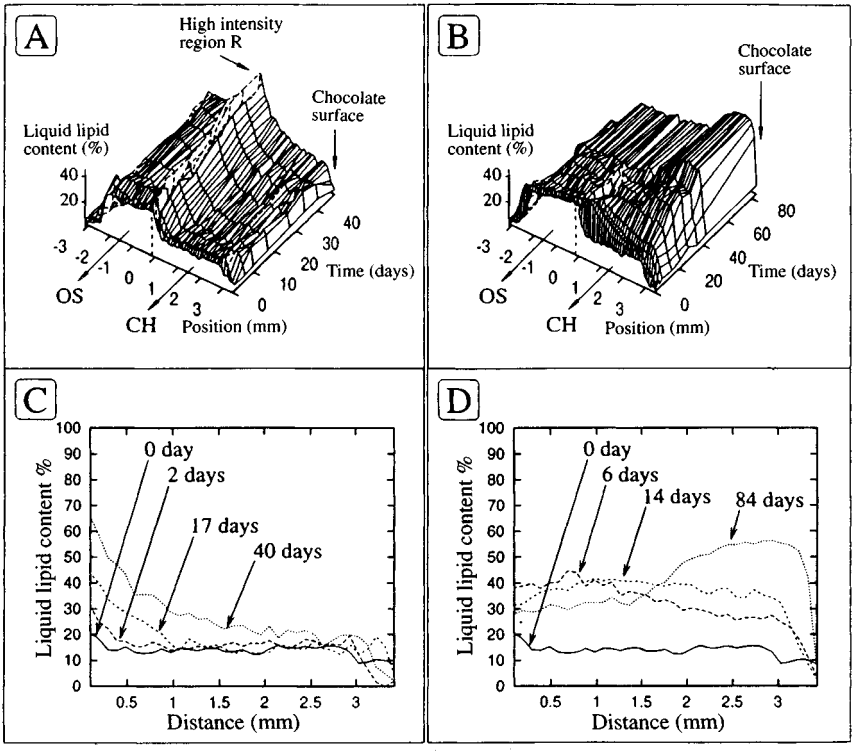

Figure 3.10. Time course of the liquid triacylglycerol content in chocolate. (A) experiment at 19°C; (B) experiment at 28°C (OS, mixture of oil and hazelnut and icing sugar); (C) migration profiles of the liquid triacylglycerol in chocolate at 19°C; (D) migration profiles of liquid triacylglycerol in chocolate at 28°C. (From Ref. 305.)

3.2.2 Time-Dependent Quality Factors in Colloidal Foods

Many foods exist as multiphase colloidal systems such as emulsions, dispersions, and foams, and in such materials the microstructure of the system affects the *kinetics* of the phase changes, such as crystallization and phase separation, and introduces a time dependence into the quality factors that can limit storage times and processing conditions.

Edible Oil-in-Water Emulsions. Edible oil-in-water emulsions such as salad spreads, creams, and sauces are very popular, yet many basic aspects, such as the role of oil droplet size distribution, surfactant, and triglyceride composition on rates of crystallization of lipids in model oil-in-water emulsions, are still poorly understood. For lipid crystallization to occur in an oil droplet, the temperature must not only be below the melting temperature (the thermodynamic condition for crystallization), but it must also be below the temperature for homogeneous nucleation (the kinetic condition for crystal growth). If not, the oil droplet remains indefinitely in a supercooled liquid state.

The homogeneous nucleation kinetics can be modeled as a zeroth-order reaction such that

$$\frac{dC}{dt} = -k_n \tag{3.6}$$

where k_n is the nucleation rate constant and C is the concentration of liquid triglyceride. Integration gives

$$\frac{C(t)}{C(0)} = 1 - \frac{k_n t}{C(0)} \tag{3.7}$$

In contrast, the rate of crystal growth, once the system is nucleated, can be expressed as a second-order reaction such that

$$\frac{-dC}{dt} = -k_g C^2 \tag{3.8}$$

where k_g is the growth rate constant. Integration of equation (3.8) gives

$$\frac{C(0)}{C(t)} = 1 + k_g C(0)t \tag{3.9}$$

MRI has been used to test these relationships by providing noninvasive real-time measurements of $C(r,t)$ in emulsions during cooling. Spatial resolution of the crystallization kinetics is important because the rate depends on the local temperature, and this varies spatially throughout the sample as it cools. Nonspatially resolved measurements such as DSC give only average values of $C(t)$ for a range of temperatures that is insufficient for detailed analysis of the crystallization kinetics.

The emulsion system used to test the kinetic model above consisted of a trimyristin oil-in-water emulsion (40:60%) containing various amounts of a trilaurin (122–124, 127). As a pure 40:60% emulsion, trimyrystin (a C_{14} homotriglyceride) freezes rapidly in minutes at 20°C because this temperature is below both the melting point and nucleation temperature. In contrast, when the trimyrystin is replaced by trilaurin, a shorter-chain-length C_{12} homotriglyceride, the pure 40:60% trilaurin emulsion does not crystallize over weeks at 20°C. This is because 20°C, although below the melting point, is above the trilaurin nucleation temperature, so it remains in a supercooled state. The MRI studies were therefore used to measure $C(r,t)$ in trimyristin emulsions containing increasing amounts of trilaurin under conditions of convective cooling. A transverse relaxation-time-weighted spin-echo imaging method was used because only the liquid lipid and water contributes to the signal, the solid lipid having too short a transverse relaxation time to contribute. Volume-localized spectroscopy based on the CHESS imaging sequence (see Chapter 1) was used in parallel with the spin-echo imaging to distinguish liquid oil and water signals from different regions of the sample (the top, middle, and bottom regions of a cylinder containing the cooling emulsion). Typical results are plotted in Figures 3.11 and 3.12, and the two straight-line segments in each plot correspond to fits of the nucleation and crystal growth equations [equations (3.7) and (3.9), respectively]. The results clearly demonstrate the transition from nucleation and crystal growth kinetics and show that the two triglycerides did not behave independently. Indeed, the resulting frozen system exhibits a single melting peak in DSC and not separate peaks from trilaurin and trimyrystin, which strongly suggests compound (or

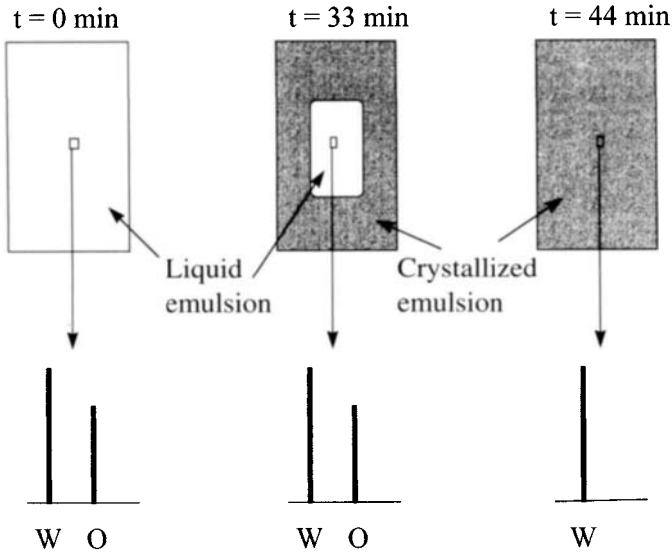

Figure 3.11. Schematic of the time course of emulsion crystallization, indicating the time course of fat-weighted images and localized spectroscopy taken from the middle part of the emulsion. Quantitative results from this type of experiment are shown in Figure 3.12. (From Ref. 127.)

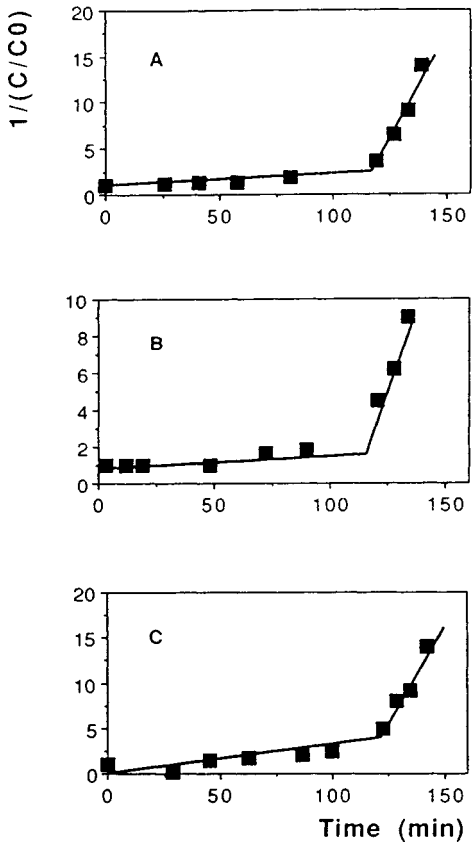

Figure 3.12. Typical samples for the observation of different kinetic regimes. The data were obtained with 80 mL per liter of trilaurin. (*A*), (*B*), and (*C*) refer to the top, center and bottom of the container (see Figure 3.11). The first and second parts of these plots were tentatively referred to as nucleation and crystal growth, respectively.

mixed) crystal formation. This is consistent with the absence of an MRI signal from residual, unfrozen trilaurin after crystallization.

Phase separation in edible oil-in-water and water-in-oil emulsions such as salad dressings, mayonnaise, milk, and ice cream is another kinetic process that affects their long-term stability, and much remains to be understood about the effect of surfactants, emulsion composition, droplet coalescence, and flocculation on the phase separation kinetics. The theoretical analysis of the rates of phase separation (creaming) of emulsions rests heavily on Stoke's law and modifications of it. According to Stoke's law, the mean velocity, v, of oil or water droplets in the direction of gravity in a phase-separating emulsion is given as

$$v = \frac{2R^2 g\,(\rho_1 - \rho_2)}{9\eta} \tag{3.10}$$

where R is the mean radius of the droplet, η the continuous phase shear viscosity, and $\rho_1 - \rho_2$ the difference in densities between the two phases. As a first approximation, v can be equated to the mean velocity of separation of the oil and water phases. However, in reality, the relationship will be complicated by a distribution of droplet sizes and by coalescence, so breaks down at high droplet concentrations. MRI can assist in the development of better models of phase separation by providing direct, noninvasive measurements of the time-dependent spatial distribution of oil fraction, $\phi(r,t)$ and in combination with PGSE diffusion measurements, of the spatial distribution of droplet size distributions (see Chapter 11).

An example of this approach has been the MRI study of phase separation in a 40% soy oil-in-water emulsion stabilized with 0.2% polyoxyethylene sorbitan monooleate surfactant (126). A linear relationship was first established between the single-exponential proton longitudinal relaxation rate and the oil volume fraction ϕ for a series of homogenized soy-oil emulsions of increasing oil fraction. The relationship conformed to that expected for fast exchange of magnetization between the oil and water phases (see Chapter 2)

$$T_1^{-1} = \phi_{oil} T_{1oil}^{-1} + \phi_{water} T_{1water}^{-1} \tag{3.11}$$

$T_1(z,t)$ profiles were then measured as a function of time along the axis of a vertical cylindrical column of creaming emulsion, and these were converted via equation (3.11) into time-dependent oil volume fractions $\phi(z,t)$, where z is the direction of gravity and of the cylinder axis. Typical results shown in Figure 3.13 show a

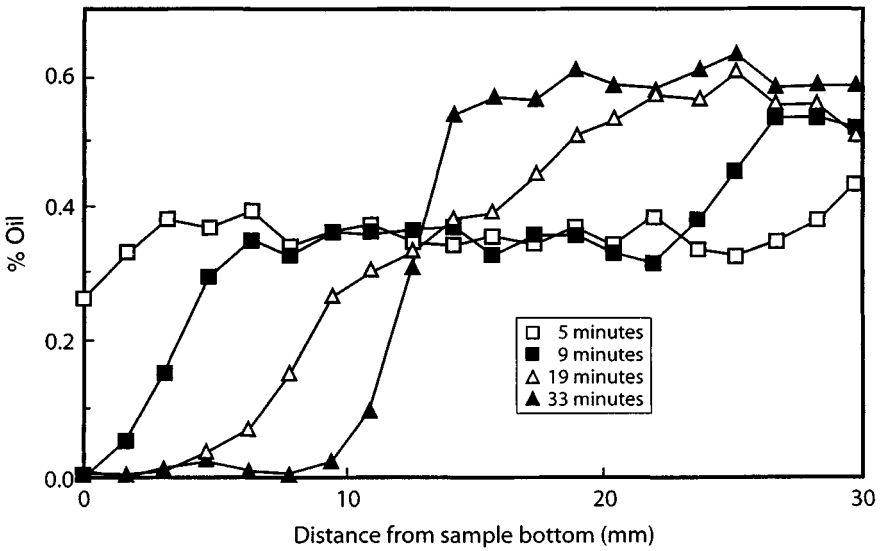

Figure 3.13. Oil volume fraction versus time and position (height from bottom) along a profile of an emulsion consisting of 40% soy oil–water–0.2% polyoxyethylene sorbitan monooleate. (From Ref. 126.)

"cream" front moving upward through the sample. Substitution of the mean velocity of the moving front into equation (3.10) gives an average droplet radius of 7 μm, which is of the correct order of magnitude. Chemical shift imaging is an alternative to T_1 mapping for determining $\phi(z,t)$, and PGSE methods also exist for determining droplet size distributions in emulsions. These are described more fully in Part Two. In principle, therefore, PGSE-weighted imaging can also be used to image the coalescence kinetics in collapsing emulsions.

Foams. Foams are another important class of colloid, and foam drainage and collapse are important phenomena in the food industry. Examples of common food foams include whipped egg white, whipped cream, and ice cream, and with these foods it is important to maintain long-term foam stability and quality. A liquid-based foam is a thermodynamically unstable state and tends to phase separate by drainage of water under gravity from the thin liquid films defining the gas bubble boundaries. This eventually leads to thin film breakage and bubble collapse. A foam can therefore be stabilized by increasing the fluid viscosity to slow the drainage and adding appropriate surfactants to stabilize the film interfaces.

MRI can contribute to these efforts by providing noninvasive measurements of the rate of drainage and fluid flow (128). The one-dimensional spin density profile of a cylindrical column of foam measured in the direction of gravity is proportional to the amount of liquid at each height in the foam (see Figure 3.14), and this information provides a critical test of theories of foam drainage. Additional information such as the spatial- and time-dependent changes in mean bubble size can, in principle, be obtained from relaxation time and/or diffusion maps provided that they are calibrated with optical methods.

Swiss cheese could be classed, somewhat loosely, as a macroscopic solid foam, and it is worth noting that MRI has also been used to investigate the relationship between cheese quality and its internal structure (302). A detailed grading system is used to determine the quality of Swiss cheese, involving the number, shape, and size of eyes, cracks, and gas holes in the body of the cheese. Currently, these quality factors are measured by physically cutting a cheese in half and visually examining the two cut surfaces. MRI, together with image processing algorithms, offers an alternative, fully automated, nondestructive method of determining the same quality features. Indeed, the longer-term objective of this research is to develop the MRI approach for use as an on-line quality measurement of Swiss cheese. The on-line aspects of MRI are discussed more fully in Chapter 6; NMR studies of the microscopic structure of cheese, regarded as a solid colloidal system, are considered in Chapter 11.

3.2.3 Quality Factors Associated with Cellular Tissue

Fish and Meat. MRI has also been used to monitor quality changes in fish and meat. MRI spin-echo imaging of whole fresh and frozen cod have been used to determine the differences in water binding and its effect on the fish texture noninvasively. This is an important storage problem because cod shows marked changes in

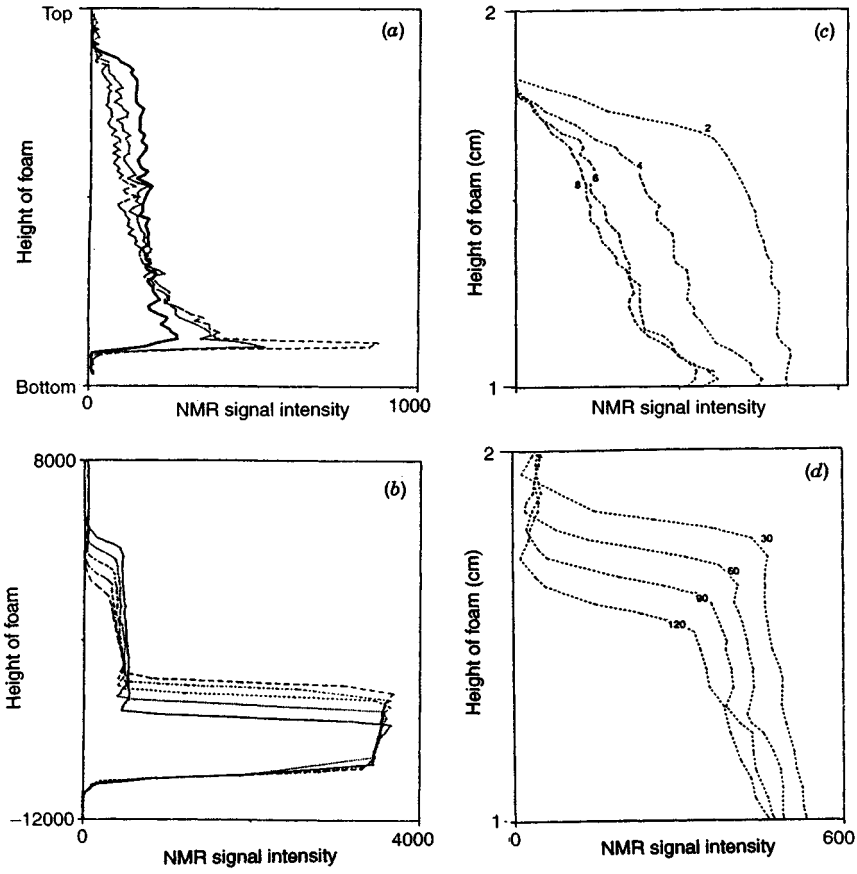

Figure 3.14. Sequential signal intensity profiles for egg white foam (*a*) and beer (*b*). Sequence times as shown on lines represent time after formation in minutes and seconds, respectively (*c*) and (*d*) are magnified profiles. (From Ref. 128.)

texture due to protein aggregation during frozen storage, thereby making the fish unpalatable (132).

Variations in the quality of cured meat, such as pork, during brining, is of primary interest to bacon manufacturers. Two- and three-dimensional ^{23}Na imaging has been used to image the spatial distribution of brine in cured rabbit muscle and in tumbled ham (300). However, the low sensitivity of the sodium ion compared to that of protons necessitated many repeat acquisitions to obtain a good signal-to-noise ratio, and this is a problem if the time course of brining and the associated changes is to be imaged. An alternative approach used by Guiheneuf and coworkers (298) involves using manganese ions as tracers to follow the brining kinetics. Manganese ions in trace amounts diffuse at a rate similar to that of the most abundant electrolyte species (i.e., sodium and chloride ions), so the time course of

manganese diffusion can be used to follow, indirectly, the diffusion of sodium and chloride into the meat. Because it is paramagnetic, only trace amounts (e.g., <20 μg per gram of meat) of manganese are sufficient to reduce the water proton longitudinal relaxation time significantly. The ingress of the manganese can therefore be visualized with a fast, null-point, inversion recovery proton MRI sequence (298). A subsequent study by the same group observed differences in the diffusion of manganese ions in pork meat that had already been cured with various brine concentrations (299). It was argued that the decreases observed in the manganese diffusion coefficient were related to increases in the density of protein binding sites in the pork and that these, in turn, are related to the salt concentration. For example, increasing the salt concentration from 53 mg/g to 193 mg/g causes the meat swelling to decrease from 33% to 6% and the manganese diffusion coefficient to fall from 0.89×10^{-10} m^2/s to 0.42×10^{-10} m^2/s. It would appear, therefore, that MRI manganese diffusion studies may be a useful probe of brined meat quality.

The amount and spatial distribution of fat in meat muscle are key factors affecting the quality of unbrined meat. Quality factors of concern include the palatability, texture, and juiciness as well as taste and aroma of the final cooked meat. Tingle and co-workers (301) have demonstrated the feasibility of using chemical shift as well as T_1-weighted imaging in visualizing the distribution of fat and water in samples of retail meat. No correlation with textural or sensory measurements was sought in these preliminary studies, but this would be an obvious avenue to explore.

Fruits and Vegetables. A number of feasibility studies have used MRI to monitor fruit and vegetable quality, such as bruising in apples, pears, onions, and peaches (173); the deterioration of apples in storage (174); water-core distribution in apples (175); and oxygen-dependent core breakdown in Bartlett pears during storage (176). A detailed analysis of the origins of image contrast in bruised apples has been made by McCarthy and co-workers (304). The bruised region in apple appears brighter than intact tissue in spin-warp images. By measuring the intrinsic transverse relaxation times with the CPMG sequence at short pulse spacings it was shown that this was not a consequence of a relaxation time difference. Indeed, the bruised region had a shorter T_2 relaxation time than that of the intact tissue, suggesting that it should appear darker rather than brighter. By comparing gradient-recalled echo images with spin-echo images it was concluded that the contrast originated from changes in tissue susceptibility. Intact apple tissue has a large number of intercellular air spaces, which means that when placed in a magnetic field, there are significant local field gradients set up around the air gaps, created by the difference in bulk magnetic susceptibility between air and water. Diffusion through these local gradients causes dephasing and therefore loss of signal intensity. When the tissue is bruised, the integrity of cell walls and membranes is lost, so fluid enters the air gaps and reduces the susceptibility-induced field gradients, resulting in an increased T_2^* and a brighter image. The effect is most pronounced in gradient-recalled images, because reversing the applied field gradient only refocuses the dephasing caused by the applied gradient, not that caused by internal gradients. In contrast, a spin-echo image refocuses the dephasing caused by all gradient inhomogeneities,

both external and internal. This suggests that gradient-recalled images may be more useful in future on-line MRI sensing of bruising in apples (see Chapter 6). Other applications of MRI to fruit and vegetables are discussed more fully in Chapter 7.

Cereals. The distribution of lipid and solute concentrations in cereal grains is one important quality factor amenable to MRI analysis. For example, Ishida and coworkers (N. Ishida, H. Kano, and H. Ogawa, National Food Research Institute, Japan, unpublished conference abstract) have used chemical shift microimaging and localized spectroscopy to image the production and spatial distribution of maltose and other metabolites in germinating barley seeds, which affects the quality of beers and spirits. A discussion of water distribution and flow in cereal grains is deferred to Chapter 9.

3.2.4 Quality Factors Affected by Biopolymer Gelation and Retrogradation

Biopolymer gelatinization is fundamental to a wide range of food manufacturing operations and affects the texture and thermal stability of the food. Many confectionery products, such as jellied sweets, contain gelatine, and a wide variety of biopolymers such as starches, carrageenans, agarose, and pectins, are used, either alone or as mixed biopolymers, as gelling agents and thickeners throughout the food industry. Because some biopolymer thickeners produce a similar mouth-feel to fat, there is much research directed at developing novel mixed biopolymers as fat substitutes in low-fat foods. As we shall see in greater detail in Chapter 12 the increased interchain cross-linking associated with gelation reduces the mobility of the biopolymer chains, which results in a reduction in the transverse relaxation times of exchangeable and nonexchangeable biopolymer protons. Because water protons are in fast exchange with biopolymer protons in hydroxyl, amino, and thiol groups, gelation also causes a reduction in the observed transverse water proton relaxation time. The spatiotemporal evolution of the gelation process can therefore be followed using MRI transverse relaxation time maps.

Calcium Alginate Gels. An interesting example of T_2 mapping of gelation involves the formation of alginate gels by the diffusion of calcium ions into a sodium alginate solution. Calcium alginate gel beads are now widely used for the immobilization of whole microbial and plant cells and have potential for the encapsulation and slow release of flavor compounds and antimicrobials. The beads are formed by dripping sodium alginate solution (containing the cells to be immobilized) into a solution of calcium chloride. Understanding the structure and stability of calcium alginate gels as well as the reaction-diffusion kinetics within them is therefore of particular importance in the biotechnology processing area. When calcium ions diffuse into a sodium alginate solution, they cross-link the alginate chains via ionic bridges formed with two negatively charged guluronate groups on the alginate backbone. The gel is spatially inhomogeneous because the calcium alginate gel is more concentrated in the region that first comes in contact with the calcium ions. The gelation stage is associated with syneresis, which is gel shrinkage resulting in

the release of hydration water as the calcium ions bind the carboxylate groups on the alginate. This is, of course, accompanied by concentration of the gel.

A simple model for these effects has been presented by Kim (116) and assumes a pseudosteady-state situation such that the flux of calcium ions into the gel equals the rate of consumption of sodium alginate solution according to a fixed stoichiometry (see Figure 3.15). For a spherical bead of radius $R(t)$ containing an outer layer of gelled calcium alginate of thickness $R(t) - r_c(t)$ and an inner spherical core of ungelled sodium alginate solution of radius $r_c(t)$, the spatial profile of the calcium ion concentration (or equivalently, the alginate concentration) through the outer gelled layer can be obtained by solving the diffusion equation for the calcium ions under steady-state conditions

$$\frac{\partial C}{\partial t} = 0 = \frac{1}{r^2}\frac{\partial}{\partial r} Dr^2 \frac{\partial C}{\partial r} \tag{3.12}$$

This is solved by setting the ion concentration to zero at $r_c(t)$ and equal to the initial concentration $C(0)$ at $R(t)$ and assumes that gel formation is fast compared to the calcium ion diffusion. For a spherical bead the solution of equation (3.12) gives a spatial profile

$$C(r) = C(0)\left[1 - \frac{Rr_c(1/r - 1/R)}{R - r_c}\right] \tag{3.13}$$

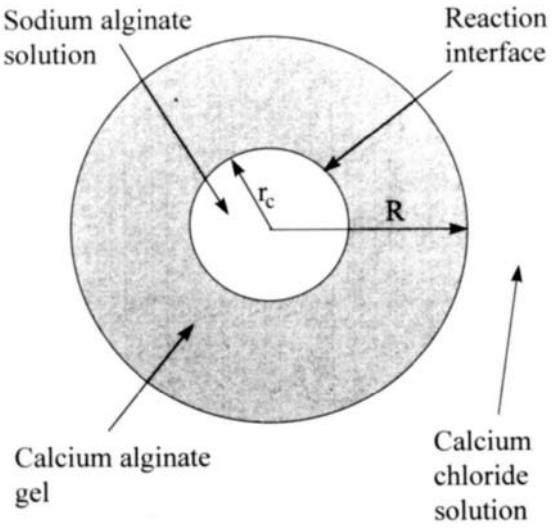

Figure 3.15. Spherical drop model for the gelation of a spherical sodium alginate drop by ingress of calcium ions from a surrounding calcium chloride solution.

The shrinkage, $R(t)$, and position of the ion front, $r_c(t)$, can be obtained by equating the fluxes of the calcium into the gel with the rate of consumption of sodium alginate solution

$$4\pi R(t)^2 D\left(\frac{dC}{dr}\right)_R = -b\frac{d}{dt}\frac{4\pi r_c(t)^3}{3} \tag{3.14}$$

Here the constant b takes account of the stoichiometry of the calcium–alginate reaction. This equation can be solved by substituting equation (3.13) and integrating to obtain a relationship between the shrinkage, $R(t)$, and the position of the calcium front, $r_c(t)$, which need not be reproduced here. A more sophisticated reaction-diffusion model has been solved numerically by Mikkelsen and Elgsaeter (250) using standard finite-difference methods, and the calcium and gel concentration profiles for various geometries and boundary conditions were presented. A notable deficiency of their model is the failure to treat syneresis and the resulting shrinkage. Nevertheless, their model agrees semiquantitatively with the gravimetric "slicing" experiments of Skjak-Braek and co-workers (251).

Because MRI gives real-time measurements of $R(t)$, $r(t)$, and the alginate concentration profile, $C(r(t),R(t))$, it is ideal for a noninvasive test of the theoretical models. An early MRI feasibility study used one-dimensional T_2 mapping to determine the concentration profile of calcium alginate in an inhomogeneous gel. The study was purely structural in content and simply required a calibration curve of T_2 versus alginate concentration to be made for a series of homogeneous calcium alginate gels (113). Subsequently, a time-dependent one-dimensional (lamellar) MRI study of the formation of calcium alginate gels by the diffusion of calcium ions into a sodium alginate solution was reported (see Figure 3.16) (114). Unlike the earlier study, the concentration profile of the calcium alginate gel was not reported or analyzed in this time-course experiment, only the position of the calcium ion front, whose estimated position showed a linear dependence on the square root of the diffusion time which agrees with the foregoing model when modified for lamellar morphology (116). The next stage in these MRI studies involves imaging not just the position of the calcium ion front, $r_c(t)$, but also the time-dependent alginate concentration profile, $C(r(t),R(t))$, and the syneresis effect, characterized by $R(t)$. It should also be possible to use MRI to study the space-time course of the peculiar volume oscillations caused by counterfluxes of ions and water that are observed when calcium alginate beads are placed in water or sodium chloride solutions (115). The sequestration of heavy metal ions by calcium alginate gels and gels containing immobilized cells has also been studied by MRI (112). Such biosorption could be useful for the removal of traces of heavy metals from wastewater.

Starch Retrogradation. The staling of bread, cookies, cakes, and other cereal products during storage is another important quality factor and is associated with the recrystallization of starch or, more precisely, amylopectin chains, into A- or B-type

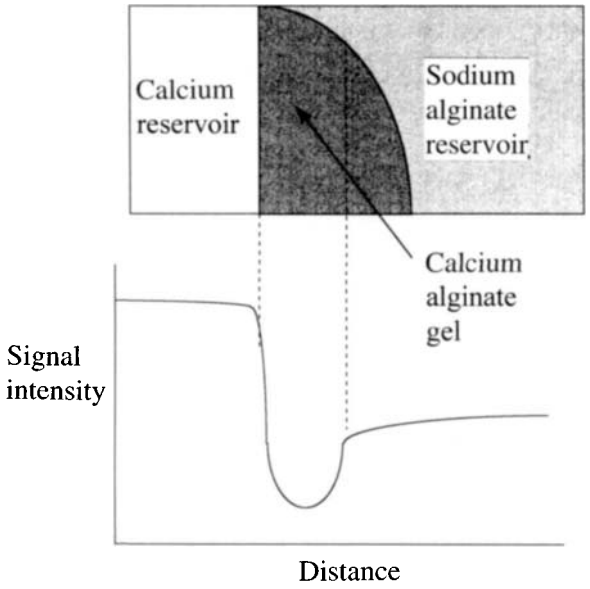

Figure 3.16. Representation of the imaging protocol used by Potter et al. (113,114) to follow the formation of calcium alginate gels. Calcium diffuses from a reservoir into a sodium alginate solution resulting in a lamellar gelation zone. The top diagram is obtained by stacking one-dimensional profiles taken at regular time intervals along the axis of the cylindrical reaction vessel. One such profile is illustrated in the lower diagram.

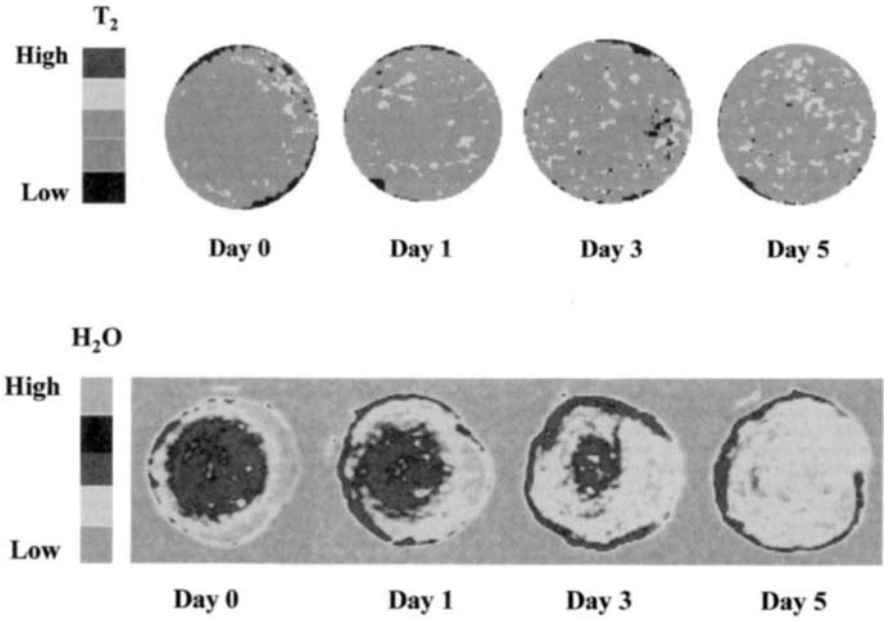

Figure 3.17. M_o maps for freshly baked sweetrolls and after 1,3, and 5 days of storage. (From Ref 133).

crystalline polymorphs from the initial gelatinized state obtained by baking. Retrogradation is associated with increased hardness and is thought to be associated with reduced biopolymer chain mobility in the amylopectin. The changes in molecular mobility associated with retrogradation are considered in greater detail in Part Three. Here we consider the spatial distribution of retrogradation rates because this can be followed by MRI. Figure 3.17 (bottom) shows the M_0 maps for freshly baked sweet rolls and after 1, 3, and 5 days of storage reported by Ruan et al. (133). They showed that staling was associated with an apparent migration of moisture from the inside to the outside of the sweet roll. Surprisingly, the corresponding T_2 maps Figure 3.17 (top) showed a longer initial T_2 time in the drier outer region of the sweet roll and a shorter T_2 time in the middle region, which gradually increased during storage. The reasons for these storage changes are still a matter of speculation. One hypothesis is that retrogradation proceeds faster in the center because of the higher initial moisture content and results in an increase in more mobile water with a longer T_2, which migrates to the outside of the sweet roll. Whatever the correct interpretation, it is clear that MRI has an important role to play in imaging the spatial changes associated with staling cereal products.

4

FLOW IMAGING AND FOOD RHEOLOGY

4.1 INTRODUCTION

Characterizing the rheological properties of liquid foods, slurries, and suspensions is an essential step in the optimization of many food manufacturing processes. Knowledge of the viscosity of a liquid food is needed when sizing equipment such as pumps, mixers, heat exchangers, and extruders. Optimization of mixing processes requires knowledge of viscosities, velocity fields, shear rates, residence times, and degrees of mixing. In the asceptic heat processing of fluids containing solid food particles it is necessary to know the distribution of residence times of both the particles and the fluid to ensure a safe product. Understanding and modeling processes such as extrusion, which, in general, involves a complex interaction between heat transfer, chemical reaction, and flow, remains an outstanding challenge in food processing science. Rheological measurements can also be used in quality control of intermediate or final products.

MRI is uniquely advantageous in flow studies of concentrated particulate or colloidal suspensions and other opaque fluids because optical methods of flow measurement, such as laser Doppler anemometry and the visual inspection of the motion of suspended particles, cannot be applied. Moreover, quantitative measurement of flow velocities by inserting probes such as hot-wire sensors, can significantly perturb the flow pattern and only give measurements at a single position at a time. By combining flow imaging sequences with other pulse sequences sensitive to NMR parameters, such as relaxation times, diffusion coefficients, or chemical shifts, it is, in principle, possible to map velocity simultaneously with other parameters, such as concentration, temperature, or reaction rate.

4.2 PRINCIPLES OF FLOW IMAGING

The principles and pulse sequences used in flow imaging have been described in a number of texts (5,18) so need only be summarized here. They can be classified as steady-state, time-of-flight, or phase-shift methods.

4.2.1 Steady-State Methods

Steady-state methods rely on the loss of signal intensity in a rapidly repeated slice-selected imaging sequence due to the flow of excited spins out of the excitation slice. The method relies on loss of intensity and is not as accurate as phase-encoding techniques.

4.2.2 Time-of-Flight Methods

Time-of-flight methods are used widely in MRI and involve a *tagging and interrogation mechanism* whereby slice selection is used either to excite (or remove) magnetization from a narrow tagged slice in the flowing liquid, and a second slice-selective interrogation pulse is used to record its position at a later time. There are many variations on this tagging–interrogation theme. The position of the interrogation pulse can be changed by shifting its frequency relative to the tagging pulse and the flow rate derived from plots of the dependence of image intensity on distance between the tagging and interrogation pulses. The velocity resolution in this method is limited by the slice width, and the method is complicated by a loss of intensity due to relaxation in the time between the tagging and interrogation pulses. Variants of the method that are particularly useful for visualizing flow patterns include imaging the subsequent flow of the tagged slice by slice selecting a plane perpendicular to the tagging plane and using phase encoding and readout gradients in this plane (188). Alternatively, a grid of spins can be excited using a double DANTE sequence in which two successive orthogonal selection gradients are used. The flow pattern is then easily followed from the distortion of the grid lines in subsequent imaging of the grid pattern. This grid-distortion method is particularly effective for visualizing complex flow patterns and testing predictions of computational fluid dynamics. Recently, it has been used to produce a video of the time-dependent three-dimensional grid patterns of a fluid flowing around two baffle plates in a tube (189). Some still frames from this video are reproduced in Figure 4.1.

4.2.3 Phase-Encoding Flow

Flow imaging using the phase-encoding method provides the most accurate quantitative information and is most readily adapted to imaging either fluid velocity or acceleration. It is therefore the method of choice for the quantitative rheological measurements discussed in the next section. It uses a spin-echo imaging sequence and

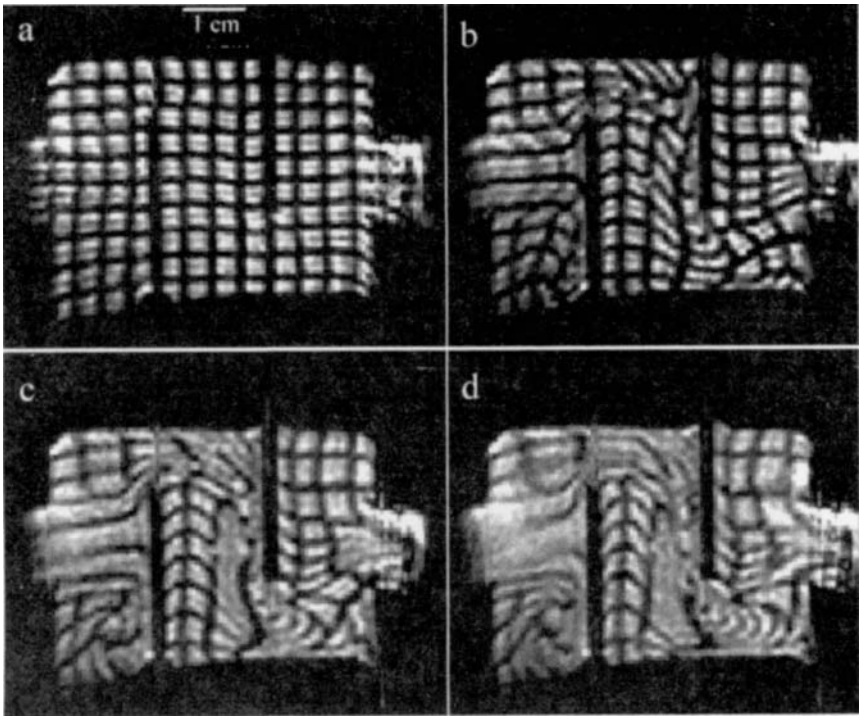

Figure 4.1. DANTE tagged echo-planar images of water flowing through a cylinder section fitted with transverse baffles. The dark tags correspond to magnetization that has been saturated at time $t = 0$; subsequent images are acquired after a delay of (*a*) 0 ms, (*b*) 400 ms, (*c*) 800 ms, and (*d*) 1200 ms. (Courtesy of Gibbs and Hall, Ref. 117.)

introduces a velocity-dependent phase shift in each image voxel by using a gradient pulse $G^*(t)$ with a nonzero first moment (see Chapter 1). If the velocity-encoding gradient amplitude is not ramped, the velocity-dependent phase shift creates a complex image, $\rho(\mathbf{r}) \exp[i\mathbf{p} \cdot \mathbf{v}(\mathbf{r})]$, where $\rho(r)$ is the spin density and $\mathbf{p}$ is the first moment of the velocity-encoding gradient, defined as

$$\mathbf{p} = \gamma \int_0^{\Delta} dt'\, t' \mathbf{G}^*(t') \tag{4.1}$$

The stimulated-echo sequence with a bipolar velocity-encoding gradient is particularly useful because the velocity phase-encoding time, Δ, can be accurately defined with hard pulses and permits extended phase-encoding times because longitudinal relaxation times are usually longer than transverse relaxation times. Various protocols exist for extracting the real and/or imaginary parts of the image, $\rho(r)$ cos $[\mathbf{p} \cdot \mathbf{v}(\mathbf{r})]$ and $\rho(\mathbf{r})$ sin $[\mathbf{p} \cdot \mathbf{v}(\mathbf{r})]$, and hence the velocity map, $\mathbf{v}(r)$. Where fast velocity imaging is required, as in mixing and turbulent flow studies, velocity-encoding variants of echo-planar imaging (EPI) and FLASH exist, but as always, the price

paid for increased speed in these sequences is loss of spatial resolution resulting from an increased acquisition bandwidth.

An alternative phase-encoding method for flow imaging uses *displacement imaging* (otherwise known as *dynamic q-space imaging*) and is based on the Fourier relationships [equations (1.18) and (1.19)] discussed in Chapter 1. This approach is slower than the previous single-shot velocity-encoding method because it necessitates repeated measurements with varying wavevector q and Fourier inversion from q- to R-space. Nevertheless, it has the advantage of providing additional molecular information, such as local diffusion coefficients. Moreover the q-space method is more resilient to artifacts such as gradient imperfections and is based on a clearly defined displacement time scale Δ.

Combinations of flow-imaging methods can also be used. A recent imaging study of thermal convection patterns set up in a layer of heated fluid (the Rayleigh–Bénard problem) used phase-encoding velocity imaging in three velocity-encoding directions, with two space dimensions, to give a two-dimensional velocity map where all three components of the velocity vector were imaged. The grid-distortion method was then used to visualize the thermal convection rolls set up in the fluid and produce video movies of the flow patterns. In this way, full qualitative and quantitative flow information was obtained (41).

Regardless of which flow-imaging method is used, the upper limit on the detectable velocity in experiments where a fluid is flowing through the receiver coil is the ratio L/TE of the receiver coil dimension L to the imaging observation time TE. At velocities greater than this the excited spins are removed from the coil before detection. The lower limit on coherent velocity flow is determined by molecular diffusion and is approximately $(D/T_1)^{0.5}$ since this longitudinal relaxation time T_1 will set the upper limit on the imaging time. For bulk water this lower velocity limit is roughly 20 μm/s.

4.3 BASIC RHEOLOGY

Flow imaging is a powerful tool for studying rheological properties, so before considering applications, we briefly review the relevant fundamentals of fluid rheology. External forces acting on a continuous volume of a solid or fluid induce stresses within the material, measured as a force per unit area, usually denoted by the vector σ. Consider the rectangular block in Figure 4.2. A shear stress σ is imposed on the block by application of the forces indicated. To prevent rotation, an equal and opposite couple must be applied to the other two faces. This combination of shear stresses causes deformation and induces a state of shear strain as indicated in Figure 4.2 and measured by the ratio $\tan \gamma = \delta l/l$. When the deformation is small, the angle γ, expressed in radians, equals the strain. If the upper surface in Figure 4.2 flows with a velocity $\mathbf{v}$ under the shear stress, $\delta l = \mathbf{v}\, \delta t$ in the time δt, and the rate of strain $d\gamma/\delta t$ is simply $\mathbf{v}/l$, or, more generally, the velocity gradient $d\mathbf{v}/dy$, where y is the vector in the direction of l. One of the objectives of simple rheological studies is to quantify the relationship between shear stress σ and strain γ or

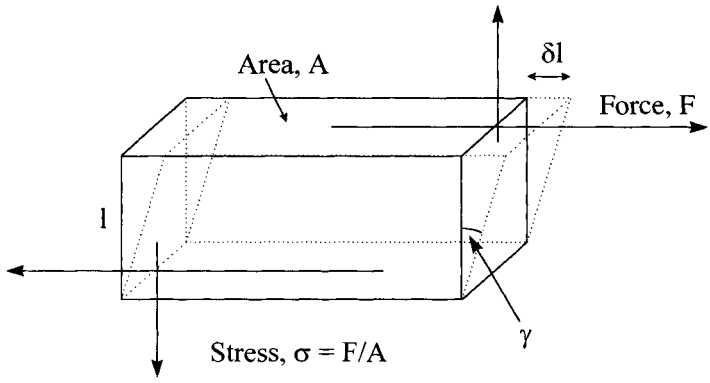

Figure 4.2. Shear deformation of a rectangular element. $\delta l/l$ is defined as the shear strain; γ is the angle of shear. For small deformations, $\gamma = \delta l/l$.

strain rate $d\gamma/dt$. The appearance of the velocity in the expression for the strain rate is the basis for the use of flow imaging in determining this rheological relationship.

For many simple, inelastic fluids, there is a single-valued relationship between the strain rate and the stress of the form $d\gamma/dt = f(\sigma)$. Various models have been proposed which differ in the functional form proposed for $f(\sigma)$. These include several described below.

4.3.1 Newtonian Model

In the Newtonian model, $d\gamma/dt = \phi\sigma$, where ϕ is a constant called the fluidity, which is the reciprocal of the shear viscosity η. This is a good model for most low-molecular-weight fluids such as water and most aqueous solutions, including sugar solutions. Examples of Newtonian fluids common in the food industry include fruit juices, milk, cream, honey, and vegetable oils. The Newtonian model is shown by the straight line (*a*) in Figure 4.3. Such lines or curves in plots of stress against strain rate are called *flow curves*. This rheological terminology should not, of course, be confused with flow profiles observed in an imaging experiment.

Other models describe various types of deviation from the simple Newtonian model and are indicated by the other flow curves in Figure 4.3. Among many such models mention should be made of three others.

4.3.2 Bingham Model

In the Bingham model, $\sigma - \sigma_y = U(d\gamma/dt)$, where σ_y is the yield stress and is given by the intercept in curve (*b*) in Figure 4.3. An ideal Bingham model fluid behaves as an elastic solid below the yield stress and then flows as a Newtonian fluid above it, characterized by a plastic viscosity U. In flow down a tube where the shear stress increases linearly with the distance from the tube axis, a Bingham fluid moves as a

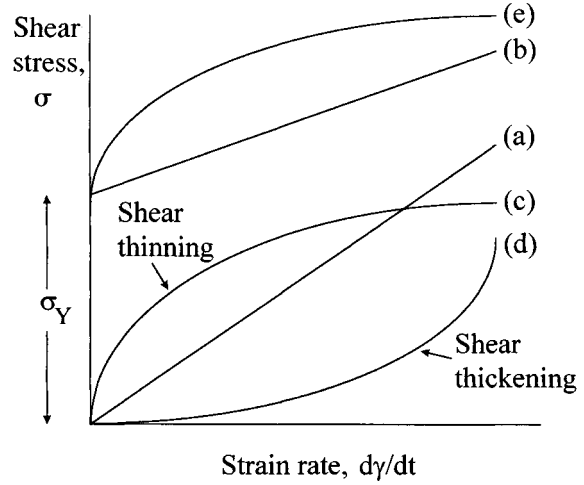

Figure 4.3. Rheological flow curves for inelastic materials. (*a*) Newtonian fluid model; (*b*) Bingham model; (*c*) power-law model, $N > 1$; (*d*) power-law model, $N < 1$; (*e*) Herschel–Bulkey model.

solid plug down the central part of the tube and like a Newtonian fluid near the edges. This gives a "flattened" velocity profile across the tube, in contrast to the parabolic profile of an ideal Newtonian fluid. Many concentrated suspensions and emulsions, including milk concentrates (36) and tomato sauce, follow this type of rheology. However, the Bingham model is only an idealization of their real behavior because the flow curve is often nonlinear and the yield point can be ill defined. Some nominally Bingham fluids also exhibit various degrees of hysteresis as the stress is decreased or increased.

4.3.3 Power-Law Fluid Model

Many polymer solutions and melts are described by the power-law relationship, $d\gamma/dt = \phi\sigma^N$, which is sometimes written in the alternative form $\sigma = k(d\gamma/dt)^n$, where $n = 1/N$ and $k = \phi^{-1/N}$. When $N > 1$, the viscosity decrease with increasing shear rate and the fluid is called *shear thinning* and is represented by curves of type (*c*) in Figure 4.3. Many semidilute polymer solutions exhibit shear thinning because the shearing reduces the effect of polymer–polymer contacts, or entanglements. If $N < 1$, the fluid is shear thickening and is represented by flow curves of type (*d*). Shear thickening can arise because shear induces particle aggregation. Cornflour–water mixtures are examples of shear-thickening mixtures. If the fluid is shear thinning ($N > 1$) the velocity profile in streamline flow down a straight tube is somewhat "blunter" than the ideal parabolic profile of a Newtonian fluid. Conversely, a shear-thickening fluid ($N < 1$) gives a sharper profile. Power-law fluids of importance in the food industry include fruit and vegetable purees, concentrated juices, mayonnaise, and mustard.

4.3.4 Herschel–Bulkey Model

In the Herschel–Bulkey model, $\sigma - \sigma_y = k(d\gamma/dt)^n$. This describes nonlinear behavior above the yield stress as shown by the flow curve (*e*) in Figure 4.3. Many other functional forms have been proposed to describe the flow curve of inelastic materials and the reader is referred to textbooks on rheology for details.

So far we have considered only simple time-independent flow curves. However, many liquids exhibit changes in their rheological behavior under a steadily applied stress, very often because of changes in their molecular or microscopic structure. For example, a thixotropic fluid shows a reversible time-dependent decrease in its shear viscosity. If the decrease is permanent, the fluid is described as having suffered *rheodestruction* (or *rheomalaxis*). Other "elastic" liquids, such as adhesives, exhibit partial recovery in the strain deformation after removal of a stress. It is beyond the scope of the present book to describe the rheological behavior of these more complex fluids, but it is important to be aware of the diversity of rheological behavior amenable to MRI flow studies. We now examine the way in which MRI can assist in rheological studies, beginning with the simple tube viscometer.

4.4 MRI AND TUBE VISCOMETERS

The rheological behavior of simple fluids can be studied in a tube viscometer in the conventional nonimaging way by measuring the flow rate V (i.e., volume per unit time), through a straight cylindrical tube under a constant applied pressure gradient P. This measurement alone cannot be used to derive the functional form of the flow curve, $d\gamma/dt = f(\sigma)$. Rather, it can only be used to measure rheological parameters once a particular model for the flow curve has been assumed, such as the Newtonian or power-law models. For example, if the Newtonian model is assumed and it is further assumed that there is no flow at the walls (called the *stick boundary condition*) and that the fluid is incompressible, the flow rate V and the pressure gradient P are related by the well-known Poiseuille formula

$$V = \frac{\pi R^4 P}{8\eta} \tag{4.2}$$

Measurements of V as a function of P then permit the shear viscosity to be determined. However, in many of the complex suspensions, slurries, and purees used in the food industry, this model-dependent approach is inapplicable because it is not known a priori which model, if any, describes the true rheological flow curve. This is the power of the flow-imaging approach because by directly imaging the velocity distribution across the tube, it is possible to deduce the flow curve in a model-free way. To see this, we must delve a little more deeply into the physics of the tube viscometer.

The shear stress at a radius r (measured from the tube axis) in the tube viscometer is

$$\sigma(r) = \frac{rP}{2} \tag{4.3}$$

and the rate of strain is simply

$$\frac{d\gamma}{dt} = \frac{-dv}{dr} \tag{4.4}$$

Since $dv/dr = (dv/d\sigma)(d\sigma/dr)$, this implies that

$$f(\sigma) = \frac{d\gamma}{dt} = \frac{-dv}{d\sigma}\frac{P}{2} \tag{4.5}$$

According to equation (4.5), the desired flow curve $f(\sigma)$ can be obtained in a model-independent way from an MRI measurement of the velocity field $v(r)$ by using equation (4.3) to change variables to $v(\sigma)$ and taking the derivative to obtain $dv/d\sigma$. This model-free approach has the added advantage that no assumption need be made about the velocity at the wall (i.e., whether slip or stick boundary conditions pertain). In fact, the boundary condition is measured in the MRI image within the resolution of one transverse pixel dimension. Furthermore, by slice selecting across the middle of the tube, all end effects resulting from flow discontinuities at the ends of the tube, which affect conventional measurements, can be removed.

Surprisingly, the MRI velocity data so far obtained from tube flow has been interpreted in a model-dependent way by assuming either a Newtonian or power-law relationship, solving these models for the theoretical velocity profile, then fitting the theory to the MRI velocity data to obtain the model parameters. For example, in a power-law fluid, the radial dependence of velocity in pipe flow is given as $v(r) = v_{max}[1 - (r/a)^{n+1/n}]$, where a is the pipe radius and $V(r)$ is the velocity component along the pipe. Fitting the MRI data with this type of expression is satisfactory in simple cases but is clearly not the best protocol for more complex food materials, especially if there is slip at the wall of the container, shear-induced phase separation, or particle aggregation. Figure 4.4 shows the MRI velocity profile for a common food thickener (a xanthan gum solution) flowing down a 2.6-mm-diameter glass pipe at different pump flow rates. It is notable that not only is the flattening of the velocity profile indicative of strong shear-thinning behavior, but the absolute velocity at the wall, measured within an image voxel, increases with increasing flow rate. This is symptomatic of apparent wall slippage. These authors measured a wide range of absolute slip velocities and showed that they depended uniquely on wall stress (311). Apparent slip results from a modification of fluid

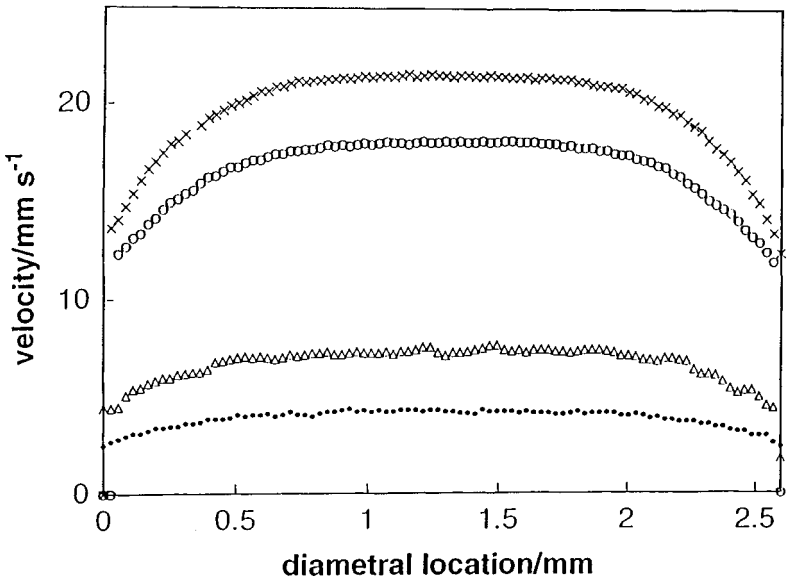

Figure 4.4. Experimental velocity profiles for 0.2% xanthan in water in a 2.6 mm diameter glass pipe. (From Ref 312.)

properties due to the proximity of a solid surface and results in a boundary layer of fluid experiencing a much higher shear rate than the bulk of the fluid, so that there is a large velocity gradient close to the wall. Clearly, it is important to be able to study apparent slip, because conventional rheological measurements require knowledge of the exact velocity boundary condition if the bulk data are to be interpreted meaningfully. It also has important practical implications because flow behavior may be controlled not so much by the bulk shear viscosity but by the apparent slip.

To date, full two-dimensional imaging with phase encoding has been used to measure the MRI velocity profiles across the tube. An example is shown in Figure 1.8, which show the real and imaginary parts of the velocity-encoded image. Although this is reassuring to see, full two-dimensional imaging is, in principle, unnecessary because the flow down the tube is cylindrically symmetric, so full information on $v(r)$ is contained in a single projection image across the tube, thereby removing the need for time-consuming phase encoding for the second spatial dimension. Instead, the radial information can be extracted from the real part of the projection by an inverse Abel transformation. This transformation was discussed in Chapter 1 in the context of radial imaging and should permit much faster flows to be imaged. A large number of MRI tube-flow studies have been reported in the literature, and some of these are listed in Table 4.1.

TABLE 4.1. Flow Imaging Studies

Fluid	Apparatus	Phenomenon	Reference
Water	Capillary tube	Newtonian flow	(31)
Poly(ethyleneoxide) solution	Capillary tube	Power-law rheology	(31)
1.5% Carboxymethylcellulose solution	Tube flow	Rheology	(32)
Tomato juice	Tube flow	Rheology	(33)
Fibrous suspensions	Tube flow	Rheology	(34)
Carboxymethylcellulose solution	Extruder	Velocity field	(44)
Water	Hollow-fiber bioreactor	Starling flow	(46,47)
	Thermal convection cell	Rayleigh–Bénard flow	(41)
	Tube flow	Turbulence	(38,42)
Particle suspensions Negative buoyancy	Tube flow	Shear-induced migration	(52)
Density matched	Tube flow	Shear-induced migration	(53)
	Couette flow between cylinders	Shear-induced migration	(54)
	Rotational viscometer	Shear-induced migration	(55)
Water	Flow between rotating cylinders	Motion in Taylor–Couette vortices	(57)
Xanthan gum	Tube flow	Shear thinning and apparent wall slip	(311)
Egg white cornflour–water, tomato sauce	Couette flow/ cone-and-plate flow	Shear-induced phase transitions	(311,312)

4.5 MRI AND ROTATIONAL VISCOMETERS

Similar considerations apply to rotational viscometers, which are the other standard means for determining stress–strain relationships. One form of rotational viscometer that is particularly convenient for flow imaging studies is the Couette cell, which consists of two concentric cylinders with fluid placed between them (see Figure 4.5). If the inner cylinder rotates under the action of a torque G while the outer one is stationary, the fluid between the cylinders undergoes streamline flow (at low Reynolds numbers) characterized by an angular velocity $w(r)$ at a radial distance r from the cylinder axis. The stress–strain rate equations for this geometry now take the form

$$\sigma(r) = \frac{G}{2\pi r^2} \tag{4.6}$$

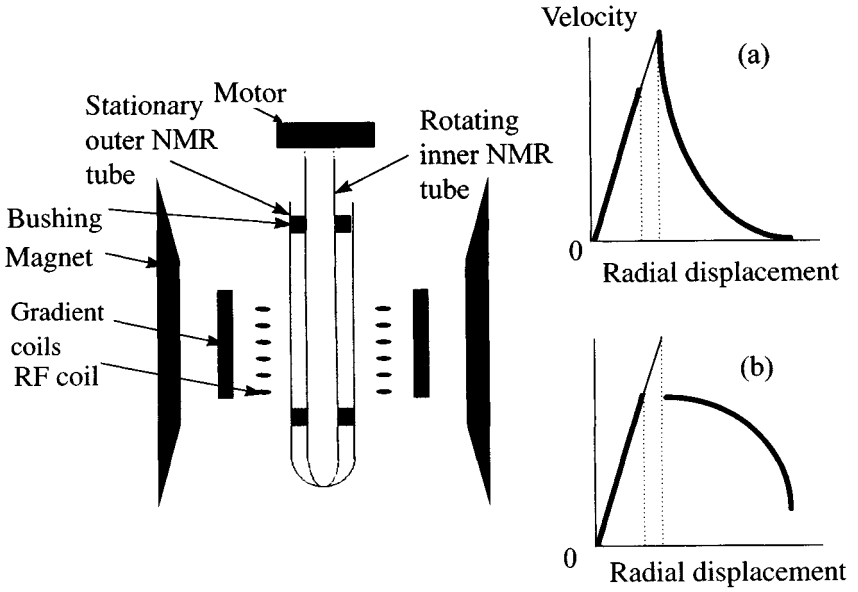

Figure 4.5. Schematic of the cylindrical NMR Couette cell used by Rofe et al. (311). Inset (*a*) shows the schematic velocity profile for water filling both the inner tube (as reference) and the gap between tubes. The break corresponds to the glass wall of the inner tube. (*b*) The same for water filling the inner tube and a shear thickening fluid filling the gap and exhibiting slip on the inner and outer walls.

and the rate of strain is simply

$$\frac{d\gamma}{dt} = r\frac{dw}{dr} \tag{4.7}$$

Since $dw/dr = (dw/d\sigma)(d\sigma/dr)$, this implies that

$$f(\sigma) = -2\sigma\frac{dw}{d\sigma} \tag{4.8}$$

Equation (4.8) permits a model-free determination of the flow curve $f(\sigma)$ to be made directly from an MRI determination of $v(r)$. All that is necessary is two changes of variables, one from $v(r)$ to $w(r)[= v(r)/r]$ and the other from r to $\sigma(r)$ using equation (4.6). This requires a separate measurement of the torque G, which can be done outside the NMR probe. In principle, therefore, flow-imaging circumvents the major problems in the conventional use of rotational viscometers: namely, that the relationship between the angular velocity of the cylinder and the applied torque can only be solved exactly for special cases, such as with a very narrow gap

between the cylinders or when the form of the flow curve is already known. It also makes no assumption about the velocity of the fluid at the walls. Indeed, the existence of slip at the wall is usually obvious in the experimental velocity profiles. The inset labeled (*a*) in Figure 4.5 shows a schematic velocity profile when the inner NMR tube contains water as a reference fluid and the gap between the inner and outer tubes also contains water. In contrast, the inset labeled (*b*) shows the velocity profile expected when the water in the gap is replaced by a shear-thickening fluid that exhibits slip at both glass walls.

MRI rheological measurements using this rotational viscometer approach offer many advantages over the imaging of flow down a tube. To begin with, there is no need for a steady flow of liquid through the apparatus, so much smaller volumes of liquid can be measured. Moreover, the fluid remains in the detector coil, so the restriction on the maximum flow rate (and therefore shear rate) imposed by the need to keep the excited spins inside the detector coil no longer applies. In the rotational viscometer the upper limit on coherent flow studies will be determined by the onset of Taylor vortices and, at higher rotation speeds, turbulence, which are both phenomena of great interest which can be imaged (see below). If microimaging facilities are available, the cylinders in the rotational viscometer can assume the size of capillary tubes, permitting the effect of very high shear rates to be studied. With fast flow imaging sequences and stroboscopic imaging methods (5), time-dependent phenomena such as thixotropy, rheomalaxis, and viscoelasticity could, at least in principle, be studied under conditions where the cylinder rotation undergoes some programmed time-dependent rotation.

Rofe and co-workers (58) have used displacement imaging (dynamic q-space microscopy) to image the radial dependence of the velocity profile in a Couette cell consisting of concentric NMR tubes (an NMR tube of about 5 mm rotated concentrically inside an NMR tube of about 10 mm). A radial resolution of about 50 μm was achieved with a maximum angular velocity of about 10 rad/s. In this pioneering experiment no attempt was made to use a model-independent approach to the data analysis. Instead, the velocity profile predicted for a power-law fluid, $v = \Omega r_{in} R(1 - R^{-2/n})/K(1 - K^{-2/n})$, was fitted to the velocity data for a 5% polyethylene oxide–water solution and used to obtain the power-law exponent n. In these experiments the inner tube was rotated with angular velocity Ω and has a radius r_{in}. The outer tube has an inside radius r_o, and $K = r_{in}/r_o$. while $R = r/r_o$ The results were shown to be in good agreement both with previous NMR measurements in tube flow and with independent rheological measurements in a cone-and-plate viscometer. Most recently, Brittin and Callaghan (312) have used this MRI–Couette cell approach to study the rheological behavior of a number of common food materials, including xanthan gum, cream, semisoft butter, egg white, cornflour–water mixtures, and tomato sauce. The xanthan gum was found to be strongly shear thinning ($n = 0.28$) and the cream only weakly shear thinning ($n = 0.8$), while the butter was shear thickening ($n = 3$). Most interesting was the observation that the egg white, the cornflour–water mixture, and the tomato sauce exhibited shear-induced phase transitions, manifested as discontinuities or changes of slope in the Couette

cell $v(r)$ profiles. Similar results were observed for the velocity field imaged within a cone-and-plate rheometer (133), which emphasizes the importance of supplementing the purely rheological measurements of torque and cylinder velocity with MRI velocity maps.

4.6 SOLID SUSPENSIONS

When there are nonrheological changes induced in the fluid by the flow, further information can be gained by combining flow imaging with the spatial distribution of other NMR parameters, such as spin density, relaxation times, or diffusion coefficients. The study of particle migration under shear stress is an example of changes in particle concentration in a solid suspension in different regions of the flow field that can be monitored from changes in either the spin density and/or relaxation times.

Diffusion theory, which describes the migration of particles in a suspension from regions of high to low concentration, is now very well developed. What is less well understood is the mechanism by which shear in a flowing fluid induces the migration of particles from regions of high to low shear stress. A number of theories have been proposed to explain the effect, including constitutive flow equations based on a model of particle interactions and diffusive scaling laws (50,56), and theories based on velocity fluctuations (51). Shear-induced particle migration manifests itself in a variety of flow phenomena, ranging from the shear resuspension of particles, particle accumulation behind an advancing meniscus, blunting of the velocity profile in Poiseuille flow, and migration of particles to the outer cylinder wall in Couette flow in wide-gap rotational viscometers.

Several researchers have used MRI to study this interesting phenomenon. Altobelli et al. (52) used MRI to study flow velocities and particle concentration maps in concentrated suspensions of small, negatively buoyant particles flowing through horizontal tubes. The velocity distribution was measured by the time-of-flight method, and at the same time, maps of the fluid volume fraction F in each $(x–y)$ pixel in a plane across the tube were obtained, after suitable normalization, by integrating the signal intensity along the tube. The map of particle volume fraction was then given as $(1 - F)$. Because of the negative buoyancy, at very slow flow velocities the particles formed a packed layer at the bottom of the tube with clear fluid above. Increasing flow rates caused the particle bed to dilate and consequently to become resuspended, eventually giving way to a plumelike structure. At high velocities the particles formed a highly concentrated core (or plug) in the tube center and the velocity profile flattened. Figure 4.6 shows the relationship between the velocity profile *bluntness* (defined here as the maximum velocity/average velocity) and the particle volume fraction. Sinton and Chow (53) investigated similar flow-induced migration except that they density matched the solid and fluid phases, which consisted of PMMA [polymethyl methacrylate] microspheres, mean diameter 131 μm, suspended in a polyether oil–water–sodium iodide mixture with a range of solid fractions up to 52%. In concentrated suspensions a blunting of the velocity profile

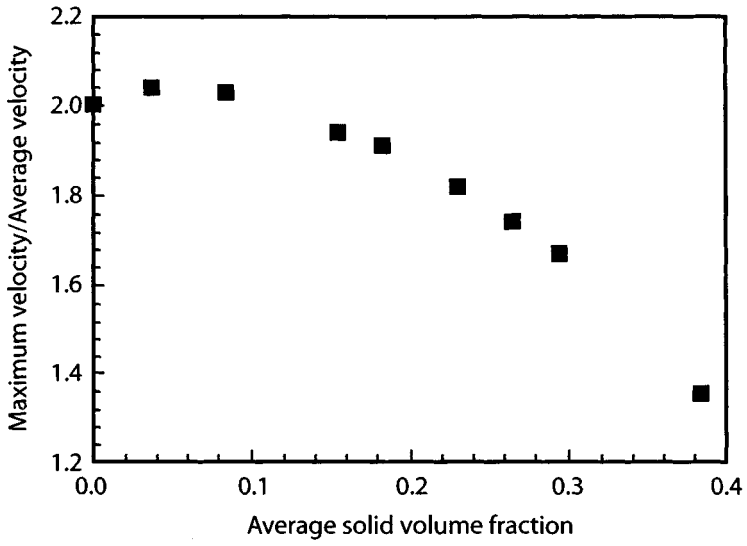

Figure 4.6. Normalized peak fluid velocity ("bluntness") versus average particle volume fraction for flowing suspensions in cylindrical tubes. (From Ref. 52.)

caused by shear-induced particle migration was observed, and this could not be quantitatively fitted by the assumption of shear thinning. Unfortunately, their maps of particle packing fraction showed anomalies that could have arisen from RF field inhomogeneities, so quantitative data analysis was not possible in this case.

A quantitative analysis of shear-induced particle migration using MRI has been made using a rotational viscometer (54). The apparatus consisted of two concentric cylinders designed so that there was no region of stagnant fluid below the central cylinder and no axial migration of particles from between the cylinders into the stagnant region. When density-matched suspensions were used it was found that particles migrated radially toward the wall of the outer cylinder regardless of which cylinder was rotated. The particle concentration near the outer wall approaches maximum packing for randomly distributed spheres at steady state. The radial particle concentration profiles after 0, 200, and 4000 revolutions of the inner cylinder at 17 rpm are plotted in Figure 4.7. The particle migration rate was found to be directly proportional to the shear rate and to increase dramatically with increasing particle size as the 2.7 ± 0.3 power of the mean particle diameter for a nearly monodisperse set of sieved particles. Moreover, the migration was irreversible, in the sense that reversing the direction of fluid flow did not cause reversal of the direction of migration. These observations are qualitatively consistent with the hydrodynamic diffusion theory proposed by Leighton and Acrivos (56). Phase encoding was also used to measure the radial distribution of the angular fluid velocity once the suspension had reached the steady state. It was found that the velocity fell off much more rapidly with increasing radial distance than the Newtonian fluid and was almost stagnant in the outer region, where the particles were close packed.

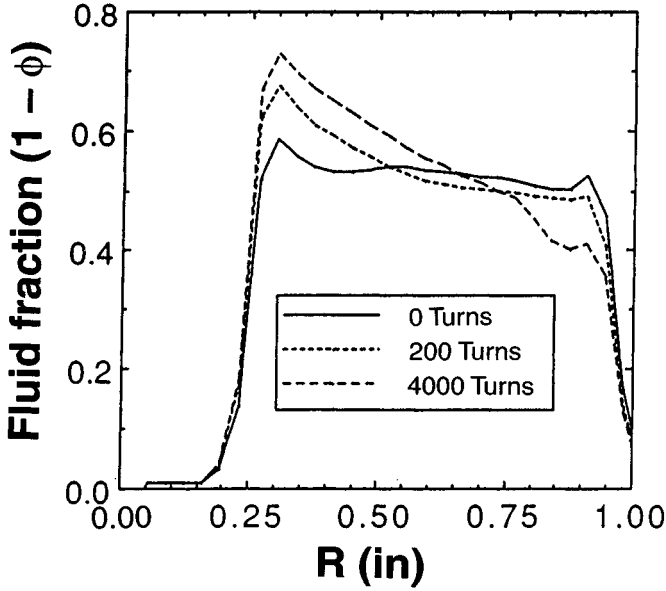

Figure 4.7. Radial concentration profile (fluid fraction) in a Couette cell for a suspension of 655-μm sieved spheres for the indicated number of turns (revolutions) of the inner cylinder at a speed of 17 rpm. (From Ref. 54.)

Most interesting was the observation that in the steady-state distribution the particles arranged themselves in concentric rings, sliding past each other.

Most recently, the axial migration of particles from between the cylinders and into the stagnant region below the central cylinder has been investigated with MRI (55). Figure 4.8 illustrates the phenomenon, which leads to a decrease in apparent viscosity under prolonged shearing. In this investigation maps of particle packing densities were determined from signal intensity distributions, but flow imaging was not undertaken. Instead, the same concentric cylinder arrangement was placed in a rheometer for conventional stress–strain measurements. The results directly confirmed the Leighton–Acrivos theory of shear-induced migration (56). Shear-induced aggregation in concentrated food emulsions such as dairy creams is another example of structural changes induced by flow that should be amenable to a combined relaxation time–flow imaging approach.

4.7 MRI AND COMPUTATIONAL FLUID DYNAMICS

Mention has already been made of the three-dimensional imaging study of flow through a tube containing two baffle plates (see Figure 4.1). Such studies are important for testing the applicability of CFD calculations of the flow of Newtonian fluids in complex geometries such as heat exchangers and pumps in the food industry. Many real liquid food systems do not obey the Newtonian model, so discrepancies

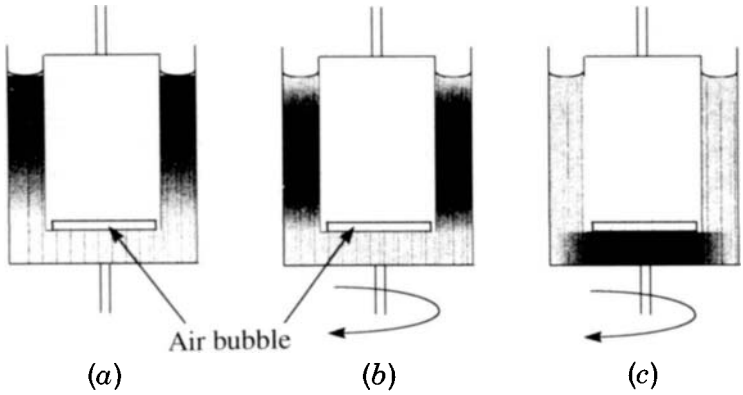

Figure 4.8. Schematic cross section of a Couette cell filled with a concentrated suspension illustrating (*a*) the nonuniform distribution that develops during sample loading; (*b*) axial shear-induced migration of the particles down the cylinder during rotation [there is also radial migration not shown in this diagram (see Figure 4.7)]; (*c*) shear-induced migration of the particles underneath the rotating cylinder. (From Ref. 55.)

between the CFD prediction and MRI flow images are of potential significance. An example of MRI used to image the velocity field in the vicinity of a sharp contraction or expansion in cylindrical pipes has been reported (31). The velocity components parallel and perpendicular to the cylinder axis were measured at various distances from the radius discontinuity. In this case the data agreed well with CFD calculations for a Newtonian fluid.

4.8 FLOW AND QUALITY ASSURANCE

Detailed quantitative measurements of rheological properties using rheometers such as the rotational viscometer are time consuming and require careful calibration. In most industrial situations more rapid rheological tests are used with the purpose of testing food quality. Such tests are necessarily empirical in the sense that they do not attempt to measure an intrinsic rheological property of the fluid, such as its shear viscosity, but some other simpler parameter, such as a flow time or flow length, that also depends on the shape and size of the apparatus. Imaging the flow in these empirical quality assurance tests can, together with mathematical analysis, assist in understanding and analyzing the rheology underlying these rapid test methods.

A good example of this approach is a combined MRI and mathematical analysis of the Bostwick consistometer presented by McCarthy and McCarthy (37). The Bostwick consistometer is used to determine the quality of pureed fruit and vegetable products and provides the standard that stipulates the grades of tomato products in the United States. In this example MRI was used to image the flow in the consistometer and test the theoretical prediction that the simple parameter measured

in the apparatus (in this case a length of flow L recorded at a specified time) is given by the expression $A(gp^3t\rho/3\eta)^{0.2}$, where A is a constant, g is the gravitational constant, ρ the fluid density, q a fluid volume per unit width, and η the shear viscosity. The details of this test are not so important in the present context (and can be found in Ref. 37) but serve to show that MRI flow studies of these empirical tests can lead to an improved understanding of which rheological factors are being measured. This, in turn, allows manufacturers to optimize processing conditions and improve product quality. Other tests that may be amenable to similar analysis include the Brabender visco-amylograph, which is used to test the consistency of starches, and the Torque plasicorder, used for dough consistency.

4.9 EXTRUSION

Extrusion is perhaps one of the least understood food processing operations, yet its use is widespread throughout the industry because it is a continuous operation, very flexible in its range of application, and gives end products of reproducible quality. Common types of extruded foods include pasta, snacks, confectionary, pet foods, and animal feeds, but its potential in the creation of new food products and in the processing of novel combinations of raw ingredients continues to be actively researched.

The simplest single-screw extruder is not unlike a rotational viscometer in the sense that it comprises an outer cylinder, called the barrel, and an inner, concentric rotating cylinder. The essential difference is that the inner cylinder has a helical screw configuration, so that as it rotates the food is pushed down the tube against the end of the barrel. The helical screw is characterized by flight height (H, the height of the helix) and the helical angle, θ. The end of the barrel contains the die, which is a shaped orifice through which the food is squeezed. A schematic of a single-screw suitable for imaging applications is shown in Figure 4.9.

During extrusion the food is fed into the barrel, where it is subjected to shear stress by the rotating screw; to a pressure gradient, because the size of the die orifice is usually smaller than the barrel; and to heating, both from external heat sources along the barrel and from internal heat generated by chemical reactions and friction. Under these conditions a complex series of physical and chemical changes take place, such as mixing, gelatinization, denaturization, evaporation, flavor production (and loss), and rheological changes. Not surprisingly, understanding and mathematically modeling these complex and rapid changes is a major challenge in food processing science. MRI can greatly assist this endeavor by providing real-time noninvasive images of the flow within the extruder and, potentially, spatial maps of other NMR parameters, such as relaxation times, chemical shifts, and diffusion coefficients as well as images of temperature and/or chemical changes. To date, only the isothermal flow aspect has been researched, so for the present, only the velocity field need be considered.

A simple theoretical model of the flow within a single-screw extruder can be developed by assuming an incompressible, Newtonian fluid with stick boundary conditions and using the Navier–Stokes equation to describe the flow (45). The geome-

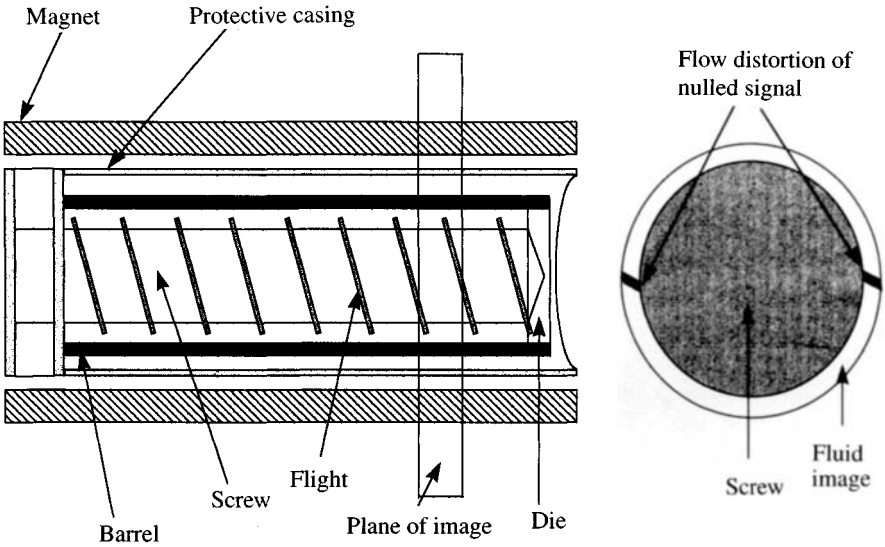

Figure 4.9. Schematic of a single-screw extruder suitable for use inside an imager. The constant-diameter screw features a shallow, wide channel; screw diameter is 3.3 cm with flight height 0.254 cm and helix angle 17.67°. The imaging coil can slide along the extruder permitting imaging of any region of the barrel. Stroboscopic signal acquisitions (one per revolution) are triggered by a microswitch in contact with the drive shaft. The right-hand figure illustrates the effect of motion on the nulled horizontal intensity band in the food.

try can be simplified by unwinding the helical flight and considering the flow down a straight channel formed between two flights on each side with the inner cylinder (screw) surface as a base and the barrel surface as the top (49). The screw motion is then equivalent to a sliding of the top barrel surface over the fluid at a helical angle θ (see Figure 4.10). We require the dependence of the velocity components on the distance between the two cylinders (now planes in Figure 4.10) in directions parallel and perpendicular to the flights. Using the coordinate system of Figure

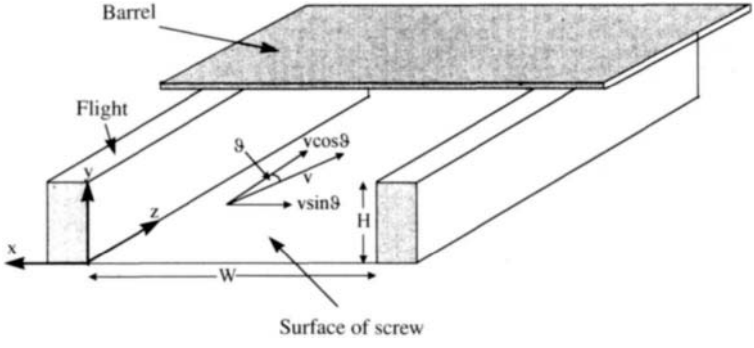

Figure 4.10. Geometry of a shallow channel in an extruder.

4.10, these are $v_z(y)$ and $v_x(y)$, respectively. In the steady state in the z-direction this reduces to

$$\frac{\partial P}{\partial z} = \mu\left(\frac{\partial^2 v_z}{\partial x^2} + \frac{\partial^2 v_z}{\partial y^2}\right) \tag{4.9}$$

where μ is the shear viscosity.

The velocity gradient in the y-direction is considerably larger than in the x-direction because the height of the channel is much less than the width, so the first term in equation (4.9) can be neglected. This is equivalent to making the width of the channel infinite and representing the motion of the screw relative to the barrel as equivalent to the sliding motion between two infinite parallel planes. With this simplification equation (4.9) can be integrated twice with the boundary conditions $v_z(0) = 0$ and $v_z\ (\mathrm{H}) = V \cos\theta$, to give

$$v^z(y) = V \cos\theta\left(\frac{y}{H}\right) + \frac{y^2 - Hy}{2\mu}\frac{\partial P}{\partial z} \tag{4.10}$$

Similarly, in the x-direction we have the equation

$$\frac{\partial P}{\partial x} = \mu\left(\frac{\partial^2 v_x}{\partial x^2} + \frac{\partial^2 v_x}{\partial y^2}\right) \tag{4.11}$$

Neglecting the term $\partial v_x/\partial x^2$ and using the boundary conditions $v_x(0) = 0$ and $v_x(H) = -V \sin\theta$, equation (4.11) can be integrated to give

$$v_x(y) = -V \sin\theta\frac{y}{H} - \frac{1}{2\mu}\frac{\partial P}{\partial x}(yH - y^2) \tag{4.12}$$

Because of the flight barriers there is no net flow in the x-direction, so we have the condition

$$\int_0^H dy\, v_x(y) = 0 \tag{4.13}$$

which gives

$$\frac{\partial P}{\partial x} = -6V \sin\theta\frac{\mu}{H^2} \tag{4.14}$$

Substituting this into equation (4.12) finally gives

$$v_x(y) = V \sin\theta\frac{y}{H}\left(2 - 3\frac{y}{H}\right) \tag{4.15}$$

In terms of these component velocities, the velocity $v_p(y)$ in the plane perpendicular to the screw, which is the slice-selected imaging plane, is given as

$$v_p(y) = V - v_z \cos\theta + v_x \sin\theta \tag{4.16}$$

Comparison between the imaging experiment and the theoretical model is easiest in the limiting cases of a completely open barrel (no die), when the pressure gradient is zero, and in the case of a completely closed barrel, when there is no net flow down the barrel. In these cases equation (4.16) simplifies to

$$\frac{v_p}{V} = 1 - \frac{y}{H} + 3\sin^2\theta\left[\frac{y}{H} - \left(\frac{y}{H}\right)^2\right] \qquad \text{(open barrel)} \tag{4.17}$$

and

$$\frac{v_p}{V} = 1 + 2\frac{y}{H} - 3\left(\frac{y}{H}\right)^2 \qquad \text{(die closed)} \tag{4.18}$$

These functions are plotted in Figure 4.11*a* and *b*, respectively, where they can be seen to agree very well with the shape of the image flow patterns in Figure 4.11*c* and *d*, respectively. These images were obtained by the time-of-flight technique by nulling the signal from a slice across the extruder in an orientation perpendicular to the barrel and taking an image of it at later times. These pioneering measurements were made by McCarthy and co-workers with a special extruder made of nonmagnetic materials and operated inside the magnet of the NMR spectrometer and using a model carboxymethylcellulose solution. The extension of these studies to more complex fluids and nonisothermal extruder conditions is to be anticipated and will aid the development of more realistic numerical models of the extrusion process.

4.10 FLOW IN BIOREACTORS

Bioreactors are devices engineered to optimize the production of biochemically synthesized products by living cells. Advances in recombinant DNA and cell fusion technologies have led to increasing demands for cost-effective means of processing large quantities of biochemicals from mammalian and plant cells. Membrane-based bioreactors are beginning to meet this demand by protecting cells from shear stress due to fluid flow and eliminating the need for cell and product separation. A problem in optimizing bioreactors is maintaining a sufficient supply of fresh nutrient fluid to the cells. The hollow fiber bioreactor (HFBR) (Figure 4.12) seeks to overcome this difficulty by exploiting *Starling flow.* In the HFBR, nutrient fluid is pumped down a hollow, microporous capillary fiber which is surrounded, concentrically, by a cell suspension in the extracapillary space. Fluid is transported through the porous fiber into the extracapillary space, where it flows axially and nourishes

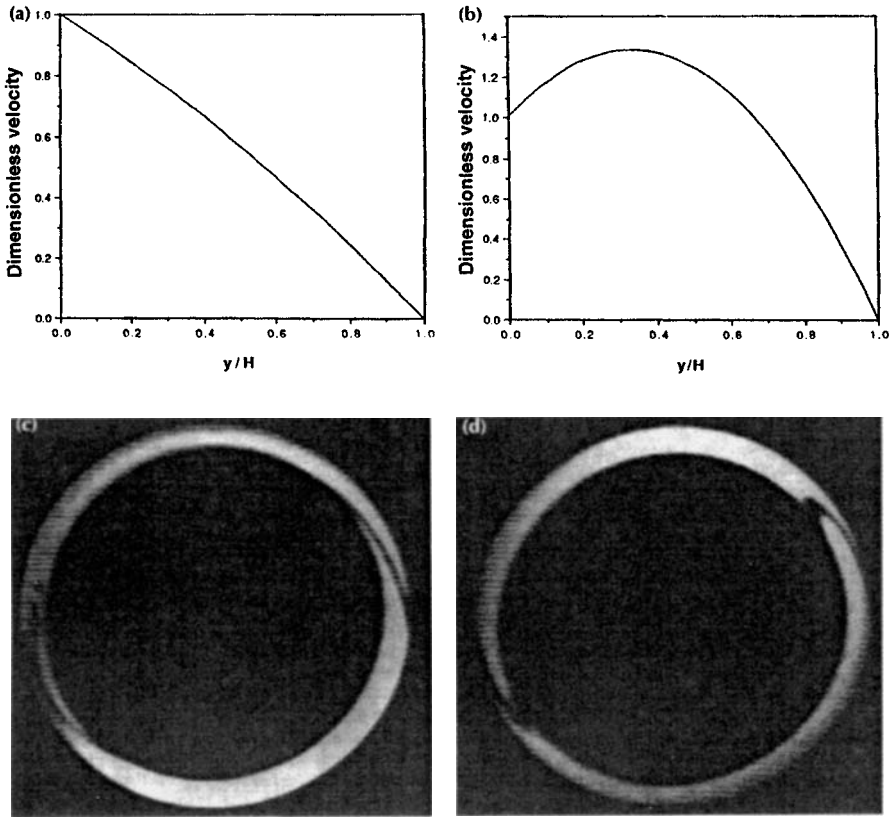

Figure 4.11. Comparison of the theoretical predictions [equations (4.17) and (4.18)] with images from the extruder in Figure 4.9. Diagrams (*a*) and (*c*) correspond to zero pressure gradient in the z-direction. Diagrams (*b*) and (*d*) correspond to zero net flow. (Courtesy of McCarthy and co-workers, Ref. 44.)

the cells. Fluid containing reaction products is transported back into the central fiber as indicated. The average flow through this system is called Starling flow because of its analogy to fluid transport in venous and arterial capillary beds (46–48). Simplified mathematical models of Starling flow through a bioreactor having a single hollow fiber have been developed by solving the Navier–Stokes equation for the fluid motion in the central tube and Darcy's flow law through the membrane and cell-containing regions. These solutions have been compared successfully with MRI velocity maps (47) but are too lengthy to reproduce here. Such comparisons between model flow calculations and MRI flow maps are useful for testing the underlying assumptions in the model. Nevertheless, the velocity fields existing in actual (as apart from model) bioreactors are usually too complicated to be predicted by computational fluid dynamics because there is often more than one fiber, and these can be bent and have an irregular distribution, permitting channeling of flow

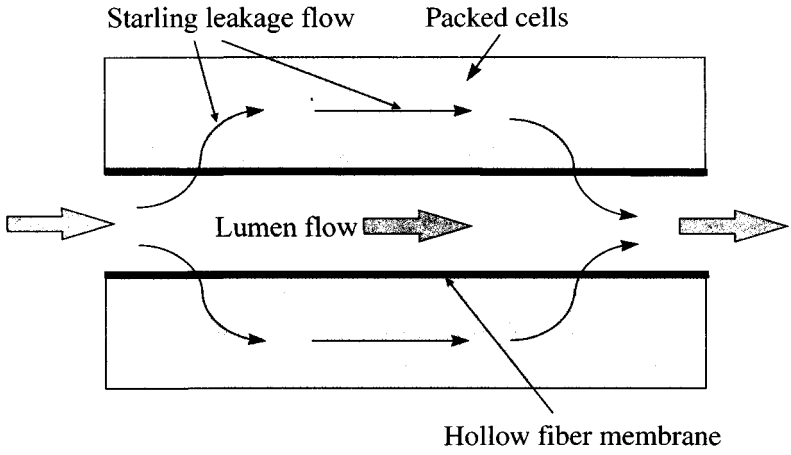

Figure 4.12. Schematic of a hollow-fiber bioreactor. Nutrient fluid flows through the central "lumen" of the hollow fiber. Cells are located in the cylindrical region surrounding the lumen and are separated from the main flow by the hollow-fiber membrane. The Starling leakage flow pattern provides nutrient to the cells and carries metabolic end products back into the lumen flow.

where the spaces between fibers, or between the fibers and the outer walls, are greatest. In this situation, noninvasive flow imaging can help improve the design and performance of bioreactors by showing which configuration (e.g., the number, distribution, size, and porosity of the fibers) maximizes the flow to each part of the cell suspension. As a case in point, Figure 4.13 shows the spatial distribution of the axial component of the mean velocity in a bioreactor containing 40 hollow capillary fibers. Here a 1-mm slice through the reactor is shown with an in-plane resolution of 20×20 μm. The spongy matrix of the hollow fibers appears as dark circles and the channeling of the fluid is clearly seen by the bright areas. In principle, volume-selective spectroscopy can also be used to monitor the distribution of nutrients and bioproducts throughout the reactor vessel, as well as to monitor the metabolic state of the cells, but there are as yet no reports of this.

4.11 MIXING AND TURBULENCE

So far we have considered time-independent steady flows where imaging is used to provide the velocity field $\mathbf{v}(r)$. We turn now to a number of important phenomena that arise when the velocity field depends explicitly on time. Consider the time-dependent velocity field $\mathbf{v}(r,t)$. The trajectory of a fluid particle initially located at $\mathbf{r}_0$ corresponds to the solution of the equation $d\mathbf{r}/dt = \mathbf{v}(\mathbf{r},t)$ with the initial condition $\mathbf{r} = \mathbf{r}_0$. However, in many situations this apparently simple equation produces chaotic behavior, such that fluid particles, no matter how close initially, separate exponentially fast or take unpredictable and aperiodic trajectories. Two examples of

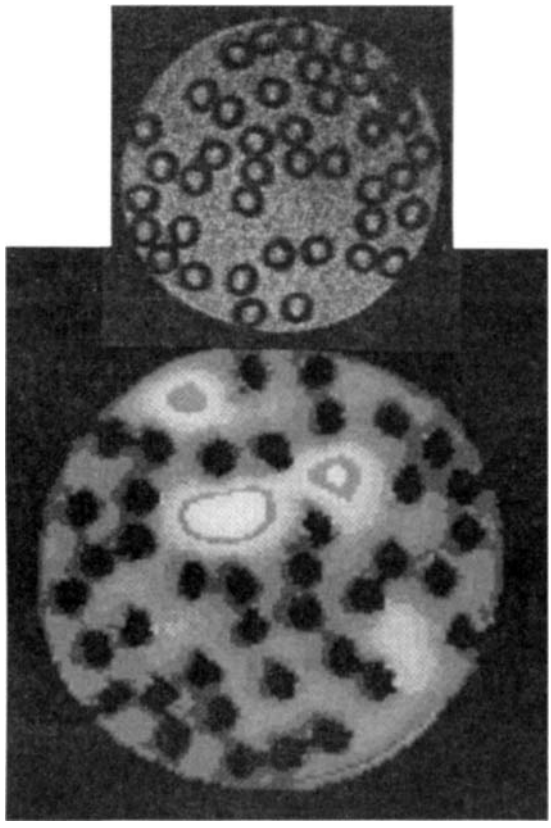

Figure 4.13. (Top) NMR image of a cross section through a multiple-fiber bioreactor containing 40 hollow fibers without flow. The spongy matrix of the hollow fibers appears as dark rings. (Bottom) Flow image of the system showing flow variations due to the irregular packing of fibers. Flow inside the fibers is outside the range of measured velocities and therefore appears black. (From Ref. 46.)

such behavior of relevance to food processing are the chaotic mixing of two (or more) fluids and the turbulent flow that arises in a single component fluid at high Reynolds numbers. Each is considered below.

4.11.1 Fluid Mixing

Understanding the fundamental physics of fluid mixing is important when designing apparatus to optimize mixing during processing. A particularly simple geometry for quantitative mixing studies arises if the inner cylinder of the rotational viscometer is made noncoaxial with the outer cylinder. The flow in this rotating eccentric cylinder arrangement is periodic and has an exact solution for creeping flow and can be simulated numerically (39). The main parameters controlling the spatial

trajectories set up in this system are the ratio of the inner and outer cylinder radii, R_{in}/R_{out}; the degree of eccentricity δ/R_{out}, where δ is the distance between the cylinder axes; and the ratio of the angular velocities, Ω_{in}/Ω_{out}. Under creeping flow conditions the streamline portrait is determined only by the ratio of angular velocities of the inner and outer cylinders. Amazingly, despite the stirring, there exist one or more coherent regions (holes or islands) of fluid that translate and deform with the flow but inside which there is very little mixing. These moving islands are surrounded by chaotic regions where mixing is effective because the fluid volume elements get stretched (see Figure 4.14). The islands in Figure 4.14 are the regions where a fluorescent tracer, injected into the fluid, is unable to penetrate. Clearly, a mixing process is optimized by minimizing the volume and lifetime of such islands. Up to now these chaotic structures in mixing fluids have been visualized using fluorescent tracer techniques, but flow imaging, especially using the flowing-grid method, provides an obvious, noninvasive way of visualizing islands and the stretching of fluid elements, not only for transparent fluids, but even with the mixing of complex, non-Newtonian fluids in realistic mixers.

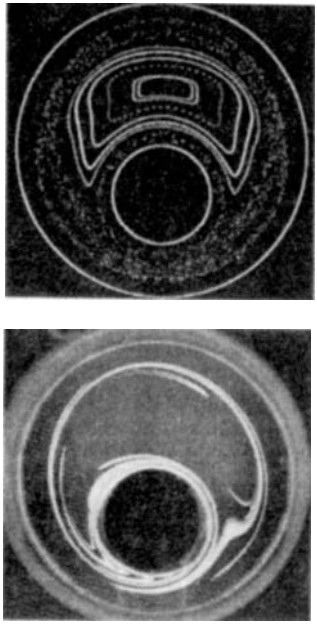

Figure 4.14. Experimental and theoretical studies of the mixing flow patterns between two nonconcentric counterrotating cylinders, characterized by $R_{in}/R_{out} = \frac{1}{3}$, $\delta/R_{out} = 0.3$, and $\Omega_{in}/\Omega_{out} = -2$; where R_{in} is the radius of the inner cylinder, δ the offset distance of the cylinder axes, and Ω_{in} the angular velocity of the inner cylinder. (Top) Computation for an angular displacement, $\theta_{out} = 165°$ showing a single saddle point. (Bottom) Stretching of a fluorescence blob initially located in the neighborhood of the saddle point. (From Ref. 39.)

One in vivo aspect of mixing that is relevant to nutrition is the effectiveness of time-periodic motions (peristaltic motions) in improving mixing of food in the duodenum during digestion. (40). Whole-body imaging studies are now being undertaken to investigate this fascinating biological mixing and flow problem and should be appearing in the literature in the near future.

4.11.2 Turbulence

The chaotic structures arising during the mixing of fluids may well have a bearing on the coherent structures appearing in turbulent flow at high Reynolds numbers. In fact, turbulence is now considered a case of spatial deterministic chaos, albeit a very complicated one, and it appears to be well represented by multifractals as originally suggested by Mandelbrot (43). Although optical flow visualization methods are useful for qualitative observations of turbulence, flow imaging is indispensible if quantitative information is required because it can measure, selectively, any velocity component at many positions at the same time. This facilitates the identification of organized fluid motions. Fast phase-encoding flow imaging sequences are mandatory in such studies, with total image acquisition times of only a few tens of milliseconds. Kose (38,42) has used such methods to image the equilibrium turbulent region produced in a straight 18-mm-inner-diameter circular pipe at Reynolds numbers around 2250 when entrance to the pipe is restricted by a 10-mm-diameter circular orifice. To observe the turbulence, 4-mm-thick slices perpendicular to the tube axis were imaged at eight fixed downstream positions. One set of images corresponded to the component of velocity along the tube; another set corresponded to the velocity components transverse to the tube axis. Figure 4.15 is a schematic showing the types of turbulent flow structures set up in the tube. The region up to about $3D$ is the upstream interface region

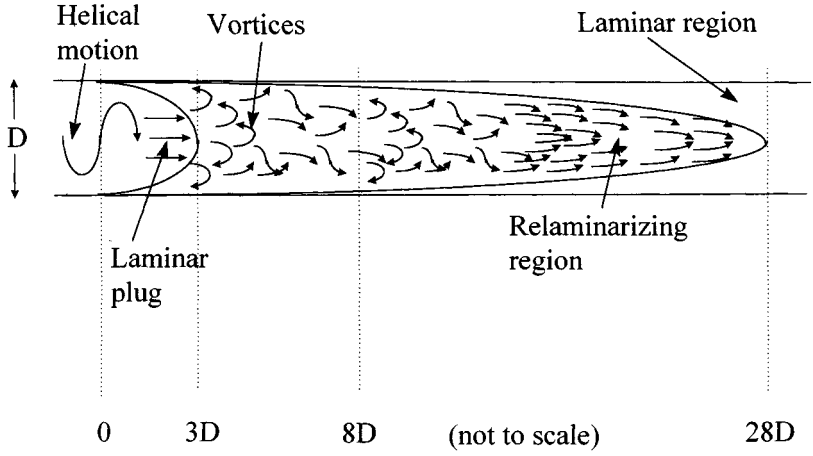

Figure 4.15. Schematic of the turbulent flow region set up in a horizontal pipe having an inner diameter D of 18 mm. Turbulence was created by placing a plate with a 10-mm orifice near the pipe inlet; 4-mm MRI slices were then taken at several downstream positions and used to construct the schematic. (From Ref. 38.)

where a clear laminar flow gives way to a turbulent interface. Just beyond the interface there is a vortex shedding process, represented by the curly arrows. This gives way to a highly turbulent region extending out to about $5D$. The third region extends to about $20D$ and involves the relaminarization of the fluid motion, where vortices are decaying toward a cone-shaped interface separating the downstream laminar flow region from the turbulent cone. To examine the nature of the vortices, the real and imaginary components of the complex image corresponding to a rotating vortex in the fluid were mathematically simulated and revealed characteristic phase patterns which depended on the vortex orientation and direction of rotation. Comparison with the imaging data permitted the number, size, and orientation of vortices to be recognized in real time at various positions in the tube. In this way a detailed model (Figure 4.15) of the turbulent regions downstream from the constriction could be constructed.

4.12 VELOCITY DISTRIBUTIONS

It is important to remember that the velocity maps produced by the phase-encoding or grid-distortion methods in the foregoing applications use only a single value of the velocity-encoding gradient and therefore measure only *average* velocities. When there is steady, coherent fluid motion, this is usually all that is required. But in phenomena such as turbulence, there can be incoherent flow on a wide range of distance scales, including distance scales smaller than an imaging voxel. Besides turbulent flow, the complicated flow in separation procedures such as chromatography and electrophoresis is another example where velocity distributions are needed and not just the mean velocity, although few have been reported to date. It is noteworthy that the flow measurements in the bioreactor discussed above actually measured the velocity distribution using equation (4.20), although only the mean velocity was reported. In these situations it is necessary to consider not just the mean velocity but the velocity distribution within a voxel, and this requires ramping through a raster of phase-encoding gradients. To understand this, let us suppose that there is a velocity distribution $P(\mathbf{v})$ within each imaging voxel, such that $P(\mathbf{v})\, d\mathbf{v}$ is the fraction of spins having a velocity between $\mathbf{v}$ and $\mathbf{v} + d\mathbf{v}$. In this case the echo amplitude $S(\mathbf{p})$ arising from the voxel is an integral

$$S(\mathbf{p}) = \int d\mathbf{v}\, P(\mathbf{v}) \exp(-i\mathbf{p} \cdot \mathbf{v}) \tag{4.19}$$

where $\mathbf{p}$ is the integral defined by equation (1.5). In the special case that the velocity distribution has the idealized distribution $\delta(\mathbf{v} - \mathbf{v}_m)$ (i.e., coherent steady flow with velocity $\mathbf{v}_m$ on all distance scales), equation (4.19) reduces to $\exp[-i\mathbf{p} \cdot \mathbf{v}_m(r)]$, which is the implicit assumption in the applications so far considered. However, in cases such as turbulence, it is the velocity distribution within a voxel, $P[\mathbf{v}(\mathbf{r},t)]$, that is needed as well as the average velocity $\mathbf{v}_m$. This distribution is obtained from the reciprocal Fourier relationship

$$P(\mathbf{v}) = \int d\mathbf{p}\, S(\mathbf{p}) \exp(i\mathbf{p} \cdot \mathbf{v}) \tag{4.20}$$

[cf. equation (1.10)]. This shows that to obtain the distribution it is necessary to measure the echo amplitude $S(\mathbf{p})$ not just at one value of the velocity-encoding gradient but over a raster of $\mathbf{p}$-space by introducing a ramped velocity-encoding gradient $\mathbf{g}^*$.

An alternative to study complex flows with velocity-encoding imaging based on the Fourier conjugates $(\mathbf{p},\mathbf{v})$ is to use displacement imaging based on the conjugates $(\mathbf{q},\mathbf{R})$, which was discussed in Chapter 1. We now consider this in greater detail.

4.13 DISPLACEMENT IMAGING OF COMPLEX FLOWS

Displacement imaging is based on the Fourier relationship

$$S(\mathbf{q}) = \int d\mathbf{R}\, P(\mathbf{R},\Delta) \exp(i\mathbf{q} \cdot \mathbf{R}) \tag{4.21}$$

and its inverse

$$P(\mathbf{R},\Delta) = \int d\mathbf{q}\, S(\mathbf{q}) \exp(-i\mathbf{q} \cdot \mathbf{R}) \tag{4.22}$$

where $P(\mathbf{R},\Delta)$ is the probability distribution for the displacement of spins through a distance $\mathbf{R}$ in time Δ (see Chapter 1). $P(\mathbf{R},\Delta)$ is a much more convenient quantity to deal with than velocity distributions when the flow patterns are very complicated, as in mixing and turbulence. Application of equation (4.22) requires that the wavevector $\mathbf{q}$, defined as $(2\pi)^{-1}\gamma\mathbf{G}\tau$, be ramped through a raster from $-\mathbf{G}_{max}$ to $+\mathbf{G}_{max}$ for each time delay Δ, which makes for a very long experiment if a large number of time delays are used. A more convenient multiple-echo pulse sequence has been devised that permits the entire $(\mathbf{q}$–$\Delta)$-space to be sampled in a single two-dimensional experiment (57), and this gives $P(\mathbf{R},\Delta)$ directly by Fourier transformation.

4.13.1 Taylor–Couette Flow

An interesting application of displacement imaging concerns the flow patterns set up in the concentric-cylinder rotational viscometer arrangement (57). When the inner cylinder is rotated at low speeds, the conventional creep flow pattern is set up between the cylinders such that there is no component of velocity in the axial direction (i.e., in the direction of the cylinder axis). But at higher rotation speeds, inertia of the fluid elements near the inner cylinder causes them to experience centrifugal forces that drive them radially outward. This sets up a pattern of circular vortices, called *Taylor–Couette vortices,* between the cylinders (see Figure 4.16). This flow pattern can be displacement imaged by slice selecting across the cylinders and applying the two-dimensional displacement pulse sequence. Figure 4.17 shows the displacement profiles observed in this experiment. When the slice bisects a Taylor vortex the displacement probability function very quickly shows two peaks, corresponding to flow in opposite directions in a vortex. Conversely, a slice selected between two vortices shows no initial displacement, as seen in the single sharp peak.

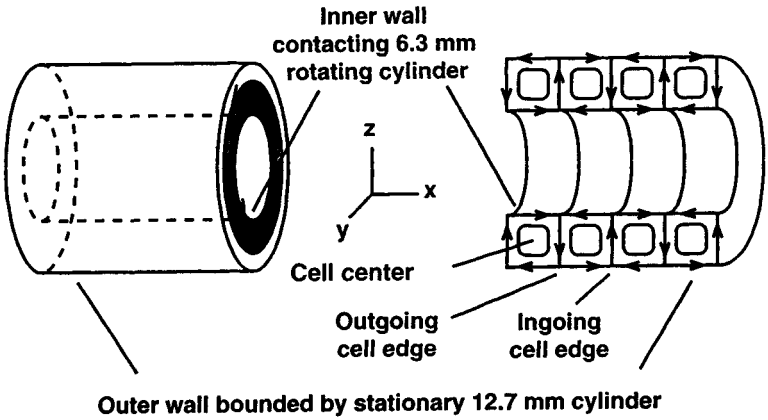

Figure 4.16. Schematic of Taylor–Couette flow. In this experiment the inner cylinder rotates sufficiently fast to create the Taylor vortices shown in the right-hand diagram.

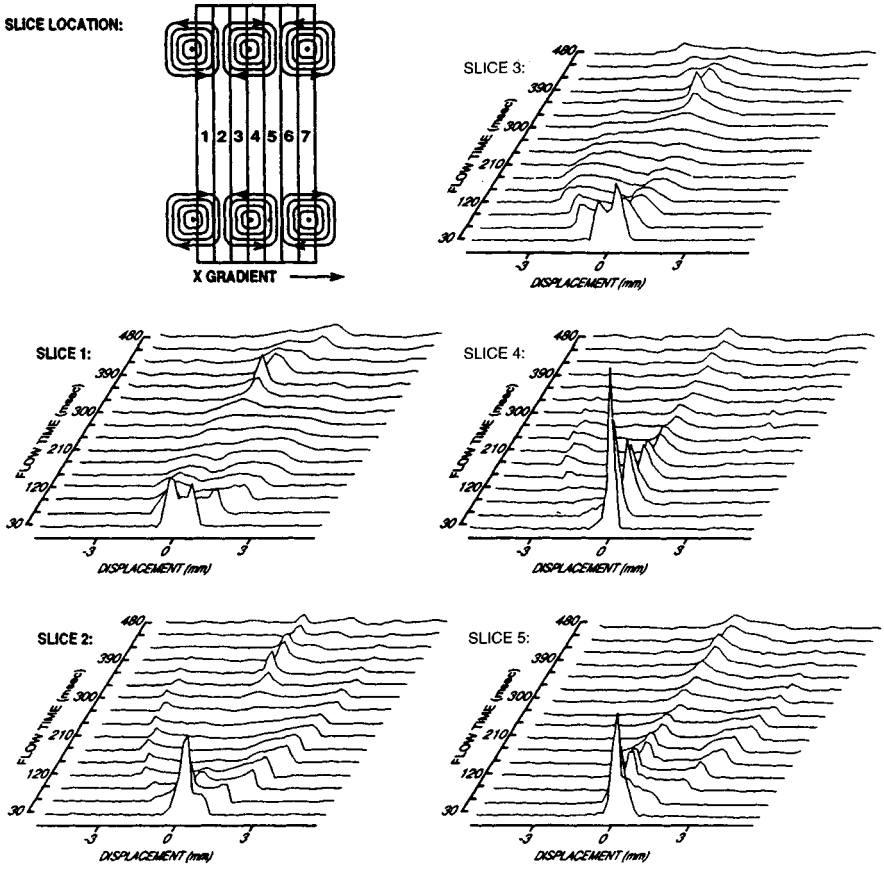

Figure 4.17. Displacement profiles observed for the Taylor instabilities in Figure 4.16.

A special three-dimensional version of the displacement-imaging experiment, based on combining *k*-space imaging and displacement imaging using the Fourier conjugates [(**q**,**R**);(**k**,**r**)] discussed in Chapter 1, has also been applied to Taylor–Couette flow (57). This results in the series of stacked two-dimensional plots illustrated in Figure 4.18. Because the variable r_0 is the initial position of the slice, the two-dimensional plots show correlations between position r and displacements R. The third time direction, obtained by varying the displacement time Δ, indicates how an entire stack of slices, sequentially located down the length of the cylinder column, evolves. The characteristic linked-chain pattern reflects the physical arrangement of the Taylor cells in the column because the edges between cells are associated with a single sharp peak, whereas slices taken through a cell are characterized by a double peak, corresponding to displacements in opposite directions. An even more complicated flow pattern is set up when the inner cylinder is not concentrically situated (see the earlier discussion), but two- or three-dimensional displacement imaging has yet to be applied to this interesting situation.

4.13.2 Flow Through Porous Media

The flow of liquids through a porous solid matrix under an external pressure gradient has immediate relevance to the extraction of oil from porous rock, where brine is pumped through oil-bearing porous rock to displace the oil. Much of the early research in this subject has therefore been stimulated by the oil industry. Nevertheless, the results are relevant to many other areas, such as fluid flow through chromatography columns, tissue perfusion, the flow of fluids in the gut, and potentially, food processing science, where the transport of water, solutes, and lipids through a solid food matrix is of concern. We therefore mention, very briefly, some of the recent applications of MRI to this fascinating area, without making any attempt to be comprehensive.

Fluid transport through a porous system is limited by the backbone percolation cluster. In a finite percolation cluster, the backbone is defined as the set of pathways conducting an electric dc current between two points, or set of points, kept at different potentials. The backbone of the percolation cluster is obtained by removing all branches and dead-ends that do not contribute to the conductivity. By providing direct three-dimensional maps of both the fluid distribution (spin density) and the velocity, MRI provides a unique tool for determining the backbone percolation cluster. This approach has been nicely illustrated on a model system by Muller et al. (313). These authors first imaged the three-dimensional spin density distribution in the water-saturated matrix under zero flow conditions; then made a three-dimensional velocity vector field by imaging the spatial distribution of the three velocity components, (v_x, v_y, v_z). From these data the three-dimensional velocity magnitude images were calculated. The exclusion of all voxels of the spin density images with velocities below the noise level provided an image of the percolation backbone. This study was particularly powerful because the model porous matrix was constructed from a computer simulation of a random site percolation network by machining out

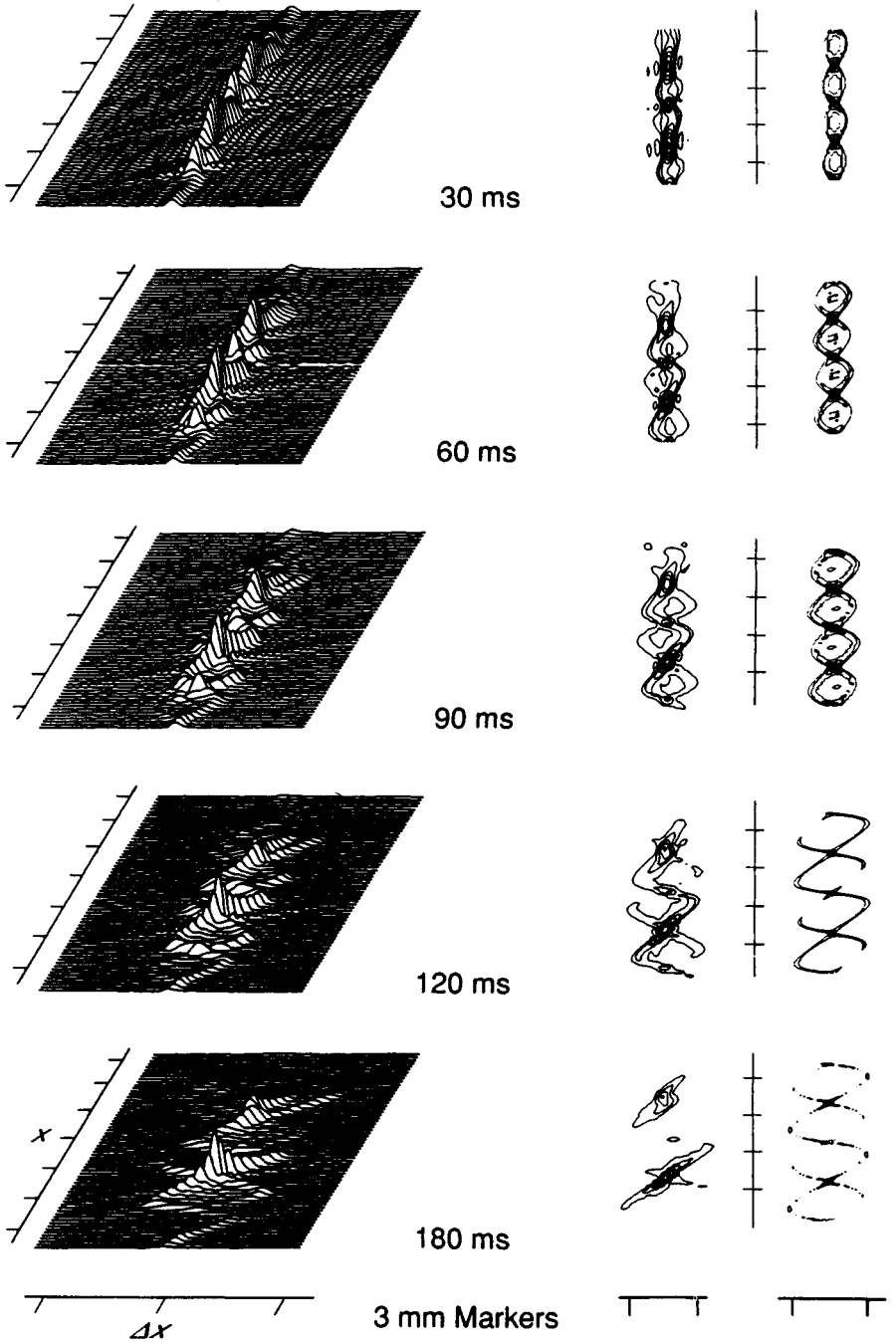

Figure 4.18. Three-dimensional flow displacements corresponding to the Taylor instabilities of Figure 4.16.

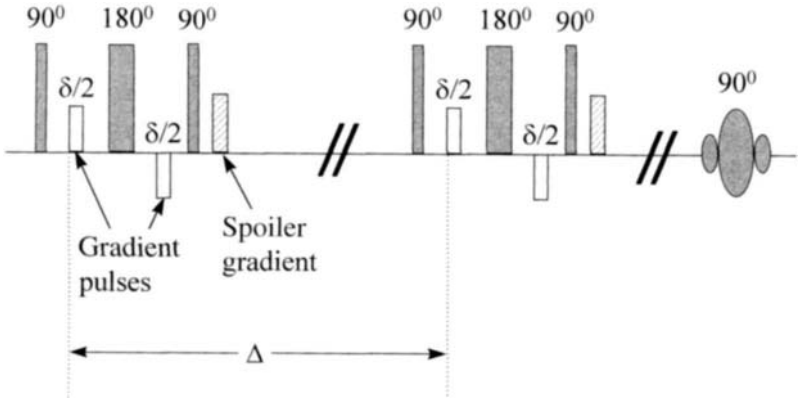

Figure 4.19. Stimulated echo-pulse sequence modified to minimize the effects of susceptibility-generated internal field gradients. The spoiler pulses destroy the FID after the 90° pulses and prevent interference with the stimulated echo. The final 90° pulse is slice selective.

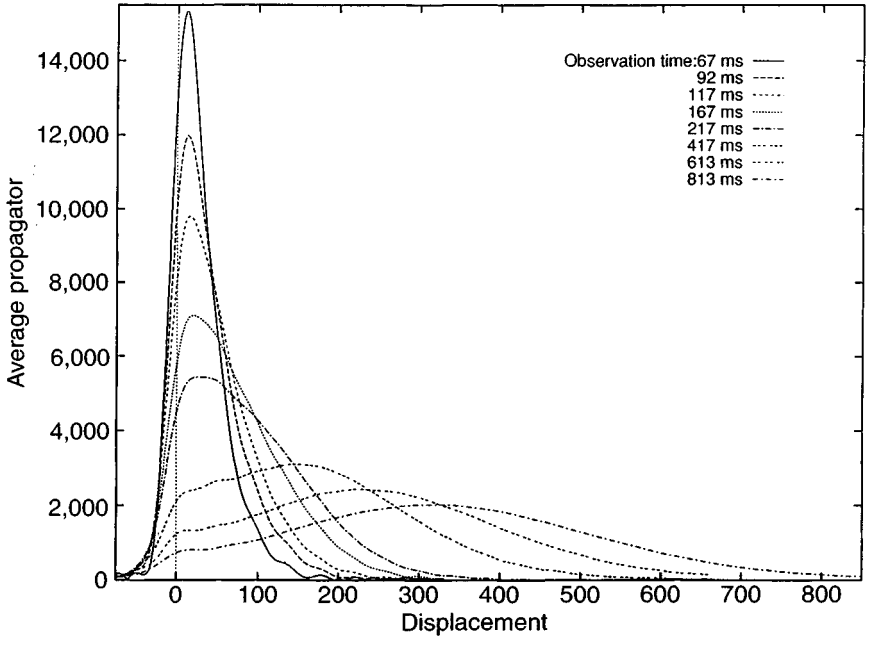

Figure 4.20. Experimental average displacement propagators $P(R,\Delta)$ for increasing displacement times Δ for a water-saturated Fontainebleau sandstone. Displacement is in microns. (Courtesy of K. J. Packer and J. J. Tessier, Ref. 314.)

holes in 32 flat polystyrene disks and then stacking the disks on top of one another according to the computer simulation. In this way the backbone percolation cluster derived from the MRI data could be compared directly with the computer simulation for exactly the same porous matrix.

The displacement imaging approach, based on equations (1.15) and (1.16) (non-spatially resolved) or (1.18) and (1.19) (spatially resolved), provides an alternative to velocity imaging. Instead of measuring velocity fields directly, the average propagator $P(R,\Delta)$, giving the probability that the spins undergo a displacement R in time Δ, is measured and compared with theoretical models. This approach has been used by Packer and Tessier (314) to study fluid displacements in a water-saturated cylinder of Fontainebleau sandstone using the modified stimulated echo-pulse sequence shown in Figure 4.19. The modifications are designed to minimize the effects of local susceptibility-induced field gradients. Figure 4.20 shows $P(R,\Delta)$, along the direction of flow (the cylinder axis) and displays a progressive shift to a broad displaced Gaussian with increasing times, Δ. These data were modeled, with reasonable success, by calculating the propagator for combined flow and diffusion in a network of connected, isotropically oriented cylindrical capillaries, assuming laminar flow within each capillary. In the absence of an applied pressure gradient, restricted diffusion determines the form of $P(R,\Delta)$, but a discussion of this aspect is deferred to Chapter 11. The propagators, $P(R,\Delta)$ for Fontainebleau Sandstone, have also been modeled using a reconstructed porous solid (332). This is a three-dimensional computer-generated random structure designed to have the same overall porosity and pore correlation function as the real sandstone (333).

5

SOLID-IMAGING TECHNIQUES

5.1 SOLID LINEWIDTHS

The end product of food processing operations such as drying, baking, and freeze-drying are low-water-content solids. Some of these, such as cookies, crackers, and pastries, can be consumed without rehydration, whereas others, including most freeze-dried foods, spray-dried powders, extruded products such as spaghetti, and cereal flakes, normally require rehydration. The advantages of lowering the water content include the reduced risk of microbial and chemical spoilage and the lower weight of water per unit solid, which facilitates transportation and distribution.

Although conventional imaging methods can be used to follow moisture migration during the early stages of baking or drying, this is not true during the later stages, as the system becomes more solidlike and the transverse water proton relaxation times shorten to less than 1 ms. For example, an attempt to image a dry cracker with the spin-warp sequence based on a Hahn echo with phase encoding and slice selection is doomed to failure because the transverse proton relaxation time is typically less than a few hundred microseconds, so all gradient pulses and excitation pulses would need to be switched on and off within this very short time span. Even assuming this were possible, the spin-warp sequence would still not produce an image of the cracker unless the applied gradients were large compared to the intrinsic spectral linewidth of the solid, approximately $1/\pi T_2$. If not, the resonance frequency shifts induced by the applied imaging gradients fall inside the natural spectral linewidth and would not therefore produce a spatially resolved image. For many solids, natural proton linewidths can be on the order of tens, or even hundreds, of kilohertz, which precludes the use of conventional imaging gradients.

In high-resolution NMR spectroscopy of solids, various line-narrowing techniques are used to remove the dipolar Hamiltonian mainly responsible for the very

short proton transverse relaxation times. The dipolar Hamiltonian for a pair of spins i and j has the form

$$H_{dd} = A_{ij}(1 - 3\cos^2\theta_{ij})(I_i \cdot I_j - 3I_{iz}I_{jz}) \tag{5.1}$$

where θ_{ij} is the angle between the internuclear vector and the applied magnetic field and I is the usual nuclear spin angular momentum operator. It can be seen from the form of equation (5.1) that the dipolar Hamiltonian can be nulled either by zeroing the geometric factor $(1 - 3\cos^2\theta_{ij})$, or by zeroing the spin-operator factor $(I_i \cdot I_j - 3I_{iz}I_{jz})$. The geometric factor can be nulled by rapid spinning at the "magic" angle, $\theta_{ij} = 54.7°$, in the *magic-angle spinning* (MAS) *technique*. In MAS, the sample, in the form of a small cylinder, is rotated at a velocity fast compared to T_2^{-1} at an angle of 54.7° to the static spectrometer field. The other general approach, called *multipulse line narrowing,* is to null the spin-operator term in equation (5.1) by a series of hard pulses carefully designed such that after a repeated cycle the time-averaged dipolar Hamiltonian is zero to first order. MREV-8 is a classic example of such a line-narrowing pulse sequence. At first sight it would therefore appear that these line-narrowing approaches could be incorporated into phase-encoding imaging sequences to permit solid imaging. This has indeed been tried with moderate success (23,24), but there are clear limitations to this brute-force approach. Obviously, the geometric restraint of having to mold the sample into a small cylinder suitable for MAS precludes its general use in imaging. Multipulse line-narrowing methods are more convenient, but the problem here is that they must be combined with strong imaging gradients and it is not possible to switch the gradients on and off between the line-narrowing pulses (which have to be applied within a period of T_2). This means that the line-narrowing pulses have to be applied in the presence of strong applied gradients, which severely degrades the performance of the line-narrowing sequence. It also requires special hardware for generating the high-power radio-frequency pulse trains.

Fortunately, a number of methods have been developed to circumvent these difficulties, and *solid imaging* is now a practical, if not yet routine technique. The solid-imaging methods of perhaps the greatest potential in food imaging include stray-field imaging (STRAFI), phase-encoding solid imaging (PSI) and variations such as JEPHI and MEPSI, and sinusoidal gradient-echo imaging and combined multipulse–sinusoidal gradient echo imaging. Each of these solid imaging schemes has its own advantages and drawbacks, and we discuss each in turn after a brief consideration of potential applications of solid imaging in food science.

5.2 SOLID IMAGING AND FOOD SCIENCE

To date, most applications of solid imaging have involved nonbiological solids such as plastics, adhesives, porous rocks, and zeolites. So before examining the techniques themselves, it is worth considering what sort of problems in food science might usefully be tackled by solid imaging. At the present time these applications

remain purely speculative, and only time will tell whether they become a reality. At least seven types of problem come to mind.

1. As we have seen in Chapter 3, conventional imaging methods, with relaxation-time compensation, are capable of producing spin-density maps (and hence moisture maps) only in the high-water regime, not in the low-water regime where transverse relaxation times fall below approximately 1ms, which is often the case toward the end of the drying curve, where quality considerations are most important. This is precisely the regime where solid-imaging techniques come into their own.

2. Many baked foods, such as bread and cookies, not only have a low water content but also a very high porosity created as gas replaces water during the baking. These highly heterogeneous, porous solids are difficult to image conventionally because of the low water content and the massive susceptibility broadening effects created around the gas pores. As we shall see, solid-imaging techniques are able to circumvent these difficulties and could perhaps be used to image the final stages of the baking process.

3. Having manufactured a freshly dried or baked food, the problem is to keep it fresh and minimize the slow ingress of water vapor by diffusion from the surrounding air into the dried product. We are all aware of the changes in texture resulting from the ingress of even small quantities of water vapor into crackers, resulting in a loss of texture ("snap"). Understanding these textural changes is important in the formulation and preservation of such products, and solid imaging offers the possibility of following the kinetics of the ingress of water vapor into the dry solid, and in the case of STRAFI, of imaging the time course of the plasticization of the biopolymer chains.

4. By relying on the signal from the unfrozen water in the central frozen core of the food, freeze-drying kinetics can be imaged with conventional methods (see Section 3.4). However, solid-imaging techniques, in principle, permit even freeze-dried solid food components, and possibly even the ice itself, to be imaged and could provide complementary information on freeze-drying kinetics.

5. Several of the nonfood applications of solid imaging have involved thin films. Examples include the ingress of organic solvents into plastic films, which is of concern in packaging, or the drying of thin films in the paint and adhesives industrial sector. However, thin films are also becoming important in the food industry. There is a continuing search for edible thin films with low water permeability so that a layer of food with high water activity can safely be placed next to one with low water activity without severe intermixing of the moisture, resulting in loss of microbial stability. Polysaccharide and protein films appear promising for this purpose, but there is a need to understand and measure the biofilm properties, especially its permeability and drying–rehydration kinetics. Here again, high-resolution solid imaging has much to offer.

6. Food cryopreservation, in either the chilled or frozen states, is another obvious area where solid imaging could have an impact. Because of their heterogeneity

and compositional complexity, there is rarely a single liquid–solid phase transition as a food is cooled. Instead, different microscopic compartments and fractions in the food freeze, or crystallize, at different temperatures. Solid imaging offers the possibility of observing the spatial distribution of these transitions as a food is cooled. An example being studied in the author's laboratory involves the freezing of raw potato. At −5°C, the cell cytoplasm, vacuolar, and extracellular water is already frozen, but unfrozen water still exists in the starch granules and cell wall compartments. Solid imaging (SPI) is being used to image the freezing of this unfrozen water as the potato is cooled below −5°C.

7. Even when there is no first-order phase transition, cooling, and/or drying, can induce glass transitions in various regions within food, profoundly affecting textural, kinetic, and dynamic properties (190). Biopolymer mobility is severely reduced below the glass transition temperature and results in a shortening of transverse relaxation times. Solid-imaging methods therefore have the potential to reveal the spatial distribution of glassy states in foods.

These seven examples should suffice to convince the reader of the important role that solid imaging is likely to have in food science in future years. It is therefore appropriate to turn to the principles underlying these relatively novel imaging methods. We begin with stray-field imaging (STRAFI).

5.3 STRAY-FIELD IMAGING

5.3.1 Introduction to the STRAFI Method

The ideas behind STRAFI have been nicely explained in a recent review by McDonald (8), who together with co-workers at the University of Surrey, has been pioneering many of the applications of STRAFI since it was proposed by Samoilenko et al. in 1988 (9). The gradient of the stray field surrounding the superconducting magnet of a commercial NMR spectrometer is orders of magnitude larger than the applied imaging gradients generated by gradient coil sets. For example, the stray-field gradient for a standard 89-mm 9.4-T (400-MHz proton frequency) magnet is on the order of 50 T/m, compared to a few hundred mT/m in a strong gradient imaging or diffusion pulse. The stray-field gradients are therefore sufficiently strong to overcome the natural linewidth of most solid food samples and permit imaging. Susceptibility broadening is also overwhelmed by the stray field, so porous heterogeneous solids are also amenable to STRAFI.

Of course, the stray-field gradients of a superconducting magnet cannot be switched on and off, and even a hard 90° excitation pulse a few microseconds in duration is slice selective in large stray-field gradients. For example, a 10-μs 90° pulse would only excite a slice about 40 μm wide in the direction of a 50-T/m fringe field. All this means that a different imaging protocol must be used whereby only a single slice in the sample is excited by a hard pulse and the total intensity

from the slice is recorded as a number. The sample is then moved a distance roughly equal to the slice thickness and the intensity from the neighboring slice in the solid again recorded. By progressively translating the sample through the stray field and plotting the slice intensity as a function of sample position, a one-dimensional profile of the solid can be built up. This protocol is illustrated by the schematic in Figure 5.1.

A few comments can usefully be made at this point. First, the slice thickness, 40 μm or less, puts the resolution on a par with conventional microimaging, so changes on a microscopic distance scale can be observed. Second, the technique is not confined to one-dimensional profiling, and commercial STRAFI probes are available which, by rotating and translating the sample, permit three-dimensional imaging via back-projection signal processing. Third, by directly measuring slice intensities, STRAFI does not involve Fourier transformation and is therefore more akin to continuous-wave spectroscopy, except that the sample is "continuously" moved instead of the frequency. Fourth, it is not possible to measure the intensity of a point on the FID from a single 90° pulse in STRAFI because the very strong field gradient causes destructive interference of the FID signal in a time short compared to the instrument dead-time. For this reason it is common to use either the quadrature echo sequence, 90^0_x–τ–$(90^0_y$–τ–echo–τ$)_n$, or the CPMG sequence 90^0_x–τ–$(180^0_y$–τ–echo–τ$)_n$, and record the intensity of the echoes. It is important that the 180° pulses in the CPMG sequence are made by doubling the amplitude of the 90° pulse and not by doubling their duration, which would also increase the slice thickness.

As with most imaging applications, it is not difficult to obtain qualitatively impressive images with STRAFI. An example is shown in Figure 5.2, showing the ingress of acetone vapor into PVC (13). It is notable that even polystyrene plastic and dry paper can be imaged. The real difficulties appear when quantitative infor-

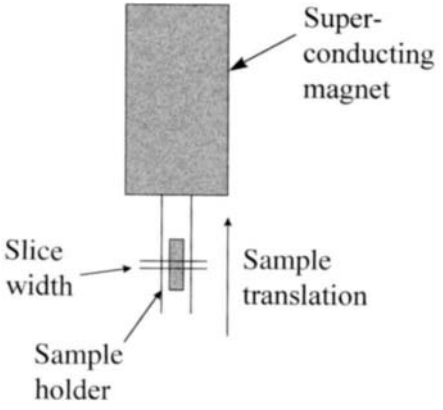

Figure 5.1. Schematic of the STRAFI equipment.

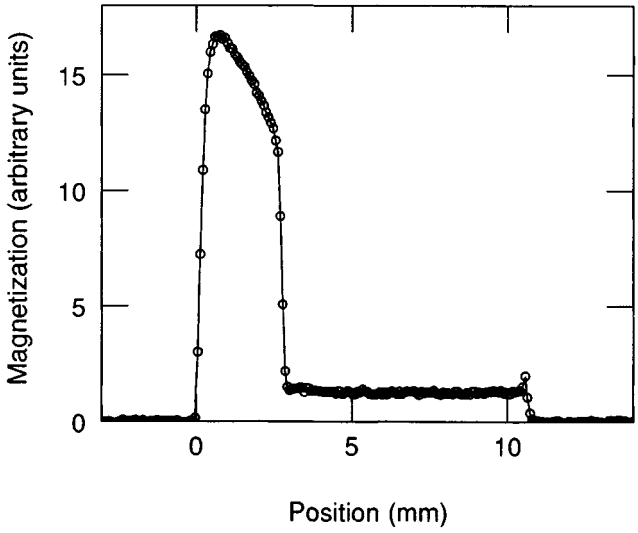

Figure 5.2. One-dimensional profile of PVC exposed to acetone vapor above a liquid acetone reservoir for 48 h at 20°C; the line connecting the data is added for ease of viewing only. (From Ref. 13.)

mation is required, which is the case with the potential applications of STRAFI in food science listed above. These difficulties fall into a number of categories.

First, imaging times can be slow, which could be a problem if real-time processing changes are to be imaged. Imaging times can be reduced by speeding up the movement of the sample through the field and by using multiecho slicing, whereby signal is acquired from a new slice while it is still recovering in the previous slices. However, moving the sample modulates the signal in a way analogous to conventional liquid flow imaging, which greatly complicates data interpretation. Second, the strong stray-field gradient modulates the amplitudes of successive echoes in multiple-echo STRAFI pulse sequences from the same slice. This makes it harder to extract quantitative relaxation times from the echo decays, especially when the sample is moved continuously through the field. To understand these complications it is necessary to delve somewhat more deeply into the theory of the STRAFI method, which is discussed elegantly in two papers by Benson and McDonald (10,11).

5.3.2 Theory of the STRAFI Method

Echo Modulation. As stated earlier, even a 10-μs 90° pulse is slice selective in the powerful gradients of the stray field of a superconducting magnet. The theory of slice selection is well known (5) and was summarized in Chapter 1. After a 90_x^0

pulse of duration t_p, the magnetization observed in the rotating frame, M'_y, has a sinc-function spatial modulation through the excited slice such that

$$M'_y(t_p) = \frac{\pi}{2}\frac{sin\theta}{\theta} \tag{5.2}$$

where $\theta = (\pi/2)(B_1^2 + B_g^2)^{1/2}/B_1$; $B_g = rG$ and the 90° pulse duration t_p is $\pi/2\gamma B_1$. This is shown in the top part of Figure 5.3. The effective slice thickness Δr is equated to the distance between the points of zero magnetization either side of the central peak, when the sinc function is zero ($\theta = \pm \pi$) and B_g is $\pm G\Delta r/2$. Substitution into equation 5.2 gives a slice thickness

$$\Delta r = \frac{\sqrt{3}}{t_p \gamma G} \tag{5.3}$$

Equation (5.3) shows that the spatial resolution can be increased simply by using longer pulse lengths t_p. However, the signal intensity is also proportional to Δr, so as with conventional imaging, a low signal-to-noise ratio eventually sets the practical limit on achievable resolutions.

The simple sinc-function spatial modulation of the magnetization in the slice selected is further modulated by precession of the magnetization in the gradient. This imposes an additional spatial modulation with a characteristic length δr given by

$$\delta r = \frac{2\pi}{\gamma G(t_p + t')} \tag{5.4}$$

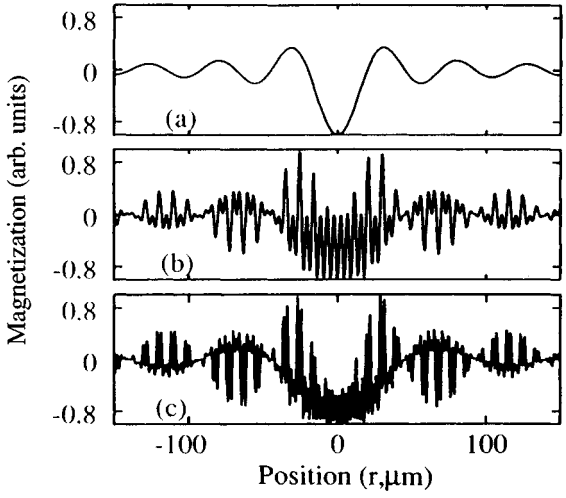

Figure 5.3. Calculated y'-component of the magnetization (*a*) immediately after the 90_x pulse, (*b*) at the first echo, and (*c*) at the second echo as a function of position. The pulse length is 10 μs, the pulse gap is 50 μs, and the gradient is 50 T/m. (From Ref. 10.)

where t' is the time after the 90° pulse. This additional modulation is shown in Figure 5.3*b* at the time of the first solid echo. In addition, there is spatial modulation due to the repetition of the 90° pulses, having a higher characteristic spatial length δr_p, given as

$$\delta r_p = \frac{2\pi}{\gamma G \tau} \tag{5.5}$$

where τ is the pulse spacing. This imposes yet another modulation which is shown in Figure 5.3*c* at the time of the second echo. The observed intensity at the second echo is obtained by spatially integrating the magnetization in Figure 5.3*c*, and shows (11) that the second, and subsequent, echoes in the quadrature sequence are, in the absence of relaxation or sample movement, 1.5 times more intense than the first echo, an effect that has been observed experimentally (10).

Similar calculations using the CPMG instead of the quadrature echo sequence show the same enhancement of the second and subsequent echoes, but in addition, there is an improvement in signal-to-noise ratio in the CPMG compared to the quadrature echo sequence (11). However, phase alternation in the CPMG sequence, which is used in liquid transverse relaxation measurements to eliminate cumulative errors in the rephasing pulses, actually leads to greatly diminished echo intensities and cannot therefore be implemented.

5.3.3 Effects of Sample Movement in STRAFI

STRAFI experiments usually involve continual movement of the sample through the field by means of a rotating screw–goniometer arrangement, and echo measurements are then taken "on the fly." Although this reduces the imaging time, it means that the gradient felt by an excited slice is continually changing. There is clearly a maximum velocity v_h at which the sample moves a slice thickness during the time between refocusing pulses. At or above this critical velocity, no sensible imaging is possible. This maximum velocity can be calculated by equating the slice thickness [equation (5.3)] to the distance moved during n echoes, $(2n\tau)v_h$, with the result

$$v_h = \frac{\pi\sqrt{3}}{(2n\tau)t_p\gamma G} \tag{5.6}$$

The value of v_h for a four-echo hydrogen experiment with a pulse length of 10 μs, a pulse gap of 50 μs, and a gradient of 50 T/m is 10 cm/s, which is sufficiently fast not to impose a restraint on most STRAFI experiments. However, the more critical velocity constraint is when the sample moves a distance $2\tau v_1$ during the first echo time, equal to the smaller of the spatial modulation lengths δr given by equation (5.5). This defines a critical velocity v_1 such that

$$v_1 = \frac{2\pi}{(2\tau)^2\gamma G} \tag{5.7}$$

For the same experimental conditions used above, v_1 is only 0.3 cm/s, which unfortunately, is within the range of velocities used in typical STRAFI experiments. The effect is to impose an additional phase increment α, given by

$$\alpha = \int_o^\tau dt\, \gamma G v t \tag{5.8}$$

analogously to the phase increment in flow imaging. The result greatly complicates the interpretation of the echo amplitudes. Figure 5.4 shows the calculated echo amplitude as a function of pulse spacing for the first three echoes in the quadrature sequence at three sample velocities, in the absence of relaxation. In practice, it is therefore easier to perform STRAFI relaxation measurements on stationary samples and move from slice to slice in a discontinuous way. This also increases the imaging time, however, which is not always desirable if continuous processing changes are being followed. Here, as with many NMR measurements, we find that there is a subtle, and frustrating, relationship between information content and imaging time.

5.3.4 Relaxation Measurements in STRAFI

If the sample velocity is kept well below v_1, the effects of transverse relaxation on the echo intensities can be calculated using the usual attenuation factor, $\exp(-TE/T_2)$, where TE is the echo time. However, the amplitude of the first echo needs to be multiplied by a factor of 1.5 to take account of the echo modulation effects discussed above. Relaxation-time measurements are of potential importance in

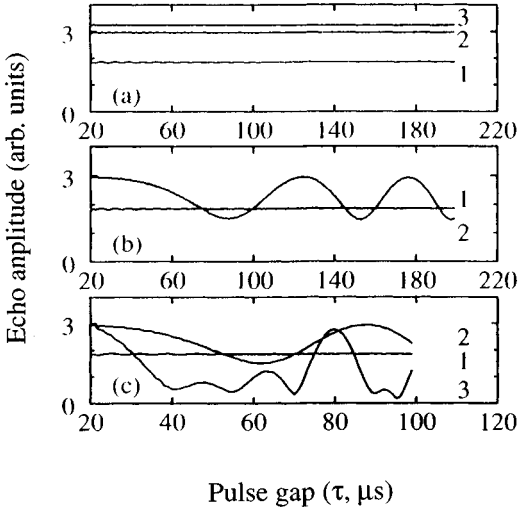

Figure 5.4. Calculated echo amplitude as a function of pulse gap for the first few echoes for (*a*) a stationary sample, (*b*) a sample velocity of 1 cm/s, and (*c*) a sample velocity of 2 cm/s. The echo numbers are given beside the appropriate curves in the figure. The pulse length is 10 μs and the gradient is 50 T/m. (From Ref. 10.)

food applications, so they will be illustrated with examples taken from the literature on the application of STRAFI in materials science.

5.3.5 Applications of STRAFI in Materials Science

One-dimensional profiles have been obtained during the time course of the drying of a 2-mm-thick film of sodium silicate, which changes from a soft, rubbery texture at higher water contents, to a brittle, glasslike solid at lower water contents (12). This behavior is also observed during the drying of biopolymer films such as gelatine, so the STRAFI results are of considerable interest, even though sodium silicate is not a food. A 16-echo quadrature-echo pulse sequence was used with a τ spacing of 50 μs and a theoretical slice width Δr of 53 μm. Because relaxation times were being quantified, the sample remained static during each slice measurement. The echo intensities at each position r were fitted with the usual single exponential function, $M(r,t) = M_0(r) \exp[-t/T_2(r)]$. In this way, profiles of the spin density $M_0(r)$ (and hence the degree of hydration, after correction for shrinkage) and relaxation time $T_2(r)$ were deduced separately. By comparing one with the other it was possible to derive the dependence of the relaxation time on moisture content and show that the water mobility in the film depends primarily on the local hydration level and not on the rate of drying.

Another materials science application of STRAFI that has considerable relevance to analogous problems in food science is a study of the diffusion of acetone vapor into PVC (13). This study is particularly interesting because it not only succeeded in measuring the acetone profiles, but also profiles of the rigid PVC and of the fraction of a more mobile, swollen PVC component. The data were used to show that the ingress obeyed case II diffusion kinetics (178), such that after ingress of acetone, the PVC was plasticized (or rubberized) at a rate $A[1 - \exp(-t/\tau_c)]$, where τ_c^{-1} is the softening rate. This example is interesting because conventional MRI has been used to show that case II rehydration kinetics also applies to the rehydration of pasta, but in conventional imaging no signal could be obtained from the dry pasta or from the rehydrated starch components. It therefore appears that STRAFI could be applied usefully to the study of biopolymer plasticization during the rehydration of foods. We turn now to the second solid-imaging method, phase-encoding solid imaging (PSI).

5.4 PHASE-ENCODING SOLID IMAGING

5.4.1 Introduction to PSI

Phase-encoding solid imaging is sometimes also called *single-point imaging* (SPI) or *constant-time imaging* (27). The simplest version of this class of solid-imaging sequence is the acquisition of an FID with a 90°_x pulse in the presence of an applied field gradient. Of course, the pulse duration must be sufficiently short that its excitation bandwidth covers the range of frequencies introduced by the applied imaging gradients, so that hard pulses are required. Turning the gradient on before

acquisition removes the problem of gradient switching artifacts. Of course, if the entire FID were acquired in the time domain and Fourier transformed, a one-dimensional projection along the direction of the applied field gradient would, in principle, be obtained. Indeed, this is what happens in the readout direction in conventional FT liquid-state imaging. This simple protocol cannot be applied to solids because their very short T_2 time limits the acquisition time, so that the maximum k value is only about $\gamma G_{max} T_2^*$, severely limiting spatial resolution. Moreover, very strong gradients would be required to overcome the effect of the natural linewidth, so the FID would decay extremely rapidly. One way around this problem is to choose a single point on the FID and introduce phase encoding by monitoring the effect of increasing applied gradients on the amplitude of this single point (hence the names *SPI, constant-time imaging,* and *PSI*). This means that at least one scan is needed for each gradient step, so imaging times with PSI can be very long, the major disadvantage of the technique. Of course, the imaging time can be reduced by using excitation pulses with smaller flip angles, so that the full $5T_1$ recycle delay can be reduced at the expense of a poorer signal-to-noise ratio. One advantage of PSI over other solid-imaging techniques is that it can be implemented on standard imaging spectrometers without special hardware, although a fast digitizer and a probe with short excitation pulses suitable for solids are required for the best results.

5.4.2 Resolution in PSI

Because the image in PSI is obtained from a single point on the FID at constant time, transverse relaxation no longer limits the spatial resolution and the image is free from distortions from magnetic field inhomogeneities, susceptibility artifacts, and chemical shifts. It is therefore of interest to investigate what factors do limit resolution in PSI. According to Nyquist's theorem, the one-dimensional pixel resolution δx in PSI is the reciprocal of the maximum wavevector, $1/k_{max}$, and the maximum wavevector is simply $\gamma G_{max} t_p / 2\pi$. It appears, therefore, that arbitrarily small pixel resolutions can be achieved in PSI by increasing the maximum field gradient G_{max} and choosing a point on the FID with as long a time delay t_p as possible. Although the pixel resolution can indeed be increased in this way, this does not mean that the true resolution of the image is increased, because it takes no account of intrinsic factors, such as diffusion, which "spread" signal between neighboring pixels. The spreading of signal caused by these intrinsic factors is described by the point-spread function PSF(x), where x is the imaging direction. PSF (x) can be thought of as the spectrum obtained from a thin section of the sample located between x and $(x + dx)$. The observed image (in one dimension) is the convolution of the PSF and the actual spatial distribution of spin density, $\rho(x)$. The true resolution is therefore defined as the full width at half-height of the PSF. The PSF is, by definition, the Fourier transform of a k-space function called the *modulation transfer function* (MTF) and it is usually easier to deduce the form of the PSF from the MTF. In k-space the overall MTF is obtained by multiplying the component MTFs corre-

sponding to diffusion, relaxation, and so on, so the total PSF is obtained as the convolution of component MTFs. We therefore write

$$\mathrm{PSF}(x) = \mathrm{PSF}_{\mathrm{dif}} \otimes \mathrm{PSF}_t \otimes \mathrm{PSF}_k \tag{5.9}$$

where $\mathrm{PSI}_{\mathrm{dif}}$ is the spreading caused by diffusion, PSF_t the spreading caused by the decay of magnetization in the time domain (caused by, e.g., relaxation, susceptibility broadening, and chemical shifts), and PSF_k the spreading caused by the finite size of the k-space sampling raster. The beauty of single-point imaging is that by keeping the time constant, the various time factors causing signal decay, such as relaxation and dephasing by susceptibility inhomogeneities, chemical shift differences, and so on, are constants in k-space. In other words, MTF_t is a constant in k-space, so that PSF_t is a delta function in real space and relaxation effects do not cause loss of spatial resolution in single-point imaging. PSF_k is also a minor factor because its MTF is a constant between $-k_{\max}$ and $+k_{\max}$ and zero elsewhere. The PSF_k obtained by Fourier transformation is therefore a sinc function with a full width at half-height of $1.2l/k_{\max}$ or $1.21\delta x$. In other words, the PSF arising from the finite size of the k-space raster causes only a 21% coarser resolution than the digital resolution. Unfortunately, it is diffusion that is the major factor limiting resolution in PSI. It is well known that unrestricted diffusion causes the FID to decay exponentially as $\exp(-D\gamma^2 G_x^2 t_p^3/3)$. Rewritten in k-space, this is the MTF, $\exp(-Dk^2 t_p/3)$. Fourier transformation therefore gives $\mathrm{PSI}_{\mathrm{dif}}$ as $\exp(-3x^2/4Dt_p)$ and the full width at half-height, which gives the diffusion-limited resolution, is $dx_{\mathrm{dif}} = 1.92(Dt_p)^{0.5}$. This sets the true resolution limit in single-point imaging and shows that resolution can be increased by increasing t_p, but only at the expense of loss of signal-to-noise ratio because of the decay of the FID. Of course, the diffusion coefficient in solidlike materials is usually much less than that of bulk water and, moreover, the derivation assumes unrestricted diffusion, which is not necessarily the case. These considerations suggest that much higher resolutions can, at least in principle, be achieved with PSI than with frequency-encoding imaging.

5.4.3 Relaxation Weighting in PSI

In PSI using a simple FID, an image can be obtained from any point on the FID, although the optimum delay for the best signal-to-noise ratio is $T_2^*/2$ (27). By acquiring images from several points on the FID and analyzing the decay as an exponential, it is possible to extract separate spin-density and transverse relaxation-time maps (although the T_2 in this case will include field inhomogeneities, so is more precisely T_2^*). Relaxation-time maps have been obtained in this way for concentrated starch gels, and the effects of starch retrogradation have been imaged (29). In this example, spatial dependence was not expected, but the T_2^* map (on a scale of 0 to 15 μs) revealed significant variations over the sample, for reasons that are, as yet, unclear.

Another application of PSI based on the simple-phase-encoded FID concerns a one-dimensional study of the kinetics of cement hardening (28). Changes in the proton density (or water content, assuming that T_2^* does not change) of a cement sample over the course of 36 days were followed. The results are particularly relevant to imaging the time course of gelation and the formation of glassy states in foods, although such applications have yet to be reported.

5.4.4 Multipulse Variants of PSI

In most practical applications of PSI with conventional imaging spectrometers, the resolution will not be diffusion limited, but limited by the digital resolution, which is the reciprocal of $k_{max} = \gamma G_{max} t_p / 2\pi$. There is therefore a definite advantage in extending the phase-encoding period, t_p, as much as possible, at least until diffusion begins to limit resolution. This is the idea behind multiple pulse variations of PSI, which, by producing coherent echoes, can extend t_p and improve resolution. Three such pulse sequences have been shown to be particularly effective: the solid-echo sequence (giving solid-echo phase-encoding solid imaging, SEPSI); the Jeener–Broekert sequence (giving Jeener–Broekert phase-encoding imaging, JEPHI) and the magic-echo sequence (giving magic-echo phase-encoding solid imaging, MEPSI). Because the essential idea is the same for all these methods, we focus on the MEPSI technique, which has been the most successful to date.

The pulse sequence for MEPSI is shown in Figure 5.5 (25,26). The magic echo consists of a sandwich of two hard 90° pulses of arbitrary phase ϕ and $-\phi$ with two burst pulses forming the sandwich contents, each of duration $2t$, tip angle α

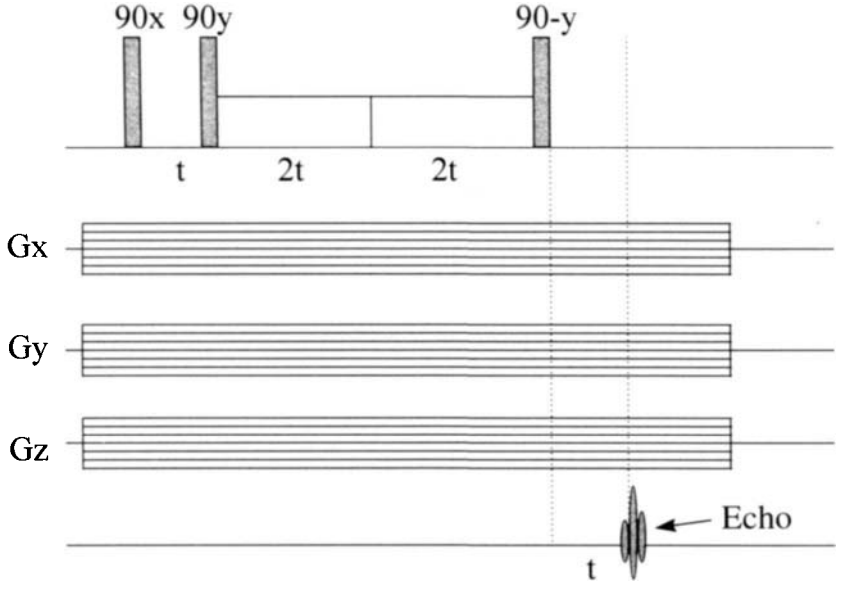

Figure 5.5. Three-dimensional MEPSI pulse sequence.

($= 2\omega_1 t$), and phase ($\phi + \pi/2$) and ($\phi - \pi/2$), respectively (26). The effect of this magic sandwich sequence is to refocus completely dephasing caused by dipolar interactions. During the first time interval t after the excitation pulse, the magnetization evolves under the dipolar Hamiltonian H_d. The effect of the first half of the sandwich is to rotate the magnetization to a tilted reference frame where the spins are locked in an effective field $\frac{1}{2}(3\cos^2\theta - 1)H_d$ for a time $2t$, where θ is the tilt angle between the effective and applied field. If the burst RF power is much greater than the dipolar fields, $\theta = 90°$ and the spins evolve under the field $-H_d$. This refocuses the dipolar dephasing and causes a rotary echo in the middle of the magic sandwich. The second half of the sandwich introduces a reversed phase, $-H_d$, which is refocused by the final evolution period under the full dipolar Hamiltonian to produce an echo a time t after the magic sandwich. The magic sandwich preserves phase encoding, which can be introduced by ramping through applied gradients and measuring the echo amplitude at a fixed time $6t$ after the excitation pulse. The three-dimensional imaging version is shown in Figure 5.5 and produces an image after Fourier transformation.

Taking a typical t value of 100 μs, the magic echo extends the phase encoding period to 600 μs, which gives substantially improved resolutions. For example, a test sample consisting of hexamethyl benzene gave resolutions of 300 μm^3 with a gradient of 20 G/cm (25). As with all single-point imaging methods, the main

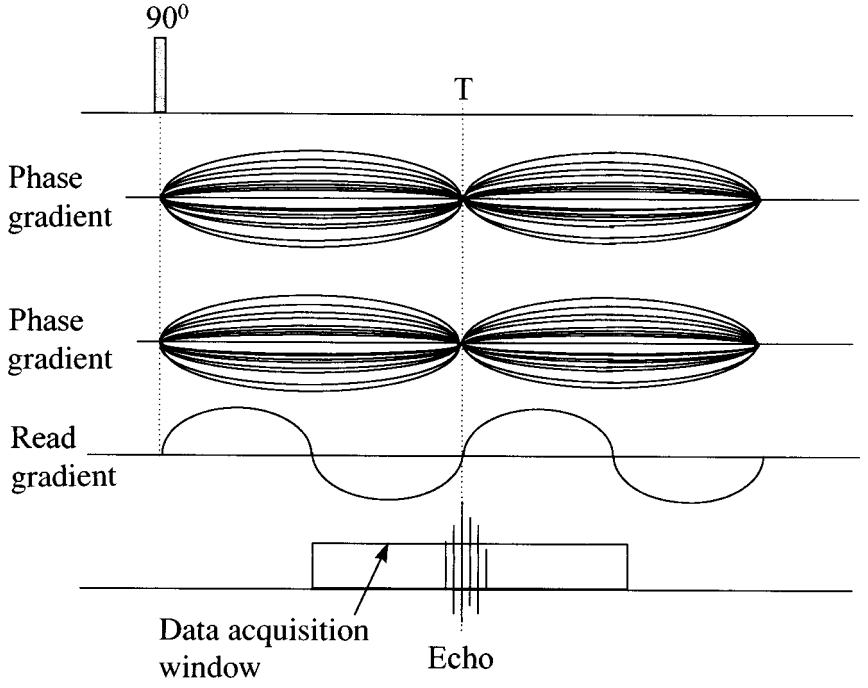

Figure 5.6. Three-dimensional oscillating field gradient solid-imaging pulse sequence. (From Ref. 20.)

disadvantage of this MEPSI is the long image acquisition time, which, for a three-dimensional experiment can be many hours. It is therefore advisable in food processing applications to exploit sample symmetry wherever possible and use one-dimensional imaging, or if radial symmetry exists, radial imaging with inverse Abel transformation, which gives the two-dimensional information. Molecular motion during application of the magic sandwich degrades its refocusing performance, so this can be exploited as an image contrast parameter related to molecular motion in the solid state. For example, the amplitude of the magic echo increases dramatically in a rubber sample as the temperature is lowered below the glass transition (30). This means that MEPSI could be used to image the spatial distribution of molecular motions and/or temperatures in solid foods below the glass transition temperature.

5.5 SINUSOIDAL GRADIENT-ECHO IMAGING

An alternative way of imaging solids with transverse relaxation times less than 1 to 5 ms was proposed by Cottrell et al. in 1990 (14). Based on the application of a sinusoidally oscillating strong field gradient, it has appropriately been called *sinusoidal gradient-echo imaging* and is comfortably able to image samples with transverse relaxation times as short as 100 μs. A repetitive pulse variant of the technique, which gives an improved signal-to-noise ratio, has been presented by McDonald et al. (15), and most recently, a three-dimensional imaging version has been presented (20).

5.5.1 Principles of Sinusoidal Gradient-Echo Imaging

The basic idea of sinusoidal gradient-echo imaging is simple to understand, although its implementation is less straightforward. Dipolar broadening in solid samples is overcome by using strong field gradient amplitudes of the order of 1T/m, and the problem of rapidly switching them on and off within the few hundred microseconds permitted by the short transverse relaxation time in solids is overcome by using sinusoidally oscillating gradients, for which tuned gradient coils, providing large gradients at moderate power, are available. Figure 5.6 shows the three-dimensional imaging version of this sequence. In the readout direction the sinusoidal amplitude variation serves to produce a gradient echo, so no refocusing RF pulse is required and echo times (*TE*) can be reduced from milliseconds in conventional liquidlike spin-echo imaging, to only about 100 μs, permitting soft solid imaging. Phase encoding is introduced using sinusoidal gradients with twice the period within the data acquisition window, as indicated in Figure 5.6. One subtlety in the data processing involves the trajectory in k-space, which, with sinusoidal gradients, produces nonlinear sampling, unlike the linear sampling obtained in the usual constant-gradient FT method. Simple relationships that linearize the k-space raster have been presented and used to extract the image (20).

5.5.2 Applications of Sinusoidal Gradient-Echo Imaging in Materials Science

To date there have been no applications of this technique to food materials, but several nonfood studies have immediate bearing on analogous problems in the transport of water in low-moisture foods. The first involves a study of water diffusion in zeolites (16) and sandstones (17). Zeolites exhibit spatial heterogeneity over a very wide range of distance scales, so an understanding of the kinetics of water transport within a zeolite bed helps the formulation of moisture transport models in heterogeneous porous food materials. Despite the fact that the water proton transverse relaxation times in a zeolite bed are too short to permit conventional imaging (one relaxation component in zeolite 4A is about 150 to 200 μs, the other about 1.5 to 2 ms), Hughes et al. (16) used the repetitive pulse variant of gradient-echo imaging with a short echo time of 216 μs to obtain one-dimensional moisture profiles through a plug of the packed zeolite. A similar study was made of the moisture profiles in sandstone (see Figure 5.7). These moisture profiles were interpreted with the model presented in Section 3.1, involving the parallel diffusion of the moisture in the vapor phase and the diffusion of water in the liquid phase, either within the zeolite crystallites, or in the case of the porous sandstone, as pore surface water. In both cases local dynamic equilibrium was maintained between the vapor and liquid phases and was described by the adsorption isotherm. The success of these studies suggests that it should be possible to use the technique to image moisture transport in foods comprising granular microporous particles, such as cookies.

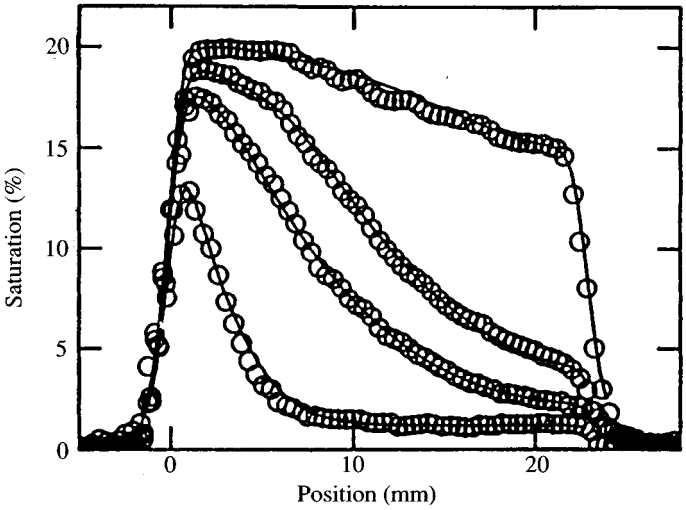

Figure 5.7. Water ingress profiles into a sandstone plug after 4 (lower trace), 24, 48, and 120 (upper trace) hours together with theoretical fits (see the text for details). The repetitive pulse variant of the oscillating field gradient solid-imaging pulse sequence was used to observe the profiles (see Figure 5.8). (From Ref. 17.)

5.5.3 Combined Multipulse Sinusoidal Gradient-Echo Imaging Methods

Although conventional multipulse line-narrowing sequences such as MREV-8 have been incorporated into imaging sequences (21), they suffer from the need for high radio-frequency pulse power, which is required, at least in part, to overcome the large spectral width induced by the presence of strong imaging field gradients. A very elegant solution to this problem has been proposed, and tested successfully, by McDonald and Tokarczuk (22). This combines a multipulse sequence that averages the dipolar Hamiltonian to zero (in first order) with a sinusoidally driven imaging field gradient. By locating the excitation pulses at the zero points of the sinusoid gradient function, much lower RF power is needed. The pulse sequence is shown in Figure 5.8. The product of the six pulses of the repeated cycle is unity. The average Hamiltonian, to first order, acting in the presence of the sinusoidal gradient of mean magnitude B_g is simply the Zeeman Hamiltonian in $B_g/3$ (22)

$$H_{av} = \frac{\gamma h B_g}{3} \sum_j I_z^j \tag{5.10}$$

so that all dipolar terms are removed. Moreover, it can be shown that this sequence does not accumulate phase from a static resonance frequency offset. This means that the sequence is insensitive to magnet inhomogeneity and to chemical shift

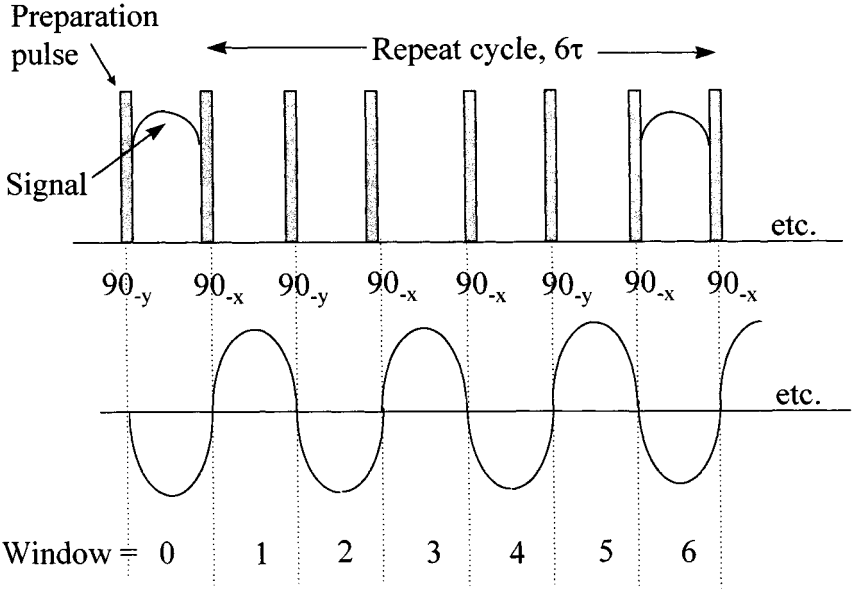

Figure 5.8. Repetitive pulse variant of the oscillating gradient solid-imaging sequence. (From Ref. 17.

broadening. Space encoding is introduced by using a linear oscillating gradient of the form

$$B_g(t,x) = \frac{\pi Gx}{2} \sin \frac{\pi t}{\tau} \tag{5.11}$$

for which the observed signal, sampled every sixth window of the repeated cycle, is

$$M(t) = M_0 \int_{-\infty}^{\infty} dx\, \rho(x) \exp\left(\frac{-i\gamma Gxt}{3}\right) \tag{5.12}$$

The one-dimensional spin density profile $\rho(x)$ can be extracted in the usual way from equation (5.12) by Fourier transformation with respect to time. By rotating the oscillating gradient between successive shots of the repeated cycle, projections in successive directions can be obtained and the two-dimensional image extracted by back projection.

6

ON-LINE MRI FOR PROCESS CONTROL AND QUALITY ASSURANCE

6.1 INTRODUCTION

The possibilities for exploiting MRI as an on-line sensor for process control and quality assurance throughout the food manufacturing sector are very great and the next few years should see rapid development in this area. The term *on-line* generally refers to a real-time measurement during processing. In this sense it includes *in-line* measurements, where an aliquot from a production line is temporarily removed for examination; *side-line* measurements, where measurements are made on a moving side stream where a fraction of the material moves parallel to, and usually more slowly than, the main production line; and what could be called *main-line* measurements, where material moving on the main production line is examined in situ. Clearly, the type of food material and the production environments vary so greatly that no single magnet design and NMR protocol will be suitable for all applications and it will be necessary to adapt spectrometer operations to each specific application.

One basic consideration is whether spatial resolution is essential to the monitoring process. If simple relaxation measurements with an FID provide all the necessary information, such as moisture or oil content, more expensive imaging facilities are superfluous. On the other hand, where discrete samples move in single file down a production line, a nonspatially resolved NMR measurement on each sample may be possible, but imaging may permit several samples to be examined simultaneously, permitting a faster throughput. Both nonspatially resolved NMR on-line detection, as well as the purely imaging aspects, will therefore need to be considered in this chapter. We begin by reviewing some of the constraints imposed on all on-line NMR/MRI measurements by spin physics and then proceed to consider some specific examples.

6.2 CONSTRAINTS IMPOSED BY SPIN PHYSICS

One obvious constraint is that the sample container should not be metallic, because radio-frequency radiation does not easily penetrate metal. The conveyor and all components therefore need be made of nonferrous materials. The first step in on-line NMR is to polarize the sample in a constant magnetic field. Polarization involves the relaxation of longitudinal magnetization from zero (or more correctly, the small equilibrium value in the earth's magnetic field, which corresponds to a proton resonance frequency of about 2 kHz) to the equilibrium value determined by the Boltzmann factor $\exp(-\gamma h B_0/k_B T)$ at temperature T in a field B_0. Complete polarization requires a time of least $5T_1$, which for pure water with a T_1 value of about 2 s requires waiting 10 s in the polarizing magnetic field. This is usually too long if on-line measurements on a fast-moving conveyor are being considered, because the polarizing magnet would need to have a length of $5T_1 v$, where v is the conveyor velocity (see Figure 6.1). There are several ways around this difficulty. The signal-to-noise ratio may be sufficient to permit less than 100% polarization; for example, 95% polarization is obtained after only $3T_1$. Alternatively, two magnets could be used, a high-field one for polarization for a short time, and a lower-field magnet for on-line detection. Fifty percent polarization in the high-field magnet may then be, for example, 90% polarization at the lower field. The other option is to redesign the conveyor system so that there is a reservoir of samples waiting in the polarizing field before entry onto the conveyor.

Once the samples are polarized, the next step is signal excitation. Here spin physics dictates that the sample has to pass through both the excitation coil and the static magnetic field simultaneously and that the static and excitation fields must be

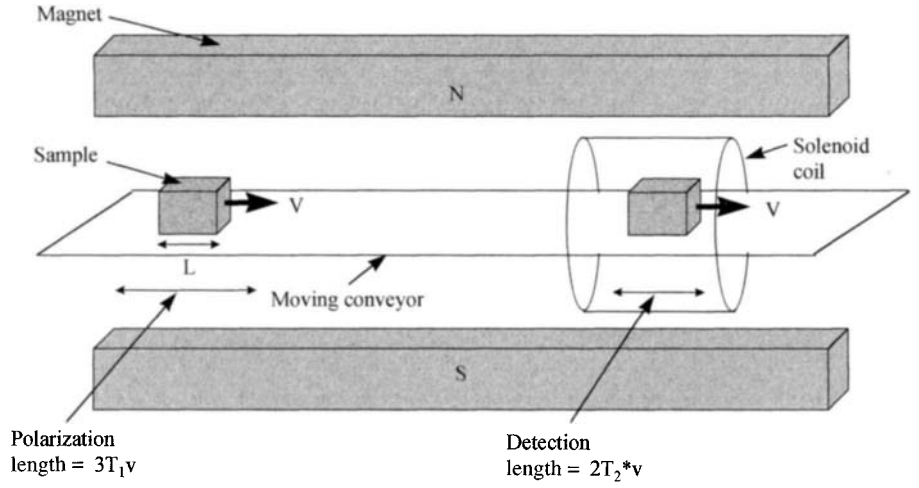

Figure 6.1. Schematic of a conventional NMR apparatus with a solenoid coil adapted for use around a moving conveyor. The sample is of length L and moves continuously with velocity v. The lengths of the polarization and measurement regions are indicated.

in orthogonal directions. This means, unfortunately, that a solenoid excitation coil located inside a solenoid electromagnet generating an axial magnetic field is not a possible configuration because both fields are parallel and along the axis. Instead, a solenoid or birdcage coil constructed around a cylinder would need to be used for the signal excitation in this geometry because the excitation field is then transverse to the static field (see Figure 6.1). Subject to this orthogonality constraint, many other designs can be considered based around superconducting magnets, electromagnets (sometimes called resistive magnets), permanent magnets, single-sided magnets, and surface coils. Permanent magnets are the cheapest, but they are heavy and are low-field. A saturated iron-core permanent magnet has a maximum field strength of about 0.25 T, corresponding to a proton resonance frequency of about 10 MHz, which may not give a high enough signal-to-noise ratio value for some applications. Electromagnets can generate higher fields but can have high power consumption and require cooling. Superconducting magnets give the highest fields, and therefore best signal-to-noise ratio with no power consumption but are very expensive and require regular filling with liquid nitrogen and helium. Low-cost, high-temperature superconductors would be the ideal for on-line applications, but despite considerable advances in high-temperature superconductivity, commercial magnets remain a future dream. The size of the region of field homogeneity is another physical constraint (see Figure 6.1). If the first part of an FID is to be measured in a time period of, say, $2T_2^*$ and the sample is of size L and moves with velocity v, the region of field homogeneity needs to be at least $2T_2^*v + L$.

The radio-frequency power needed to excite the resonance is another major consideration. Large samples will require large magnets and large excitation coils, and this, in turn, increases the amount of power needed to generate the excitation pulses. To excite the entire sample it is better to excite the resonance with a short, high-power radio-frequency pulse with a wide excitation bandwidth than one with low power applied for a longer period, especially if the sample has a low T_2^* value. This can be achieved either by using expensive, high-power RF amplifiers and/or by using highly tuned excitation coils (i.e., coils with a high quality factor or Q value). Detection of the signal also requires a rapid receiver recovery after the excitation pulse (i.e., a short ring-down time), and this generally requires a lower Q value or active damping technology. Alternatively, separate receive and transmit coils could be used. Rapid data collection and analysis are needed for real-time monitoring, and in some cases this could become the rate-limiting step.

One other consideration in the design of on-line instruments is the need to minimize acoustic ring-down. A conductor carrying an RF current in a static magnetic field is subject to an oscillating force at the radio frequency. These forces vibrate the conductors and generate ultrasonic waves within them. When the RF excitation pulse is turned off in the transmitter, the ultrasonic waves reverberate, and because the vibrations occur in a static field, a voltage is developed across it and is detected in the receiver. Other vibrating conductors will radiate RF fields that can be sensed by the detector coil. These effects give rise to spurious ring-down effects which dominate the dead time and require special techniques to minimize them.

The standard design of NMR spectrometers, whereby the sample is placed inside a magnet and RF coil, is based on spectrometers built in the 1940s. However, this standard configuration is not necessarily the best for on-line studies, especially with large samples. For many applications an inside-out design is more appropriate, in which excitation and detection does not have to occur inside the magnet and detector coil. One possible design, presented by Kleinberg et al. (191), has found application in the oil industry. Figure 6.2 shows a schematic of the basic features and how excitation and detection occur in the outer region. Details of systems design are outside the scope of this book, but the reader wishing to pursue these aspects may find the articles by McDonald (97), Bjokstam and Listerud (102), and Fukushima and Roeder (103) helpful.

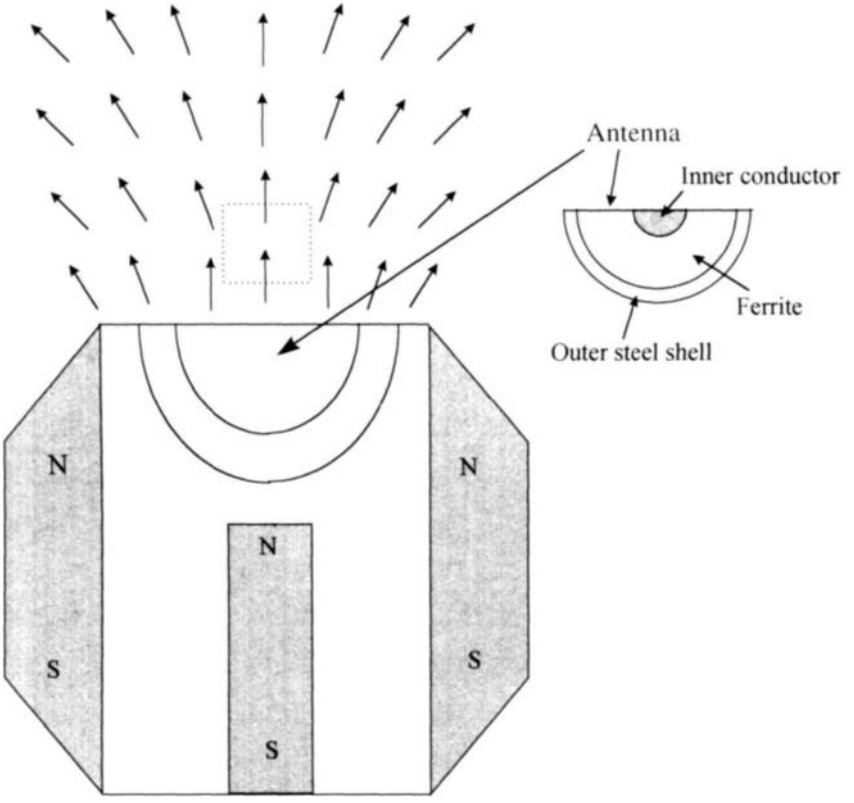

Figure 6.2. Schematic of an inside-out NMR spectrometer suitable for use with a moving conveyor belt. The three magnets project the field indicated by the small arrows, and the antenna, shown in amplified cross section, provides radio-frequency radiation orthogonal to the magnetic field in the square box indicated. (From Ref. 191.)

6.3 NONSPATIALLY RESOLVED ON-LINE NMR

This subject has been considered in a useful review by McDonald (97). One of the first nonspatially resolved, on-line NMR instruments was developed in the 1960s by Nelson et al. (192) and is now used for monitoring the composition of a liquid steam using the chemical shift spectrum. The spectrum was recorded every 6 s using a continuous-wave instrument because pulsed NMR was not available at that time. Fluid was diverted through the spectrometer in a side-line arrangement and a small reservoir within the magnet was used for polarization. The system was locked onto one line in the spectrum, and changes in a second spectral line were related to compositional changes. A similar side-line method has been reported by Tellier and co-workers (193) and used to monitor the fat content in flowing fine meat pastes. More recently, a French research group (104) has been developing a side-line nonspatially resolved NMR method for monitoring fat content based on the acquisition of the FID. The spectrum obtained by Fourier transformation and resolution enhancement resolves the fat and water peaks and, with careful calibration, permits the amount of fat to be determined. This measurement is needed for both regulatory and quality control purposes.

Nichols and De Los Santos (100) have described an on-line system that sits below the production line and samples from it by lowering a mechanical piston so that the sample falls into a cylindrical NMR sample chamber. After measurement, the sample is returned to the production line by raising the piston. A schematic of the apparatus is shown in Figure 6.3. The system is well suited for finer, dry products

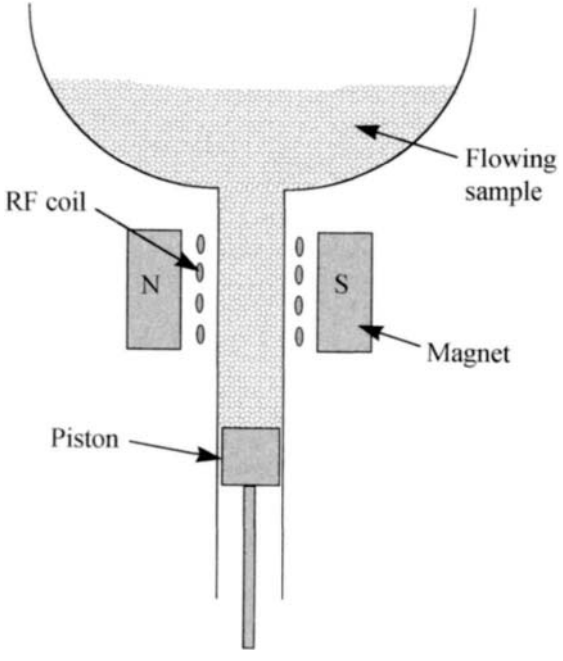

Figure 6.3. Piston off-line sampling arrangement patented by Nichols and DeSantos and adapted from Ref. 100.

such as powders (e.g., in gluten drying) but could, in principle, be used with fluids. Chen et al. (99) succeeded in measuring an on-line FID of whole avocado traveling on a conveyor belt using a surface coil. They showed that the oil/water spectral peak ratio was unaffected by velocities up to 250 mm/s. A portable nonimaging spectrometer for quality assurance has also been described by Snoddy (101).

6.4 SPATIALLY RESOLVED ON-LINE NMR

Earlier we mentioned how internal defects in fruits and vegetables, such as bruises, disease, stages of ripeness, and worm damage, can, at least in principle, be detected noninvasively in MRI from changes in some NMR parameter, such as signal intensities, relaxation times, or diffusion coefficient. A more detailed account of plant imaging on the macroscopic and microscopic scales is given in Chapters 7 and 9. In this section we explore the possibilities for building on-line MRI sensors of fruit or vegetable quality suitable for use with a moving conveyor belt in an industrial factory.

Pitting fruit such as cherries, plums, and olives is an important industrial process, usually performed by holding the fruit and pushing the pit (or stone) out of the fruit with a mechanical plunger. It is, of course, important that any samples still containing pits are detected with as high an efficiency as possible. An on-line imaging system for detecting pits in cherries has been described by Zion and co-workers (194). It involves taking one-dimensional projection images using a spin-echo imaging sequence. A schematic of the apparatus is shown in Figure 6.4. Cherries are positioned in the grove of a moving belt and a sagittal slice is taken through the cherries, followed by transverse projections through the slice. The presence of a pit is shown by an additional central peak in the projection. Of course, the echo time has to be less than the T_2 value of the pit if it is to be detected. Unfortunately, this simple concept is complicated by additional peaks in the projection arising from

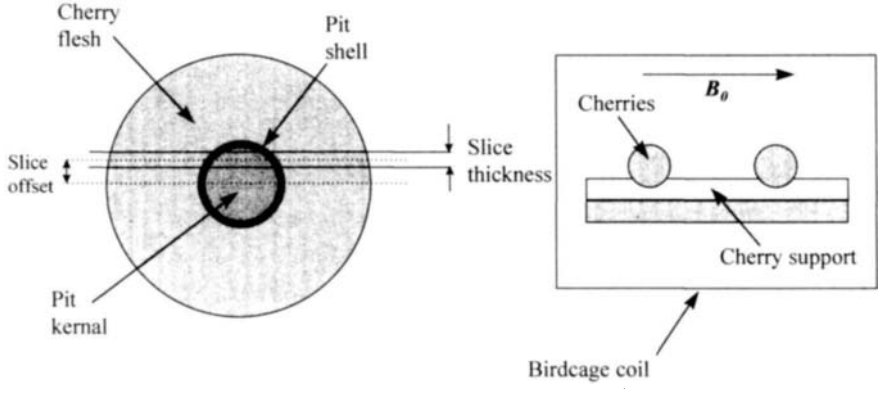

Figure 6.4. Schematic of the birdcage coil with cherries. The inset shows an idealized view of a cherry, indicating slice offsets. (From Ref. 98.)

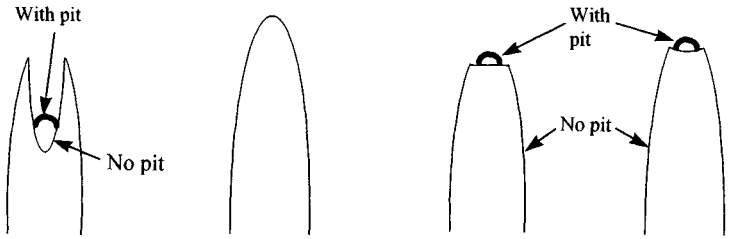

Figure 6.5. Schematic projections for a pitted and depitted cherry. The extra intensity arising when there is a pit is indicated by the thick line. Profiles correspond to the indicated values of slice thickness and slice offset for a relative cherry diameter of 2.0, pit diameter of 0.8, and pit shell thickness of 0.1 (see Figure 6.4 for a definition). (From Ref. 98.)

noise, shape distortions, and missing flesh parts, so it is not always straightforward to distinguish between a pitted and an unpitted cherry. This difficulty was circumvented by using a more sophisticated classification based on simulations of projection lineshapes. Figure 6.5 shows the theoretical projections for a pitted and an unpitted cherry based on an idealized, spherical cherry. Figure 6.6 shows experimental projections from three pitted and three unpitted cherries. It can be seen that two of the cherries without pits still gave a three-peak projection, but the relative heights of the middle and outside peaks is lower than that for a genuine cherry containing a pit. For this reason a criterion for deciding between the pitted or unpitted states was based on calculating the intensity ratio of the middle peak(s) to the outer peak(s).

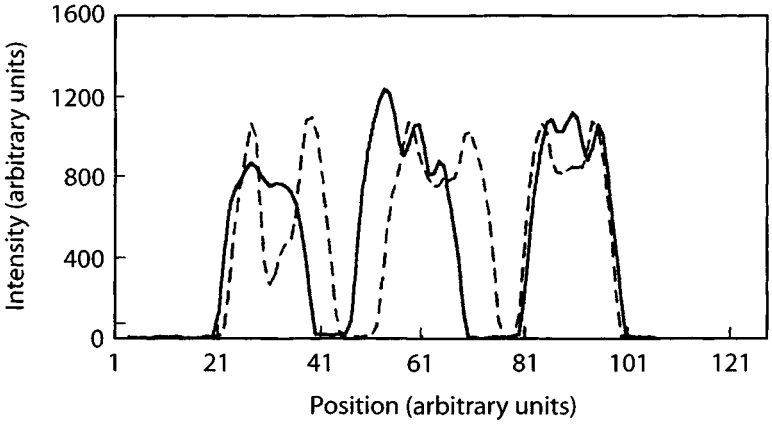

Figure 6.6. Experimental image projections for a set of three stationary pitted and depitted cherries, acquired with a slice thickness of 2 mm. (From Ref. 98.)

This more sophisticated criterion succeeded in correctly distinguishing 88% of cherries with pits. At present this success rate is only moderate, and it relies on the use of expensive superconducting magnets equipped with slice selection facilities. Moreover, these feasibility studies were undertaken on static samples placed inside the magnet. Motion of the cherries through the magnet would be expected to degrade the quality of the projections further by introducing additional dephasing caused by movement through field inhomogeneities. This study therefore highlights some of the practical difficulties in implementing on-line detection methods. Nevertheless, a number of research groups are now actively developing on-line MRI, and rapid progress in this exciting field is expected in the near future.

7

WHOLE-PLANT FUNCTIONAL IMAGING

7.1 INTRODUCTION

Optimizing the production of food crops in the field requires detailed knowledge of the effects of environmental factors on plant development. These environmental factors include osmotic stress caused by drought, as well as nutritional requirements and the effects of herbicides, pollutants, and disease. By permitting noninvasive, in vivo monitoring of the whole plant as it develops under realistic environmental conditions, functional imaging has become a powerful tool in the plant physiologists' armory. In this chapter some of the recent developments in functional whole-plant imaging are summarized.

There are various experimental protocols for imaging a living plant under realistic environmental conditions. One possibility is to bring the spectrometer to the plant growing in the field. This has been done using portable, low-field (e.g., 10 MHz) permanent-magnet spectrometers in which the magnet poles are split so they can be placed around the plant stem or leaf system (62). Such portable spectrometers are excellent for some applications, such as flow imaging, but are obviously unsuitable for applications such as chemical shift imaging at high resolution, where high, well-shimmed fields are needed. The other approach is to bring the living plant to the spectrometer, but here the problem is to maintain the root system bathed in nutrient and the whole plant in an environment of controlled humidity, temperature, and luminescence intensity. Figure 7.1 shows a schematic of how this can be done for stem imaging, where the root and leaf system are outside the magnet. Clearly, each crop type presents a new challenge in instrument design, but with smaller seedlings it is possible to grow them inside adapted NMR tubes. A third possibility, which has yet to be fully exploited,

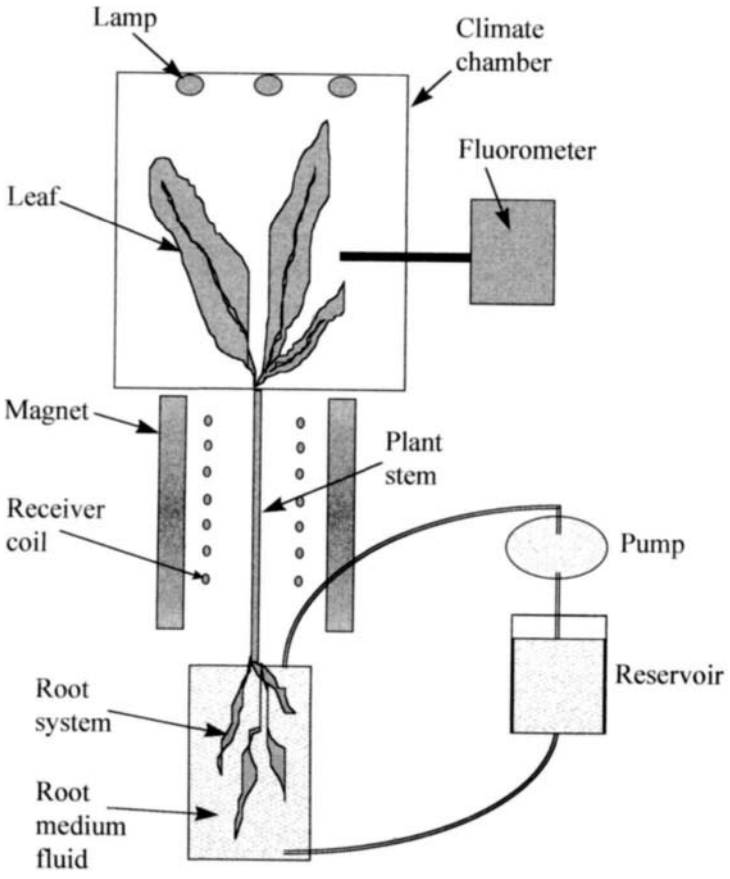

Figure 7.1. Schematic of a probe arrangement suitable for whole-plant functional imaging. The climate box permits control of humidity, temperature, and light intensity. The root system is supplied with circulating nutrients (as illustrated), or the root system is kept in soil.

is the use of surface coils attached to various parts of the plant, and the recent commercial development of superconducting coils (65) offers several exciting possibilities for doing this.

In our discussion of whole-plant functional imaging, we try to follow the physiology of plant development. We begin with the development and physiology of the root system, then consider the transport of water and nutrients through the plant, which leads to a consideration of water balance and the responses of the plant to environmental stresses, such as water depletion, osmotic stress, exposure to heavy metals, oxygen deprivation, and the effects of variable luminescence. Plant nutrition is the final topic of discussion. We begin with the root system.

7.2 FUNCTIONAL ROOT IMAGING

By placing a vessel containing soil and roots inside the spectrometer magnet, the development of a plant root system can be followed, noninvasively, in real time (59,60,105). In this way the relationship between the root development and water depletion zones set up in the soil as the root extracts water and nutrients can be studied quantitatively. The noninvasive aspect is mandatory because any disturbance of the soil by removal of a root can change the soil porosity, the spatial distribution of water and nutrient, and the distribution of microbiological populations within it. A recent application of this underground functional MRI has been to follow the development of pine roots using three-dimensional T_1-weighted images to distinguish the soil and root (105). The water depletion zones around the tap root, lateral roots, and fine roots were quantified for water content and volume, and the effects on water uptake of symbiotic relationships such as infection with mycorrhizal fungus has been investigated. The time dependence of the root network volume and surface area was determined using seeding algorithms from three-dimensional images. Surprisingly little is known about the factors controlling the spatial distribution and development of the root network, and this approach will help clarify them. The potential for investigating root viability using NMR microimaging and chemical shift imaging remains to be explored. A very similar approach could be used to image the development and physiology of underground crops such as carrots and potatoes. This is an obvious, if unexplored, area and is essential if we are to understand and optimize the effect of irrigation patterns and soil types on the growth of carrots, potatoes, and other tubers.

7.3 TRANSPORT IN INTACT PLANTS

The function of the root system is, of course, to extract water and nutrients from the soil. The next aspect to be considered is therefore the transport of water and nutrients through the stem in the xylem and phloem sieve tubes that comprise the vascular bundles. The flux of nutrient through a plant stem (in mmol/h) equals the product of the flow rate (in μL/h) and the nutrient concentration (in mmol/μL). The flow rate can be measured with flow microimaging; while the nutrient concentration is obtained by chemical shift microimaging. A good example of this combined flow and shift imaging approach is the recent study of nutrient transport in a 6-day-old castor bean seedling (195). The seedlings were grown in specially designed glass tubes that fitted inside the imaging probe head and permitted nutrients to be supplied to the roots. The velocity distribution through the vascular bundles in the stem was observed with q-space phase encoding at an in-plane resolution of 47 μm. Flow in opposite directions corresponding to phloem and xylem counterflow in the vascular bundles was also resolved. The sucrose concentration was determined with an in-plane resolution of 47 μm using chemical shift imaging. The resulting sucrose flux analysis strongly supported the hypothesis of an osmotically driven translocation process within the seedling. At the same time a correlation peak imag-

ing sequence based on combining the conventional two-dimensional COSY spectra with imaging was used to map the spatial distribution of other metabolites, including glucose, glutamine/glutamate, lysine, arginine, and valine. The results revealed surprising spatial compartmentation of these metabolites within the tissue. Investigations on the dynamic changes in nutrient fluxes as the plant was subjected to various environmental conditions and stresses, such as osmotic stress, and varying luminescence have also been reported.

The effect of time-dependent illumination conditions on water transport and the flux of sugar in the stem of a 6- to 8-week-old tobacco plant has been monitored using a combination of phase-encoded flow and chemical shift imaging (63). The sugar concentration maps revealed the highest concentrations in the outer pith region, probably in the phloem tissue. An in vivo MRI study of the effect of osmotic stress induced by replacing normal root medium by well-aerated PEG-6000 medium on 4-week-old cultured maize and pearl millet plants has been reported by Meulenkamp et al. (61). These two plants were chosen because they show very different drought tolerances. The time course of water uptake was measured over a 30-h period by weighing the root medium vessel outside the magnet, and photosynthetic activity was measured on the second top leaf in a fixed position using a modulated fluorometer under high (100 lux) and low (10 lux) light conditions. Quantitative proton spin density and T_2 maps of a 2.5-mm slice across the stem were acquired at regular time intervals. The Millet showed a strong correlation between the proton and T_2 maps, water uptake, and osmotic stress, revealing subtle differences between different types of tissue in the stem. This is no doubt a result of adaptation by elastic shrinking under osmotic stress in combination with changes in membrane permeability, leading to a slower, gradual loss of water from all parts of the plant, delaying necrosis of the leaves and irrecoverable loss of photosynthetic ability, which are the results of severe osmotic stress. In contrast, the NMR parameter maps in maize hardly changed during stress periods.

An in vivo functional MRI study of the dynamic effects of nutritional stress has been reported for sucrose starvation in intact seedlings of *Ricinus communis* when the supply tissue, the endosperm, was removed (64). Sugar concentration maps were measured using chemical shift microscopy in the phoem region of the cell division zone 1 cm behind the cotyledons. First the intact seedling was imaged, then the endosperm removed and replaced with a 100-mmol sucrose solution. Finally, the dynamic effect of replacing the sucrose solution by a simple buffer solution was monitored. It was found that after an initial decrease in stem sucrose concentration, it increased and finally stabilized at about 100 mmol once again. This is direct evidence that the plant is activating the starch degradation pathway to maintain a constant flow of sucrose.

Of course, one reason for the flow of water and nutrients through the plant is to supply the developing fruit and grain. The microscopic flow of water within a ripening wheat grain was imaged in a classic study by Jenner et al. (66). Wheat plants were raised in small pots under controlled environment conditions and the ears selected about 14 days after anthesis, when they were approximately halfway through the grain-filling stage. The pot was inverted and a wheat ear inserted into

the spectrometer probe. Illumination at about 100 W/m was provided by a lamp standing 2.3 m from the plant. Water proton density, velocity, and diffusion maps were then obtained within an attached grain using combined velocity and q-space microscopy. These were compared with the results for a detached grain. The analysis of flow patterns within the grain suggested that it was associated with the unloading and/or distribution of assimilates in the vicinity of the furrow of the grain, and this involved extensive recirculation of water throughout the grain. The ability to observe flow and diffusion within a single grain, in vivo, is remarkable, but much remains to be done in exploiting this technique for understanding the relationship between intragrain flow, grain development, and environmental stresses imposed on the plant. It is disappointing that little appears to have been done in imaging intragrain flow in vivo since the original work was reported in 1988.

7.4 FUNCTIONAL BRAIN IMAGING AND CONSUMER SCIENCE

The applications described above illustrate how functional imaging can assist in optimizing the production of food crops in the field. It is worth noting, in passing, that functional imaging also has a great deal to say about the other end of the food chain, namely, the food consumption step. This is every bit as important, because there is obviously no point in optimizing the production of a particular crop in the field, or the subsequent processing stages, if the end product has a terrible taste. It is therefore important to understand human physiological responses during food consumption, and functional brain imaging can, potentially, reveal this in exquisite detail.

The application of functional imaging in real-time monitoring of brain activity is now well documented in clinical imaging (317). The usual contrast mechanism in functional brain imaging involves BOLD, an acronym for *blood oxygenation level –dependent effects*. When a region of the brain, such as the visual cortex, is stimulated, there is a local increase in oxygen uptake by hemoglobin, resulting in a decrease in local deoxyhemoglobin concentration. Now the Fe^{2+}-containing heme group in deoxyhemoglobin is paramagnetic, unlike the oxygenated state, which is diamagnetic. A reduced concentration of deoyhemoglobin is therefore associated with a reduction in the local concentration of paramagnetic centers, and this, in turn, results in a lengthening of the apparent transverse relaxation time, T_2^*. The net result is an increase in signal intensity in T_2^*-weighted images in active regions of the brain. The exact mechanism by which a decrease in paramagnetic concentration gives a longer T_2^* is debatable. One mechanism thought to be at work involves a reduction in magnetic susceptibility differences between the oxygenated blood and the surrounding tissue. This reduces the local susceptibility-generated magnetic field gradients and therefore the diffusive attenuation of the signal by diffusion processes. For this reason functional imaging is usually based on fast pulse sequences that are sensitive to dephasing by local field inhomogeneities, such as gradient-recalled echo planar imaging, where images can be obtained in hundreds

of milliseconds (see Chapter 1). Fast imaging methods are essential to minimize artifacts such as head movement, especially in experiments where images are compared under conditions of stimulation and no stimulation. For this reason considerable effort is required to reregister the brain images and obtain statistically significant signal intensity differences. Despite the nontrivial nature of functional brain imaging, it has already been employed successfully to observe the stimulation of the visual cortex, the motor cortex, the auditory cortex, and in studies of brain activity in epilepsy and during higher cognitive tasks. The two areas that, to date, are missing from this list are those associated with brain stimulation by taste and smell. Nevertheless, the author is aware of at least two research groups actively researching these topics, so results should soon be forthcoming.

If functional brain imaging of taste and smell responses is successful, it raises the exciting prospect in consumer science of being able to explore the relationship between the actual magnitude of the concentration of taste or aroma compound(s) in the mouth, the physiological brain response, and the perceived response. This could lead to "designer" foods, tailored to optimize taste and aroma sensations of individual consumers. Whether this futuristic scenario is desirable is another issue. Nevertheless, a true understanding of the physiological responses of both plants and the human brain ultimately requires an understanding not just of gross changes on the macroscopic distance scale but also of the underlying microscopic changes at the cellular and subcellular scales. These distance scales are explored in Part Two.

8

UNCONVENTIONAL MRI TECHNIQUES

8.1 INTRODUCTION

The use of the adjective *unconventional* in the title to this chapter will, no doubt, raise the ire of regular practitioners of these MRI techniques. The word is used in the loosest sense, however, and in future years what is now unconventional may well become commonplace. Although there are as yet few reported applications of these techniques in food science, this situation will, no doubt, soon be rectified as their various advantages are realized. It is felt some mention of these alternative imaging techniques, however brief, is therefore warranted.

8.2 ROTATING-FRAME IMAGING

Conventional laboratory-frame, *k*-space imaging spatially encodes the spin phase with applied linear field gradients **G**, defined as $\mathbf{G} = \nabla B$, such that the external magnetic field $\mathbf{B}(\mathbf{r})$ is $\mathbf{B}_0 + \mathbf{G} \cdot \mathbf{r}$. During the readout step in a gradient, the resonance frequency therefore becomes spatially dependent and given as $\omega(\mathbf{r}) = \gamma\mathbf{B}(\mathbf{r}) = \gamma(\mathbf{B}_0 + \mathbf{G} \cdot \mathbf{r})$. In analogy, rotating-frame imaging spatially encodes spin phase with linear gradients in the radio-frequency amplitude $\mathbf{G}_1$, defined as $\mathbf{G}_1 = \nabla B_1$, such that the applied radio-frequency field $\mathbf{B}_1(\mathbf{r})$ is $\mathbf{B}_1^0 + \mathbf{G}_1 \cdot \mathbf{r}$ and the nutation frequency in the rotating frame becomes spatially encoded such that $\omega_1(\mathbf{r}) = \gamma\mathbf{B}_1(\mathbf{r}) = \gamma(\mathbf{B}_1^0 + \mathbf{G}_1 \cdot \mathbf{r})$.

Figure 8.1 shows a simple pulse sequence that can be used for rotating-frame imaging. In the absence of an applied radio-frequency gradient ($\mathbf{G}_1 = 0$) the sequence reduces to that used to measure the rotating-frame relaxation times $T_{1\rho}$, so

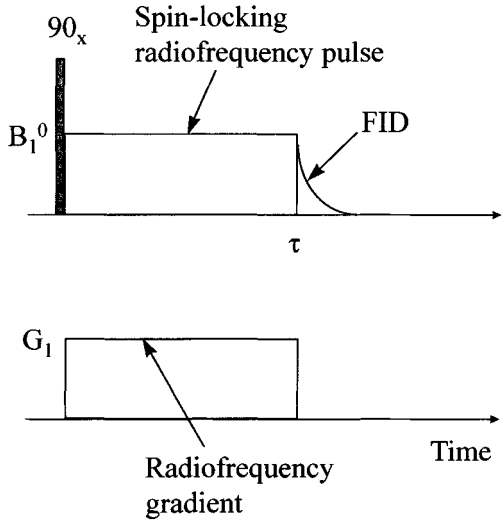

Figure 8.1. Simple pulse sequence for rotating-frame imaging.

we first consider this conventional nonspatially resolved $T_{1\rho}$ measurement before introducing the imaging aspects. In a $T_{1\rho}$ measurement, an initial hard on-resonance 90°_{x} pulse rotates the equilibrium magnetization along the y-axis in the frame rotating at the Larmor frequency. This magnetization is then spin-locked for a time τ by irradiation with a radio-frequency field of amplitude B_1^0 shifted in phase by 90° from the initial excitation pulse, so that the effective field experienced by the on-resonance spins is actually B_1^0 and not the main magnetic field B_0 and is parallel to the magnetization. During the time interval τ the spin-locked magnetization decays exponentially with a time constant $T_{1\rho}(\omega_1)$, where ω_1 is γB_1^0. After a time τ the radio-frequency field is turned off and the transverse magnetization, freed from the spin-locking pulse, now gives the usual FID. $T_{1\rho}(\omega_1)$ is obtained by recording the exponential decay in the amplitude of the FID as a function of increasing τ.

It is worth noting in passing that as the amplitude of the radio-frequency spin-locking pulse increases and ω_1 approaches the main resonance frequency ω_0, $T_{1\rho}(\omega_1)$ will asymptotically approach the value of the longitudinal relaxation time $T_1(\omega_0)$. In the opposite limit of very weak B_1^0 amplitudes, $T_{1\rho}(\omega_1)$ will approach the transverse relaxation time T_2. In other words, $T_{1\rho}(\omega_0)$ is T_1 and $T_{1\rho}(\omega_1 = 0)$ is T_2. The ω_1 frequency dispersion of $T_{1\rho}$ therefore lies between the limits of T_1 and T_2 and contains valuable dynamic information on the ω_1 frequency scale. This aspect is considered in greater detail in Chapter 12.

The experiment described above assumes that the magnetization is spin-locked along the y-axis, at 90° to the main spectrometer field B_0. However, this does not

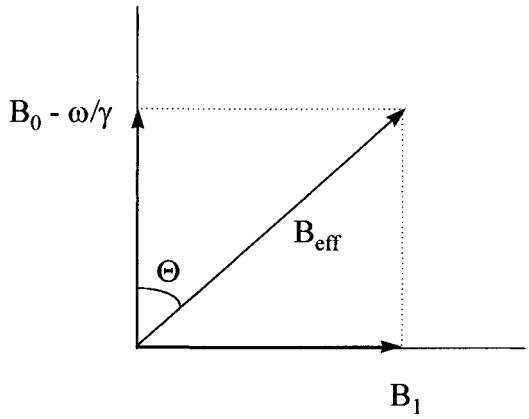

Figure 8.2. Relationship between the resonance frequency offset ω_z, the radio-frequency field strength ω_1, and the spin-lock angle θ in the rotating frame.

need to be the case, and the magnetization in the rotating frame can be spin-locked at any angle θ to the B_0 direction by varying the resonance frequency offset ω_z, defined as $\omega - \omega_0$, where ω is the frequency of the radio-frequency radiation and ω_0 is the resonance frequency γB_0. Figure 8.2 shows that $\tan\theta$ is simply (ω_1/ω_z). More generally, we therefore need to define a rotating-frame relaxation time, $T_{1\rho}(\omega_0,\omega_1,\omega_z)$, that depends on three frequencies. A discussion of the dynamic aspects probed by these frequency dispersions is deferred to Chapter 12. Having considered the conventional nonspatially resolved aspects of the rotating-frame spin-locking experiment, we are now in a position to discuss rotating-frame imaging.

In the simplest form of rotating-frame imaging the radio frequency is set on-resonance so that $\omega_z = 0$ and the magnetization is spin-locked at $\theta = 90°$. An additional radio-frequency gradient, $\mathbf{G}_1(\mathbf{r})$ is then superposed during the spin-locking interval, τ, so that $\mathbf{B}_1^0$ becomes $\mathbf{B}_1(\mathbf{r}) = \mathbf{B}_1^0 + \mathbf{G}_1 \cdot \mathbf{r}$. This has the effect of imposing a spatial variation in the effective magnetic field in the rotating frame so that the nutation frequency of the spins in the rotating frame, $\omega_1(\mathbf{r})$, becomes a function of position. To extract the positional information the single-point imaging strategy discussed in Section 5.4 is used, according to which the amplitude of an initial point on the FID is recorded as a function of increasing $\mathbf{G}_1$(at fixed τ) or of increasing τ (at fixed $\mathbf{G}_1$). The image is then extracted from the pseudo-FID, $S(\mathbf{k})$, obtained from the single-point amplitudes, by the usual Fourier transform relationship

$$S(\mathbf{k}) = \int d\mathbf{r}\, \rho(\mathbf{r}) \exp(i\mathbf{k} \cdot \mathbf{r}) \tag{8.1}$$

Here the wavevector $\mathbf{k}$ is $\gamma\mathbf{G}_1\tau$. To keep the attenuation by rotating-frame relaxation constant, it is obviously better to fix τ and vary $\mathbf{G}_1$ between acquisitions rather than varying τ at fixed $\mathbf{G}_1$, although either strategy will generate an image.

Because B_1 fields are usually much weaker than the main spectrometer field B_0, rotating-frame imaging is not subject to the susceptibility-generated imaging artifacts that can plague conventional B_0 imaging. This can be a major advantage when imaging heterogeneous foods. It is also free of eddy-current artifacts arising from rapid switching of strong applied laboratory-frame field gradients. Another advantage is that the FID is acquired in the absence of field gradients, so it retains full spectroscopic information. Fourier transformation of the FID during the imaging experiment therefore permits rotating-frame chemical shift imaging. Strong radio-frequency field gradients can be created using fringe fields of surface coils, so the technique is especially valuable for depth profiling of surface layers. This could be particularly important in monitoring changes in food surfaces during processes such as drying and cooking.

Rotating-frame imaging does, however, suffer from a number of disadvantages. The radio-frequency fringe fields of surface coils are linear only over a small sample volume, so that images can be severely distorted. To some extent these distortions can be corrected during the image-processing stage, but it nevertheless complicates image interpretation. Two- or three-dimensional imaging is also difficult to implement with surface coils. Back-projection methods must therefore be used, whereby the image is reconstructed from projections taken as the sample is rotated relative to the surface coil or, conversely, the coil is rotated around the sample. This is satisfactory as long as the sample does not experience rapid (processing) changes. If it does, a fast rotating-frame imaging sequence must be used. One such sequence involves breaking up the continuous $\mathbf{G}(\mathbf{r})$-radio-frequency spin-locking pulse of duration τ into a series of n much shorter spin-locking gradient pulses of amplitude $\mathbf{G}(\mathbf{r})$ and duration τ/n, each separated by $n - 1$ very short time periods δ. A single point on the FID is acquired during each δ time period. In this way the space-encoded FID, $S(\mathbf{k})$, is acquired in a single multiphase acquisition step of duration $\tau + (n - 1)\delta$.

Contrast in a rotating-frame imaging experiment also differs from conventional (i.e., nonrotating frame) imaging. The imposition of a B_0 gradient in conventional imaging creates a spatial variation in resonance frequency ω_0, so that in theory, because T_1 and T_2 can depend on ω_0 (see Chapter 12), the longitudinal and transverse relaxation rates could also vary spatially, even in a perfectly homogeneous sample. In practice, the dependence of T_1 and T_2 on ω_0 is too slight to be detected in most imaging experiments. On the other hand, the imposition of a B_1 gradient in rotating-frame imaging creates a spatial variation in ω_1, and in this case, the dependence of $T_{1\rho}$ on ω_1 cannot necessarily be neglected. For example, Figure 12.17 shows that the $T_{1\rho}(\omega_1)$ dispersion, even for a dilute glucose solution, can be quite considerable and could give spatially varying relaxation contrast even in a spatially homogeneous sample. This suggests that the frequency dispersion of the rotating-frame relaxation time could be mapped in the spatial dimension in an imaging experiment. This idea has been exploited by Kimmich and co-workers in the SLOAFI technique, which is an acronym for *spin-lock adiabatic field-cycling imaging* (320). The pulse sequence for this elegant experiment is shown in Figure 8.3. In addition to the conventional $T_{1\rho}$ sequence in Figure 8.1, there is now an imposed B_0 field gradient G which is switched

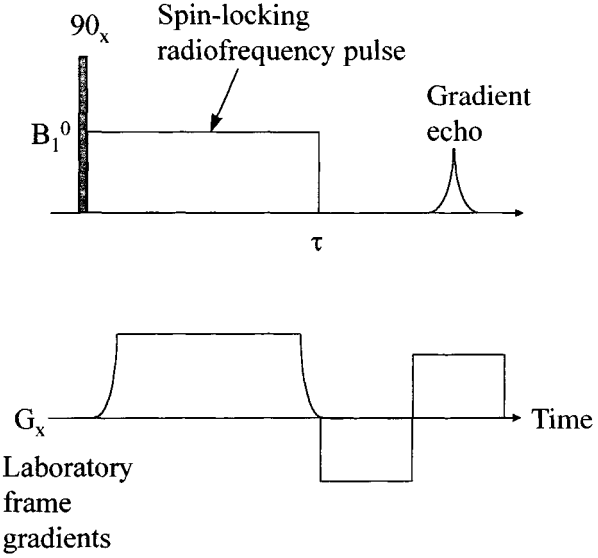

Figure 8.3. SLOAFI pulse sequence.

on and off adiabatically (i.e., without inducing spin transitions, so that the magnetization follows the effective field direction). The G-gradient means that the resonance offset frequency $\omega_z(r)$ and hence the spin-locking angle $\theta(r)$ vary spatially. Because $T_{1\rho}$ also depends on $\omega_z(r)$ [or equivalently, $\theta(r)$], the signal will be attenuated to different extents at different positions. The spatial variation can be imaged using the gradient-echo sequence shown in Figure 8.3 and the dependence of $T_{1\rho}$ on $\theta(r)$ can therefore be obtained by repeating the experiment with increasing spin-locking intervals t_{sl}. If the B_1 field strength is made too small compared to the resonance frequency offset created by the laboratory field gradient G, the experiment above will not succeed because only a narrow slice of spins will be spin locked in the field gradient. In this limit the sequence can be used as a means of slice selection, which is an aspect considered in Chapter 12 (see, e.g., Figure 12.16).

8.3 MULTINUCLEAR IMAGING

8.3.1 MRI with Other Nuclei

Most nuclei other than protons cannot be used for MRI either because of a low gyromagnetic ratio, a low natural abundance, or very short relaxation times. However, a few nuclei, such as ^{23}Na, have large gyromagnetic ratios and sufficiently high natural abundance to permit direct imaging. Other nuclei, such as ^{19}F and ^{2}H, can be introduced in the form of labeled compounds because they have high gyro-

magnetic ratios but negligible natural abundance. There are, as yet, few applications to foods, but a noteworthy exception is the use of ^{23}Na imaging to monitor the ingress of brine into meat during curing (300). Natural sodium concentrations in meat are too low to permit imaging, but the high concentrations typically used in brining meat (about 5 *M*) are ideal for imaging. The effect of various traditional processing operations, such as tumbling and cooking, on the brine distribution in ham was therefore investigated after immersion of the freshly excised meat in 5 *M* NaCl. It was shown that tumbling helps to even out the distribution of salt throughout the meat, but that even after 1 h of tumbling the distribution of Na^+ was not completely uniform. On the other hand, cooking created a spatially uniform salt distribution throughout the meat. Because of the plethora of organic compounds in foods, the most important nonproton nucleus is carbon, and special methods have been developed for imaging the spatial distribution of organic compounds.

8.3.2 Proton-Detected Localized ^{13}C Spectroscopy and Imaging

The natural abundance of ^{13}C nuclei is too low to permit direct imaging, but the signal from the ^{13}C nuclei can be detected indirectly through protons chemically bonded to them, and this can be done in a spatially selective way. One particularly successful approach involves polarization transfer via the Hartmann–Hahn condition in the double-rotating frame and is illustrated in Figure 8.4. The proton magnetization is first spin locked in the rotating frame with an on-resonance radiofrequency field of strength B_{1H}, and at the same time the carbon nuclei are

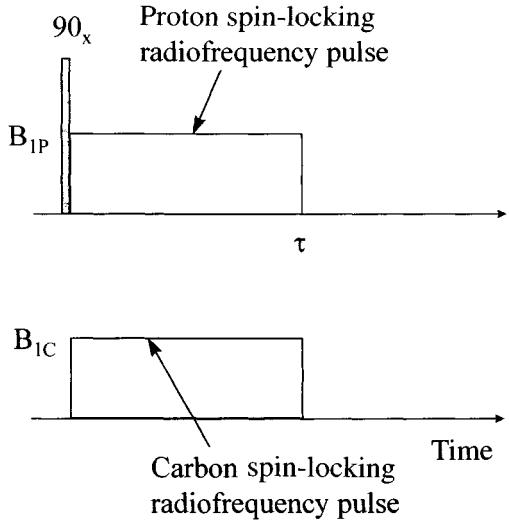

Figure 8.4. Pulse sequence for Hartmann–Hahn cross polarization.

irradiated in a double-resonance experiment. If the amplitude of the on-resonance carbon radio-frequency field B_{1C} is adjusted to fulfill the Hartmann–Hahn matching condition, $|\gamma_H| B_{1H} = |\gamma_C| B_{1c}$, energy-conserving (secular) flip-flop transitions between the proton and carbon spins can occur, transferring magnetization between the two pools. This cross-polarization process can be spatially localized by imposing external B_0 (or B_1) field gradients, because these create a spatial distribution of resonance frequencies, so that the Hartmann–Hahn matching condition will only be fulfilled at one spatial location. The pulse sequence in Figure 8.5, known as CYCLCROP (cyclic cross-polarization) shows how this can be used to produce localized carbon spectra (CYCLCROP-LOSY). Magnetization transfer from hydrogen to carbon is first achieved with the Hartmann–Hahn matching condition (Figure 8.4), with the difference that the transfer is spatial localized in the z-direction by imposing a field gradient G_z. The carbon magnetization is then stored as longitudinal magnetization with a 90°_{-x} pulse and all hydrogen magnetization destroyed with a comb of 90° pulses in combination with homospoil gradients. The carbon magnetization is then transferred back to the coupled hydrogens in a reverse polarization transfer in a spatially localized way by spin locking the carbon magnetization and irradiating the proton pool in a gradient G_y. The proton magnetization is then stored in the longitudinal direction with a 90°_{-x} pulse and all other magnetization removed with a spoiler gradient. A proton Hahn echo with a slice-selective

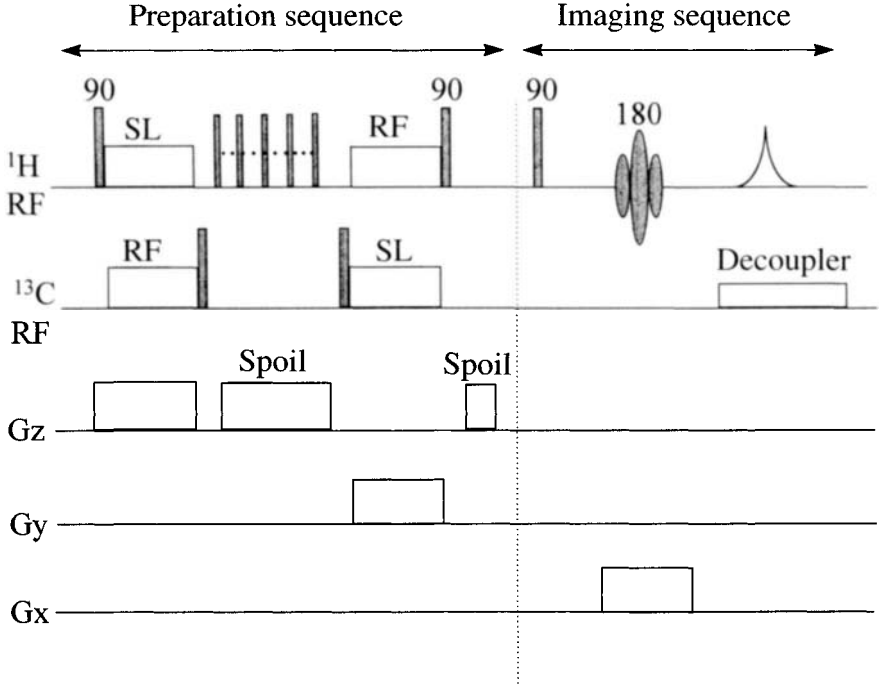

Figure 8.5. CYCLCROP–LOSY sequence for proton-detected ^{13}C localized spectroscopy.

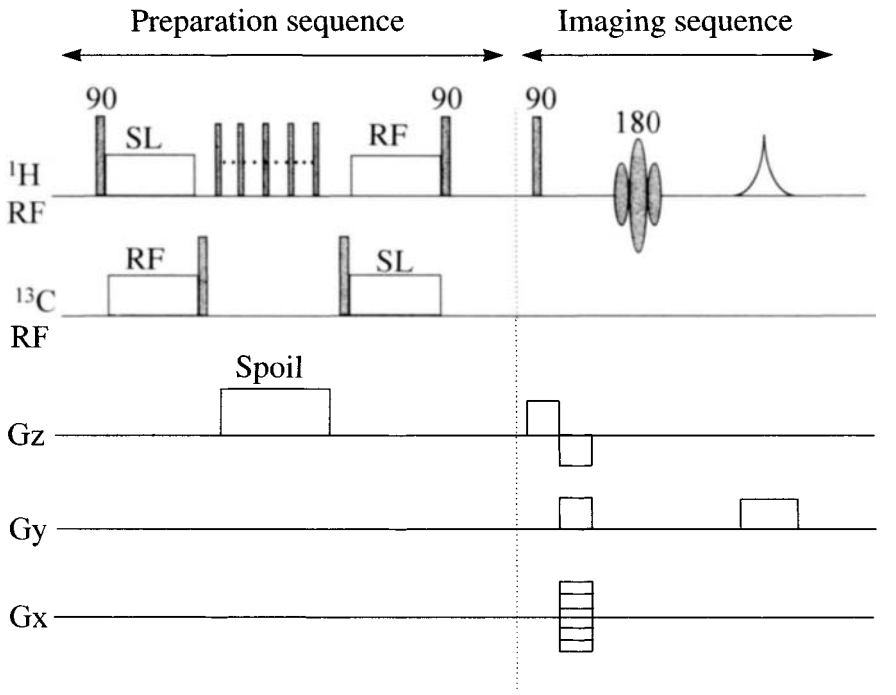

Figure 8.6. CYCLCROP-imaging sequence for proton-detected ^{13}C imaging.

180° pulse in a G_x gradient gives spatial localization in the x-direction. In this way, a spectrum of protons bonded to ^{13}C nuclei is obtained from a localized region within the sample.

This cyclic cross-polarization methodology can be generalized to three-dimensional proton-detected ^{13}C imaging using a procedure known as CYCLCROP imaging, shown in Figure 8.6 (323). The first, "preparation" part of the sequence prepares longitudinal magnetization only in those protons bonded directly to ^{13}C nuclei. This nonspatially resolved proton magnetization is then used to produce an image. In Figure 8.6 this is done with the three-dimensional spin-warp pulse sequence. The power of proton-detected ^{13}C imaging has yet to be exploited in food processing. One obvious application is to follow the spatial gradients of sugars and metabolites set up during processes such as air drying, rehydration, and cooking.

8.4 NMR FORCE MICROSCOPY

NMR force microscopy promises the highest spatial resolutions of all the NMR imaging techniques, so it is appropriate that we discuss it before turning to the microscopic distance scale in Part Two. The basic arrangement of the NMR force microscope as used by Rugar and co-workers (324,325) is illustrated in Figure 8.7.

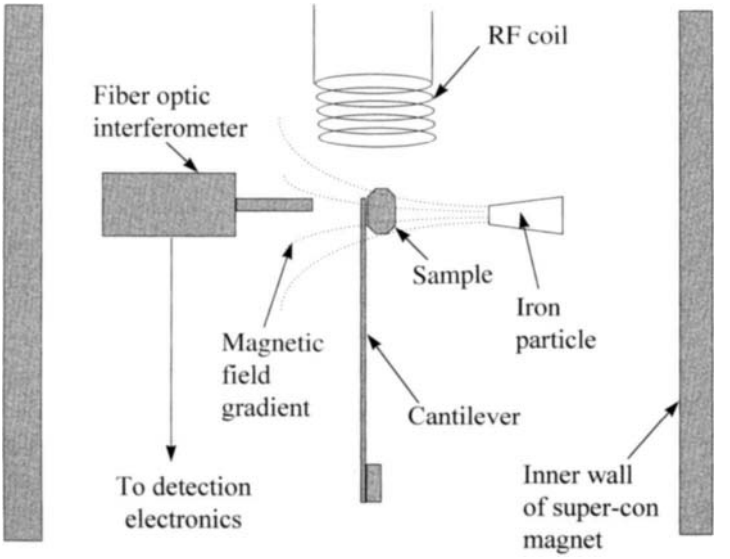

Figure 8.7. Schematic of an NMR force microscope.

The sample, typically only a few hundred microns in size, is fixed to the end of an extremely sensitive cantilever only 900 Å thick, so that it has a very small spring constant. A 1-mm iron particle is positioned a few hundred microns from the sample and the entire arrangement is inserted in the bore of a superconducting magnet. The iron particle creates a powerful field gradient G on the order of 600 T/m, and this field, together with the main superconducting field polarizes the sample protons, inducing a magnetic moment m. Because the induced moment is in a field gradient, there is a constant force mG exerted on the cantilever. If the magnetization undergoes resonance, however, the moment $m(t)$, and therefore the force, vary in time and cause the cantilever to move. This movement is detected by a fiber optic interferometer. In this way the magnetic resonance is detected by mechanical force changes. The modulation scheme used by Rugar and co-workers (324,325) is based on cyclic adiabatic inversion of the magnetization induced with a radio-frequency coil placed less than 1 mm away from the sample. In the coordinate frame of Figure 8.7 this generates the effective rotating-frame field

$$B_{eff} = B_1\mathbf{x} + \left[\frac{B_0 - \omega(t)}{\gamma}\right]\mathbf{z} \tag{8.2}$$

where the radio frequency, $\omega(t)$, is modulated sinusoidally around the resonance frequency, ω_0, such that $\omega(t) = \omega_0 + \Omega \sin \omega_c t$. Here Ω is the maximum frequency deviation and ω_c is the cantilever resonance frequency. The effect of this is to make the magnetization oscillate above and below the **x**-axis in the rotating frame at the

cantilever resonance frequency. This, in turn, causes the cantilever to experience an oscillating force and vibrate at the same frequency. The amplitude of the cantilever vibration is recorded by the interferometer and is proportional to the number of on-resonance spins in the sample. The imaging aspect follows the basic idea of the STRAFI technique (see Section 5.3). Because of the very powerful field gradient, only a narrow slice of spins will be on-resonance and the force will be proportional to the number of spins in that slice. By moving the iron particle relative to the sample, the resonance slice will move through the sample and the distance dependence of the amplitude of the cantilever vibration will be equivalent to a spatial map of the spin density through the sample. Rugar and co-workers (324) have developed this technique and achieved spatial resolutions of 2.6 μm with a grain-sized sample of ammonium nitrate. This is an order of magnitude better than the resolutions in conventional NMR microimaging and the use of higher field gradients, more sensitive cantilevers, and lower temperatures to reduce thermal vibration is expected to give even better resolution. Of course, merely achieving high spatial resolution on a static sample is not sufficient in itself, because electron microscopy already far exceeds these resolutions. The true potential lies in monitoring changes noninvasively on the (sub-)micron distance scale, but further development is needed before this can be achieved.

PART TWO

MICROSCOPIC DISTANCE SCALE

9

MICROIMAGING AND NMR MICROSCOPY

9.1 INTRODUCTION

The NMR microscope is one of the most exciting developments in MRI and was anticipated by early workers in the field (21). The dictionary definition of *microscopic* is "not visible with the unaided eye," and since the average human eye can detect objects as small as about 40 μm, it is sensible to confine the terms *NMR microscopy* and *NMR microimaging* to images where one or more of the spatial voxel dimensions is less than about 40 μm. The qualifier "one or more spatial dimensions" is necessary because it is not unusual to find high spatial resolution in two dimensions at the expense of low resolution in the third, slice-selected direction. The terms *NMR microimaging* and *NMR microscopy* are otherwise interchangeable and do not imply differences in spatial resolving power, which are typically on the order of 5 to 40 μm. Because of the point-spread function arising from water diffusion, resolutions much better than about 5 μm will be very hard to achieve. A detailed discussion of the physical factors limiting resolution in NMR microscopy can be found in Callaghan's book (5) and in a number of discussion papers (196).

9.2 APPLICATIONS OF NMR MICROIMAGING TO CELLULAR TISSUE

Because of their relatively high water content, which gives a high signal-to-noise ratio and therefore high-resolution images, most applications of NMR microscopy have focused on cellular tissue of either animal or plant origin. In cellular tissue the cell is the natural unit of length, so microimaging studies can be further classified into tissue studies and intracellular studies. As its name implies, *tissue studies* are

those where resolutions are sufficient to distinguish different tissue types, such as vascular and parenchyma tissue, but are insufficient to resolve intracellular organelles, although in favorable cases the outline of individual cells can be resolved. *Intracellular microimaging* studies succeed in resolving one or more intracellular organelles, such as the cell nucleus or vacuoles, and include single-cell studies. We consider each application in turn.

The quality factors of relevance to vegetables and fruit are often popularly collected together into adjectives such as *unripe, ripe,* or *overripe,* with the implication that the desirable quality factors associated with ripeness are to be preserved as long as possible during storage, transportation, and display. There are also negative quality factors to be considered, such as bruising, fungal infection, and stress injury. Of course, terms such as *ripening* and *bruising* encompass a wide range of detailed tissue changes, such as alterations in the concentrations of sugars and low-molecular-weight metabolites in vascular and parenchyma tissue during ripening or the filling of intercellular air spaces with cellular fluid during bruising. Conventional histological approaches for the study of plant development and postharvest damage are difficult and unsatisfactory in a number of ways. Both optical and electron microscopy are highly invasive, requiring various combinations of fixing, drying (e.g., in ethanol or acetone), infiltration (e.g., with wax or resin), embedding, slicing, and staining, all of which are destructive and do not permit the continuous observation of developmental or processing changes. Moreover, many mature fruit samples, such as ripe raspberries, are very difficult specimens to prepare for conventional histology (67). The mesocarp cells are large and have thin cell walls and high water content, making fixation difficult, and distortions can occur during dehydration and embedding. Wax- or resin-embedded fruits are also difficult to section where soft parenchyma cells of the mesocarp are adjacent to hard, lignified secondary walls of sclerids in the endocarp surrounding the embryo. It is also difficult, or impossible, to extract quantitative information such as the volume of particular tissues, or the concentration of sugars, from optical or electron micrographs. Being noninvasive and quantitative, NMR microimaging offers solutions to all these difficulties.

Two other applications where the noninvasive aspect of NMR can be put to good use include the regular testing of the viability of seeds in seed banks. These banks are important repositories of seed varieties and it is clearly undesirable to have to germinate the seeds repeatedly to test their viability. The potential for NMR microscopy, including chemical shift microscopy, in this area is therefore great. Another application, just beginning to be explored, is the use of noninvasive MRI to follow the development of roots (including underground crops such as carrots and potatoes). The macroscopic aspects of this were discussed in Chapter 8, but the potential for determining root viability at microscopic resolutions using NMR microimaging remains to be explored.

To be able to examine and quantify quality factors in plant tissue with NMR microimaging requires three steps. First, it is necessary to identify NMR contrast parameters, such as the water proton spin density, water proton longitudinal or transverse relaxation time, or water self-diffusion coefficients or intensities in chemically shifted

images, which permit the various tissue types, such as epidermal, parenchyma, vascular tissue (including the phloem and xylem), seed, and endosperm, to be distinguished in the NMR image. This image-contrast step permits only qualitative changes to be monitored in images weighted with the selected NMR parameter. The second step involves the determination of quantitative NMR parameter maps for the various tissues. The third and final step involves elucidation of the quantitative relationship between the NMR parameter maps and changes in the tissue quality factor of interest, such as degree of ripeness. When all three steps have been achieved, it is possible to use NMR microscopy as a quantitative probe of quality factors in fruit and vegetables. It may then be feasible to exploit the quantitative relationship between the NMR parameter and the physiological parameter in an on-line sensor, though probably not at the microscopic distance scale.

Few reports in the literature have succeeded in fulfilling all three steps, but considerable progress is being made. The second step (calculating quantitative parameter maps) appears to be a point of weakness in the current research literature. One reason for this is undoubtedly the long acquisition times needed to obtain a NMR parameter map at microscopic resolution. Consider, for example, the measurement of a transverse relaxation time map at microscopic resolution. Because the voxels are of microscopic dimensions, the signal-to-noise ratio is reduced so that more accumulations are required. Assuming that the relaxation is single exponential (which, as we discuss in Chapter 10, is not, in general, to be expected), at least five or six points per voxel measured at increasing delay time will be needed to calculate a relaxation time from the exponential decay and obtain the spin density by extrapolation to zero delay. This means that an already long image acquisition time needs to be multiplied by a factor of at least 5 or 6 for quantitative T_2 mapping. It is not, therefore, surprising that acquisition times of several hours may be needed in NMR microscopy. While considering transverse relaxation-time maps, it should be noted that because NMR microscopy usually involves high field strengths, care is needed to ensure that transverse relaxation-time maps are obtained in the absence of artifacts from dephasing by diffusion through internal field gradients generated by susceptibility discontinuities. Where changes in these local susceptibility-generated gradients are the NMR parameter of interest, as with bruising, they can be quantified by measuring the difference $(T_2^* - T_2)$, where T_2 is measured with a CPMG preparation sequence with a short 90 to 180° pulse separation. Alternatively, gradient-echo imaging intensities can be used, as this sequence is sensitive to dephasing by internal field gradients.

Before considering examples of steps 1 to 3, it is worth noting that samples will usually have to be removed and replaced in the spectrometer repeatedly if slow processes, such as ripening in a particular specimen, are to be followed in real time. This means that full three-dimensional images are required if difficulties in reproducibly positioning the sample in the spectrometer are to be avoided. Three-dimensional imaging is also advantageous because it permits the application of powerful image construction algorithms (96), such as multiplanar reformatting and cluster analysis, that facilitate visualization and quantification of the tissue changes. Many commercial three-dimensional software packages for image analysis also

have "seeding" algorithms for volume or surface rendering. This enhances the visualization of particular structures, such as the vascular network, by allowing the operator to preselect an initial voxel as a starting point for segmentation. The program then traverses the three-dimensional data set and accepts only connected voxels having an intensity within an operator-determined range, setting the intensity of all other voxels to zero. This permits intricate vascular networks to be visualized in three dimensions (74). Care must be taken when measuring image volumes with this technique to ensure that the user-defined criterion for choosing voxels is compatible with the real volume in the specimen. Once again, however, the price paid for three-dimensional information is usually extended image acquisition time, although multislice imaging techniques partially alleviate this problem.

We now consider several examples of microimaging quality factors taken from the recent literature, using as the framework for discussion the three steps discussed above. Step 1 is nicely illustrated by recent work on cultivated strawberry fruit (70). Because of differences in water relaxation rates in vascular and parenchyma tissues, the major structural features of the fruit could be identified (see Figure 9.1). Moreover, NMR images selectively displaying the three-dimensional spiral arrangement of the vascular supply (carpellary traces) to the achenes ("seeds") could be obtained. Having thus qualitatively discriminated the different tissue types in the fruit, it was possible to monitor contrast changes resulting from infection, bruising, and ripening. Unfortunately, step 2, the calculation of relaxation time and spin density maps, was not attempted; nevertheless, the qualitative changes in image contrast indicated that infection with the fungus *Botrytis cinerea* caused an increase in the T_2^* of the parenchmya tissue, consistent with the reduction of local magnetic susceptibility inhomogeneities as a result of filling of the intercellular gas spaces with intracellular fluid released through cell

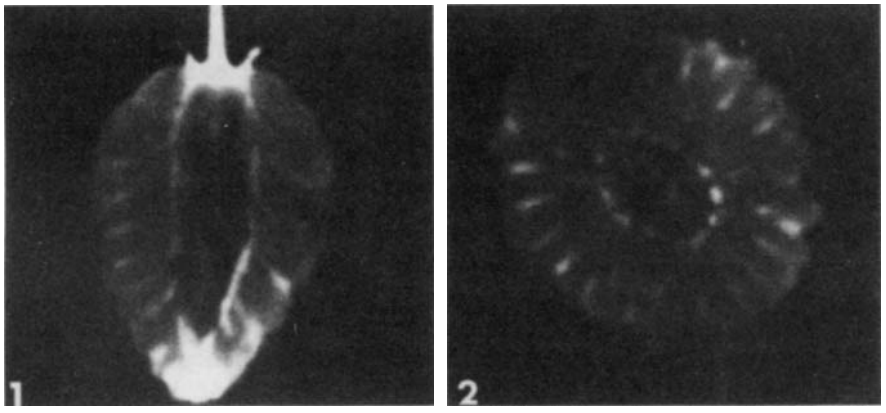

Figure 9.1. Image 1 shows a longitudinal slice through a ripe strawberry. A bright spindle-shaped vascular cylinder surrounds a central darker pit with large eccentric gas space. The bright carpellary traces depart from the vascular cylinder and radiate to the surface of the receptacle, each to terminate as a cone-shaped structure at the base of a deep invagination of the fruit surface within which a single achene is located. Image 2 shows a transverse slice. (From Ref. 70.)

wall damage. This permitted the diseased and healthy tissue to be T_2^*-contrasted and the rate of progress of the disease to be quantified as the rate of increase in the volume of infected tissue (70). As discussed in Chapter 6, the ability to discriminate diseased, bruised, and healthy tissue is essential for the development of on-line MRI quality monitoring.

The ripening process was shown to change the relative magnitudes of T_1 and T_2 for parenchyma and vascular tissue in green and red-ripe strawberries. The reasons for this are not yet fully understood, but it is known that ripening involves an overall 40% increase in soluble solids and a 150% increase in total sugar (74). Because the vascular system supplies nutrients and sugars to the parenchyma tissue during development, and the sugar content of the parenchyma tissue increases during ripening, it is expected that the differences between vascular and parenchyma tissue sugar content will decrease and cause changes in the relative water proton relaxation times (see Chapter 12). However, further work is needed before this explanation can be tested and put on a quantitative basis.

The connection between ripening and sugar content suggests the use of chemical shift NMR microscopy for separating water and sugar proton signals. This was not attempted in the strawberry study but has been applied successfully to the ripening of grapes (73). Separate images of water (at 4.6 ppm) and a resonance at 3.4 ppm, assigned to sugars, were obtained (Figure 9.2). A uniform sugar distribution was found in the unripe and fully ripe grape, but during the final ripening stage sugar gradients were found in the parenchyma tissue around the seeds. Kockenberger and Metzler (76) have discussed the potential of obtaining two-dimensional COSY spectra from each voxel in an image. So far this combination of two-dimensional NMR spectroscopy and microimaging, called *correlation peak imaging* (CPI), has been used to determine the spatial distribution not just of sucrose, but also of α- and β-glucose, glutamine/glutamate, lysine, arginine, and valine in castor bean seedlings grown in an NMR tube, but the technique should have application to a wide range of other plant materials.

One quality factor of importance in the export of grapes from the Mediterranean countries is stalk-end rot. As its name implies, this is a shriveling and wilting of the grape tissue from the stalk end after a few days. The reasons for this are as yet unknown but could be related to excessive use of sulfur dioxide as a preservative during transportation. Here again NMR microscopy could help elucidate this process.

Step 2, the calculation of quantitative MR parameter maps, is nicely illustrated in the work of Kochenbrod et al. (197), who reported spin density, T_1, T_2, and diffusion maps of intact young maize plants. A noteworthy feature of this work is the observation that because of geometric restrictions, water diffusivity in the vascular bundles is less in the direction transverse to the bundle axis than along the axis. This emphasizes the need to exploit the directional aspects of the diffusion tensor, by applying the diffusion gradient pulses in all three directions when probing plant quality factors. Curiously, the T_2 map permitted the xylem and phloem regions in the vascular bundles to be distinguished, but no difference could be observed in the T_1 map. Understanding such observations requires a more fundamental analysis of the origins of image contrast in cellular tissue and is deferred to Chapters 10

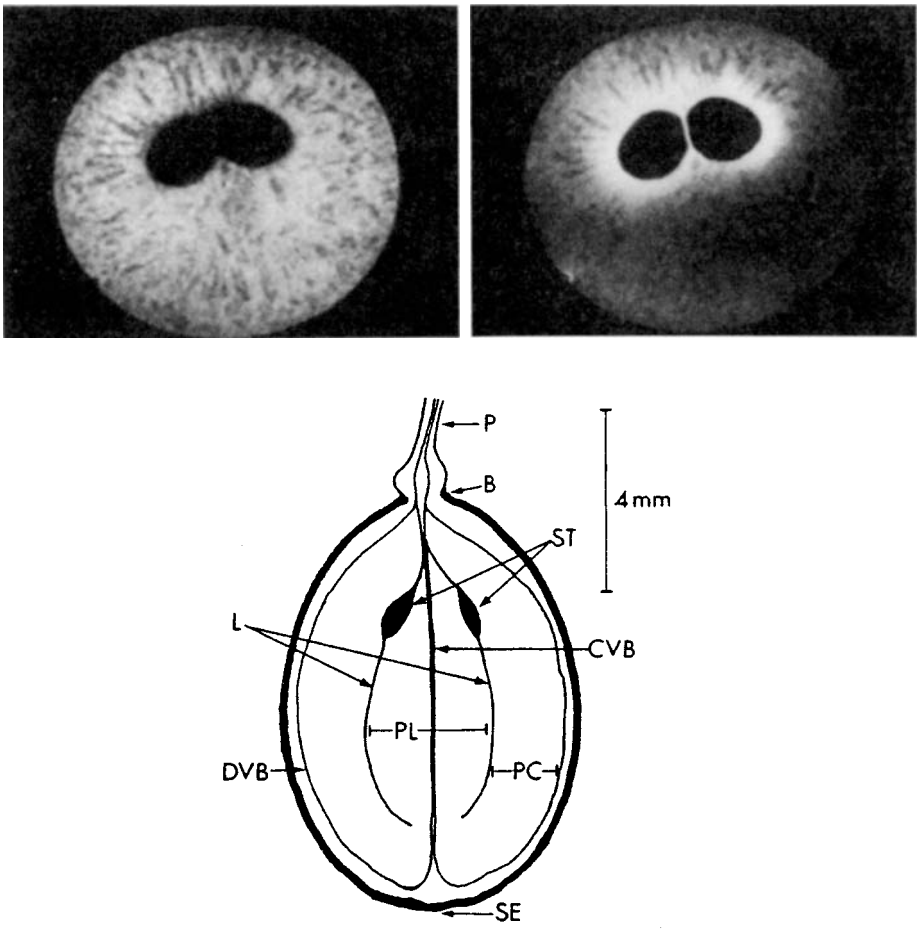

Figure 9.2. Chemical-shift-resolved images of a ripe grape (Black Hambourg). In the photos at top, the left-hand image shows the water image at 4.6 ppm taken through the seed trace. The right-hand image is the sugar image at 3.4 ppm. Note the concentration of sugar around the two seed traces. The schematic (bottom) defines the main tissue types in the grape. PL, placenta; PC, pericarp; P, pedicel; CVB, central vascular bundle; DVB, dorsal vascular bundle; L, locule; ST, seed trace; SE, stylar end; B, brush. (From Ref. 73.)

and 12. The work on intact maize plants succeeded in illustrating the use of quantitative parameter maps, but it made no attempt at step 3, which is establishing the relationship between changes in the parameter maps and changes in tissue quality factors. In fact, only the healthy, maize plant was studied.

All three steps can be found in the work of Ishida et al. (78) on the ripening of barley seeds. These workers imaged ripening barley seeds with and without diffusion weighting and thereby calculated quantitative maps of the effective water self-diffusion coefficient over a 44-day period during the ripening of a barley seed. Effective diffusion coefficients were obtained for the major tissue types: the glume

and seed coat, vascular bundles, the endosperm, and the water cavity in the seed. The most notable effect was the decrease in the diffusivity of water in the endosperm and seed coats during the last 8 days of maturation. In this study the diffusion-pulsed field gradients were applied parallel to the slice-selecting imaging gradient, so only a single component of the diffusion tensor was measured. However, an attempt was made to investigate the extent to which the water diffusion in each tissue type was restricted by repeating the measurements with increasing diffusion times, Δ. Figure 9.3 shows the results of this experiment after 32 days of incubation. The authors proceeded to interpret these changes in diffusivity using a model for restricted diffusion of Meerwall and Ferguson (198) involving diffusion between compartments separated by permeability barriers. The results permitted an analysis of the effects of ripening on the compartment sizes and membrane permeability coefficients. Discussion concerning the assumptions behind this model is deferred until Chapter 11.

Another quantitative study where proton density and relaxation-time maps were calculated considered the effects of ripening and bruising of strawberry fruit by Maas and Millard (71). These authors showed that bruising is associated with a lengthening of T_2, suggesting that subcellular compartmentation is disrupted and water enters the intercellular spaces. Indeed, the apparent spin density in the

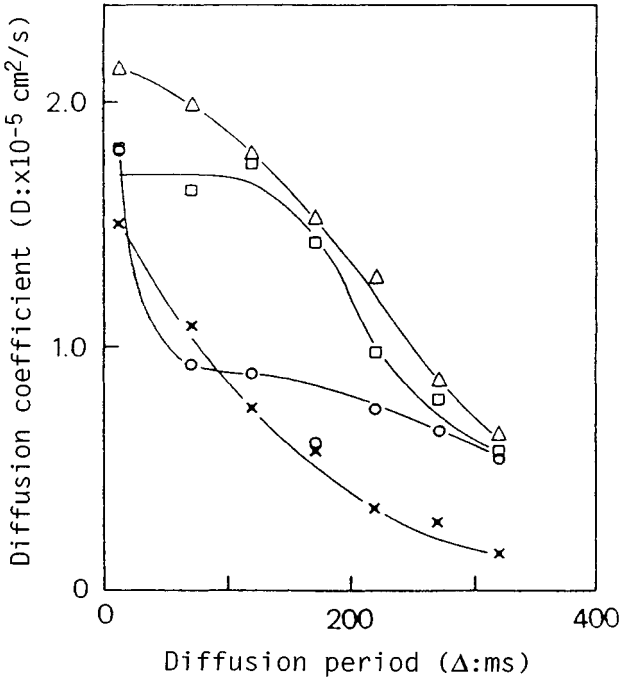

Figure 9.3. The Δ dependence of the water diffusion coefficient in various tissues of a barley seed after 32 days of ripening. Circles, vascular bundles; squares, endosperm; triangles, water cavity; crosses, glume and seed coat. (From Ref. 78.)

bruised region increased. However, susceptibility artifacts could not be discounted in these measurements, so some caution is needed in interpretating the quantitative changes. Ripening was associated with an increase in T_2 from about 16 to 25 ms in the immature green fruit to 25 to 100 ms in the ripe red fruit. Possible reasons for this are discussed in Chapter 10 and require consideration of the numerical cell model of water compartmentation. A similar increase in T_1 was observed in the pericarp tissue (the edible part) of cherry during ripening by Ishida and co-workers (80). At the same time the T_1 of the cherry pit, or stone, decreased from an initially high value to a low value just before reaching maturity. This rather dramatic change was assigned to a decrease in water content in the pit and an increase in the pericarp as the cherry reached maturity, but no quantitative relationship was established between T_1 and the gravimetric water content, so this interpretation must for the moment be regarded as tentative. Volume-selective spectroscopy was also used to image the distribution of sugars and oil in the cherry. It was observed that sugars accumulated in the pericarp just after the decrease in pit T_1 and that soon after this, a peak assigned to oil appeared in the pit. These various observations suggest that there are metabolic triggers that turn off the pit development and turn on the pericarp maturation, and that MRI can provide a noninvasive probe of these triggers and when they are activated. Such knowledge can aid in determination of the optimum harvest time.

One other quantitative study is worthy of discussion because the authors succeeded in showing the relationship between the proton spin density map and other quantifiable measures of the degree of ripeness of tomato fruit (81). This was done in the hope of using MRI as an on-line sensor of tomato ripeness. Tomato ripeness has been placed on a more definite basis by first classifying the fruit according to its external color as: 1, mature green (MG); 2, breaker; 3, turning; 4, pink; 5, light red; 6, red-ripe (95). Four additional substages of the first mature-green (MG) stage have been identified on the basis of the internal color and tissue consistency. These substages are MG1, characterized by firm green locular tissue and soft seeds that cut easily; MG2, characterized by soft green locular tissue and hard seeds that do not cut when the tissue is sliced with a sharp knife; MG3, characterized by some gel in the locule but no internal red color; and MG4, where locular tissue is predominantly gel-like with some red visible. The *locular tissue* referred to here is indicated in Figure 9.4, which shows the main tissue types in the tomato. Additional quantifiable measures of tomato ripeness include the amount of plant hormone (ethylene) produced, the amount of CO_2 produced, and the firmness (measured by the displacement in millimeters of a 500-g weight resting on the fruit for 10 s). Table 9.1 summarizes the relationship between these measures and the maturity stages referred to above. Perhaps the most important stage from the MRI perspective is the liquefication of the locular tissue during stages MG1 to MG4, since this heralds the onset of the later ripening stages. If this change could be detected rapidly and nondestructively, it would greatly reduce the variability in the ripeness of tomatoes marketed for international export. Such tomatoes are picked at the MG stage and transported in boxes gassed with ethylene. But on arrival the tomatoes display the entire range of ripeness up to 6 (red-ripe) and require a second costly

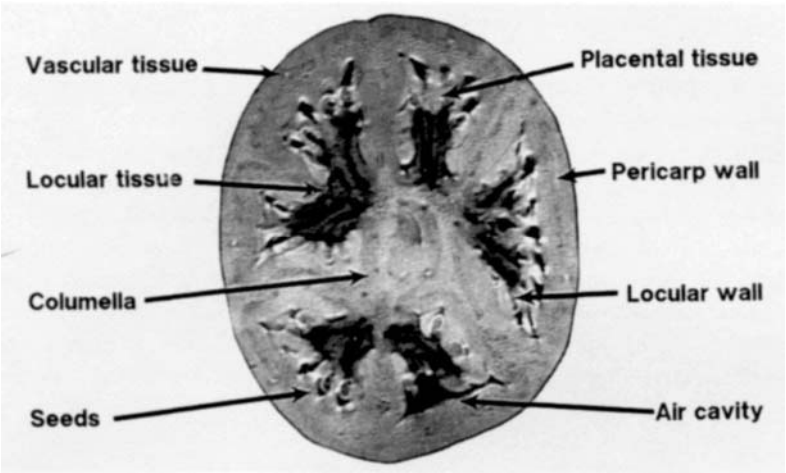

Figure 9.4. Main tissue types in a tomato fruit.

(and damaging) hand-sorting stage. If the tomatoes, when picked, could be classified on the MG1 to MG4 scale, ripening would be more uniform and the second sorting stage would be rendered unnecessary (81). This was the motive for the MRI study, which showed that as the locular tissue ripened from stage MG1 to MG3 its water content increased, as seen as an increased intensity in the spin density map recorded in the absence of significant relaxation attenuation. Later stages of ripening were associated with an increasing graininess in the pericarp tissue as small air pockets developed in the tissue. The next stage is to exploit these MRI changes in an on-line automated monitor of tomato maturity. This is not yet possible if it requires full two-dimensional imaging, because each image required about 6 min to acquire. However, it may not always be necessary to obtain a two-dimensional image if a carefully chosen imaging protocol is chosen.

TABLE 9.1 Quantitative Indicators of Tomato Quality

Maturity	External Color[a]	Internal Maturity[b]	nL ethene/g·h	μL CO_2g·h	Firmness[c]
Red-ripe	6	—	9.8	24.5	1.8
Turning	3	—	5.7	23.9	1.6
Breaker	2	—	2.6	28.8	1.3
Mature-green	1	3	0.4	17.9	0.8
Mature-green	1	1	0.03	11.7	0.7

Source: Ref. 81.

[a]External color subjectively rated as: 1, mature-green; 2, breaker; 3, turning; 4, pink; 5, light red; 6, red-ripe.

[b]Internal maturity subjectively rated on firmness of locular tissue and color of seeds, with 1 being green firm tissue and seeds cut by knife; and 3 being green, reddish tissue with seeds not cut by knife.

[c]Firmness measured as the displacement in millimeters of a 500-g weight resting on the fruit for 10 s.

9.3 MICROIMAGING PROCESSING EFFECTS IN TISSUE

The majority of food microimaging studies to date have been concerned with quality factors such as ripeness, bruising, and infection and not with the microscopic effects of processing operations such as drying, freezing, freeze-drying, rehydration, or heating. This is a pity because a microscopic understanding of the effects of these processing operations is essential for the development of transport models and for an understanding of the macroscopic MRI food processing results. The long image acquisition times, often several hours, required to achieve sufficient signal at very high spatial resolutions makes it difficult to use NMR microscopy to follow small-scale changes during fast processes such as freezing. The sort of information available will be considered for a few selected processing operations, beginning with freezing.

9.3.1 Freezing

The freezing operation is of commercial importance for the preservation and transport of a wide range of vegetables, such as potato, carrots, and beans, as well as for fruit, such as raspberries, black currants, and gooseberries. At the tissue level we need to know the freezing characteristics of each type of tissue, including the amount of unfrozen water in each tissue, as a function of temperature. At the (sub-) cellular level, different organelles, such as vacuoles, granules, cytoplasm, and cell wall regions, have different freezing characteristics and it is important to know which, if any, remain unfrozen at any specified subzero temperature, both for thermal transport modeling as well as for understanding slow spoilage processes during long-term storage. Given its importance, it is surprising that there appear to be few reports where microimaging is used to study the effect of freezing at a microscopic tissue level. A hint of the rich information to be gained in such studies is to be found in the work of Brennan (77). Although this work was concerned primarily with environmental freezing injury in crops of black currant, it showed that the freezing injury was localized in the stylar and ovular regions of the flower buds and is one of the few examples where microimaging has been used to monitor the freezing and thawing of different tissue types.

A more recent example involves the use of T_1-null microscopy to observe changes in sugar and water distributions in blueberry fruit tissue before and after freeze-thawing (94). An image of the sugar distribution was obtained by introducing a hard 180° pulse before a standard spin-warp imaging sequence, and exciting the sugar protons at the null point of the water proton magnetization (i.e., after a time period at which the inverted magnetization has recovered to zero). Before treatment there were high sugar concentrations in the thin exocarp, the placenta, and the locules. Freeze-thawing disrupted the cell walls and membranes, permitting the sugar to diffuse out of the placental tissue into other tissues, including the mesocarp. The changes are indicated in Figure 9.5. At the subcellular level, nonspatially resolved NMR water proton relaxometry has already provided valuable information about the freezing behavior of different organelles and the reader is directed to Chapter 10 for a fuller discussion of this approach.

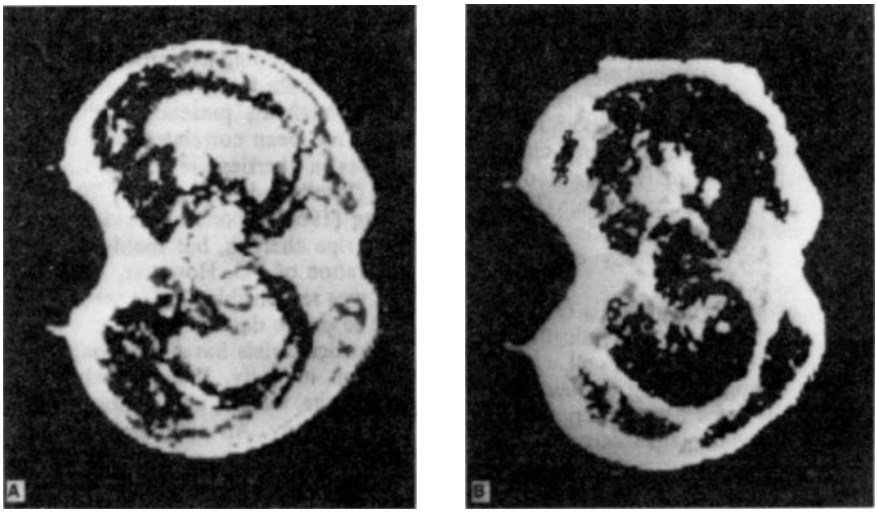

Figure 9.5. The left image shows a water-weighted image of a fresh blueberry fruit. The right image shows the sugar-weighted image of a frozen-thawed blueberry. Note the almost complementary distributions. (From Ref. 94.)

9.3.2 Rehydration and Drying

Drying, rehydration, and cooking of plant material such as seed is an important industrial operation and requires knowledge of moisture diffusion throughout the material. This is especially true for wheat and rice grains as well as soybeans. Conventional gravimetric determinations of moisture diffusivity in such cellular foods provide only an effective, average moisture diffusivity since it takes no account of the mechanisms of transport through different tissues types, such as vascular bundles, parenchyma tissue, endosperm, epidermal tissue, cuticles, and air spaces. What is needed is spatially resolved information on water transport through different tissues in different regions of the seed or plant material. This information is contained in the time course of the water proton spin density map at a resolution sufficient to discriminate different tissue types. Additional information is contained in water self-diffusion maps at diffusion distances long compared to cellular size but still short enough to discriminate tissue types.

The pioneering study of water diffusion in wheat grains by Jenner et al. (66) demonstrated the feasibility of this type of measurement, but this classic study was concerned with the physiology of grain development. Mention has already been made in Section 2.4.3 of the recent comparative study of rehydration of wheat grains by boiling and steaming (199). The results showed that during boiling, water penetrates evenly into the wheat grain from all points on the boundary, including the inside of the crease, and gives a clearly defined water front ingressing into the center of the grain. In contrast, steaming gives slower rehydration and a gradually increasing water content throughout the grain, suggesting that the grain surface presents a greater water permeability barrier to steam than liquid water, although the

reasons for this are, as yet, unknown. The moisture images were obtained by compensating the signal for transverse relaxation and by calibration of the spin density map with gravimetric measurements of water content.

Wheat grains are usually partially rehydrated by soaking in water, a process known as *tempering*, prior to milling. However, some wheat varieties, such as the Scout 66, Karl, and Newton varieties, are very resistant to the ingress of water during soaking after harvesting and require many weeks or even months of storage before they can be tempered. The reasons for this phenomenon (called the *new crop syndrome*) are being investigated by NMR microimaging. Preliminary studies (200) show that during soaking, the water first penetrates the embryo, then is drawn into the vascular tissue in the grain, and finally, enters the ventral (but not dorsal) endosperm tissue. However, the reasons for the resistance of some varieties is yet to be elucidated. It was not necessary to progress beyond stage 1 in these qualitative studies, so the water ingress was inferred from the changes in Hahn-echo image intensity. Similar qualitative microimaging studies were used to distinguish dormant from nondormant grains. Dormancy in immature grains is a very desirable characteristic because it prevents early sprouting under moist conditions (including rain), which leads to starch damage. Microimaging indicated that water could penetrate the root cap region of the nondormant (germinatable) grains during soaking, but not the dormant kernals (200).

Watanabe and Yoshida (79) have used chemical-shift-resolved microimaging to produce separate water and oil images during the rehydration of soybeans (see Figure 9.6). This study did not attempt to quantify the moisture or oil images, but the time course of the chemically shifted images showed that rehydration proceeded from the outside of the seed and was accompanied by expulsion of oil from the central intercotyledon and the transient formation of a gas-filled space between the cotyledons, presumably due to unbalanced stresses during disproportional swelling of the seed.

Other examples where chemical shift microscopy has been used to observe the effects of drying on the water and metabolite distributions include a three-dimensional chemical shift study of fresh and dried feenal fruit (92). In this study the spatial distribution of anethole, reserve oil, and water in fresh and dried feenal fruit mericarps with an in-plane resolution down to 30 μm and with a spectral resolution of 0.4 ppm. was achieved (see Figure 9.7). In the undried fruit, water was confined mainly to the outer pericarp, which was free of anethole and reserve oil. In the dried fruit the signals from anethole oil were located in the oil canals of the mericarp and reserve oil in the endosperm tissue. This study emphasized the importance of suppressing the water signal to avoid dynamic range problems and baseline problems due to extended wings of a strong water peak. In fact, this is mandatory in this example because the anethole peak intensity was approximately 250 times lower than the water peak intensity in the undried fruit.

Separate oil and water signals have also been obtained for the intact fruit of coffee (93). The oil signal is located in the coffee bean itself and the water is present in the unripe bean and in the fruit wall (Figure 9.8). Although no processing changes were observed in this study, its relevance to drying and roasting of coffee beans is obvious.

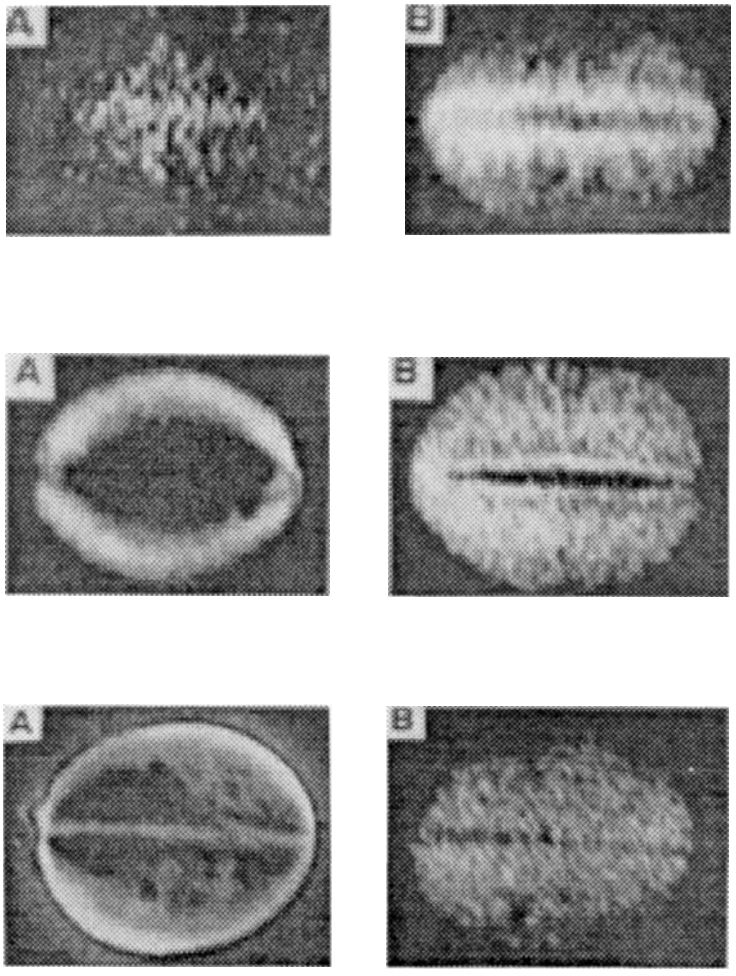

Figure 9.6. Chemical-shift-resolved images of soybean seeds. Series A shows the water image and series B the oil image. Top, the dry bean; middle, after 2 h of soaking; bottom, after 24 h of soaking. (From Ref. 79.)

The distribution of water in sultana grapes before and after drying for 24 h at 40°C has been reported in a preliminary drying study by Pope et al. (72). Loss of water from the peripheral layers was evident, as was shrinkage of the grape (Figure 9.9). Chemical shift microscopy can also be used to image the sugar distribution in the grape (72). However, a systematic study on water and sugar distribution for various drying times and conditions was not undertaken despite its potential importance in the dried fruit industry, where rapid drying with minimum chemical degradation by browning reactions is essential for good dried fruit quality. Another obvious example where chemical shift microscopy would be of value in drying studies

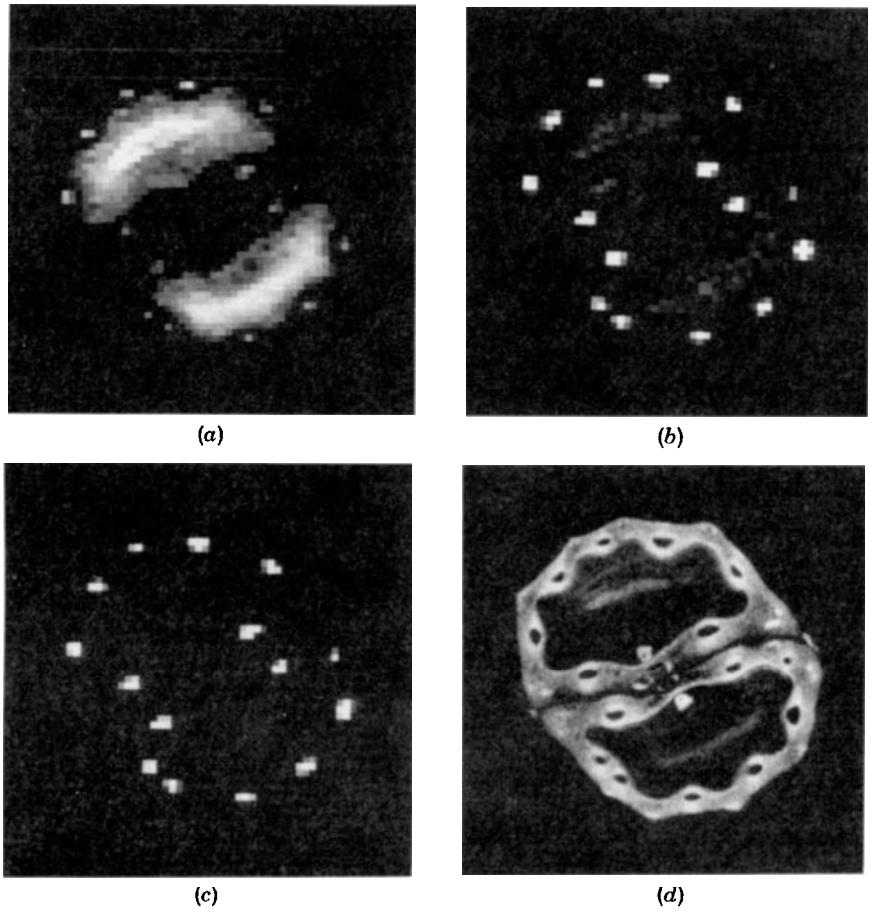

Figure 9.7. Water-suppressed three-dimensional chemical-shift-resolved microimages of fresh fennel mericarp. Top left image, methylene groups of reserve oil ($\delta = 1.3$ ppm); top right image, methyl groups of anethole ($\delta = 1.8$ ppm); bottom left, aromatic and olefinic resonances of anethole ($\delta = 7$ ppm); bottom right, normal nonselective image of the same slice (in-plane resolution = 15.6 μm). (From Ref. 92.)

is in monitoring countergradients of sugars and other metabolites set up in tissue during surface air drying. When drying is very fast it leads to case hardening at the surface due to the formation of crystalline or glassy layers as the surface water is removed.

9.3.3 Thermal Processing

There is also a surprising paucity of investigations on the microscopic effects of heating and cooking cellular plant tissue. Joyce et al. (82) have imaged the effects of heating ripening mango fruit in hot water because this is a more acceptable way

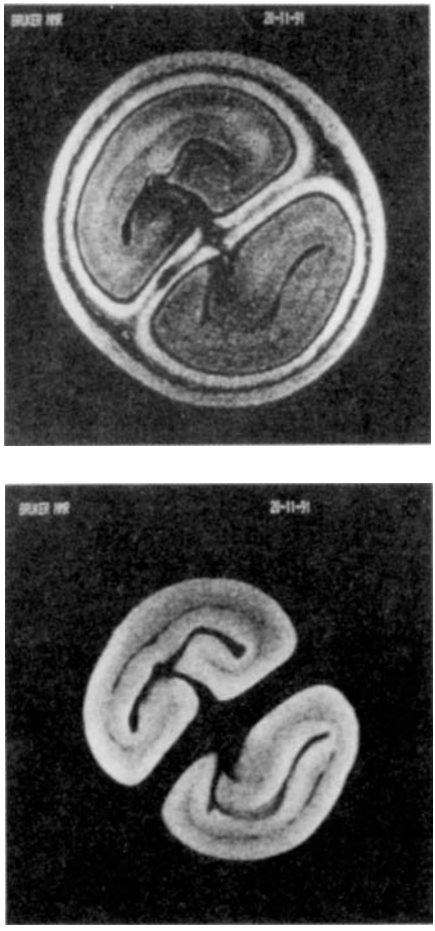

Figure 9.8. Chemical-shift-resolved images of the fruit of coffee. Top image, water distribution; bottom image, oil distribution. Voxel dimensions are 60×60 μm with a 1-mm slice thickness. (From Ref. 93.)

of insect disinfestation than using chemical insecticides but can lead to heat-induced tissue damage. The qualitative changes in spin-echo image contrast (see Figure 9.10) showed the initiation of heat injury around vascular traces in the mesocarp (the white spots in Figure 9.10), possibly because they form a network for rapid heat transfer and/or retain heat longer than do surrounding cells. In Figure 9.10 heat-damaged mesocarp tissue is manifest as a darkening because transverse relaxation times are shortened, although the reasons for this are unknown. The very dark area at the top corresponds to damaged pulp. Heat treatment also resulted in eventual formation of air-filled cavities and islands of starchy mesocarp. Although there was no attempt to calculate spin-density or relaxation-time maps and quantify

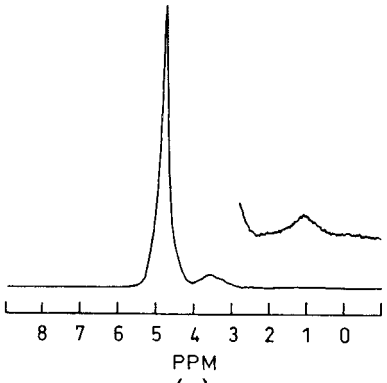

(a)

(b)

(c)

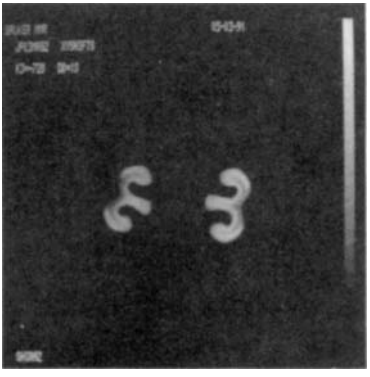

(d)

Figure 9.9. Spectrum and images of a sultana grape berry. The spectrum shows a water peak at 4.8 ppm, a sugar peak at 3.6 ppm, and an oil peak at 1.1 ppm (expanded scale). Top right image, water image; bottom left, sugar image; bottom right, oil image. Voxel dimensions are 60×60 μm with a 1-mm slice thickness. (From Ref. 93.)

the changes, the results provide a nice illustration of the need for microscopic information when developing models of heat transfer in cellular tissue.

A quantitative study (corresponding to stage 3 in our classification) of heat injury in papaya has been reported by Suzuki and co-workers (316). Imported papayas are subjected to quarantine vapor heat treatment at 47.2°C for 30 min for disinfection of fruit fly eggs and larvae. The problem was to find a nondestructive method for distinguishing injured and healthy fruit after the heat disinfection, MRI (and X-ray CT) being obvious possibilities. Figure 9.11 shows proton density and T_1 and T_2 maps of unripe papaya (G), a ripe papaya [C (control)], a wrapped heat-treated fruit (W), and a thermally injured fruit (T). The unripe and ripe samples have almost equal proton densities and equal and uniform T_1 and T_2 values. How-

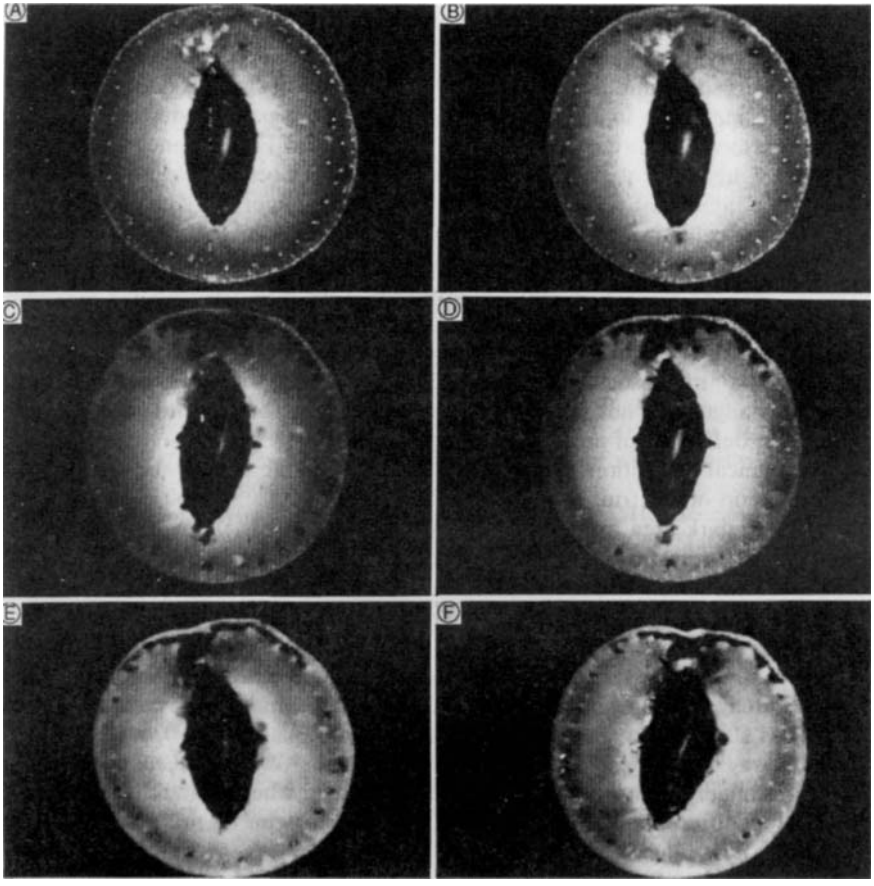

Figure 9.10. Water proton images of ripening, heat-treated mango (Kensington Pride Fruit). Images A to F are for 0, 1, 4, 6, 8, and 11 days of ripening after heat treatment. (From Ref. 82.)

ever, heat damage caused irregularities to appear in each map. Black areas appeared in the proton density maps, corresponding to low-proton-density regions. Similarly, T_1 maps showed regions of long and short T_1, the short areas corresponding to lower polygalacturonase enzyme activity, which is responsible for the softening of the ripening tissue. Regions of longer T_2 (white in Figure 9.11) appeared to correspond to crumbled parts of overripe tissue. It appears, therefore, that MRI can be a useful nondestructive sensor for regions of heat injury. If we adhere to our earlier definition of microimaging as having at least one voxel dimension less than 40 μm, the investigations on mango and papaya thermal injury described above are not strictly microimaging studies and therefore fall outside this part of the book. Nevertheless, they point to the need for truly microscopic information on the effects of heat on plant tissue. Whether the temperature dependence of relaxation times and water diffusion coefficients will permit NMR temperature mapping at the

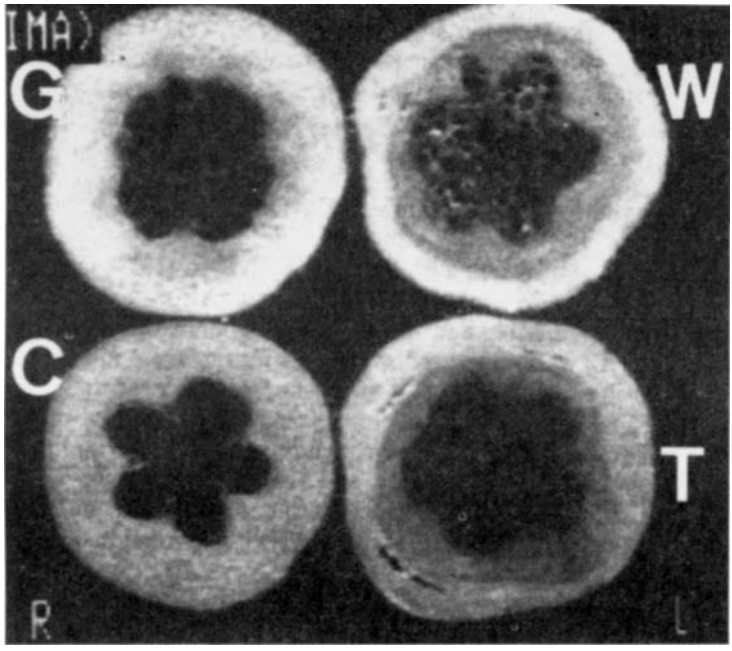

Figure 9.11. Images of papaya fruit showing the effects of heat injury. G, unripe fruit; C, control (ripe or normal fruit); W, injured fruit wrapped with Saran wrap; T, thermally injured fruit. Note the darker contrast around the placental region in the mesocarp tissue resulting from heat injury.

microscopic level remains to be investigated. Such information would be especially valuable in the development of thermal transport models in cellular tissue, addressed in the next section. Table 9.2 lists a number of references to recent work on microimaging cellular plant tissue. The list is not intended to be exhaustive, merely representative, and serves to illustrate the extent of the work remaining to be done.

Flow imaging at microscopic resolutions has also been used to image water and nutrient flow in plant stems and seeds. To be meaningful, these studies have to be made on the whole, intact plant under realistic environmental conditions, which requires controlled environment boxes for the transpiring leaves and controlled nutrient supply to the root system. For this reason they were discussed in Section 7.3.

9.4 INTRACELLULAR MICROIMAGING

9.4.1 Intracellular Resolution in Tissues

In small tissue samples at high fields it is possible to achieve spatial resolutions in one or more directions on the order of 5 to 20 μm, which is considerably smaller than the size of a typical plant cell or large mammalian cell. It should therefore be possible to resolve large intracellular organelles such as the nucleus and vacuoles,

TABLE 9.2 Representative Microimaging Studies of Processing Changes in Plant Tissue

Plant	Process	NMR Parameter	Step	Reference
Red raspberry	Ripening	Spin-echo signal intensity	1	(67,68)
Gooseberry fruit	None	Gradient-echo signal intensity	1	(69)
Strawberry	Ripening, bruising, infection	T_1, T_2	1	(70)
	Ripening, bruising	Spin density, T_2	3	(71)
Grape berries	Ripening, drying	Chemical shift	1–3	(72,73)
Fig, okra, potato, kiwi, apple, persimmon, sugar beet	Three-dimensional vascular structure	Various	1	(74)
Red raspberry fruit	Fungal infection	Gradient-echo signal intensity	1	(75)
Barley seeds	Ripening	Diffusion coefficients	1–3	(78)
Soybean seed	Rehydration	Chemical shift	1	(79)
Wheat grains	Ripening	Diffusion and flow	2	(66)
	Steaming and boiling	Spin density	3	(199)
Tomato fruit	Ripening	Spin density	3	(81)
	Ripening	T_1	3	(80)
Mango fruit	Heat treatment	Relaxation-time weighted signal intensity	1	(82)
Blueberry fruit	Freezing-thawing	T_1 discrimination of sugar and water	1	(94)
Cherry	Ripening	T_1, D and volume selective spectroscopy	2	(201)
Papaya	Heat injury	Spin density, T_1, T_2	3	(316)

although smaller organelles such as the mitochondria, chloroplasts, ribosomes, and nucleoli will fall within one voxel and not be resolved. In this section we review the progress that has been made in these subcellular explorations.

Figure 9.12 shows an NMR microimage of a layer of onion (*Alium cepa*) skin cells, obtained in 1 h with a resolution of $5 \times 5 \times 70$ μm reproduced from the work of Glover and co-workers (202). The cells were soaked in $CC1_4$ to eliminate artifacts due to dephasing in the local fields induced by the susceptibility discontinuity across the air–water interface around intercellular air gaps. Somewhat disappointingly, no intracellular structures are visible in Figure 9.12, and the authors suggest

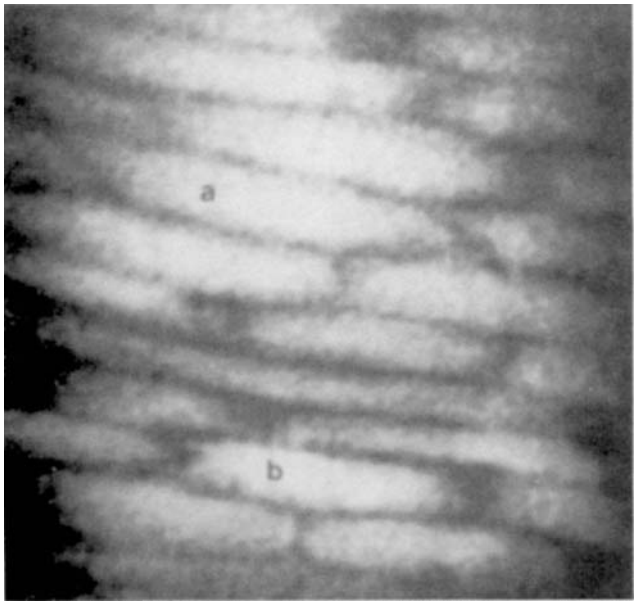

Figure 9.12. NMR microimage of a layer of onion skin cells obtained in 1 h with a resolution of $5 \times 5 \times 70$ μm. The cells were soaked in a solution of CCl_4 to eliminate susceptibility artifacts and highlight the boundaries (dark lines) between the cells. (From Ref. 202.)

that this is because no slice selection was used, so the image involves considerable volume averaging. Nevertheless, the fact that dark outlines of each cell can be seen, even in the susceptibility-matched situation, confirms the shorter relaxation times of the cell wall region previously found in nonspatially resolved NMR relaxation measurements on isolated cell wall extracts. In subsequent experiments (203), plasmolysis was initiated by placing the cells in a hypertonic sucrose solution and the rate of cell volume shrinkage was followed. This type of experiment has the potential of providing accurate cell permeabilities, which are needed in theoretical models for tissue drying and rehydration.

9.4.2 Single-Cell Studies

The first image of a single cell was published in *Nature* by Aguayo et al. in 1986 (83), and over the last decade several research groups have responded to the challenge of imaging other intracellular structures, studies listed in Table 9.3. The real value of single-cell microimaging is not in providing information about subcellular structure because this is already known from electron microscopy at far higher resolution. Rather, their value lies in what they reveal about the intrinsic relaxation behavior of subcellular water compartments. This information is needed for the devel-

TABLE 9.3 Single-Cell Microimaging Studies

Cell Type	Intracellular Structures Imaged	Reference
Frog oocytes	Cell nucleus, animal and vegetal poles of the cytoplasm	(83)
	Cell nucleus and cytoplasm	(85)
	Cell lineage during embryonic development	(86)
Marine alga *Acetabularia mediterranea*	Cap structure of vacuole and cytoplasm during cell maturation	(84)
	Cell wall and central organelles	(87)
Neuron from *Aplysia californica*	Nucleus and cytoplasm	(88–91)

opment of cell models of tissue relaxation (and contrast), discussed in Chapter 10. Progress in this direction has, however, been slow and the few studies on frog oocytes, single algal cells, and neurons have in many ways raised more questions than answers. One question of particular relevance in the context of food processing is the effect on the relaxation times of the intracellular compartments of changing extracellular conditions such as water activity and temperature. Another question discussed in greater detail in Part Three deals with factors affecting the intrinsic compartment relaxation times, such as biopolymer concentration and rigidity, magnetization transfer, and so on, and how these factors are affected by environmental and processing conditions. In principle, single-cell microimaging can answer these questions, but few systematic studies have been reported to date. We consider briefly next the various studies that have been undertaken.

9.4.3 Frog Oocytes

The first single-cell image, published by Aguayo et al. (83), was of a frog ova and showed that T_2 of the cell nucleus was longer than that for the surrounding cytoplasm. Subsequent studies by Posse and Aue (85) used chemical shift microscopy to produce separate images of the lipid and water components in the frog oocyte cell and showed that the cytoplasm was rich in lipid compared to the nucleus (see Figure 9.13). Whether this is the major factor contributing to the relaxation-time difference remains to be determined. Although it is somewhat of a side issue in the present context, it is interesting to note that Jacobs and Fraser (86) used microimaging of the frog oocyte to trace cell lineage. A fertilized frog oocyte was permitted to develop into a 16-cell embryo, then one of the cells was microinjected with the contrast agent Gd-DTPA, which is unable to cross the cell membrane. The subsequent embryonic development was imaged and the descendants of the labeled cell were traced from the relaxation contrast. This experiment clearly opens up many exciting possibilities in embryology.

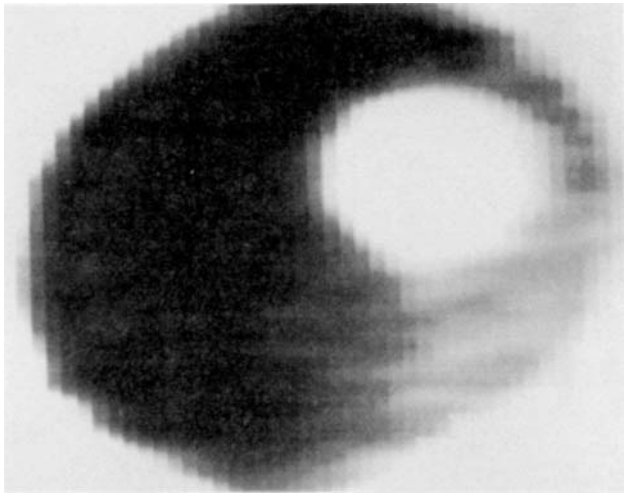

Figure 9.13. NMR microimage of a single frog ova obtained in 8 min with a spatial resolution of $16 \times 27 \times 250$ μm. The bright central nucleus is surrounded by darker cytoplasm. The cytoplasm has a graduated signal intensity with the animal pole brighter than the vegetal pole. (From Ref. 83.)

9.4.4 Single-Celled Alga

The rather curious phenomenon of the intracellular formation of raylike projections containing cytoplasm arranged around a central vacuole during the reproductive cycle of the single-celled marine alga *Acetabularia mediterranea* was imaged by Harrison et al. (84). T_1 weighted images were taken during the various stages of cell growth. Subsequent investigations (87) on the single-celled green alga *Micrasterias*, reproduced in Figure 9.14, identified the cell wall region and revealed a central dark region believed to arise from central organelles.

9.4.5 Neurons

Neurons are the only other single-cell type imaged so far. The first NMR microimage of a single neuron was reported by Schroeniger et al. using a cell isolated from the marine gastropod *Aplysia californica* (88). These authors succeeded not only in observing qualitative image contrast but in producing quantitative maps of T_1, T_2, and water diffusion coefficients. Like the oocyte, this showed that the nucleus has a longer T_1, T_2, and diffusion coefficient than the cytoplasm (see Table 9.4). Using a CPMG-weighted imaging sequence, Bowtell et al. (89) subsequently verified that the T_2 contrast is intrinsic and not caused by dephasing by diffusion through susceptibility-generated local field gradients generated by the high imaging fields. At present, one can only speculate about the causes of these nuclear and cytoplasmic differences. In view of the later discussion in Part Three, it is very unlikely that this reflects different states of "mobility" of water in these environments, attractive

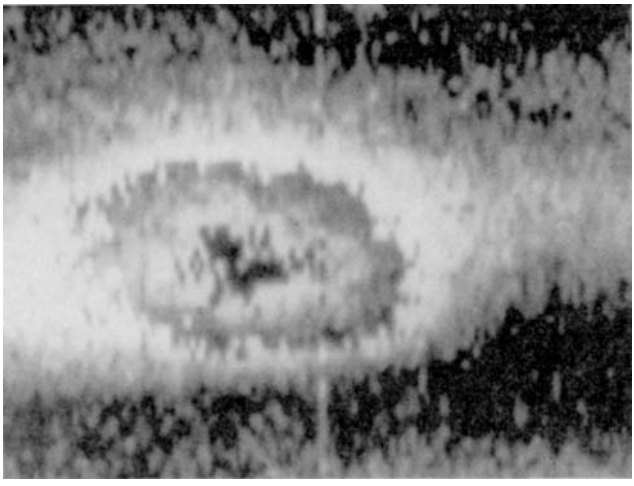

Figure 9.14. NMR microimage of the single-celled green alga *Micrasterias*. The image resolution is $6 \times 8 \times 12$ μm and was obtained in 3 h 38 min. The cell wall is evident as an oval ring of lower intensity. The central dark region is thought to arise from central organelles with short T_2 relaxation times. (From Ref. 87.)

as this concept may be. It is far more likely that water protons are relaxing by fast proton exchange with biopolymer protons and by diffusive exchange with a few water molecules of hydration found within the biopolymer structures. If so, the differences reflect the different composition and concentration of biopolymers in the subcellular compartments. Qualitative support for this interpretation comes from magnetization contrast imaging, which shows similar contrast to the transverse relaxation (90). It could also provide the explanation for the decrease in T_2 observed as the age and weight of the cell increase (91).

Clearly, the area of single-cell microimaging is still in its early days and many questions remain unanswered. Nevertheless, valuable complementary information about subcellular water compartmentation can be gleaned from nonspatially resolved relaxation and diffusion measurements, and it is to these topics that we turn in the next two chapters.

TABLE 9.4 T_1 and T_2 Relaxation Times and Water Diffusion Coefficients for the Nuclear and Cytoplasmic Compartments of a Single Neuron (*Aplysia californica* L7)

	Nucleus	Cytoplasm
T_1	1.9 ± 0.1	1.36 ± 0.15 s
T_2	78 ± 15 ms	29.2 ± 1.5 ms
D	1.5 ± 0.2 mm^2/s	0.28 ± 0.04 mm^2/s

Source: Ref. 88.

9.5 MICROSCOPIC TRANSPORT MODELS FOR CELLULAR TISSUE

In Chapter 3 we discussed a number of theoretical models for the macroscopic moisture gradients set up during the drying of plant tissue. These used a thermodynamic approach which essentially ignored the cellular microstructure of plant tissue and used quantities such as the effective moisture diffusivity. In this section we consider models of mass and heat transport that explicitly acknowledge the microstructure of cellular tissue.

Mattea et al. (326) suggested that plant tissue microstructure could be modeled as a two-dimensional collection of convex, irregular polygons (see Figure 9.15), because this resembles the actual picture of cellular tissues seen in optical micrographs. The formal mathematical definition of this geometry is two-dimensional Voronoi tessellation (325) and is illustrated in Figure 9.15. The cellular arrange-

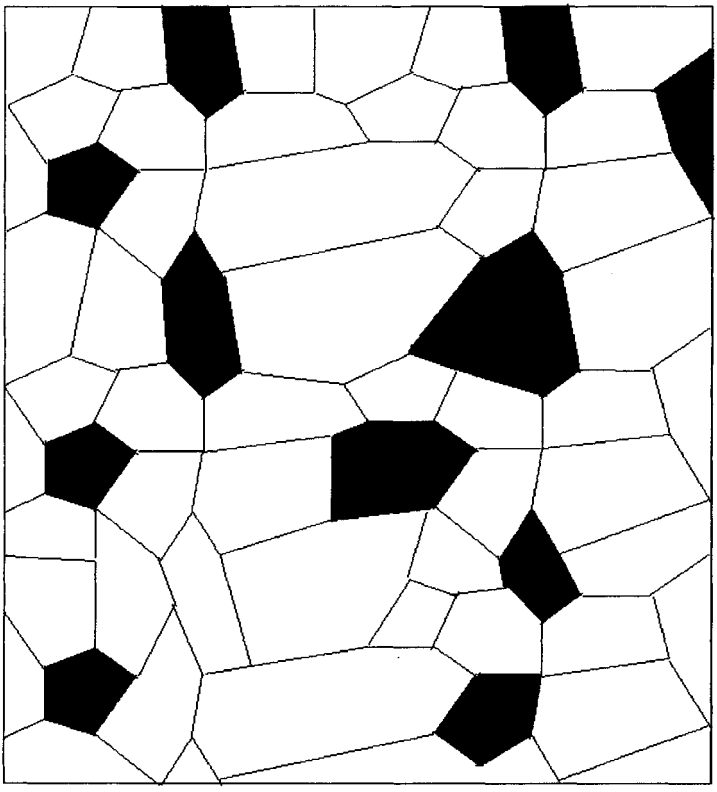

Figure 9.15. Voronoi tessellation of polygons representing cellular tissue. Shaded polygons are air-filled pores, others are cells. (From Ref. 326.)

ment is then defined by randomly selecting N polygons as cells and $N_{total} - N$ as pores (or intercellular gaps), subject to the condition that the fraction of the total area occupied by pores equals the tissue porosity, located so as to avoid oversized pore clusters. The initial work assumed that the tissue was uniformly dehydrated and set about calculating the dependence of the thermal conductivity on porosity. This was done using two different approaches. The first assumed that dehydration has the effect of converting some of the cell polygons into pores, with no change of geometry. The second assumed that dehydration removed water from the cells, causing them to shrink, while the polygons representing pores expand. Because each cell is supporting an internal pressure (turgor pressure), the configuration that minimizes the cell perimeter is chosen as the solution to the deformation process at each moisture content. As we shall see in Chapter 10, NMR relaxometry supports the shrinkage model rather than the substitution model, and a comparison of theoretical and experimental predictions confirms the superior nature of this assumption. The dependence of the thermal conductivity on water content was calculated for apple and pear tissue using a finite-element procedure (326) by assigning the thermal conductivity of air to all the pores and that of an equivalent glucose solution for the cells. The extension of this approach to nonequilibrium drying processes looks very promising, although this will require additional assumptions about the mechanism of cell water loss, including the diffusion of water between

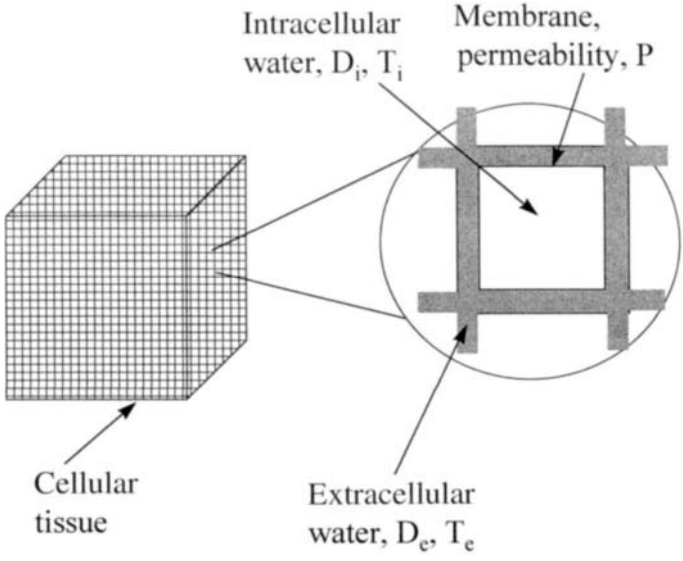

Figure 9.16. Lattice model of cellular tissue. A cell is represented by a box surrounded by a membrane of permeability P. Intracellular water has a diffusion coefficient D_i and transverse relaxation time T_i. The cells are in a cubic array. Extracellular water is characterized by D_e and T_e. (From Ref. 328.

cells through cell wall and membrane barriers. This "transport" aspect has been studied by Szafer et al. (328), who calculated the apparent water diffusion coefficient in tissue by explicitly acknowledging the existence of intra- and extracellular water compartments separated by a semipermeable membrane. In this case, however, the tissue was modeled as a periodic array of cuboid cells, as illustrated in Figure 9.16. A Monte Carlo method was then used to simulate the diffusion of water throughout the tissue. The apparent diffusion coefficient for both short and long diffusion times was calculated and compared with various limiting formulas. The authors were concerned primarily with understanding the changes observed in water diffusivity following ischemic insults to brain tissue (and observed with diffusion-weighted MRI). However, the approach will undoubtedly be of value in modeling processing changes in plant tissue. In Chapters 10 and 11 a Monte Carlo method is used on a yet smaller distance scale, to interpret water proton relaxation and diffusion inside isolated plant cells, where the focus is now on the exchange of water, by molecular diffusion, between subcellular plant cell organelles, such as the vacuole, the cytoplasm, and the cell wall region.

10

MICROSTRUCTURE AND RELAXOMETRY

10.1 INTRODUCTION

Chapter 9 ended with a discussion of single-cell microimaging using specially built high-resolution NMR microscopes and highlighted the difficulties of achieving resolutions of just a few microns. Imaging microstructure on this distance scale is obviously never going to be a routine procedure with k-space imaging, and we must look for alternative NMR protocols. In this chapter and the next we discuss water proton relaxometry and diffusometry. Somewhat surprisingly, these nonimaging NMR methods can reveal aspects of microstructure hidden to even the best NMR microscope. Knowledge of food microstructure is important because it affects macroscopic transport rates and food functionality, such as texture. It is also important for understanding how image contrast, especially relaxation-weighted contrast, is related to microstructure and water compartmentation because most processing operations are associated with microstructural changes and a microscopic redistribution of water and/or lipid. In this chapter we explore the relationship between water proton relaxation and microstructure.

10.2 WATER PROTON RELAXATION IN MICROSCOPICALLY HETEROGENOUS SYSTEMS

10.2.1 Bloch–Torrey Equations

Figure 10.1 shows a schematic of a system consisting of two microscopic compartments labeled with the subscripts 1 and 2. The compartments could represent any number of microporous food matrices, such as subcellular organelles in cellular

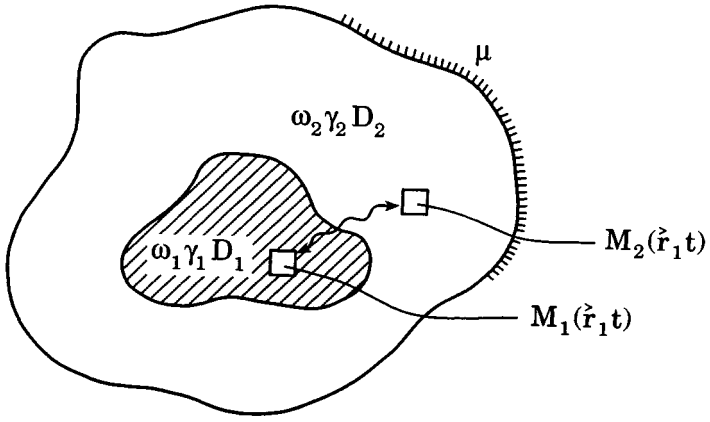

Figure 10.1. Schematic illustrating the relationship between relaxation and microstructure. The two microscopic compartments, labeled $i(i = 1,2)$, are characterized by different intrinsic resonance frequencies ω_i, relaxation rates γ_i, and self-diffusion coefficients D_i, and spins are free to diffuse between the compartments. The overall relaxation behavior is obtained by solving the Bloch–Torrey equations for the space-time evolution of the magnetization density, $M_i(\mathbf{r},t)$. Surface relaxation, characterized by a surface relaxation strength μ, often needs to be taken into account.

tissue or microscopic water-filled pores in a granular bed. Each compartment, i, is characterized by an intrinsic water proton resonance frequency ω_i, a relaxation rate γ_i for either longitudinal, transverse, or rotating-frame water proton magnetization, and a water self-diffusion coefficient, D_i. A discussion of the molecular factors determining the magnitude of the intrinsic parameters γ_i and D_i within each compartment is deferred to Part Three. For present purposes it is sufficient to assume that they are constants within each compartment. Using the formalism of nonequilibrium thermodynamics, each compartment can be spatially coarse-grained into voxels that are large compared to molecular dimensions but small compared to the dimensions of the compartments themselves. A voxel located at a point $\mathbf{r}$ will be associated with a magnetization density vector, $\mathbf{M}_i(\mathbf{r},t)$. Various situations can now be envisaged. If the two compartments are actually immiscible phases such as oil and water, there is no exchange of magnetization between compartments and the observed relaxation behavior will simply be the sum of the relaxation of the isolated phases, which in this example would give biexponential relaxation. This is also the case if the compartments can exchange molecules (such as water or solutes) but are of macroscopic dimensions so that diffusive exchange between compartments is extremely slow on the observational time scale of an NMR experiment, which is, at most, $5T_1$ or $5T_2$. In the other extreme of very fast diffusion between the phases, which can occur if the compartments are so small that the NMR measurement time scale is long compared to the diffusion time scale (roughly, r^2/D for a compartment of size r), the relaxation will become single exponential, with a

relaxation rate given by the weighted volume average of the two intrinsic relaxation rates. The interesting behavior occurs at intermediate exchange rates, because then the observed distribution of relaxation times will be sensitive to the morphology of the system and will, in general, be multiple exponential, characterized by an infinite hierarchy of relaxation times, even in a simple two-compartment system (134).

The relaxation behavior of a multicompartment system such as that in Figure 10.1 can be calculated by solving the Bloch–Torrey equations (234) for the time evolution of the magnetization density. The transverse relaxation is most conveniently calculated by defining the complex transverse magnetization densities, $M^+(\mathbf{r},t)$ and $M^-(\mathbf{r},t)$. $M^+(\mathbf{r},t)$ is the complex sum $M_x(\mathbf{r},t) + iM_y(\mathbf{r},t)$ in a voxel located at $\mathbf{r}$, and $M^-(\mathbf{r},t)$ is its complex conjugate, $M_x(\mathbf{r},t) - iM_y(\mathbf{r},t)$. The space-time evolution of the transverse magnetization density is then described by the Bloch–Torrey equations within each compartment, i

$$\frac{\partial M_i^+}{\partial t} = -i\omega_i M_i^+ - \gamma_i M_i^+ + D_i \nabla^2 M_i^+ \qquad i = 1, 2 \tag{10.1}$$

and there is a corresponding complex conjugate equation for M_i^-. These equations are best envisaged with a vectorial representation of the magnetization, whereby each volume element is associated with a vector representing its complex magnetization density. The term in ω_i describes precession of the vector at the resonance frequency ω_i. The second term describes the decrease in the length of the magnetization density vector at a rate γ_i; the third term describes the diffusion of the vectors between voxels. These coupled equations must be solved subject to initial conditions appropriate to the NMR pulse sequence. For example, a hard 90° pulse excites x-magnetization in all compartments, but selective excitation experiments can be designed so that transverse (or longitudinal) magnetization is excited in only one type of compartment. For example, the Goldman–Shen pulse sequence can be used to excite magnetization in the compartment with the longest transverse relaxation time. This sequence is discussed in detail later in the chapter. The Bloch–Torrey equations must also be solved with spatial boundary conditions appropriate to the compartment size and geometry, and it is in this way that microstructure affects the relaxation behavior. For solid boundaries that act as a surface relaxation sink, the spatial boundary condition states the equality of the flux of magnetization normal to the surface with the rate of destruction of magnetization on the surface

$$\mathbf{n} \cdot \mathbf{D} \cdot \nabla M = -\mu M \cdot \mathbf{n} \tag{10.2}$$

where $\mathbf{n}$ is the unit vector normal to the surface and μ is defined as the surface relaxation strength. The boundary condition for unhindered diffusion between two neighboring compartments, i and j, such as that between a gel and water phase, is simply the equality of fluxes across the interface

$$\mathbf{D}_i \cdot \nabla M_i = \mathbf{D}_j \cdot \nabla M_j \tag{10.3}$$

Where a semipermeable lipid membrane separates compartments, as in cellular tissue, one can either attempt to treat the membrane as an additional, albeit very thin compartment, and use equation (10.3) at each interface, or alternatively, the boundary condition at a boundary at $z = a$ can be written in one dimension as

$$D_j\left(\frac{\partial M_j}{\partial z}\right)_{z=a} = P[M_2(a,t) - M_1(a,t)] \tag{10.4}$$

where P is the membrane permeability, given as $D_m K/L$, where D_m is the diffusion coefficient in the membrane, L the membrane thickness, and K the equilibrium distribution coefficient for the spins. This shows that under suitable circumstances, NMR relaxometry can be used to determine membrane permeabilities.

Analytic solutions of the Bloch–Torrey equations with one or other of the spatial boundary conditions have been derived for the simplest morphologies, such as for diffusion between two adjacent lamellar phases (134) and for single lamellar, cylindrical, and spherical compartments where relaxation occurs by diffusion to the compartment boundary, which acts as a surface relaxation sink of strength μ (135). Some of the more important limiting cases are discussed in the next few sections. In more complicated morphologies the Bloch-Torrey equations must be solved by numerical methods, such as finite-element or Monte Carlo techniques (205,208). The Monte Carlo method is worth further comment because it has hardly begun to be exploited in relaxation and diffusion simulations, yet has enormous computational flexibility. In the Monte Carlo method the microstructure is represented by some idealized morphology, such as packed spheres, cylinders, or lamellar regions inside a cube (see Figure 10.2). The space inside the cube is then coarse-grained in N^3 volume elements which are small compared to the distance scale of the microstructure but large compared to molecular distances. Magnetization density vectors are then randomly distributed over the voxels and assigned a resonance frequency ω_i, relaxation rate γ_i, and diffusion coefficient D_i corresponding to their position. Initially, the effect of a single, hard 90° pulse is simulated by assigning to each magnetization vector an initial x-magnetization equal to the inverse of the number of vectors while assuming that the initial y-magnetization is zero. The subsequent time evolution is determined by giving every magnetization vector a probability p of jumping randomly to a neighboring volume element in each of the three Cartesian directions in a time step Δt with zero probability of jumping outside the cube. The jump probability p is calculated from the diffusion coefficient as $p = D_i \Delta t/(\Delta x)^2$, where Δt is the incremental time step and Δx is the volume element length. The length of each vector decays exponentially with the relaxation rate γ_i and precesses with frequency ω_i corresponding to its position. The new total magnetization after time Δt is obtained by summing over all vectors, taking into account their precession and relaxation. The effects of various pulse sequences can be introduced directly as phase changes on the individual magnetization vectors during the simulation. For example, the effect of a hard 180°_x pulse applied at a time τ is to reverse the y-direction of all magnetization vectors. External applied gradient pulses, chemical exchange, and surface relaxation can all be simulated by appropriate changes in the basic model.

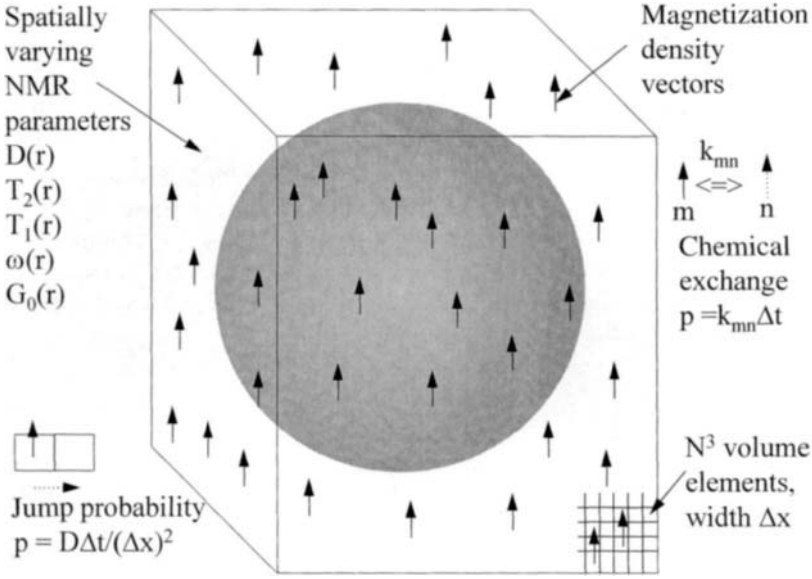

Figure 10.2. Monte Carlo simulation for relating relaxation to microstructure. A cube is divided into N^3 volume elements and magnetization density vectors are distributed randomly between them. The morphology is defined and NMR parameters assigned to the compartments. Magnetization density vectors then diffuse between voxels with a probability $D_i\Delta t/(\Delta x)^2$ and can chemically exchange with a probability $k_{mn}\ \Delta t$. In this illustration the morphology is simply a spherical region inside the cube, with exchange between the regions inside and outside the sphere.

The effect of diffusion in limiting the resolution in NMR microscopy has been analyzed with Monte Carlo simulation (252). This was done by considering the effect of water diffusion between two neighboring microscopic compartments on a one-dimensional image acquired either with a Hahn spin-echo pulse sequence or a multiple-echo imaging sequence. It was shown that diffusion between adjacent microscopic regions separated by semipermeable interfaces or membranes could limit image resolution to a few tens of microns by averaging the relaxation contrast differences between the compartments. The diffusion also has the effect of partly averaging the frequency differences set up by applied field gradients in the image acquisition step (252).

The Monte Carlo method has also been used to calculate echo-decay amplitudes in the CPMG sequence and relate the transverse relaxation components to microstructure (208). When comparing the numerically simulated echo decay envelopes for these sequences with experiment, it is important to analyze the time decay of the volume-integrated magnetization, predicted by these numerical methods, with the same relaxation-time deconvolution software as used for the experimental

data. It then does not particularly matter whether this is by maximum entropy methods (MEM), constrained deconvolution, least squares methods, or by some other method, because only differences between theory and experiment are being compared. The author prefers to use the CONTIN software package (235), based on constrained deconvolution, since this produces a continuous distribution of relaxation times resembling a one-dimensional spectrum. Subtleties such as shoulders and peak distortions are then easy to pick out. Of the many possible applications of NMR relaxometry in microstructural studies, we will select a few examples where a comparison of the theoretical and experimental relaxation behavior in spatially heterogeneous systems can give both morphological information and information about the diffusive exchange rate.

10.2.2 Saturated High-Permeability Systems

A randomly packed bed of Sephadex beads is a model two-compartment system of this type. Sephadex consists of granules of chemically cross-linked polysaccharide (dextran) chains that swell up in water to form microspheres of dextran gel which are freely permeable to water. The two compartments therefore consist of the water located outside and inside the microspheres, and boundary condition (10.3) applies. Sephadex is a particularly good model system for testing relaxation theory because the microsphere radius can be varied systematically and the intrinsic relaxation time inside the microspheres can be altered by changing the gel concentration or, in the case of transverse relaxation, by changing the pulse spacing in the CPMG sequence (see Chapter 12). Figure 10.3 shows a comparison of the theoretical and experimental multiple exponential relaxation behavior for water-saturated randomly packed beds of Sephadex of differing radii but having the same dextran concentration. The Monte Carlo method, based on a single Sephadex microsphere centrally located inside a cube, was used for the theoretical predictions, and a simple least squares multiple exponential deconvolution method was used to extract the relaxation times. Increasing the Sephadex sphere radius increases the diffusion distance between water in the compartments inside and outside the spheres. This slows down the diffusive exchange and leads to more pronounced multiple exponential relaxation (see Figure 10.3).

It is less obvious why the relaxation in the largest sphere category is triple exponential even though there are only two aqueous compartments. One possibility is that the random packing of the spheres creates intersphere pores of various shape and size categories associated with different exchange rates and effective relaxation times. Alternatively, the intermediate relaxation-time component could arise from water in the interfacial region that cannot reach the center of the sphere or completely exchange with the bulk water outside the spheres.

The dependence of the multiple exponential transverse relaxation on CPMG pulse spacing is also interesting because the intrinsic relaxation rate inside the Sephadex microsphere shows a dispersion as the pulse spacing is varied. That is, a plot of transverse relaxation rate against CPMG pulsing frequency shows a strong frequency dispersion (see Figure 10.4). This effect is analyzed quantitatively in

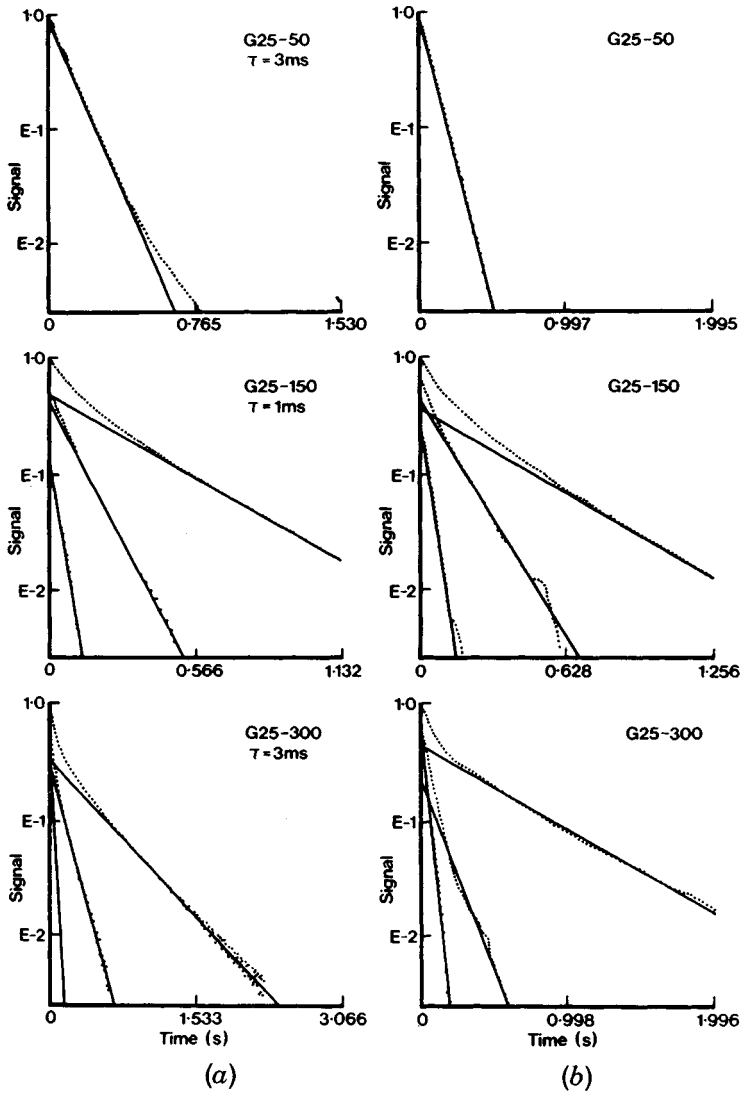

Figure 10.3. Gradual transition from the fast to slow exchange regimes in a water-saturated randomly packed bed of Sephadex G25 microspheres as the sphere radius increases from 25 μm (top), 90 μm (middle), to 150 μm (bottom row). The left-hand column shows the experimental CPMG echo-decay envelopes on a log scale. The right-hand column shows the theoretical predictions based on solution of the Bloch–Torrey equations. Data acquired with CPMG 90 to 180° pulse spacings of 1 or 3 ms (as indicated) at a spectrometer frequency of 300 MHz. (From Ref. 205.)

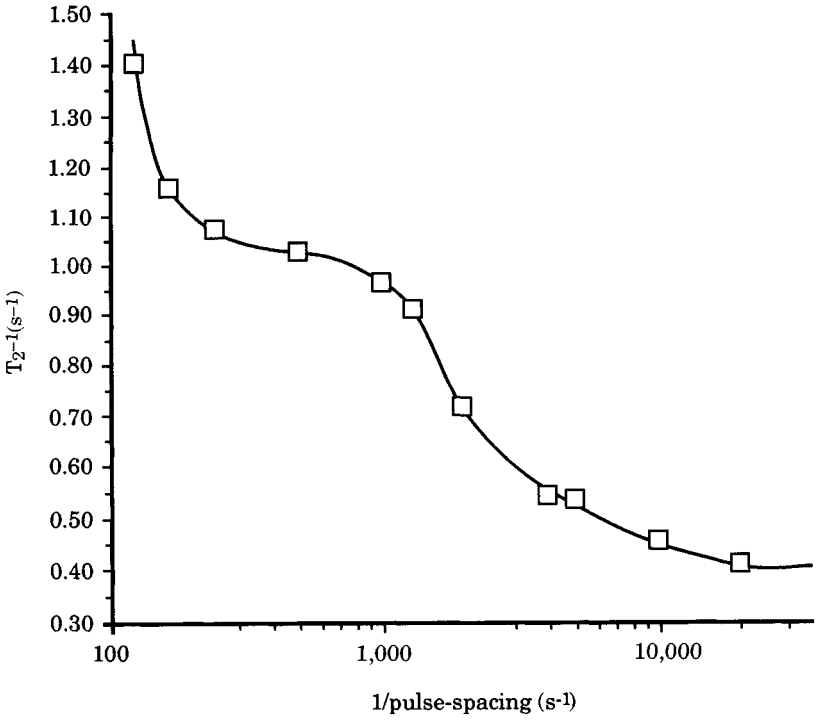

Figure 10.4. Transverse relaxation double dispersion for a randomly packed bed of Sephadex G200-50 microspheres measured at 100 MHz at 298 K. The *x*-axis shows the 90 to 180° CPMG pulsing rate. The inflection at high pulsing rates arises from proton exchange between water and Sephadex hydroxyl protons. The increase at slow pulsing rates originates from diffusive exchange between water compartments inside and outside the microspheres. (From Ref. 221.)

Chapter 12, but qualitatively, it originates from the dephasing of water proton transverse magnetization due to the fast exchange of water protons with Sephadex hydroxyl protons, which differ slightly in resonance frequency. The midpoint on the dispersion curve corresponds to the mean proton exchange rate. Pulsing at a frequency faster than the proton exchange rate removes the dephasing effect by continually refocusing the transverse magnetization, resulting in a decrease in the transverse relaxation rate. Pulsing slower than the proton exchange rate causes increased dephasing between refocusing pulses and gives an increased transverse relaxation rate. In a microstructured system there can also be additional dephasing because of the exchange of water molecules between microscopic compartments whenever the compartments differ slightly in resonance frequency. Analogously to a proton chemical exchange dispersion, there can therefore be a diffusive exchange dispersion. Figure 10.4 shows an example of this in the water proton transverse relaxation data for a randomly packed bed of Sephadex G200-50, which because of fast diffusive exchange and a small microsphere size, gives essentially single expo-

nential relaxation (208). The first inflection, between reciprocal CPMG pulse spacings of 10^3 and 10^4 s^{-1}, arises from proton exchange at a rate of about 2.5×10^3 s^{-1} and is analyzed quantitatively in Part Three. The change in relaxation rate between reciprocal pulse spacings of 10^2 and 10^3 s^{-1} arises from fast diffusive exchange between the inside and outside water compartments, which differ slightly in resonance frequency. Here the effective, diffusive exchange rate D/R^2, where R is the mean Sephadex sphere radius, is only about 6.25 s^{-1}. Because this is three orders of magnitude slower than the chemical exchange rate, the diffusive dispersion is well separated from the proton exchange dispersion (see Figure 10.4). Despite the complexity of combined chemical and diffusive exchange, Monte Carlo simulation has been used to reproduce this complicated relaxation behavior. Figure 10.5 shows the Monte Carlo simulated double dispersion arising from combined chemical and diffusive exchange.

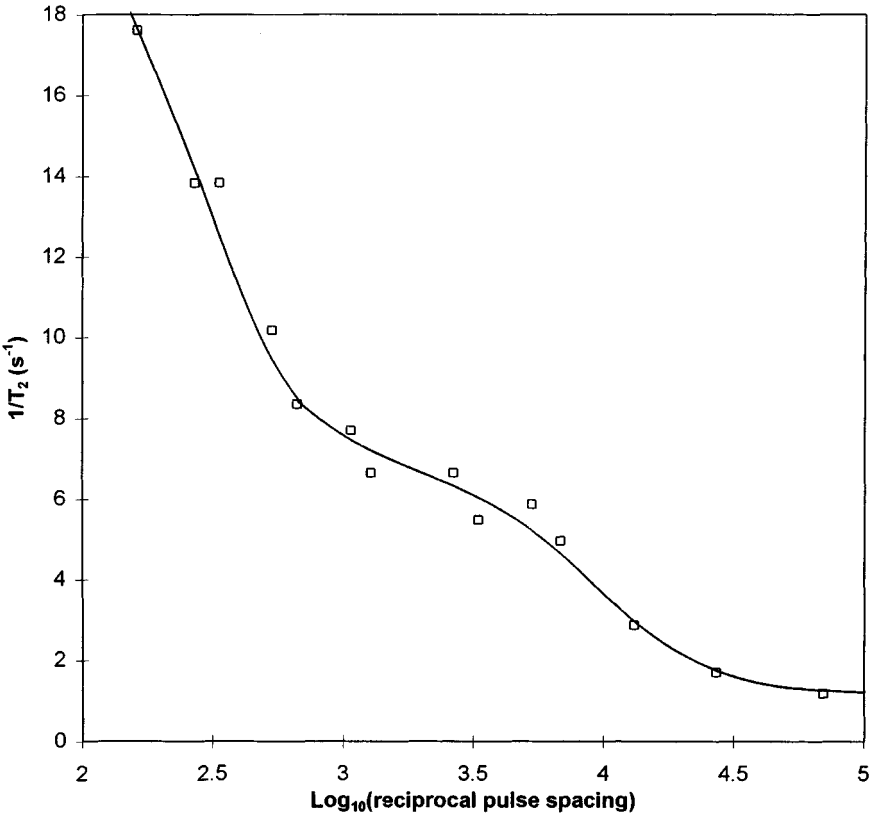

Figure 10.5. Double dispersion predicted by Monte Carlo simulation (Figure 10.2). A lamellar morphology was assumed whereby a 40-μm-wide cube was divided into two equal halves. Proton exchange between two equal populations occurred in only one-half of the cube. Parameter values can be found in Ref. 205.

Although for didactic purposes we have focused on Sephadex beds, similar relaxation phenomena are expected to arise with many other microporous systems. Multiple exponential water proton transverse relaxation is indicative of a multicompartment system, and information on the number and size of the compartments can be obtained by analyzing the relaxation data. A dependence of the component relaxation rates on CPMG pulsing rate shows that there are populations of water protons differing in resonance frequency, either because of chemical shift differences or because there are local induced field gradients in the system. In both cases a detailed analysis of the frequency dependence gives valuable information about the dynamical state of the system on the CPMG pulsing time scale of 0.1 to 100 ms. We consider this in greater detail in the next section.

The dependence of transverse relaxation time on pulse spacing can be used to manipulate image contrast. Figure 10.6 shows how the transverse relaxation-time-weighted contrast in the image of a courgette can be changed simply by reducing the CPMG pulse spacing while keeping the total echo time (*TE*) constant. This was achieved by increasing the number of refocusing 180° pulses between the initial 90° excitation pulse and the echo, as indicated in Figure 10.7 (215).

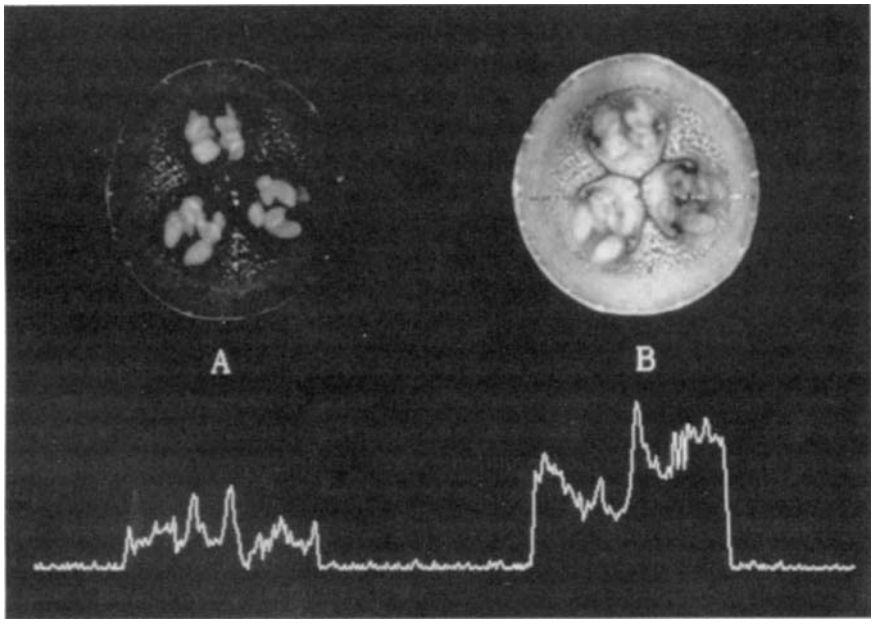

Figure 10.6. (*A*) 256 × 256 images of fresh courgette acquired with pulse sequence A in Figure 10.7. $TE = 100$ ms, $TR = 6$ s, $\tau = 50$ ms. (*B*) 256 × 256 image of fresh courgette acquired using pulse sequence B in Figure 10.7. $TE = 100$ ms, $\tau = 1.1$ ms, $\delta = 5$ ms. Traces were taken through the center of each image. (From Ref. 215.)

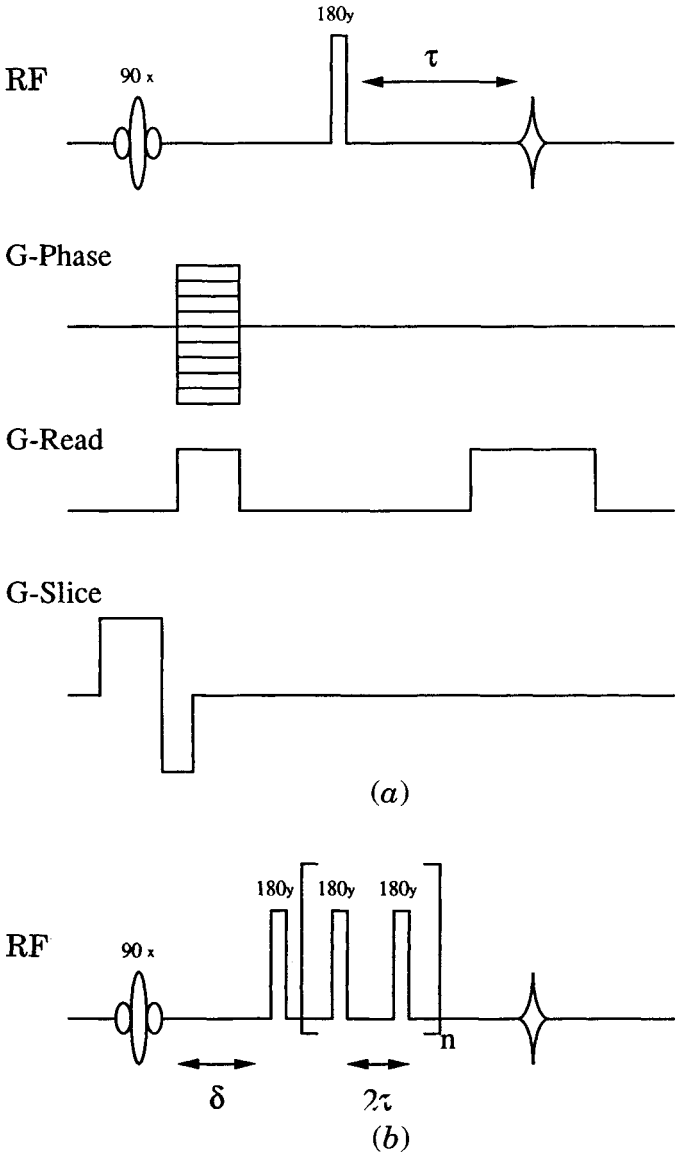

Figure 10.7. Spin-warp imaging pulse sequences used to acquire the images in Figure 10.6. Sequence B differs from A in the inclusion of a train of hard 180° spin-echo refocusing pulses which effectively reduces the T_2. (From Ref. 215.)

10.2.3 Unsaturated High-Permeability Systems

So far we have discussed only water-saturated beds of randomly packed Sephadex microspheres. If the initially water-saturated bed is progressively dried, osmotic and capillary forces dictate that air first replaces the water outside the microspheres, and only after all external water has been removed will water begin to be removed from the gel inside the microspheres and cause sphere shrinkage. The associated changes in the water proton transverse relaxation-time distributions for a bed of Sephadex G25-300 (in this case extracted with the CONTIN constrained deconvolution method) are shown in Figure 10.8 and agree reasonably well with the distributions calculated with the Bloch–Torrey equations for combined chemical and diffusive exchange (221). A similar approach can be used to follow the microscopic redistribution of water and air during the drying of microporous food materials. As part of an industrially sponsored project, the author has even used the relaxation methodology to follow microscopic water redistribution during the drying of compressed horse-feed pellets, although it is stretching a point to describe this material as a typical food.

Changes in microstructure and in the air–water distribution in microporous foods can greatly complicate the interpretation of quantitative imaging studies during drying and rehydration. The conventional imaging approach assumes linear proportionality between the initial magnetization, $M(0)$, and the water content, and determines $M(0)$ with a spin-echo imaging sequence by extrapolating a log plot of the echo amplitude against echo time TE to zero echo times. Unfortunately, this simple protocol can break down with microporous samples if there is sample shrinkage and changes in packing density. For example, drying a bed of Sephadex microspheres first removes external water without sample shrinkage and results in bead shrinkage once all external water is removed. Bead shrinkage means that more microspheres can be packed into the imaging voxel, which partly compensates for the loss of signal intensity due to water loss. Moreover, the microspheres tend to aggregate in clumps at low water contents and this alters the packing density. The result of these factors is a highly nonlinear relationship between $M(0)$ and water content which cannot be used for imaging moisture distributions (224). The alternative is to exploit the relationship between water proton transverse relaxation time and water content to image the water distribution in the bed. However, the conventional way of doing this, by measuring an effective single-exponential transverse relaxation time by recording echo amplitude as the echo time, TE, is increased in a spin-echo imaging sequence, will also be an unreliable measure of water content, because the true transverse relaxation changes from multiple to single exponential relaxation and attenuation of the echo amplitude by diffusion in local susceptibility-generated field gradient inhomogeneities becomes more severe as more air enters the food and increases porosity. For this reason it is often better to obtain true T_2-weighted maps using a CPMG preparation sequence before the imaging sequence (see Chapter 1) and then convert the T_2 map to a moisture map with a calibration curve determined by applying the CPMG sequence to spatially homogeneous samples (224).

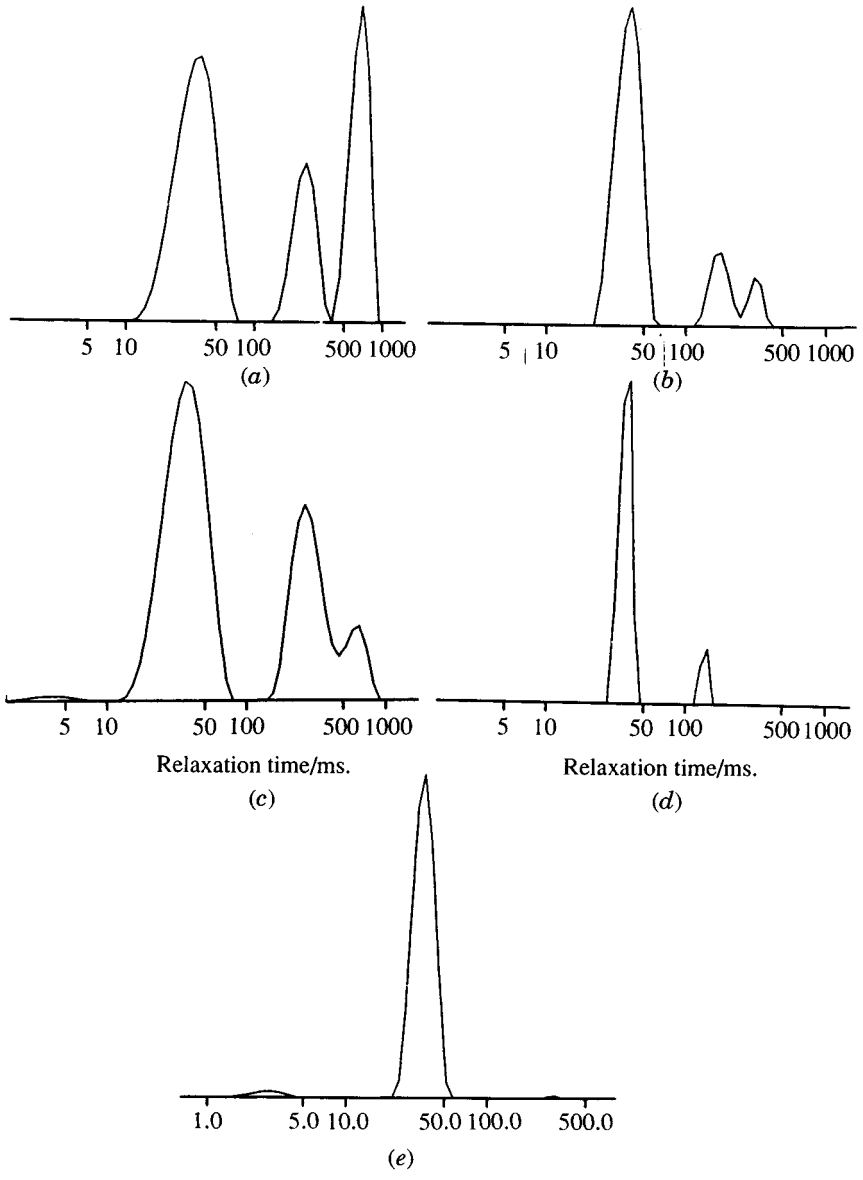

Figure 10.8. Distributions of water proton transverse relaxation times for a randomly packed bed of Sephadex G25-300 microspheres as a function of water content. Data acquired at 300 MHz with a CPMG 90 to 180° pulse spacing of 200 μs. Echo-decay envelopes were analyzed with the CONTIN constrained deconvolution method. Water contents correspond to (*A*) $W = 4$ (saturated); (*B*) $W = 3.5$; (*C*) $W = 3.0$; (*D*) $W = 2.5$. (From Ref. 221.)

As we have seen, ice has a very short transverse proton relaxation time of a few tens of microseconds, so that on the millisecond relaxation time scale associated with the CPMG or inversion-recovery pulse sequences, freezing a particular microscopic water compartment removes the signal from that compartment. This is associated with the disappearance of the corresponding relaxation-time peak in the CONTIN distribution. The temperature dependence of the relaxation-time distribution can therefore be used to monitor both the amount, and microscopic distribution, of unfrozen water, air, and ice in a partly frozen food matrix. This idea has been applied to the Sephadex microsphere beds and used to monitor the amount of ice and unfrozen water inside the microspheres as a function of temperature (222). Figure 10.9 shows how freezing at 272 K freezes all water outside the Sephadex microspheres but not that inside, but that further cooling to 248 K freezes even water inside the microsphere, apart from residual nonfrozen water associated with the dextran chains and having a short relaxation time of about 1 to 2 ms. Note that the CONTIN plots in Figure 10.9 have arbitrary vertical scales determined by fixing the

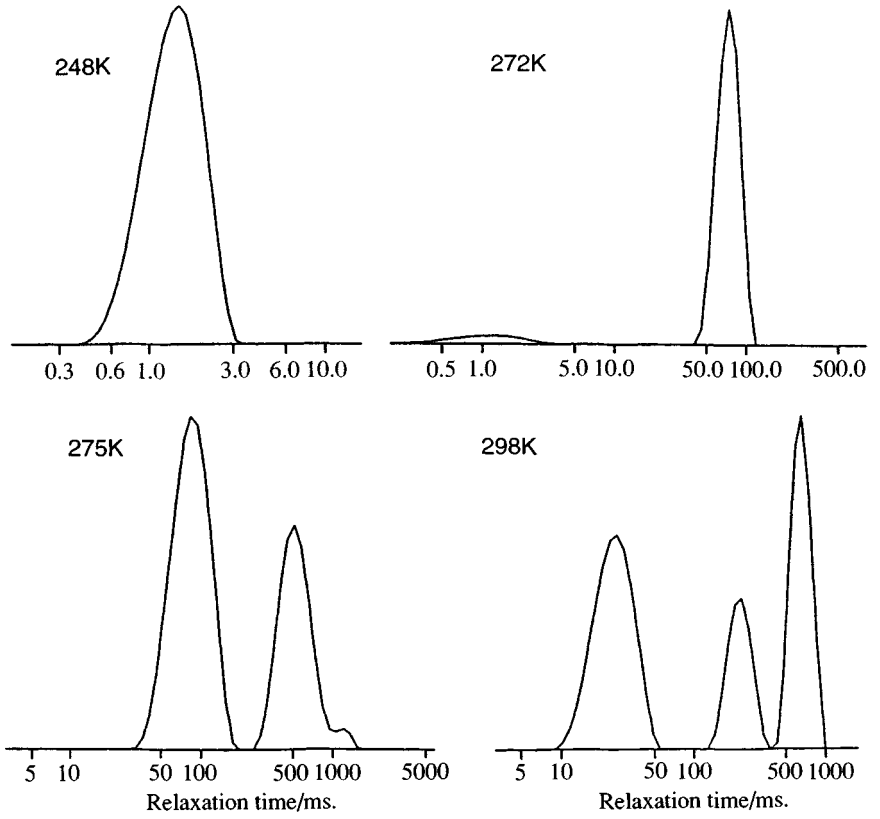

Figure 10.9. Representative water proton transverse relaxation dispersions in saturated beds of Sephadex G25-300.

maximum intensity to the top of the plot. By comparing the relaxation times of Sephadex beds where ice and air surround water-filled Sephadex microspheres, it has been possible to show that the ice–water interface acts as a significant source of surface relaxation for water proton transverse magnetization (222). The effect of surface relaxation sinks is considered in the next section.

10.2.4 Saturated Low-Permeability Systems

Another type of relaxation behavior arises when one or more of the phases is solid and has a surface that acts as a relaxation sink for water proton magnetization. Equation (10.2) defines the boundary condition for this class of system of which water-saturated granular beds, porous glasses, sandstones, and partly frozen materials are representative examples. The same theory applies to the relaxation of nonaqueous solvents in freeze-dried food matrices, provided that the solvent does not cause collapse of the food matrix. Because solvent proton relaxation now proceeds by diffusion to a solid surface, larger liquid-filled pores are associated with longer relaxation times than smaller liquid-filled pores, so that the observed multiple exponential relaxation reflects the pore size distribution and the ease with which liquid in one pore can diffuse through connecting throats or channels into neighboring pores (the *pore connectivity*). In principle, fitting the observed relaxation-time distribution with solutions to the Bloch–Torrey equations can give the pore size distribution and the pore connectivity. The major problem is realistically modeling the complex three-dimensional morphology of a randomly packed bed or irregularly shaped particles or pores. Various approaches have been used to analyze this problem.

The simplest approach is to neglect pore connectivity and regard the pores as isolated liquid-filled spheres. This is an attractive option because analytic solutions to the Bloch–Torrey equations for water diffusing in spherical pores of radius R, characterized by a surface relaxation strength μ, have been presented in a seminal paper by Brownstein and Tarr (135). These authors also presented solutions for cylindrical and lamellar-shaped pores. The solutions are in the form of an infinite series of relaxation–diffusion modes, each mode being associated with a characteristic transverse relaxation time. In general, therefore, a single water-filled pore is associated with an infinite number of relaxation times, but the multiple exponential character becomes prominent only in the slow-diffusion limit, when the rate-limiting step is diffusion of the water to the pore walls. Even then, the higher-order relaxation terms contribute less than 20% of the decay and can be ignored for many practical purposes. The expressions for two limiting cases are especially simple. When the surface is a strong relaxation sink, diffusion to the surface is the rate-limiting step, so we can write

$$M(t) = M_0 \exp\left(\frac{-Dt}{R^2}\right) \tag{10.5}$$

In the opposite extreme, the rate-limiting step is relaxation at the surface, so the decay depends linearly on the surface-to-volume ratio, S/V

$$M(t) = M_0 \exp\left(-\mu t \frac{S}{V}\right) \tag{10.6}$$

where μ is the surface relaxation strength. In principle, equation (10.6) provides a means of determining the ratio S/V, but the difficulty is the unknown nature of the surface relaxation strength. In Chapter 11 we shall see how a combination of relaxation and diffusion measurement may provide a way around this difficult problem. Using the Brownstein–Tarr formalism, Davis and Packer (137) have developed a numerical method for rapidly converting the continuous distribution of relaxation times into the corresponding distribution of pore sizes. This was applied to the determination of pore size distributions in porous sandstones. In principle, the same approach could be used to determine pore size distributions in porous freeze-dried foods, using organic solvents rather than water.

The assumption that all pores are magnetically isolated is not always valid, especially when the diffusion-time scale R^2/D is longer than the relaxation-time scale μ/R. Analytic solutions to the Bloch–Torrey equations have been derived for diffusion between two neighboring lamellar-shaped pores (134), but this fails to treat a pore size distribution. McCall et al. (259) have approached this complicated problem by assuming that each pore is in the fast diffusion limit and then applying perturbation theory, effective-medium theory, and matrix diagonalization methods to explore the effects of interpore exchange on the relaxation-time distributions. The approach gave quantitative predictions in terms of the interpore coupling rate ω_c, defined as the ratio $S_t D/Vl$, where S_t is the cross-sectional area of the throats connecting the pores, D the water diffusion coefficient, V the mean pore volume, and l the mean interpore distance. The effects of increasing the interpore coupling rate on the relaxation-time distributions were calculated and in many ways resembled the effects of increasing chemical exchange averaging of spectral peaks in the frequency domain. Thus a very fast interpore exchange rate collapsed the multiple-exponential relaxation-time spectrum to a single narrow peak (259). An alternative approach to modeling the effects of pore connectivity and incorporating a pore size distribution is to simplify the geometry by mapping it onto a one-dimensional problem, as illustrated in Figure 10.10. The pores are then characterized by a width l_i with a distribution $P(l)$ connected by throats. For simplicity the throats are assumed to have the same mean size δ and a self-diffusion coefficient D_t. Because δ is constant, D_t effectively controls the pore connectivity and in this model can be taken to define it. Surface relaxation is described within the one-dimensional model by assigning a relaxation rate γ_t to the throats such that the surface relaxation strength μ is $\delta(\gamma_t - \gamma_w)$. This *unit-cell model* of relaxation and diffusion was used to analyze the multiple-exponential relaxation observed in a model system consisting of a water-saturated bed of randomly packed silica particles (218). In this system the silica surface behaves as a powerful relaxation sink because of fast proton exchange between water and silanol (Si—OH) protons. Because the silanol protons are in a rigid matrix they have a short transverse, a long longitudinal relaxation time, and a

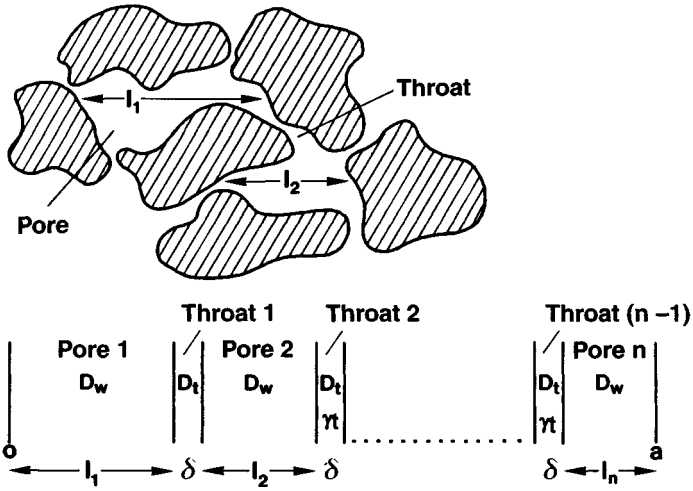

Figure 10.10. Illustrative cross section through a randomly packed bed of water-impenetrable particles showing pores and throats. The one-dimensional model corresponding to this complex morphology is also shown. (From Ref. 218.)

frequency-dependent rotating-frame relaxation rate. The effect of varying the surface relaxation strength μ can therefore be investigated by comparing transverse, longitudinal, and rotating-frame relaxation at various frequencies. The results for a silica bed comprising coarse particles of size 130 to 250 μm is shown in Figure 10.11, where it compares favorably with the predictions of the unit-cell model for a pore connectivity D_t of 10^{-6} cm ^{2}/s.

A similar approach has been used to investigate pore connectivity and microstructure in water-saturated randomly packed beds of monodisperse glass microspheres as the sphere radius is varied. Figure 10.12 shows the water proton transverse relaxation distributions for various glass microsphere radii. There are a number of noteworthy features in these distributions. First is the observation of four relaxation-time peaks with the 402-, 200-, and 103-μm bead sizes, which implies the existence of four different pore size categories in these beds. This is surprising since this does not agree with computer simulations of the pore size distribution, where the pore size is defined as the radius of the largest sphere that can be accommodated inside the pore (236) and which predict a continuous distribution of pore sizes (and associated relaxation times), as shown by the hatched distribution in Figure 10.14. The explanation of this discrepancy lies in the pore geometry and susceptibility-induced local field gradients. The pores in a randomly packed bed of spheres are not spherical but consist of distorted octahedra, tetrahedra, and triangles having six, four, and three "corners," respectively. In a static magnetic field, highly inhomogeneous field gradients are induced within each pore, and diffusion through these local distorted gradients is a source of dephasing, in other words, of transverse relaxation. The pores are therefore distinguished on the basis of their size and geometry. The longest relaxation-time peak corresponds to the distorted octahedral pores, the middle one to the distorted tetrahedral pores, and the third peak to the

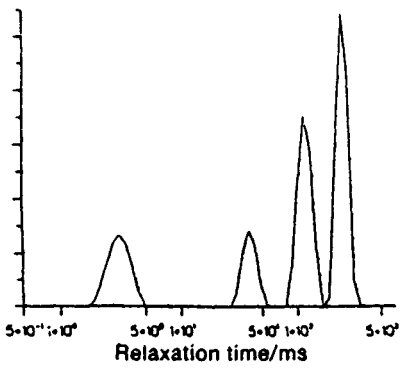

(*a*)

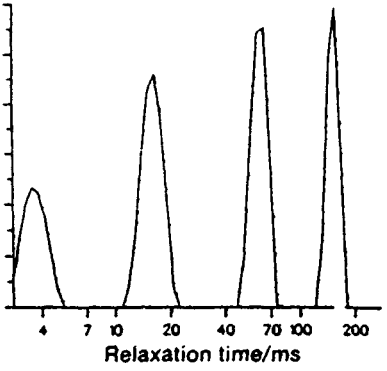

(*d*)

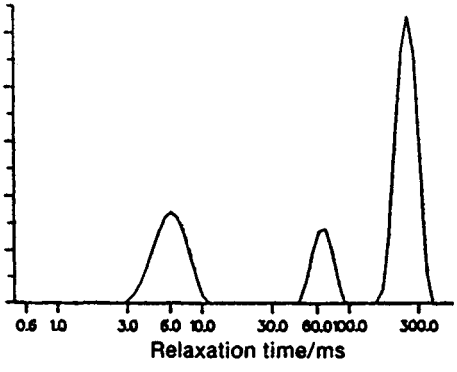

(*b*)

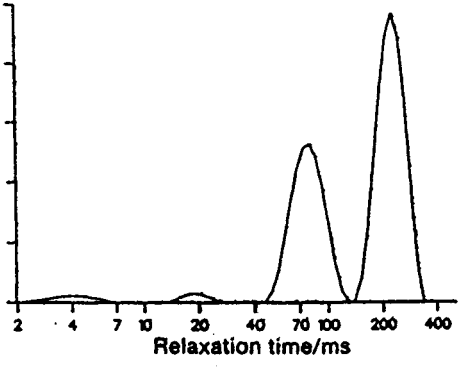

(*e*)

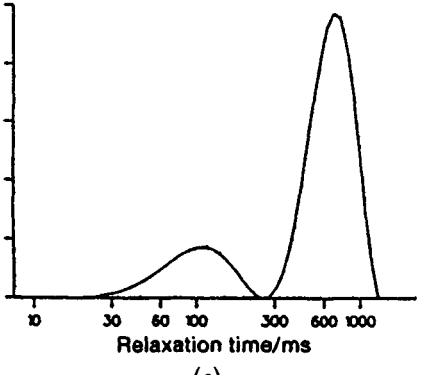

(*c*)

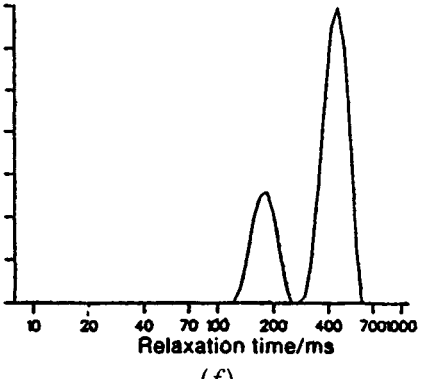

(*f*)

Figure 10.11. Comparison of the experimental (left column) and theoretical (right column) relaxation distributions for a saturated packed bed of coarse silica. (*a*) and (*d*) Transverse relaxation; (*b*) and (*e*) rotating-frame ($T_{1\rho}$) relaxation-time distribution at $\omega_1 = 5.32$ kHz; (*c*) and (*f*) longitudinal relaxation at 100 MHz. Theoretical results were based on the unit-cell model in Figure 10.10 with a pore connectivity D_t of 10^{-6} cm^2/s, with $\gamma_t =$ (*d*) 3400 s^{-1}, (*e*) 150 s^{-1}, and (*f*) 30 s^{-1}. (From Ref. 218.)

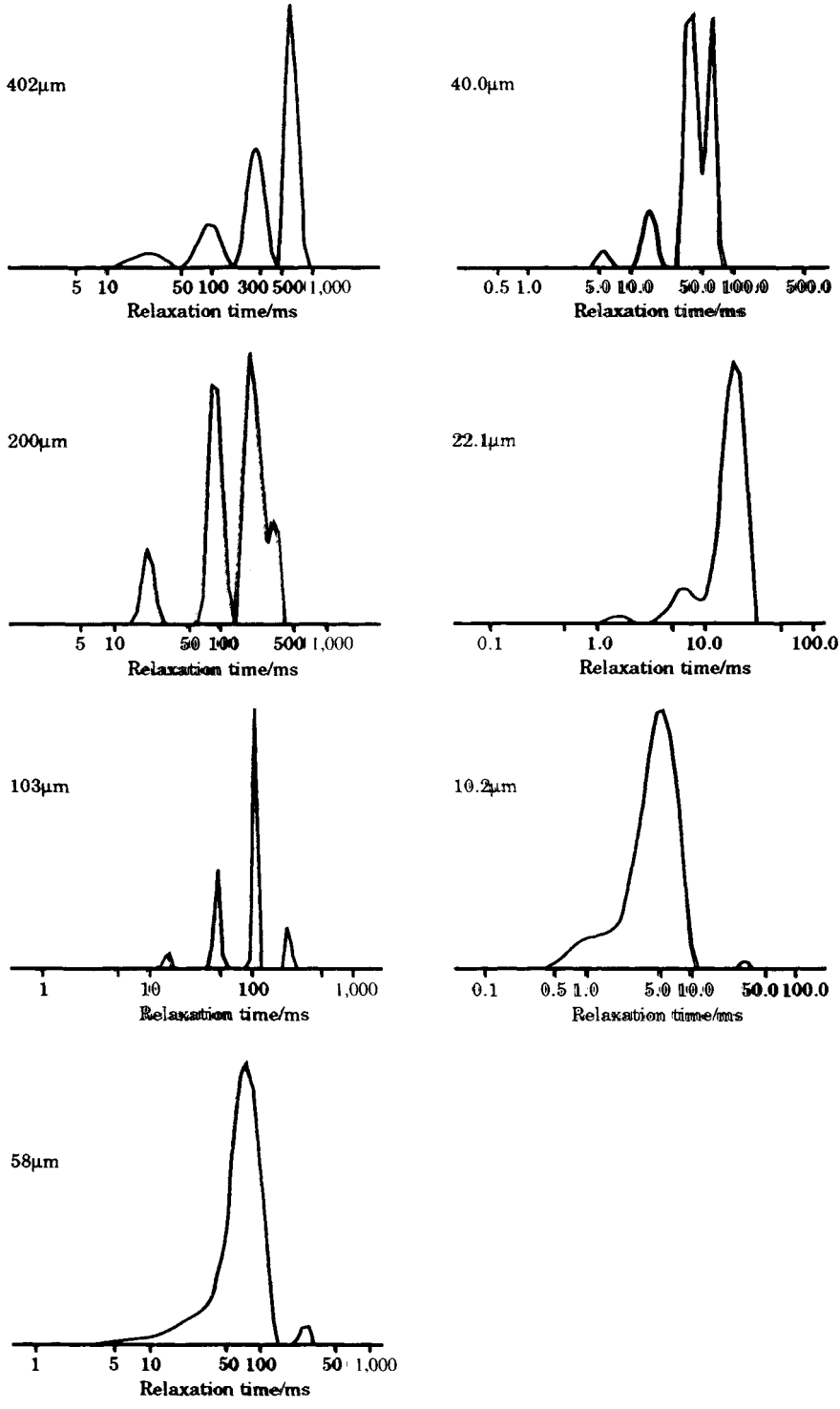

Figure 10.12. Experimental transverse relaxation distributions for water in randomly packed saturated glass microsphere beds having the monodisperse sphere diameters indicated. (From Ref. 216.)

small triangular pores. The origin of the fourth and shortest relaxation peak is still uncertain, but it could arise from higher-order diffusive modes or from relaxation of water in the edges formed by two touching spheres. Because the induced geometry-dependent field gradients increase with increasing external field strength, relaxation distributions measured at low resonance frequencies such as 20 MHz do not distinguish between the pores, and the CONTIN transverse relaxation times show only a single broad featureless peak (see Figure 10.13). There is therefore an advantage to

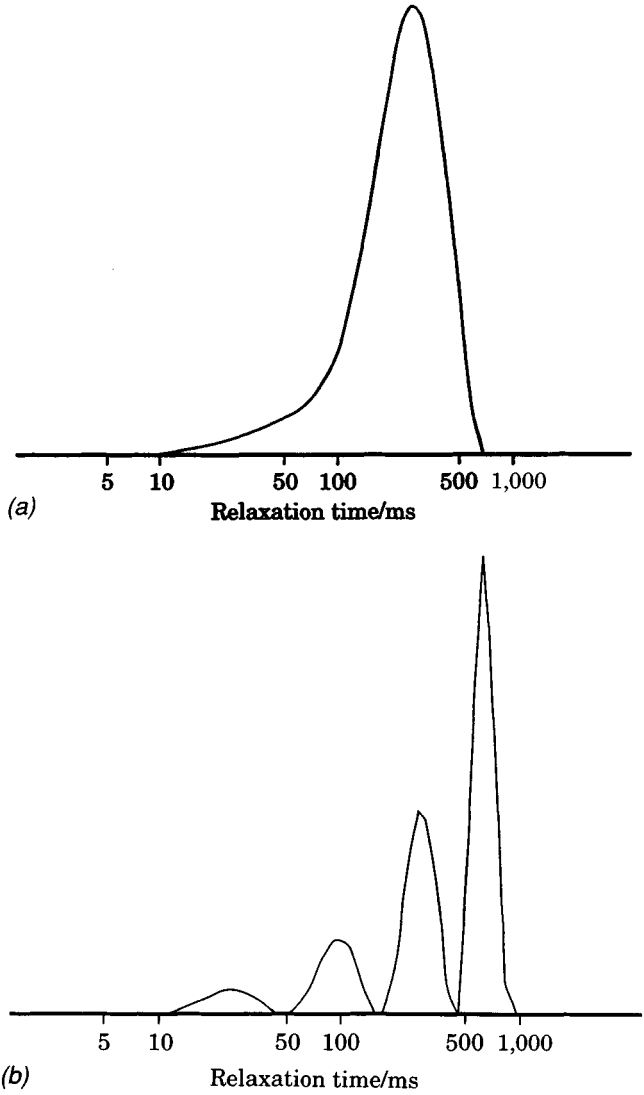

Figure 10.13. Distribution of water proton transverse relaxation times for a water-saturated, randomly packed bed of 200-μm-radius monodisperse glass microspheres measured at two spectrometer frequencies: (*A*) 20 MHz; (*B*) 300 MHz.

working at high field strengths for distinguishing pores on the basis of their size and geometry (233). A quantitative analysis of induced field gradients is deferred to Section 10.3.

The effect of pore connectivity is seen in the partial averaging of the relaxation-time peaks of the smallest bead sizes (22.1 and 10.2 μm) in Figure 10.12. Here diffusive distances are small enough to permit substantial mixing of magnetization between pores. The 58-μm bead category is anomalous and thought to be a result of a lower surface relaxation strength in this particular sample of glass. Pore connectivity can be determined more directly by measuring the rate of diffusion of magnetization between neighboring pores. This can be done by exploiting the difference in transverse relaxation times between large and small pores to excite magnetization in the large pore selectively and following its subsequent diffusion into the small pores. A modified Goldman–Shen pulse sequence is convenient for this (218). This uses the pulse sequence 90°_x–$(t_1$–$180°$–$t_1)_{n1}$–90°_{-x}–t_2–90°_x–$(t_3$–$180°$–$t_3)_{n2}$–acquire, which combines the CPMG and Goldman–Shen (138) sequences. By setting the time period $(2t_1 \times n_1)$ to be $5T_2$ for the smallest pores, magnetization is selectively destroyed by transverse relaxation in the smallest pores, while that in the largest pores is only slightly reduced. The 90°_{-x} pulse then returns the magnetization to the z-direction, where it diffuses into the smaller pores during the contact time t_2. The resulting magnetization distribution is monitored by the subsequent CPMG

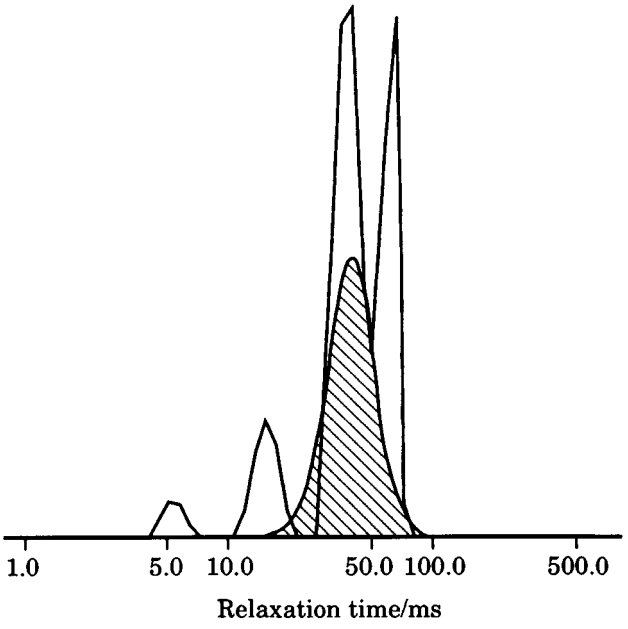

Figure 10.14. Comparison of the four-peak experimental transverse relaxation-time distributions for a 40-μm-diameter glass microsphere bed with the continuous distribution (gray shade) predicted assuming a continuous pore size distribution defined as the radius of the largest sphere that can fit in the pore. (From Ref. 216.)

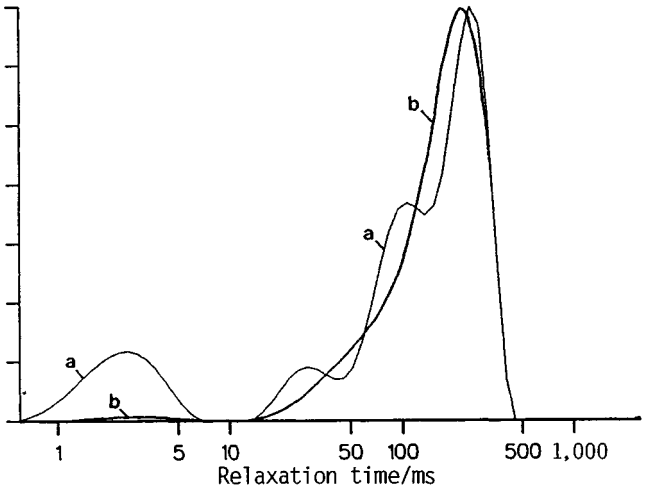

Figure 10.15. Removal of magnetization from the smallest pores by the Goldman–Shen CPMG sequence described in the text. $t_1 = t_3 = 200$ μs, $t_2 = 2$ μs, $n_2 = 1024$. (*a*) $n_1 = 1$; (*b*) $n_1 = 48$. (From Ref. 218.)

sequence. Phase errors can be minimized by phase cycling. Figure 10.15 shows the selective removal of water proton transverse relaxation times from the smallest pores for the water-saturated silica bed. As the contact time, t_2, is increased, the intensity of the peak from the smallest pores increases as more magnetization diffuses into them. The recovery data can be analyzed by defining the recovery ratio $A(t_2)$ as $[I(t_2) - I(t_2 = 0)]/[I(t_2 = \infty) - I(t_2 = 0)]$, and Figure 10.16 shows the plot of $A(t_2)$ against increasing t_2. The line in Figure 10.16 shows the theoretical fit of the unit cell model to the experimental data for a pore connectivity D_t of 4×10^{-6} cm^2/s.

10.2.5 Unsaturated Low-Permeability Systems

If an initially water-saturated porous material such as a granular bed of nonpermeable particles is dried, the changing microscopic air–water distribution among the pores will be reflected in changes to the water relaxation-time distributions. By modeling these changes it is possible to distinguish between various pore-emptying mechanisms (219,226). For example, with hydrophilic materials, capillary forces are expected to determine the air–water distribution, and these dictate that air will first displace water from the largest pores and penetrate smaller pores only after all larger pores are entered. This displacement continues until the *funicular state* is reached, when all pores contain air but there is still a continuous connected phase of water throughout the bed (see Figure 10.17). Further drying progressively breaks the connectivity of the water phase until the *pendular state* is reached, when water is located only at the points of contact between particles. If hydrophobic forces dominate, as with fat or lipid surfaces, air is expected to displace water in the nar-

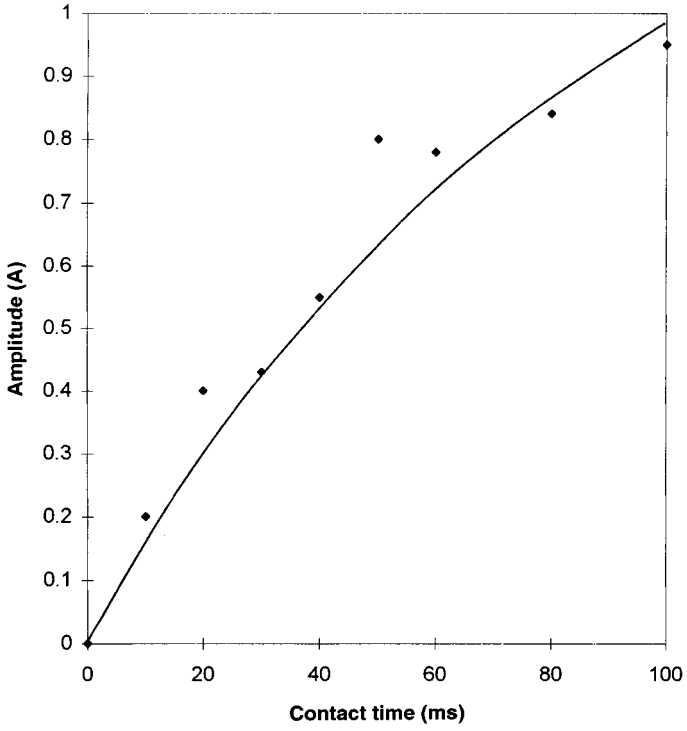

Figure 10.16. Dependence of the recovery ratio A on contact time t_2 (ms) describing diffusion of longitudinal magnetization from the large to smallest pores of the coarse silica bed. The solid line shows the theoretical result for a pore connectivity D_t of 4×10^{-6} cm^2/s calculated with the unit-cell model of Figure 10.10. (From Ref. 218.)

row throats and capillaries before entering larger pores. The changing amplitudes in the CONTIN distributions of water proton transverse relaxation times for beds of silica and of monodisperse glass microspheres conform to the capillary model of pore emptying. Figure 10.18 shows the changing distributions for coarse silica beds containing the indicated amounts of water; while Figure 10.19 compares the experimental water contents at which each relaxation peak disappears during drying with those predicted from the pore size distributions (219,226).

10.2.6 Granular Starch Pastes

The previous model systems are illustrative of the principles relating microstructure and water relaxation, but they are not food-based materials. Starch–water systems are perhaps the simplest model food-based system and illustrate how the same principles apply. The CONTIN proton transverse relaxation-time distribution for a water-saturated randomly packed bed of potato starch granules is bimodal when

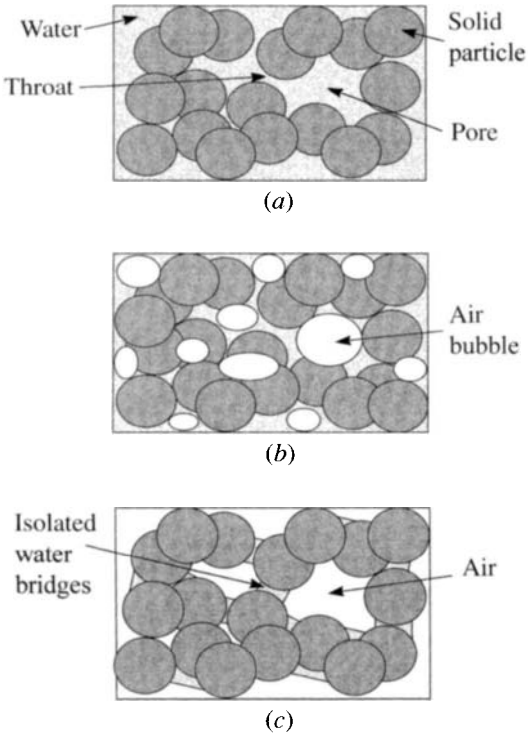

Figure 10.17. Illustrative cross section through randomly packed particle beds showing the distribution of particles, water, and air in the (*a*) saturated, (*b*) funicular, and (*c*) pendular states. (From Ref. 219.)

measured with the CPMG sequence with a 90 to 180° pulse spacing of 200 μs at 300 MHz. The most reasonable assignment of the two relaxation peaks is to water inside and outside the starch granules. This assignment is supported by the observation that the decrease in the long relaxation-time peak area matches the decrease in electrical conductivity of the bed when the water is replaced by a dilute KCl solution and by the disappearance of the outside water peak at 273 K when the outside water freezes, leaving unfrozen water inside the granules. Native potato starch granules, which are spheroidal in shape, vary is size between about 10 to 20 μm and are bound by a lipid bilayer membrane. The observation that the shorter relaxation-time peak at room temperature does not shift significantly on removal of outside water suggests that the relaxation is in the slow exchange regime. The nonexchanging starch proton pool has a short T_2 of only a few hundreds of microseconds, so does not contribute to CPMG measurements at high water contents, but it appears as the fast relaxing component in the FID of powdered starches containing only surface-adsorbed water (213). The major features of the transverse

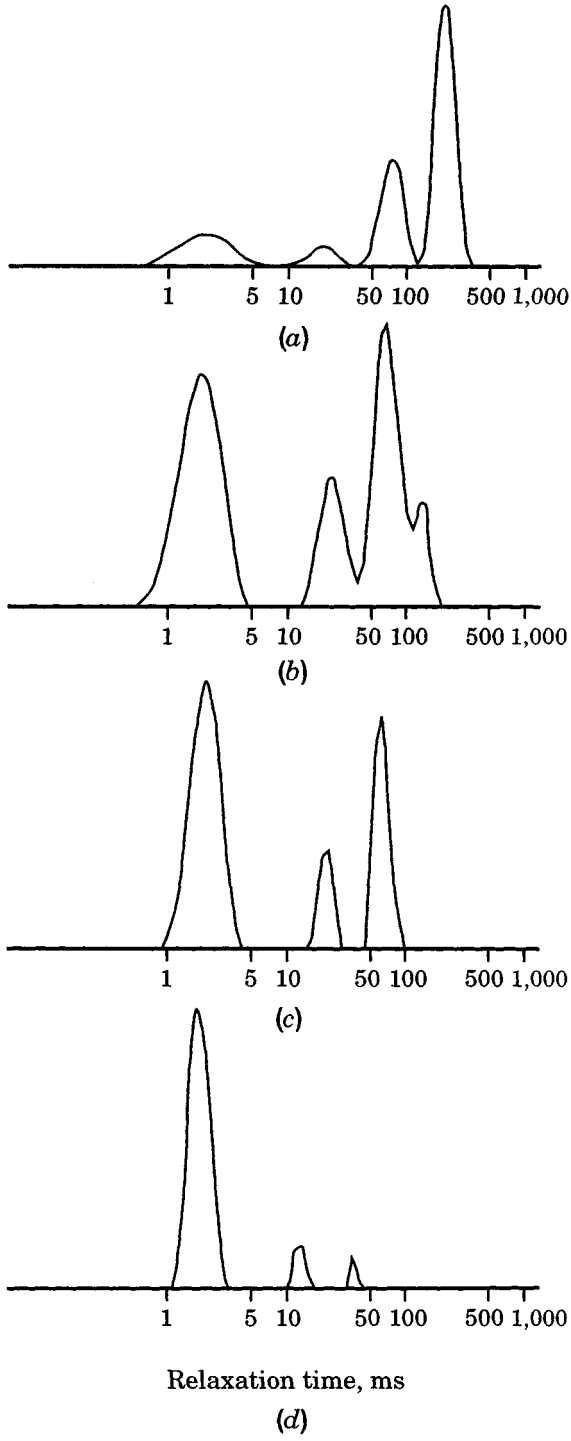

Figure 10.18. Experimental transverse relaxation-time distributions for water in coarse silica beds showing the progressive removal of water from larger to smaller pores. (*a*) Water content $W = 1.08$ (saturated); (*b*) 0.58; (*c*) 0.48; (*d*) 0.34. (From Ref. 219.)

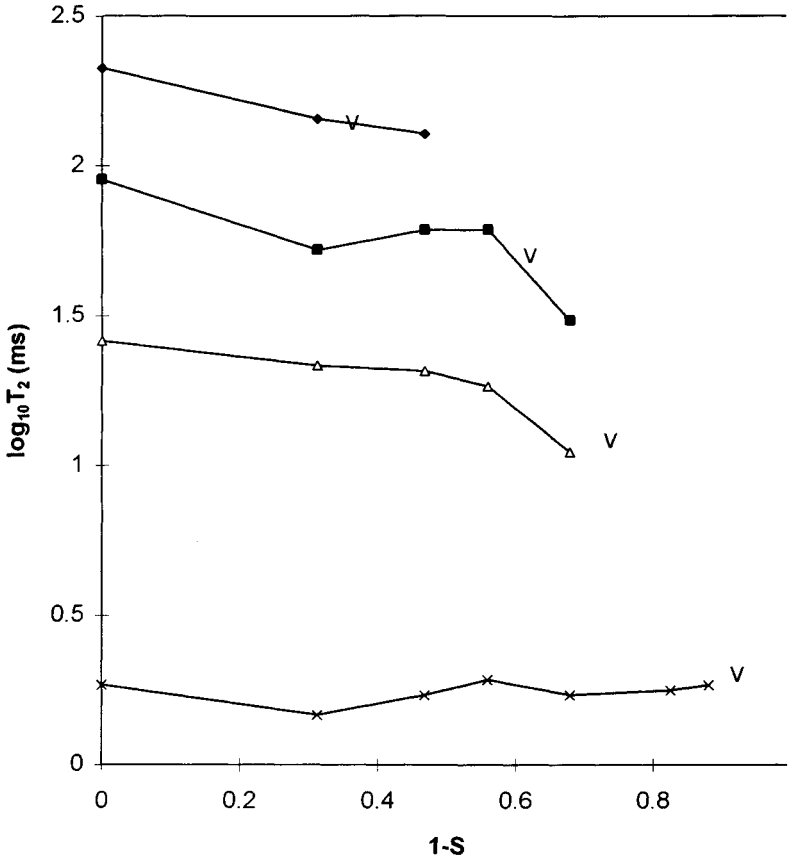

Figure 10.19. Dependence of the positions of the peak maxima in the transverse relaxation-time distributions in Figure 10.18. Arrows show the theoretical compositions at which the peaks vanish. (From Ref. 219.)

relaxation are therefore fairly straightforward to assign, but much remains to be done in understanding the relaxometry of starch gelatinization and retrogradation processes as well as the effect of using starches from different plant sources. Because starch granules are important constituents of most plant cells it is appropriate at this point to consider the more complex relaxation behavior of the intact plant tissue.

10.2.7 Plant Tissue

Water relaxation in plant tissue combines features from each of the above-mentioned categories of material. There are three principal aqueous compartments: the vacuoles, the cytoplasm, and the cell wall region (including the extracellular water). These compartments are separated by the tonoplast and the plasmalemma

membranes, respectively. In many tissues, such as potato, there are additional starch-containing granules. As a first approximation the relaxation behavior of plant tissue can be modeled by ignoring intercellular diffusion and solving the Bloch–Torrey equations numerically for the isolated spherical cell model shown in Figure 10.20. For plant tissue the cell morphology is readily observed with light or electron microscopy, so there is little point in trying to probe microstructure with NMR relaxometry. What is not readily available by light or electron microscopy is the magnitude of the plasmalemma and tonoplast membrane permeabilities, which are largely responsible for controlling water transport through the tissue during drying. To determine the membrane permeabilities the morphological parameters from light and electron microscopy are fed as input into the numerical cell model, together with the intrinsic compartment relaxation times measured by separating out the cell components, such as the cell wall; the cytoplasmic fluid; and any intracellular granules, such as starch granules. The multiple-exponential water proton relaxation is then fitted by numerically solving the Bloch–Torrey equations in the cell model by adjusting the membrane permeabilities. A number of subsidiary experiments can be performed to verify the fit. These include water diffusion measurements using the Stejskal–Tanner or stimulated echo-pulse sequences. These sequences are discussed in more detail in Chapter 11. In addition, there are a number of supplementary experiments to determine the plasmalemma permeability involving measuring the effect of reducing the relaxation time of the extracellular water by the addition of paramagnetic ions such as Cu^{2+} or Mn^{2+}, which also eventually diffuse into the cells, or of ions such as dysprosium tripolyphosphate, which do not. These methods and several other NMR protocols for measuring membrane permeabilities in cells, vesicles, and micelles have been reviewed by the author (253). These protocols have been used to measure membrane permeabilities in apple tissue (216,257), but the effects of processes such as ripening and dehydration on the membrane permeabilities have yet to be investigated by NMR relaxometry. The complications of polydiversity in cell sizes and geometries observed in actual plant tissues are completely ignored in the single numerical cell model in Figure 10.20. The calculated parameters pertain only to an "average" cell and assign all relaxation peaks to intracellular compartments. At the expense of increased complexity it may be possible to combine the intracellular model with the Voronoi tessellation model of the tissue, discussed in Chapter 9. Whether this increased complexity is numerically tractable remains to be investigated.

Like the model Sephadex system, the intrinsic water proton transverse relaxation rates of the vacuolar fluid and cytoplasm can show large dispersions as the CPMG pulsing rate $1/\tau$ is varied. This is not surprising because they consist essentially of solutions of carbohydrates, proteins, polysaccharides, and low-molecular-weight metabolites with exchangeable protons. These frequency dispersions in the intrinsic relaxation rates result in a CPMG pulse-spacing dependence of the overall multiple exponential relaxation rates for the whole tissue, and once again a Monte Carlo or finite-element model needs to be used to interpret the relaxation data. Dispersive multiple exponential transverse relaxation has been observed, for example, in onion, tomato, and apple (212).

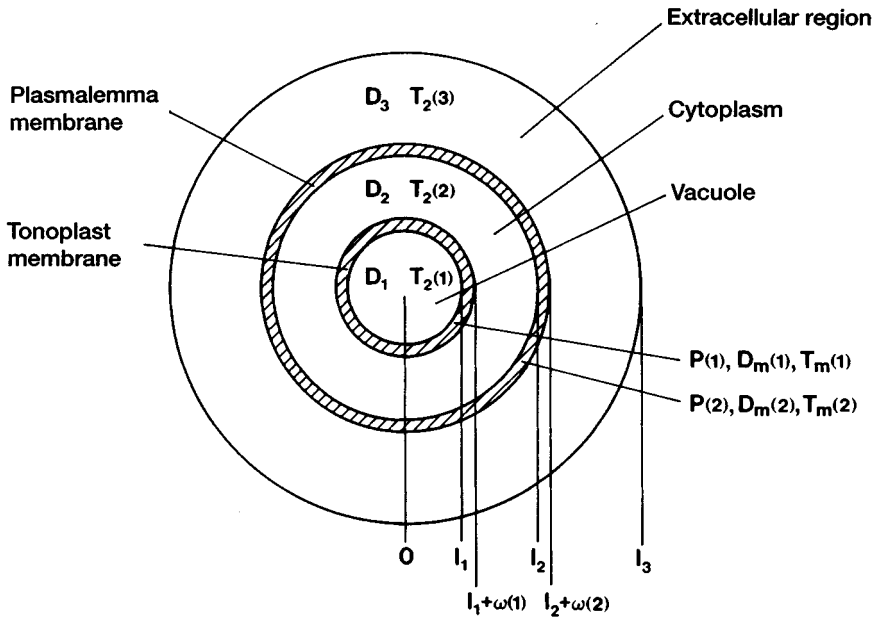

Figure 10.20. Spherical cell model. The vacuole, cytoplasm, and cell wall compartments within an idealized plant cell are each characterized by intrinsic water self-diffusion coefficients D, relaxation rates γ, and resonance frequencies ω. The plasmalemma and tonoplast membranes are assigned water permeability coefficients P and intrinsic relaxivities. Relaxation within the whole cell can be modeled by numerical solution of the coupled Bloch–Torrey equations for each compartment.

The effect of freezing on the relaxation behavior of plant tissue has potential importance in food cryopreservation. Figure 10.21 shows the dependence of the water proton transverse relaxation times (at a fixed 90 to 180° pulse spacing of 200 μs and a spectrometer frequency of 100 MHz) on temperature for fresh potato tissue, together with tentative peak assignments based on the relaxation of isolated cell components. It is evident that even at −15°C there is still unfrozen water in the starch granules and cell walls, and this can affect rates of freezing and freeze-drying.

10.2.8 Ice-Crystal Size Distributions in Frozen Foods

In Section 3.4 it was pointed out that imaging can be used to follow the rate of freezing and freeze-drying on a macroscopic distance scale. It was pointed out that the porous structure of freeze-dried foods is determined by the distribution of ice crystal sizes, which in turn is related to the rate of freezing and the nature of the food matrix. On the microscopic distance scale, relaxometry can be used to gain information about the pore size distribution (and hence ice crystal size distributions) provided that the pores are filled with a chemically inert nonaqueous solvent such as octane or acetone. Unfortunately, water causes collapse of the freeze-dried food

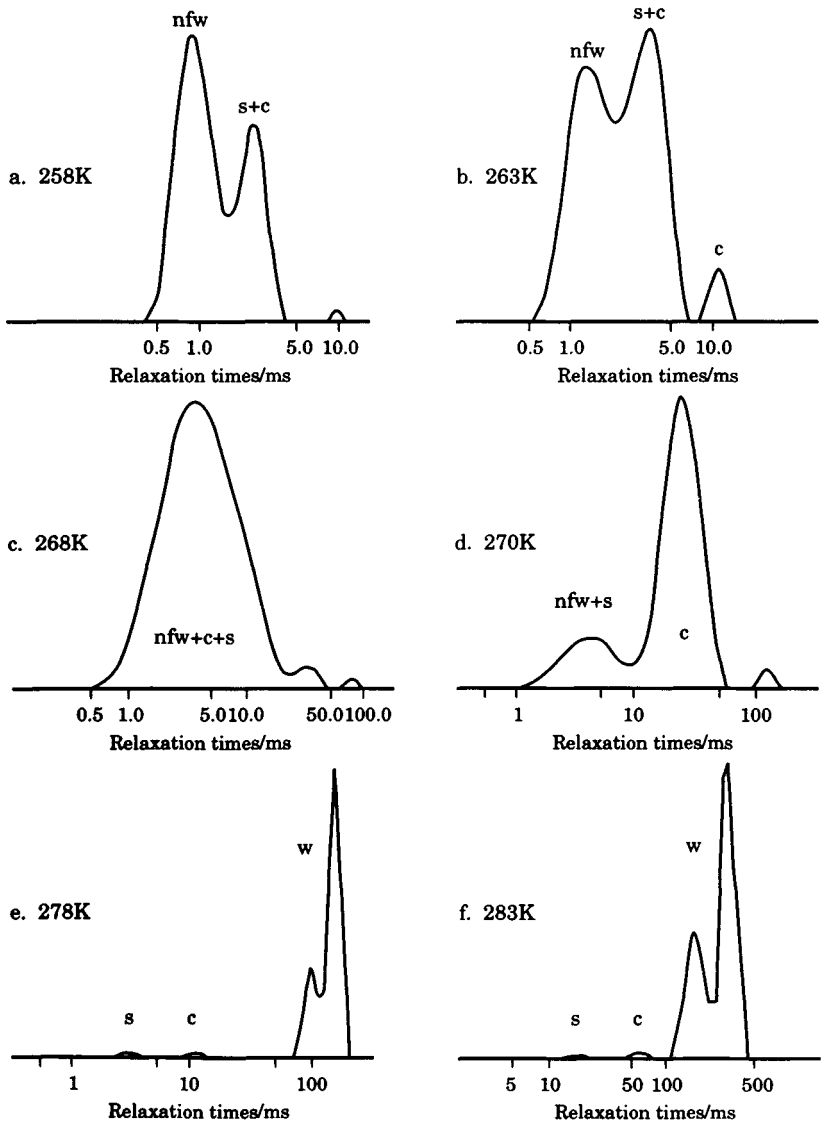

Figure 10.21. Water proton transverse relaxation-time distributions for uncooked potato tissue for various temperatures during freezing. Note the change of scale and that peak intensities are always scaled on the maximum peak intensity. Peak assignments are as follows: s, starch granules; c, cell wall compartment; w, cytoplasm and vacuole; nfw, nonfreezing water associated with biopolymers. (From Ref. 223.)

matrix and cannot therefore be used. Figure 10.22 shows the distribution of transverse relaxation times for a cylinder of freeze-dried starch gel immersed in bulk liquid acetone as the amount of external liquid acetone is reduced. The sharp peak with a relaxation time of approximately 1 s arises from bulk liquid acetone. As this bulk acetone is progressively removed, strongly shifted relaxation peaks

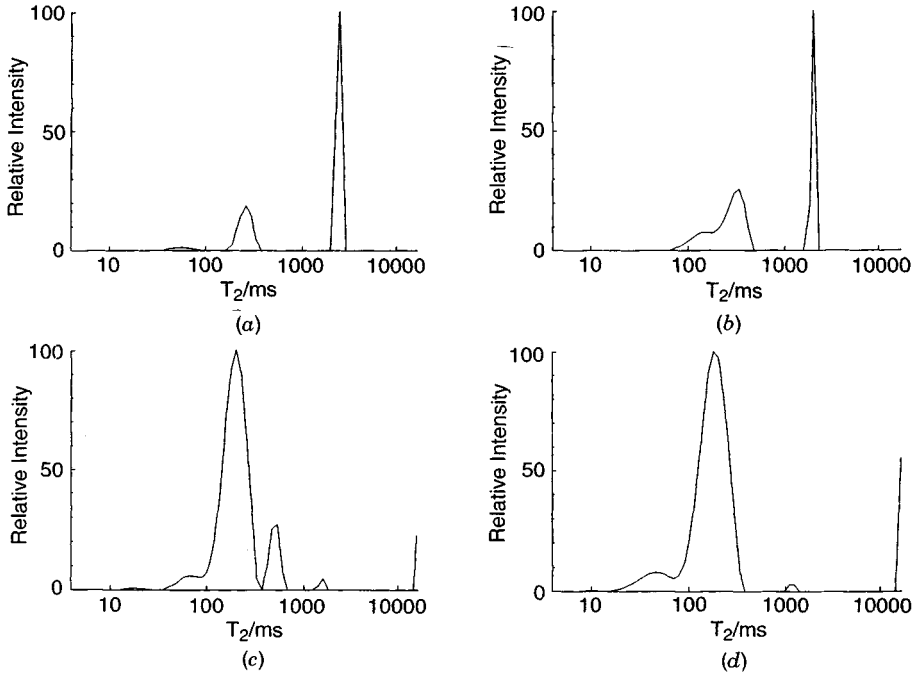

Figure 10.22. Representative transverse relaxation distributions for acetone in freeze-dried starch gels containing various amounts of bulk acetone as interstitial and surface layers. (*a*) 92.4%, (*b*) 81.4, (*c*) 75.2, and (*d*) 65.4% acetone, by weight. The peak at 2.5 s corresponds to the bulk acetone. The peaks between 20 and 500 ms correspond to acetone inside the pores of the freeze-dried gel.

corresponding to acetone inside the starch gel pores become more clearly resolved. These shifted peaks, when analyzed with the Brownstein–Tarr theory (135), can in principle be used to determine the pore size distribution and hence the original ice crystal size distribution in the frozen starch gel. It is interesting to note that the surface relaxation strength for acetone at the starch surface shows a strong frequency dispersion with the CPMG pulsing rate, and this can be exploited to sensitize the pore distribution measurements. The results, so far, are preliminary and the protocol is still being researched by a number of groups, including the authors.

10.3 RELAXATION EFFECTS OF INTERNAL FIELD GRADIENTS

Mention has already been made of the geometry-specific internal magnetic field gradients generated across phase boundaries differing in bulk magnetic susceptibility. In this section we examine to what extent the enhanced dephasing effect of these internal gradients can be analyzed and used for microstructural determination. Consider once again the water-saturated randomly packed bed of silica particles.

Because the bulk magnetic susceptibilities of silica and water are different, placing the sample in a static magnetic field induces a highly localized magnetic field gradient around each silica particle. Glasel and Lee (269) have shown that for an isolated sphere surrounded by a continuous medium, the average field gradient G_{av} is proportional to the spectrometer field and inversely proportional to the sphere radius R

$$G_{av} = \frac{\mu_0 H_0 \Delta\chi}{4R} \tag{10.7}$$

where μ_0 is the magnetic permeability of vacuum, H_0 the applied magnetic field strength, and $\Delta\chi$ the difference between the volume magnetic susceptibilities. If we ignore the fact that the gradient is actually spatially inhomogeneous and assume unrestricted diffusion and no surface relaxation, this internal gradient causes an enhanced CPMG transverse relaxation rate proportional to the square of the 90 to 180° pulse spacing τ (7)

$$T_2^{-1} = T_{2w}^{-1} + \frac{D(\gamma G_{av}\tau)^2}{3} \tag{10.8}$$

The assumption of unrestricted diffusion, which is rarely observed in heterogeneous systems, has been removed by a number of authors. Robertson (270), Neuman (271), and Kleinberg and Horsfield (268) have presented solutions for the decay of transverse magnetization where diffusion is restricted within isolated lamellar, cylindrical, and spherical pores containing a constant linear field gradient G_{av}. The solutions are complicated, so we quote them only for a spherical pore of radius R and for the CPMG sequence

$$T_2^{-1}(\tau) = T_{2w}^{-1} + 2\left(\frac{\gamma^2 G^2 R^4}{D}\right) \sum_{i=1}^{\infty} \frac{1}{\alpha_i^4(\alpha_i^2 - 2)} \left[1 - \frac{3 - 4\exp(-a/2) + \exp(-a)}{a}\right] \tag{10.9}$$

where

$$a = \frac{2\tau\alpha_i^2 D}{R^2} \tag{10.10}$$

and α_i are numerical coefficients defined as the roots of the equation

$$\tan\alpha_i = \frac{2\alpha_i}{2 - \alpha_i^2} \tag{10.11}$$

It is noticeable that restricting the diffusion has the effect of placing the diffusion coefficient D in the denominator and the simple τ^2 dependence is lost. At first sight, the complexity of this expression, even for a single spherical pore, precludes its use for microstructural determination. However, in the limit that the CPMG pulse spacing is much longer than the mean diffusion time within a pore, $\tau \gg R^2/D$, the expressions simplify considerably, and Yu (267) showed that for restricted diffusion within an isolated lamellar pore

$$T_2^{-1}(\tau) = T_2^{-1}(\text{Hahn}) - \left(\frac{17}{13{,}440}\right)\frac{R^6\gamma^2G_{av}^2}{D^2\tau} \tag{10.12}$$

where T_2^{-1}(Hahn) is the relaxation rate extracted from the simple 90°–τ–180° Hahn-echo-decay envelope, which for $\tau \gg R^2/D$ was shown by Robertson (270) to be

$$T_2^{-1}(\text{Hahn}) = \frac{R^4\gamma^2G_{av}^2}{120D} \tag{10.13}$$

Equation (10.12) shows that in the absence of surface relaxation, a plot of the CPMG relaxation rate against the pulsing rate $1/\tau$ should give a straight line whose slope will give the ratio R^3G_{av}/D and whose intercept, T_2^{-1}(Hahn), gives the ratio $R^4G_{av}^2/D$. These two ratios, together with an independent measurement of D for the pure fluid (see Chapter 11), give estimates of the pore size R and the average field gradient within the pore, G_{av} (267). It is certainly worth attempting such a simple analysis, but it should be remembered that there are still four more complications that can invalidate the results. These are surface relaxation, a pore size distribution, pore connectivity (since pores are rarely in true isolation), and the fact that the internal gradients are not actually uniform within a pore but highly inhomogeneous and geometry sensitive. Despite these complexities, Kleinberg and Horsfield (268) have attempted to incorporate at least some of these additional factors by writing

$$M(2n\tau) = M(0)\int_0^\infty \exp\left[-\left(\frac{R}{R_0}\right)^2\right]\exp\left(\frac{-3\rho t}{R}\right)\exp[-tT_2^{-1}(\tau)] \tag{10.14}$$

This expression assumes a Gaussian pore size distribution, represented by the exponential term in $(R/R_0)^2$, where R_0 is a characteristic pore size. The second factor describes surface relaxation in a spherical pore in the fast diffusion limit [see equation (10.6)]. The last factor describes restricted diffusion in a uniform internal gradient, where $T_2^{-1}(\tau)$ is given by equation (10.9). This combination of effects was shown to provide a reasonable description of the effects of pulse spacing on the CPMG relaxation rates in a number of porous rocks at various spectrometer frequencies (268). Two important effects that equation (10.14) fails to address is the spatial inhomogeneity of the susceptibility-induced field gradient within the pores and the effect of pore connectivity. LeDoussal and Sen (318) have solved the Bloch–Torrey equation for relaxation in spherical pores containing a parabolic field gradient

$$\frac{\delta \mathbf{M}(\mathbf{r},t)}{\delta t} = D\nabla^2\mathbf{M}(\mathbf{r},t) + i\gamma(G_1 z + G_2 z^2)\mathbf{M}(\mathbf{r},t) \tag{10.15}$$

Here the factor $\exp(i\omega_0 - 1/T_{2b})t$ has been factored out and g_1 and g_2 are the linear and parabolic parts of the gradient, respectively. The results of this analysis can be summarized as follows. At very short τ values the relaxation rate increased quadratically as

$$T_2^{-1} = \frac{2D\gamma^2 G_2^2 R^2 \tau^2}{3} \tag{10.16}$$

where R is the pore radius. This quadratic dependence might have been anticipated from equation (10.8). However, this initial quadratic dependence quickly changed to a linear dependence at longer t values, and at very long pulse spacings the relaxation rate eventually approached a constant value given as

$$T_2^{-1} \text{ (long } \tau) = \frac{\gamma^2 G_2^2 R^6}{8D} \tag{10.17}$$

The data in Figure 10.23 showing the τ dependence of the acetone proton transverse relaxation rate at 300 MHz in an acetone-saturated freeze-dried starch gel (see Section 10.2) conform to the predicted linear τ dependence, and the negative intercept is consistent with an initial increase proportional to τ^2. However, the

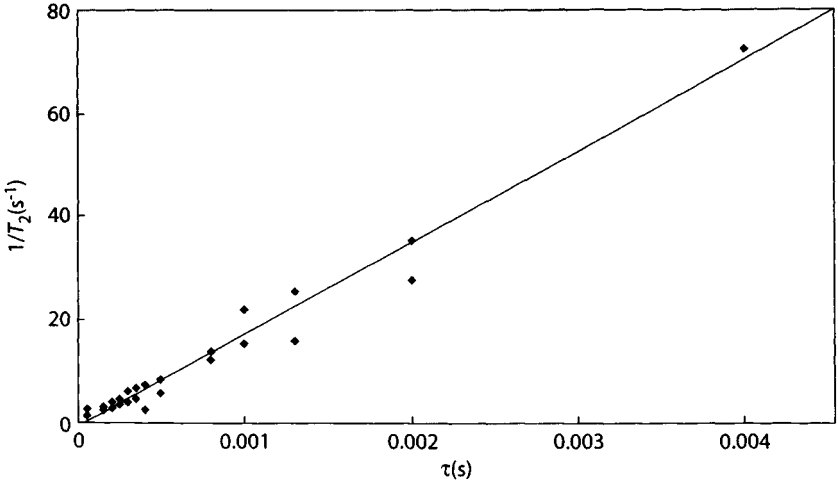

Figure 10.23. Dependence of the proton transverse relaxation rate of acetone on CPMG pulse spacing τ measured at 300 MHz for an acetone-saturated freeze-dried starch gel. The linear dependence and negative intercept are consistent with strong nonlinear magnetic field gradients within the pores.

asymptotic approach to a constant relaxation rate at long pulse spacings was not observed in this experiment.

Before leaving this topic, it is worth noting that the complexities of internal field gradients tend to be severe when there is excess water (or fluid) surrounding solid granules or air bubbles. This is the usual situation in wet porous rocks but is not common in porous foods, apart from cellular tissue such as apple, which contains many intercellular air gaps. Consider, for example, a randomly packed bed of starch granules that has been dried so as to remove most of the external water and leave only water inside the granules. It is well known from textbooks on electromagnetism that the field induced inside an isolated ellipsoid in an external uniform static magnetic (or electric) field is itself uniform and parallel to the external field, regardless of the orientation of the ellipsoid. This implies that the susceptibility effects discussed above will be small in such a system and that the CPMG relaxation decays will be insensitive to pulse spacing. It should also be remembered that a CPMG pulse spacing dependence can also arise from chemical exchange, and this is analyzed in Chapter 12. If susceptibility-induced gradients are an unwanted problem, it is always possible to use longitudinal relaxation, since this cannot be dephased by frequency offsets and is unaffected by susceptibility-induced internal, or external, gradients. Although this would appear to circumvent the entire problem, surface relaxation strengths μ for longitudinal relaxation at biopolymer surfaces tend to be weak compared to those for transverse relaxation (see, e.g., Figure 12.1), at least in the absence of paramagnetic impurities, so longitudinal relaxometry tends to be an insensitive probe of microstructure.

Up to this point the discussion of nonspatially resolved relaxation-time distribution has assumed that the NMR signal is taken from the entire sample and that the sample is heterogeneous only on the microscopic distance scale. In other words, repeating the relaxation-time measurements on smaller subvolumes of the sample would give the same relaxation-time distribution. This assumption will break down if the heterogeneity extends over a wide range of distance scales, from the microscopic to the macroscopic. In such cases the observed relaxation-time distribution will depend on the volume from which the signal is taken. The easiest way to vary the sampling volume is, of course, to combine the relaxation-time measurements with k-space microimaging and acquire spatial maps of relaxation-time distributions. If the water proton relaxation-time distribution from a single voxel is still multiple exponential, it confirms that there are water compartments on a scale smaller than the voxel size. On the other hand, if the relaxation-time distribution changes from multiple to a single exponential at a resolution d, this shows that the water compartment heterogeneity exists on a distance scale greater than d. Fractal geometries present an interesting example of the relationship between spatial resolution and relaxation-time distributions because they exhibit heterogeneity over every distance scale. One of the few studies of relaxation in fractal systems is that reported by Rigby and Gladden (329). These researchers used relaxation-time-weighted imaging and fractal geometry to characterize the porous structures of various water-saturated silica and alumina pellets. The entire pellet was first imaged with a spatial resolution of 40 μm, at which resolution the longitudinal relaxation-

time distribution within a voxel was single exponential, within experimental error. A spatial map of the longitudinal relaxation time was then calculated and showed heterogeneity in the form of random homogeneous clusters over distance scales ranging from 40 to 1000 μm. A fractal dimension d was then extracted from the T_1 map by fitting the relationship between the cluster area (A) and cluster perimeter (P) with the fractal $A \propto P^{2/d}$, where d is the fractal dimension. For Euclidean-type geometries d is unity, but for a fractal geometry, d will be greater than 1. In fact, for the T_1 maps of porous silica, d values on the order of 1.64 to 1.68 were found by estimating the gradient of the log area versus log perimeter using a form of the boundary extraction method (330). Many real foods are also heterogeneous over a wide range of distance scales, so it would be interesting to use similar relaxation-time mapping methods to explore the extent to which their heterogeneity conforms to fractal geometry.

10.4 MICROSTRUCTURE AND THE MICROBIAL SAFETY OF FOODS

Microbial safety and spoilage is an essential food quality factor that has been ignored earlier in the book. We are all aware of food poisoning outbreaks caused by

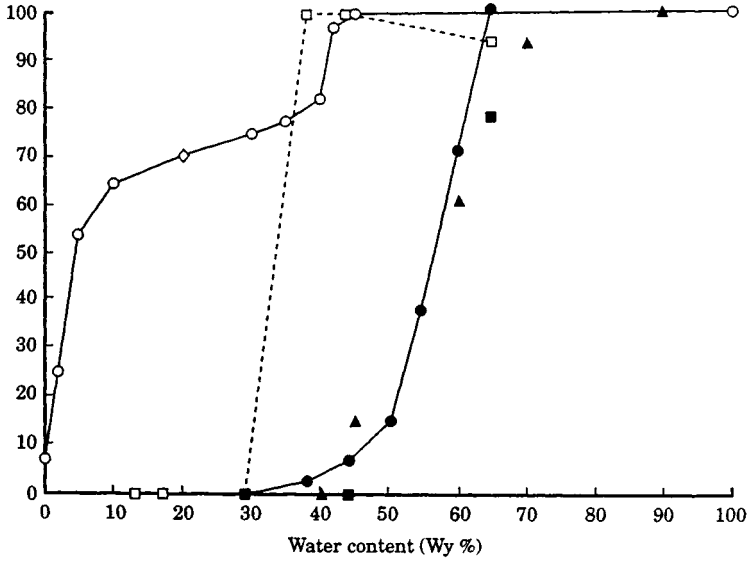

Figure 10.24. Comparison of the drop in % recovery (▲) of *Salmonella typhimurium LT2* in a randomly packed bed of 40–63 μm silica with the decrease in water activity, a_{av}*100 (○), % electrical conductivity relative to the saturated bed (●) and NMR peak areas relative to the saturated bed. (□), % relative peak area corresponding to all water outside the silica particles: ■, % relative peak area corresponding to water in the largest pores.

bacterial pathogens such as *Salmonella, Listeria,* and *Escherichia coli* 157 and their severe consequences in terms of human suffering. Microbial spoilage of foods by bacteria, yeasts, and fungi is also a major factor limiting food shelf life, and this has major economic implications. Not surprisingly, food manufacturers and distributors are making intense efforts to prevent microbial survival and growth in their foods. The usual strategy is to maintain a chemical environment that is hostile to the growth of microorganisms by, for example, the addition of chemical preservatives, the use of low pH, and through addition of humectants to lower the water activity, a_{av}. An aspect that is less well understood is the role of food microstructure and the microscopic air–water distribution in limiting microbial survival and growth. Figure 10.24 shows that the survival of *Salmonella typhimurium* when its innoculum is suddenly added to silica powder is correlated with the amount of water in the largest pores as measured by the area of the NMR water proton transverse peak in a CONTIN plot or by electrical conductivity. Similar results are seen in Figure 10.24 for the silica beds. Clearly, if a bacterial cell happens to end up in a water-filled pore, it will survive, whereas if, by chance, it finds itself in an air-filled pore, it will experience osmotic shock, and possibly oxygen toxicity, and lose viability. This

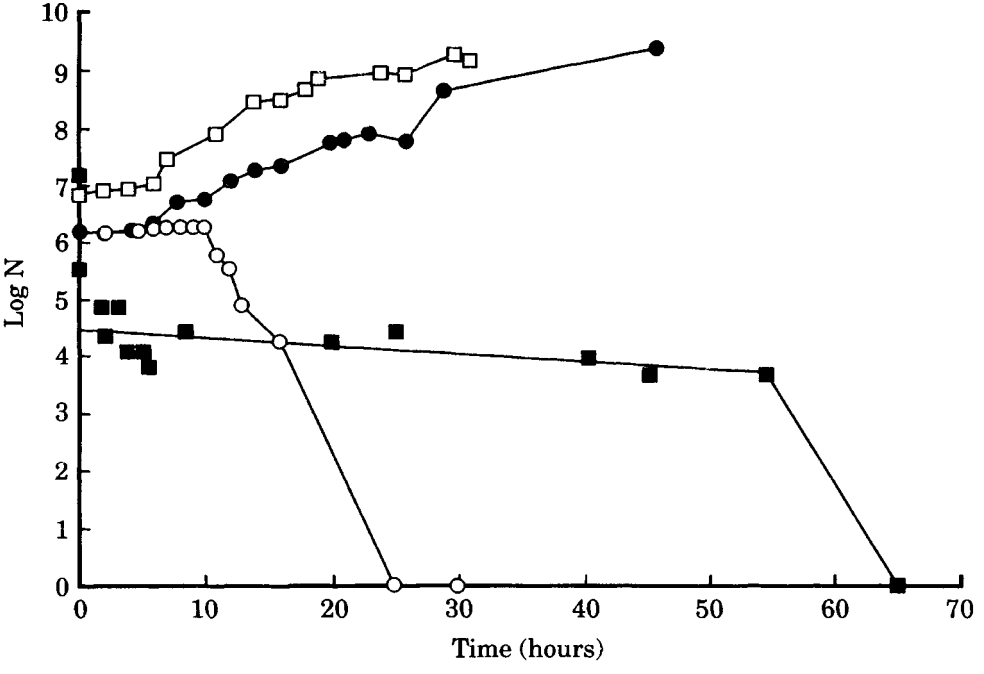

Figure 10.25. Growth data for *Salmonella typhimurium LT2* in various model systems. An inoculum containing 10^7 cells/ml. was added to dry Sephadex G25-50 powder so as to give the indicated final water contents. Aliquots were taken for plate counting at the indicated times. (□) 80% water content, (●) 60%, (■) 40%. The corresponding recovery data for a dextran solution is included (○).

simple experiment illustrates how microstructure and the air–water distribution can affect microbial survival in an osmotic shock situation (272). Figure 10.25 shows the longer-term effects of exposing the *Salmonella* to partially saturated porous matrices and shows the time course of the cell viability measured in a Sephadex bed and a dextran solution containing 40% water over the course of a few days. The dramatic decrease in viability in the dextran solution after about 10 h is noteworthy and corresponds to the point at which the dextran solution undergoes a phase transition to a rubbery solid, presumably by chain entanglement (273). This type of observation suggests a strong relationship between food microstructure and the microscopic air–water distribution and the microbial stability of foods, but much work remains to be done in clarifying the relationship.

11

PROBING MICROSTRUCTURE WITH DIFFUSION

11.1 INTRODUCTION

Many microstructural features in foods exist on a scale of 0.1 to 10 μm, which is less than the best resolutions achievable with an NMR microscope. These small-scale microstructural features are important in controlling transport over macroscopic distances and affect quality factors such as texture. In Chapter 10 we showed how NMR relaxometry could give valuable microstructural information. In this chapter we analyze how the restriction of water diffusion by barriers, interfaces, and membranes can be used to probe microstructure at resolutions far exceeding those available with *k*-space imaging or relaxometry. The methodology is less direct than *k*-space imaging and depends on knowing the relationship between microstructure and the attenuation of a diffusion-weighted NMR signal. Unfortunately, this relationship is model dependent and usually very complicated. Nevertheless, considerable progress is being made in extracting microstructural information from the NMR diffusion data, and this has been reviewed by Price (149) and Callaghan (5). An earlier article by Karger et al. (152) is also very helpful in giving an overview of the subject. We begin by considering the basic, nonspatially resolving, diffusion-weighted pulse sequences and their relationship to microstructure.

11.2 DIFFUSION-WEIGHTED PULSE SEQUENCES

Figure 11.1 shows the simplest pulsed field gradient spin-echo (PGSE) sequence for measuring self-diffusion, introduced by Stejskal and Tanner (153). As mentioned in Chapter 1, the introduction of two short pulsed field gradients of amplitude G and duration δ separated by a time Δ introduces a phase change, $\mathbf{q} \cdot (\mathbf{r}' - \mathbf{r})$,

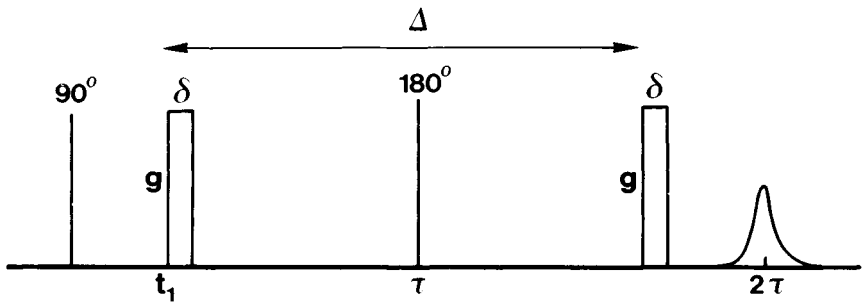

Figure 11.1. Stejskal–Tanner (pulsed gradient spin-echo) sequence.

where the wavevector $\mathbf{q}$ is the area under the pulsed gradient, $(2\pi)^{-1}\gamma G\delta$, and $(\mathbf{r}' - \mathbf{r})$ is the displacement experienced by the spins in the diffusion time Δ. The observed spin-echo amplitude is obtained by integrating over all spins and is therefore

$$S(\mathbf{q},\Delta) = \iint d\,\mathbf{r}\, d\mathbf{r}'\, \rho(\mathbf{r})P(\mathbf{r} \mid \mathbf{r}',\Delta) \exp[i2\pi\mathbf{q} \cdot (\mathbf{r}' - \mathbf{r})] \tag{11.1}$$

Here $\rho(\mathbf{r})$ is the spin density and $P(\mathbf{r} \mid \mathbf{r}',\Delta)$ is the conditional probability that a spin initially at $\mathbf{r}$ will be at $\mathbf{r}'$ a time Δ later. This expression neglects transverse relaxation effects and assumes that the gradient pulses are narrow, $\delta \ll \Delta$. Provided that the system is translationally invariant (i.e., independent of the initial position of the spins), equation (11.1) can be transformed to the displacement variable $\mathbf{R} = \mathbf{r}' - \mathbf{r}$ by introducing the average propagator

$$P_{\text{av}}(\mathbf{R},\Delta) = \int d\mathbf{r}\, \rho(\mathbf{r})P(\mathbf{r} \mid \mathbf{r}',\Delta) \tag{11.2}$$

With this transformation, equation (11.1) becomes the Fourier relationship (5)

$$S(\mathbf{q},\Delta) = \int d\mathbf{R}\, P_{\text{av}}(\mathbf{R},\Delta) \exp(i\mathbf{q} \cdot \mathbf{R}) \tag{11.3}$$

and the average probability distribution for the displacement of spins through a distance $\mathbf{R}$ in time Δ can be obtained by Fourier inversion of the NMR echo amplitude

$$P_{\text{av}}(\mathbf{R},\Delta) = \int d\mathbf{q}\, S(\mathbf{q},\Delta) \exp(-i\mathbf{q} \cdot \mathbf{R}) \tag{11.4}$$

Equations (11.3) and (11.4) were presented in Chapter 1, where it was pointed out that they are analogous to the k-space Fourier relationships used in spatial imaging. Instead of imaging $\rho(r)$ using the conjugate k-space, we now "image" the average propagator $P_{\text{av}}(\mathbf{R},\Delta)$ using the conjugate q-space. Provided that the relationship between $P_{\text{av}}(\mathbf{R},\Delta)$ and microstructure is known, equations (11.3) and (11.4) can be used to probe microstructure, and this protocol is called q-space microscopy,

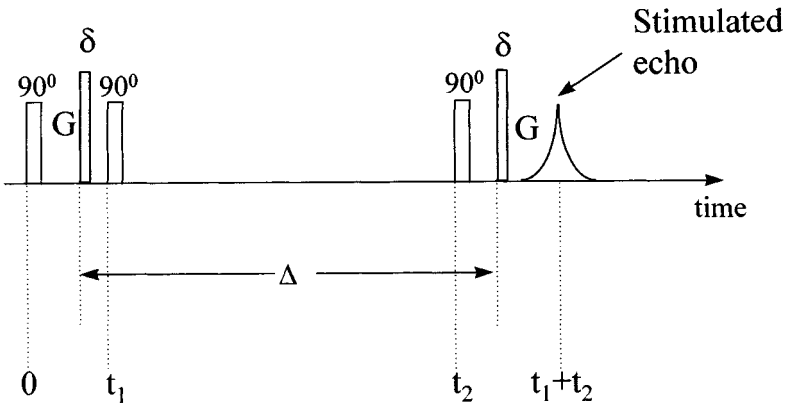

Figure 11.2. Pulsed gradient stimulated-echo sequence.

in analogy with *k*-space microimaging. Unfortunately, the relationship between $P_{av}(\mathbf{R},\Delta)$ and microstructure is usually very complicated, so *q*-space microscopy is still in its developmental stages and far from routine.

The spin echo is attenuated not only by diffusion but also by relaxation, which for single-exponential relaxation introduces the factor $\exp(-TE/T_2)$ in the spin-echo diffusion sequence. This factor can be removed by measuring the ratio $S(q,\Delta,TE)/S(q = 0, TE)$. However, this simple expedient is not necessarily valid for multicompartment systems, where the relaxation is, in general, multiple exponential. We return to this point later. Transverse relaxation places an upper limit on the maximum diffusion time possible in the Stejskal–Tanner sequence, and in heterogeneous systems with short T_2 times, this can be a problem, because the diffusion distance needs to be larger than the scale of the structural heterogeneity being probed. For this reason, the stimulated echo, rather than the spin echo, has advantages, because this is attenuated mainly by longitudinal relaxation, which is usually much slower than transverse relaxation. The typical stimulated echo–pulsed field gradient sequence (158) is shown in Figure 11.2. The second 90° pulse converts *y*-magnetization to longitudinal magnetization, which undergoes longitudinal relaxation during the time interval $(t_2 - t_1)$ and transverse relaxation during the shorter t_1 intervals. The diffusion time is controlled by Δ, which needs to be less than $5T_1$ for measurable echo amplitude. Otherwise, equation (11.4) remains valid for the pulsed gradient–stimulated echo sequence.

11.3 DIFFUSION PROPAGATOR AND MICROSTRUCTURE

We now explore the relationship between the diffusion propagator and microstructure for several simple model systems.

11.3.1 Unrestricted Diffusion

The simplest situation is the spatially homogeneous system where there is no microstructure and the diffusion is unrestricted. In this case the average propagator $P(\mathbf{R},\Delta)$ is the spreading Gaussian function

$$P(z,\Delta) = (4\pi D\Delta)^{-1/2} \exp\left(\frac{-z^2}{4D\Delta}\right) \tag{11.5}$$

where z has been taken as the direction of the applied field gradient. Substitution into equation (11.3) gives the Gaussian function

$$S(q,\Delta) = \exp(-4\pi^2 q^2 D\Delta) \tag{11.6}$$

A more rigorous derivation that does not assume narrow gradient pulses introduces a small correction whereby Δ is replaced by $(\Delta - \delta/3)$ (153). Equation (11.6) shows that provided there is unrestricted diffusion, the diffusion coefficient can be obtained as the slope of a plot of $-\ln[S(q,\Delta)/S(q=0)]$ against $4\pi q^2\Delta$ and it then does not matter whether one varies q or Δ or some combination of them. Some authors assume that a very similar protocol can be applied to restricted diffusion in structured systems provided that the diffusion time Δ is fixed and only the wavevector q is varied. The result is then an apparent diffusion coefficient $D(\Delta)$ that depends on the diffusion time Δ, and this dependence is used to extract information about microstructure. This protocol is, however, suspect for a number of reasons. First, it ignores the complexity of spatially inhomogeneous relaxation, and second, it is logically inconsistent to use an equation derived on the assumption of unrestricted diffusion to probe structure in systems that are known to be restricted. Nevertheless, an apparent diffusion coefficient does lend itself to intuitive understanding, which is advantageous because rigorous mathematical solutions of coupled relaxation and diffusion in restricted geometries are usually extremely complicated.

11.3.2 Restricted Diffusion in Pores with Reflective Walls

One of the few cases for which exact analytical solutions have been derived is diffusion in a closed rectangular box of width a. The conditional probability obtained by solving the diffusion equation with appropriate boundary conditions when substituted into equation (11.1) gives

$$S(q,\Delta) = \frac{2[1 - \cos(2\pi qa)]}{(2\pi qa)^2} + 4(2\pi qa)^2 \sum_{n=1}^{\infty} \exp\left(\frac{-n^2\pi^2 D\Delta}{a^2}\right) \left\{\frac{1 - (-1)^n \cos(2\pi qa)}{[(2\pi qa)^2 - (n\pi)^2]^2}\right\} \tag{11.7}$$

In the limit of short diffusion times, $\Delta \ll a^2/2D$, equation (11.7) reduces to equation (11.6), describing unrestricted diffusion. Conversely, in the limit of long diffusion times, $\Delta \gg a^2/2D$, we find that the echo amplitude becomes a sinc function

$$S(q,\infty) = |\ \mathrm{sinc}(\pi qa)\ |^2 = \frac{4\sin^2(\pi qa)}{(2\pi qa)^2} \tag{11.8}$$

We shall return to this long time limit in the next section. Meanwhile, it is interesting to note that if an apparent diffusion coefficient is extracted from equation (11.7) in the regime of weak applied gradients, such that $2\pi qa \ll 1$, the diffusion coefficient depends on the diffusion time, decreasing with increasing Δ from the unrestricted value at very short times to $a^2/12\Delta$ at long times. A decrease in the apparent diffusion coefficient $D(\Delta)$ with increasing diffusion time Δ is usually regarded as the signature of restricted diffusion, but as we shall show, a similar decrease can arise with unrestricted diffusion when there is chemical or diffusive exchange in multicompartment systems. Care is therefore needed when probing microstructure from the Δ dependence of the apparent diffusion coefficient. Exact solutions also exist for restricted diffusion in cylinders and spheres with perfectly reflecting boundaries, as well as when the boundaries act as relaxation sinks (257,266). Figure 11.3 shows the Δ-dependence of the signal amplitude for various q values calculated for diffusion inside an isolated spherical pore with reflecting walls.

11.3.3 Q-Space Microscopy in the Long Time Limit

Regardless of the geometry of the confining space, in the long time limit $\Delta \rightarrow \infty$ all spins lose memory of their initial positions, so

$$P(\mathbf{r}' - \mathbf{r}, \infty) = \rho(\mathbf{r}') \tag{11.9}$$

In this limit the average propagator reduces to the density–density autocorrelation function

$$P_{\mathrm{av}}(\mathbf{R},\infty) = \int d\mathbf{r}\ \rho(\mathbf{r})\rho(\mathbf{r} + \mathbf{R}) \tag{11.10}$$

Substitution of equation (11.10) into (11.3) shows that the echo amplitude is now the static structure factor

$$S(\mathbf{q},\infty) = \int d\mathbf{r}\ \rho(\mathbf{r}) \exp(-i\mathbf{q} \cdot \mathbf{r}) \int d\mathbf{r}'\ \rho(\mathbf{r}') \exp(i\mathbf{q} \cdot \mathbf{r}') \tag{11.11}$$

$$= |\ S(\mathbf{q})\ |^2 \tag{11.12}$$

As first pointed out by Cory and Garroway (258), equation (11.12) is analogous to the theory for optical and X-ray diffraction. Interference patterns are observed in $S(\mathbf{q},\infty)$ due to the cancellation of spin phases, and the interference pattern is related to microstructure via the static structure factor. At long diffusion times the spins are

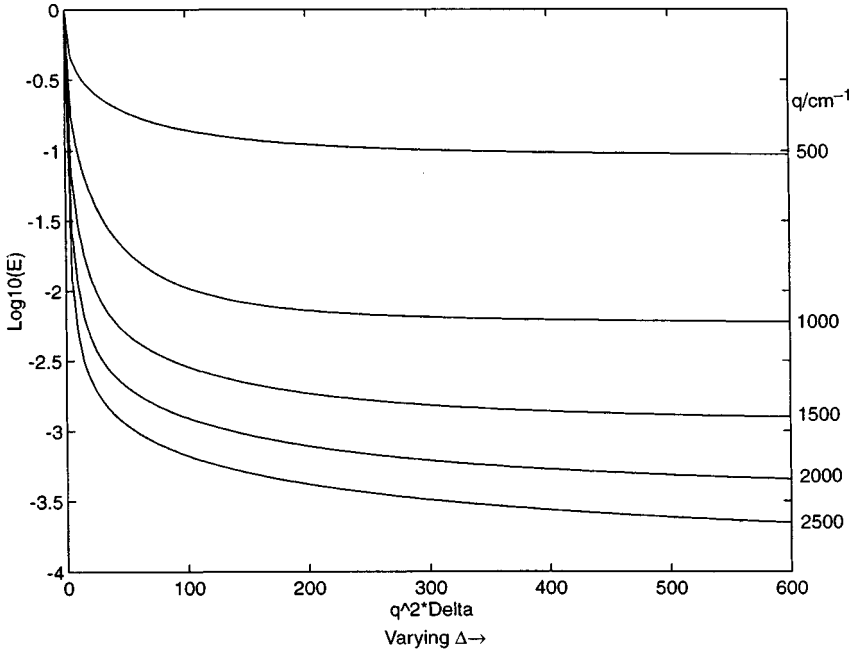

Figure 11.3. PGSE signal attenuation calculated for spins confined within a spherical pore of radius 10 μm with nonrelaxing reflecting walls. The x-axis corresponds to $q^2\Delta$ for fixed q and increasing Δ. The curves correspond to q values of 500 (top), 1000, 1500, 2000, and 2500 cm^{-1} (bottom), respectively.

reflected many times off the confining boundaries, so their displacement is no longer determined by the diffusion coefficient. Instead, their probability distribution is determined by the morphology of the container. Consider, for example, the case of diffusion in a closed rectangular box of dimension a. For this container $\rho(\mathbf{r})$ is simply a top hat function whose Fourier transform is the sinc function, $\text{sinc}(\pi qa)$. Equation (11.12) therefore gives equation (11.8), which, of course, it must do for consistency. Equation (11.8) shows that $S(\mathbf{q},\infty)$ has nodes at $qa = 1,2,\ldots,n$ due to spin phase cancellation and the position of the nodes can be used to determine the size of the container, a. Expressions for $S(\mathbf{q},\infty)$ for other, more realistic microstructures, including closed spherical pores, systems with connected pores, branched networks, and fractal geometries, can be found in Callaghan's book (5). Figure 11.4 shows the signal attenuation calculated for spins in an isolated spherical pore of radius 10 μm as the surface relaxation strength of the pore increases. The dashed line corresponds to nonrelaxing walls. It can be seen that the major effect of the increasing surface relaxation is to make the apparent radius of the pore decrease due to loss of magnetization in an increasingly thick surface layer. This results in a shift of the diffraction minima to larger values of qa. The example of connected pores is of special significance in microporous foods so will be considered in greater detail.

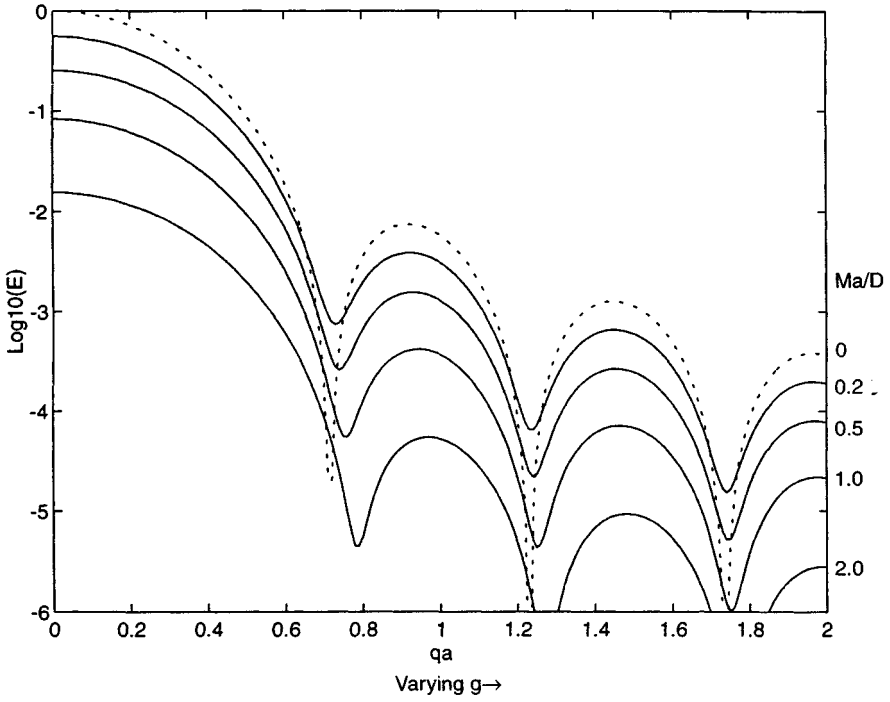

Figure 11.4. PGSE signal attenuation calculated for spins confined within a spherical pore of radius 10 μm as the surface relaxation of the pore wall, $\mu a/D$, increases. The x-axis corresponds to increasing qa at a fixed $\Delta = a^2/D$ for the solid lines and for $\Delta = 100a^2/D$ for the dashed line. The curves correspond to surface relaxation strengths $\mu a/D$ of 0 (top, dotted), 0.2, 0.5, 1.0, and 2.0 (bottom), respectively.

11.3.4 Systems with Connected Pores

So far we have discussed the propagator for the extreme cases of unrestricted diffusion and for diffusion confined within closed pores. Many real microstructures fall between these two extremes such that there is water inside larger regions, or "pores," connected by smaller "throats" or "necks." An obvious example is a water-saturated bed of randomly packed water-impermeable microspheres, but a more realistic example for many foods would, perhaps, be a randomly packed bed of starch granules, dried to the pendular state, such that most water outside the granules has been removed, leaving water "bridges" at the points of contact. In such a structure the water-saturated starch granules represent the pores and the points of contact between granules represent the throats. In principle, the structure could be probed with the q-space formalism in the long time limit, $\Delta \rightarrow \infty$, as presented in Section 11.3.4. However, because of the pore connections, the static structure factor would need to be that for the entire sample, not just for a single pore, so unrealistically long diffusion times would be needed. The long-time-limit case is therefore inap-

propriate. Instead, the microstructure can be probed using diffusion times sufficient for spins to diffuse from one pore into a neighboring pore. If the mean interpore spacing is b, this is roughly $b^2/2D_{eff}$, where D_{eff} is the effective long-time "macroscopic" diffusion coefficient. The propagator theory for this case has been presented elegantly by Callaghan et al. (260). Using a pore-hopping model, they showed that the echo attenuation can be expressed as

$$\frac{S(q,\Delta)}{S(q=0)} = |S_0(q)|^2 \exp\left(\frac{-6D_{eff}\Delta}{b^2 + 3\xi^2}\right)\left[\frac{1 - \exp(-2\pi^2 q^2 \xi^2)\sin(2\pi qb)}{2\pi qb}\right] \quad (11.13)$$

where ξ is the standard deviation in the interpore spacing, b, and $|S_0(q)|^2$ is the static structure factor for an isolated pore. Equation (11.13) contains a number of important concepts. It assumes pore *equilibration:* that the time scale required for the spins to probe the internal structure within a single pore of radius a, $a^2/2D_{eff}$, is much less than the time scale needed to diffuse to a neighboring pore, $b^2/2D_{eff}$. This is why the static structure factor for a single pore, $|S_0(q)|^2$, multiples the right-hand side of equation (11.13). In addition, the possibility of interpore hopping introduces an additional diffractionlike effect described by the sine-function term. At high q, and at times $\Delta > b^2/2D_{eff}$, this introduces a "diffraction" maximum when $qb \approx 1$ in the echo attenuation plot shown in Figure 11.5. It is also interesting to note that the interpore diffusion introduces a q-dependence into the apparent diffusion coefficient, defined as the ratio

$$D_{app} = \frac{-(1/4\pi^2 q^2) d\, ln[S(q,\Delta)/S(q=0)]}{d\Delta} \quad (11.14)$$

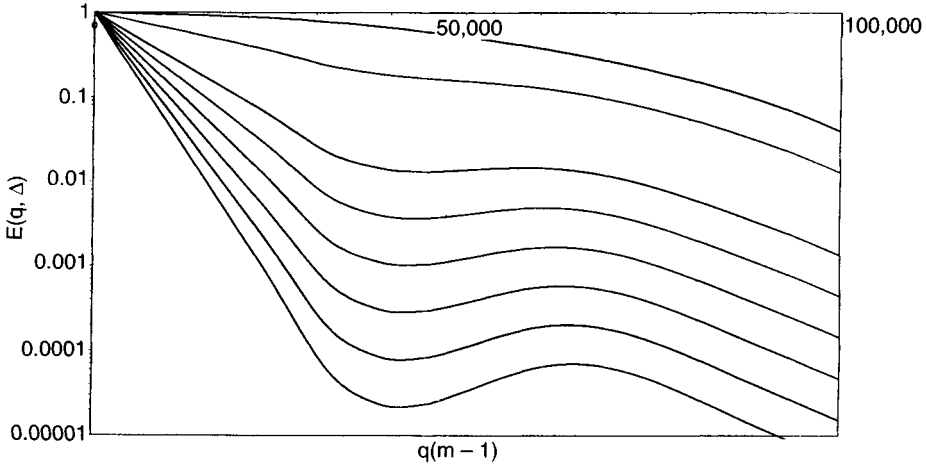

Figure 11.5. Signal attentuation calculated using the pore-hopping model, equation (11.13), for several diffusion times Δ. Note the diffraction minima arising from interpore diffusion. Δ increases from the top to bottom curves.

For unrestricted diffusion, D_{app} is equivalent to D, the intrinsic molecular self-diffusion coefficient of the pure fluid, whereas at long Δ and small q, D_{app} becomes equivalent to D_{eff}. The (q–Δ)-dependence of this variation gives information on the pore size and interpore spacing.

11.3.5 Q-Space Microscopy in the Short Time Limit

It would appear from the earlier discussion that probing microstructure on a distance scale b requires a diffusion time of at least b^2/D and that measurements with diffusion times much less than b^2/D will only result in measurements of unrestricted diffusion. Somewhat surprisingly, this is not the case, and in a series of papers Mitra and co-workers (262–265) have shown that a PGSE measurement of the apparent diffusion coefficient at very short times is a uniquely powerful way of determining the surface-to-volume ratio S/V of microporous materials. The physical reason for this is easy to understand and is illustrated in Figure 11.6. At short times Δ, only molecules in a surface layer of thickness equal to the diffusion length $(D\Delta)^{1/2}$ sense the presence of the walls. If the wall area is S, a fraction of spins $S(D\Delta)^{1/2}/V$ deviate in their behavior from free diffusion and are associated with a non-Gaussian propagator. What Mitra and co-workers showed using a complicated

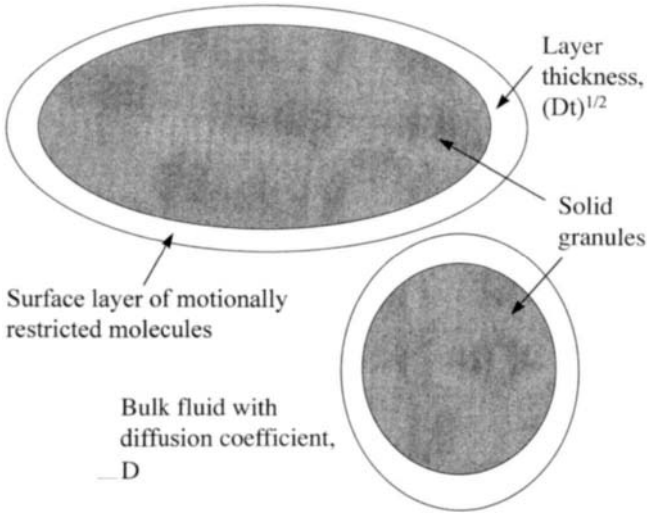

Figure 11.6. Origin of $\Delta^{1/2}$ behavior in the PGSE apparent diffusion coefficient. At short Δ only molecules in a surface layer of thickness equal to the diffusion length $(D\Delta)^{1/2}$ are sensitive to the restrictions due to the pore walls. The fraction of restricted molecules at short times is given by $(S/V)(D\Delta)^{1/2}$. (From Ref. 264.)

perturbative expansion of the diffusion propagator was that this resulted in a short-time diffusion coefficient $D(\Delta)$ that was proportional to the S/V ratio such that

$$\frac{D(\Delta)}{D_0} = 1 - \left(\frac{4}{9\pi^{1/2}}\right)(D\Delta)^{1/2}\left(\frac{S}{V}\right) + \text{higher-order terms in } \Delta \text{ and } \Delta^{3/2} \quad (11.15)$$

This expression is especially noteworthy because the coefficient of $(D\Delta)^{1/2}$ does not contain the surface relaxation strength μ of the wall because magnetization lost at the wall does not contribute to the diffusion measurement. This contrasts with the relaxation analysis of Chapter 10, where the relaxation rate in the fast diffusion limit was enhanced by a factor proportional to $\mu(S/V)$. In other words, a measurement of the absolute surface-to-volume ratio by relaxometry is hindered by our ignorance of the surface relaxation strength μ. But this is not the case with short-time measurements of the apparent diffusion coefficient and suggests that a combination of the two types of measurement would be an excellent way of measuring the surface relaxation strength. Of course, short-time diffusion measurements give the surface-to-volume ratio but not details of the microstructure. For microstructural determination longer diffusion times are necessary, as discussed above. Nevertheless, many important processes, such as the rates of surface spoilage reactions, depend on S/V ratios, so this approach has considerable potential value.

11.4 SUSCEPTIBILITY EFFECTS ON DIFFUSION MEASUREMENTS

In Section 11.3 we showed how deviations of the diffusion propagator from a simple Gaussian can be used to probe microstructure or surface-to-volume ratios. Unfortunately, diffusion in an inhomogeneous field also causes the propagator to depart from a Gaussian form so that D_{app} depends on the diffusion time and wavevector. This makes it easy to confuse the effects of inhomogeneous background gradients from those of microstructure. As we saw in Chapter 10, local magnetic field distortions arise from susceptibility discontinuities across phase boundaries. In the presence of the main magnetic field B_0, these discontinuities induce local field gradients, or background gradients, which can be labeled $\mathbf{G}_0$. Assuming that these are linear gradients (which is not usually the case; see below), their effect in a diffusion pulse sequence can be incorporated by replacing the wavevector $\mathbf{q}$ by $(\mathbf{q} + \mathbf{q}_0)$, where $\mathbf{q}_0$ is $(2\pi)^{-1}\gamma\mathbf{G}_0\delta$. Because the echo attenuation involves the vector product $\mathbf{q} \cdot \mathbf{q}$, the presence of background gradients introduces terms in q_0^2 and $\mathbf{q} \cdot \mathbf{q}_0$. The former are independent of the applied gradient and enter along with transverse relaxation. Their effect on transverse relaxation was discussed in Chapter 10. The linear vector cross terms in $\mathbf{q} \cdot \mathbf{q}_0$ introduce the $(q\text{–}\Delta)$-dependence, which can be confused with microstructural effects. In some cases their effect can be minimized by acquiring the echo with positive and negative applied gradient and canceling the cross terms in the data processing step by first taking the logarithm of the echo attenuation and adding the results for the positive

and negative gradients. This exploits the fact that reversing the direction of the applied field gradient changes $\mathbf{q} \cdot \mathbf{q}_0$ to $2 - \mathbf{q} \cdot \mathbf{q}_0$ (227). An alternative approach is to design pulse sequences that minimize the effect of background gradients. Several such pulse sequences have been suggested with varying degrees of success (156,261).

Although background gradients are usually considered a nuisance factor to be minimized, recent work has shown that they can also enhance our ability to resolve microstructure (233). This exploits the highly inhomogeneous nature of internal field gradients, an aspect that has been ignored when they are modeled as an effective linear gradient of average strength $\mathbf{G}_0$. The results show that water-filled pores in a porous solid can be resolved on the basis of their different apparent transverse relaxation times when measured in a high B_0 field corresponding to a proton frequency of 300 MHz, whereas they were not resolved at a lower B_0 value of 20 MHz. The reason for this enhanced pore resolution is believed to be the existence of highly inhomogeneous field gradients localized at the pore edges and dependent in magnitude and orientation on the pore geometry. Diffusion of water molecules through these gradients enhances their transverse relaxation rate to an extent that depends on pore geometry, permitting different pores to be distinguished. The same inhomogeneous background gradients cause the apparent water diffusion coefficient within each pore to be greatly enhanced compared to that of bulk water, to an extent that also depends on pore size and geometry. These pore-resolved diffusion coefficients are obtained by analyzing the effect of applied gradients on each resolved relaxation peak in the distribution of transverse relaxation times measured with the CPMG pulse sequence. The pore-dependent diffusive enhancements can be reproduced theoretically by numerically solving the Bloch–Torrey equations with gradient terms and assuming that the applied linear field gradient behaves like a parabolic-shaped gradient within each pore. The parabolic form of the applied gradient arises not because of distortion of the linear gradient by the microstructure, but rather, because its linearity is masked by the nonuniform background gradient within each pore. At the pore edge the background gradient G_0 far exceeds the applied gradient G, which therefore has little or no effect, whereas in the pore center, the background gradient is smallest and the applied gradient exceeds it in magnitude. The net result as far as water protons within the pore are concerned is an apparent applied gradient that is zero at the pore edges and maximum at the pore center. This nonuniform applied gradient results in an apparently enhanced diffusivity if the data are analyzed assuming a linear applied gradient. The greatest distortion appears with the smallest pores, so this may also be a useful mechanism for probing pore size distributions and even pore geometry (281).

11.5 COUPLED RELAXATION AND DIFFUSION

Provided that the system is spatially homogeneous (i.e., lacks microstructure on the diffusion distance of interest), the relaxation is single exponential and the echo

attenuation by relaxation and diffusion is simply factorizable. For the Stejskal–Tanner spin-echo sequence in Figure 11.1, the echo amplitude is then

$$S(q,\Delta) = \exp\left[-4\pi^2 q^2 D\left(\Delta - \frac{\delta}{3}\right) - \frac{TE}{T_2}\right] \tag{11.16}$$

The corresponding expression for the stimulated-echo sequence in Figure 11.2 is

$$S(q,\Delta) = 0.5S(0)\exp\left[-q^2 D\left(\Delta - \frac{\delta}{3}\right) - \frac{(t_2 - t_1)}{T_1} - \frac{2t_1}{T_2}\right] \tag{11.17}$$

In equation (11.16) $S(0)$ is the initial equilibrium magnetization, and the factor of 0.5 arises because the second 90° pulse only converts y-magnetization to the longitudinal direction, not x-magnetization. Relaxation effects in spatially inhomogeneous systems are harder to eliminate and can have significant effects. For example, the diffraction effects predicted by equation (11.12) at long diffusion times are completely lost when the box walls act as strong relaxation sinks because the magnetization is destroyed at the boundary rather than reflected back into the container. Microstructure can then be probed, in the absence of applied field gradients, using the relaxation-time distribution as discussed in Chapter 10. One of the outstanding challenges is to develop robust NMR protocols for probing microstructure when relaxation and diffusion effects are both present. The author has explored the potential of combining relaxation and diffusion effects using constant gradient CPMG and stimulated echo pulse sequences (281). However, data interpretation then requires numerical solution of the Bloch–Torrey equations for the postulated microstructure, and this is computationally very challenging.

11.6 DIFFUSION IN MULTICOMPARTMENT SYSTEMS

A rigorous analysis of coupled diffusion and relaxation in multicompartment systems such as cellular tissue and porous structures requires numerical solution of the coupled Bloch–Torrey equations for each compartment along lines similar to those discussed for pure relaxation in Chapter 10. The echo amplitude is, in general, a multiple-exponential function of the diffusion time Δ, but the relationship between the component decays and microstructure is exceedingly complex. Some simplification is afforded if the diffusion between compartments is treated as a chemical exchange process characterized by the mean lifetime of spins in each compartment. Despite the loss of morphological information, this is a useful first approximation and results in the following closed analytic expression for the spin-echo amplitude arising from unrestricted diffusion with two chemically exchanging species characterized by intrinsic diffusion coefficients D_i, proton fractions P_i, and reciprocal lifetimes k_i, where i (= 1,2) is the species label (160)

$$S(\Delta) = P_1' \exp(-a_1\Delta) + P_2' \exp(-a_2\Delta) \tag{11.18}$$

where

$$a_{12} = 0.5[\gamma^2\delta^2G^2(D_1 + D_2) + \frac{1}{T_1} + \frac{1}{T_2} + k_1 + k_2 + \left\{-\left[\gamma^2\delta^2G^2(D_2 - D_1) + \frac{1}{T_1} - \frac{1}{T_2} + k_1 - k_2\right]^2 + 4k_1k_2\right\}^{1/2} \quad (11.19)$$

$$P_2' = \frac{P_1(\gamma^2\delta^2G^2D_1 + 1/T_1 + P_2(\gamma^2\delta^2G^2D_2 + 1/T_2) - a_1}{a_2 - a_1} \quad (11.20)$$

Here $P_1' + P_2' = 1$ and $P_1k_1 = P_2k_2$. Note that in equations (11.18) and (11.19) the subscripts on T_1 and T_2 refer to the species (compartment) designation, not to longitudinal or transverse relaxation.

It is interesting to note that a Δ-dependent effective diffusion coefficient can be obtained from equation (11.18) if it is assumed that the compartment with the smaller diffusion coefficient has the longer relaxation time. This is a consequence of the nonfactorizability of relaxation and diffusion in multicompartment systems, which means that relaxation effects cannot be removed by the simple expedient of taking the ratio $S(q,\Delta)/S(q = 0)$.

11.7 ANOMALOUS DIFFUSION

For unrestricted diffusion the mean-square displacement of the phase-labeled spins is proportional to the time and the conditional probability assumes the Gaussian form of equation (11.5). However, when the migration space accessed by the spins has a fractal geometry, the mean-square displacement of the spins has the more general form (151)

$$< (\mathbf{r} - \mathbf{r}_0)^2 > = \alpha t^{2/d} \quad (11.21)$$

where d is called the anomalous diffusion exponent. Normal, unrestricted diffusion corresponds to $\alpha = 6D$ and $d = 2$, but in fractal networks motion is restricted and $d > 2$. In the narrow pulse regime, $\delta \ll \Delta$, equation (11.21) corresponds to a stretched exponential attenuation function,

$$S(q,\Delta) = S(0)\exp\left[-\frac{\alpha}{6}(2\pi q)^2\Delta^{2/d}\right] \quad (11.22)$$

Fringe-field stimulated-echo attenuation in biological tissue can often be fitted by introducing an effective anomalous diffusion coefficient d, especially in the small q region. However, this may be no more than a convenient empirical representation of the effects of restricted multicompartment diffusion and relaxation than a true consequence of fractal geometry. It can, however, be argued that the range of distance scales characterizing structural heterogeneity in cells, ranging from macromolecu-

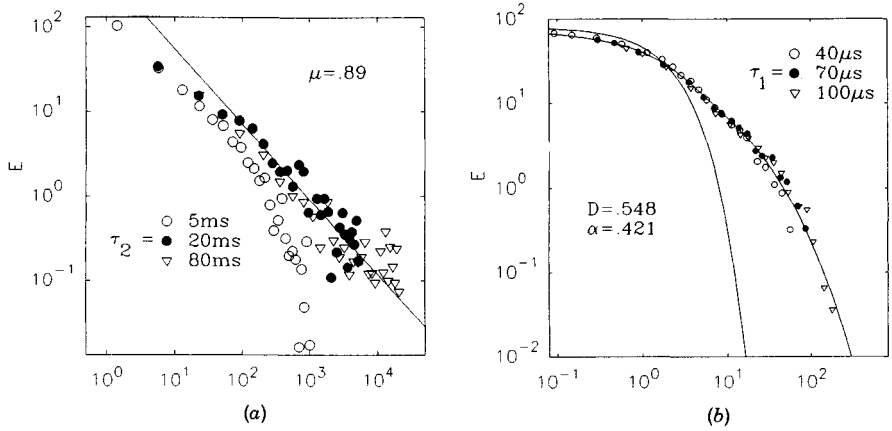

Figure 11.7. Fringe-field stimulated-echo decays for liver tissue. (*A*) q variation at fixed Δ. The straight line corresponds to the function $q^{-2\mu}$ with $\mu = 0.89$. Simple unrestricted diffusion would correspond to $\mu = 1$. (*B*) Δ variation at fixed q. The line fitting the data corresponds to equation (11.23). For comparison the curve for the second term in equation (11.23) corresponding to anomalous diffusion with the same scaling is displayed. The notation is such that E is $S(q,\Delta)/S(q = 0)$, b is $(2\pi q)^2 D\Delta$, τ_1 is δ, and τ_2 is Δ.

lar networks to small and large organelles, gives rise to a fractal-type geometry. Figure 11.7 shows the fringe-field stimulated-echo attenuation data for mammalian liver tissue taken from Kopf et al. (282). The data for Δ-variation of the echo attenuation were fitted as a superposition of the expression for unrestricted diffusion [equation (11.6)] and a stretched exponential function corresponding to anomalous diffusion in a fractal geometry [cf. equation (11.22)]

$$\frac{S(q,\Delta)}{S(0)} = C_1 \exp[-(2\pi q)^2 D\Delta] + C_2 \exp[-(2\pi q)^2 D\Delta]^a \qquad (11.23)$$

Figure 11.7*b* shows that this expression provides a reasonable fit to the data for Δ-variation at fixed wavevector q. In contrast, the data for q-variation at fixed Δ (actually, δ-variation at fixed fringe-field gradient G and fixed Δ) changed from a simple unrestricted diffusion form at short Δ to a power-law dependence at long Δ when the microstructure begins to be probed (Figure 11.7*a*). Clearly, much theoretical work is still required if these changes are to be understood at a more fundamental, nonempirical level. They do, however, present exciting future possibilities for monitoring cell and tissue changes at a subcellular level.

11.8 MICROSTRUCTURE-WEIGHTED k-SPACE IMAGING

In Chapter 3 it was shown how the temperature dependence of the diffusion coefficient could be used to produce temperature maps from diffusion-weighted k-space imaging sequences. In like manner, spatial maps of microstructure can, in principle,

be generated by using the pulse sequences above to weight voxel intensities in k-space imaging sequences. One problem with this approach is the large amount of data generated by exploring (q–Δ)-space within each k-space imaging voxel. The other problem is the extraction of microstructural information from the (q–Δ)-weighted images. To simplify the problem it has been proposed (150) that the q–Δ data should be analyzed with one of three idealized models, each representative of a different type of microstructure. The first is the *fractal microstructure*, for which equation (11.22) provides the best-fitting function. Spatial maps of the parameters $\alpha(\mathbf{r})$ and $d(\mathbf{r})$ are then the end product of image analysis. The second is the *barrier microstructure* which usually generates complicated infinite series such as equation (11.7) for the case of boxes, spheres, and cylinders with reflective walls. It is proposed that these barrier-type microstructures can be represented by the simplified function

$$S(q,\Delta) = S(0)[(1 - R)\exp(-q^2D\Delta) + R] \tag{11.24}$$

where R is the residual attenuation observed at long Δ, which is related to barrier spacing and barrier permeability. Barrier-type microstructures are therefore quantified by parameter maps of $R(\mathbf{r})$ and $D(\mathbf{r})$. *Multicompartment systems* are the third major type of microstructure used to generate parameter maps. Equation (11.18) to (11.20) are simplified to the biexponential function

$$S(q,\Delta) = S(0)[P_S\exp(-q^2D_S\Delta) + (1 - P_S)\exp(-q^2D_F\Delta)] \tag{11.25}$$

which corresponds to two microscopic compartments characterized by fast and slow diffusion coefficients D_F and D_S and populations P_F and P_S, respectively. Parameter maps of $P_S(\mathbf{r})$, $D_S(\mathbf{r})$, and $D_F(\mathbf{r})$ characterize this type of microstructure. More components can be treated if the quality of the data permits the extraction of more than two exponentials. Of course, if there is good reason to suspect a particular type of microstructure, such as the connected pore structure, the appropriate idealized function, such as a simplified pore-hopping function, can be introduced, together with its associated parameter maps.

To date these various microstructural parameter maps have been generated only in the clinical context (actually, for intact duck embryos), where they have been shown to provide much improved contrast over a conventional map of the apparent diffusion coefficient derived assuming unrestricted diffusion (150). It remains to be investigated which, if any, of the parameter maps are useful in quantifying changes in food microstructure during processing and storage.

11.9 CONSTANT-GRADIENT CPMG AND STIMULATED-ECHO STUDIES

Many variants on the Stejskal–Tanner and stimulated-echo pulse sequences have been proposed (156). The constant-gradient versions of these pulse sequences are worth considering in greater detail because these are easy to automate. Instead of

gradient pulses, the gradients are applied during the entire sequence and can be ramped from $-G$ through to $+G$ between acquisition cycles. The constant-gradient CPMG sequence is especially valuable for studying coupled transverse relaxation and diffusion in complex systems, (281). When G is zero, the CPMG echo-decay envelope can be analyzed as a multiple-exponential decay, and as discussed in Chapter 10, this can be related to microstructure. By repeating the entire CPMG sequence in the presence of a constant gradient G, each transverse relaxation-time peak becomes diffusion weighted in a microstructurally sensitive way. In this way, relaxation and restricted diffusion can be used to probe microstructure simultaneously (281). Even when acquired in a constant gradient, the echo-decay envelope can still be analyzed as a multiple-exponential decay function, but the exponential coefficients are no longer simple transverse relaxation rates. Indeed, we can write

$$S(q,\omega,t) = \sum_i A_i(q_i,\omega) \exp[-R_i(q,\omega) - \alpha_i(q,\omega)]t \tag{11.26}$$

where $R_i(q,\omega)$ is a generalized wavevector and frequency-dependent relaxation rate and $\alpha_i(q,\omega)$ is a generalized wavevector and frequency-dependent diffusion term. The frequency ω in equation (11.25) is the CPMG pulsing frequency $2\pi/\tau$ (i.e., the reciprocal of the 90 to 180° pulse spacing). The generalized diffusion term α_i can be related to a frequency-dependent diffusivity (256,281) such that

$$\alpha_i(q,\omega) = \frac{\pi^2}{4} q^2 t \left[D(0) + 2\left(\frac{2}{\pi}\right)^4 D_i(\omega) \right] \tag{11.27}$$

In the absence of external gradients, $q = 0$, α_i is zero and equation (11.26) reduces to the conventional expression for multiple-exponential transverse relaxation discussed in Chapter 10. In general, however, equation (11.26) shows that by varying the CPMG pulsing frequency in the presence of applied gradients, the frequency dependence of the apparent diffusion coefficient $D(\omega)$ can be probed. In heterogeneous systems this frequency dependence arises because there are diffusive modes set up by the microstructure and these diffusive modes exist in the presence of spatially nonuniform background gradients. For any geometry the frequency dependence can, in principle, be calculated by solving the Bloch–Torrey equations for the CPMG sequence in the presence of applied gradients G and background gradients G_0. Figure 11.8 shows the frequency dependence calculated for isolated lamellar pores of the sizes indicated in the presence of a parabolic nonlinear field gradient (281). The frequency dependence becomes most pronounced for small pores and has been observed experimentally in a water-saturated model system consisting of randomly packed 22.1-μm-diameter glass microspheres (see Figure 11.9). The break in the data in Figure 11.9 arises because the CPMG decay envelope becomes biexponential at low pulsing frequencies, with the major part of the decay amplitude in the slower-decaying component, which is plotted in Figure 11.9. The diffusion coefficient $D(\omega)$ also depends on pore size. In fact, the presence of local background gradients within the pores makes $D(\omega)$ apparently increase with decreasing pore size, as the experimental data in Figure 11.10 confirm (281). Although the

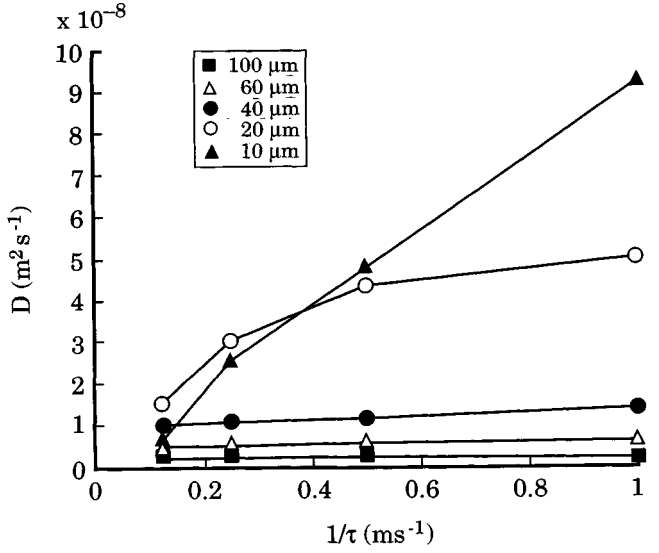

Figure 11.8. Theoretical frequency dependence of D_{app} ($x10^{-8}$ m^2/s) calculated for lamellar pores of the sizes indicated for a parabolic internal field gradient and a pulse spacing of 1 ms. (From Ref. 227.)

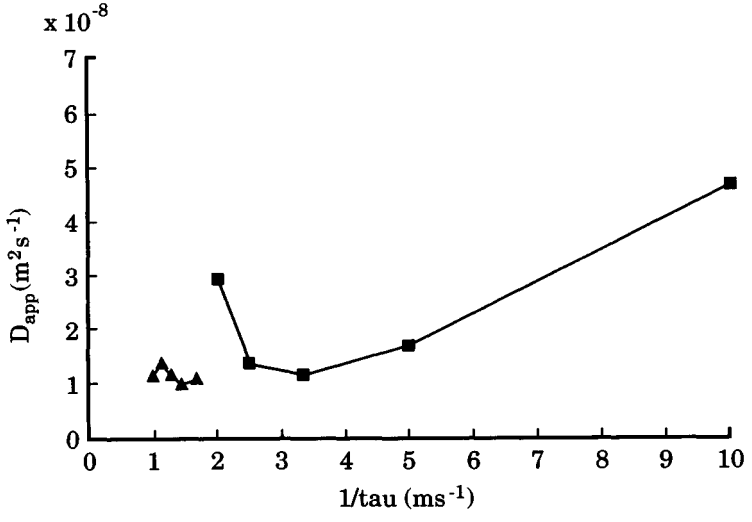

Figure 11.9. Experimental frequency dependence of D_{app} ($x10^{-8}$ m^2/s) for a water-saturated bed of 22.1-μm-diameter glass microspheres measured at 300 MHz. The frequency is expressed as the reciprocal CPMG pulsing rate. The break in the data arises because the decay for $\tau < 500$ μs becomes double exponential with the major part of amplitude (70%) in the slower-relaxing component, which is the one shown. (From Ref. 227.)

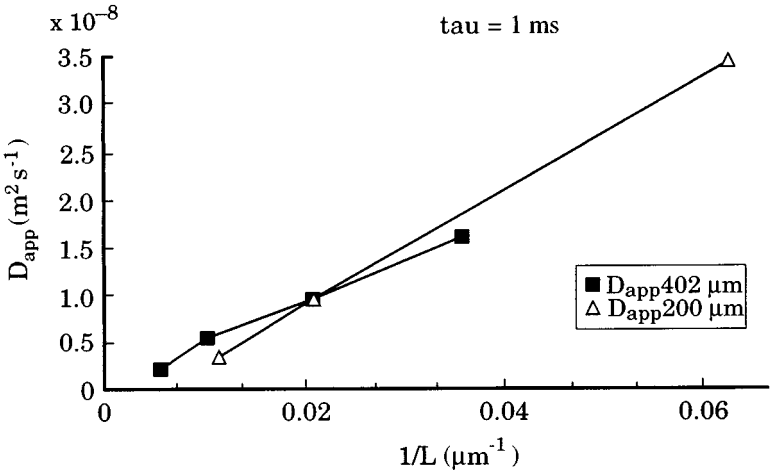

Figure 11.10. Experimental dependence of D_{app} (x 10^{-8} m^2/s) on reciprocal pore size for water-saturated beds of glass microspheres of the diameters indicated. A fixed pulse spacing τ of 1 ms and a spectrometer frequency of 300 MHz were used throughout. (From Ref. 227.)

magnitude and frequency dependence of $D(\omega)$ is sensitive to microstructure, the effects are subtle and their interpretation requires extensive numerical simulation. For this reason it will be some time before they can be exploited for routine microstructural determination.

The constant-gradient CPMG and stimulated-echo sequences can also be used in the fringe field of a superconducting magnet. Because this field gradient is created by the spatial decay of the main spectrometer field B_0, it is orders of magnitude greater than any pulsed gradient generated through gradient coils. A strong field gradient G corresponds to a high wavevector q ($= \gamma G\delta/2\pi$) and to short, submicron distance scales (144). One problem with such fringe field diffusion studies is that even a conventional 1- or 2-μs hard 90° pulse becomes slice selective, and because the gradient cannot be turned off, special iterative fitting methods are needed to compensate for relaxation effects (144). Some examples of fringe-field methods are presented in the applications section.

11.10 MICROSTRUCTURAL DETERMINATIONS IN FOOD MATRICES

In this section we review the use of restricted diffusion in microstructural determinations for several types of food-based materials, beginning with gels.

11.10.1 Gels

Ohtsuka and co-workers have been particularly active in NMR diffusion studies of gel microstructure (141–143). The stimulated-echo pulsed field gradient method

was applied to concentrated gels with varying diffusion times Δ up to 1010 ms and variable gradient amplitudes G at fixed δ and t_1. An effective water diffusion coefficient $D(\Delta)$ was extracted using the standard equation

$$ln\left[\frac{S(q,\Delta)}{S(q=0)}\right] = -D(\Delta)(4\pi q)^2\left(\Delta - \frac{\delta}{3}\right) \tag{11.28}$$

Plots of $\ln[S(q,\Delta)/S(q=0)]$ against $(4\pi q)^2[\Delta - 1/3\delta]$ resulted in a series of straight-line plots for increasing q at fixed Δ (Figure 11.11) whose slopes, $D(\Delta)$, decreased with increasing Δ (Figure 11.12). The decrease in $D(\Delta)$ with increasing Δ was assumed to result from restricted diffusion by the gel microstructure. Microstructural information was extracted using a simplified model in which the gel is represented as a series of parallel permeable barriers. Diffusion through these barriers is described by an expression by Meerwall and Ferguson (198)

$$\frac{S(\Delta)}{S(q=0)} = \exp\left[\frac{-\theta D_0\Delta}{a^2(\sin^2\alpha + A)}\right]\frac{2}{\pi^2 d^2} + 1 - \cos\pi d + 2\sum_{n=1,m}\left[1 - \frac{(-1)^n\cos\pi d}{(1 - n^2/d^2)}\right]\exp\left(\frac{-n^2\pi^2 D_0 B\Delta}{a^2}\right) \tag{11.29}$$

where a is the barrier spacing, D_0 the diffusion coefficient of water in the interbarrier spaces, $\theta = \gamma G\delta a$, α is the angle between the barrier and the field gradient, and

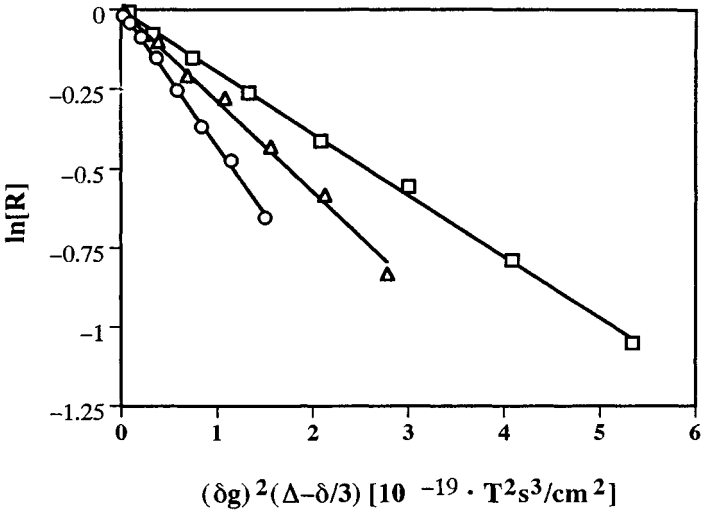

Figure 11.11. Plots of stimulated-echo attenuation versus $q^2(\Delta - \delta/3)$ for randomly packed beds of Sephadex G25 containing 30% water (weight of water/weight of total %) for three diffusion times Δ: circles, 60 ms; triangles, 110 ms; squares, 210 ms. (From Ref. 143.)

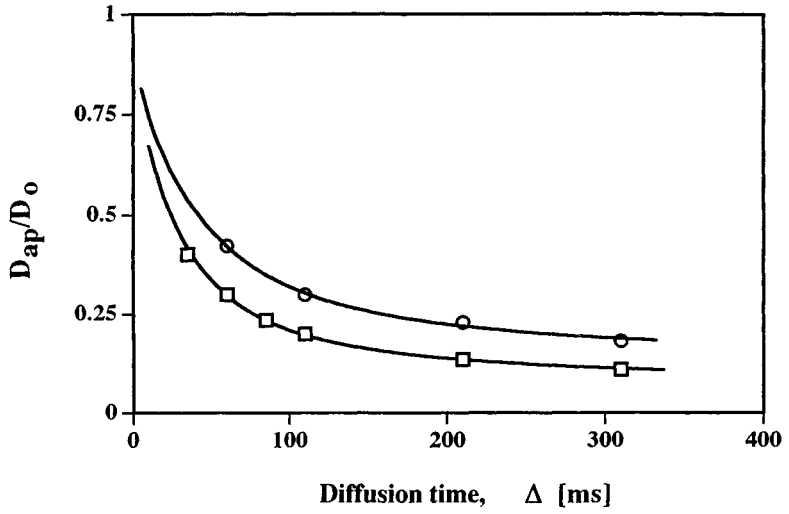

Figure 11.12. Dependence of the apparent water diffusion coefficient derived from the slope of the lines in Figure 11.11 on diffusion time Δ for Sephadex G25 at two water contents: squares, 30%; circles, 50% (weight of water/weight of total %). (From Ref. 143.)

$d = (\theta/\pi)\,|\cos\alpha|$. The coefficients A and B are related to the barrier permeability coefficient P as

$$A = \frac{\cos^2\alpha}{1 + (1/P)}$$

$$B = \frac{1}{1 + P} \tag{11.30}$$

Values of a, P, and D_0 were derived by fitting the observed data. This approach has been used with concentrated potato starch gels (141), dextran gels introduced by interaction with potassium ions (142), and gellan gum hydrogels (143). The dependence of a, P, and D_0 on gel concentration and in the case of starch, on changes induced by retrogradation were reported. Barrier spacings deduced from equation (11.29) are typically on the order of 10 to 15 μm (starch gels), 6 to 10 μm (dextran gels), and 5 to 15 μm (gellan gums), and vary slightly with gel concentration and in the case of the charged polysaccharide dextran and guar-gum gels, on ionic concentration. These pore spacings would appear to be rather large for such concentrated gels. Pores on the order of 5 to 15 μm should be visible with confocal light microscopy, but this has yet to be confirmed. Whether these pore sizes are an artifact of an oversimplified model or actually exist remains to be investigated more thoroughly. With starch it would be of interest to investigate the dependence of the mean pore spacing and permeability on the origin of the starch and on processing and storage conditions and whether they depend on the present of low-molecular-weight species such as sugars, which are known to affect retrogradation rates.

Curiously, there is no evidence of pores in the range 1 to 10 μm in protein gels such as gelatine and cross-linked bovine serum albumin (BSA). Kimmich and coworkers (144) used the stimulated-echo sequence in the fringe-field of a superconducting magnet to investigate water diffusion in these systems. The diffusion did not appear anomalous, and no significant dependence of the diffusion coefficient on diffusion time was observed. The dependence of D on protein concentration was measured and showed breaks at about 50 and 85% w/w protein. These were interpreted in terms of obstruction effects by protein molecules at high water contents and by the topologically two-dimensional diffusion in the network of overlapping hydration shells around protein molecules at lower concentrations. The percolation threshold appeared at about 15% water. A more detailed discussion of the molecular factors determining water diffusion coefficients is deferred to Part Three.

Anomalous diffusion with an anomalous coefficient d of 2.63 in equation (11.22) was observed in protein aerogels obtained by freeze-drying. This suggests that diffusion of water over the surface of the freeze-dried porous protein surface is akin to diffusion in a fractal space.

11.10.2 Cellular Tissue

During the falling-rate period of the drying of cellular tissue such as fruits and vegetables, the drying rate is limited by diffusion through internal structures within the tissue. For plant tissue this includes water transport through semipermeable membranes such as the tonoplast membrane surrounding the vacuole and the plasmalemma membrane surrounding the cytoplasm. In addition, there are obstruction effects to water diffusion from the cell walls and internal organelles. NMR spin-echo and stimulated-echo diffusion measurements are ideally suited for studying these effects and for determining the membrane permeabilities, especially when they are combined with the relaxation measurements discussed in Chapter 10. The experimental echo amplitude $S(q,\Delta)$ for cellular tissue can be modeled by solving the Bloch–Torrey equations numerically either for the subcellular compartments within a single cell or for diffusion between cells. We first consider the single-cell model. Here the compartments include the vacuole, the cytoplasm, and the cell wall region, including the extracellular water. These compartments are separated by the tonoplast and plasmalemma membranes, respectively (see Figure 10.20). It is usually straightforward to use electron microscopy to determine average cell morphology in plant tissue, but the membrane permeabilities are more difficult to measure in vivo. By fitting the observed $S(q,\Delta)$ with the numerical cell model and known cellular morphology, it is therefore possible to determine the membrane permeabilities. The feasibility of this approach has been demonstrated for fresh apple tissue (216), but it has yet to include the effects of processing or ripening. A major assumption of the method is cell uniformity throughout the tissue. This is only very approximately true, and subsequent work will need to measure the $(q–\Delta)$-dependence of k-space imaging pixels. Another major assumption is that intercell diffusion is negligible during the measurement time scale, so that cells can be treated in isolation. In fact, some workers have interpreted their $S(q,\Delta)$ data by

combining the tonoplast, cytoplasm, plasmalemma, and cell wall regions into a single effective permeability barrier to intercell diffusion. For example, Stapley et al. (303) have used the pulsed gradient stimulated-echo sequence to investigate the effect of electrical and conventional heating on intercell permeabilities in carrot tissue. A cylindrical plug of the interior region of carrot containing phloem and xylem vascular tissue was examined; as well as the remaining outer cylinder, consisting of exterior cortex cells. Diffusion was measured in axial and radial directions relative to the cylinder axis. The echo attenuation gave evidence of restricted diffusion and was interpreted using numerical solutions of the Bloch–Torrey equations for lamellar cell model in which carrot cells were represented as lamellar regions of width L containing water of diffusivity D and separated by an effective barrier of permeability P. The barrier spacings L for raw carrot were comparable to actual cell sizes, about 90 μm for the larger cells in the interior vascular region and 45 μm for the exterior cortex region. Cooking the samples increased the apparent diffusion coefficients and the barrier permeability, resulting in less restricted diffusion, consistent with a breakdown of cell structure. There were only small, but statistically significant differences between samples cooked electrically and conventionally, but this was much less than the difference between cooked and uncooked material.

11.10.3 Emulsions

In a seminal paper Packer and Rees (146) showed how the Stejskal–Tanner pulsed gradient spin-echo pulse sequence could be used to determine the distribution of droplet sizes in water-in-oil and oil-in-water emulsions. The experiment is based on the relationship between the echo attenuation ratio R, which is $S(q,\Delta,\tau)/S(q = 0,\tau)$, and the droplet size distribution $P(a)$, where a is the droplet radius

$$R = \frac{\int da\, P(a)a^3R(a)}{\int da\, P(a)a^3} \tag{11.31}$$

Here $R(a)$ is the echo attenuation ratio for a droplet of radius a given as a function of the NMR parameters G, Δ, and δ and of the unrestricted, bulk phase diffusion coefficient D by a complicated infinite series expansion which can be found in their original paper (146). The signal from the continuous phase can be removed, in the case of an oil-in-water emulsion, by the use of D_2O, and in the case of a water-in-oil emulsion, by using echo times 2τ longer than $5T_2$(oil), which exploits the fact that the T_2 of the oil is usually much shorter than that of water. Fitting the dependence of R on diffusion time Δ permits $P(a)$ to be extracted. When doing this it is usual to assume a log-normal distribution for $P(a)$.

Several improvements to this basic protocol have been suggested subsequently. Van den Enden et al. (147) proposed a more rapid method suitable for routine droplet size measurements on large numbers of water-in-oil emulsion samples. They replaced the spin-echo by the stimulated-echo sequence and eliminated the continuous-phase oil signal by the T_1 null method (i.e., an initial nonselective 180° pulse followed by a delay chosen to give zero magnetization for the oil but not

water protons). The echo attenuation was then examined only in the long Δ limit where R is independent of Δ, and the dependence of R on q was examined by varying δ at fixed G, analogously to q-space microscopy.Tables of R versus δ were calculated for different log-normal droplet size distributions, which facilitated data analysis.

The pulsed gradient spin-echo method has also been used to investigate the much more complex microstructure of cheddar and Swiss cheeses by Callaghan and co-workers (148). Cheese consists essentially of an emulsion of fat droplets in a protein–water matrix, and the NMR method was used to study the fat droplet size distribution and the microscopic distribution of water. The echo attenuation of the fat in the absence of water was measured by using an echo spacing of 160 ms, much longer than the T_2 of water in the cheese (12 ms) but shorter than of the fat. The water signal was obtained at shorter echo times by Fourier transforming the echo, which resulted in separate peaks for the fat and water. The (Δ–q)-dependence of the water signal was shown to be consistent with one-dimensional diffusion of the water along the protein chains and from one chain to another in the cross-linked protein matrix. This contradicted earlier work using electron microscopy which suggested that the water concentrated at the fat–casein interface. A Gaussian droplet size distribution was assumed for the fat, and the echo attenuation analysis gave a very broad size distribution with mean values consistent with those observed in electron micrographs, showing significant differences between the Swiss and cheddar cheeses.

PART THREE

MOLECULAR DISTANCE SCALE

12

MOLECULAR ORIGINS OF RELAXATION CONTRAST

12.1 INTRODUCTION

In Part Two we considered the multiple-exponential water proton relaxation usually observed in food materials that are heterogeneous on the microscopic distance scale of tens to hundreds of microns. The relaxation analysis was based on solution of the Bloch–Torrey equations for the exchange of magnetization between each constituent microscopic compartment, as illustrated in Figure 10.1. The compartments themselves were assumed to be spatially homogeneous and characterized by a single transverse rotating frame or longitudinal relaxation rate, labeled γ_i, within compartment i. In this chapter we present the theory for these intrinsic compartmental relaxation rates by considering the molecular origins of water proton relaxation for solutions, gels, rubbers, and glasses. The chapter begins with a consideration of dilute solutions and gels since the theory is most developed for these. The final part deals with more concentrated systems such as rubbers and glasses.

12.2 RELAXATION IN A SINGLE PROTON POOL

It is conventional when discussing the molecular origin of relaxation to start with a system where there is only one proton pool, such as pure water or the CH proton pool of a biopolymer dissolved in D_2O, and consider the effect of varying molecular mobility on the protons transverse, longitudinal, and rotating-frame relaxation rates. In water, for example, each proton experiences a randomly fluctuating local magnetic field due to transient dipolar interactions with other protons as the water molecules rotate and translate. The randomly fluctuating fields induce transitions between quantum spin states that result in magnetic relaxation. The relationship

between the rate of relaxation and the amplitude and frequency of the fluctuating fields has been discussed in numerous NMR textbooks (5,7) at various degrees of difficulty, so only the results need be quoted here. Assuming that the fluctuating magnetic fields arise solely from homonuclear dipolar interactions, it can be shown that (7)

$$T_1^{-1} = 0.4A[J(\omega_0,\tau_c) + 4J(4\omega_0,\tau_c)] \tag{12.1}$$

$$T_2^{-1} = 0.1A[6J(0,\tau_c) + 10J(\omega_0,\tau_c) + 4J(4\omega_0,\tau_c)] \tag{12.2}$$

$$T_{1\rho}^{-1} = 0.2A[3J(\omega_1,\tau_c) + 5J(\omega_0,\tau_c) + 2J(4\omega_0,\tau_c)] \tag{12.3}$$

where the J functions are spectral densities characterizing the frequency spectrum of molecular motion modulating the dipolar interaction, such that

$$J(n\omega,\tau_c) = \frac{\tau_c}{1 + n\omega^2\tau_c^2} \tag{12.4}$$

Here ω_0 is the spectrometer frequency, ω_1 ($= \gamma B_1$) the radio-frequency field strength, and τ_c a correlation time characterizing the molecular motion modulating the interaction. The amplitude of the random field fluctuations is determined in this case by the dipolar interaction constant A, which for two nuclei of spin I separated by a distance r has the form

$$A = \left(\frac{\mu_0}{4\pi}\right)^2\left(\frac{h}{2\pi}\right)^2\frac{\gamma_r^4 I(I+1)}{r^6} \tag{12.5}$$

where μ_0 is the magnetic field constant, γ_r the gyromagnetic ratio, and h is Planck's constant. Other relaxation mechanisms give expressions for the relaxation rates that differ in detail, but the principles are the same. Figure 12.1 shows the dependence of T_1, $T_{1\rho}$, and T_2 on the product $\omega_0\tau_c$, predicted by equations (12.1) to (12.3). When $\omega_0\tau_c \ll 1$, all relaxation rates are equal, $T_1 = T_2 = T_{1\rho}$. This is called the *motionally narrowed regime* because the long transverse relaxation time is equivalent to a narrow spectral linewidth in the frequency domain. This is the situation with pure liquid water. The slow-motion regime arises when $\omega_0\tau_c \gg 1$, and Figure 12.1 shows that T_1 then becomes much longer than T_2, and the spectral linewidths, proportional to $1/T_2$, become very large, sometimes many kilohertz in width. This is the situation in solid and semisolid phases such as the nonexchanging CH protons of cross-linked protein and polysaccharide gels, and ice. As mentioned in Chapter 8, rotating-frame relaxation characterizes the decay of the magnetization spin-locked in a radio-frequency field of amplitude ω_1 ($= \gamma B_1$). When ω_1 is zero, $T_{1\rho}$ is simply T_2; and in the hypothetical case that ω_1 is made as large as ω_0, $T_{1\rho}$ approaches T_1. The rotating-frame relaxation rate $T_{1\rho}(\omega_1)^{-1}$ for a pure phase therefore displays a frequency dispersion in ω_1 between a maximum value of T_2^{-1} when $\omega_1 = 0$ and minimum value of T_1^{-1} when $\omega_1 = \omega_0$ (7).

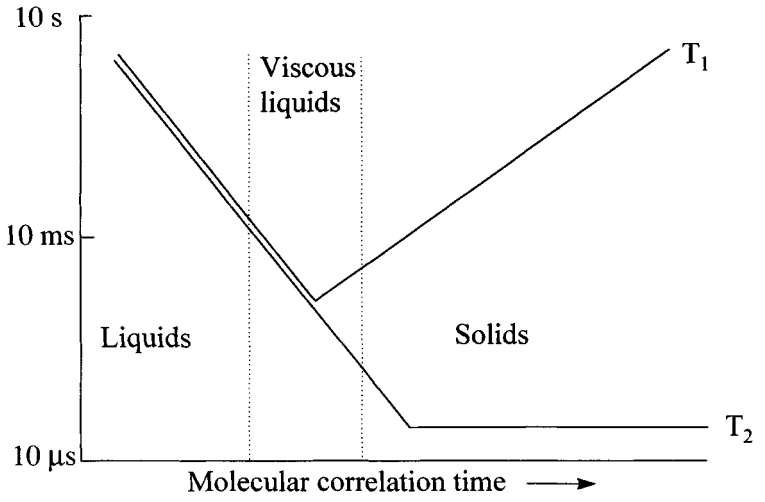

Figure 12.1. Schematic diagram of the relationship between the NMR relaxation times T_1 and T_2 and the correlation time τ_c characterizing molecular mobility in a single-component system

By measuring the ratio of the transverse, longitudinal, and rotating-frame relaxation rates and/or their frequency dependence, the correlation time τ_c can be determined by fitting the data with equations (12.1) to (12.3) or their equivalent. In this way, NMR relaxation measurements provide a powerful tool for investigating molecular dynamics. The longitudinal relaxation rate shows a dispersion when the spectrometer frequency ω_0 is varied. Conventional spectrometers operate on the megahertz frequency scale, but field-cycling spectrometers exist in which ω_0 can be reduced to the kilohertz frequency range. This permits molecular motions on the time scale of milliseconds to nanoseconds to be investigated. Rotating-frame relaxation rates are, perhaps, the richest source of information on molecular dynamics, because they have characteristics of both longitudinal and transverse relaxation. They can therefore display frequency dispersions in both ω_1 and ω_0 and permit molecular motions on intermediate time scales to be probed. These various frequency dispersions are valuable in MRI because they permit relaxation contrast to be manipulated. For example, T_1 contrast in cellular tissue tends to be minimal when working at spectrometer frequencies greater than 40 MHz but becomes greatly enhanced at lower spectrometer frequencies. Rotating-frame relaxation contrast can also be substantially greater than high-field T_1 contrast and is not as sensitive to susceptibility effects as transverse relaxation.

Whereas equations (12.1) to (12.3) and Figure 12.1 are useful for understanding relaxation in a single proton pool such as pure water, they are inadequate as a

description of water in foods because foods invariably contain more than one pool of protons which can interact both magnetically and chemically. Consider, for example, a starch gel: There is the pool of nonexchanging starch CH protons, the pool of chemically exchanging starch hydroxyl protons, and the water proton pool. Within the water proton pool we may have to consider various classes of hydration water having different residence lifetimes in the starch matrix but in diffusive exchange with pure water. The starch proton pool may also contain domains of varying mobility, depending on the degree of gelatinization and/or retrogradation. Similar proton pools can be identified within most microscopically homogeneous compartments in foods because the water inevitably contains dissolved metabolites such as sugars, amino acids, oligosaccharides, enzymes, globular proteins, and polysaccharides. It is therefore necessary to develop the theory of water proton relaxation when there are multiple proton pools within spatially homogeneous solutions and gels. We begin the analysis with transverse relaxation.

12.3 WATER PROTON TRANSVERSE RELAXATION

It has long been recognized that addition of a solute such as a globular protein to water causes an increase in the water proton transverse relaxation rate, and that at low solute concentrations the enhancement in relaxation rate is proportional to the solute concentration. There are two main reasons for the enhancement. The first is the lengthening of the water rotational and translational correlation times when the water resides in the solvation shell of the solute. This does not result in multiple-exponential relaxation because the lifetime of water molecules in the hydration shell is usually very short on the NMR observational time scale. The second possible reason for enhanced relaxation rates is proton chemical exchange between water and exchangeable solute protons such as those in hydroxyl and amino groups on the solute. One of the difficulties in interpreting water proton relaxation times in solutions and gels is knowing to what extent these two mechanisms contribute to the enhancement. We therefore begin the analysis by considering water proton transverse relaxation in one of the simplest binary solutions, methanol–water mixtures, and in subsequent sections deal with increasingly complex binary solutions and gels.

12.3.1 Methanol–Water Mixtures

A mixture of CD_3OH and water contains two proton pools, the hydroxyl protons on the water and methanol, which can be assigned transverse relaxation rates γ_a and γ_b, respectively. In the absence of exchange between these two proton pools one would expect to observe biexponential relaxation with rates γ_a and γ_b. However, at room temperature the relaxation is single exponential, indicative of fast exchange of protons between the two pools on the NMR observational time scale. There is also a chemical shift difference between the two exchanging proton pools; this has very important consequences for the magnitude of the observed transverse relaxation rate as measured by the CPMG pulse sequence. Figure 12.2 shows the dependence

of the single-exponential transverse relaxation rate for several methanol–water mixtures as a function of the CPMG pulsing frequency, $1/\tau$. As the pulsing frequency is increased the observed transverse relaxation rate shows a strong dispersion characteristic of chemical exchange. If the pulsing frequency is much greater than the proton exchange rate, the dephasing caused by the proton switching between two sites differing in resonance frequency is completely refocused by the train of 180° pulses in the CPMG sequence, so proton exchange has no additional dephasing effect. On the other hand, if the pulsing rate is much less than the proton exchange rate, the frequency variation experienced by a proton as it switches between methaonol and water causes rapid dephasing of its transverse magnetization and the observed transverse relaxation rate increases to a maximum value. The midpoint of the dispersion arises when the pulsing and proton exchange rates are equal. The observed dispersion curves can be analyzed quantitatively with the general two-site exchange expressions of Carver and Richards (136), which are reproduced in a modified form in Appendix A. These expressions relate the observed dispersion

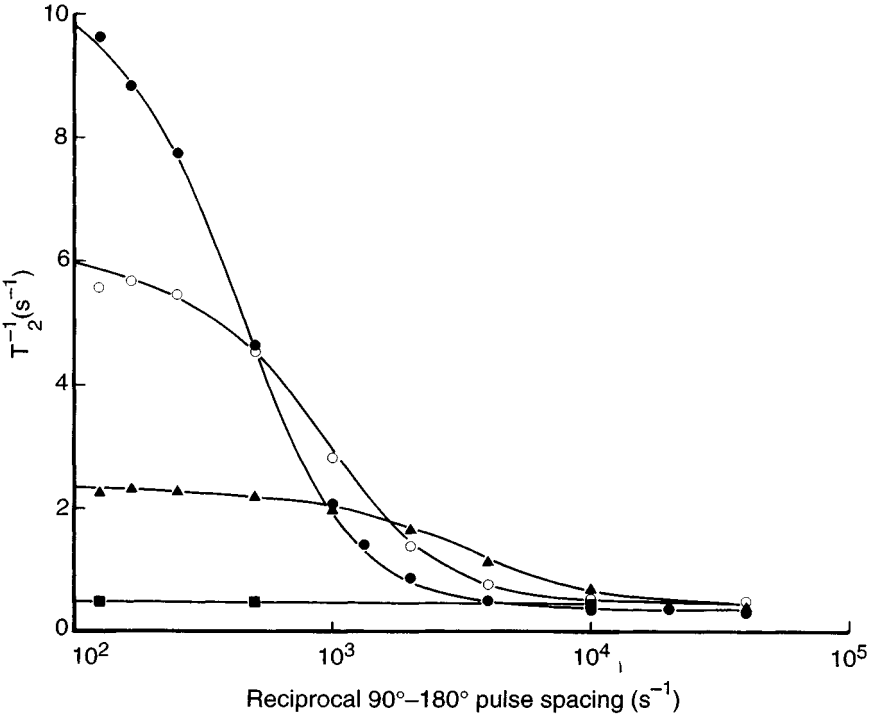

Figure 12.2. Experimental and calculated transverse hydroxyl proton relaxation dispersions for some representative mixtures of CD_3OH and water of varying composition: closed circles, $P_b = 0.9234$, pH 7.3; open circles, $P_b = 0.8152$, pH 7.3; closed/open wedge, $P_b = 0.5497$, pH 7.3; closed squares, $P_b = 0.0418$, pH 10.75. Solid lines are the theoretical curves calculated with the proton exchange theory in Appendix A. (From Ref. 139.)

curve to the intrinsic relaxation rates γ_a and γ_b, the fractions of hydroxyl protons on the water (P_a) and methanol (P_b), where $P_a + P_b = 1$, and the frequency difference between methanol and water hydroxyl protons, δ (in ppm). In addition to these parameters the dispersion depends critically on the average lifetimes of the protons on water (τ_a) and methanol (τ_b), or their corresponding reciprocals, the exchange rates, $k_a = 1/\tau_a$ and $k_b = 1/\tau_b$. These are not independent variables since $P_a k_a = P_b k_b$, which merely states that the proton exchange fluxes must be equal. The curves in Figure 12.2 are fits of these expressions to the relaxation data for the methanol–water mixtures. It is apparent that there are more unknown parameters than can be determined uniquely simply by fitting a dispersion curve. However, P_b is known from the composition of the mixture, and the relaxation rates γ_a and γ_b in the mixture are expected to be close to that of pure water and methanol, respectively. The limiting relaxation rate at fast pulsing rates γ is related to γ_a and γ_b as

$$\gamma = P_a\gamma_a + P_b\gamma_b \tag{12.6}$$

Once P_b, γ_a, and γ_b are known, the values of the parameters k_b and δ can be determined by fitting the rest of the dispersion curve, since their individual effects on the shape of the curve are quite different. k_b determines the position of the midpoint of the dispersion curve, so that increasing k_b at constant frequency difference δ has the effect of shifting the dispersion to shorter pulse spacings while causing a simultaneous drop in the relaxation rate at long pulse spacings. This effect is similar to that shown in Figure 12.2. In contrast, increasing the frequency offset δ at a constant exchange rate causes the relaxation rate at long pulse spacings to increase while leaving the midpoint of the dispersion unchanged. By fitting the entire dispersion curve it is therefore possible to obtain the values of k_b and δ as a function of state variables such as temperature, composition, and pH. Figure 12.3 shows the dependence of the proton exchange rate on pH for a methanol–water mixture of fixed composition; while Figure 12.4 shows the dependence of the proton exchange flux k ($= P_b k_b$) on composition at a fixed pH of 7.3 at 298 K (139). The data in these diagrams can be fitted to an equation of the form

$$k = P_b k_1[H_3O^+] + \frac{P_b k_2 K_w}{[H_3O^+]} + k_3 P_b^3(1 - P_b)^3 \tag{12.7}$$

The first two terms correspond to acid-base catalysis of the proton exchange and the last term to a neutral cyclic exchange mechanism, shown in Figure 12.5. The other curves in Figure 12.4 correspond to theoretical predictions for neutral exchange mechanisms involving random proton exchange for which $k = CP_b(1 - P_b)$ and for all possible five- and six-membered rings of methanol and water molecules, but these clearly fail to fit the experimental data. This type of kinetic analysis can be extended systematically to many other types of exchanging system, such as ethanol, propanol, and butanol–water mixtures and can give useful insights into solution structure, but so far only the simplest methanol–water system has been explored in this way.

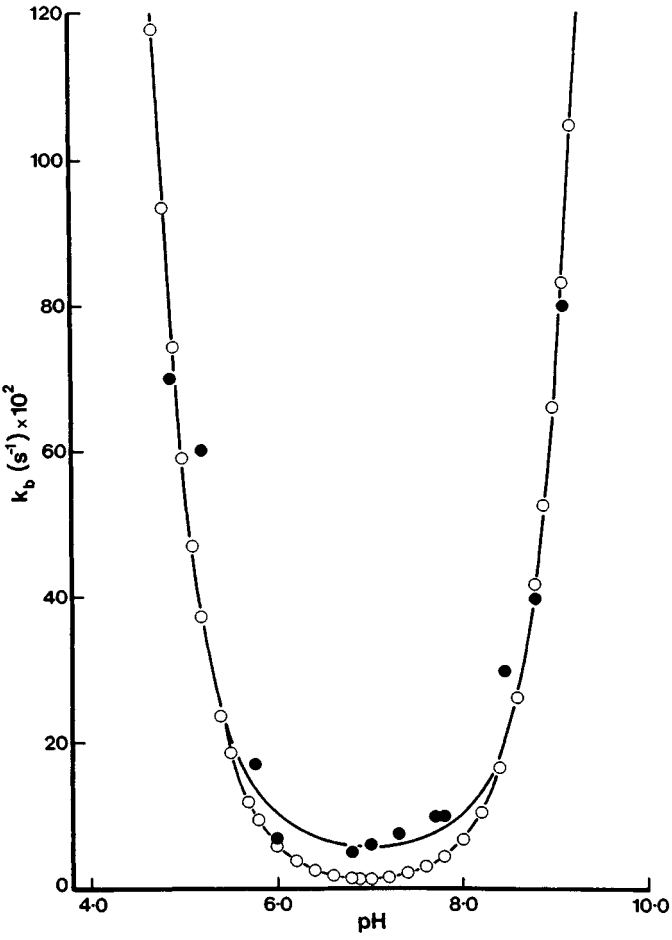

Figure 12.3. Dependence of the exchange rate k_b on pH for methanol–water mixtures of fixed composition ($P_b = 0.04186$). The solid circles are experimental points. The open circles mark the least-squares best fit of the pure acid-base-catalyzed mechanism corresponding to $k_1 = 5.9 \times 10^8$ dm^3/mol · s and $k_2 = 6.6 \times 10^8$ dm^3/mol · s. The unmarked curve shows the effect of including a neutral exchange mechanism and corresponds to $k_1 = 5.1 \times 10^8$ dm^3/mol · s, $k_2 = 5.7 \times 10^8$ dm^3/mol · s and $k_3 = 5 \times 10^2$ s^{-1}. (From Ref. 139.)

12.3.2 Monosaccharide Solutions

Like methanol, the exchangeable hydroxyl protons on monosaccharides such as glucose give rise to a transverse relaxation-time dispersion that can be used to investigate the kinetics of proton exchange in monosaccharide solutions. These dispersions dominate the transverse relaxation behavior of plant tissues such as carrot, which have significant concentrations of low-molecular-weight sugars. Indeed, the cells in carrot are sufficiently small that the transverse relaxation can be regarded as

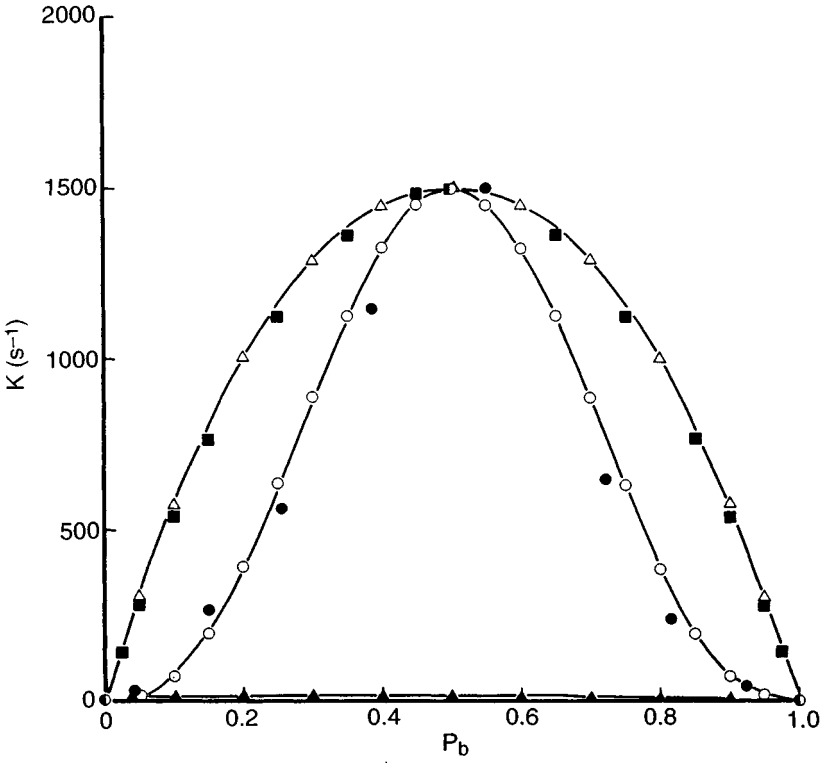

Figure 12.4. Experimental and calculated dependence of the proton exchange flux k on composition in CD_3OH–water mixtures at pH 7.3 at 298 K. Solid circles, experiment; open circles, calculated dependence for the function $k = \beta P_b^3 (1 - P_b)^3$, corresponding to the transition state in Figure 12.5 with $\beta = 9.6 \times 10^4$ s^{-1}; solid squares, calculated dependence for the function $k = CP_b(1 - P_b)$ corresponding to random proton exchange, with $C = 6 \times 10^3$ s^{-1}; open triangles, the exchange flux calculated for all five- and six-membered cyclic transition states; solid/open wedges, the exchange flux calculated for pure acid-base catalysis using the rate constants k_1 and k_2 of Figure 12.3. (From Ref. 139.)

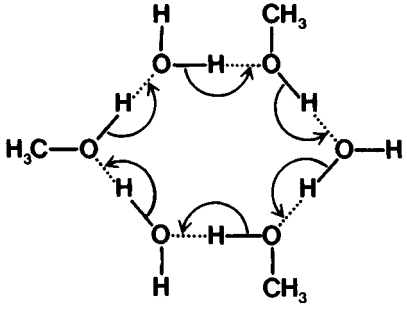

Figure 12.5. Neutral cyclic proton exchange mechanism used to fit the data in Figure 12.4. (From Ref. 139.)

single exponential to a good approximation, and the effect of processing operations such as drying and freezing on the transverse water proton relaxation of carrot mirrors the effect of concentrating and cooling a simple glucose solution.

There are, of course, three proton pools to be considered in a glucose solution. In addition to the exchangeable water and glucose hydroxyl protons, there are the nonexchanging sugar CH protons so that the transverse relaxation is biexponential, except in dilute solutions when the CH proton signal is of too low intensity to be observed. The CH relaxation time is best determined in D_2O solution, where it appears as a major component along with the residual HDO signal, which is difficult to eliminate completely even by repeated lyophilization in D_2O. Its transverse relaxation behavior can be analyzed with equation (12.2) or its analog since it is essentially an isolated proton pool. However, transverse relaxation of the exchangeable protons requires the two-site formalism already discussed for methanol–water solutions. Indeed, analysis of the dispersion data for the exchangeable protons as a function of pH gives a curve similar to that for methanol in Figure 12.3, showing acid-base catalysis (209). Like the aqueous methanol mixtures there is also evidence for a cyclic neutral exchange process involving the transition state in Figure 12.6. One difficulty in the quantitative dispersion analysis is the existence of nonequivalent hydroxyl groups on the sugar, each of which is associated with a characteristic dispersion. The observed dispersion is therefore an average of all of them.

Cooling is expected to slow the proton exchange rate k_b and decrease T_{2b} and should have predictable consequences for the dispersion curves. Figure 12.7 compares the dispersion curves for a 6% w/v glucose solution at pH 5.8 at various temperatures, together with the best fits of the equations in Appendix A. The dispersion analysis for these temperatures and for several others is summarized in Table 12.1 and confirms that the proton exchange rate decreases with temperature. However, the two major effects are seen to be the decrease in T_{2b} with decreasing temperature

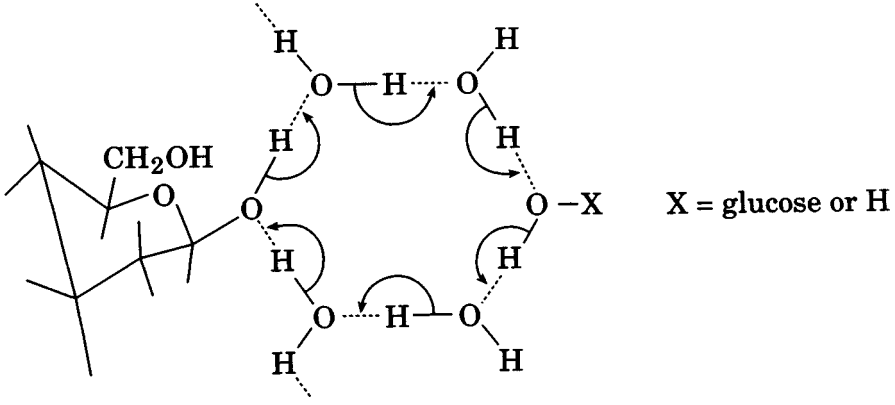

Figure 12.6. Neutral cyclic proton exchange mechanism in glucose solutions derived from an analysis of proton exchange dispersions at neutral pH. (From Ref. 209.)

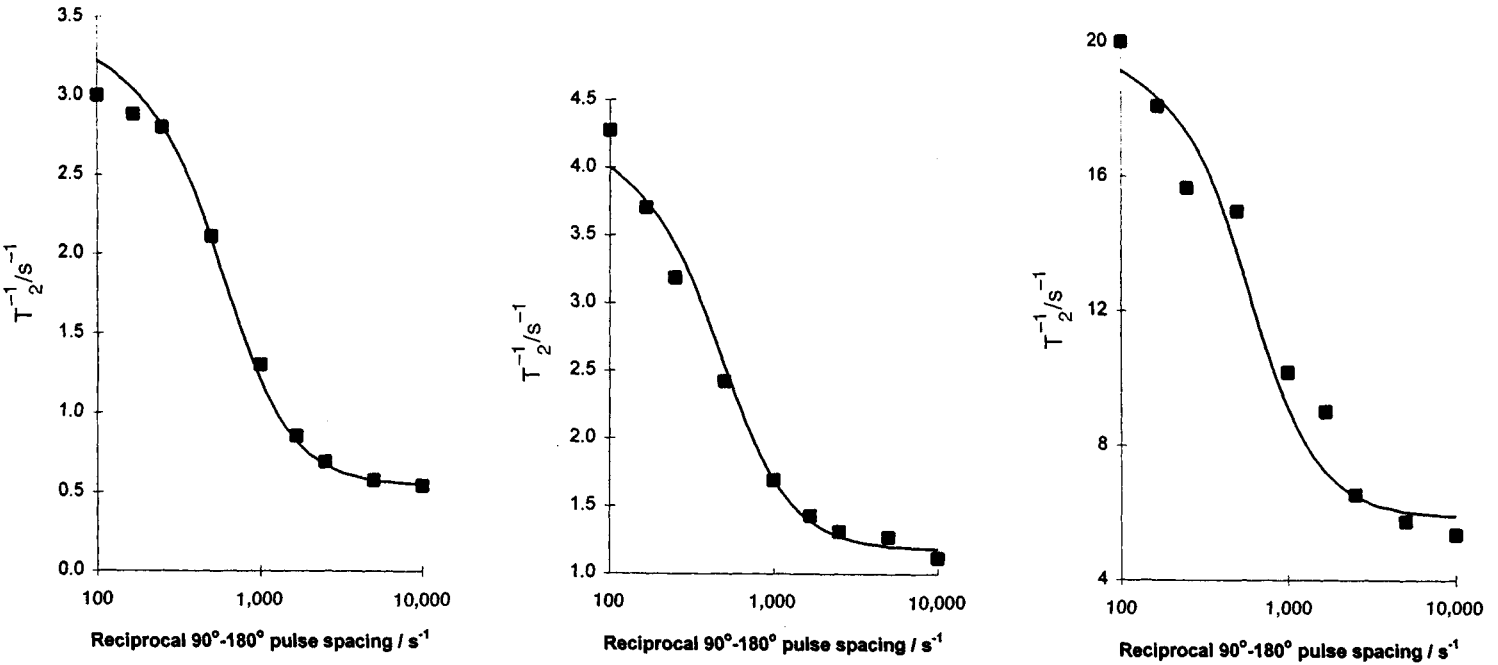

Figure 12.7. Transverse relaxation dispersions for a 6% glucose solution (pH 5.8) observed at 100 MHz at temperatures of 283 K (left), 270 K (middle), and 263 K (right). Lines are fits of the proton exchange theory in Appendix A. (From B. P. Hills and K. Nott, unpublished data.)

TABLE 12.1. Parameters Used to Model the Temperature Dependence of the Transverse Relaxation Dispersion of a 6% Glucose Solution[a]

Temperature (K)	T_{2b} (ms)	P_a	ω_b (ppm)	k_b (s^{-1})
298	500	0.9857	0.97	850
283	285	0.9857	0.76	800
278	110	0.9857	0.70	750
274	80	0.9857	0.54	730
270	35	0.9382	0.55	650
263	10	0.9169	0.98	600

[a]Measured at pH 5.8 at 100 MHz. T_{2a}, corresponding to pure water, was fixed at 2 s throughout.

and the decrease in P_a below 273 K as ice crystals form and concentrate the solution. By way of comparison, Figure 12.8 shows the relaxation dispersion for cooling uncooked parenchyma carrot tissue, taking the relaxation rates from the dominant vacuolar compartment, and Table 12.2 shows the dispersion analysis for carrot juice taken from the phloem tissue. The dramatic fall in P_a below 273 K due to ice crystal formation is quite marked, as is the drop in the proton exchange rate.

A similar dispersion analysis can be used to analyze tissue drying. For example, drying raw carrot parenchyma tissue removes water mainly from the vacuole and concentrates the sugars within the vacuole, resulting in a decrease in the intrinsic vacuolar transverse relaxation time. This results in a changing multiple exponential transverse relaxation time distribution observed for the entire tissue. These complicated changes can be modeled by noting that drying increases P_b in the vacuolar compartment, so the proton exchange formalism can be used to calculate the resulting reduction in the vacuolar T_2. Once this is known, the multiple exponential behavior of the entire tissue during drying can be calculated by inputting the vacuolar T_2 into the numerical cell model, discussed in Chapter 10.

12.3.3 Biopolymer Solutions and Gels

Because polysaccharides and proteins have exchangeable hydroxyl and/or amino protons, the principles discussed for methanol and monosaccharides apply equally well to aqueous solutions and gels of these more complex systems. Detailed dispersion studies have been undertaken for dilute solutions of globular protein such as lysozyme and bovine serum albumin (206). Perhaps the most important new feature is the possibility of using the water proton transverse relaxation as a probe of changes in the conformation and mobility of the biopolymer chains in solution during gelation, denaturation, and retrogradation. Conformational changes can alter the accessibility of the exchangeable biopolymer protons to chemical exchange with the solvation water, and this is reflected in altered values for the proton fraction P_b. Reducing the biopolymer chain mobility also reduces the intrinsic transverse relax-

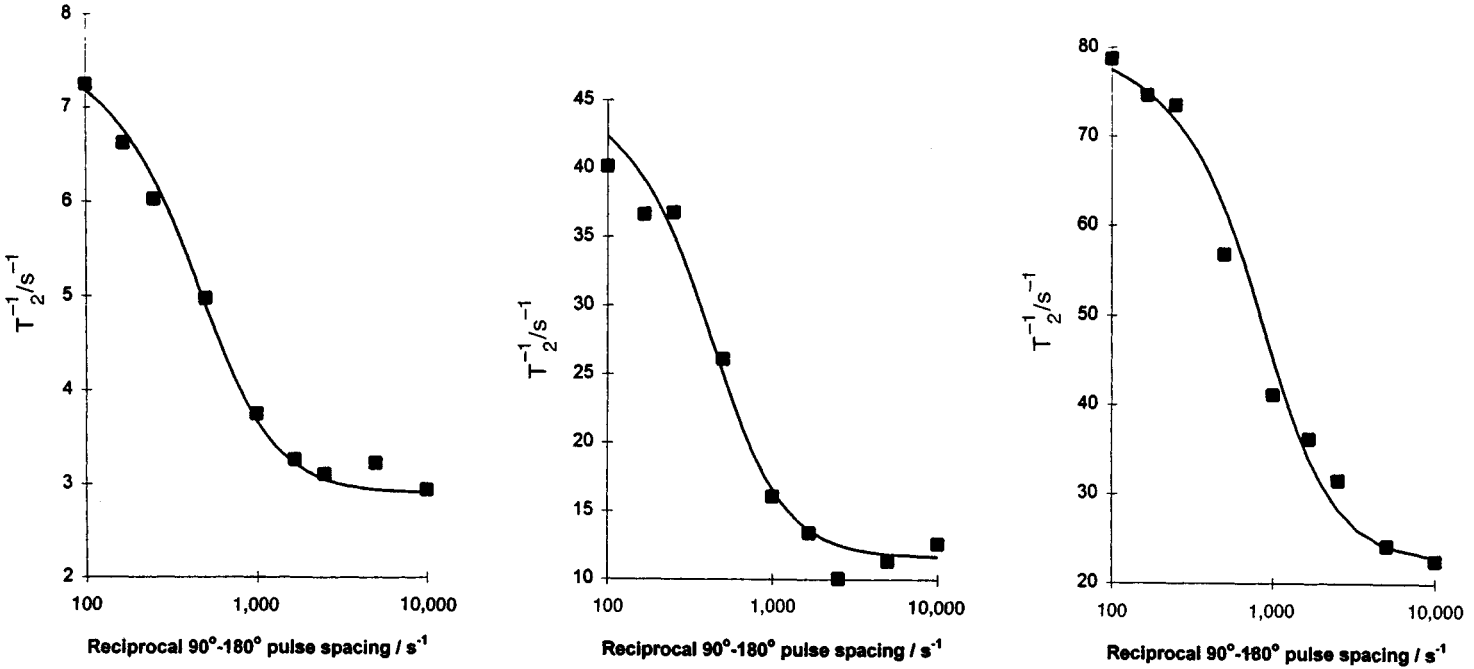

Figure 12.8. Transverse relaxation dispersions for uncooked parenchyma carrot tissue observed at 100 MHz at temperatures of 283 K (left), 270 K (middle), and 263 K (right). Lines are fits of the proton exchange theory in Appendix A. (From B. P. Hills and K. Nott, unpublished data.)

TABLE 12.2. Parameters Used to Model the Temperature Dependence of the Transverse Relaxation Dispersion of Carrot Juice (pH 6.7) Obtained from Phloem Tissue[a]

Temperature (K)	T_{2b} (ms)	P_a	ω_b (ppm)	k_b (s^{-1})
283	62.7	0.920	0.34	3200
278	67.5	0.920	0.32	2790
270	49.2	0.390	0.48	700
263	19.7	0.390	0.78	500
258	8.3	0.100	1.10	250

[a]Measured at 100 MHz. T_{2a}, corresponding to pure water, was fixed at 2 s throughout.

ation time T_{2b} of the exchangeable biopolymer protons. Because of exchange this also reduces the observed transverse relaxation time of the exchangeable proton pool, loosely described as the water proton relaxation time.

Dextran solutions are good examples of very flexible random-coil polysaccharide molecules which, being hydrophilic, are freely soluble in water. Dextrans are 1:6-linked polyglucans, and because of their flexibility, their hydroxyl protons have a long T_{2b}. The CPMG dispersions for various dextran solutions are shown in Figure 12.9, and the smooth lies are the fits to the data of the exchange equations in Appendix A. Figure 12.10 shows the dispersion behavior of two quite different polysaccharides, laminaran and schleroglucan, which are both polysaccharides made from a backbone of 1,3-linked glucose units. Laminaran is water soluble but does not form gels. It has a β1,3 linkage, and chains with more than about 49 glucose units exist as a rigid triple-helix conformation, chains shorter than about 49 glucose units exist as random coils. This is confirmed by the dispersion curve (Figure 12.10, curve *a*), which can be used to deduce the fraction of hydroxyl protons accessible to proton exchange, which is, in turn, related to the amount of triple-helix formation (211). In contrast to laminaran, schleroglucan gives a relatively flat dispersion curve (Figure 12.10, curve *c*). This flattening is indicative of chain rigidity. In fact, schleroglucan, which has an α1,3 linkage, forms rigid gels consisting of a high percentage of rigid triple-helix regions, with few hydroxyl protons accessible to exchange. To understand this dispersion behavior, consider the effect of progressively reducing the relaxation time T_{2b}, which is the inevitable result of increasing chain rigidity. In the limit of a very short T_{2b}, the rate-limiting step for water proton relaxation is exchange onto the biopolymer, because as soon as a water proton exchanges onto the biopolymer, it relaxes. In other words, the dephasing effect of the frequency difference between the water and biopolymer protons is lost in this limit, which means that the relaxation becomes independent of pulsing rate. Similar effects are observed during gelation. Gelation cross-links biopolymer chains and is often associated with the formation of more rigid *junction*

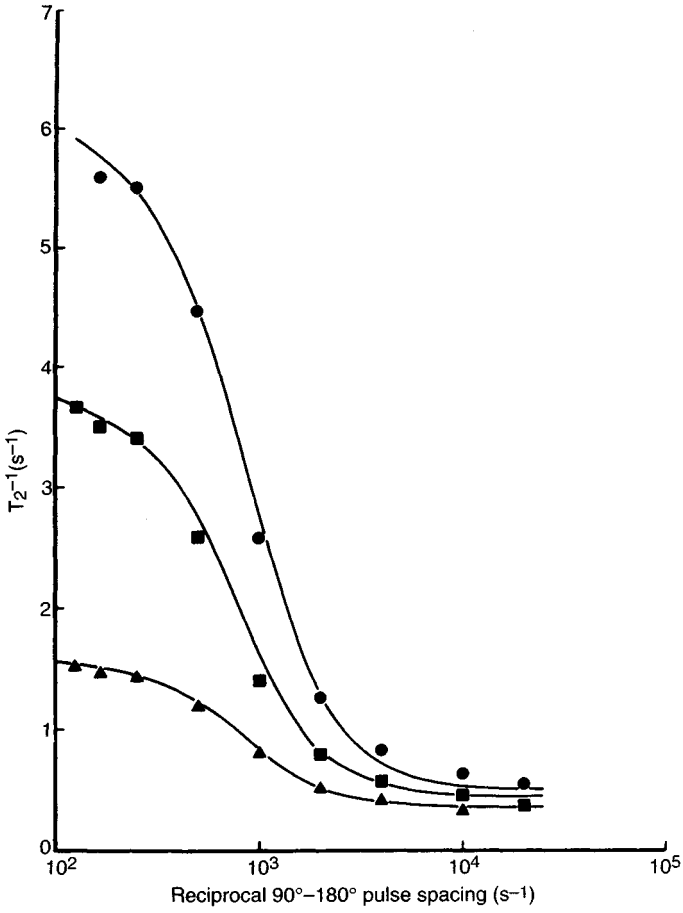

Figure 12.9. Experimental and theoretical relaxation dispersions for solutions of dextran (average MW 9000), pH 6 to 7, 300 K, at a spectrometer frequency of 100 MHz. Solid circles, 9.85% w/w dextran, $P_b = 1.615 \times 10^{-2}$, $k_b = 1.1 \times 10^3\ s^{-1}$, $\delta\omega = 1.25$; solid squares, 6.40% dextran, $P_b = 1.055 \times 10^{-2}$, $k_b = 1.0 \times 10^3\ s^{-1}$, $\delta\omega = 1.15$; closed/open wedges, 6.40% dextran, $P_b = 3.255 \times 10^{-3}$, $k_b = 1.0 \times 10^3\ s^{-1}$, $\delta\omega = 1.3$. Other parameters are $T_{2a} = 3$ s and $T_{2b} = 94$ ms. (From Ref. 211.)

zones where many chains associate together as a bundle. The formation of junction zones and cross-links inevitably increases chain rigidity and results in a flattening of the dispersion curve and in many cases a shift to an increased overall relaxation rate γ. The effect has been analyzed quantitatively for a gelatin solution as it undergoes a sol-to-gel phase transition (214). The gelatin protein chains are in the random coil state in solution, but gelation creates rigid junction zones and cross-links.

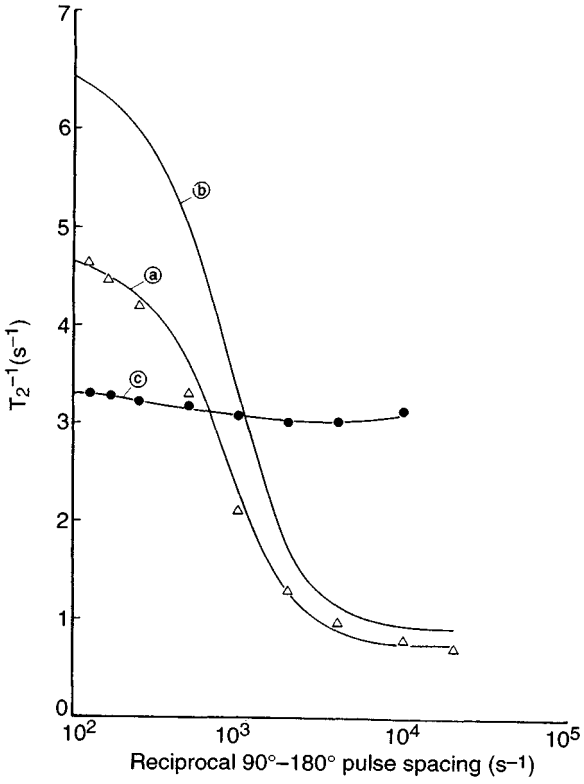

Figure 12.10. Water proton transverse relaxation dispersions for laminaran and schleroglucan observed at 100 MHz. Curve *a*: Theoretical dispersion for a 10.78% w/w laminaran solution, pH 6.5, 300 K, calculated assuming only a 70% accessibility to hydroxyl protons. Triangles are experimental points. Curve *b*: Same as curve *a*, except a 100% hydroxyl proton accessibility has been assumed. Curve *c*: The experimental relaxation rates for a 2.6% w/w schleroglucan gel at 300 K. The curve in this case is only a guide to the eye. (From Ref. 211.)

The associated changes in their dispersions are shown in Figure 12.11, and the smooth lines are the best fit of the exchange equations. The sensitivity of the dispersions to gelation means that NMR can be used to study the kinetics of the gelation process.

The denaturation of globular proteins, which destroys their tertiary structure, can also result in decreased transverse proton relaxation times. This effect has been observed in dairy products (283) and is probably the effect of chain entanglement, resulting in protein aggregation and reduced chain mobility. It means that NMR transverse relaxation-time measurements can be used to follow the denaturation

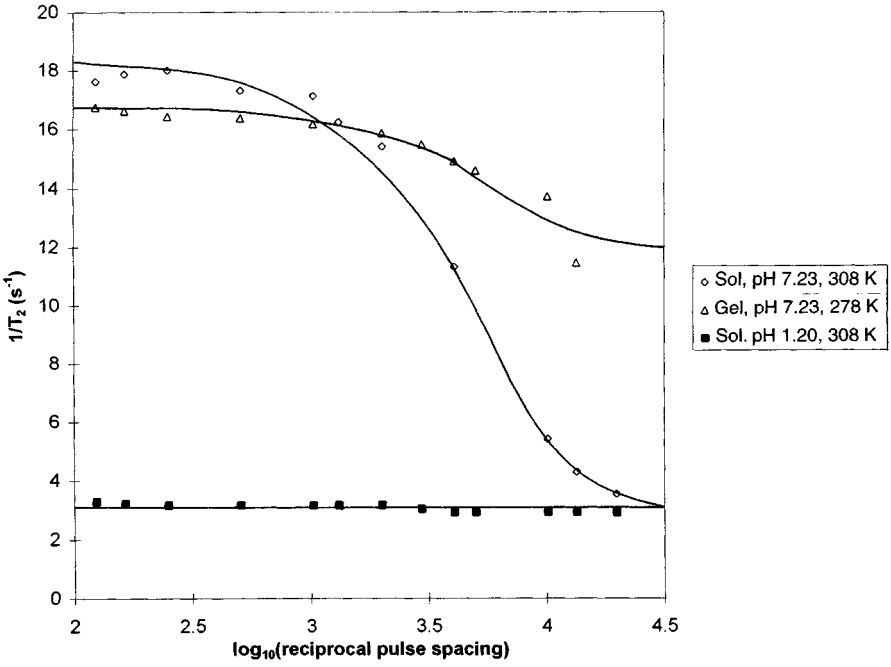

Figure 12.11. Transverse relaxation proton dispersions for 19.48% w/w gelatine at a spectrometer frequency of 300 MHz. Curve *a*: The sol state at 308 K, pH 7.23. Curve *b*: The sol state at 308 K, pH 1.20. Curve *c*: The gel state at 278 K, pH 8.20. Lines are the theoretical fits using the equations in Appendix A. (From Ref. 140.)

kinetics and could provide a useful, noninvasive, on-line monitor of the degree of denaturation. The increase in water proton transverse relaxation rate on gelation and denaturation means that on the macroscopic distance scale, these processes can be imaged in space and time by calibrating transverse relaxation time maps with the degree of gelation and/or denaturation. The example of imaging the gelation of alginate gels was discussed in Section 2.4.

The complicated temperature and concentration dependence of the water proton relaxation of ionic polysaccharide sols and gels can also be rationalized with the proton exchange model. Figure 12.12 shows the effect of increasing KCl concentration on the T_2 of a 5% solution of κ-carrageenan measured at a short CPMG pulse spacing at 16 MHz (284). For the present we ignore the possibility of strongly hydrogen-bonded hydration water with long residence times, in which case the minimum arises from the exchangeable proton pool. In the limit of short pulse spacings the equations in Appendix A reduce to

$$T_2^{-1} = \frac{P_a}{T_{2a}} + \frac{P_b}{T_{2b} + \tau_b} \tag{12.8}$$

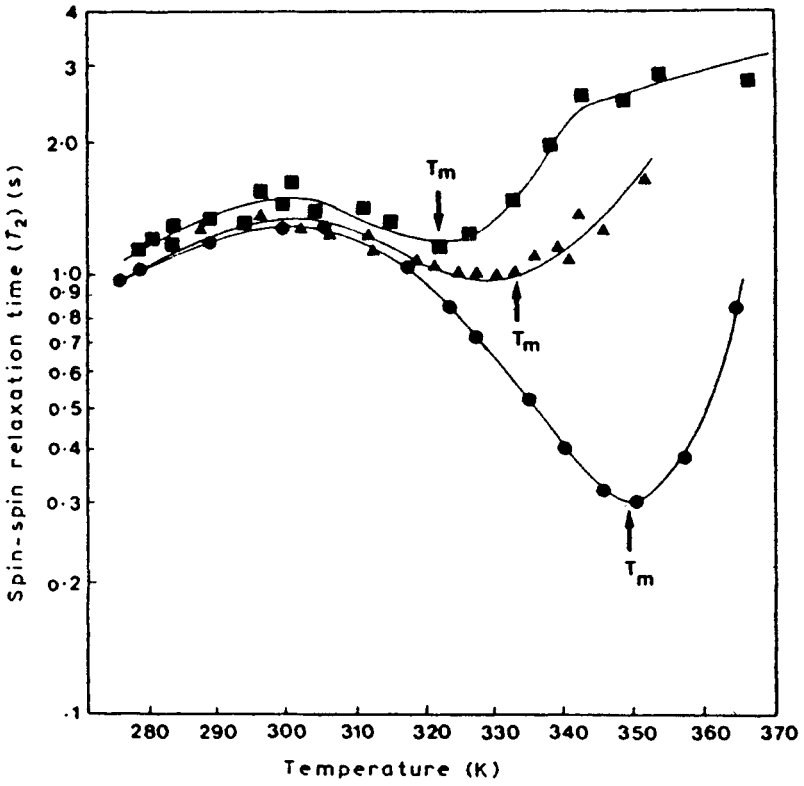

Figure 12.12. Effect of KCl concentration on the T_2 value of water in a 5% κ-carrageenan gel: solid circles, 0.2 *M*; solid triangles, 0.1 *M*; solid squares, 0.05 *M*. The melting points are indicated. (From Ref. 284.)

where τ_b is the mean lifetime of an exchangeable hydroxyl proton on the carrageenan backbone ($= k_b^{-1}$). With increasing temperature the intrinsic relaxation times T_{2a} and T_{2b} increase as the correlation time characterizing the water dynamics decreases. This explains the overall increase in T_2 in Figure 12.12 in the absence of the minimum. The minimum arises because the lifetime, τ_b, also decreases with increasing temperature, and according to equation (12.8), the minimum will occur when τ_b equals T_{2b}. In practice, the observed T_2 value can increase before the theoretical exchange minimum because the gel melts. In fact, the minima in Figure 12.12 arise from gel melting and indicate that increasing KCl concentration strengthens the gel and raises the gel–sol transition temperature. Similar ideas should apply to other gelling polysaccharides, proteins, and mixed polysaccharide–protein systems, but the very large number of possible systems created by varying the nature of the biopolymer(s), their concentration, the nature and concentration of counterions, and the temperature and pH means that even in the dilute regime, much remains to be done in elucidating the relaxation behavior of food biopolymer systems.

Before leaving the subject of water proton transverse relaxation, a word of caution is needed. Some researchers have attempted to interpret gel relaxation with the Brownstein–Tarr theory discussed in Chapter 10 and extract information about the pore structure of the gel. In view of the success of the proton exchange model, there would appear to be little justification for this approach. Moreover, it is conceptually somewhat arbitrary to attempt to define a pore size distribution and a surface relaxation strength in the three-dimensional network of cross-linked chains characterizing a gel. Nor is there justification for neglecting proton exchange altogether and assuming that the relaxation rate is a result of fast exchange between free water and water hydrating the biopolymer. Such molecular exchange undoubtedly exists and is included, implicitly, in slight changes in the parameter T_{2a} in the exchange equations. However, this effect should be analyzed only after the effects of proton exchange have been taken into account. Many of the relaxation contrast changes observed in clinical imaging of human tissues have been assigned to changes in various types and states of water within the cells without proper attention being paid to the important effects of proton exchange. Nevertheless, one of the remaining outstanding problems in these biopolymer systems is to extend these quantitative studies to lower water contents where proton exchange rates may well be slowed and the contribution from strongly hydrogen-bonded hydration water increased. We return to low-water-content systems in Section 12.6.

12.4 WATER PROTON LONGITUDINAL RELAXATION

Unlike water proton transverse relaxation, longitudinal proton magnetization can be exchanged by a direct through-space dipolar interaction as well as by actual chemical exchange of protons. This through-space interaction can be thought of as a mutual flipping of opposed proton spins, which is an energy-conserving process. Figure 12.13 summarizes the various possible transfer pathways in a solution or gel having three proton pools: water (labelled a) and exchangeable (b) and nonexchangeable (m) solute protons. The rate constants k_a and k_b refer to chemical proton exchange, the others to the secular dipolar interaction pathway. P_m and T_{1m} refer to the pool of nonexchanging solute protons. Fortunately, the equality of fluxes in the stationary state means that only the four rate constants k_b, k'_b, k_m, and k'_m are independent. Moreover, k_b can be determined by fitting the transverse relaxation dispersion. Similarly, the proton fractions P_a, P_b, and P_m can be determined from the composition of the solution and the relation $P_a + P_b + P_m = 1$. T_{1m} can be measured directly for the biopolymer dissolved in D_2O and T_{1b} is expected to be similar to T_{1m} since both are determined by intramolecular dipolar interactions within the biopolymer. This leaves only T_{1a} and the three dipolar cross relaxation rates k'_b, k_m, and k'_m either to be evaluated theoretically or determined from the longitudinal relaxation data. The Bloch equations corresponding to Figure 12.13 can be written

$$\mathbf{M} = \mathbf{A} \cdot \mathbf{M} + \mathbf{B} \tag{12.9}$$

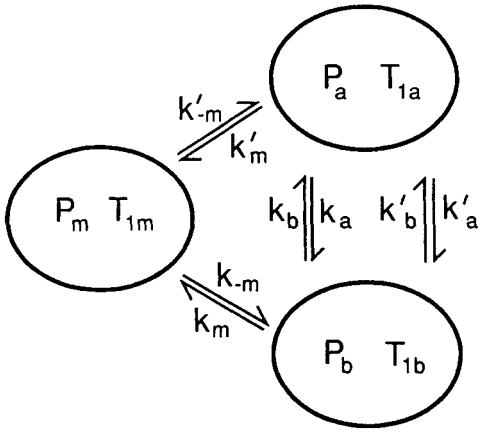

Figure 12.13. Main exchange processes contributing to longitudinal proton relaxation in an aqueous biopolymer solution or gel. See the text for details.

where **A** is the matrix

$$A = \begin{bmatrix} -(T_{1a}^{-1} + k'_m + k_a + k'_a) & k + k'_b & k'_{-m} \\ k_a + k'_a & -(T_{1b}^{-1} + k_m + k_b + k'_b) & k_{-m} \\ k'_m & k_m & -(T_{1m}^{-1} + k'_m + k_{-m}) \end{bmatrix}$$

and

$$B = \begin{bmatrix} T_{1a}^{-1} M_a^0 \\ T_{1b}^{-1} M_b^0 \\ T_{1m}^{-1} M_m^0 \end{bmatrix} \quad \text{and} \quad M = \begin{bmatrix} M_a \\ M_b \\ M_m \end{bmatrix}$$

where $k_a = P_b P_a^{-1} k_b$, $k_{-m} = P_b P_m^{-1} k_m$, $k'_{-m} = P_a P_m^{-1} k'_m$, and $k'_a = P_b P_a^{-1} k'_b$. Here M_i^0 ($i = a,b,m$) are the equilibrium magnetizations. These coupled equations must be solved for initial conditions $M_i(t = 0)$ appropriate for selective or nonselective excitation. In general, the solutions will give triple-exponential relaxation since there are three coupled pools of protons. In practice, various limiting cases can be observed with less complicated relaxation behavior. Consider, for example, the case of a dilute solution of a globular protein. It will be shown in Chapter 13 that the dipolar cross-relaxation rates from hydration water, k'_b and k'_m, are negligible and that the dipolar cross-relaxation rate between exchangeable and nonexchangeable biopolymer protons is very slow (on the order of 1 s^{-1}). This means that the pool of nonexchanging biopolymer protons, m, is uncoupled from the combined pool of

exchangeable water and biopolymer protons, $a + b$. This is observed to be the case with lysozyme solutions at 25°C, where the nonexchanging proton pool gives a faster relaxing component in the inversion recovery experiments. Since k_b is large (on the order of 10^3 to 10^4 s^{-1}) the slower-relaxing component can be written as the fast exchange average of the relaxation rates of free water (f), hydration water (bw) and exchangeable biopolymer proton pools such that

$$T_{1w}^{-1} = (1 - P'_{bw} - P'_b)T_{1f}^{-1} + P'_{bw}T_{1bw}^{-1} + \frac{P'_b}{T_{1b} + k_b^{-1}} \tag{12.10}$$

where

$$P'_{bw} = \frac{P_{bw}}{P_{bw} + P_f + P_b} \tag{12.11}$$

and

$$P'_b = \frac{P_b}{P_{bw} + P_f + P_b} \tag{12.12}$$

where $P_f + P_{bw} + P_b + P_m + 1$. One particularly important consequence of these equations is that the observed longitudinal relaxation rate of the exchangeable proton pool (loosely described as the water relaxation) will show a frequency dispersion as the spectrometer frequency ω_0 is varied. This follows because T_{1b}^{-1} exhibits a dispersion according to equation (12.1), where in this case τ_c is the rotational correlation time of the protein. Since τ_c is typically on the order of a few nanoseconds for globular proteins in dilute solution, the spectral density will vary on the frequency scale of tens of megahertz. These $T_1(\omega_0)$ dispersions have been observed in classic papers by Koenig and co-workers (249), and their observations have been the subject of widely differing theoretical interpretation. Although it appears that proton exchange contributes to the T_1 frequency dispersion, it needs to be added that the relative contributions of proton exchange and exchange between free and hydration water is not always straightforward to decide. There is increasing evidence from high-resolution NMR that a small number of water molecules have long residence times, on the order of microseconds to milliseconds, within globular proteins. These more slowly exchanging water molecules could contribute significantly to the observed T_1 frequency dispersions alongside the proton exchange. However, they will not contribute significantly to the CPMG transverse relaxation dispersions because their exchange rate is too fast for the transverse relaxation dispersion time scale and their resonance frequency is unlikely to be significantly shifted from that of free water.

The cross relaxation–proton exchange model can also be used to interpret the effect of biopolymer gelation on the T_1 dispersion. Gelation is caused by cross-linking of the macromolecules so that rotation on the nanosecond time scale no longer determines the frequency dependence of T_{1b} (ω_0). Instead, $T_{1b}(\omega_0)$ will be

determined by the complicated dynamics of the gel network, and this is expected to be characterized by much longer correlation times. The midpoint of the $T_{1b}(\omega_0)$ dispersion will therefore be shifted to lower frequencies and have a functional form reflecting the gel network dynamics (140). The dispersive behavior in gels is further complicated by the dependence of the cross-relaxation rate k_m, on ω_0. Figure 12.14 shows the dispersions observed for fibrin gels obtained by the gelation of fibrinogen solutions of various concentrations (319). In agreement with the analysis above, the effective dispersion frequency was indeed observed to decrease by an order of magnitude on gelation.

The existence of T_1 frequency dispersions is not merely of academic interest but has the important implication in MRI that T_1 contrast in any food materials depends on the spectrometer frequency and not just on parameters characterizing the food. Increasing spectrometer frequency decreases the longitudinal relaxation rate and leads to loss of T_1 contrast. Measurements of T_1 frequency dispersions are therefore useful for identifying the spectrometer frequency for optimum T_1 contrast. Fortunately, measurements of the complete T_1 frequency dispersion are now a relatively straightforward exercise using a field-cycling (FC) spectrometer. The essential feature of an FC spectrometer is its ability to switch the strength of the main, B_0, magnetic field rapidly. By polarizing the sample in a high magnetic field, B_P, then rapidly transferring it to a low field, B_E, corresponding to a resonance frequency ω for a time t_E before returning the field to a higher value, B_D, for signal detection with a 90° pulse, it is possible to measure T_1 at a fixed frequency ω by measuring the exponential decay of the signal as t_E is stepped out and then determine the frequency dependence of $T_1(\omega)$ by repeating the entire experiment for different B_E

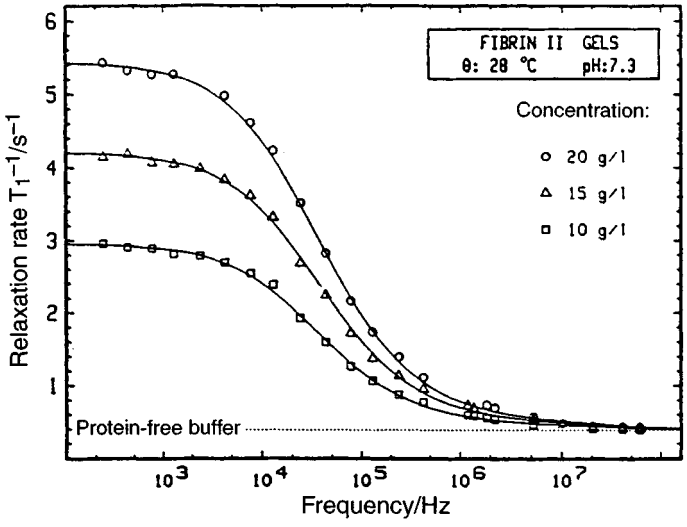

Figure 12.14. T_1 (ω_0) dispersions for fibrin gels at 28°C and pH 7.3 for three protein concentrations: open circles, 20 g/L; open triangles, 15 g/L; open squares, 10 g/L. (From Ref. 319.)

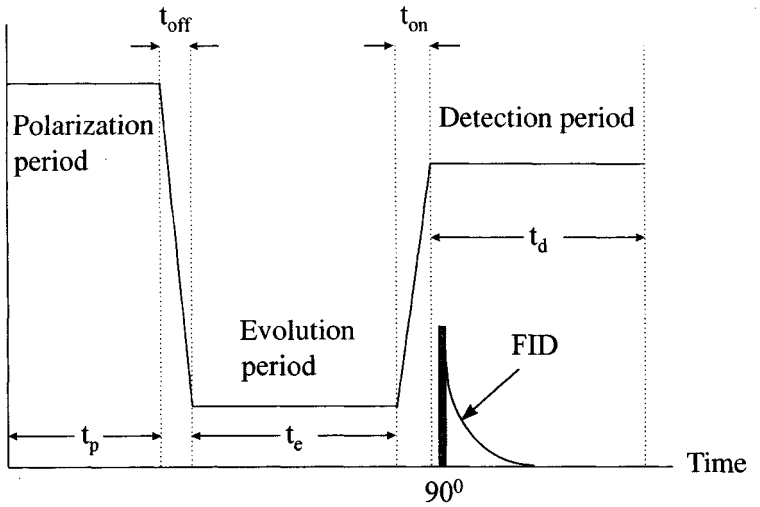

Figure 12.15. Simple field-cycling protocol for measuring the frequency dispersion of the longitudinal relaxation.

values. Figure 12.15 shows a schematic of this simple field-cycling protocol for measuring $T_1(\omega)$.

12.5 WATER PROTON ROTATING-FRAME RELAXATION

Whereas transverse and longitudinal relaxation-weighted maps are widely used in imaging, rotating-frame relaxation contrast is less exploited, despite the fact that it has many potential advantages. Rotating-frame relaxation time maps can be made simply by inserting the conventional $T_{1\rho}$ spin-locking sequence as a preparation sequence before an imaging sequence (see Chapter 1). However, it is worth noting that because of the low field strength of the radio-frequency (B_1) spin-locking field, it can be made slice selective simply by performing $T_{1\rho}$ spin locking in the presence of a field gradient G. A suitable three-dimensional $T_{1\rho}$ imaging sequence is shown in Figure 12.16. The initial excitation can be performed with a hard 90° pulse, but in the presence of the field gradient, all transverse non-spin-locked magnetization will be destroyed. Only magnetization with a resonance frequency ω such that $|\omega - \omega_0| < \gamma B_1$ will be spin locked and immune to destructive dephasing. This corresponds to a slice width ΔL of $2B_1/G$. The slice width is therefore independent of the duration of the spin-locking pulse, so that $T_{1\rho}$ maps can be created by acquiring images with increasing spin-locking durations (285). Of course, rotating-frame imaging (Chapter 8) is an alternative means of generating $T_{1\rho}$ weighting.

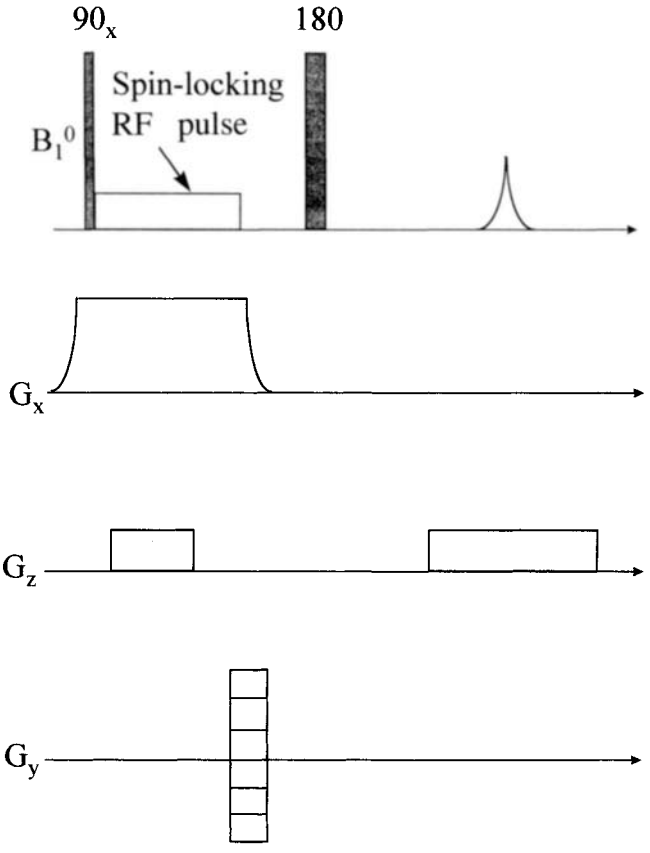

Figure 12.16. Pulse sequence for $T_{1\rho}$-weighted imaging. (From Ref. 285.)

$T_{1\rho}$ maps are potentially rich sources of dynamic information, especially in water-rich biological (food) materials, where both proton exchange and cross relaxation dominate the relaxation. To analyze the dynamics, consider Figure 12.13 once again. This also describes relaxation in the rotating frame, with the important differences that all three components (x,y,z) of magnetization must be considered and frequency offsets between the three pools explicitly included (140). The 3×3 matrix equation must therefore be replaced by a 9×9 matrix equation, which is given in Appendix B. Although the 9×9 form of the A matrix complicates the theoretical interpretation, it also makes the rotating-frame relaxation a rich source of information because it depends on three independent frequencies: the spectrometer frequency ω_0, the radio-frequency field strength ω_1, and the spin-locking angle θ [where $\theta = \tan^{-1}(\omega_1/\omega_z)$ and ω_z is the radio-frequency resonance frequency offset].

Nevertheless, there is a paucity of experimental data on rotating-frame relaxation in biopolymer and biological systems. As with longitudinal relaxation, rotating-frame dipolar cross-relaxation rates in dilute solutions of globular proteins are predicted to be negligibly small, so the proton exchange pathway should dominate and give rise to dispersions when $T_{1\rho}$ is plotted against radio-frequency field strength ω_1. The $T_{1\rho}$ dispersions for 20% glucose solutions at various pH values are shown in Figure 12.17 together with the fits of the equations in Appendix B. In more-rigid biopolymer systems the rotating-frame cross-relaxation rates are expected to increase so that the exchangeable proton pool becomes coupled to the nonexchanging proton pool. In this situation the ω_1 dependence of $T_{1\rho}$ should be particularly revealing since there are potentially four sources of ω_1 dependence: (1) The explicit ω_1 dependence arising from solution of the foregoing coupled Bloch equations, (2) an implicit ω_1 dependence arising because the rotating-frame cross-relaxation rates themselves depend on ω_1, (3) an ω_1 dependence of the spectral densities characterizing the biopolymer nonexchanging proton pool which originates from chain motion in the ω_1 frequency range, and (4) an ω_1 dependence arising from the variable extent of spin locking of the biopolymer proton because spin locking will occur only if ω_1 is greater than the biopolymer proton linewidth. The author has observed large $T_{1\rho}$ versus ω_1 dispersions for agarose gels at a resonance frequency of 100 MHz (unpublished), and earlier investigators reported large dispersions in tissues such as mouse spleen (321). Several authors [e.g., Santyr et al. (322)] have reported large $T_{1\rho}$ dispersions against ω_1 in muscle tissue even at quite low spectrometer frequencies of about 17 MHz. which has been assigned to hydration water having correlation times as long as 10^{-5} to 10^{-6} s in muscle tissue. However, the possibility of proton exchange and dipolar cross relaxation was not taken into account, so this conclusion has to be regarded as tentative. There is clearly a great deal of research needed before reliable quantitative interpretation of rotating-frame relaxation rates can be made in aqueous biopolymer systems. Two aspects that may facilitate the interpretation are noteworthy. The first is that dipolar interactions are independent of spectrometer frequency, unlike the magnitude of proton exchange dispersions, which increase with spectrometer frequency because the frequency offset between proton pools is proportional to spectrometer frequency. This could be useful in separating proton exchange and dipolar cross-relaxation contributions. The second point is that dipolar interactions and therefore rotating-frame dipolar cross relaxation, can, in principle, be removed by spin locking at the magic angle by choosing the resonance offset ω_z so that $\tan^{-1}(\omega_1/\omega_z) = 54.7°$. Magic-angle spin locking therefore leaves only the proton exchange cross-relaxation pathway.

12.6 LOW-WATER-CONTENT HOMOGENEOUS SYSTEMS

Earlier we analyzed the molecular factors determining water proton relaxation times in the dilute regime, which are needed in the interpretation of relaxation in conventional liquid-phase imaging. In this section we extend the relaxation analysis

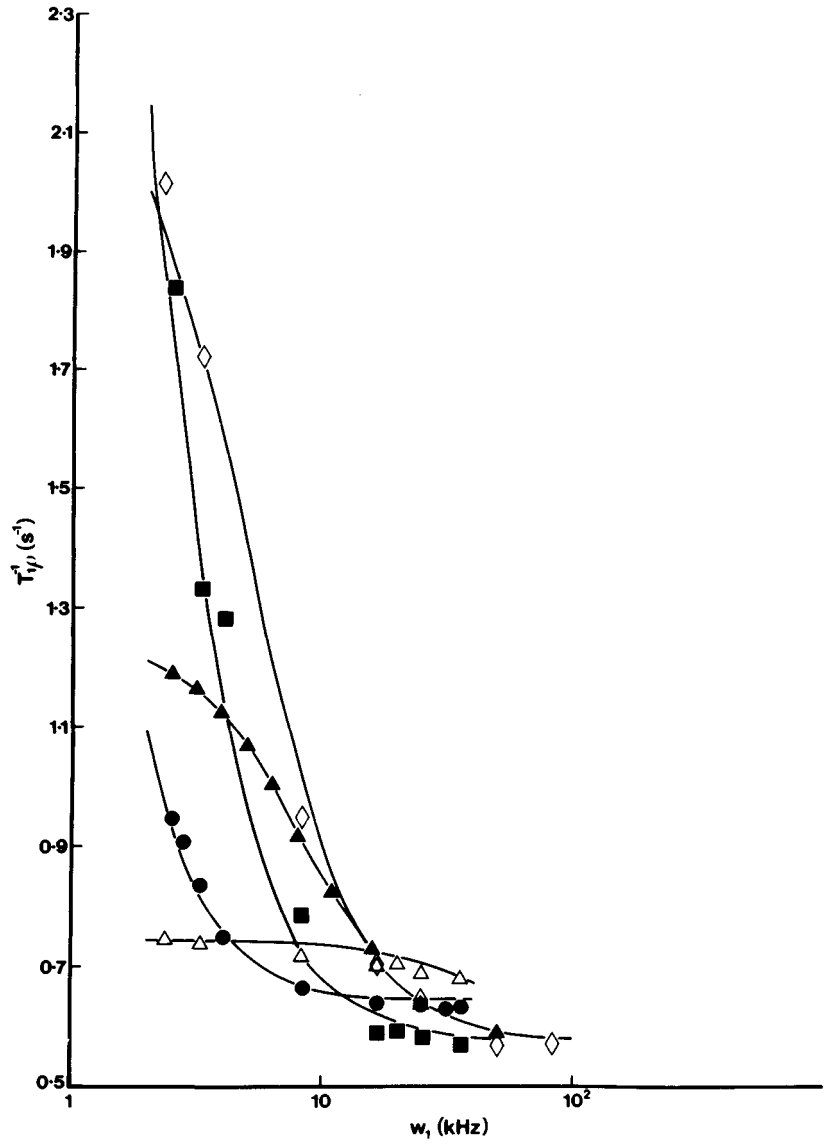

Figure 12.17. Rotating-frame relaxation dispersions for a 20% glucose solution observed at 100 MHz and 296 K for the following pH values: solid circles, 6.25; solid squares, 3.76; open diamonds, 3.23; solid/open wedges, 2.8; open triangles, 1.75. Lines are fits of the equations in Appendix B. (From Ref. 209.)

to low-water-content food systems, which is relevant to solid imaging (see Chapter 5). Emphasis is placed on low-water-content biopolymer–sugar–water systems because these are useful representations of many real food systems and have been studied extensively by several research groups.

12.6.1 Hydration Water and Biopolymer Plasticization

Consider the case of gelatin gels. At high water contents the FID is dominated by the pool of exchangeable water and gelatin protons, and the signal from nonexchanging gelatin protons is either not detected or appears only as a minor rapidly decaying component with a relaxation time of a few 100 μs which is not detected in the CPMG sequence even with short echo spacings of 400 μs. However, at lower water contents, between 0 and 50% (weight of water per weight of dry gelatin) the signal from the nonexchangeable protons on the gelatin can no longer be ignored in the FID and can be analyzed as the sum of two Gaussian components, one of which has a relaxation time of only a few tens of microseconds while the longer Gaussian component has a relaxation time of a few hundred microseconds. The fastest-relaxing component is believed to arise from rigid nonexchanging gelatin protons, while the second Gaussian component arises from more mobile protons, including hydration water with long residence times, exchangeable biopolymer protons, and the more mobile biopolymer (side-) chains. What is particularly significant is the observation that the relaxation time of the short solidlike component increases with increasing water content. This increase in polymer chain mobility with increasing water content, known as *plasticization*, permits high-energy "strained" interchain conformations to be relaxed and can result in a subsequent increase in the degree of local order in the biopolymer network, such as the increased formation of ordered helical regions. This increased ordering can be observed in both low-angle X-ray diffraction and in intensity changes in the amide bands in the FTIR spectrum, and also results in a sharpening of spectral lines in the high-resolution solid NMR spectrum measured with the CPMAS technique. Plasticization by small amounts of water has also been investigated in a number of cereal proteins that are important in controlling the functional behavior of doughs and breads, such as glutenin in wheat (286,287) and chordein in barley (288). Much remains to be done in developing quantitative models for biopolymer plasticization by small molecules such as water and sugars, but one promising approach involves glass-transition theory, considered in Section 12.6.2.

As mentioned above, the slower-relaxing component in the gelatin FID arises from more mobile protons and includes hydration water with a long residence lifetime. Plots of the effective transverse relaxation rate of this slower-relaxing component against water content shows a distinct inflection at about 20% w/w water (331). This can be seen in Figure 12.18, where the transverse relaxation rate from the slower-relaxing component of the FID is combined with that from CPMG measurements at higher water contents. In like manner, Figure 12.19 shows that the normalized amplitude of the slow-relaxing component in the FID, obtained by extrapolating to zero time, also shows an inflection at about 20%. Moreover, sodium relaxation-time measurements in gelatin gels containing sodium chloride show a similar break (see Figure 12.19). These observations strongly suggest that below water contents of about 20% the water exists as a (sub-)monolayer on the gelatin and is characterized by long residence lifetimes. Above about 20%, water begins to form more mobile, liquidlike multilayers, characterized by much shorter correlation

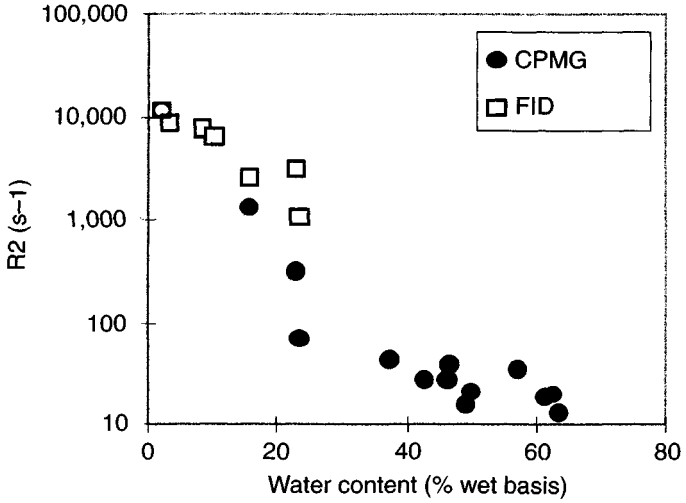

Figure 12.18. Proton transverse relaxation rates of the slow-relaxing component in concentrated gelatin gels as a function of water content, measure at 20 MHz and at 298 K. Closed circles, FID data; open squares, CPMG data. (From M.-C. Vackier, B. P. Hills, and D. N. Rutledge, unpublished data.)

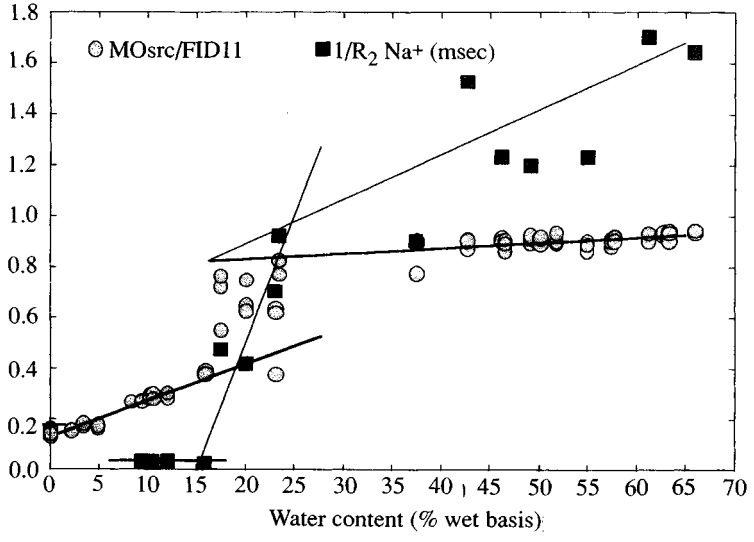

Figure 12.19. Solid circles, initial, normalized signal amplitude of the slow-relaxing component in the FID of concentrated gelatine gels as a function of water content, measured at 298 K. (From Ref. 331.) Also shown by the solid squares is the transverse relaxation time of sodium ions in gelatin gels as a function of water content.

times. The sodium relaxation data are then consistent with the hypothesis that the ion mobility increases dramatically as soon as multilayer water is formed, and some evidence exists (see below) that proton exchange between water and biopolymer protons begins to influence relaxation rates only when multilayer water exists.

12.6.2 Glass Transition Theory of Starch Retrogradation

In amylopectin gels, plasticization of the amylopectin chains permits their partial recrystallization into A or B crystallites of amylopectin double helices, which is responsible for the phenomenon of retrogradation and results in the staling of bread and cake products. This important phenomenon is best analyzed with the polymer science approach based on glass–rubber transition theory. Mention has already been made in Chapter 5 of the use of single-point imaging to follow the space-time evolution of starch retrogradation. In this section we consider the molecular origin of the changes in relaxation time associated with retrogradation. Figure 12.20 shows the effect of increasing storage time on the transverse water proton relaxation rate measured as a single-exponential CPMG decay for a waxy maize starch extrudate which consists mainly of gelled amylopectin containing 35% water. The corresponding increase in the relaxation rate for the solid nonexchanging proton

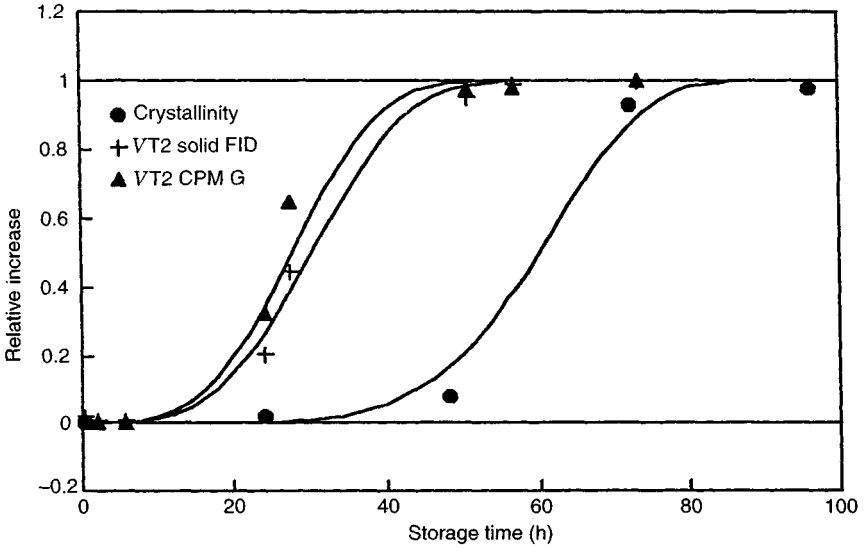

Figure 12.20. Effect of storage time on the CPMG water-exchangeable proton transverse relaxation rate (solid/open wedges); the CH proton relaxation time measured from the FID (pluses); and the crystallinity index measured by X-ray diffraction for an amylopectin extrudate containing 35% water. Only relative increases are shown and the lines are the fits of the Avrami equation (12.13). (From Ref. 289.)

component of the amylopectin, obtained from a Gaussian analysis of the FID, is included. At a molecular level, retrogradation corresponds to an increased crystallization of the amylopectin into either A or B crystallites (depending on the water content and temperature), which causes the textural change associated with staling and results in decreased biopolymer proton mobility and a corresponding shortening of the FID relaxation time. The degree of crystallinity, measured by X-ray crystallography, is included in Figure 12.20. Because there is fast proton exchange between water and amylopectin hydroxyl protons (as well as between hydration and bulk water), the shortening of the amylopectin proton relaxation time is also associated with a shortening of the CPMG water proton relaxation time, and the decrease is expected to be described by the exchange model discussed previously.

At a phenomenological level the rate of amylopectin crystallization (and hence the relaxation-time changes) can be modeled with the Avrami equation, which has the form

$$R(t) = R_{max} - (R_{max} - R_0)\exp[-(Gt)^n] \tag{12.13}$$

Here G is the rate of retrogradation and the index n typically assumes values between 1 and 4. R_{max} and R_0 are the asymptotic relaxation rates at infinite and zero storage time, respectively. The smooth lines in Figure 12.20 are the fits of the Avrami equation to the data. Because the rate of crystallization G depends on biopolymer chain mobility, it is appropriate to use the polymer science approach (130) and analyze it with glass–rubber transition theory (129). At or below the glass transition temperature T_G, the G value is expected to be zero because the extremely low chain mobility prevents growth of the amylopectin crystallites. The relationship between G and $T - T_g$ is expected to follow a modified version of the empirical Williams–Landel–Ferry (WLF) (131) equation, which relates kinetic properties to $T - T_g$. Applied to retrogradation the modified equation can be written

$$\log_{10}\left(\frac{G_{ref}}{G}\right) = \frac{-C_1(\Delta T - \Delta T_{ref})}{C_2 + (\Delta T - \Delta T_{ref})} \tag{12.14}$$

Here $\Delta T = (T - T_g)$ and ΔT_{ref} is $(T - T_{ref})$, where T_{ref} is an arbitrary reference temperature. The log-linear plot predicted by equation (12.14) is shown in Figure 12.21. Because the glass transition temperature is itself a function of water content and sugar content, the rate of retrogradation G will also depend on the system composition, increasing with increasing water contents because of the reduction in T_g. More quantitatively, the compositional dependence of the glass transition temperature can be estimated by equations such as that of ten Brinke (290) or modifications of it. The ten Brinke equation has the form

$$T_g = \frac{\Sigma_i W_i \Delta C_{pi} T_{gi}}{\Sigma_i W_i \Delta C_{pi}} \tag{12.15}$$

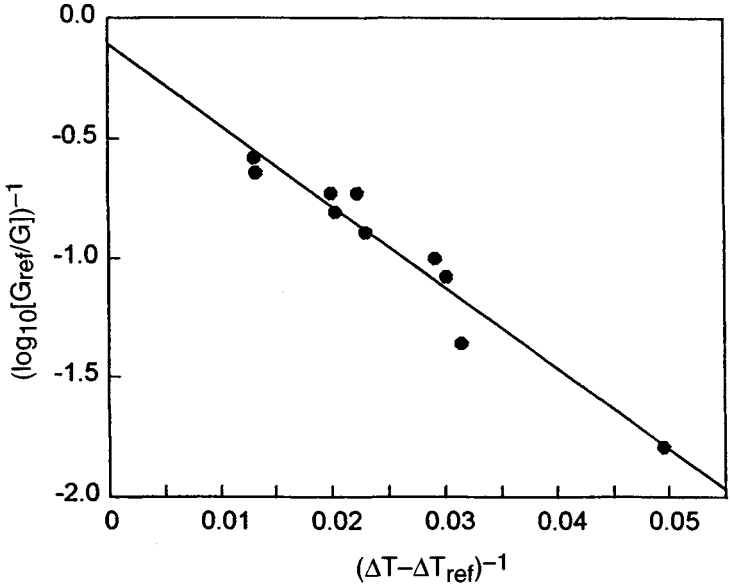

Figure 12.21. WLF plot [equation (12.14)] of the retrogradation rate derived from the Avrami fits to the CPMG exchangeable proton transverse relaxation rate (see Figure 12.20) for amylopectin–water extrudates. (From Ref. 289.)

where W_i is the weight fraction of component i and ΔC_{pi} is the difference in the specific heat capacity between the liquid and glassy states at T_g. Equation (12.15) shows that the introduction of lower-molecular-weight species such as water and sugars with low intrinsic T_g values results in a lowering of the overall T_g value for the mixture. This, in turn, leads to an increased rate of retrogradation via the WLF equation.

The ten Brinke equation is only a first approximation in most food systems because it assumes that there is no selective partitioning of water between biopolymer or sugar molecules. In fact, the sorption isotherm for the amylopectin and sugar show that this assumption is not strictly valid, with water preferably hydrating the biopolymer at low water contents and sugar at high water contents. The analysis

Figure 12.22. Temperature dependence of the T_2 relaxation times for (*a*) 89.4% maltotriose; (*b*) 90.8% maltoheptaose; (*c*) 91.8% pullulan. Asterisks, T_2 relaxation time of the slowly relaxing exchangeable proton component; pluses, T_2 relaxation time of the fast-relaxing CH component. The vertical line shows the glass transition temperature determined by differential scanning calorimetry. (From Ref. 159.)

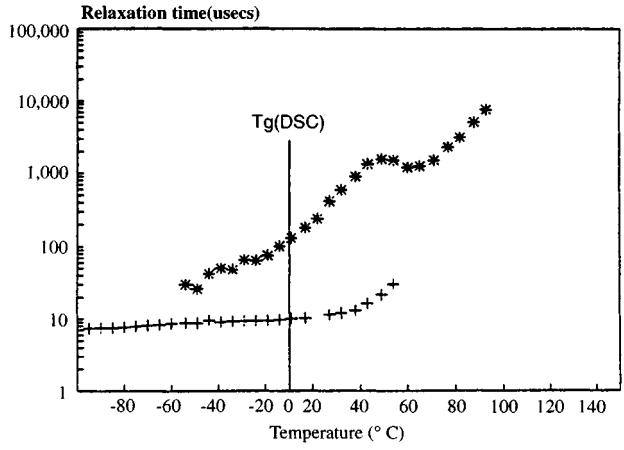
Relaxation time(usecs)
100,000
10,000
1,000
100
10
1
Tg(DSC)
-80 -60 -40 -20 0 20 40 60 80 100 120 140
Temperature (° C)

(*a*)

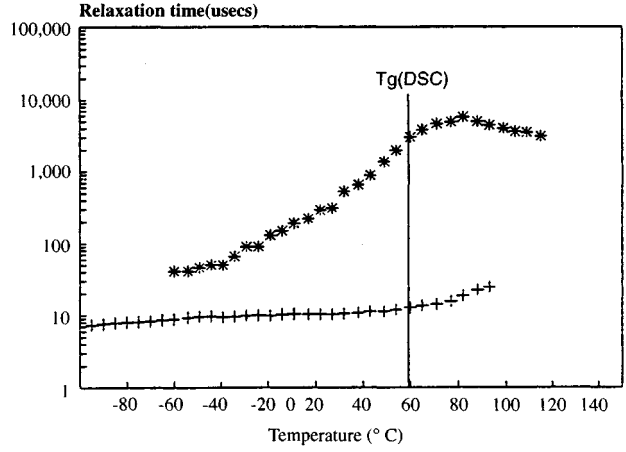
Relaxation time(usecs)
100,000
10,000
1,000
100
10
1
Tg(DSC)
-80 -60 -40 -20 0 20 40 60 80 100 120 140
Temperature (° C)

(*b*)

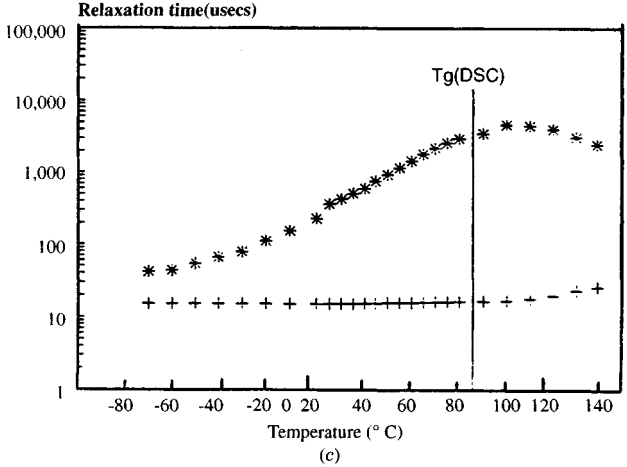
Relaxation time(usecs)
100,000
10,000
1,000
100
10
1
Tg(DSC)
-80 -60 -40 -20 0 20 40 60 80 100 120 140
Temperature (° C)

(*c*)

above also assumes that the rate-limiting step in retrogradation is the growth of amylopectin crystalline regions within the biopolymer network and not the rate of crystal nucleation, which decreases up to the amylopectin melting point. If nucleation is rate limiting the rate of retrogradation will be expected to decrease with increasing temperature, which is sometimes observed in cake products. Despite these complexities it is clear that glass–rubber transition theory offers exciting possibilities for the prediction of the effect of water content, sugar content, and temperature on the rate of staling of baked products, and that NMR and MRI provide the means for a detailed investigation of the space and time changes in molecular mobility associated with the staling process.

12.6.3 Water Dynamics in the Glassy State

Ablett et al. (159) have measured the temperature dependence of water proton transverse and longitudinal relaxation times in concentrated malto-oligomers as they pass through the glass transition temperature (as measured by DSC) and some of their data are reproduced in Figure 12.22. The maximum in T_2 as the temperature is decreased is characteristic of the removal of proton exchange and shows that all proton exchange ceases at and below the glass transition temperature in these systems. What is remarkable is the high mobility of the water even below the glass transition temperature, and this suggests that solid-imaging techniques should permit water in glassy states of food to be imaged. This high water mobility has also been observed in 10% maltose–water glasses in which the water gives a narrow spectral peak sitting on top of the broad spectrum arising from the more rigid maltose protons (229). Analysis of the dipolar cross-relaxation rates between water and maltose protons in this glass measured with the Goldman–Shen experiment gives a mean lifetime for water molecules at a particular maltose OH group of only about 10^{-5} s. These data suggest that in the glassy state the biopolymer or solute (e.g., maltose) has formed a rigid lattice with rotationally (and translationally; see section 13.2.3) mobile water molecules diffusing in the interstitial spaces formed by the lattice. Clearly, the water dynamics no longer correlates with the macroscopic shear viscosity, and this is confirmed by NMR translational diffusion measurements in glassy-state systems.

APPENDIX A

The observed transverse relaxation rate $1/T_2$ for two-site chemical exchange can be calculated as follows

$$\frac{1}{T_2} = \frac{1}{2\tau} \ln \lambda$$

$$\ln \lambda = -\tau\alpha_+ + \ln[(D_+ \cosh^2 \xi - D_- \cos \eta^2)^{1/2} + (D_+ \sinh^2 \xi + D_- \sin^2 \eta)^{1/2}]$$

$$2D_{\pm} = \pm 1 + \frac{\psi + 2\delta\omega^2}{(\psi^2 + \zeta^2)^{1/2}}$$

$$\xi = \left(\frac{\tau}{\sqrt{2}}\right)\{\pm[+\psi + (\psi^2 + \zeta^2)^{1/2}]^{1/2}\}$$

$$\zeta = 2\delta\omega\alpha_-$$

$$\eta = \frac{\tau}{\sqrt{2}}\{\pm[-\psi + (\psi^2 + \zeta^2)^{1/2}]^{1/2}\}$$

$$\psi = \alpha_-^2 - \delta\omega^2 + \frac{4}{\tau_a\tau_b}$$

$$\alpha_+ = \frac{1}{T_{2a}} + \frac{1}{T_{2b}} + \frac{1}{\tau_a} + \frac{1}{\tau_b}$$

$$\alpha_- = \frac{1}{T_{2a}} - \frac{1}{T_{2b}} + \frac{1}{\tau_a} - \frac{1}{\tau_b}$$

$$\delta\omega = \omega_b - \omega_a$$

where T_{2a} and T_{2b} are the transverse relaxation times of the a and b sites, respectively; τ_a and τ_b are the lifetimes on the a and b sites, respectively, such that $P_a/\tau_a = P_b/\tau_b = 1/\tau$.

APPENDIX B

The Bloch equations for the cross relaxation–proton exchange model of rotating-frame relaxation in aqueous biopolymer systems are as follows

$$\mathbf{M} = \mathbf{A} \cdot \mathbf{M} + \mathbf{M}'$$

and

$$M = \begin{bmatrix} M_a \\ M_b \\ M_m \end{bmatrix} \quad \text{and} \quad M_i = \begin{bmatrix} M_x^i \\ M_y^i \\ M_z^i \end{bmatrix} \quad i = a, b, m$$

A is the 9×9 matrix

$$A = \begin{bmatrix} a & \pi & \pi \\ \pi & b & \pi \\ \pi & \pi & c \end{bmatrix}$$

where π is the 3×3 identity matrix and

$$a = \begin{bmatrix} -(T_{2a}^{-1} + k_a + \kappa_a + \kappa'_m) & \omega - \omega_a & \omega_1 \\ -(\omega - \omega_a) & -(T_{2a}^{-1} + k_a + \kappa_a + \kappa'_m) & 0 \\ -\omega_1 & 0 & -(T_{1a}^{-1} + k_a + \kappa_a + \kappa'_m) \end{bmatrix}$$

$$b = \begin{bmatrix} -(T_{2b}^{-1} + k_b + \kappa_b + \kappa_m) & \omega - \omega_b & \omega_1 \\ -(\omega - \omega_b) & -(T_{2b}^{-1} + k_b + \kappa_b + \kappa'_m) & 0 \\ -\omega_1 & 0 & -(T_{1b}^{-1} + k_b + \kappa_b + \kappa_m) \end{bmatrix}$$

$$c = \begin{bmatrix} -(T_{2c}^{-1} + \kappa'_{-m} + \kappa_{-m}) & \omega - \omega_c & \omega_1 \\ -(\omega - \omega_c) & -(T_{2c}^{-1} + \kappa'_{-m} + \kappa_{-m}) & 0 \\ -\omega_1 & 0 & -(T_{1c}^{-1} + \kappa'_{-m} + \kappa_{-m}) \end{bmatrix}$$

$$M' = \begin{bmatrix} M_a^0 T_{1a}^{-1} \\ M_b^0 T_{1b}^{-1} \\ M_m^0 T_{1m}^{-1} \end{bmatrix} \quad \text{where} \quad M_i^0 = \begin{bmatrix} 0 \\ 0 \\ M_z^{i0} \end{bmatrix} \quad i = a, b, m$$

The resonance frequencies ω_i $(i = a, b, m)$ are most conveniently expressed in terms of the independent variables $\delta\omega = (\omega_b - \omega_a)$, $\delta\Omega = (\omega_m - \omega_b)$, and radio-frequency resonance offset $\omega_z = (\omega - \omega_{av})$, where ω_{av} is the average resonance frequency $\omega_{av} = \Sigma_1 P_i \omega_i (i = a, b, m)$. Then

$$\omega - \omega_a = \omega_z + (1 - P_a)\,\delta\omega + P_m\,\delta\Omega$$

$$\omega - \omega_b = \omega_z - P_a\,\delta\omega + P_m\,\delta\Omega$$

13

MOLECULAR FACTORS INFLUENCING THE DIFFUSION AND TRANSFER OF WATER MAGNETIZATION

13.1 INTRODUCTION

It is appropriate that the last chapter should be devoted to the molecular factors influencing the transfer of water proton magnetization through space, by diffusion, and between proton pools, by magnetization transfer, because these two processes are fundamental in the MRI of foods. In Part One we saw how diffusion of water through foods on the macroscopic distance scale controls processes such as drying and rehydration and could be used in temperature mapping. In Part Two we saw how restricted molecular diffusion could be used to probe food microstructure, and in Chapter 12 we showed that the transfer of transverse, longitudinal, and rotating-frame magnetization between water and biopolymer–solute proton pools was fundamental in determining relaxation contrast in the MRI of foods. This final chapter ties together a number of otherwise disparate themes.

13.2 MOLECULAR FACTORS INFLUENCING DIFFUSION CONTRAST

Figure 13.1 shows the dependence of the water self-diffusion coefficient on protein concentration for solutions (in some cases, gels) of BSA and gelatine (144). These data were obtained with the fringe-field stimulated-echo diffusion pulse sequence discussed in Chapter 11. Changes of slope are apparent at protein concentrations of about 50 and 85% w/w and can be related to the changing importance of three molecular mechanisms: obstruction effects, exchange processes, and percolation cluster effects.

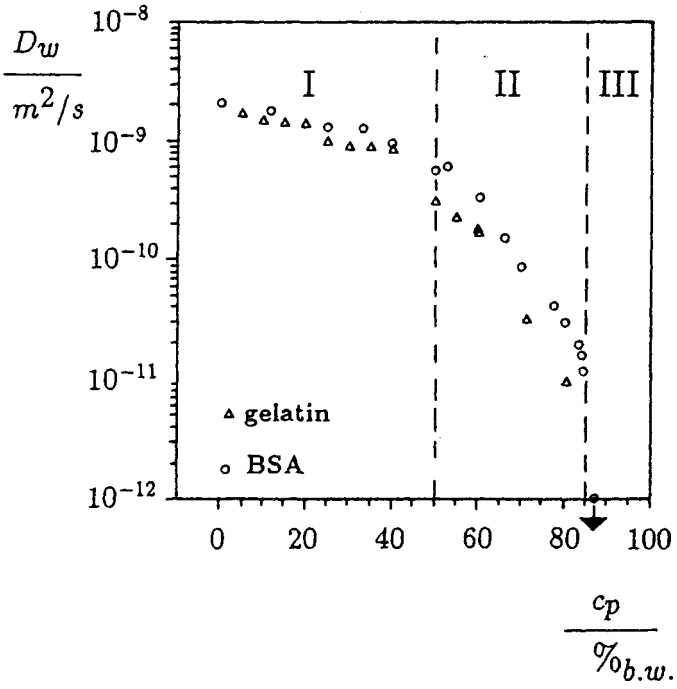

Figure 13.1. Dependence of the average water diffusion coefficient in aqueous BSA and gelatine solutions (gels) on protein concentration, $c_p = 100 - c_w$ at 20°C. The data point for 87% BSA (marked by an arrow) is the lower limit of the measuring range in these fringe-field experiments since no detectable diffusion occurred. (From Ref. 144.)

13.2.1 Obstruction Effects

In the dilute regime, bulk water dominates the diffusion behavior. Diffusion of water molecules is obstructed by the presence of much more slowly moving macromolecules. This difficult problem was tackled, theoretically, in a classic paper by Wang (155), who represented the protein solution as a suspension of randomly oriented ellipsoids and showed that their combined obstruction effect in dilute systems was described by an equation of the form

$$D_{ob} = D_0(1 - \alpha\phi) \tag{13.1}$$

where D_{ob} is the obstructed water self-diffusion coefficient, D_0 the unhindered diffusion coefficient of bulk water, ϕ the total volume fraction occupied by the protein molecules, and α a geometric factor related to the principal-axis ratio of the ellipsoids. Equation (13.1) predicts a linear concentration dependence at low protein concentrations, which is seen in the first part of Figure 13.1.

13.2.2 Exchange Effects

Wang also considered the problem of the exchange of water molecules between the bulk "free" phase and those in the hydration shell of the macromolecule and derived the linear relationship

$$D_{app} = D_{ob}\left(1 - \frac{c_h}{c_0}\right) \tag{13.2}$$

where D_{app} is the observed water self-diffusion coefficient and c_h and c_0 are the concentrations of hydration and total water, respectively. This equation is derived with the assumption that the exchange of water between the hydration and bulk states is fast on the NMR measurement time scale and that the diffusion of the macromolecule is much smaller than that of water (155). Proton exchange and in the stimulated echo sequence, magnetization transfer by dipolar coupling between the water and macromolecular proton pools will also contribute to equation (13.2), although this effect was not explicitly treated by Wang. We consider this aspect in greater detail in Section 13.3.

Kimmich and co-workers used the exchange effect to interpret the second part in Figure 13.1, generalizing it to the form, $D_{app} = p_h D_h + p_f D_f$, where p_f is the fraction of free water, D_f the diffusion coefficient of free water, and D_h, the diffusion coefficient of hydration water. Fitting the data in segment II of Figure 13.1 gave $D_f = 2.2 \times 10^{-9}$ m^2/s and $D_h = 1.2 \times 10^{-10}$ m^2/s. Note that D_h refers to diffusion in the three-dimensional Euclidean space, while the actual water molecule displacements in the macromolecule hydration shell occur in the topologically two-dimensional surface layers.

13.2.3 Percolation Cluster Effects

In the concentration range 85 to 100% protein in Figure 13.1, the diffusion coefficient becomes immeasurably small on the NMR measurement time scale of milliseconds. The crossover between regions II and III in Figure 13.1 coincides with the percolation threshold in dielectric studies of protein conductivity. Kimmich and co-workers (144) have therefore concluded that during this phase the surface layers of water molecules hydrating the macromolecule break up into finite-sized "patches" or "pools" and their connectivity is reduced correspondingly. This results in a transition from infinite to finite cluster sizes. The extension of these ideas to polysaccharide systems is still "work in progress."

It might be thought that in view of the reciprocal relationship between the diffusion coefficient and shear viscosity predicted by the Stokes–Einstein equation and the relationship between shear viscosity η and temperature embodied in the WLF equation (190)

$$\log \frac{\eta}{\eta_g} = \frac{C_1(T - T_g)}{C_2 + (T - T_g)} \tag{13.3}$$

there should be a corresponding relationship between the water self-diffusion coefficient and $T - T_g$. A number of NMR experiments show that this is not, in fact, the case. Instead, the water continues to show considerable rotational and translational mobility at temperatures far below the glass transition temperature in many biopolymer systems. The rotational mobility of water in the glass state of biopolymer systems and simple sugars was mentioned in Chapter 11. Direct measurements of the water translational mobility with the pulsed field gradient spin-echo technique confirms that this is also true for translational mobility. Figure 13.2 shows the dependence of the temperature dependence of the water translational diffusion coefficient in a 80.9% pullulan gel. This not only confirms much higher water mobility than predicted by the shear viscosity, but also shows that there is no break or change of slope at the glass transition temperature. The molecular interpretation of this observation is, perhaps, related to the large difference in molecular weights of the water and pullulan molecules, which permits the water dynamics to "uncouple" from that of the long-chain molecule. Much more work is needed to clarify this dynamic uncoupling phenomenon, which is relevant to processes such as drying and rehydration and loss of volatile aroma molecules above and below the glass transition temperature.

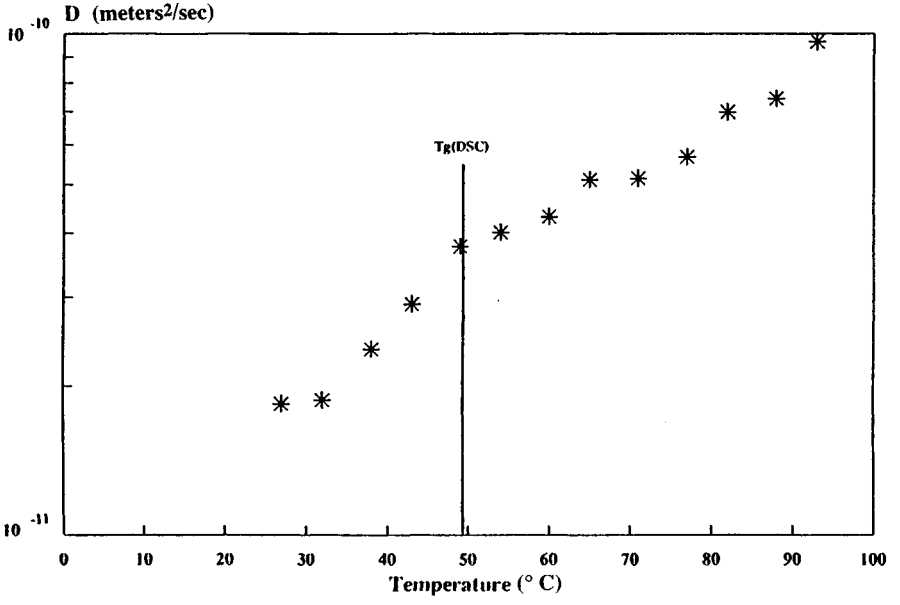

Figure 13.2. Temperature dependence of the water self-diffusion coefficient in 80.9% pullulan as it goes through the glass transition temperature. (From Ref. 159.)

13.3 MAGNETIZATION TRANSFER

13.3.1 Magnetization Transfer Contrast Imaging

The transfer of longitudinal magnetization between water and macromolecule proton pools can be used to create image contrast in MRI (239–241,244,245). This is usually done by selectively saturating the macromolecular protons and allowing the magnetization to exchange with water protons that are imaged. In regions where magnetization transfer is fast, the water proton signal is attenuated by exchange with the saturated macromolecular proton pool. The selective saturation of the macromolecular proton pool can be achieved by either continuous or pulsed irradiation (242,243). In the continuous approach the macromolecular protons are irradiated with a long (0.1 to 1.0 s) low-intensity off-resonance RF pulse before each excitation of the water proton imaging sequence. The long imaging times necessitated by the long saturation pulses is the major disadvantage of this approach. A faster protocol is to use multiple short-duration (1 to 20 ms) higher-intensity pulses distributed throughout a spin-echo or gradient-echo imaging sequence. If shaped RF pulses are used, bandlimited off-resonance saturation of the macromolecular proton pool can be achieved (14,24). If binomial on-resonance RF pulses are used, the macromolecular proton pool is symmetrically saturated while producing a net zero excitation of the water proton pool.

Pike and co-workers (242,247) has presented a phenomenological analysis of magnetization transfer contrast based on solution of the coupled Bloch equations for the exchange of longitudinal magnetization between the water (or exchangeable proton) pool and the more rigid nonexchanging macromolecular proton pool. They simplified the analysis used in Chapter 12 by combining the proton exchange and secular dipolar cross-relaxation exchange processes into effective forward and reverse exchange rates, k_f and k_r, respectively. With this simplification we can write

$$\frac{dM_f}{dt} = R_{1f}(M_{0,f} - M_f) - k_f M_f + k_r M_r \tag{13.4}$$

$$\frac{dM_r}{dt} = R_r(M_0 - M_r) - k_r M_r + k_f M_f \tag{13.5}$$

where the subscripts f and r refer to the water pool and the more-rigid macromolecular proton pool, respectively. These equations were solved subject to appropriate initial conditions for the MT-imaging sequence, which involved partial saturation of the macromolecular proton pool and steady-state excitation appropriate to rapid repetition of the imaging sequence. In this way the conditions needed to maximize magnetization transfer contrast could be calculated. While these simplified, two-site exchange equations can be used to predict MT contrast in many systems, they also require an understanding of the molecular factors controlling the effective exchange rate constants, k_f and k_r. The proton exchange contribution was considered in Chapter 12. We now need to look at the factors controlling the magnitude of the dipolar cross-relaxation rate.

13.3.2 Secular Dipolar Cross-Relaxation Rates

The analysis of the dipolar cross-relaxation rate is based on slight modifications of the theory of the nuclear Overhauser effect (NOE) (237). The cross relaxation rate between a particular pair of protons $|\sigma|$ is given as

$$|\sigma| = \frac{C_p^2}{10} |J(0,\tau) - 6J(2\omega_0,\tau)| \tag{13.6}$$

where the J functions are the spectral densities defined by equation (12.4), and in this case the correlation time τ characterizes the motion that modulates the dipolar interaction between the pair of protons and C_p is the dipolar coupling constant. Figure 13.3 shows a schematic of the dependence of $|\sigma|$ on the correlation time τ. For

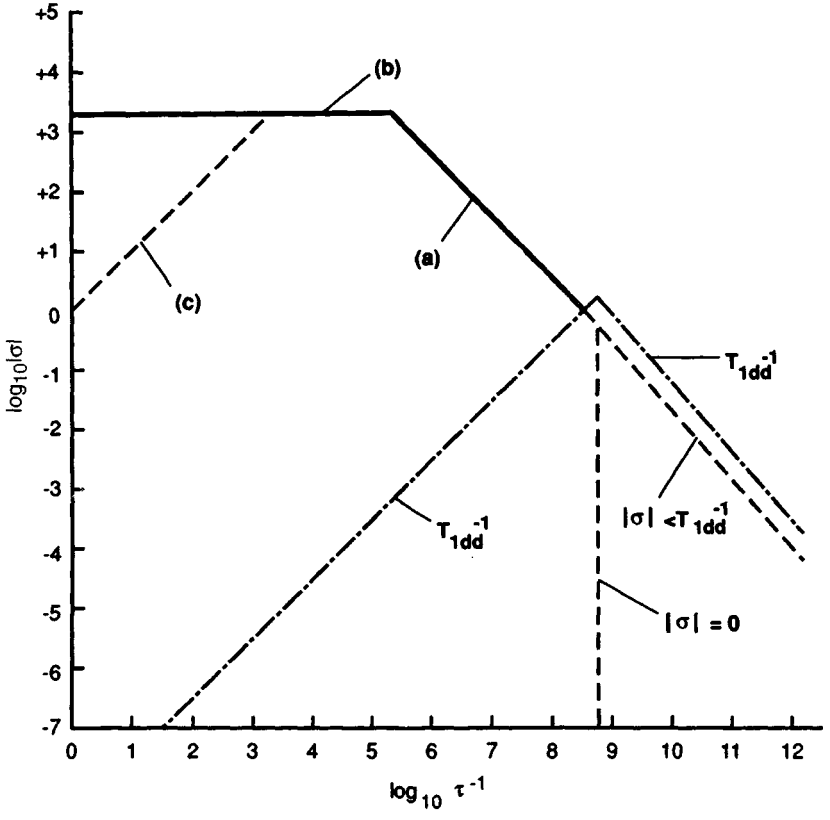

Figure 13.3. Dependence of the pairwise longitudinal secular dipolar cross-relaxation rate $|\sigma|$ on the correlation time modulating the interaction. Line *a* is given by equation (13.6) line *b* is the rigid lattice limiting value assuming a nonexchangeable proton linewidth of 30 kHz. The dotted-dashed line shows the region where $|\sigma| < T_{1dd}^{-1}$, so there is no cross relaxation. For comparison, the dotted line (*c*) shows the proton exchange rate (*k*) when $\tau = \tau_b$.

dipolar cross relaxation between surface hydration water and biopolymer protons, τ corresponds to the mean lifetime of a particular water molecule at the biopolymer surface, which is extremely short, typically much less than 1 ns as determined by high-resolution two- and three-dimensional NOESY spectroscopy (274), so that $|\sigma|$ is negligible, at least in dilute solution. Recent work suggests that in addition to the hydration water, there are a few more strongly hydrogen-bonded water molecules inside the crevasses and coils of globular proteins having lifetimes of microseconds or longer. However, with these water molecules the dipolar interaction is not modulated by the lifetime but by the rotational motion of the biopolymer, which for dilute globular proteins is on the order of a few tens of nanoseconds. This means that dipolar cross relaxation from hydration water in globular protein solutions is negligible. Similar arguments apply to the dipolar cross relaxation between the exchangeable and nonexchangeable biopolymer protons, which will also be modulated by rotational motion of the globular protein.

The situation becomes less straightforward when the water content is lowered or when the rotational motion of the protein molecule is stopped by gelation, for example. In these cases there could well be significant dipolar cross relaxation from the hydration water as well as between the biopolymer proton pools. Much work remains to be done in measuring these rates and in separating the contributions of proton exchange and dipolar cross relaxation. Cross-linked protein gels, such as chemically cross-linked BSA, have been found to be excellent models of the relaxation behavior of tissue, such as the human spleen, both showing similar $T_1(\omega_0)$ dispersions (see, e.g., Figure 12.14). At resonance frequencies ω_0 above about 40 MHz, the intrinsic T_1 values of the nonexchanging proton protons and of the water are comparable, so that magnetization transfer, either by proton exchange or by dipolar cross relaxation, has little effect on image contrast. However, at lower frequencies, between 0.01 and 1 MHz, the nonexchanging and water protons have very different longitudinal relaxation times (because one is in the rigid lattice regime, and the water is in the motionally narrowed regime). In this case cross relaxation can have a dominant role in determining the observed exchangeable proton relaxation times, and hence image contrast.

13.3.3 Measurement of Dipolar Cross-Relaxation Rates

One very useful way of measuring dipolar cross-relaxation rates is to excite longitudinal magnetization selectively in the water proton pool and monitor its transfer into the pool of nonexchanging biopolymer protons. If the transverse relaxation time of the biopolymer protons is much less than that of the water protons, this can be conveniently done with the Goldman–Shen pulse sequence (138). This consists of three nonselective 90° pulses ($90°_{+x}$–D4–$90°_{-x}$—t_d–$90°_{+x}$–FID). By setting the time delay D4 longer than five times the biopolymer transverse relaxation time, all transverse magnetization in the nonexchanging biopolymer proton pool is removed while leaving water and exchangeable biopolymer proton magnetization essentially unchanged. The $90°_{-x}$ pulse returns this residual water and exchangeable proton magnetization to the z-axis, where it cross relaxes to the nonexchanging biopolymer

proton pool during the mixing time t_d. The third 90°_x pulse generates an FID from which the rate of recovery of the nonexchanging magnetization can be measured as a function of mixing time. Fitting this recovery curve gives the cross-relaxation rate. Longitudinal relaxation during the mixing time can also contribute to the recovery, but this contribution can be partly eliminated by alternating the sequence above with the sequence 90°_x–D4–90°_x–t_d–90_{-x}–FID and adding the result (292).

An alternative method for measuring the cross-relaxation rate involves *Z-spectroscopy* (238). This involves the acquisition of the water FID or spectrum with a single 90° hard pulse immediately after selective irradiation of the system with a long preparation pulse at a frequency offset $\Delta\omega$ from the water resonance. Because of cross relaxation between the water and biopolymer proton pools, the FID amplitude of the water depends on the cross-relaxation rate, on $\Delta\omega$, and on the relaxation characteristics of the biopolymer component. In fact, the $\Delta\omega$ dependence of the water signal mirrors the solid spectrum of the solid component, which is very useful since it can be acquired with a high-resolution spectrometer equipped with a decoupling channel (293).

13.4 MULTISTATE THEORY OF WATER RELATIONS IN FOODS

The compositional complexity of many real foods often prevents a detailed analysis of the molecular and microstructural factors determining relaxation, diffusion, and magnetization transfer rates between the numerous proton pools. Nevertheless, the situation is far from hopeless because physical insights gained from the study of simpler model systems permits the development of (semi-)empirical relationships applicable to more complex systems. In this final section we explore one of these approaches, the *multistate theory of water relations*, and indicate how it can be used to correlate a wide variety of otherwise unconnected physical and microbiological observations.

13.4.1 Multistate Theory of Water Activity

Both high-resolution NMR spectroscopy (274) and low-resolution relaxometry suggest that in dilute and moderately concentrated biopolymer systems, water interacting with biopolymers exchanges with water in the bulk phase with a spectrum of exchange lifetimes ranging from nanoseconds to microseconds, or possibly even milliseconds, with very strongly hydrogen-bonded water essential for the structural integrity of the macromolecule. Neglecting the complexities of cross relaxation and proton exchange, and assuming fast diffusive exchange of water molecules between the various states of interaction with the food matrix, we can write, somewhat naively

$$T_{\text{av}}^{-1} = \sum_i p_i T_i^{-1} \tag{13.7}$$

where we assume i discrete states of hydration water of fractional population p_i and intrinsic relaxation times T_i. Specializing to the simple two-state case where bulk water exchanges with hydration water, equation (13.5) becomes $T_{av}^{-1} = x_h T_h^{-1} + x_b T_b^{-1}$, where $x_h + x_b = 1$ and x_h and x_b are the volume fractions of hydration and bulk water, respectively. This equation can be rewritten to show the linear dependence of the observed relaxation rate on solid content W^{-1}

$$T_{av}^{-1} = T_b^{-1} - \frac{m_0 (T_b^{-1} - T_h^{-1})}{W} \tag{13.8}$$

where m_0 is the weight of hydration water per unit weight of dry biopolymer and W is the water content, defined as the weight of water per unit weight of dry solid. This linear relationship has been observed in many systems; Figure 13.4 gives examples for a variety of model systems. Changes of slope between otherwise linear segments suggests, according to equation (13.8), that one of the states of water has either been lost or a new one introduced. It is important to note that equation (13.8) is applicable only when the water relaxation is single exponential. As discussed in Chapter 10, this requires rapid diffusive exchange between any microscopic compartments.

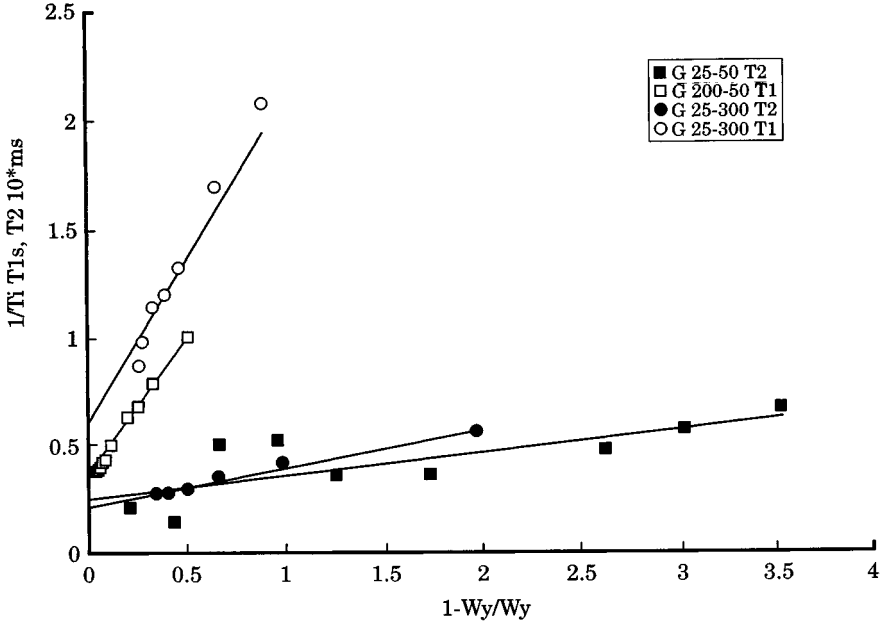

Figure 13.4. Dependence of the water proton relaxation rate (s^{-1}) on solid content expressed as $(1 - W_y)/W_y$ for randomly packed beds of Sephadex microspheres. The relaxation is single exponential throughout the range. T_1 is in units of seconds, T_2 in units of 10 ms. W_y is defined as the total mass of water per unit mass of water and dry solid. (From Ref. 231.)

It has long been suspected that relaxation times are also related to water activity and may provide a useful measure of what is loosely called *water availability*. If such a relationship exists, it would find many important applications because it is well known that correlations already exist between equilibrium water activity and the rates of enzymatic and nonenzymatic reactions as well as the rates of microbiological growth or death (275,278). To seek a relation between water activity and NMR relaxation rates, we can, as a working hypothesis, assume that each of the i states of hydration water are also characterized by different intrinsic activities a_i and write, in analogy with equation (13.7), that the average water activity a_{av} observed is given as

$$a_{av} = \sum_i p_i a_i \tag{13.9}$$

This is, in fact, consistent with the ergodic theorem of statistical thermodynamics, which states that at equilibrium, the time-averaged property of one water molecule is the same as the ensemble averaged property, equation (13.9) being the ensemble-averaged expression. Specializing to the simple two-state case where bulk water exchanges with hydration water, equation (13.9) becomes, analogously to equation (13.8), the sorption isotherm

$$a_{av} = a_b - \frac{m_0(a_b - a_h)}{W} \tag{13.10}$$

Equation (13.10) is only valid for $W > m_0$, because W values less than m_0 correspond to the removal of hydration water and the formalism is no longer applicable. It is then necessary to revert to conventional gas-phase kinetic theories of sorption isotherms such as the BET theory (279). Figure 13.5 shows how the theory gives

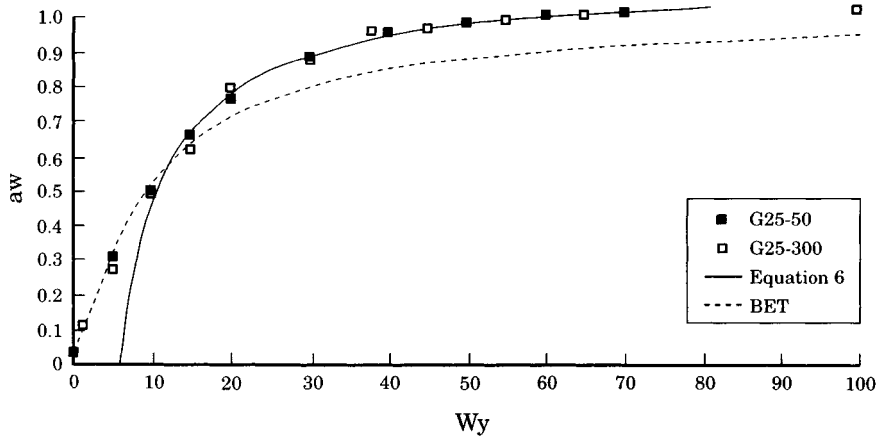

Figure 13.5. Fit of equation 13.10 to the sorption isotherm data for Sephadex G25-50 and G25-300 (which differ only in particle size). The dashed curve shows the BET fit.

satisfactory agreement with the sorption isotherm data for Sephadex G25-50 for activity values above about 0.4, which corresponds roughly to the surface water activity. The dashed line in Figure 13.5 is the fit of the BET isotherm, which gives good agreement with activities below 0.4, but not at higher water activities.

The correspondence between equations (13.8) and (13.10) implies that NMR relaxation rates are linearly related to water activity according to the equation

$$T_{av}^{-1} = T_b^{-1} + C(1 - a_{av}) \tag{13.11}$$

where the constant C is $(T_h^{-1} - T_b^{-1})/(1 - a_h)$. This equation is valid for $W > m_0$ only under conditions of fast diffusive averaging of the magnetization density, so that the observed relaxation is single exponential. Equation (13.11) has been verified for a number of model systems, such as beds of Sephadex microspheres, silica particles, and starch granules. Typical results are shown in Figures 13.6 and 13.7. The breaks in the silica data in Figure 13.7 are actually consistent with the model because they correspond to the points in the sorption isotherms where all external bulk water ($aw = 1$) is removed, leaving only water in micropores within the silica particles. Clearly, much work is required to explore the limits of usefulness of

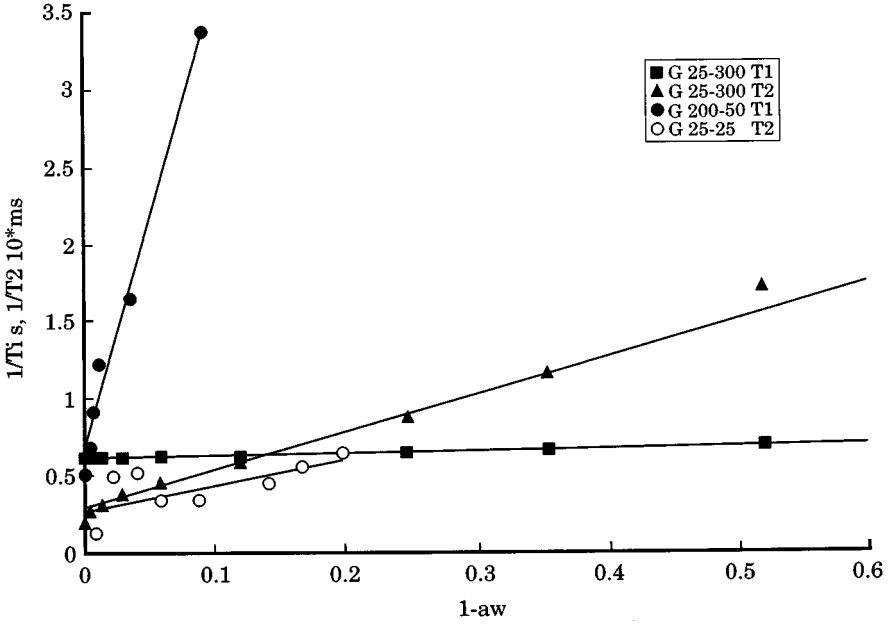

Figure 13.6. Linear relationships between relaxation rates in the fast exchange regime and $(1 - av)$ predicted by equation (13.11) for randomly packed beds of Sephadex microspheres differing in cross-linking density and particle size. T_1 is in units of seconds, T_2 in units of 10 ms.

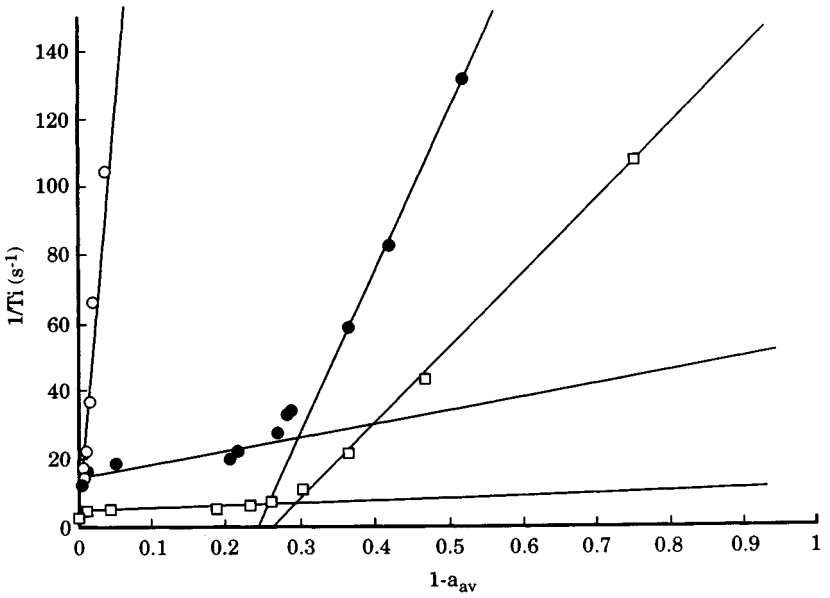

Figure 13.7. Dependence of the water proton transverse relaxation rates on water activity, expressed as $(1 - a_{av})$ for several randomly packed beds of silica particles. Solid circles, 10 to 40 μm particle size, T_2^{-1} data divided by 10; open squares, 40 to 63 mm particle size, T_1^{-1} data; open circles, 0.5 to 10 μm particle size, T_2^{-1} data divided by 10. The lines are the best fits of equation (13.11) to the data. (From Ref. 231.)

equation (13.11) in food systems. The fact that proton exchange has been ignored in equation (13.7) may at first sight appear to invalidate the approach. This objection remains to be more fully explored, but it may be the case that exchange effects merely alter the magnitude of the effective component T_{2i} so that subsequent relationships, such as (13.11), remain applicable, at least over certain ranges of water content.

13.4.2 Electrical Conductivity and NMR Water Relaxation

We saw in Section 2.3.3 how in the falling-rate period of drying, transport of moisture through a food matrix becomes rate limiting. As a capillary-porous solid becomes drier, the connections between water-filled pores in the matrix become progressively broken, until in the pendular state, all fluid-phase conductivity is lost and moisture transport occurs only via the vapor phase. The gradual loss of fluid-phase

connectivity is reflected not only in decreasing effective macroscopic moisture diffusivity, but also in decreasing electrical conductivity if the water is replaced by a conducting solution such as dilute KCl. According to Archie's law (276), the dependence of the electrical conductivity λ of a porous medium is related to water content as

$$\frac{\lambda}{\lambda_{sat}} = \phi^p S^p \tag{13.12}$$

where λ_{sat} is the electrical conductivity of the porous matrix saturated with the conducting solution, ϕ the porosity (the ratio of the total void volume to the total volume), S the degree of saturation, and p and q are constants of the order of 2 to 3. Archie's law has been derived for saturated beds by purely geometric arguments; however, the extension to unsaturated systems is empirical. Figure 13.8 shows that Archie's law is reasonably well obeyed for many porous systems containing varying amounts of a dilute potassium chloride solution. If Archie's law is combined with equation (13.8), we deduce that the water proton relaxation rates are related to conductivity as

$$\frac{\lambda}{\lambda_{sat}} = \phi^q \left(\frac{T_{av}^{-1} - T_b^{-1}}{T_{sat}^{-1} - T_b^{-1}} \right)^p \tag{13.13}$$

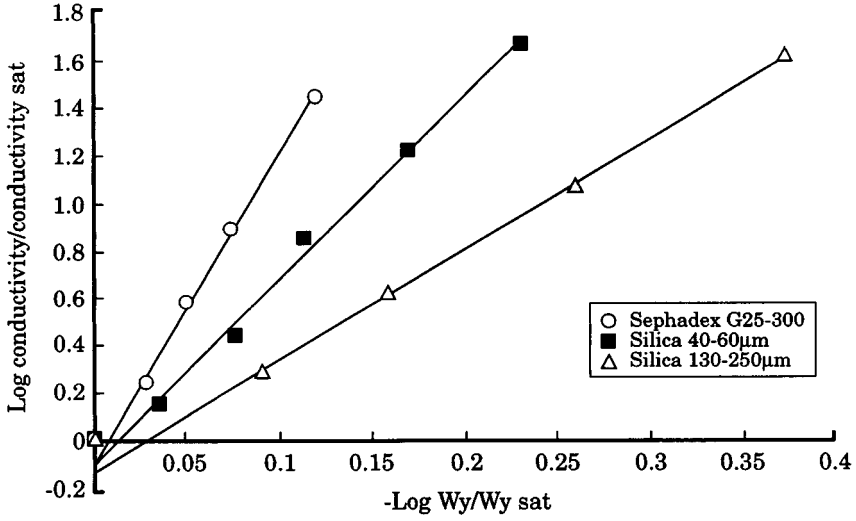

Figure 13.8. Log-log plot of Archie's law for the model porous beds indicated. The lines are best fits with equation (13.12).

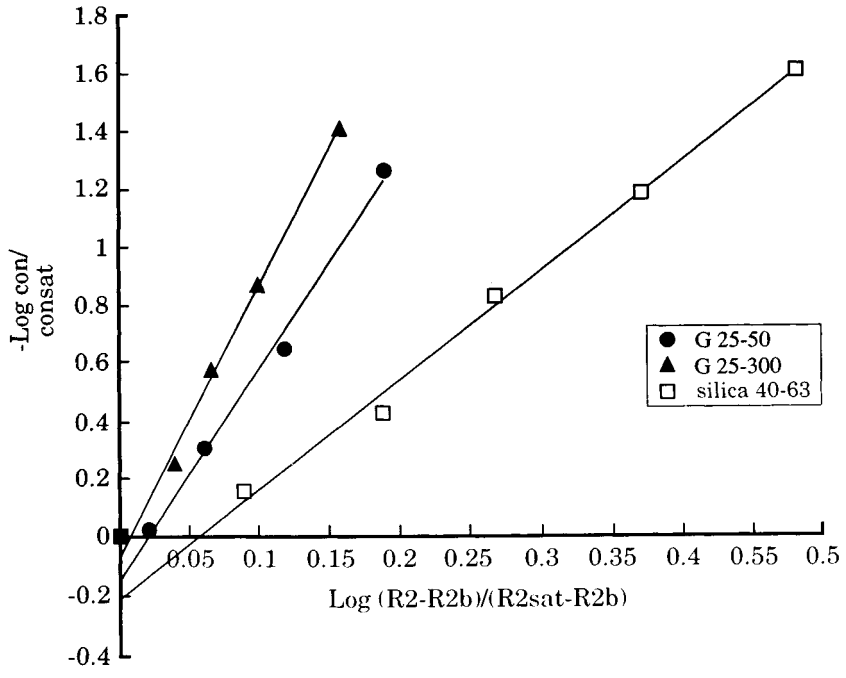

Figure 13.9. Log-log plot of equation (13.13) for water/oxygen-17 relaxation rates in randomly packed beds of Sephadex G25-50 and 25 to 300 and 40 to 63 μm silica particles. (From Ref. 231.)

where T_{sat}^{-1} is at the relaxation rate in the water-saturated system. Equation (13.13) remains valid as long as the exchange is fast on the NMR time scale and the relaxation is single exponential. Figure 13.9 shows that the single-exponential water proton transverse relaxation times for beds of Sephadex G25-50 conform satisfactorily to equation (13.13). When the NMR exchange is slow, the changing intensities of the relaxation-time peaks are not so obviously related to conductivity, and much work remains to be done in elucidating the relationship. In Sephadex and silica beds, for example, Figures 13.10 and 10.24 show that the decrease in electrical conductivity correlates very well with the decrease in the relative amplitude of the transverse relaxation-time peak for water in the largest pores, as measured by a CONTIN relaxation-time distribution (see, e.g., Figures 10.8 and 10.18). Evidently, the largest pores are most effective in creating connections throughout the matrix. It is interesting to observe that Figures 13.10 and 10.24 include microbiological data on the survival of the foodborne bacterial pathogen *Salmonella typhimurium* LT2. This correlates with the NMR and conductivity data because the removal of water from a pore causes the bacteria within a pore to suffer osmotic shock. Similar rela-

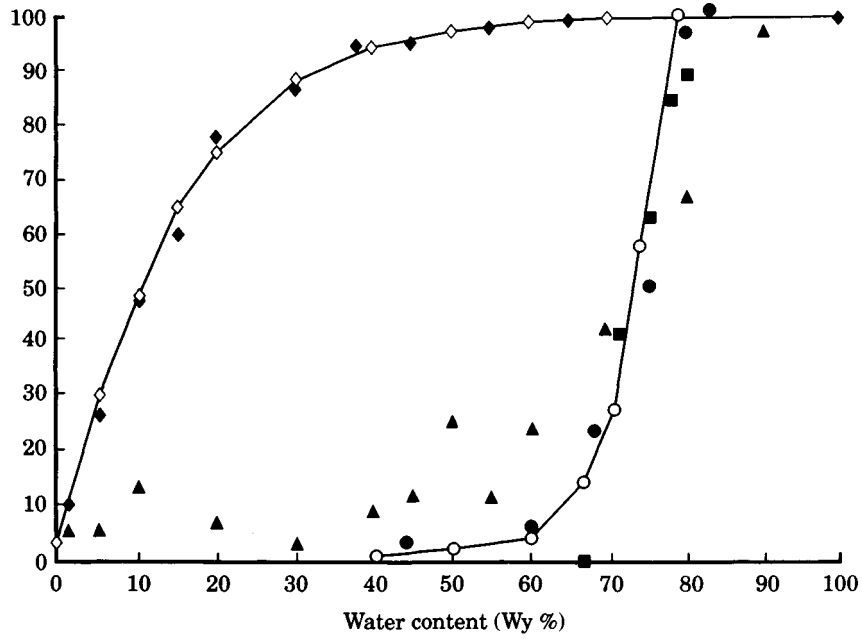

Figure 13.10. Comparison of the drop in percent recovery (solid/open wedges) of *Salmonella typhimurium* LT2 in a randomly packed bed of Sephadex G25-50 with the decrease in water activity, $a_{av} \times 100$ (solid diamonds), % electrical conductivity relative to the saturated bed (solid circles), and the NMR measurements of the amount of water outside the microspheres (solid squares) measured from the % peak area (relative to the saturated bed) in the CONTIN water proton transverse relaxation time distributions (see Figure 10.8). The sorption isotherm data for Sephadex G25-300 have been included (open diamonds).

tionships are expected for microbial spoilage organisms which can limit food shelf life. This suggests the exciting possibility that NMR relaxation times (and hence relaxation-time-weighted MRI) might be useful indicators of microbial stability of different regions within a food. Clearly, much more extensive NMR and microbiological data are required before this potentially important application can be placed on a reliable footing.

REFERENCES

1. Callaghan, P. T., and Manz, B. Velocity exchange spectroscopy. *J. Magn. Reson.* **A106** (1994), 260–265.
2. Ernst, R. R., Bodenhause, G., and Wokaun, A. *Principles of NMR in One and Two Dimensions*. Oxford University Press, Oxford, 1988.
3. Callaghan, P. T., and Stepisnik, J. Frequency-domain analysis of spin motion using modulated-gradient NMR. *J. Magn. Reson.* **A117** (1995), 118–122.
4. Weiner, N. *The Fourier Integral and Certain of Its Applications*. Dover, New York, 1958.
5. Callaghan, P. T. *Principles of Nuclear Magnetic Resonance Microscopy*. Oxford Science Publications, Oxford 1991.
6. Rutledge, D. N. *Signal Treatment and Signal Analysis in NMR*. Elsevier, Amsterdam, 1996.
7. Abragam, A. *Principles of Nuclear Magnetism*. Oxford University Press, Oxford, 1978.
8. McDonald, P. Stray field MRI: A powerful technique for quantitative, high resolution imaging of solids. *Spectros. Eur.* **7** (1995), 25–30.
9. Samoilenko, A. A., Atremov, D. Y., and Sibeldina, L. A. *JETP Lett.* **47** (1988), 417.
10. Benson, T. B., and McDonald, P. J. Profile amplitude modulation in STRAFI. *J. Magn. Reson.* **A112** (1995), 17–23.
11. Benson, T. B., and McDonald, P. J. The application of spin-echoes to STRAFI. *J. Magn. Reson.* **A109** (1995), 314–317.
12. Hughes, P. D. M., McDonald, P. J., Rhodes, N. P., Rockliffe, J. W., Smith, E. G., and Wills, J. A STRAFI study of the drying of sodium silicate films. *J. Colloid Interface Sci.* **177** (1996), 208–213.
13. Perry, K. L., McDonald, P. J., Randall, E. W., and Zick, K. Stray field MRI of the diffusion of acetone into polyvinyl chloride. *Polymer* **35** (1994), 2744–2748.

14. Cottrell, S. P., Halse, M. R., and Strange, J. H. *Meas. Sci. Technol.* **1** (1990), 624.
15. McDonald, P. J., Perry, K. L., and Roberts, S. P. *Meas. Sci. Technol.* **4** (1993), 896.
16. Hughes, P. D. M., McDonald, P. J., Halse, M. R., Leone, B., and Smith, E. G. Water diffusion in zeolite 4A beds measured by broad-line MRI. *Phys. Rev.* **B51** (1995), 11332–11338.
17. McDonald, P. J., Pritchard, T., and Roberts, S. P. Diffusion of water at low saturation levels into sandstone rock plugs measured by broad-line magnetic resonance profiling. *J. Colloid. Interface Sci.* **177** (1996).
18. Grant, D. M., and Harris, R. K. *Encyclopedia of NMR.* John Wiley, New York, 1996.
19. Power, E. A. *Introductory Quantum Electrodynamics.* Longman Group, Harlow, Essex, U.K. 1974.
20. Mallett, M. J. D., Codd, S. L., Halse, M. R., Green, T. A. P., and Strange, J. H. Three-dimensional NMR imaging using large oscillating field gradients. *J. Magn. Reson.* **A119** (1996), 105–110.
21. Mansfield, P., and Grannell, P. K. *Phys. Rev.* **B12** (1975), 3618–3634.
22. McDonald, P. J., and Tokarczuk, P. F. An NMR multipulse sequence for the imaging of solids using sinusoidally driven magnetic field gradients. *J. Phys.* **E22** (1989), 948–951.
23. Cory, D. G., Van Os, J. W. M., and Veeman, W. S. NMR Images of rotating solids. *J. Magn. Reson.* **76** (1989), 543–547.
24. Veeman, W. S., and Cory, D. G. Proton NMR imaging of solids with MAS. *Adv. Magn. Reson.* **13** (1989), 43–56.
25. Hafner, S., and Barth, P. Magic-echo phase-encoding solid imaging with improved time resolution. *Magn. Reson. Imaging* **13** (1995), 441–445.
26. Demco, D. E., Hafne, S., and Kimmich, R. Spatially resolved homonuclear solid-state NMR:III. Magic-echo and rotary-echo phase-encoding imaging. *J. Magn. Reson.* **96** (1992), 307–322.
27. Gravina, S., and Cory, D. G. *J. Magn. Reson.* **B104** (1996), 53.
28. Bogdan, M., Balcom, B. J., Bremmer, T. W., and Armstrong, R. L. Single point imaging of partially dried, hydrated white portland cement. *J. Magn. Reson.* **A116** (1995), 266–269.
29. Eads, T. M., and Axelson, D. E. Nuclear cross relaxation spectroscopy and single point imaging measurements of solids and solidity in foods. In P. S. Belton, I. Delgadillo, A. M. Gil, and G. A. Webb (Eds.), *Magnetic Resonance in Food Science.* Royal Society of Chemistry, Cambridge, 1995, pp. 230–242.
30. Barth, P., Hafner, S., and Kuhn, W. Magic-echo phase-encoding solid imaging of rubber materials below the glass transition temperature. *J. Magn. Reson.* **A110** (1994), 198–201.
31. Callaghan, P. T., Jeffrey, K. R., and Xia, Y. Translational motion imaging with pulsed gradient spin-echo methods. In B. Blumich and W. Kuhn (Eds.), *Magnetic Resonance Microscopy.* VCH, Weinheim, Germany, 1992.
32. McCarthy, K. L., Kauten, R. J., McCarthy, M. J., and Steffe, J. F. Flow profiles in a tube rheometer using MRI. *J. Food Eng.* **16** (1992), 109–125.
33. Maneval, J. E., Seymour, J. D., Powell, R. L., McCarthy, M. J., and McCarthy, K. L. Application of NMR to the rheological characterization of non-Newtonian fluids. *Am. Inst. Chem. Eng. Conf. Abstr.,* Florida, 1992.

34. Seymour, J. D., Maneval, J. E., McCarthy, K. L., and McCarthy, M. J. NMR velocity phase-encoded measurements of fibrous suspensions. *Phys. Fluids* **A5** (1993), 1–4.
35. Lips, A., Westbury, T., Hart, P. M., Evans, I. D., and Campbell, I. J. On the physics of shear-induced aggregation in concentrated food emulsions. In E. Dickinson and P. Wastra (Eds.), Food Colloids and Polymers: *Stability and Mechanical Properties.* Royal Society of Chemistry, Cambridge, 1993, pp. 31–44.
36. Horne, D. S. Viscosity of milk and its concentrates. In E. Dickinson and P. Wastra (Eds.), *Food Colloids and Polymers: Stability and Mechanical Properties.* Royal Society of Chemistry, Cambridge, 1993, pp. 260–265.
37. McCarthy, M. J., and McCarthy, K. L. Quantifying transport phenomena in food processing with NMR imaging. *J. Sci. Food Agr.* **65** (1994), 257–270.
38. Kose, K. Instantaneous flow-distribution measurements of the equilibrium turbulent region in a circular pipe using ultrafast NMR imaging. *Phys. Rev.* **A44** (1991), 2495–2504.
39. Ottino, J. M., Leong, C. W., Rising, H., and Swanson, P. D. Morphological structures produced by chaotic flow. *Nature* **333** (1988), 419–425.
40. Macagno, E. O., and Christensen, J. A. *Rev. Fluid Mech.* **12** (1980), 139–158.
41. Weis, J., Kimmich, R., and Muller, H. P. NMR imaging of thermal convection patterns. *Magn. Reson. Imaging* **14** (1996), 319–327.
42. Kose, K. Visualization of turbulent motion using echo-planar imaging with a spatial tagging sequence. *J. Magn. Reson.* **98** (1992), 599–603.
43. Mandelbrot, B. B. Intermittent turbulence in self-similar cascades: Divergence of high moments and dimensions of the carrier. *J. Fluid Mech.* **62** (1974), 331–358.
44. McCarthy, K. L., Kauten, R. J., and Agemura, C. K. Application of NMR imaging to the study of velocity profiles during extrusion processing. *Trends Food Sci. Technol.* **3** (1992), 215–219.
45. Landau, L. D., and Lifshitz, E. M., *Fluid Mechanics.* Pergamon Press, New York, 1959.
46. Hammer, B. E., Heath, C. A., Mirer, S. C., and Belfort, G. Quantitative flow measurements in bioreactors by NMR imaging. *Biotechnology* **8** (1990), 327–330.
47. Heath, C. A., Belfort, G., Hammer, B. E., Mirer, S. D., and Pimbley, J. M. MRI and modelling of flow in hollow-fibre bioreactors. *Am. Inst. Chem. Eng.* **36** (1990), 547–558.
48. Starling, E. H. On the absorption of fluids from the connective tissue spaces. *J. Physiol.* **19** (1896), 312–326.
49. Harper, J. M. *Extrusion of Foods.* CRC Press, Boca Raton, Fla., 1981.
50. Philips, R. J., Armstrong, R. C., Brown, R. A., and Graham, A. L. A constitutive equation for concentrated suspensions that accounts for shear-induced particle migration. *Phys. Fluids* **A4** (1992), 30.
51. Jenkins, J. T. and McTigue, D. F. Transport processes in concentrated suspensions: The role of particle fluctuations. In D. D. Joseph and Schaeffer (Eds.), *Two-Phase Flows and Waves.* Springer-Verlag, New York, 1990.
52. Altobelli, S. A., Givler, R. C., and Fukushima, E. *J. Rheol.* **35** (1991), 721–734.
53. Sinton, S. W., and Chow, A. W. NMR flow imaging of fluids and solid suspensions in Poiseuille flow. *J. Rheol.* **35** (1991), 735–771.

54. Abbott, J. R., Tetlow, N., Graham, A. L., Altobelli, S. A., Fukushima, E., Mondy, L. A., and Stephens, T. S. Experimental observations of particle migration in concentrated suspensions: Couette flow. *J. Rheol.* **35** (1991), 773.

55. Chow, A. W., Sinton, S. W., Iwamiya, J. H., and Stephens, T. S. Shear-induced particle migration in Couette and parallel plate viscometers: NMR imaging and stress measurements. *Phys. Fluids* **6** (1994), 2561–2576.

56. Leighton, D., and Acrivos, A. The shear-induced migration of particles in concentrated suspensions. *J. Fluid Mech.* **181** (1987), 415–439.

57. Chingas, G. C., Frydman, L., Barrall, G. A., and Harwood, J. S. In E. Blumich and W. Kuhn (Eds.), *Magnetic Resonance Microscopy*. VCH, Weinheim, Germany, 1992.

58. Rofe, C. G., Lambert, R. K., and Callaghan, P. T. NMR imaging of flow for a shear-thinning polymer in cylindrical Couette geometry. *J. Rheol.* **38** (1994), 875–887.

59. Bottomley, P. A., Rogers, H. H., and Foster, T. H. NMR imaging shows water distribution and transport in plant root systems in situ. *Proc. Natl. Acad. Sci. USA* **83** (1986), 87.

60. Omasa, K., Onoe, M., and Yamada, H. NMR imaging for measuring root system and soil water content. *Environ. Control Biol.* **23** (1985), 99.

61. Meulenkamp, L., Vergeldt, F., de Jager, P. A., van Dusschoten, D., and van As, H. Quantitative NMR microscopy, chlorophyll fluorescence and water uptake rate measurements to study water-stress tolerance in plants. *Conf. Abstr.: Towards Whole Plant Functional Imaging*, Amsterdam, 1996.

62. van As, H., Reinders, J. E. A., de Jager, P. A., and van de Sanden, P. A. C. M. In situ plant water balance studies using a portable NMR spectrometer. *J. Exp. Bot.* **45** (1994), 61–67.

63. Meininger, M., Landschutz, W., Jacob, P. M., Thurmer, W., Zimmermann, U., and Haase, A. Functional NMR imaging of tobacco plants at 7T. *Conf. Abstr.: Towards Whole Plant Functional Imaging*, Amsterdam, 1996.

64. Verscht, J., Kalusche, B., Kockenberger, W., Haase, A., and Komor, E. Sucrose concentrations in *Ricinis communis* hypocotyls under different supplying conditions measured by non-invasive NMR spectroscopic imaging. *Conf. Abstr.: Towards Whole Plant Functional Imaging*, Amsterdam, 1996.

65. Black, R. D., Early, T. A., Roemer, P. B., Mueller, O. M., Mogro-Campero, A., Turner, L. G., and Johnson, G. A. A high temperature superconducting receiver for NMR microscopy. *Science* **259** (1993), 793.

66. Jenner, C., Xia, Y., and Eccles, C. Circulation of water within wheat grain revealed by NMR microimaging. *Nature* **336** (1988), 399–402.

67. Williamson, B., Goodman, B. A., and Chudek, J. A. NMR microimaging of ripening red raspberry fruits. *New Phytol.* **120** (1992), 21–28.

68. Goodman, B. A., Williamson, B., and Chudek, J. A. NMR microimaging of raspberry fruit: Further studies on the origin of the image. *New Phytol.* **122** (1992), 529–535.

69. Williamson, B., Goodman, B. A., and Chudek, J. A. The structure of mature gooseberry fruits revealed non-invasively by NMR microscopic imaging. *Micron* **24** (1993), 377–383.

70. Goodman, B. A., Williamson, B., Simpson, E. J., Chudek, J. A., Hunter, G., and Prior, D. A. M. High field NMR microscopic imaging of cultivated strawberry fruit. *Magn. Reson. Imaging* **14** (1996), 187–196.

71. Maas, J., and Millard, M. NMR microimaging of strawberry fruit. *Acta Hortic.* **348** (1993), 375–377.

72. Pope, J., Jonas, D., and Walker, R. Applications of NMR microimaging the study of water, lipid and carbohydrate distribution in grape berries. *Protoplasma* **173** (1993), 177–186.

73. Goodman, B. A., Williamson, B., and Chudek, J. A. Identification of the distribution of sugars in grapes using chemical shift selective NMR microscopy. *Magn. Reson. Imaging* **11** (1993), 1039–1041.

74. MacFall, J. S., and Johnson, G. A. The architecture of plant vasculature and transport as seen with magnetic resonance microscopy. *Can. J. Bot.* **72** (1994), 1561–1573.

75. Goodman, B. A., Williamson, B., and Chudek, J. A. Non-invasive observation of the development of fungal infection in fruit. *Protoplasm* **166** (1992), 107–109.

76. Kockenberger, W., and Metzler, A. NMR microimaging as a non-invasive approach to measuring transport and metabolite concentrations within plants. *Bruker Rept.* **141** (1995), 21–23.

77. Brennan, R. Freezing events in flowers of *Ribes nigrum* L. revealed by NMR microimaging. *J. Hortic. Sci.* **68** (1993), 919–924.

78. Ishida, M., Ogàwa, H., and Kano, H. Diffusion of cell associated water in ripening barley seeds. *Magn. Reson. Imaging* **13** (1994), 745–751.

79. Watanabe, H., and Yoshida, M. Moisture diffusion in soya bean seed measured by NMR. In R. P. Singh and M. A. Wirakartakusumah (Eds.), *Advances in Food Engineering*. CRC Press, Boca Raton, Fla., 1992, pp. 79–83.

80. Ishida, M., Kobayashi, T., Koizumi, M., and Kano, H. Proton NMR imaging of tomato fruits. *Agr. Biol. Chem.* **53** (1989), 2363–2367.

81. Saltveit, M. E. Determining tomato fruit maturity with non-destructive in-vivo NMR imaging. *Postharvest Biol. Technol.* **1** (1991), 153–159.

82. Joyce, D. C., Hockings, P. D., Mazucco, R. A., Shorter, A. J., and Brereton, I. M. Heat treatment injury of mango fruit revealed by non-destructive MRI. *Postharvest Biol. Technol.* **3** (1993), 305–311.

83. Aguayo, J. B., Blackband, S. J., Schoeniger, J., Mattingly, M., and Hintermann, M. NMR imaging of a single cell. *Nature* **322** (1986), 190–191.

84. Harrison, L. G., Luck, S. D., Munasinghe, B. D., and Hall, L. D. MRI approaching microscopic scale: Maturation stages of *Acetabularia mediterranea* reproductive caps. *J. Cell Sci.* **91** (1988), 379–388.

85. Posse, S., and Aue, W. P. Spectroscopic imaging and gradient-echo microscopy on a single cell. *J. Magn. Reson.* **83** (1989), 620–625.

86. Jacobs, R. E., and Fraser, S. E. Magnetic resonance microscopy of embryonic cell lineages and movements. *Science* **263** (1994), 681–684.

87. McFarland, E. W., and Mortara, A. Three-dimensional NMR microscopy: Improving signal to noise with temperature and microcoils. *Magn. Reson. Imaging* **10** (1992), 279–288.

88. Schroeniger, J. S., Aiken, N., Hsu, E., and Blackband, S. J. Relaxation time and diffusion NMR microscopy of single neurons. *J. Magn. Reson.* **103** (1994), 261–273.

89. Bowtell, R. W., Peters, A., Sharp, J. C., Mansfield, P., et al. NMR microscopy of single neurons using spin-echo and line-narrowed 2-D FT imaging. *Magn. Reson. Med.* **33** (1995), 790–794.

90. Hsu, E. W., Aiken, N. R., Schoeniger, J. S., and Blackburn, S. J. Magnetization transfer microimaging of single neurons. *Society of Magnetic Resonance in Medicine,* 11th annual meeting, 1992, p. 974.

91. Aiken, N., Hsu, E. W., Blackburn, S. J., and Horsman, A. Maturation effects on the NMR characteristics in the microscopy of single neurons. *Society of Magnetic Resonance,* 2nd annual meeting, San Francisco, 1994, p. 711.

92. Rumpel, H., and Pope, J. M. The application of 3D chemical shift microscopy to non-invasive histochemistry. *Magn. Reson. Imaging* **10** (1992), 187–194.

93. Pope, J. Applications of chemical shift microscopy to non-invasive histochemistry of plant materials. In B. Blumich and W. Kuhn (Eds.), *Magnetic Resonance Microscopy.* VCH Press, Weinheim, Germany, 1992.

94. Gamble, G. R. Non-invasive determination of freezing effects in blueberry fruit by MRI. *J. Food Sci.* **59** (1994), 571–573.

95. USDA, Color classification requirements in United States standards for grades of fresh tomatoes. *USDA Visual Aid TM-L-1,* 1975.

96. Argiro, V. J. *Pixel* **1** (1990), 35.

97. McDonald, P. J. The use of NMR for on-line process control and quality assurance. In A. G. Gainker (Ed.), *Food Processing: Recent Developments.* Elsevier, Amsterdam, 1995.

98. Zion, B., McCarthy, M. J., and Chen, P. Real-time detection of pits in processed cherries by magnetic resonance projections. *Food Sci. Technol.* **27** (1994), 457–462.

99. Chen, P., McCarthy, M. J., Kim, S. M., and Zion, B. Development of high-speed NMR techniques for sensing fruit quality. *Am. Soc. Agr. Eng. Paper 95-3613,* 1995.

100. Nicholls, C. I., and De Los Santos, A. *Drying Technol.* **9** (1991), 849.

101. Snoddy, M. L. *Spectroscopy* **8** (1993), 41.

102. Bjorkstam, J., and Listerud, *J. Adv. Instrum.* **8** (1993), 41.

103. Fukushima, E., and Roeder, S. B. W. *Experimental Pulse NMR: A Nuts and Bolt Approach.* Addison-Wesley, Reading, Mass., 1981.

104. Donnat, J. P., Beauvallet, C., Foucat, L., Veyres, F., Martin, G., and Renou, J. P. On-line NMR determination of fat content in ground beef. *Abstr. 3rd Int. Conf. NMR in Foods,* Aveiro, Portugal, 1995.

105. MacFall, J. S., Kramer, P. J., and Johnson, G. A. *New Phytol.* **119** (1991), 551.

106. Bowtell, R., Mansfield, P., Sharp, J. C., Brown, G. D., McJury, M., and Glover, P. M. NMR microscopy at 500 MHz: Cellular resolution in biosystems. In B. Blumich and W. Kuhn (Eds.), *Magnetic Resonance Microscopy.* VCH Press, Weinheim, Germany, 1992, pp. 427–439.

107. Von Recklinghausen, I. R., de Jager, P. A., van der Meer, Y., van Dusschoten, D., Hoekstra, F. A., and van As, H. Water relations in the Resurrection plant, *Craterostigma plantagineum* Hochst. Poster at the workshop *Towards Whole Plant Functional Imaging,* Amsterdam, 1996.

108. Dumoulin, C. L. A method for chemical shift selective imaging. *Magn. Reson. Med.* **2** (1985), 583–585.

109. Rutledge, D. N., Rene, F., Hills, B. P., and Foucat, L. MRI studies of the freeze-drying kinetics of potato. *J. Food Process Eng.* **17** (1994), pp. 325–352.

110. Athanasios, I. L., and Bruttini, R. Freeze drying. In A. S. Mujumdar (Ed.), *Handbook of Industrial Drying.* Dekker Publishers, New York, 1995, pp. 304–343.

111. Wolff, E., and Gibert, H. Freeze drying. In *Encyclopedia of Food Science, Food Technology and Nutrition.* Academic Press, London, 1993, pp. 2035–2043.

112. Nestle, N. F. E. I., and Kimmich, R. NMR imaging of heavy metal absorption in alginate, immobilized cells and kombu algal biosorbents. *Biotechnol. Bioeng.* **51** (1996), 538–543.

113. Potter, K., Carpenter, A., and Hall, L. D. Mapping of the spatial variation in alginate concentration in calcium alginate gels by MRI. *Carbohydr. Res.* **246** (1993), 43–49.

114. Potter, K., Balcom, B. J., Carpenter, A., and Hall, L. D. The gelation of sodium alginate with calcium ions studied by MRI. *Carbohydr. Res.* **257** (1994), 117–126.

115. Velings, N. M., and Mestdagh, M. M. Physico-chemical properties of alginate gel beads. *Polymer Gels Networks* **3** (1995), 311–330.

116. Kim, H.-S. A kinetic study on calcium alginate bead formation. *Korean J. Chem. Eng.* **7** (1990), 1–6.

117. Gibbs, S. J., and Hall, L. D. What roles are there for MRI in process tomography? *Meas. Sci. Technol.* **7** (1996), 827–837.

118. Duce, S. L., Carpenter, T. A., and Hall, L. D. NMR imaging of chocolate confectionery and the spatial detection of polymorphic states of cocoa butter in chocolate. *Food Sci. Technol.* **23** (1990), 545–549.

119. Lambelet, P. Comparison of NMR and DSC methods for determining solid content of fats. *Food Sci. Technol.* **16** (1983), 200–202.

120. Lambelet, P., Desarzens, C., and Raemy, A. Comparison of NMR and DSC methods for determining the solid content of fats: III. Proton transverse relaxation times in cocoa butter and edible oils. *Food Sci. Technol.* **19** (1986), 77–81.

121. Gribnau, M. C. M. Determination of solid/liquid ratios of fats and oils by low-resolution pulsed NMR. *Trends Food Sci. Technol.* **3** (1992), 186–190.

122. Simoneau, C., McCarthy, M. J., Reid, D. S., and German, J. B. Measurement of fat crystallization using NMR imaging and spectroscopy. *Trends Food Sci. Technol.* **3** (1992), 208–211.

123. Simoneau, C., McCarthy, M. J., Kauten, R. J., and German, J. B. Crystallization dynamics in model emulsions from MRI. *J. Am. Oil Chem. Soc.* **68** (1991), 481–487.

124. Simoneau, C., McCarthy, M. J., Reid, D. S., and German, J. B. Influence of triglyceride composition on crystallization kinetics of model emulsions. *J. Food Eng.* **19** (1993), 365–387.

125. Huyghebaert, A., and Hendrickx, H. Polymorphism of cocoa butter, shown by differential scanning calorimetry. *Food Sci. Technol.* **4** (1971), 59–63.

126. Kauten, R. J., Maneval, J. E., and McCarthy, M. J. Fast determination of spatially localized volume fractions in emulsions. *J. Food Sci.* **56** (1991), 799–801, 847.

127. Ozilgen, S., Simoneau, C., German, J. B., McCarthy, M. J., and Reid, D. S. Crystallization kinetics of emulsified triglycerides. *J. Sci. Food Agr.* **61** (1993), 101–108.

128. German, J. B., and McCarthy, M. J. Stability of aqueous foams: Analysis using MRI. *J. Agr. Food Chem.* **37** (1989), 1321–1324.

129. Karel, M., Buera, M. P., and Roos, Y. Effect of glass transition on processing and storage. In J. M. V. Blanshard and P. J. Lillford (Eds.), *The Glassy State in Foods.* Nottingham University Press, Loughborough, Leicestershire, U.K., 1993.

130. Slade, L., and Levine, H. Beyond water activity: Recent advances based on an alternative approach to the assessment of food quality and safety. *Crit. Rev. Food Sci. Nutr.* **30** (1991), 115–360.

131. Williams, W., Landel, R. F., and Ferry, J. D. The temperature dependence of relaxation mechanisms in amorphous polymers and other glass forming liquids. *J. Am. Chem. Soc.* **77** (1955), 3701–3707.

132. Howell, N., Shavila, Y., Grootveld, M., and Williams, S. High-resolution NMR and MRI studies on fresh and frozen cod and haddock. *J. Sci. Food Agr.* **72** (1996), 49–56.

133. Ruan, R., Almaer, S., Huang, V. T., Perkins, P., Chen, P., and Fulcher, R. G. Relationship between firming and water mobility in starch-based food systems during storage. *Cereal Chem.* **73** (1996), 328–332.

134. Belton, P. S., and Hills, B. P. The effects of diffusive exchange in heterogeneous systems on NMR lineshapes and relaxation processes. *Molec. Phys.* **61** (1987), 999–1018.

135. Brownstein, K. R., and Tarr, C. E. Importance of classical diffusion in NMR studies of water in biological cells. *Phys. Rev.* **19** (1979), 2446–2453.

136. Carver, J. P., and Richards, R. E. A general 2-site solution for the chemical exchange produced dependence of T2 upon the Carr–Purcell pulse sequence. *J. Magn. Reson.* **6** (1972), 89–105.

137. Davis, S., and Packer, K. J. Pore-size distribution from NMR spin-lattice relaxation measurements of fluid-saturated porous solids. *J. Appl. Phys.* **67** (1990), 3163–3170.

138. Goldman, M., and Shen, L. Spin-spin relaxation in LaF3. *Phys. Rev.* **144** (1966), 321–31.

139. Hills, B. P. NMR relaxation studies of proton exchange in methanol–water mixtures. *J. Chem. Soc. Faraday Trans.* **86** (1990), 481–487.

140. Hills, B. P. The proton exchange cross-relaxation model of water relaxation in biopolymer systems. *Molec. Phys.* **76** (1992), 489–508.

141. Ohtsuka, A., Watanabe, T., and Suzuki, T. Gel structure and water diffusion phenomena in starch gels studied by pulsed field gradient stimulated echo NMR. *Carbohydr. Polymers* **25** (1994), 95–100.

142. Watanabe, T., Ohtsuka, A., Murase, N., Barth, P., and Gersonde, K. NMR studies of water and polyer diffusion in dextran gels. Influence of potassium ions on microstructure formation and gelation mechanism. *Magn. Reson. Med.* **35** (1996), 697–705.

143. Ohtsuka, A., and Watanabe, T. The network structure of gellan gum hydrogels based on the structural parameters by the analysis of the restricted diffusion of water. *Carbohydr. Polymers* **30** (1996), 135–140.

144. Kimmich, R., Klammler, F., Skirda, V. D., Serebrennikova, I. A., and Fatkulin, N. Geometric restrictions of water diffusion in aqueous protein systems: A study using NMR field gradient techniques. *Appl. Magn. Reson.* **4** (1993), 425–440.

145. Watanabe, H., and Fukuoka, M. Measurement of moisture diffusion in foods using pulsed field gradient NMR. *Trends Food Sci. Technol.* **3** (1992), 211–215.

146. Packer, K. J., and Rees, C. Pulsed NMR studies of restricted diffusion: 1. Droplet size distributions in emulsions. *J. Colloid Interface Sci.* **10** (1972), 206–218.

147. Van den Enden, J. C., Waddington, D., van Aalst, H., van Kralingen, C. G., and Packer, K. J. Rapid determination of water droplet size distributions by PFG-NMR. *J. Colloid Interface Sci.* **140** (1990), 105–113.

148. Callaghan, P. T., Jolley, K. W., and Humphrey, R. S. Diffusion of fat and water in cheese as studied by pulsed field gradient NMR. *J. Colloid Interface Sci.* **93** (1983), 521–529.

149. Price, W. S. Gradient NMR. *Ann. Rep. NMR spectros.* **32** (1996), 53–142.

150. Cheng, K. H. Quantitation of non-Einstein diffusion behaviour of water in biological tissues by proton MR diffusion imaging: Synthetic image calculations. *Magn. Reson. Imaging* **11** (1993), 569–583.

151. Metzler, R., Glockle, W. G., and Nonnenmacher, T. F. Fractional model equation for anomalous diffusion. *Physica* **A211** (1994), 13–24.

152. Karger, J., Pfeifer, H., and Heink, W. Principles and application of self-diffusion measurements by NMR. *Adv. Magn. Reson.* **12** (1988), 1–89.

153. Stejskal, E. O., and Tanner, J. E. Spin diffusion measurements: Spin echoes in the presence of a time-dependent field gradient. *J. Chem. Phys.* **42** (1965), 288–292.

154. Tanner, J. E., and Stejskal, E. O. Restricted self-diffusion of protons in colloidal systems by the pulsed-gradient, spin-echo method. *J. Chem. Phys.* **49** (1968), 1768–1777.

155. Wang, J. H. Theory of the self-diffusion of water in protein solutions: A new method for studying the hydration and shape of protein molecules. *J. Am. Chem. Soc.* **76** (1954), 4755–4765.

156. Karlicek, R. F., and Lowe, I. J. A modified pulsed field gradient technique for measuring diffusion in the presence of large background gradients. *J. Magn. Reson.* **37** (1980), 75–91.

157. Callaghan, P. T., and Jolley, K. W. Diffusion of water in the endosperm tissue of wheat grains as studied by pulsed field gradient NMR. *Biophys. J.* **28** (1979), 133–141.

158. Tanner, J. E. Use of the stimulated echo in NMR diffusion studies. *J. Chem. Phys.* **52** (1970), 2523–2526.

159. Ablett, S., Darke, A. H., Izzard, M. J., and Lillford, P. J. Studies of the glass transition in malto-oligomers. In J. M. V. Blanshard and P. J. Lillford (Eds.), *The Glassy State in Foods,* Nottingham University Press, Loughborough, Leicestershire, U. K., 1993, pp. 189–206.

160. Karger, J. Der Einfluss der Zeibereichdiffusion auf die Spinechodampfung unter Berucksichtigung der Relaxation bei Messungen mit der Methode der gepulsten Feldgradienten. *Ann. Phys.* **7** (1971), 107–109.

161. Belton, P. S., Colquhuon, I. J., and Hills, B. P. Applications of NMR to food science. *Ann. Rept. NMR Spectros.* **26** (1993), 1–53.

162. Scher, L. I., Fazio, P., and Hsieh, M. W. *Am. Inst. Chem. Eng. Symp. Ser.* **297** (1993), 1–32.

163. Song, H., and Litchfield, J. B. *Cereal Chem.* **67** (1990), 580–584.

164. Hulbert, G. J., Litchfield, J. B., and Schmidt, S. J. Temperature mapping in carrot using T1 weighted MRI. *J. Food Sci.* **60** (1995), 780–785.

165. Sun, X., Schmidt, S. J., and Litchfield, J. B. Temperature mapping in potato using half-Fourier transform MRI of diffusion. *J. Food Process Eng.* **17** (1994), 423–437.

166. Sun, X., Litchfield, J. B., and Schmidt, S. J. Temperature mapping in a model food gel using MRI. *J. Food Sci.* **58** (1993), 168–172.

167. Schwarzbauer, C., Zange, J., Adolf, H., Deichmann, R., Noth, U., and Haase, A. Fast measurement of temperature distributions by rapid T1 mapping. *J. Magn. Reson.* **B106** (1995), 178–180.

168. De Poorter, J. Non-invasive MRI thermometry with the proton resonance frequency method: study of susceptibility effects. *Magn. Reson. Med.* **34** (1995), 359–367.

169. De Poorter, J., De Wagner, C., De Deene, Y., Thomsen, C., Stahlberg, F., and Achten, E. Non-invasive MRI thermometry with the proton resonance frequency method: In vivo results in human muscle. *Magn. Reson. Med.* **33** (1995), 74–81.

170. Litchfield, J. B. Chemical shift temperature mapping. *Conf. Abstr.: 3rd Intern. Conf. NMR in Food,* Nantes, 1997.

171. McCarthy, M. J., and Kauten, R. J. MRI applications in food research. *Trends Food Sci. Technol.* **1** (1990), 134–139.

172. Duce, S. L., Amin, A., Horsfield, M. A., Tyszka, M., and Hall, L. D. NMR imaging of dairy products in two and three dimensions. *Int. Dairy J.* **5** (1995), 311–319.

173. Chen, M. J., McCarthy, M. J., and Kauten, R. *Trans. Am. Soc. Agr. Eng.* **32** (1989), 1747–1754.

174. Duce, S. L., Carpenter, T. A., and Hall, L. D. 31st Exp. NMR Spectros. *Conf. Proc.,* 1990, p. 193.

175. Wang, C. Y., Wang, P. C., and Faust, M. *Sci. Hortic.* **35** (1988), 227–234.

176, Potter, K., Carpenter, T. A., and Hall, L. D. Magn. Reson. *Imaging* **12** (1994), 309–311.

177. Liapis, A., and Bruttini, R. Freeze drying. In A. S. Mujumdar (Ed.), *Handbook of Industrial Drying.* 1995, pp. 304–343.

178. Crank, J. *Mathematics of Diffusion.* Oxford University Press, Oxford, 1983.

179. McCarthy, M. J., Perez, E., and Ozilgen, M. Model for transient moisture profiles of a drying apple slab using data obtained with MRI. *Biotechnol. Prog.* **7** (1991), 540–543.

180. Ruan, R., Schmidt, S. J., Schmidt, A. R., and Litchfield, J. B. Nondestructive measurement of transient moisture profiles and the moisture diffusion coefficient in a potato during drying and absorption by NMR imaging. *J. Food Process Eng.* **14** (1991), 297–313.

181. Schrader, G. W., and Litchfield, J. B. Moisture profiles in a model food gel during drying: Measurement using MRI and evaluation of the Fickian model. *Drying Technol.* **10** (1992), 295–332.

182. Song, H., and Litchfield, J. B. NMR imaging of transient three-dimensional moisture distribution in an ear of corn during drying. *Cereal Chem.* **67** (1990), 580–584.

183. Chen, P., McCarthy, M. J., and Kauten, R. NMR for internal quality evaluation of fruits and vegetables. *Trans. Am. Soc. Agr. Eng.* **32** (1989), 1747–1753.

184. German, J. B., and McCarthy, M. J. Stability of aqueous foams: Analysis using MRI. *J. Agr. Food Chem.* **37** (1989), 1321–1324.

185. Song, H., and Litchfield, J. B. Measuring stress cracks in corn by MRI. *Am. Soc. Agr. Eng. Paper 91-6052,* 1991.

186. Heil, J. R., McCarthy, M. J., and Ozilgen, M. MRI and modelling of water up-take into dry beans. *Food Sci. Technol.* **25** (1992), 280–285.

187. Sahimi, M. *Applications of Percolation Theory.* Taylor & Francis, London, 1994.

188. Axel, L., Shimakawa, A., and McFall, J. *Magn. Reson. Imaging* **4** (1986), 199.

189. Gibbs, S. J., and Hall, L. D. What roles are there for MRI in process tomography? *Meas. Sci. Technol.* **7** (1996), 827–837.

190. Blanshard, J. M. V., and Lillford, P. J. *The Glassy State in Foods.* Nottingham University Press, Loughborough, Leicestershire, U. K., 1993.

191. Kleinberg, R. L., Sezginer, A., Griffin, D. D., and Fukuhara, M. Novel NMR apparatus for investigating an external sample. *J. Magn. Reson.* **97** (1992), 466–485.

192. Nelson, F. A., Reilly, C. A., and Savage, W. E. *Ind. Eng. Chem.* **52** (1960), 487.

193. Tellier, P. C., Trierweiler, J., Lejot, J., and Martin, G. J. Etude de la réponse quantitative d'une sonde RMN haute résolution a écoulement libre. *Analusis* **18** (1990), 67–72.

194. Zion, B., Kim, S. M., McCarthy, M. J., and Chen, P. Detection of pits in olives under motion by NMR. *J. Sci. Food Agr.* in press (1997).

195. Kockenberger, W. Long distance transport in plants measured by NMR microscopy. *Conf. Abstr. Towards Whole Plant Functional Imaging,* Amsterdam, 1996.

196. Hills, B. P., Wright, K. M., and Belton, P. S. The effects of restricted diffusion in NMR microscopy. *Magn. Reson. Imaging* **8** (1990), 755–765.

197. Kockenbrod, E., Haase, A., Benkert, H., Schneider, H., and Zimmermann, U. Quantitative NMR microscopy on intact plants. *Magn. Reson. Imaging* **13** (1995), 447–455.

198. Meerwall, E., and Ferguson, R. D. Interpreting PGSE diffusion experiments with permeable membranes. *J. Chem. Phys.* **74** (1981), 6956–6959.

199. Shapley, A. G. F., Hyde, T. M., Gladden, L. F., and Fryer, P. J. NMR imaging of diffusion and reaction in wheat grains. *J. Magn. Reson. Anal.* **2** (1996).

200. Himmelsbach, D. S. Proton NMR imaging of the hydration of wheat and rice grains. *J. Magn. Reson. Anal.* **2** (1996), 163–164.

201. Ishida, N Ogawa, H., Koizumi, M., and Kano, H. Ontogenic changes in water status and accumulated soluble compounds in growing cherry fruits by NMR imaging. *J. Magn. Reson. Anal.* **2** (1996), 168–169.

202. Glover, P. M., Bowtell, R. W., Brown, G. D., and Mansfield, P. A microscope slide probe for high resolution imaging at 11.7 tesla. *Magn. Reson. Med.* **31** (1994), 423–428.

203. Bowtell, R., Mansfield, P., Sharp, J. C., Brown, G. D., McJury, M., and Glover, P. M. NMR microscopy at 500MHz: Cell resolution in biosystems. In B. Blumich and W. Kuhn (Eds.), *Magnetic Resonance Microscopy.* VCH Press, Weinheim, Germany, 1992, pp. 427–439.

204. Hills, B. P., and Belton, P. S. NMR studies of membrane transport. *Ann. Rep. NMR Spectros.* **21** (1989), 99–159.

205. Hills, B. P., Wright, K. M., and Belton, P. S. NMR studies of water proton relaxation in Sephadex bead suspensions. *Molec. Phys.* **67** (1989), 193–208.

206. Hills, B. P., Takacs, S. F., and Belton, P. S. The effects of proteins on the proton NMR transverse relaxation times of water: I. Native BSA. *Molec. Phys.* **67** (1989), 903–918.

207. Hills, B. P., Takacs, S. F., and Belton, P. S. The effects of proteins on the proton NMR transverse relaxation times of water: II. Protein aggregation. *Molec. Phys.* **67** (1989), 919–937.

208. Hills, B. P., Wright, K. M., and Belton, P. S. Proton NMR studies of chemical and diffusive exchange in carbohydrate systems. *Molec. Phys.* **67** (1989), 1309–1326.

209. Hills, B. P. Multinuclear NMR studies of water in solutions of simple carbohydrates: I. Proton and deuterium relaxation. *Molec. Phys.* **72** (1991), 1099–1121.

210. Belton, P. S., Ring, S. G., Botham, R. L., and Hills, B. P. Mulinuclear NMR studies of water in solutions of simple carbohydrates: II. Oxygen-17 relaxation. *Molec. Phys.* **72** (1991), 1099.

211. Hills, B. P., Cano, C., and Belton, P. S. Proton NMR relaxation studies of aqueous polysaccharide systems. *Macromolecules* **24** (1991), 2944–2950.

212. Hills, B. P., and Duce, S. L. The influence of chemical and diffusive exchange on water proton transverse relaxation in plant tissue. *Magn. Reson. Imaging* **8** (1990), 321–331.

213. Tanner, S. F., Hills, B. P., and Parker, R. A study of the interaction of sorbed water with starch using proton NMR spectroscopy. *J. Chem. Soc. Faraday Trans.* **87** (1991), 2613–2621.

214. Hills, B. P. The proton exchange-cross relaxation model of water relaxation in biopolymer systems: The sol and gel states of gelatine. *Molec. Phys.* **76** (1992), 509–523.

215. Duce, S. L., Carpenter, T. A., Hall, L. D., and Hills, B. P. An investigation of the origins of contrast in spin-echo images of plant tissue. *Magn. Reson. Imaging* **10** (1992), 289–297.

216. Hills, B. P., and Snaar, J. E. M. Dynamic q-space microscopy of cellular tissue. *Molec. Phys.* **76** (1992), 979–994.

217. Hills, B. P., Smart, S. C., Quantin, V. M., and Belton, P. S. NMR microimaging studies of water diffusivity in saturated microsporous systems. *Magn. Reson. Imaging* **11** (1993), 1175–1184.

218. Hills, B. P., Belton, P. S., and Quantin, V. M. Water proton relaxation in heterogeneous systems: I. Saturated, randomly packed suspensions of impenetrable particles. *Molec. Phys.* **78** (1993), 893–908.

219. Hills, B. P., Belton, P. S., and Quantin, V. M. Water proton relaxation in heterogeneous systems: II. Unsaturated suspensions. *Molec. Phys.* **79** (1993), 77–93.

220. Hills, B. P., Wright, K. M., Wright, J., and Hall, L. D. An MRI study of drying in granular beds of non-porous particles. *Magn. Reson. Imaging* **12** (1994), 1053–1063.

221. Hills, B. P., and Babonneau, F. A quantitative study of water proton relaxation in packed beds of porous particles with varying water content. *Magn. Reson. Imaging* **12** (1994), 909–922.

222. Hills, B. P., and LeFloch, G. NMR studies of non-freezing water in randomly packed beds of porous particles. *Molec. Phys.* **82** (1994), 751–763.

223. Hills, B. P., and LeFloch, G. NMR studies of non-freezing water in cellular plant tissue. *Food Chem.* **51** (1994), 331–336.

224. Hills, B. P., and Babonneau, F. Quantitative radial imaging of porous particle beds with varying water content. *Magn. Reson. Imaging* **12** (1994), 1065–1074.

225. Hills, B. P., and Snaar, J. E. M. Water proton relaxation studies of pore microstructure in monodisperse glass bead beds. *Molec. Phys.* **84** (1995), 141–157.

226. Snaar, J. E. M., and Hills, B. P. Water proton relaxation studies of air–water distributions in beds of randomly packed monodisperse glass microspheres. *Molec. Phys.* **86** (1995), 1137–1156.

227. Hills, B. P., Wright, K. M., and Snaar, J. E. M. Dynamic NMR q-space studies of microstructure with the multigrade CPMG sequence. *Magn. Reson. Imaging* **14** (1996), 305–318.

228. Hills, B. P., Babonneau, F., Quantin, V. M., Gaudet, F., and Belton, P. S. Radial NMR microimaging studies of the rehydration of extruded pasta. *J. Food Eng.* **27** (1996), 71–86.

229. Hills, B. P., and Pardoe, K. Proton and deuterium NMR studies of the glass transition in a 10% water–maltose solution. *J. Molec. Liquids* **63** (1995), 229–237.

230. Hills, B. P., Manning, C. E., and Ridge, Y. A new theory of water activity in heterogeneous systems. *J. Chem Soc. Faraday Trans.* **92** (1996), 979–983.

231. Hills, B. P., Manning, C. E., Ridge, Y., and Brocklehurst, T. NMR water relaxation, water activity and bacterial survival in porous media. *J. Sci. Food Agr.* **71** (1996), 185–194.

232. Hills, B. P., Manning, C. E., Ridge, Y., and Brocklehurst, T. Water availability and the survival of *Salmonella typhimurium* in porous media. *Int. J. Food Microbiol.* **36** (1997), 187–198.

233. Hills, B. P., Wright, K. M., and Snaar, J. E. M. Extraordinary susceptibility effects in high field NMR relaxation and diffusion studies of porous media. *J. Magn. Reson. Anal.* **2** (1996), 305–310.

234. Torrey, H. C. Bloch equations with diffusive terms. *Phys. Rev.* **104** (1956), 563–565.

235. Provenchar, S. W. A constrained regularization method for inverting data represented by linear algebraic or integral equations. *Comput. Phys. Commun.* **27** (1982), 213.

236. Barke, G. C., and Mehta, A. *Phys. Rev.* **A45** (1992), 3435.

237. Edzes, H. T., and Samulski, E. D. The measurement of cross-relaxation effects in the proton NMR spin-lattice relaxation of water in biological systems: Hydrated collagen and muscle. *J. Magn. Reson.* **31** (1978), 207–229.

238. Grad, J., and Bryant, R. G. Nuclear magnetic cross-relaxation spectroscopy. *J. Magn. Reson.* **90** (1990), 1–8.

239. Wolff, S. D., and Balaban, R. S. Magnetization transfer contrast and tissue water proton relaxation in vivo. *Magn. Reson. Med.* **10** (1989), 135–144.

240. Eng, J., Ceckler, T. L., and Balaban, R. S. Quantitative proton magnetization transfer imaging in vivo. *Magn. Reson. Imaging* **17** (1991), 304–314.

241. Wolff, S. D., Eng, R. S., and Balaban, R. S. Magnetization transfer contrast: Method for improving contrast in gradient recalled echo images. *Radiology* **179** (1991), 133–137.

242. Pike, G. B., Glover, G. H., Hu, B. S., and Enzmann, D. R. Pulsed magnetization transfer spin-echo MR imaging. *Magn. Reson. Imaging* **3** (1993), 531–539.

243. Yeung, H. N., and Aisen, A. M. Magnetization transfer contrast with periodic pulsed saturation. *Radiology* **183** (1992), 209–214.

244. Balaban, R. S., and Ceckler, T. L. Magnetization transfer contrast in MRI. *Magn. Reson. Q.* **8** (1992), 116–137.

245. Wolff, S. D., and Balaban, R. S. Magnetization transfer imaging: practical aspects and clinical applications. *Radiology* **192** (1994), 593–599.

246. Henkelman, R. M., Huang, X., Xiang, G. J., Stanisz, S. D., and Swanson, S. D. Quantitative interpretation of magnetization transfer. *Magn. Reson. Med.* **29** (1993), 759–766.

247. Pike, G. B. Pulsed magnetization transfer contrast in gradient echo imaging: A two pool analytic description of signal response. *Magn. Reson. Imaging* **36** (1996), 95–103.

248. Brown, R. D., and Koenig, S. H. T1-rho low-field T1 of tissue water protons arise from magnetization transfer to macromolecules solid-state broadened lines. *Magn. Reson. Imaging* **28** (1992), 145–152.

249. Koenig, S. H., Brown, R. D., Adams, D., Emerson, D., and Harrison, C. G. Magnetic field dependence of T1 of protons in tissue. *Invest. Radiol.* **19** (1984), 76–81.

250. Mikkelsen, A., and Elgsaeter, A. Density distribution of calcium alginate gels: A numerical study. *Biopolymers* **36** (1995), 17–41.

251. Skjak-Braek, G., Grasdalen, H., Dragnet, K. I., and Smidsrod, O. Inhomogeneous calcium alginate beads. In V. Crescenzi, I. C. M. Dea, S. Paoletti, S. S. Stivala, and I. W. Sutherlands (Eds.), *Biomedical and Biotechnological Advances in Industrial Polysaccharides*. Gordon and Breach, New York, 1988, pp. 345–363.

252. Hills, B. P., Wright, K. M., and Belton, P. S. The effects of restricted diffusion in NMR microscopy. *Magn. Reson. Imaging* **8** (1990), 755–765.

253. Hills, B. P., and Belton, P. S. NMR studies of membrane transport. *Ann. Rep. NMR Spectros.* **21** (1989), 99–159.

254. Cotts, R. M., Hoch, M. J. R., Sun, T., and Markert, J. T. Pulsed field gradient stimulated echo methods for improved NMR diffusion measurements in heterogeneous systems. *J. Magn. Reson.* **83** (1989), 252–266.

255. Joseph, P. M. A spin-echo chemical shift MR imaging technique. *J. Comp. Assisted Tomogr.* **9** (1985), 651–658.

256. Stepisnik, J. Measuring and imaging of flow by NMR. *Prog. NMR Spectros.* **17** (1985), 187–209.

257. Snaar, J. E. M., and van As, H. NMR self diffusion measurements in a bounded system with loss of magnetization at the walls. *J. Magn. Reson. Anal.* **A102** (1993), 318–326.

258. Cory, D. G., and Garroway, A. N. Measurement of translational displacement probabilities by NMR: An indicator of compartmentation. *Magn. Reson. Med.* **14** (1990), 435–444.

259. McCall, K. R., Johnson, D. L., and Guyer, R. A. Magnetization evolution in connected pore systems. *Phys. Rev.* **B44** (1991), 7344–7355.

260. Callaghan, P. T., Coy, A., Halpin, T. P. J., MacGowan, D., Packer, K. J., and Zelaya, F. O. Diffusion in porous systems and the influence of pore morphology in pulsed gradient spin-echo NMR studies. *J. Chem. Phys.* **97** (1992), 651–662.

261. Latour, L. L., Li, L., and Sotak, C. H. Improved PFG stimulated echo method for the measurement of diffusion in inhomogeneous fields. *J. Magn. Reson.* **B101** (1993), 72–77.

262. Mitra, P. P., Sen, P. N., Schwartz, L. M., and LeDoussal, P. Diffusion propagator as a probe of the structure of porous media. *Phys. Rev. Lett.* **68** (1992), 3555–3558.

263. Mitra, P. P., and Sen, P. N. Effects of microgeometry and surface relaxation on NMR pulsed field gradient experiments: Simple pore geometries. *Phys. Rev.* **B45** (1992), 143–156.

264. Latour, L. L., Mitra, P. P., Kleinberg, R. L., and Sotak, C. H. Time-dependent diffusion coefficient of fluids in porous media as a probe of surface-to-volume ratio. *J. Magn. Reson.* **A101** (1993), 342–346.

265. Mitra, P. P., Sen, P. N., and Schwartz, L. M. Short-time behaviour of the diffusion coefficient as a geometrical probe of porous media. *Phys. Rev.* **B47** (1993), 8565–8574.

266. Callighan, P. T. Pulsed-gradient spin-echo NMR for planar, cylindrical and spherical pores under conditions of wall relaxation. *J. Magn. Reson.* **A113** (1995), 53–59.

267. Yu, I. A method of analysing restricted diffusion from spin-echo measurements. *J. Magn. Reson.* **A104** (1993), 209–211.

268. Kleinberg, R. L., and Horsfield, M. A. Transverse relaxation processes in porous sedimentary rock. *J. Magn. Reson.* **88** (1990), 9–19.

269. Glasel, J. A., and Lee, K. H. *J. Am. Chem. Soc.* **96** (1974), 970.

270. Robertson, B. *Phys. Rev.* **151** (1966), 273.

271. Neuman, C. H. *J. Chem. Phys.* **60** (1974), 4508.

272. Hills, B. P., Manning, C. E., Ridge, Y., and Brocklehurst, T. NMR water relaxation, water activity and bacterial survival in porous media. *J. Sci. Food Agr.* **71** (1996), 185–194.

273. Hills, B. P., Manning, C. E., Ridge, Y., and Brocklehurst, T. E. Water availability and the survival of *Salmonella typhimurium* in porous systems. *Int. J. Food Microbiol.* **36** (1997), 187–198.

274. Brunne, R. M., Liepinsh, E., Otting, G., Wuthrich, K., and van Gunsteren, W. F. Hydration of proteins, a comparison of experimental residence times of water molecules solvating the bovine trypsin inhibitor with theoretical model calculations. *J. Mol. Biol.* **231** (1993), 1040–1048.

275. Chirife, J., and del pilar Buera, M. Water activity, glass transition and microbial stability in concentrated/semi-moist food systems. *J. Food Chem.* **59** (1994), 921–927.

276. D'Orazio, F., Bhattacharja, S., Halperin, W. P., and Gerhardt, R. Fluid transport in partially filled porous sol-gel silica glass. *Phys. Rev.* **B42** (1997), 6503–6508.

277. Franks, F., and Grigera, J. R. *Water Sci. Rev.* **5** (1990), 187.

278. Franks, F. Water activity: a credible measure of food safety and quality? *Trends Food Sci. Technol.* **2** (1991), 68.

279. Bruauer, S., Emmett, P. H., and Teller, E. *J. Am. Chem. Soc.* **60** (1938), 309.

280. Ishihara, A. *Statistical Physics*. Academic Press, New York, 1971.

281. Hills, B. P., Wright, K. M., and Snaar, J. E. M. Dynamic NMR q-space studies of microstructure with the multigrade CPMG sequence. *Magn. Reson. Imaging* **14** (1996), 305–318.

282. Kopf, M., Corinth, C., Haferkamp, O., and Nonnenmacher, T. F. Anomalous diffusion of water in biological tissues. *Biophys. J.* **70** (1996), 2950–2958.

283. Lambelet, P., Berrocol, R., and Ducret, F. Denaturation of proteins. *J. Dairy Res.* **56** (1989), 211.

284. Lewis, G. P., Derbyshire, W., Ablett, S., Lillford, P. J., and Norton, I. T. Investigation of the NMR relaxation of aqueous gels of the carrageenan family and of the effect of ionic content and character. *Carbohydr. Res.* **160** (1987), 397–410.

285. Rommel, E., and Kimmich, R. T1-rho dispersion imaging and volume-selective T1-rho dispersion weighted NMR spectroscopy. *Magn. Reson. Med.* **12** (1989), 390–399.

286. Belton, P. S., Duce, S. L., and Tatham, A. S. Proton NMR relaxation studies of dry gluten. *J. Cereal Sci.* **7** (1988), 113–122.

287. Belton, P. S., Colquhuon, I. J., Field, J. M., Grant, A., Shewry, P. R., and Tatham, A. S. Proton and deuterium NMR relaxation studies of a high molecular weight subunit of wheat glutenin and comparison with elastin. *J. Cereal Sci.* **19** (1994), 115–121.

288. Belton, P. S., and Gil, A. M. Proton NMR lineshapes and transverse relaxation in a hydrated barley protein. *J. Chem. Soc. Faraday Trans.* **89** (1993), 4203–4206.

289. Farhat, I. A. Molecular mobility and interactions in biopolymer–sugar–water systems. Ph.D. thesis, University of Nottingham, Sutton Bonnington Campus, 1996.

290. ten Brinke, G., Karasz, Z., and Ellis, T. S. *Macromolecules* **16** (1983), 244.

291. Williams, M. L., Landel, R. F., and Ferry, J. D. *J. Am. Chem. Soc.* **77** (1955), 3701.

292. Kenwright, A. M., and Packer, K. J. *Chem. Phys. Lett.* **173** (1990), 471.

293. Wu, X., Bryant, R. G., and Eads, T. M., *J. Agr. Food Chem.* **40** (1992), 449.

294. Heil, J. R., Ozilgen, M., and McCarthy, M. J. MRI analysis of water migration and void formation in baking biscuits. *Am. Inst. Chem. Eng. Symp. Ser.* **297** (1993), 39–45.

295. Duce, S. L., Ablett, S., Darke, A. H., Pickles, J., Hart, C., and Hall, L. D. NMR imaging and spectroscopic studies of Wheat Flake Biscuits during baking. *Anal. Tech. Instrumentation* **72** (1995), 105–108.

296. Farkas, B. E., Singh, R. P., and McCarthy, M. J. Measurement of oil/water interface in foods during frying. In R. P. Singh and A. Wirakartakamasuma (Eds.), *Advances in Food Engineering*. CRC Press, Boca Raton, FL, 1992.

297. Melton, S. L., Trigiano, M. K., Penfield, M. P., and Yang, R. Potato chips fried in canola and/or cottonseed oil maintain high quality. *J. Food Sci.* **58** (1993), 1079–1083.

298. Guiheneuf, T. M., Duce, S. L., Gibbs, S. J., and Hall, L. D. The use of manganese ions in interdiffusion studies of cured meat. *Int. J. Food Sci. Technol.* **30** (1995), 447–459.

299. Guiheneuf, T. M., Gibbs, S., Fischer, A., and Hall, L. D. Measurement of the diffusion coefficient of manganese ions in cured pork by one-dimensional proton MRI. *Int. J. Food Sci. Technol.* **31** (1996), 195–203.

300. Renou, J. P., Benderbous, S., Bielicki, B., Foucat, L., and Donnat, J. P. Sodium MRI: Distribution of brine in muscle. *Magn. Reson. Imaging* **12** (1994), 131–137.

301. Tingle, J. M., Pope, J. M., Baumgartner, P. A., and Sarafis, V. MRI of fat and muscle distribution in meat. *Int. J. Food Sci. Technol.* **30** (1995), 437–446.

302. Kim, S.-M., McCarthy, M. J., and Chen, P. Determination of structure of eyes and texture of Swiss-type cheeses using MRI analysis. *J. Magn. Reson. Anal.* **1** (1996), 281–289.

303. Stapley, A. G. F., Goncalves, J. A. S., Hollewand, M. P., Gladden, L. F., and Fryer, P. J. An NMR pulsed field gradient study of the electrical and conventional heating of carrot. *Int. J. Food Sci. Technol.* **30** (1995), 639–654.

304. McCarthy, M. J., Zion, B., Chen, P., Ablett, S., Darke, A. H., and Lillford, P. J. Diamagnetic susceptibility changes in apple tissue after bruising. *J. Sci. Food Agr.* **67** (1995), 13–20.

305. Guiheneuf, T. M. Visualization of liquid triacylglycerol migration in chocolate by MRI. *J. Food Sci. Technol.* **73** (1997), 265–273.

306. De Groot, S. R., and Mazur, P. *Non-equilibrium Thermodynamics.* North-Holland, Amsterdam, 1969.

307. Maneval, J. E., McCarthy, M. J., and Whitaker, S., Observation of large-scale structures in unsaturated materials. *Mat. Res. Soc. Symp. Proc.* **195** (1990), 531–536.

308. Guiheneuf, T. M., Tessier, J. J., Herrod, N. J., and Hall, L. D. MRI of meat products: I. Automated quantitation of the NMR relaxation parameters of cured pork by bulk and MRI methods. *J. Sci. Food Agr.* **71** (1996), 163–173.

309. Callen, H. P. *Thermodynamics.* John Wiley, New York, 1970.

310. Okos, M. R., Narsimham, G., Singh, R. K., and Weitnaver, A. C. Food dehydration. In D. R. Heldman and D. B. Lund (Eds.), *Handbook of Food Engineering.* Marcel Dekker, New York, 1992.

311. Rofe, C. J., De Vargas, L., Perez-Gonzalves, J., Lambert, R. K., and Callaghan, P. T. *J. Rheol.* **40** (1996), 1115.

312. Brittin, M. M., and Callaghan, P. T. NMR microscopy and the non-linear rheology of food materials. *Magn. Reson. Chem.*, in press (1997).

313. Muller, H. P., Weis, J., and Kimmich, R. Computer simulation and 6-dimensional spin density and velocity NMR microimaging of lacunar systems: A comparative analysis of percolation properties. *Phys. Rev.* **E52.5** (1995), 5195–5204.

314. Packer, K. J., and Tessier, J. J. The characterization of fluid transport in a porous solid by pulsed gradient stimulated echo NMR. *Molec. Phys.* **87** (1996), 267.

315. Thomas, N. L., and Windle, A. H. A theory of case II diffusion. *Polymer* **23** (1982), 529–542.

316. Suzuki, K., Tajima, T., Takano, S., Asano, T., and Hasegawa, T. Non-destructive methods for identifying injury to vapour heat-treated papaya. *J. Food Sci.* **59** (1994), 855–875.

317. Turner, R., and Gadian, D. G. Functional MRI: Theory and practice. In D. M. Grant and R. K. Harris (Eds.), *Encyclopedia of NMR.* John Wiley, New York, 1996.

318. LeDoussal, P., and Sen, P. N. Decay of nuclear magnetization by diffusion in a parabolic field: An exactly soluble model. *Phys. Rev.* **B46** (1992), 3465–3485.

319. Conti, S. Proton magnetic relaxation dispersion in aqueous biopolymer systems: II. Fibrin gels. *Molec. Phys.* **59** (1986), 483–505.

320. Kimmich, R., Barenz, J., and Weis, J. *J. Magn. Reson.* **A117** (1995), 228.

321. Knispel, R. R., Thomas, R. T., and Pintar, M. M. *J. Magn. Reson.* **14** (1974), 44.

322. Santyr, G. E., Henkelman, R. M., and Bronskill, M. J. Variation in measured transverse relaxation in tissue resulting from spin-locking with the CPMG sequence. *J. Magn. Reson.* **79** (1988), 28–44.

323. Kunze, C., and Kimmich, R. *Magn. Reson. Imaging* **12** (1994), 805.

324. Rugar, D., Zuger, O., Hoen, S., Yannoni, C. S., Vieth, H. M., and Kendrick, R. D. Force detection of NMR. *Science* **264** (1994), 1560–1563.

325. Rugar, D., Yannoni, C. S., and Sidles, J. A. Mechanical detection of magnetic resonance. *Nature* **360** (1992), 563–566.

326. Mattea, M., Urbicain, M. J., and Rotstein, E. Prediction of thermal conductivity of cellular tissue during dehydration by a computer model. *Chem. Eng. Sci.* **45** (1990), 3227–3232.

327. Voronoi, M. G. Nouvelles applications des paramètres continue à la théorie des formes quadratiques. *J. Reine Angew. Math.* **134** (1908), 198–287.

328. Szafer, A., Zhong, J., and Gore, J. C. Theoretical model for water diffusion in tissue. *Magn. Reson. Med.* **33** (1995), 697–712.

329. Rigby, S. P., and Gladden, L. F. NMR and fractal modelling studies of transport in porous media. *Chem. Eng. Sci.* **51** (1996), 2263–2272.

330. Wang, Z.-Y., Konno, M., and Saito, S. *J. Chem. Eng. Japan* **24** (1991), 256–258.

331. Vackier, M. C., and Rutledge, D. N. Hydration state of gelatine studied by time domain NMR: A preliminary study. *Food Chem.* **57** (1996), 287–293.

332. Adler, P. M. Porous media: Geometry and transports, Butterworth-Heinemann, Boston, 1992.

333. Tessier, J. J., Packer, K. J., Thovert, J.-F., and Adler, P. M. *AIChEJ,* 1997 (in press).

334. Dignan, D. M., Berry, M. R., Pflug, I. J., and Gardine, T. D. Safety considerations in establishing aseptic processes for low acid foods containing particulates. *Food Technol.* **43** (1989), 118.

Index

C